University of Strathclyde

Department of Naval Architecture, Ocean and Marine Engineering

An Automated Methodology for Optimisation with Respect to Vessel Manoeuvring

Anthony Romanowski

A thesis presented in fulfilment of the requirements for the degree of Doctor of Philosophy

2021

This thesis is the result of the author's original research. It has been composed by the author and has not been previously submitted for examination which has led to the award of a degree.

Signed: *Date:*

Acknowledgements

After completing my masters and the University of Strathclyde I found myself naturally leaning towards studying a PhD. Over this period, I have learnt an exceptional amount surrounding this topic and the practicalities of research. This has come mostly from my colleagues and supervisors who I would like to thank for their friendship, advice and assistance.

I'd like to thank my supervisors, without whom none of this would have been possible. I would like to start by thanking Professor Tashin Tezdogan who provided support and guidance as my first supervisor, while allowing me to explore alternate and less conventional research methods. I am incredibly grateful for this is, as it allowed a less rigid and more creative research environment to be built. I would like to thank Professor Osman Turan, firstly for providing me this opportunity and secondly offering a wealth of experience that supported and reinforced my methodologies. Both supervisors provided a wealth of knowledge and experience.

I would like to thank my colleagues and friends who assisted me throughout this PhD. Matthias Maasch, Emil Shivachev, Peter Cameron, Kaan Ilter, George Atzampos, Kurt Mizzi, Naz Yilmaz, and Batuhan Aktas.

I would like to thank FREINDHIP Systems for providing with access to their complete CAESES software suite which was vital to achieving the aims of this research (https://www.caeses.com/).

I would like to thank the University of Strathclyde Faculty of Engineering for providing accesess to the ARCHIE WeST high performance computer. The CFD Results were obtained using the Archie-WeST High Performance Computer (www.Archie-WeST.ac.uk) based at the University of Strathclyde .

I would like to thank my family for their support and motivation throughout this time, along with their patience, and my girlfriends' mother for her thoughts and care throughout this long period. Finally, I would like to thank the two who have been beside me through it all. My dog Sherlock who has helped me mentally and physically through walks, play and just being him. To the one who has supported me the most and given me the belief in myself when I struggled most, my dearest Maria, thank you, none of this would have been possible without you.

Contents

List of Figures

List of Tables

Nomenclature

V_A	Velocity Amplitude
y_{0A}	Lateral motion amplitude
ω	Oscillation Frequency
ψ_A	Yaw Amplitude
$\dot{r}$	Yaw acceleration
g	Gravity
ρ	Density
k	Kinetic energy
$\overline{\boldsymbol{v}}$	Mean velocity
μ	Dynamic Viscosity
σ_k	Model Coefficient
P_k	Production Term
φ	Model Coefficient
f_{β^*}	Free-shear Modification Factor
ω_{SPR}	Specific Dissipation Rate
S_k	User Specified Source Term
σ_ω	Model Coefficient
S_ω	User Specified Source Term
U_v	Validation Uncertainty
U_D	Desired Validation Uncertainty
U_{SN}	Simulation Uncertainty
E	Comparison Error
X'	Nondimensional X Coefficient
$F_{x\ measured}$	Measured X Force
T_m	Vessel Draft

L_{BP}	Length Between Perpendiculars
Y'	Nondimensional Y Coefficient
$F_{y\ measured}$	Measure Y Force
N'	Nondimensional Z axis Moment
$M_{z\ measured}$	Measured Z Moment
M	Vessel Mass
$\dot{u}$	Surge Acceleration
r	Yaw rate
v	Sway velocity
Y_G	Distance from CG to model rotation point transverse
X_G	Distance from CG to model rotation point longitudinal
I_Z	Moment of inertia
$\dot{v}$	Sway acceleration
u	Surge velocity
$C(t)$	NURBS Curve
$N_{i,p}$	B-Spline basis functions
w_i	Control point weights
P_i	Control points
ΔZ	Distance between Lateral Area centroid and LCB in Z direction
ΔX	Distance between Lateral Area centroid and LCB in X direction
SAC_{Aft}^{N3}	Aft sectional area coefficient
SAC_{mid}^{N4}	Midship sectional area coefficient
SAC_{Frwd}^{N5}	Forward sectional area coefficient
$Lateral_{\ Area}$	Hull cross sectional area along the centreline

Appendix i

$S_J(\omega)$	JONSWAP spectrum in frequency domain
$S_{PM}(\omega)$	Pierson-Moskowitz spectrum in frequency domain
A_γ	Normalising factor
ω_w	Wave frequency
T_p	Peak period
H_s	Significant wave height
γ	Non-dimensional peak shape parameter
$\eta(t)$	Wave amplitude with respect to time
A_j	Amplitude at specific frequency
ε_j	Randomness factor
$T_{Min\,\lambda}$	Minimum observed wavelength period
$NZ_{Min\,\lambda}$	Number of cells required for minimum wave height
δ_{SN}	Numerical error
δ_I	Iterative convergence error
δ_g	Grid spacing convergence error
δ_t	Time step convergence error
U_{SN}	Simulation uncertainty
U_I	Iterative uncertainty
U_G	Grid spacing uncertainty
U_T	Time step uncertainty
R_k	Convergence ratio
ε_{K21}	Difference between medium and fine solution
S_{k2}	Medium solution
S_{k1}	Fine solution
ε_{K32}	Difference between coarse and medium solutions

S_{k3}	Coarse solution
U_K	Uncertainty estimate
S_U	Maximum observed error in convergence study
S_L	Minimum observed error in convergence study

Publication List

Development of a CFD methodology for the numerical simulation of irregular sea-states

November 2019, Ocean Engineering 192(1):106530

A. Romanowski, T. Tezdogan, O. Turan

* This publication is positioned as Chapter 10 in *Appendix i - Development of a CFD methodology for the numerical simulation of irregular sea-states* within this study.

Abstract

Over the past two decades the marine industry has been facing ever more stringent and radical environmental aims. These are not only been defined by the International Maritime Organisation (IMO), but also by individual countries defining limitations to greenhouse gases emitted by vessels. To combat this the industry has turned towards the use of more complex fluid analysis tools, both model scale tests and computational simulations. This analysis has not only focused on hull design, but also on hull roughness, hull propeller rudder interaction and the marine environment. The focus of this PhD research is to develop methodologies that can be utilised within the industry to optimise vessel performance. With this research optimisation aimed towards improving vessel manoeuvring, with focus away from the traditional nondimensional methodologies. To do so, this research aims to lean heavily on the utilisation of Reynolds Averaged Navier Stokes (RANS) method within Computational Fluid Dynamics (CFD).

Towing tests have been considered the primary means of evaluating designs, not only for resistance but also for vessel motions. This includes the analysis forces and motions from both waves and manoeuvring tests. These tests however can be time consuming and financially costly. Therefore, the industry has begun to utilise CFD analysis at the early design stage as a low-cost and fast alternative. Not only this, but in recent years CFD has begun to achieve a level of accuracy matching towing tank tests. Due to these factors this research has a focus on the use of such computational means to improve vessel performance, with extensive validation against multiple towing tank tests.

The research has a focus on developing and understanding that can be used to quickly evaluate a potential ship design's manoeuvring characteristics. The methodology for simulating a captive harmonic test is presented, which has been validated against towing tank data conducted for the SIMMAN 2014 conference. This methodology is used in conjunction with a fully parametric hull form, developed within this research, to create and evolve equations used for ranking the hull forms manoeuvring performance. These unique equations are used in two optimisations cycles, one on the NPL hull and a further one on a custom hull to improve the vessels performance and efficiency. The optimum NPL hull forms are evaluated through a virtual turning circle manoeuvring simulation in CFD to quantify the improvements made through optimisation.

This research developed a novel methodology for ranking manoeuvring characteristics that significantly reduced the overall optimisation time, as well as producing manoeuvring gains

over 20% when evaluated in a simulated turning circle manoeuvre. In addition, the research has also presented best practice approaches for developing such a scheme and how to create a parametric setup that enables quick and accurate CFD simulations for complex manoeuvring simulations. This has been extensively validated against benchmark studies of the DTMB hull form from the SIMMAN 14 towing tank data.

1. Introduction

This chapter provides a brief overview, along with insight into the key issues which have led to this research being conducted. The motivations for each chapter is be presented, followed by the overall structure of the thesis.

1.1. General Perspectives

The naval industry is seeing ever increasing pressure from both new regulations and the public. As Cogliolo & Moretti (2011) state "the shipping sector is experiencing a situation where great focus and attention are placed on environmental issues by regulators, charterers, investors, insures, banks and, last but not least, the public and the media". This is causing naval architects to modify the priorities of the design, thereby focusing evermore greatly on improving efficiency. As regulations become ever tighter, the naval architect must consider every aspect of the design process to improve efficiency. The drive for ever more efficient vessel's is not limited to the large ocean going cargo vessels and cruise liners, but rather the smaller marine vehicles are finding innovative solutions to cover running costs. Due to the characteristics of the smaller vessels, primarily the smaller travel range, many of these smaller companies and design firms are turning towards electrical power sources Khan (2019). This is not only due to the regulations surrounding the vehicle emissions, but also to reduce daily running and maintenance costs. It is ever more important that these vessels are as efficient as possible to stretch the new electrical systems to their full potential.

The traditional approach to evaluating vessels performance before the trials was to conduct towing tank model scale tests. These have been conducted for decades with huge success, however there are noticeable problems when considering using such evaluation methods in the early design stage. Firstly, to truly benefit from learning from towing tank tests a clear and accurate hull form must be developed that can be made into the model. This inevitably means that the design process has passed the early design stage, and thus negate any benefit of conducting these tests for early evaluations. Secondly, to run such tests incurs a considerable financial cost. This is due to a model hull needing to be accurately replicated, including correctly scaling weight distribution to match the required displacement and moment of inertia. All of this occurs prior to even a single test being conducted. Due to these factors model scale testing is often only considered when multiple tests are required rather than just simple resistance analysis. Thirdly, when scaling a vessel for towing tank test, a specific scaling similarity is to be selected. This is split between Reynolds or Froude scaling, with a compromise being applied to one when the other is selected. Due to the scaling issues, it is

almost impossible to maintain an adequate level of similarity for the nondimensional parameters between the full-scale and model. This leads to most towing tank tests been conducted at Froude scaling similarity, as this is the most practical option Tezdogan (2015). Therefore, naval architects have turned to using computational means for quick and cost-effective analysis of multiple hull variants. These methods can include potential flow and computational fluid dynamics (CFD) methods.

Due to this desire for improved efficiency there has been an increase in the use of computational fluid dynamics to evaluate ship designs through the use of design optimisation, with ever greater focus towards the early design stage. As well as the ability to overcome scaling issues, with one alternative being full-scale simulations. This is not the only advantage CFD has over experimental fluid dynamics (EFD). Simple CFD simulations can be completed in under a day with current computational power, providing rapid analysis at any time. This also enables engineers to evaluate designs in one would normally be downtime, i.e. overnight. Such a procedure would be rarely considered for EFD and only in most urgent circumstances. With the advent of high performance computers using parallel cores, simple simulations can be run in minutes or even multiple simulations run in parallel. This is something that practical tests could never match. Another significant benefit to using computational analysis over practical tests is the ability to quickly modify the geometry. An example of such may be the evaluation of bulbous bow designs. Unless all bulbous bow designs have been considered and in turn built then the practical test would need to reconfigure or even remodel the hull form for each test, this is not only impractical but also highly time intensive. To contrast this, computational geometry can be easily and quickly modified and then reimported into the CFD to be evaluated, an example of such research is Park, et al. (2015).

With these factors naval architects and engineers have begun to utilise computational analysis in the early design stages. This not only helps to significantly reduce the overall design process time, but by considering the green credentials in the early design stage great improvements can be made. It is said that once a plan has gained momentum it is very difficult to stop or even change the direction, this also directly applies to efficient hull design. If the sign process does not initially start or consider efficiency and becomes ever more difficult for these goals to be achieved later in the design process, at which point compromises may have to be made to other factors.

From here this thesis utilises unsteady Reynolds Averaged Navier Stokes (RANS) CFD to develop methodology that enables engineers to evaluate and understand vessel dynamics within the real world. This leads to evaluating and determining a methodology for optimising

the manoeuvring characteristics of the vessel based on a numerical model defined within this research. Both of these focuses aim to improve manoeuvring performance, as well as allowing rapid evaluation of the early design stage.

This is based on the author's knowledge that this thesis on research introduces novel ideas and methodologies built upon the current literature. Which are presented in greater detail in Chapter 1.2.

The research here in utilises the commercial CFD software package Star CCM+, using versions 10.06 through to 15.02, developed and distributed by Siemens AG at the writing of this thesis. To fully utilise Star CCM+ the simulations are run on the high performance computer Archie-WeST managed by the University of Strathclyde. This allows more complex simulations to be run, and thus moving the current research forward.

1.2. Motivation behind this work

This section provides a brief overviews of the key motivational factors driving this work. Within this brief overview there are highlights as to how a gap in the literature relating to this motivation are filled.

- The marine industry has been utilising optimisation techniques to improve performance directly relating to hull design for the past decades. This has led to significant improvements, as well as standard operating principles, for many vessel types. This optimisation analysis however has been primarily focused on cruising speed large container vessels or cruise ships. These improvements are beginning to plateau; therefore, engineers have begun to focus on less conventional vessel optimisation and performance profiles. An area of research is now being focused on is offshore maintenance and surveying. These vessels spend a significant portion of time manoeuvring at low-speed in between offshore structures. This has motivated this research to develop methodology for rapidly evaluating a vessel's manoeuvring performance. To date there is no specific research presenting a clear methodology for evaluating virtual captive manoeuvring tests in CFD.
- It is critical to be able to evaluate a vessel's manoeuvring abilities accurately in the early design stage, to not only speed up the design process, but to also ensure the performance profile on the vessel being designed is also optimised. By conducting such valuations, significant performance improvements can be made. These improvements can only be achieved using the parametric model that can be easily modified within a certain degree of accuracy. Although parametric models are

commonly used within the industry, the overall design flexibility is relatively limited. Based on this, a fully parametric hull model is be developed that can be extensively modified to be quickly and easily evaluated has yet to be presented within the literature.

- As mentioned above, manoeuvring can play a key role in smaller craft where energy-efficient design is even more vital. The ability to evaluate the manoeuvring capabilities easily, and more importantly, rapidly between hull forms and designs in the early design stage is key to making these improvements. The current literature focuses on utilising towing tank tests or CFD to determine nondimensional manoeuvring coefficients. This methodology can achieve high level of accuracy; however, this can be time-consuming, thus negating any benefit in the early design stage. To the authors knowledge there has been no attempt in developing a method that can quickly evaluate a vessel's key manoeuvring factor in comparison to a neighbouring design. A methodology for ranking enables rapid optimisation independent of extensive towing tank or CFD analysis.
- Small craft are often more greatly affected by the vessels manoeuvring characteristics than the resistance and propulsion. This is due to the power units often being overpowered for the craft to ensure the vessel meets the minimum design requirements, this however is not the case for manoeuvring. Therefore, although resistance optimisation is commonly the focus in such studies, a shift of focus to manoeuvring can have a greater impact on the overall vessel performance.
- Optimisation is considered a standard tool for naval architects when attempting to achieve the energy-efficient requirements laid out by the IMO. These optimisations are primarily focused on resistance making factors, such as fictional or wave making. Due to this, a large area research is primarily focused upon bow or stern design. There is limited research directly looking at optimisation of the whole hull design with large geometric variations, and to the authors knowledge no research looking at manoeuvring optimisation. As vessel designs become ever more complex, multi-objective optimisations including manoeuvring will become vital to future designs. Evaluating and investigating the optimisation of a vessels manoeuvring capabilities provide a significant increase in filling the current gap in literature.

1.3. Thesis Structure

The structure of the research presented in this thesis is briefly reviewed is discussed. This thesis is built over 9 chapters that present the workflow used to develop the novel manoeuvring

optimisation that is the primary aim of this research. Following this chapter, Chapter 2 presents a literature review on the key aspects influencing the development of the manoeuvring optimisation tool. The review focuses initially on vessel manoeuvring and how it can be determined by the design process from the past and with current technology. A presentation of the literature surrounding the optimisation within the marine sector is discussed, followed by the current methods and techniques for parametric modelling and the uses in the marine industry. The final discussion presents how the literature has been lacking and how this thesis research aims to complete the literature.

Following this the thesis focuses on the stages and methodologies used to develop the final tool for manoeuvring optimisation. The initial focus of the methodologies is the creation of a tool for accurately simulating captive model tests that can be simulated in either calm water or wave conditions. Using this setup, a greater understanding of the key geometric factors influencing manoeuvring characteristics are observed.

To fully utilise the optimisation process a fully parametric hull has been created, chapter 5. This hull form is fully customizable based on specific input parameters, this is significantly more versatile than geometric morphing techniques, such as the Lackenby Shift. This hull form is designed towards the NPL parent hull, and is created in full scale. Upon completion of the parametric hull, this model is integrated into the manoeuvring setup such that the vessel design parameters also influence the manoeuvring setup to create a unified parametric model.

The next stage, chapter 6, in achieving the manoeuvring optimisation has been the development of the manoeuvring ranking equations. This section presents the evolutionary process used to create these equations through CFD manoeuvring simulations. These equations are based off the principle of being used solely in an optimisation form. Upon achieving the desired level of accuracy in these ranking equations the focus moves to the manoeuvring optimisation.

The section, chapter 7, starts by discussing the how the optimisations were conducted followed by an overview of the various models that can be used in such a set up. Following this an initial test optimisation using the ranking equations is shown which leads on to two case study optimisations, the first of the NPL hull and second of a custom monohull. The second study is to highlight the methods versatility. Upon completing these studies, the optimised hull forms from the NPL parent hull evaluation are further investigated in a free running turning circle manoeuvre. These simulations have six degrees of freedom and contain both a virtual disk and rudder. This chapter (8) helps to quantify the gains made in the manoeuvring optimisation.

Chapter 9 presents an overview of the results obtained throughout this research. Followed by a discussion on how these results can be further improved upon through future work.

2. Literature review

This chapter discusses and present the current literature on how and when the industry employs optimisation. An initial discussion on the overall design process is presented, followed by a discussion on the marine environment and how such an environment can me modelled to improve vessel performance. A detailed discussion is presented focused on the current methodologies and literature surrounding the evaluation of a vessel manoeuvring capabilities. The chapter is completed by presenting a review around the key factors of optimisation in the marine industry and how parametric modelling is integrated into this. The main conclusion drawn from this review are presented at the end.

2.1. Industry standards in early design stage

The development and design of marine vehicles is a highly complex and time intensive process. This process can be further complicated when considering greener technologies to achieve the current and future International Maritime Organisation (IMO) regulations (IMO, 2021). There are many technologies on the market that allow for significant improvements in vessels efficiency, examples include kite sail system, solar sail systems, improved hull paints and exhaust scrubbers Marine Digital (2021) to name a few. These technologies can allow for significant reductions to a retrofitted hull form, a reduction of around 5% may be seen for improved hull surface coatings Almeida (2020). These however are additional factors that help to reduce the vessels emissions on top of dominant factor, namely the hull design. It is by combining both green technologies and optimised hull form design that a vessel can meet the stringent regulations and even surpass them to ensure greater future stability.

To achieve such standards, ship owners and shipyards must focus on the design of the vessel SIEMENS (2020). It is therefore vital that the preliminary design stages are focused on creating the greenest and most efficient vessel. This however may become difficult as it is presented by SIEMENS (2020) that the classical design spiral is inefficient within itself, which in turn can lead to greater inefficiencies within the ship. It is discussed by Ang, et al. (2015) that although the simulation driven design is nothing new to the marine industry, a more automated and systematic approach improves the design process using the hull form design optimisation. Further into the research by Ang, et al. (2015) it is discussed that although this approach should implement over the classical methods, using computationally heavy simulations to optimise may limit the design flexibility. As shown by the research conducted by Kim, et al. (2016) using 2D linear potential method to initially calculate in the early design

stages improve design diversification which can then be validated against higher fidelity methods.

As noted by Naval Architecture (2014), the design spiral is a key element for any naval architect or marine engineer to understand. As noted above the classical design spiral, although vital, can be inefficient. By incorporating optimisation at the early stages of design spiral, i.e., the concept design, as conducted by Raihunen, et al. (2019) design spiral may be reduced. This research primarily focused on structural design using finite element analysis. The results show that this methodology helped to speed up the overall design process while also allowing multiple variations to be considered in the early design stage. Such a method may also be referred to as holistic ship design, this technique is discussed by Papanikolaou (2009) where optimisation is applied at the early stages of the design process for multiple criteria. This optimisation provided a strong and solid base to develop a more efficient vessel in the later design stages. From these studies it can be seen that design spiral is considered the most common technique for the process of designing a vessel from early conceptual stages to the final complete design. To counter this, the research performed by Bruinessen, et al. (2013) noted to derivatives of the design spiral can be considered alternatives to the standard approach. The first approach is known as system-based design, this process was first presented by Levander (1991) and then a newer addition by Erikstad & Levander (2012). The basis of this approach is to straighten the design spiral with a focus on minimising the number of design iterations to more quickly find a feasible technical and economical design. This method is significantly limited with respect to the hull form optimisation, as "*the system definition, the geometric sizing, weight balance and data set are based on regression based information, implicitly using a pre-defined geometric definition. This automatically limits the newly developed vessel to known designs*" Bruinessen, et al. (2013). Therefore, may not be applicable to real-world optimisation focused on the hull form, however may be used to great advantage to further improve the vessels efficiency upon completion of an initial optimisation study. This the second method is known as the 'Requirement Elucidation' Bruinessen, et al. (2013). The basis of this method is to focus on initial design stages independently of any other future phases. This method is also not limited by predefined requirements, but rather the requirements occur at the same time as the vessel design. It is also based upon the convention that purely focusing on a design process based on requirements and functionalities is limited compared to a method focused on the relationship between form and requirement. Although this method may allow for greater flexibility, a continuous and stable engineering process must be maintained throughout all phases of the design so as not to hinder and slow the design process.

Within the literature there are limited variations between methodologies, with the methodology being in essence split between concept design, preliminary/mid design, and detailed design. By considering the vessel's green credentials at an early stage with a tool that allows for rapid and comprehensive design evaluations, significant improvements can be made commonplace. An example of such methodology, although not directly related to green technologies, is used by Schachter, et al. (2016) when evaluating dynamic motions for a planing hull form using the Savitsky methodology, (Savitsky, 1964). The research conducted by Schachter, et al. (2016) used the Savitsky equations to rapidly evaluate multiple hull forms at the early design stages. From this it can be seen that using such techniques yields better results further down the design process.

From here the various techniques for evaluating conceptual vessel dynamics with respect to resistance in waves, regular and irregular, as well as vessel dynamics relating to manoeuvring and steady state conditions are discussed in greater detail below.

2.2. Manoeuvring

From literature discussed above, along with waves impacting the vessels green credentials, the manoeuvring characteristics can also play a key role in improving vessel performance. Therefore, the manoeuvring methodologies commonly used within the marine industry are discussed. In addition to potential application techniques the early design stages. Prior to these discussions a presentation of the fundamentals of ship manoeuvring is reviewed.

The analysis and understanding of a vessels manoeuvring characteristics is a complex and multi layered problem. A preliminary discussion on the classical methods for determining the manoeuvring characteristics is presented herein. The classical approach focuses on the determination of manoeuvring coefficients either through model tests or full-scale sea trials, this evolved to include computational methods of recent such as CFD Mohammadafzali (2015). Within this study Mohammadafzali (2015) discuss the key focus of using captive model tests, such as PMM towing tests, to evaluate the forces acting on the hull form. These forces are converted to nondimensional coefficient that are used in conjunction with specific equations to estimate the vessels manoeuvring characteristics Sahoo (2007).

The literature is heavily populated with research with respect to the estimation and analysis of classical manoeuvring estimation. As the topic of vessel manoeuvring can be split into multiple factions, these include the hull design, rudder design, hull rudder interaction and propeller rudder interaction, to name a few. An example of such analytical research can be seen by Obreja, et al. (2010). Within this research a fishing vessel is evaluated through classical towing

tank teste to determine the various manoeuvring coefficients, these tests included the rudder to help evaluate the turning circle capabilities. These results were used to develop a computational code that was found to be within 6% accuracy when estimating the key characteristics of the turning circle manoeuvre. Alongside the design of the hull form and selection of the rudder profile, the effect of the propeller can also influence the manoeuvring characteristics of a vessel, particularly in shallow water. It is discussed by Trodden, et al. (2016) how the selection of propeller can help to reduce the carbon footprint of a vessel in the early design stages. It is concluded in this research that the correct propeller selection with respect to manoeuvring can save around 3.22% for the test hulls, however this is primarily due to the inefficiency of the propeller at these manoeuvring speeds. As these studies show, analysis with respect to appendages can be limited due to the performance profiles of the vessel, in addition, appendages can be varied and modified throughout the life span of the vessel. This is supported by the research conducted by Liu, et al. (2015) that discuss the various impacts different rudder profiles can make to the manoeuvring performance of a vessel. This is not the case for the design of the hull, which contributes predominantly to the manoeuvring characteristics of the vessel. This is the basis for the determination of the key coefficients and the research conducted by Burcher (1991), who uses a holistic approach using both towing tank tests and fluid force predictions based of various geometries to determine and predict the manoeuvring characteristics of a vessel. Its is also concluded by Burcher (1991) that the classical derivative approach to manoeuvring prediction can be limiting and may require a hybrid method.

As noted above, vessel manoeuvring is a multifaceted topic which encompasses all aspects of the performance profiles of a vessel. This research is primarily focused of turning and dynamic characteristics over stopping and acceleration. As stated, the vessel geometry is the primary driver in how a vessel manoeuvres at low speed, this is not the case for high speed plaining vessels due to the thrust vectoring commonly used (Coop, 1995). It is discussed by (Ships Business (2005) the dominant factors influencing the a turning circle characteristics, the primary factor is structural design and vessel length, followed by the draught and trim. It is therefore the primary focus of the optimisation when reducing the carbon footprint of a vessel to influence the geometric shape and design of the hull over the appendages. It can also be seen that the classical derivate approach to vessel manoeuvring estimation may be limited and require further discussion

2.2.1. Towing Tank Tests

Throughout the design process of the ship there may be at some point a detailed investigation into the manoeuvring characteristics of the potential vessel. A hull form may not be evaluated in great detail with respect to manoeuvrability, as this characteristic of the vessel may not be as crucial to the daily routine. For example, a container ship transiting from China to the UK may take between 32-35 days Shippo (2021) with a median time spent 41 Porthcawl being below 24 hours with bulk carriers, spending three times the median time United Nations (2019). With these respective proportions for a one-way voyage less than 3% of the time is spent import, with the remaining 97% at operational speeds. This however can be clearly contrasted by focusing on a crew transfer vessel (CTV) in support of offshore facilities where the vessel may have 12 hours available, of which three hours can be considered for transiting with the remaining nine moving from wind turbines and docking University of Strathclyde (2015). This shows that potentially 75% of the operational time may be spent in conditions where manoeuvrability is of importance. This highlights the importance of focusing specific analysis and early design stages optimise the final design.

Before the development computational fluid dynamics and numerical modelling, physical testing was required to be able to predict the manoeuvring characteristics of a hull form. These physical tests were backed up with thousands of years of knowledge and intuition passed down through the generations. Towing tank tests can be split into three categories Vantorre (1999):

1. stationery straight-line tests
2. harmonic tests
3. stationery circular tests

Each of the various categories discussed in detail below. It is aimed through this literature to highlight the key factors influencing these tests and in turn the advantages and disadvantages to the various captive tests.

2.2.1.1. Stationary straight-line tests

The stationery straight-line tests consist of a further four variations, two of which should be conducted fully appended including a rotating propeller and variable rudder. The initial test may also be considered the standard towing tank test, namely straight towing. Unlike the standard resistance test, the straight towing also records and evaluates lateral forces and moments to observe any potential flow imbalance along the hull. This test can then be conducted fully appended with a scaled propeller and rudder to further evaluate the flow field entering the aft region and transiting into both appendages. The final two variants under the

stationery straight-line tests are known as oblique towing Vantorre (1999). Within these tests the vessel is rotated at an angle relative to the flow. This causes variable flow passing over the underwater hull as well as an imbalance between the bow and aft, from here the moments can be calculated and then nondimensionalised. In addition to having a constant rudder deflection it is also possible to have variable rudder deflection with the hull form constrained in either a straightforward or oblique position. It is observed by ITTC (2017) that tests involving minimal appendages are conducted with less runs than those with appendages that are allowed to oscillate.

The stationery straight-line primarily focuses on calculation of the slow motion derivatives. These slow motion derivatives are focused on slow moving vessel motions, for example the sway displacement (y) of the ship can be regarded as slow Bishop & Parkinson (1970). At a given instant of time the velocity and acceleration ratios, $\frac{v}{y}$, $\frac{\dot{v}}{v}$ and $\frac{\ddot{v}}{\dot{v}}$, are significantly smaller than $\frac{U}{l}$ Bishop & Parkinson (1970). Therefore, not only the relative velocities small but also respective rate of change in these factors are also small. Due to the small region of these derivatives only the position, velocity and acceleration terms are needed to be retained in the Taylor series expansion. Due to this limitation such a towing tank test is unsuitable for calculating the oscillatory coefficients. These slow motion derivatives are often considered adequate for most vessels, however, oscillatory coefficients are often required when vessels manoeuvre in sinusoidal pattern frequently. Additionally, these coefficients help to determine the vessels characteristics when operating closely to an oscillatory stability boundary Bishop & Parkinson (1970). Due to the nature of these coefficients, they also have valuable relationships with the seakeeping characteristics of the vessel. Therefore, towing tank tests may conduct both stationary straight-line tests accompanied by harmonic tests.

2.2.1.2. Harmonic tests

Further to the stationery straight-line tests are the harmonic towing tank tests. The basic principle of these tests is to report a sinusoidal movement in either the transverse or vertical plane. To achieve this a special mechanism is required known as a planar motion mechanism (PMM). Before discussing the various details of the various test types that can be conducted using a PMM setup, the kinematics and ship control parameters are presented. Unlike the stationery straight-line test, the hull form experiences a variation in the forward velocity as the carriage controlling the PMM system maintains a constant velocity (u) Vantorre (1999). For the pure sway tests the lateral motion amplitude (y_{0A}) and the oscillation frequency (ω) are

used to determine this way velocity amplitude (V_A) and sway acceleration amplitude ($\dot{V}_A$), Vantorre (1999), these equations are shown in (2-1) and (2-2).

$$V_A = y_{0A}\omega \tag{2-1}$$

$$\dot{V}_A = y_{0A}\omega^2 \tag{2-2}$$

For tests involving yaw additional equations are required focusing on the yaw amplitude (ψ_A) and oscillation frequency (ω) to determine the yaw velocity (r_A) and yaw acceleration amplitudes ($\dot{r_A}$). These equations are given in (2-3) and (2-4).

$$r_A = \psi_A\omega \approx \frac{y_{0A}\omega^2}{u} \tag{2-3}$$

$$\dot{r_A} = \psi_A\omega^2 \approx \frac{y_{0A}\omega^3}{u} \tag{2-4}$$

For a standard pure sway PMM towing tank test, the carriage moves a constant velocity (u) at which point the planar motion mechanism begins to oscillate the vessel laterally or to the direction of motion. As mentioned above this can be purely Y direction or it can also be conducted in the Z direction to induce an intentional heaving motion. While the test is running the vessel's heading remains parallel to the direction of travel for the main carriage. Unlike the stationery straight-line tests which in essence follow the same basic setup as a resistance simulation, all harmonic tests need to be carefully considered with respect to the towing tank size ITTC (2017). The conventional procedure when conducting tests is to maximise the size of the model hull in an attempt to eliminate as many scaling effects as possible, as noted form ITTC (2002b) "*The model should generally be as large as possible for the size of the towing tank with respect to wall effects, shallow water, model mass and the maximum speed of the towing carriage*". Due to the lateral oscillation of the PMM, more often than not the hull form is scaled down in an attempt to mitigate wall interaction effects. This is considered one of the major drawbacks to running a PMM test in a standard towing tank, as the hull form is scaled for the PMM tests which add additional uncertainty when running standard resistance tests, making the whole model less cost-effective.

The next test iteration is the pure yaw tests, these follows the same procedures as written as above for the pure sway however the hull form rotates around the attachment point to the mechanism. The rotation aims at maintaining the heading the matches oscillation path itself, i.e. the sinusoid path. As with the pure yaw test, careful consideration needs to be taken when

selecting a scale for the hull form that can be used, due to rotation it is possible the bow and stern may fall within a region where wall interference occurs. This again adds further potential limits to the tests being conducted such that more tests may be required. As presented by ITTC (2017) “most steady straight line and harmonic tests are carried out in a towing tank with a length of 37 times the ship model length and more. A mean value of the model length to tank with ratio (L/b) is 0.46”. For both the pure yaw and pure sway tests, the hulls can either be bare or fully appended with rudders and rotating propellers. When introducing rotating propellers and rudders the Reynolds scaling becomes a factor which determines the minimum model dimensions ITTC (2017).

As noted, the pure yaw tests can be conducted with a rudder, this in turn leads to a specific test where model ship follows the same procedure pure yaw test, however, the rudder is maintained at a specific angle of deflection Vantorre (1999). This in turn can lead to the final harmonic test where rather than the rudder being maintained at a specific angle, the hull is rotated to a specific of drift which is maintained for the full sinusoid path. This can help in the determination of slip. To accurately understand the interactions between yawing and drift, it is typical that a minimum of four drift angles between -30 and positive 30 degrees are used. From the research conducted by Vantorre (1999) these are typically 0 and 16 degrees. It is also seen that to avoid nonstationary and memory effects the value of the oscillation frequency (ω) should result in 1-2 oscillations for pure sway 2- 3 for pure yaw in the possible steady state test period Vantorre (1999).

2.2.1.3. Stationary circular tests

Unlike the previous PMM tests the carriage is maintained at a stationary position with the PMM creating all the motion for the hull form. As with the previous tests, this test can also have multiple variants. These can include pure yawing and yawing with drift, both these variants can also be conducted with appendages. This is the least common PMM test to be conducted as it is the least efficient and all the different test types. This lack of efficiency is due to the requirement that the hull form does not interact with the wake generated by itself from the initial starting point. Due to this, a very limited angle range is used for obtaining results, Vantorre (1999) has found that this is typically less than 180°, with 120 to 180° required for acceleration and around 60° for settling ITTC. (2017) suggest that half a circle is dedicated to acceleration, deceleration and settling with the other half focused on obtaining results. It is suggested however from Vantorre (1999) that there is no requirement for a specific deceleration phase, and thus attempt to maximise the results phase. In both cases it is suggested that between 10 and 20 minutes is required to ensure the free surface settled enough for more

test to be conducted. This highlights the inefficiency of this test and thus why Vantorre (1999) found less towing tanks conducting this type of test.

2.2.1.4. Concluding remarks on towing tank tests

From the literature, towing tank tests allow exceptional flexibility when evaluating the manoeuvring characteristics of a vessel. It is presented by Putra, et al. (2017) that although numerical alternatives are becoming ever more important within the industry, towing tank test are still an essential part of all design workflows. However, from the above literature some key limitations to physical towing tank simulations exist. Some of these limitations can be overcome through the creation of larger towing tanks or even wave basins, these alternatives all significantly increase the price of running tests making them ever more niche. Based on these limitations the industry has been moving ever more towards virtual towing tanks.

2.2.2. CFD Manoeuvring

As advancements in computer technology enable quicker and more advanced simulations to be modelled, an ever-greater proportion of the industry is turning towards using CFD to evaluate preliminary designs. This is due to multiple factors, however, a clear statement of the advantages of CFD to the engineer is "*CFD is best used in cases where the system behaviour cannot be calculated using conventional calculation – not necessarily because of the complexity of the maths theory – but because of the complexity of the overall system or its geometry*" Hanson (2017). This highlights an important mindset when using CFD. As the world becomes ever smarter and more efficient it is up to the engineer to pass these efficiencies onto not only the project but also the methodology used in the project. There are many cases where CFD has great advantages over physical towing tank tests, and many where the inverse is true. It is also true that there are problems when using CFD may be considered excessive.

The first consideration when evaluating CFD as a tool is to consider the limitations. With respect to what can be simulated there are very limited to no limitations for most of the engineering community. CFD simulations have been used to reduce development time for high performance vehicle engines Industrial technology (2020), enabling the development of lighter, stronger, and more efficient engines. Towards the other end of the spectrum, CFD has been used to evaluate flow around hypersonic vehicles for NASA (ANSYS Inc, 2021). These two examples highlight the flexibility of CFD as well as its ability to model complex small flows and the most extreme fluid conditions. However, most of these simulations focus on a single fluid, whereas ship based CFD must consider two fluid regions along with the respective

interface. This adds extra complexity when simulating, along with the same complications when scaling as is seen with towing tanks.

The literature is diversely split between replicating towing tank results and simulating open ocean manoeuvring tests. As technology has improved there have been more focused projects investigating the ability of CFD to replicate and advance towing tank tests. Some of the most extensive direct manoeuvring CFD evaluations were conducted for the SIMMAN workshops. The purpose of these workshops was to "benchmark the capabilities of different ship manoeuvring simulation methods including systems and CFD based methods through comparisons with results for tanker, container ship and surface combatant hull form test cases. Systems based methods compared with free-model test data using provided PMM and CMT (circular motion mechanism/rotating-arm) data, whereas CFD based methods are compared with both PMM/CMT and free-model test data" (SIMMAN, 2008). As mentioned in these workshops focused on three types of vessels and multiple test variations. In certain cases, the hull forms are appended or bare, but the tests being conducted in both deep water equivalent and shallow. From this initial workshop was found that RANS CFD had the potential to replicate the results observed for the PMM/CMT test data, however, the initial SIMMAN 2008 workshop lacked an extensive range CFD results to directly support this observation (Stern, et al. (2011). This is further supported through the research conducted by Dai & Li (2019), who used the methodologies developed for the SIMMAN 2008 workshop to derive the coefficients for the KVLCC2 and found good agreement with the numerical results compared with the experimental.

Following the initial SIMMAN workshop a further workshop was conducted in 2014. This second workshop used the same hull forms, the KVLCC2 tanker hull, the KCS containership and the DTMB 5415 frigate hull form, with most of the research following a similar pattern to the previous 2008 workshop. These are primarily focused on deep water IMO manoeuvres and the effects of shallow water (SIMMAN, 2014). In addition to these compulsory test new tests were conducted to again be evaluated in CFD, these included new free sailing and captive model tests. The free sailing tests included zigzag manoeuvre and the turning circle. The greatest difference between the two workshops is a significant increase in diversity in towing tanks being involved to produce more experimental data can be used to validate the CFD results. This additional focus on free sailing experimental tests led to an increase in CFD simulations attempting to replicate and evaluate these more advanced manoeuvring tests, in addition to duplicating the appendaged PMM tests. Cura-Hochbaum & Uharek (2014) focused on evaluating the KCS PMM deflected rudder tests to determine the manoeuvring coefficients

which were then used to predict specific three sailing manoeuvres. It is noted by Stern, et al. (2011), the in-house developed CFD codes found better agreement with the test results in 2008, this observation was matched by Cura-Hochbaum & Uharek (2014) who found exceptional agreement using the RANS code the authors developed to evaluate the PMM tests. Although the empirical free sailing simulations ignored scaling effects due to being conducted in full-scale, they were able to fulfil the requirements set out by IMO for deep water manoeuvres Cura-Hochbaum & Uharek (2014). Following on from this research Shen & Wan (2014-B) presented their results for the validation of the three hull forms for free sailing CFD simulation validated against the towing tank results published for the SIMMAN 2014 workshop. The research used six degrees of freedom ruefully rotating propeller for each hull form to run both zigzag and turning circle manoeuvres, research does not present a comparison with the results obtained through the workshop. This research primarily focuses on methodology and the comparison between the hull forms using the same technique. In comparison, to this the research conducted by Mofidi (2017) extensively evaluates the merits of using CFD as an evaluation tool for ship manoeuvres of a fully appended vessel. As this research is a completed thesis, there is a specific chapter for the validation and verification of the self propulsion simulation. Within this chapter Mofidi (2017) found exceptional comparison between the simulation and self propulsion. This highlights the effectiveness of using CFD for not only deriving manoeuvring coefficients but also evaluate the free running and highly dynamic manoeuvring tests.

The SIMMAN workshops have enabled extensive validation methodologies to be developed for manoeuvring CFD simulations. With the assistance of such results, research design conducted by Mucha (2017) would not have been possible. This research developed a simulation-based framework to predict ship manoeuvring characteristics in deep and shallow water. Within this thesis is presented that virtual modelling of towing tank tests enables accurate prediction of the manoeuvring derivatives, however, CFD enables analysis of full-scale flow that is not possible until the vessel has been constructed. Due to the requirement of Froude similarity while scaling due to the dominance of pressure-based forces, scale effects while the ship is manoeuvring remain modest Mucha (2017). However, Oldfield & Larmaei (2014) suggest that this may not be a constant for all vessels, as the forces when manoeuvring include strong viscous components, therefore reducing the validity of Froude scaling methodologies. This research uses the raw results data produced for SIMMAN 2014 by FORCE Technology for the DTMB 5415 frigate hull to evaluate how practical CFD is predicting manoeuvring forces and moments Oldfield & Larmaei (2014). To complete such an evaluation Oldfield & Larmaei (2014) focus solely on the PMM towing tank tests conducted

by FORCE Technology with a bare hull form. From this report it can be concluded that the results of the accuracy and feasibility of CFD being used for analysis early design stage, not only this but the repeatability for the CFD simulations matches or exceeds model tests themselves Oldfield & Larmaei (2014). This can be noted as significant improvement over other such research which found errors more than 10% for steady drift test, and even greater for unsteady tests. Further to this the focus on purely PMM validation shows the flexibility of such a test type when used in conjunction with CFD. This is supported by the research of (He, et al. (2016), who find that using PMM simulations produce good agreement. Along with this, simulations focused on shallow water provide detailed evaluation of how these effects contribute to the changes in manoeuvring performance seen in restricted waters.

A key factor in using CFD over the towing tank tests is the improved accuracy for detecting small dynamic motions. These motions may be potentially lost due to test uncertainty, which can be more prevalent when running slow speeds. Flexibility of CFD allows these potential uncertainties to be accounted for and in turn corrected. These small motions are specifically focused on by Lui, et al. (2017) research, they first concluded that including dynamic sinkage and trim on the comparison between CFD and EFD can reduce the discrepancies between results. It is also concluded that the discrepancies between EFD with dynamic motions and without have greater discrepancies than the simulations, to which they suggest the CFD has greater validity. A trend towards including additional degrees of freedom is becoming more consistent, as it is being established that there is a direct link between manoeuvring characteristics and the dynamic motions. Although towing tank tests have shown to be accurate, this more limitation further highlights the advantage of using CFD over captive towing tank test. Larger and more complex towing tank tests are being conducted to ensure these extra degrees of freedom are being captured. An example of such research was conducted by Araki, et al. (2012), who used a wave tank basin with a free running four degrees of freedom model to evaluate the manoeuvring coefficients. This research found a high degree of agreement between CFD results and the corresponding EFD data. Araki, et al. (2012) also concluded that a small number of free running CFD simulations are able to replace large number of virtual captive model tests. This methodology also highlights how the marine industry can follow the aerospace industry with CFD becoming the primary tool of experimental tests Morton (2011). The advice from ITTC (2011c) further supports this by recommending full 6 degrees of freedom simulations when the computational power has been achieved.

After replicating and evaluating captive towing tank tests in CFD, the next advancement is to evaluate free running and standard manoeuvring tests. Some of these simulations have been mentioned above, namely self-propulsion turning circle and zig zag tests. These simulations require the most computational power, as all degrees of freedom are counted for as well as additional rotating bodies. Along with complex overset meshes, either a large or moving outer domain is required. All these factors contribute to significantly increasing the simulation time. This is discussed by Araki, et al. (2012), who suggest that such complex relations may take a few weeks or even months to fully compute. Since then computation power has noticeably increased, along with CFD codes becoming ever more efficient, both of which helped to reduce the overall run time of such simulations. Such a simulation has been researched by (Carrica, et al. (2015), within this research they evaluate how shallow water effects the KCS hull form while performing a zigzag manoeuvre in shallow water. The hull form is full 6 degrees of freedom, with rotating propeller and rudder. This research was first conducted as experiments by FHR, to which the CFD was validated against. The uncertainty between the experimental and CFD results for the self propulsion were below 3%, however this uncertainty increased to between 15 and 20% when focused on yaw and yaw rate. A similar study conducted by Broglia, et al. (2015) evaluated the turning ability of a fully appended twin screw vessel. This research also used full 6 degrees of freedom with rotating rudder, however, rather than using a fully modelled and rotating propeller, two actuator discs representing the twin screws were used instead. This can only reduce the complexity of the simulation, but also the number of cells required. The results obtained from this study were predicted to be less than 10%, showing a substantial improvement over Carrica, et al. (2015). However previous research by Broglia, et al. (2012) found better comparison between experimental results when simulating turning circle manoeuvres. This research focused on the effects of different propeller models on the manoeuvring characteristics of the simulated hull, the research achieved less than 9% deviation from experimental. A further study using the turning circle manoeuvre that was used as a means to evaluate a combined CFD and potential flow model, was conducted by White, et al. (2019). This research found sufficient agreement with experimental results, however, along with conducting the turning circle manoeuvre in calm water was also simulated in head waves. This adds a further level of complexity to the overall simulation, with both the RANS simulation matching the trajectory well.

The additional real world conditions, be it waves or wind or a combination of both, the next evolution in how CFD simulations can be used to evaluate a vessel at the early stages of design. This area of research is the most limited, however, research on both zigzag and turning circle manoeuvres in waves have been conducted. Before evaluating the free running manoeuvres,

research conducted by Woolliscroft & Maki (2016) focused on evaluating the effects of waves on the vessel while conducting a PMM towing test in CFD. The results found for this research match closely with the experimental data, to which they conclude that CFD is a valid method for evaluating such problems. Wang & Wan (2018) use OpenFOAM CFD software to evaluate the ONR Tumblehome hull form with superstructure. The vessel is fully appended with rotating rudder and propellers. This research evaluates three manoeuvres, course keeping, zigzag and turning circle, all of which conducted in various wave headings. The initial course keeping simulation uses a module for OpenFOAM to emulate a PID controller. All manoeuvres are validated against experimental tests conducted by the Iowa Institute of Hydraulic Research (IIHR). The course keeping manoeuvre showed good agreement with the experimental results, with Wang & Wan (2018) highlighting that not only do the results accurately replicate the EFD, but with CFD a greater understanding of the flow around the hull form as well as improved propulsion performance can be obtained. The zigzag manoeuvre has an error compared to EFD of below 5%. With the addition of waves in the amplitude of the first and second harmonics of the manoeuvre were significantly increased, up to 80.5%, highlighting the influence of waves. The final manoeuvre research by Wang & Wan (2018), the turning circle, also achieved exceptional comparison with the EFD. This test error deviation is just below 10%, with an overestimation of 6.57% for the turning diameter Wang & Wan. (2018) also conclude that by using CFD, a greater understanding of fluid flow around the hull form, as well as the development of the free surface can be drawn. This further solidifies the ability of using CFD to evaluate complex manoeuvring problems at any stage of the design process.

It can therefore be concluded that CFD can be used as an invaluable tool for designers and engineers to evaluate potential designs in various stages throughout the design process. The literature has also highlighted that careful work CFD results can fall within the experimental uncertainty range. Along with exceptional accuracy, the ability to evaluate all flow characteristics below and above the hull can allow for improved evaluations not only on the hull but also on the vessel's appendages. Although no full-scale manoeuvring simulations that have been validated with real-world data had been presented, multiple papers have noted potential focuses on this region for future work.

2.3. Optimisation

The next base point of the literature is focused on the marine industry, as well as other engineering industries, and how optimisation is used within the sectors. It is presented by VPO (2018) for vessels between efficient this is completed at two points, firstly the design process

and secondly the maintenance of the vessel. Later in the discussion it is presented that direct design optimisation can yield good results, while also being applied to the maintenance plan of the vessel. This shows that not only can an optimisation be applied within the design process, but optimisation can also be an integral part across the working life of the vessel. As this research is primarily focused on utilising optimisation in the design process, particularly the early design stages, optimisation with respect to maintenance is not be discussed in this review but should be considered for future investigation.

Optimisation within the engineering community can be as diverse as the community itself, although it is not be discussed in the literature raw experience within the field of the engineer can be used as a basic implicit optimisation Parkinson, et al. (2013). The first stage in any optimisation is a selection of a quantitative model, this model computes the response then be used within the selected optimisation algorithm. Parkinson, et al. (2013) state that "*Obtaining a valid, accurate model of the design problem is the most important step in optimization*".

This statement can cause significant problems within the marine industry as the quantitative model being evaluated becomes more and more complex as the optimisation trends towards evaluating real world applications. However, as technology progresses so does the development and improvement of optimisation algorithms. Genetic algorithms are at this point the most popular algorithm used for optimisation Roy, et al. (2008). Although genetic algorithms are the most prevalent method for optimisation currently, other methods such as simulated annealing were used to great effect by Roy, et al. (1995) to develop global optimisation model that was used to optimise not only performance, but also steel weight and manufacturing time for a container ship.

Diez & Peri (2010) present a robust design optimisation method for ship conceptual design that uses a particle swarm optimisation technique. The aim of the robust design optimisation method is to overcome the major deficiency within the optimisation methodology, namely an optimisation can cause specialisation which in turn is the opposite of robustness. This research aims to develop a technique where good performance is still maintained even with large uncertainties with parameters. Overall, this shows good agreement with other design optimisation research. A similar study conducted by Beyer & Sendhoff (2007) found that there were many applications for robust optimisation methodologies, however, the quantitative model remains the limiting factor with large uncertainties surrounding CFD and the corresponding uncertainty emulation. To which excessive noise can be unintentionally brought into the methodology reducing its efficacy. With the increase in computational power, as well

as the literature surrounding the improvements of CFD uncertainty above, there is a steady increase in the use of CFD for optimisation.

Before evaluating the literature surrounding optimisation within the marine industry that uses CFD to evaluate the quantitative model, the research around empirical and other numerical methods is briefly discussed. Such a study was conducted by Nikolopulos & Boulougouris (2018), where they calibrated the Holtrop and Mennen power prediction method for full form and low Froude number vessels. The optimisation was briefly touched upon however, the focus was improving the quantitative model for later use in optimisation. Such prediction methods are also used by Moraes, et al. (2007). Within the research they used standard techniques to predict the power requirements and in turn the power plants required for the given hull form. This empirical method was combined with a goal programming optimisation algorithm to optimise multiple criteria for the vessel. The optimisation found noticeable improvements over the base hull. Before fully moving to using CFD as the evaluation method, a more advanced numerical model was used by Zhang (2009). This research focused on using the Rankine source method to optimise the wave making resistance of the hull form. This method not only accounts for better hull form resolution but can also be programmed to account for nonlinear effects. Such a technique is still significantly more computationally heavy than any empirical or statistical method like the Holtrop and Mennen method Birk (2019). This optimisation achieved a reduction in wave making resistance of just below 25%, showing the effectiveness of such a technique. However Zhang (2009) continues to highlight that due to the viscous terms being ignored in the Rankine source method, further improvement can be achieved. Such viscous terms can be accurately captured when using CFD.

More recently the literature has trended towards using CFD as a quantitative model for the optimisations. The number of published literatures surrounding this technique has increased exponentially since the early 2000s. An early example of such research was completed by Peri, et al. (2001) who used towing tank data to validate the initial baseline CFD simulation as well as the final optimised hull form. This can be considered the best practice when optimising a hull form, however this can be financially very expensive due to 2 additional hull models having to be created and tested. To vary the geometry a perturbation service was used, this was primarily focused on the bow region of the hull form. Additionally, three algorithms were used to evaluate the efficiency and accuracy of the different methods. The results found a reduction of 21% and 18% for the sequential quadratic programming and the steepest descent algorithm respectively. From this research Peri, et al. (2001) concluded that a CFD solver coupled with an optimisation algorithm generate valid results for ship resistance and wave

pattern. Following this research by nearly a decade Grigoropoulos & Chalkias (2010) utilised the parametric modelling capabilities of the FRIENDSHIP-Modeler coupled with the CFD solver SHIPFLOW to optimise a hull form in both calm water and waves. The research used an evolutionary multi-objective optimisation algorithm, as allowed for an optimised hull form with superior characteristics for both calm and rough waters Grigoropoulos & Chalkias (2010). Further to this it is also concluded that incorporating "inexact pre-evaluations" and "importance factors" within the optimisation could potentially lead to faster optimisations Grigoropoulos & Chalkias (2010). Following on from this Park, et al. (2015) use parametric modification and a specific region of the KSUEZMAX tanker hull form, namely the bow region and bulbous bow. Unlike for parametric modelling, parametric modification simply uses transformations specific points along given axis. This requires significantly less setup prior to optimisation, as almost any remodelled hull geometry can have these modifications applied to it. Not only this but the optimisation also considered self propulsion as a key evaluation was the percentage of reduction in delivered power. Park, et al. (2015) achieved a 3.7% reduction in delivered power through this research and coupling with CFD.

Along with the noticeable improvements made through CFD optimisation, method in which hull forms are modified in varied is also evolving and becoming more efficient. One of the most efficient forms of hull modelling for the marine industry is the use of T-Splines geometry. Common spline base geometry uses mathematical equations to determine the position of the new point along a curve, service and solid. If the user aims to refine a specific region of the surface through the addition of a point, a common spline surface would add additional points to generate a single point, however, T-Splines allows addition of a single point. This type of geometry is particularly good at representing complex characters such as hull forms. This background knowledge is presented as Kostas, et al. (2015) use this geometric representation to great effect when optimising a container ship based hull form. Using T-Splines reduces the computational demand for generating a hull forms in turn helping to speed up the overall optimisation. It is concluded from this research that "tested cases demonstrate that the developed optimization procedure can be efficiently used for real-life hull-forms solving real-life problems arising in the shipbuilding industry" Kostas, et al. (2015). The previous research is focused primarily on mono hull, but Yang & Huang (2015) conducted an optimisation coupled with CFD to evaluate a Triswach hull. This hull form not only has complex hull interaction, but also due to the large central swath hull additional complexity at resolving the underwater forces is encountered. Due to these complexities the only feasible and accurate way outside of model tests was to use CFD. The optimisation achieved noticeable improvements across a range of speeds from not only the variation of the hull shapes, but also

the positioning with respect to each other. The parent hull the optimisation of model tested to ensure CFD validity.

As technology continues to increase the focus of the quantitative model begins to become more complex. As can be seen from the above literature the focus has been purely focused on resistance with evermore increasingly complex geometries. This methodology was put to good use by Huang & Yang (2016), where a cargo ship was optimised only with CFD simulations as the quantitative model. Both the parent hull and optimum were tested in a towing tank to validate the results. This research found a resistance reduction in the range between 3.8% and 14.5% for varying Froude numbers. Not only were the forces validated by the towing tank data, but the respective dynamic motions also matched closely from the CFD. However, in recent years there has been a shift towards optimising vessels with the propeller and rudder included in the simulation. Up to this point in the literature above have included in the appendages for the optimisation geometry. Chen, et al. (2016) use the CFD simulations to not only optimise the hull form for frictional and wave resistance but to also optimise the flow into the propeller. Due to the complexity of the twin skeg hull form, around 100 had to be used to generate such a hull form parametrically. Although no rotating propellers were simulated, wake field was recorded and used as an evaluation for the optimisation algorithm. This allowed the optimisation to achieve an 8.6% reduction in resistance, along with a significant improvement to the flow entering the propeller region.

The above literature highlights the flexibility and range of optimisation within the marine industry. As technology advances so do the complexities of the algorithms as well as the quantitative models used for the evaluations. However, there is a clear void in the literature surrounding any optimisation using CFD with respect to manoeuvring. It is one of the aims of this research to develop methodology for optimising a vessel's manoeuvring capabilities using CFD within the process.

2.4. Parametric Modelling

The final focus on the literature discusses the marine industry's use of the parametric modelling. As discussed above, many of the optimisation studies involving CFD utilised some form for parametric modelling, be it fully parametric Chen, et al. (2016), or parametric modification Park, et al. (2015). Parametric modelling is not a recent development within the marine industry, a discussion surrounding the use of parametric modelling to develop 'A One Week Ship Design' was presented by Abt, et al. (2001). The research presented the three key levels that characterise the ship design process, specification, definition, and realisation. Abt, et al. (2001) propose that the parametric model should be developed in the definition stage of

the design process. This basis is used by Katsoulis, et al. (2019) to develop a parametric hull form using T-splines to improve fairness and reduce computational time. By using T-splines topology problem areas in vessel modelling, both parametrically or not, such as the bow and stern can easily be modelled in varied while maintaining a consistent level fairness. Additionally, Katsoulis, et al. (2019) used only 27 parameters, compared to 196 for an equivalent parametric model in CAESES.

As the focus of this review in the parametric modelling is primarily aimed towards hull form geometries that influence the vessel's performance. However, parametric modelling can be used to design the structural components quickly and efficiently for hull form. This was used to great effect by Bole & Forrest (2005) to evaluate a fully parametric vessel structure quickly, while also using the flexibility of the model to evaluate the performance characteristics of the vessel. In addition, parametric modelling can be used for less traditional hull form characteristics that can be easily evaluated and changed with minimal effort from the engineer. An example of such research was conducted by Ghassabzadeh & Ghassemi (2013), used fully parametric modelling to evaluate planing tunnel hull forms. This research compares the various types of hull with one another, along with how the parametric model generates such a hull form. It was found that all hull forms were able to be accurately modelled for the parametric method presented by Ghassabzadeh & Ghassemi (2013). As noted above, parametric modelling is more often than not partnered with optimisation. Scamardella & Piscopo (2014) utilise a fully parametric model from the NPL systematic series. With this parametric hull the Overall Motion Sickness Incidence (OMSI) is evaluated and optimised. This research uses mathematical methods to evaluate the OMSI with respect to JONSWAP spectrum. The results show a good improvement over the parent hull, as well as promoting the importance of both the prismatic coefficient and the longitudinal central buoyancy with respect to motion sickness and vessel seakeeping performance.

2.5. Concluding remarks

An overview of the literature surrounding key elements for this research has been presented. This is by investigating the standard procedures in the early design stage, followed by the determination of key elements which make up the marine environment. The literature then focused on manoeuvring with respect to ships. With optimisation and parametric modelling closing the literature review. From the literature it can be concluded that there are clear gaps within each of the areas:

I. no direct study focused on optimising vessel manoeuvring in the early design stage was conducted

II. with ever-increasing technological advancements there is a greater pressure to accurately simulate real-world conditions in CFD
III. there has been no study performed to accurately simulate and maintain a fully irregular sea state in CFD
IV. there has been no study presenting a methodology for parametrically setting up an irregular sea state simulation, along with the determination of the accuracy level
V. no study has been conducted where an unknown irregular free surface to evaluate a vessel's motion and added resistance
VI. no study has presented a parametric methodology for accurately replicating captive towing tank tests in CFD
VII. there has been no study where a fully parametric model has been coupled to an optimisation algorithm to evaluate the manoeuvring capabilities of the vessel

It is the primary aim of the following chapters to fill these gaps in literature develop methodologies to utilise the ever-advancing CFD.

3. Aims and Objectives

The primary aim of this research is to develop a methodology and best practices for integrating CFD analysis into an automated optimisation process to help improve vessel efficiency while manoeuvring. Due to the complexity of the problem there may be many opportunities for tangential research to influence the overall process, however this aim and objectives ensures that the research maintains its focus.

1. Develop a methodology and best practices for integrating CFD analysis into an automated optimisation process to help improve vessel efficiency while manoeuvring
    a. Investigate the limitations of current literature surrounding CFD manoeuvring simulations and optimisation, along with the main advantages to using CFD over other potential codes
    b. Develop an adaptive MRF scheme that describes a combination of pure yaw, pure sway and static drift carriage motions
    c. Develop an automated CFD domain generation tool, that generates all the key CFD volumes based upon the adaptive MRF variables
    d. Develop an automated mesh scheme that is validated and adapted against multiple towing tank results conducted by SIMMAN 2014
    e. Conduct tests to investigate various factors affecting manoeuvring variables, such as wave interference
    f. Develop a methodology for optimising with respect to key manoeuvring factors, such as turning circle factors, rather than specific manoeuvring numerical variables
    g. Couple the parametric vessel with an automated manoeuvring setup to build the base of the optimisation scheme
    h. Test the optimisation methodology to determine its accuracy in optimising for the desired factors
    i. Conduct multiple optimisation cycles to improve vessel manoeuvring performance and evaluate the newly developed methodology

4. Development of a parametric CFD manoeuvring methodology

4.1. Introduction

In this chapter the development of the manoeuvring CFD methodology is presented along with the key numerical models. The key aims and objectives for this methodology are given below:

- the primary aim is to develop methodology to simulate different vessel types in CFD to analyse various marine vessel manoeuvring tests

To achieve this main aim multiple objectives must be completed, these are as follows:

1. to choose hull form to be analysed and validated against
2. to define and select a motion description method
3. to choose solvers and equations of motion
4. to select motion capture method, i.e. overset scheme
5. to create mesh refinement
6. to set up results recording for key vessel characteristics, i.e. Y force and moment around Z axis
7. to create parametric field functions to develop fully automated CFD setup

To ensure the setup is versatile and accurate the simulation is extensively validated against towing tank tests. Due to the limited number of comprehensive open-source bare hull manoeuvring test data, the hull selection was limited to either the KCS or DTMB hull. The selection of the hull form is discussed in greater detail in chapter 4.2.

Once these key objectives have been achieved, the simulations are thoroughly tested to ensure stability as well as accuracy. In addition, the Y+ scheme is investigated for both full-scale and model scale simulations, this is due to the White Paper presented by Star CCM+ on accurately modelling full-scale marine simulations (Peric, 2020).

This methodology is also aimed at accurately predicting pure resistance, along with resistance in waves, for marine vessels. This section, along with the creation of the mesh refinements are directly linked to the methodology proposed in Chapter 10 (*Appendix i - Development of a CFD methodology for the numerical simulation of irregular sea-states*). Further to this, the methodology proposed here is to act as the building blocks for the final manoeuvring simulations in chapter . It is therefore vital that the methodology presented below is highly flexible as well as easily adaptable.

4.2. KCS and DTMB CFD methodology

Before developing and modelling a manoeuvring CFD simulation, the desired test to be replicated needs to be selected. As shown in the literature review, the most versatile towing tank test was found to be the planar motion mechanism (PMM) test. This test works by keeping the carriage at a constant X velocity, while oscillating the vessel laterally along a sinusoidal path. This test can allow up to 3 degrees of freedom, heave, pitch and roll. While surge and sway are constrained by the motion of the carriage, and yaw can be defined as either parallel to the carriages path in X direction or follow the full-size path of the vessel.

As mentioned in the literature review, by combining various oscillation frequencies and amplitudes for the PMM test a large majority of manoeuvring coefficients can be calculated. However, this methodology is not aiming to purely calculate the coefficients, but rather the overall manoeuvring capabilities of the vessel through its motions and direct forces acting on various parts of the hull. Therefore, these manoeuvring coefficients are not be the primary analysis method. This is where CFD has an advantage over previous strip-theory based methods. Along with this, specific flow characteristics beside and around the hull can be actively investigated with relative ease due to working in CFD.

Before proceeding with the creation of the CFD simulations the hull form that is used to validate and verify the accuracy of the simulations needs to be selected. Unlike other literature surrounding CFD, there is significantly fewer published results for vessel manoeuvring simulations. It was therefore decided that the largest results database would be used for this investigation, as it enables the most thorough validation and verification study to be conducted. This led to one database been selected, and in turn a choice of two hull variants. The results database was produced for SIMMAN 2014, with the two most compatible vessels being the KCS and DTMB. Both have Froude numbers close to the final desired hull's range. In addition, the DTMB hull has had thorough manoeuvring analysis conducted on it at increased speeds, thus allowing this methodology to be thoroughly tested.

Out of the two hull forms discussed above, it was decided that the KCS would be more suitable for the initial setup. This was due to its slightly lower speed, and thus closer to the final hulls speed range. Although the final simulations are conducted in full-scale, to match the investigation done for the irregular seas and a primary aim of this whole research, the SIMMAN 2014 tests were conducted in model scale. The hull selected was built by SVA and had a scale factor of 52.667, this equates to a Lpp of 4.3671 m. The model data for the KCS is given in the table below, Table 4-1, and the model data for the DTMB 5415 given in Table 4-2

Table 4-1 KCS SVA Model Data

	Full Scale	*KCS Hull*
Lpp (m)	230	4.3671
Lwl (m)	232.5	4.4141
Bwl (m)	32.2	0.6114
D (m)	19	0.45
T (m)	10.8	0.2051
Displacement (m3)	52030	0.3562
S w/o rudder (m2)	9530	3.4357
CB	0.651	0.651
CM	0.985	0.984
LCB (%), fwd+	-1.48	-1.48

Table 4-2 DTMB Force Model Data

	Full Scale	*DTMB Hull*
Lpp (m)	142	4.002
Lwl (m)	142.18	4.008
Bwl (m)	19.06	0.538
T (m)	6.15	0.174
Displacement (m3)	84244	0.19
S w/o rudder (m2)	2972.6	TBD
CB	0.507	0.651
CM	0.821	0.984
LCB (%), fwd+	-0.683	-0.652

4.2.1. Domain size and motion selection

Upon selecting hull form an initial idea of the domain size can be estimated. Throughout the CFD literature there is significant variation between the domain size and different research. Therefore, as this is an untested methodology, best practices from other literature are taken as the base for the initial setup. This in turn may be reduced or increased to find the optimum size for this study. A brief sensitivity study is conducted once a stable simulation has been set up. The initial domain size is based on two references, the first are the recommendations put forward by Simonsen, et al. (2012), the second is taken based on research conducted by He, et al. (2016). The relative distances to the inlet and respective outlets are shown in Table 4-3. It should be noted that there is a noticeable difference between the two research papers, this

however does act as a good starting point for the domain size creation as it provides clear upper and lower bounds for the main domain.

Table 4-3 PMM Domain size comparison

	Inlet L_{PP} factor	*Outlet L_{PP} factor*	*Side Outlet L_{PP} factor*	*Vertical +Ve T factor*	*Vertical -Ve T factor*
(Simonsen, et al., 2012)	4	6.4	5	NA	NA
(He, et al., 2016)	1	2	2	NA	20
This study	1	2.5	2	15	25

Based on the literature an initial domain was created for the KCS hull, the limits for this hull are shown in Table 4-3 row three. As can be seen the initial domain was set to match closely to the work conducted by He, et al. (2016). This is for two reasons, firstly the accuracy shown in their results and secondly the mesh size and mesh number are unknown for the setup, so the smaller domain helps to speed up the setup iterations. In addition, it has become from common practice within the CFD community to run very similar VOF ship simulations with this initial domain size. Extra forward length is to account for the use of an overset mesh scheme. This is the largest change compared with previous work conducted in this area.

Along with defining the domain size the method for defining the carriage and vessels motion needs to be chosen. Three approaches have been considered, along with three approaches to enable multiple degrees of freedom. The standard method for allowing multiple degrees of freedom within Star CCM+ for a resistance simulation uses a small mesh morphing scheme that allows small changes to the vessels or objects orientation. This method was instantly discarded, as the vessels orientation while manoeuvring is not known and therefore cannot be assumed to be small. In addition, this research also aims to investigate manoeuvring in waves and thus the standard small motion scheme simply not sufficient for this method. There are two other schemes that can be implemented within Star CCM+, these are overset and moving mesh. The moving mesh scheme was also instantly discarded, as this scheme requires two regions to maintain perfect contact with each other, the scheme is primarily used for propeller and turbine simulations. This therefore leaves only one scheme that allows the desired motion freedom for the vessel and flexibility, namely the overset mesh.

To reduce the overall domain size the use of the Moving Reference Frame (MRF) technique is applied to the domain. The MRF is most commonly used for rotating fans or other such rotating objects. However, MRF is now being used for more complex motion capture. It is

common practice within CFD that the object being analysed is considered a static point with the domain/rest of world moving around it. This is a very stable and accurate method for pure resistance, wave resistance and other simple vector simulations. However, for more complex motions and variable speeds the MRF technique is significantly more suitable. It is important to note that uniform inflow conditions are vital when working with moving reference frame techniques, (Kobayashi, et al., 2011). To ensure uniform flow is achieved the boundary conditions for the domain are carefully selected, and flow passing close to boundaries are carefully monitored.

This technique applies the simple concept that the object is moving, and in turn applies this motion to the reference frame of the domain, thus allowing the domain to move along with the object. The finer details for applying this technique are be described in more detail below, this is a brief description to maintain continuity in the simulation setup description. The MRF method is a highly versatile technique that can be applied to multiple regions at the same time, while also being able to be applied singularly to a domain to act similarly as the standard resistance technique, an advanced resistance analysis technique is also presented below utilising MRF.

By using the MRF technique the largest and most common problem observed when attempting to replicate PMM simulations can be overcome, especially when coupled with an overset mesh scheme. This problem being the complication when attempting to accurately model the roll motion of vessel. In both the previous research discussed above, He, et al. (2016) and Simonsen, et al. (2012), the roll motion has been neglected. This has been justified by saying that the roll motion is not a dominant factor with regards to these investigations. However, for this research it is vital to include roll, as it is planned to investigate how waves interact with vessels while conducting the PMM tests. To accomplish this the MRF technique coupled with an overset mesh are to be applied. The PMM motion is applied to the hull and overset mesh, with the multi-degrees of freedom being allowed. To reduce the domain size as much as possible the domain moves with the hull, but only with its X and Y motions. This allows the rotational effects due to the PMM motion to be captured. It is important to begin optimising every feature of the CFD simulation to be as efficient as possible, as potentially hundreds of final simulations may be required for this research.

Although this technique has significant advantages over other methods, there are complications relating to inlet flow and waves. These have to be overcome using other techniques, but the maximum possible degrees of freedom have been achieved, allowing a closer step to modelling real-world conditions in greater detail.

As mentioned earlier, there are three methods that have been considered for describing the path/motion of the carriage and vessel. Along within the literature review, the path for a PMM towing tank test is defined by the carriage speed, oscillation amplitude and oscillation frequency. The first method uses table data to define the position of the vessel based on the centre of gravity, using the coordinate system shown in Figure **4-1**. An example of the table data is shown in Figure 4-2, the blue line (YDisp) defines the X and Y position with respect to time. The orange line (RA) shows the vessel angle with respect to the X axis, however, to use this the rate of rotation (R) must be used in the input table, this is shown as the yellow line. These values were calculated in Matlab with the plan to link the two programs, Star CCM+ and Matlab, with a Java script to automate the path of definition. This proved to be unsuitable but was used as a validation method for checking the two other motion description schemes.

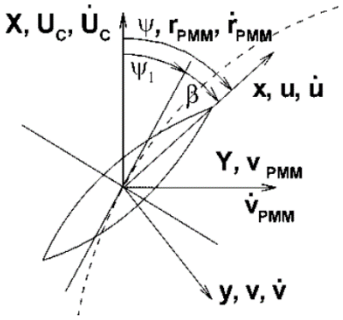

Figure 4-1 **Vessel local coordinate system (Simonsen, et al., 2012)**

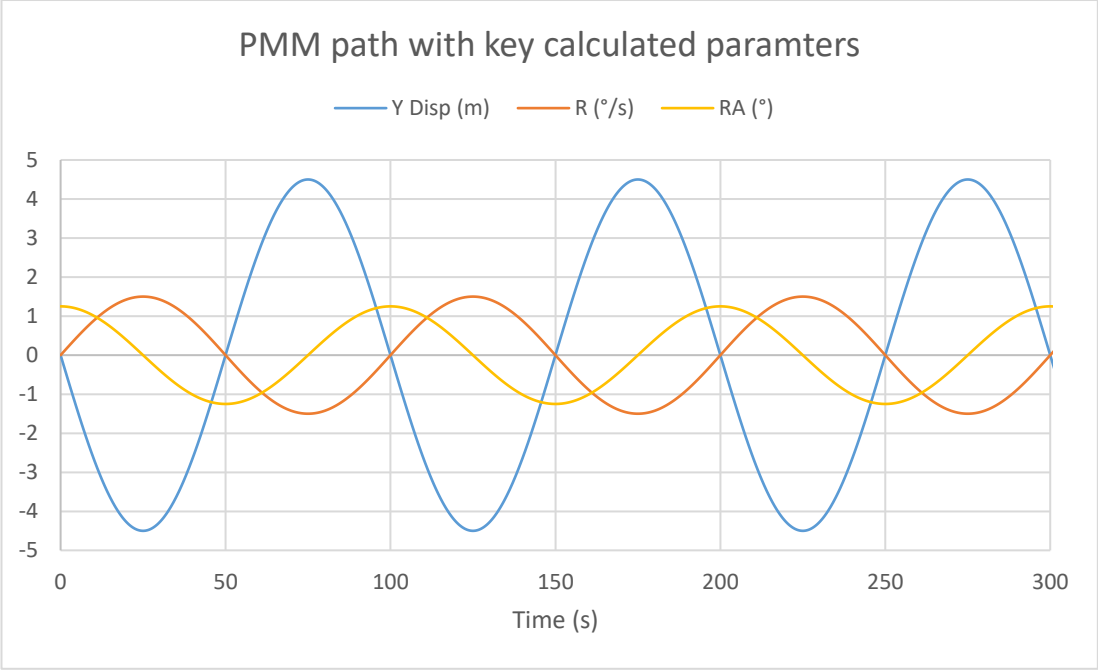

Figure 4-2 PMM Tabulated path with the magnitude of all factors given on the y-axis

The second method is aimed to automate the generation of the paths and data, shown in Figure 4-2, directly within the CFD program itself. To do this, the use of field functions within Star CCM+ were applied. These functions directly calculated the numerical equation outputs describing these trigonometric curves based on the inputted PMM values of carriage speed, carriage lateral amplitude and oscillation frequency. All these values were calculated with respect to time to produce a final set of values matching those shown in Figure 4-2, for example. This method, unfortunately, proved to be inaccurate and unstable, it was therefore discarded for the final method to be used.

As this specific section of the research is focused directly on PMM towing tank results replication, the best option for describing the motion of the vessel is to utilise the PMM settings built into Star CCM+ for the DFBI model. As the DFBI model is required for the multi-degrees of freedom, no extra computation is required for calculating the DFBI PMM motion. The planar motion carriage is described as followed by Star CCM+, "*Planar Motion Carriage option simulates a captive motion in the X-Y plane of the laboratory coordinate system. This mechanism drives the body along a prescribed trajectory in the X-Y plane, while the body is optionally allowed to move freely in the directions of heave, pitch, and roll*" Star CCM+ (SIEMENS Star CCM+, 2020-C). This method encompasses all the key aspects that are required to replicate the towing tank tests conducted for SIMMAN 2014.

4.2.2. Mesh setup

4.2.2.1. Parametric mesh refinement

For the mesh setup, the key theories and methodology developed in chapter 10 are adapted through the use of more complex volumetric regions. Along with this, the creation of the overset region and corresponding refinement volumes are also discussed. As an object is now be introduced to the methodology described in Chapter 10, the development and calculation of accurately modelling the boundary layer flow is also presented.

As discussed in Chapter 10 the free surface is vital to ensuring accurate volume of fluid simulations. Unlike simulating irregular sea states, only waves be modelled on this point the waves generated by the vessel. It is imperative that these are accurately modelled to capture all elements that make up the forces acting on the hull. In addition, the free surface has a dynamic effect on the moving hull, thus making the free surface resolution a vital point in achieving the accuracy required for this research.

Before creating the volumetric mesh refinement regions, a basic understanding of how the free surface flow changes compared to a normal resistance simulation is needed. As the PMM

towing tank test follows a very strict motion path it is possible to predict the profile that likely flow. An initial 3D model was created with a simple PMM path modelled, along with the path a simple triangle representing the wake of a normal vessel was modelled based on the Kelvin angle. The 3D model was created using the parametric add-on Grasshopper for Rhinoceros 3DM software, this allows rapid and highly flexible modelling for a simple problem such as this. The triangle can be scaled accordingly to account for the vessel size with respect to the PMM path. The wake triangle was arrayed along the PMM path at a distance they can be varied by the user. This allowed for quick resolution control on how the wake moved along the path. This analysis is shown in Figure 4-3 with varying path amplitudes, with amplitude of 1.0 equating to 10% of the PMM path length. This figure highlights the key points along the path that need to be focused on, namely the inside edge on the point maximum rotation, i.e. 0.5 and 1.5 π along the sinusoidal curve.

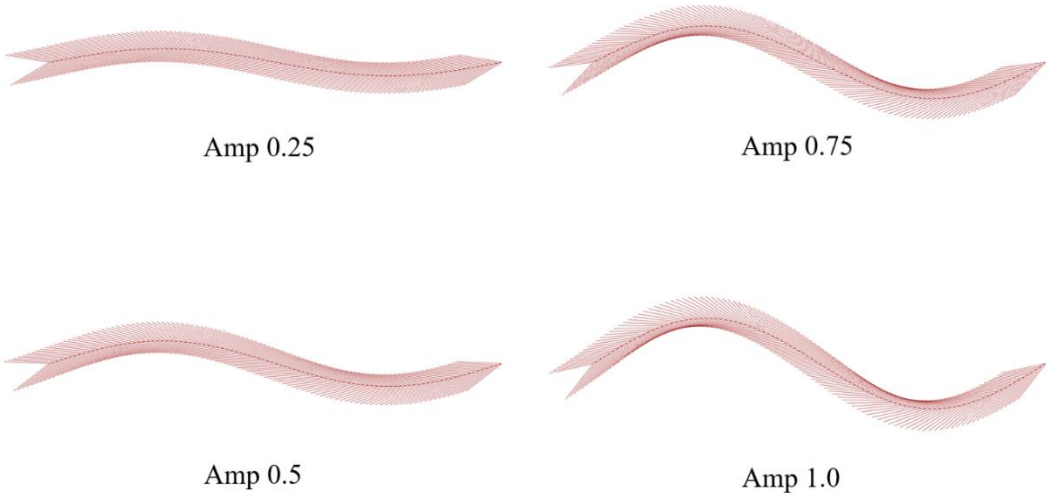

Figure 4-3 Wake profile moving along PMM path

The paths shown in Figure 4-3 are extreme examples of potential PMM paths, however these are used to highlight the potential wave compression affect that may occur when the vessel is turning. This also helps to highlight how the wave fronts closer and further away from the vessel. This effect is to be accounted for modelling the week profile of the vessel. Based on the investigation conducted in Rhinoceros 3DM wake refinement region has a sinusoidal curve applied to it, rather than the standard triangular wake. In addition, the rear of the volumetric region has an arc curve applied to it to also account for the rotation of the waves. Although the vessel follows simple sinusoidal path, the tips of the wake profile do not follow the same path. This path is distorted in both the X and Y axis. This becomes significantly more pronounced as the Y amplitude over X translation ratio gets closer to one. This is a very unrealistic PMM

path; however, all conditions should be accounted for. This extreme distortion can be seen in Figure 4-4. This distortion is accounted for in the parametric model.

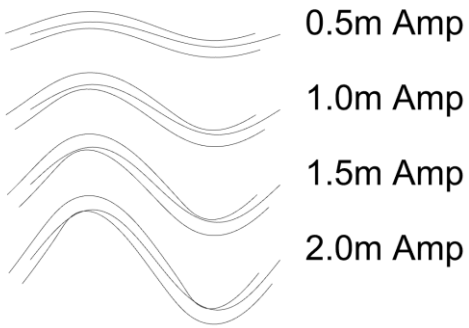

Figure 4-4 PMM Wake path distortion for varying Y amplitudes

This variation in the wake could be simply adapted and overcome by increasing the Kelvin angle. This would be the simplest method however, depending on PMM test setup there may be the extra mesh refinement in areas that is not required. This extra and useless mesh refinement is shown in Figure 4-5, with the hatched area highlighting the extra cells that would add no benefit to the simulation is. This figure also shows the initial concept the wake refinement. This concept simply applies part of the sinusoidal curve that defined the PMM path as the wake refinement edges. This curve is the first quarter, which has then been rotated at the Kelvin angle to create the wake triangle.

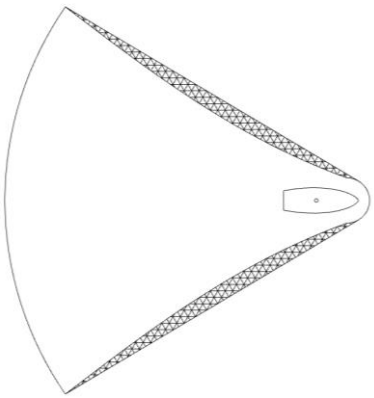

Figure 4-5 Unrequired mesh refinement in highlighted area

As mentioned above the overall domain does not rotate, whereas the overset region within the domain does rotate around the centre of gravity of the vessel. This also means that the standard overset mesh refinement is not be suitable, as it is commonly taken as a rectangular box. The overset mesh region was defined as 1.5 times the length of the vessel, this is a common size and was used by Tezdogan, et al. (2015). To account for this rotation another parametric

volume is created to ensure the overset region does not leave the specific mesh size that is used to ensure stable flow between the overset region and the outer domain.

To create this parametric volume and initial parametric overset box is modelled, the overset box can be varied in X, Y & Z proportions to allow for a variety of hull forms, i.e. an overall length factor of 1.75 rather than 1.5 for a less slim hull form. Once the box has been created, it is moved such that the centre lines up with the midship. Both the ship and the box is then be rotated to the maximum angle seen along the PMM path with respect to the flow moving along the X vector. This then highlight maximum rotational displacement observed at the corners of the overset box. Based on this a parametric volume is created using arcs and sweeps, rather than a simple circle with a radius touching the rotated corner points. This is again done to efficiently account for the motion created by the PMM path, and thus the lowest possible cell numbers. An example of this rotation is shown in Figure 4-6, it should be noted that this rotation is an extreme, as such an angle is unlikely to occur for a PMM test following recommended procedures.

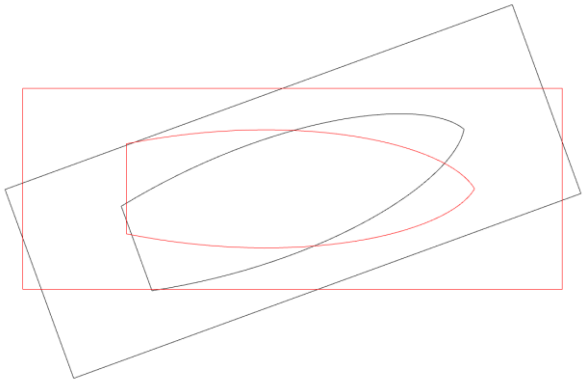

Figure 4-6 Overset region rotation, red = 0' black = 30'

The rotation around the vertical axis has now been accounted for, however as the simulations have multiple degrees of freedom is also important to now account for the overset region having motion in the vertical plane. Unlike the rotation of the overset which is predefined, the vertical motion is not be known until preliminary tests have been completed. To create a simple and intuitive way of modifying the overset refinement region, the volume above and below overset region is controlled based upon the cell size used within this refinement region. For example, rather than specifying a specific vertical length set number of cells are defined based on the simulation setup. The main reason for using this method over the simpler method of purely defining vertical dimension, is to eradicate the potential for meshing problems when generating this region of refinement.

Now that the plan has been developed for volumetric regions for the PMM tests, it is now time to start modelling these volumes in Friendship Framework CAESES parametric modeller. The base file created when developing the parametric modelling scheme for irregular seas is used. The first step in creating the volumetric refinements is importing/selecting the hull geometry. From here the overset region can be parametrically modelled using the same methodology developed in Chapter 10. By selecting the hull form the corresponding PMM parameters can be set up and in turn the path can be calculated. For this investigation specific amplitudes and oscillation frequencies were used to match the SIMMAN towing tank tests. The PMM path was simply created from an FGenericCurve in CAESES, with the Y value represented by a sinusoidal equation, with the oscillation frequency varying the length and amplitude controlling the peaks and trough heights. An FGenericCurve is "a generic curve type which can contain arbitrary coordinate definitions for x, y- and z" (Freindship Systems, 2020).

To create the wake refinement a specific part of the sinusoidal path must be taken, in addition, the curve being used for the wake refinement has to be slightly adapted to account for the compression discussed above. It was found that only very slight variation was required for realistic PMM paths, around 5% reduction in length and in 2 to 4% in amplitude increase. This was found by inputting a selection of PMM towing tank tests conducted by SIMMAN 2014 into the Grasshopper parametric model to find the upper limits of the compression effect from real world tests. This compression was then applied to a copy of the PMM path. This curve would then have an evaluation put on it to find the curve section that can be used for the wake refinement. This evaluation uses a Brent optimisation algorithm, coupled with the desired length parameter, to find the length along the curve that is desired by the user. For example, the initial length was set to 2 times the overall ship length. This value is then ran through the Brent algorithm to find a point between the start (0) and the first peak (0.25) on the compressed curve. These points are then used as the upper (0.25) and lower bounds for taking a copy of the compressed curve. This new curve acts as the outside edges of the wake refinement. The wake refinement along with curve section is shown in Figure 4-7. To close off the refinement, an arc blend curve function is used for the bow and a simple arc for the aft were used, with the midpoint at a specified distance aft of the ship. This created a closed 2D polyline that can be extruded to specified vertical height to create the closed wake volume. The vertical height, like the overset refinement, specified as a function of cell heights rather than a specific vertical dimension. This is also used to connect up the free surface refinement developed in Chapter 10 and this wake refinement.

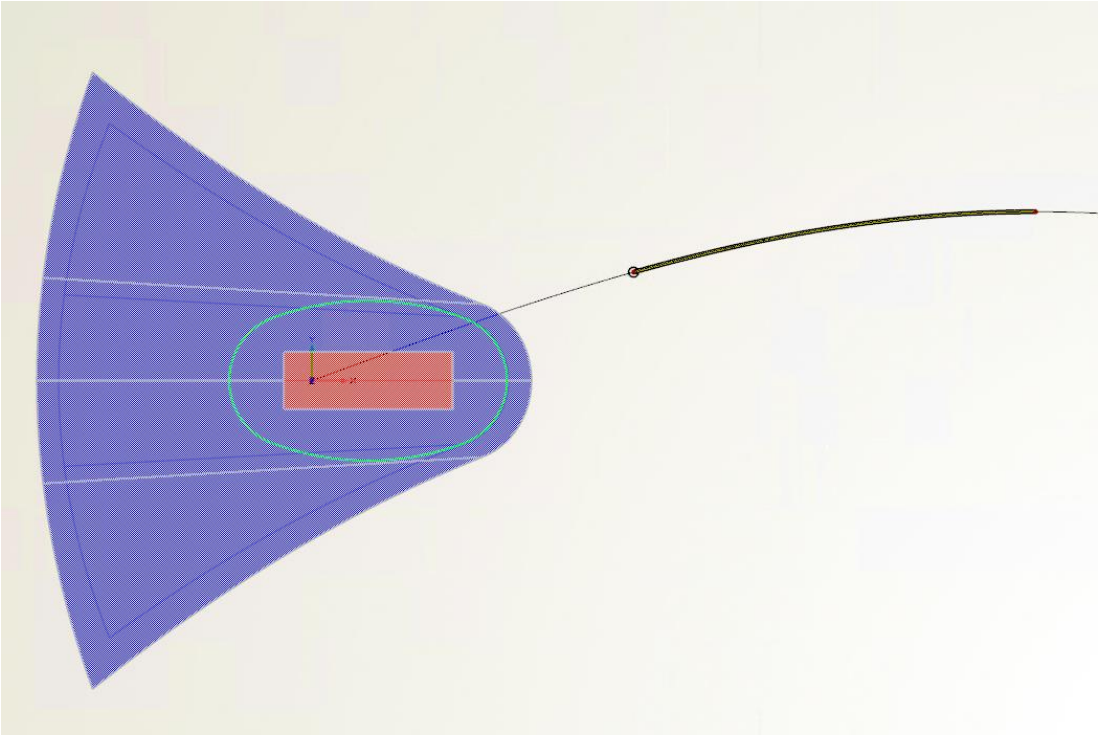

Figure 4-7 Sinusoidal wake refinement and evaluated curve section

Common practice within CFD when using volumetric refinements, is to have steadily increasing volumes on the same shape to allow for smooth transition from the highly refined region within the volume to larger cells and faster growth rates in the outer domain. This method was used to achieve great accuracy in Chapter 10, of the two integrated methods when evaluating a ship hull.

4.3. Automated optimisation for manoeuvring

The first stage in the optimisation is to create a fully parametric hull form based on an existing hull. The hull form is selected due to its performance characteristics and previous CFD validity. This hull form is then be validated using the setup developed above rather than a specific validation CFD simulation.

Once the parametric hull has been developed, the method for evaluating the manoeuvring characteristics can be chosen. Based on the research for the previous aims it was selected that a hybrid method would be most suitable. This method involves the creation of custom equations developed to rank the hull forms in terms of manoeuvring performance. To develop such an equation, the parametric hull form is used in conjunction with the CFD manoeuvring tool to find the key characteristics of the hull geometry that influence manoeuvring forces. These key geometric characteristics are then be developed into the equations that are used within the optimisation. These equations go through an iterative process to refine the accuracy

and validity. To conduct this iterative process the Sobol sequence is used to efficiently evaluate the design space. Specific stages through the process genetic differences are encouraged between the generations to improve the equation's flexibility.

The optimisation then use these equations to rank the hull forms. Upon completing the optimisation using this ranking scheme, the optimum hull forms are then evaluated in CFD to solidify improvements made for this optimisation. In addition to this, a separate optimisation are conducted with a completely unique hull form with stricter constraints to evaluate the equations' ability to be used for a variety of hull forms.

The final analysis of the optimisation results is the evaluation of the first hull forms and optimum results in a free running manoeuvring test. This includes appendages and virtual propellers. This fully quantifies the improvements made in the optimisation, along with validating the methodology developed throughout this research.

Development of a CFD methodology for the numerical simulation of irregular sea-statesas well as helping to significantly reducing the mesh numbers. Unlike other methods, the method shown in Chapter 10 uses the cell number coupled with a desired number of cells to calculate the vertical distance increase for the volume. This distance is then converted to a scale factor, this factor is not applied evenly to the whole volume but purely to the vertical. The X and Y factor is calculated to maintain an even distance around smaller volume. This method helps to carefully control the mesh numbers which is vital to this research.

The overset refinement volume is modelled in a similar way, except to arc functions are used for the bow and stern, with two arc blend functions being used to interpolate between them. The forward and aft arcs are defined based on the calculated rotational corners of the overset, as mentioned above, with the midpoint of the arc being defined by a specific length from the overset box. This can be carefully calibrated to create an elliptical shape, as seen in Figure 4-7, or a circle based on the length away from the overset box. This overset refinement is then scaled in the X and Y direction before being extruded vertically. Both the overset and wake refinement are now parametrically linked to the PMM path parameters. This linking is shown in Figure 4-8, which shows 4 different groups of volumetric refinements at varying amplitude percentages with respect to the PMM X length travelled by the carriage.

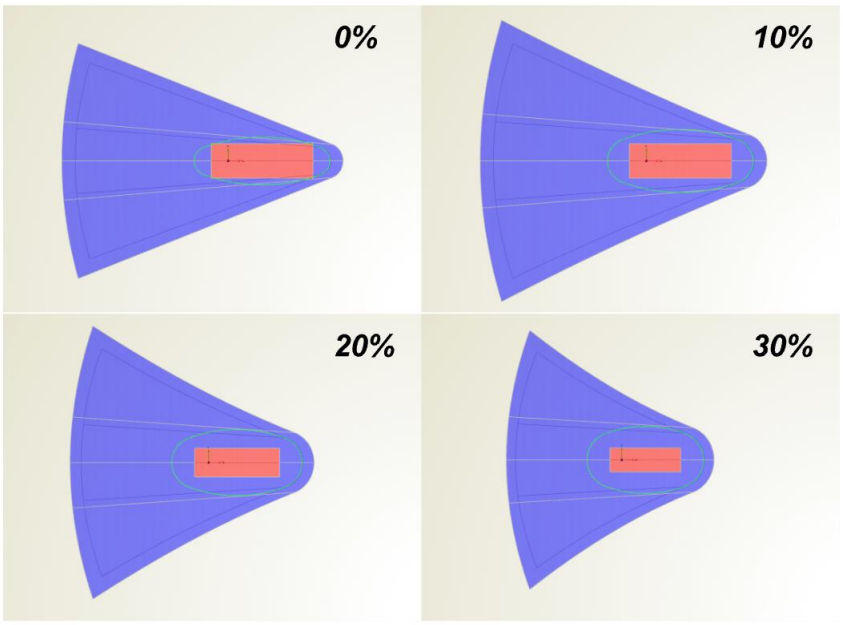

Figure 4-8 Wake and overset refinement at varying amplitudes shown as a % of single PMM wavelength X travel length, blue = wake, red = overset & green = overset refinement

As the amplitude increases with respect to a single PMM X displacement, the eccentricity of the sinusoidal curve increases and has a greater effect on the wake refinement along with the overset volume. To ensure even more stability in the simulations, with respect to the mesh, the overall domain size is also linked to the vessel length but is applied to a virtual bounding box surrounding the wake refinement. This ensures that no matter what PMM parameters are inputted the wake refinement never exceed the outer domain. The distance between the virtual box in the outer domain is controlled by another parameter based on the ship length. For most simulations, this value is set between 1 and 1.25. This factor is also important when considering how damping is applied within the domain.

4.3.1.1. Meshing model selection

As in chapter 10.2.3, the trimmed mesh method is used, as no accurate alternatives for capturing the free surface when using VOF solvers has been found. A potential method, primarily focused on simple resistance simulations, had been presented by Star CCM+. This method did not use the trimmed mesh method but rather a polyhedral/tetrahedral meshing scheme which then had an interface free surface which allowed for boundary layer to be modelled. This boundary layer would then act in a similar fashion to the trimmed mesh scheme at to free surface, however, this method did not allow for such detailed refinement. In addition, this method was also no longer compatible with the latest versions of Star CCM+. Some research relating to this method was conducted but this is discussed in future research.

To ensure stable flow between the outer domain in the overset region, the maximum cell size generated in the overset region correspond exactly to the minimum cell size generated in the overset refinement region. To further improve the resolution of flow around the hull, an extra volumetric refinement was created in the overset region based on the imported hull geometry. This refinement was simply a scaled version of the hull, which was translated down to capture the underwater region around the hull. This region would have half the cell size or smaller than the overset region.

To ensure accurate boundary layer computation, a body conformal prism layer mesh is used. The input values for this boundary layer are calculated based on the non-dimensional wall distance (y+). This calculation has been set up in CAESES to be based on the inputted PMM parameters. This ensured an accurate boundary layer was created for any potential vessel. In addition, a high y+ value is used rather than the low y+ value, this is based on the White Paper presented by Peric (2020) as well as a sensitivity study conducted below. An example of the resultant data for the boundary layer is shown in Figure 4-9.

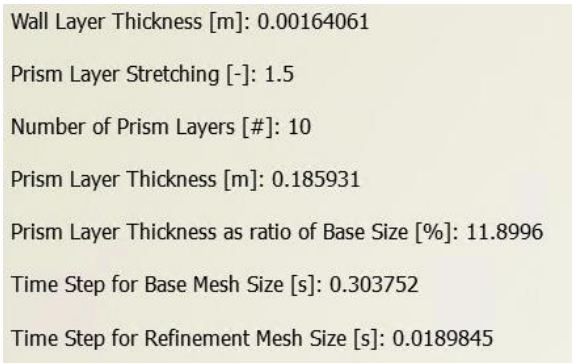

Figure 4-9 An example of calculated boundary layer mesh input data

The final mesh number varies significantly dependent on PMM test being replicated, along with whether waves is simulated. It is aimed to maintain a mesh number below 5 million cells, based on cell numbers seen in Chapter 10. The table showing various cell numbers along with breakdown for each region is shown below, Table 4-4.

Table 4-4 Breakdown of cell numbers for flat and wave PMM simulation for KCS & DTMB 5415

Cell Numbers	*Overall*	*Outer Domain*	*Overset*
KCS Flat	5,541,200	4,312,714	1,228,486
KCS Waves	3,664,132	2,714,566	949,566
DTMB Flat	2,056,785	1,516,106	540,679
DTMB Waves	3,267,142	2,332,092	935,050

As can be seen from the table the KCS hull form and simulations had a significantly higher mesh count. This is due to the hull form being changed midway through the meshing optimisation. The hull form was switched from the KCS to the DTMB 5145 hull, as KCS did not have any available bare hull test data. As this research is primarily aimed towards hull form analysis, the addition of a rudder and propeller in the PMM tests would hinder the analysis and the future steps. To overcome this the DTMB 5145 hull was used instead, although it had no rotating appendages it did have the addition of bilge keel is along the hull.

To accurately replicate towing tank simulations with a bare hull, an obscure model scale had to be chosen. This meant that there were very limited data about the position and size of the bilge keels. The data was taken from the model test report created by FORCE Technology, Agdrup (2004). A comparison of 3D model used in CFD and the towing tank model are shown in Figure 4-10. The sectional diagram for the bilge keels are shown in Appendix v Figure 15-1.

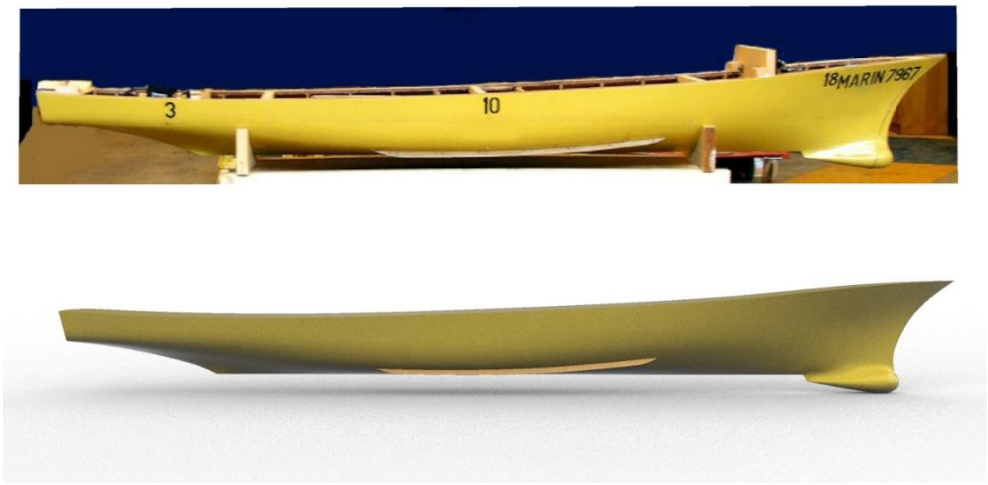

Figure 4-10 DTMB 5415 MARIN Hull 7967 towing tank model compared with 3D Rhinoceros model (below)

Details of the final mesh for the DTMB calm water PMM simulations are shown in Figure 4-11 & Figure 4-12. With Figure 4-11 highlighting how the volumetric controls presented above affect and refine volume mesh for a given PMM test, this figure also shows the increased size of the boundary layer due to the high Y+ value being used.

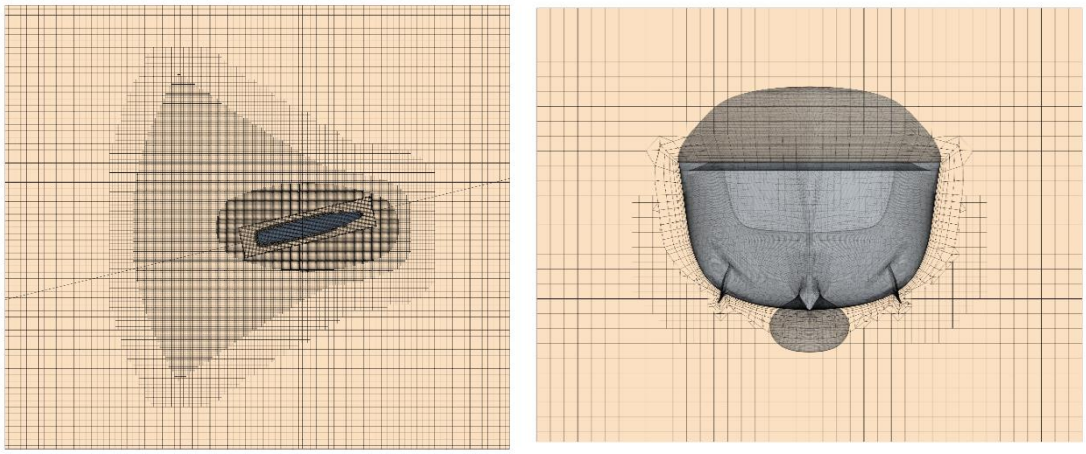

Figure 4-11 DTMB 5415 Volume mesh for free surface (left) and prism layer & overset mesh cross section (right)

Figure 4-12 DTMB 5414 Surface mesh for hull and bilge keels

4.3.1.2. Numerical setup and governing equations

For this research, the governing equations remain the same as presented in the chapter 10.2.4. The turbulent model however is selected as the standard K-Omega model. This is a two-equation model which solves the equations of transport for the turbulent kinetic energy k and the specific dissipation rate ω to calculate the turbulent eddy viscosity. A notable advantage when using this model over the K-Epsilon, is the performance improvements in the boundary layer under adverse pressure gradients. Further to this, this turbulence model can be applied throughout the boundary layer without modification, this includes viscous dominated regions. In addition, the standard model does not require the computation of all distances for the simulation. This model is also well suited for high y+ schemes, as presented by Siemens Star CCM+ (2020-A). The transport equations for the K-Omega model are given in equations (4-1) & (4-2) Siemens Star CCM+ (2020-B). The only potential disadvantage to using the K-Omega over the K-Epsilon, is the K-Omega's sensitivity to inlet boundary conditions for internal flows Siemens Star CCM+ (2020-B).

$$\frac{\partial}{\partial t}(\rho k) + \nabla \cdot (\rho k \overline{\boldsymbol{v}}) = \nabla \cdot [(\mu + \sigma_k \mu_t) \nabla k] + P_k - \rho \varphi^* f_{\varphi^*}(\omega k - \omega_0 k_0) + S_k \tag{4-1}$$

$$\frac{\partial}{\partial t}(\rho \omega) + \nabla \cdot (\rho \omega \overline{\boldsymbol{v}}) = \nabla \cdot [(\mu + \sigma_\omega \mu_t) \nabla \omega] + P_\omega - \rho \varphi f_\varphi(\omega^2 - \omega_0^2) + S_\omega \tag{4-2}$$

4.4. DTMB systematic studies and validation and verification results

Within this section, the different systematic studies with respect to volumetric refinements, geometry, turbulence models and hull motions is presented. Along with the validation and verification study for the selected hull geometry compared with the towing tank tests conducted by SIMMAN 2014.

The systematic studies include how the overall domain size effects the simulation, with a focus on stability, accuracy and simulation time. A specific study focuses on the shape of overset region, from the standard rectangular box to the cylindrical box with flat ends and a cylindrical box with domed ends. This is primarily to study how the flow entering the overset region may be producing downstream errors. The wake box developed above compared with the standard triangle or a fully covered free surface with no extra refinement but the smaller cell size. Once these mesh studies have been completed the focus then switches to the comparison between turbulence models. All these studies are compared to towing tank tests which is used for the final validation and verification study.

After the final validation and verification study is presented a final motion-based study is conducted. This study is focused on the roll damping and the roll characteristics of the defined simulation to this point. The study is not a separate simulation but uses all the aspects developed for the PMM towing tank tests. This is vital as this study takes a further step forward than the towing tank tests conducted by SIMMAN 2014, by including all in the degrees of freedom.. The hull is then be rotated along the x-axis and released to show the roll decay of the hull form in this mesh setup. Once this is matched to a certain degree of accuracy to other research, such as Lungu (2019), validation and verification study focusing on grid spacing and time step is presented. Similar to the research conducted in Chapter 10, the transient and less restricted nature of the simulations does not lend itself well to having an iterative study conducted.

4.4.1. Outer domain size systematic study

The initial systematic study focuses on overall outer domain size and how the mesh number along with how the accuracy is affected. The limits of the study were based on

recommendations put forward by both He, et al. (2016) and Peric (2020), with the recommendations taken from Peric (2020) likely to be unsuitable but set as the lower limit due to the final simulations being then in full-scale. This is the first systematic study to be completed as the outer domain size has the ability to be slightly varied based on PMM setup, as noted in section 4.2.2.1, this is merely to define the initial starting point.

An initial simulation which was achieving a consistent 5% error margin with respect to towing tank simulations was selected as the baseline for the systematic study. The turbulence model was kept as the K-Omega, along with all other variables in constant. Table 4-5 shows the three different domain sizes used with respect to the ship's overall length. The length overall factors shown in Table 4-5 correspond to the dimensions shown in Figure 4-13.

The factors for the base/medium domain size are based upon extensive resistant simulation experience and preliminary PMM towing tank simulations. The aft length ensures there is sufficient damping to the outlet without impacting the wake while the vessel is rotating. This is also the case for lateral Y dimension being two. The vertical factors are set to match resistance simulations; however it is common practice that some manoeuvring simulations are conducted in shallow water and therefore this vertical dimension easily adapted to account for this.

Table 4-5 Domain size systematic study LOA and draft factor comparison table

	LOA and vertical draft factors		
	Min	*Base*	*Max*
X-1	1	1	2
X-2	1	2.5	5
Y	1	2	4
Z-1	10	15	20
Z-2	15	25	35

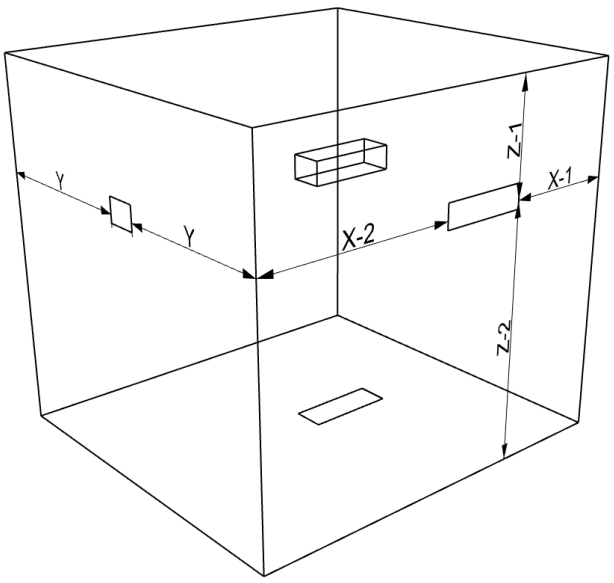

Figure 4-13 Domain dimension layout

Based on the factors used in Table 4-5 three meshes were generated. Due to only domain size increasing the overall cell number did not greatly vary between the different simulations. This is mainly due to only the free surface be noticeably affected by the domain size variation, which is not a highly dense cell region. This however becomes a significant factor when considering waves as the free surface can become extremely dense, as shown in the research from Chapter 10. The cell numbers for the freeze in relations are given in Table 4-6. As can be seen there has only been an increase of around 60,000 cells from smallest domain to the medium/final simulation. Whereas there is an increase of around 400,000 cells from the medium/final too the largest domain size simulation.

These variations in cell numbers equate to minor changes in the runtime on flat 2 degrees of freedom simulations. There is a less than 1% speed increase from the minimum domain to the medium/final domain simulation. This would be considered a small advantage however, due to the proximity of the boundaries to the hull the damping required to maintain stable simulation the direct impact on the accuracy of the simulation. The minimum domain size simulation was run a total of 11 times. This was due to simulation stability and having to restart simulation, along with fluctuating accuracy. Only six of these 11 simulations reached the desired stopping criteria. Although there is only an increase of 60,000 cells, the medium domain size was significantly more stable with zero failed or fluctuating simulations. This meant that the smallest domain size was discarded from any future simulations.

When comparing the medium and maximum domain size simulations the accuracy remains the same between the two with respect to the towing tank test results. This meant the simulation

runtime would be the deciding factor between these two domain sizes. The maximum domain size had an increase in runtime of 4.5% when compared to the medium, which equates to an extra hour on an HPC supercomputer for no added accuracy or noticeable stability. This becomes significantly more exaggerated when waves are included, due to the increased cell numbers, which in turn means the maximum domain size simulation is also unfeasible for this study. The three different domain sizes are shown in Figure 4-14, with smallest to largest shown left to right, with the cell count break down given in Table 4-6.

Table 4-6 Outer domain sensitivity study mesh numbers

Cell Numbers	*Overall*	*Outer Domain*	*Overset*
Min	1,997,338	1,458,884	538,454
Mid/Final	2,056,785	1,516,106	540,679
Max	2,410,572	1,872,118	538,454

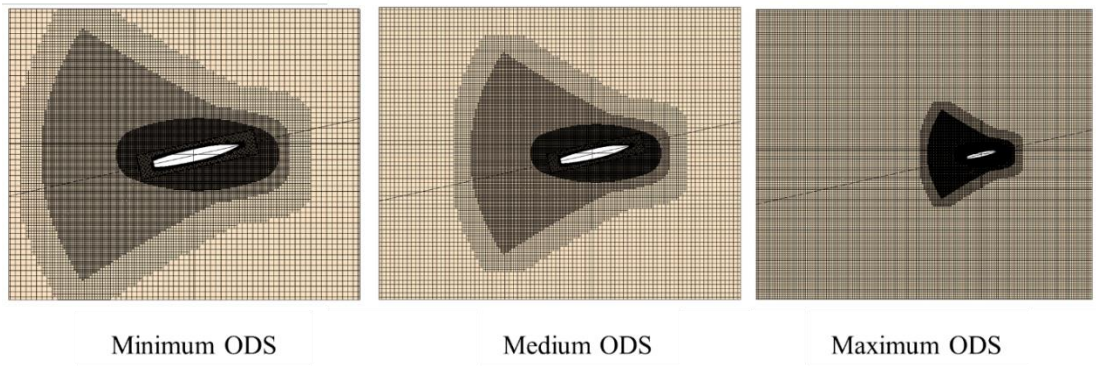

Figure 4-14 Comparison of varying outer domain free surface size and mesh

Unlike the calm water PMM simulations, simulations which include waves the free surface becomes a dense cell region. This can be seen when comparing the final cell numbers of the medium and maximum domain size as shown in Table 4-7. This equates to a 65% increase in overall cell number, with around 99.6% of this focused in the other domain.

Table 4-7 Comparison of the final cell numbers for wave simulations

Cell Numbers	*Overall*	*Outer Domain*	*Overset*
Mid/Final	5,247,648	4,312,598	935,050
Max	8,633,393	7,685,582	947,811

This study shows the importance of analysing the outer domain size, and its overall effect on the simulation. From here greater focus is now be aimed towards overset region and the flow directly around the vessel.

4.4.2. Overset region systematic study

One of the key aspects focused on throughout this work is how roll influences the manoeuvring dynamics of a vessel. Due to this, and due to the complexity of this problem, there was a question surrounding the shape of the overset region. It is common practice when simulating vessels moving through waves to have a standard rectangular box acting as the overset region. These exact dimensions for this box vary depending on the research, however a standard approximation is to have a length 1.5 times the vessels and a width 1.5 - 2 times that of the vessels beam. This width is also applied to the vertical height commonly creating a square cross-section. Such an overset method was used to great effect by Shen, et al. (2015) and Wang & Wan (2020) for both multi-degrees of freedom when investigating ship manoeuvres. However, Wang & Wan (2020) did not account for roll within their simulations. Shen, et al. (2015) did account for roll however the simulation setup was very specific and would not be suitable for potential optimisation due to the highly refined grid.

In addition to the volumetric shape study, a further study focused on the interpolation method for the overset interface was also conducted. This was conducted after the most stable volumetric shape had been found. Within Star CCM+ there are four overset interpolation options, all variants ran for both the KCS and the DTMB hull forms. The interpolation option is used to find a donor cell set for each acceptor cell for the overset interface SIEMENS Star CCM+ (2020-D).

The four available options are: distance weighted, linear, linear quasi 2D and least-squares. The distance weighted method uses the closest cells to give the largest contribution to the donor cell, with three donor cells for two-dimensional and 4 donor cells for three-dimensional simulations. The linear interpolation method uses shape function based on a triangle (2D) or at tetrahedron (3D) based around the centroid of the donor cells. The linear method is more computationally heavy but has a higher accuracy. It is most suitable for simulations involving moving meshes, as it ensures that no interpolation elements overlap. For minimal motions, the linear method can recalculate the interpolation factors rather than evaluating the complete overset calculation SIEMENS Star CCM+ (2020-D). Due to this the linear interpolation method has improved runtime for small motions between time steps, which is required when

attempting to simulate a stable DFBI simulation. The linear quasi 2D method follows the same principle as the linear method however is only used for 3D meshes with a single layer of cells acting as the interface SIEMENS Star CCM+ (2020-E). The final method is the least squares function, this is based off the cost function to approximate solution feels there the acceptor cell. The cost function evaluation is based on a first order Taylor series, that approximates the solution field centred in **a**, as shown in Figure 4-15 with corresponding first order Taylor series equation given as eq (4-3) SIEMENS Star CCM+ (2020-F).

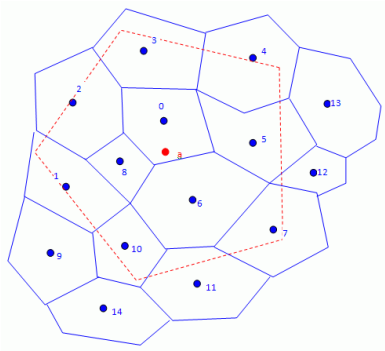

Figure 4-15 Least squares interpolation example (SIEMENS Star CCM+, 2020-F)

$$f(X) \approx (f(X_a) + (X - X_a) * \nabla f(X_a) \tag{4-3}$$

As mentioned, the study was applied to the KCS first, and then DTMB in both calm water and wave conditions. The most notable differences between the interpolation methods were seen for the KCS hull form in wave conditions. This variation can be seen in the graph shown in Figure 4-16. As seen from this graph, both the linear and least-squares method produce identical results, whereas the other two methods have significant variation and noise to the other two methods. As mentioned previously there was no noticeable difference between the four methods in calm water simulations, therefore the linear quasi 2D and distance weighted methods is considered unsuitable for future simulations.

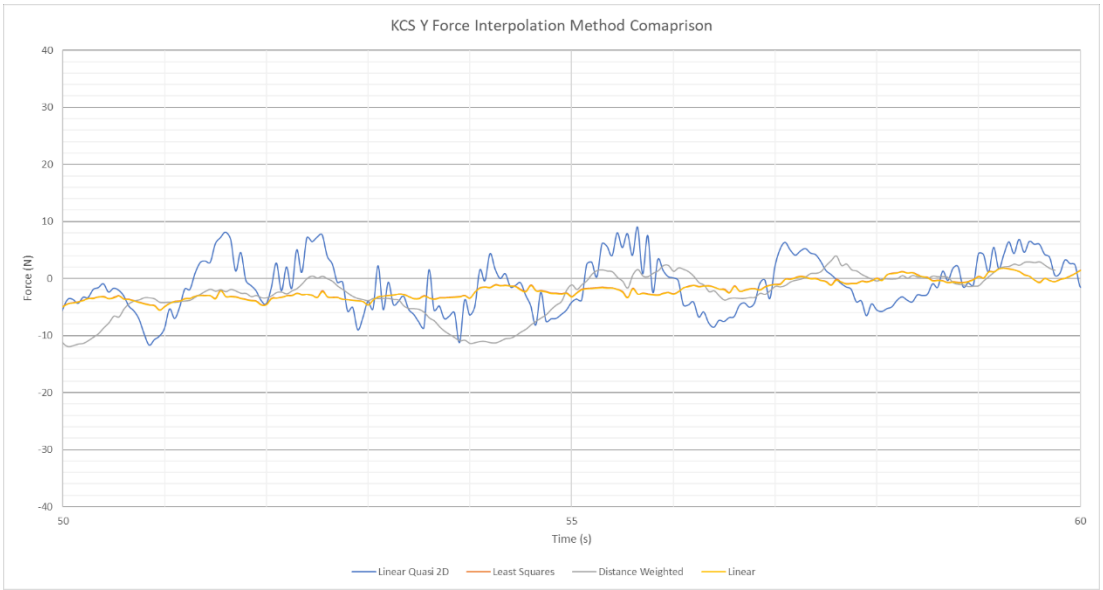

Figure 4-16 KCS Y force interpolation method comparison graph

As the linear and least-squares methods were found to be identical for both the KCS and DTMB simulations, the next consideration is the runtime efficiency. For the KCS simulations the linear method was found to be around 1.2% faster than the least-squares method. This was backed up by the DTMB simulations following closely with the linear being 1.3% faster. In addition, with improved stability and interpolation optimisation the linear method can also have fewer inner iterations per time step, and therefore be further sped up compared to the least-squares method.

The final confirmation that the linear method would be the better option, was on comparing the turbulence entering the overset region. The linear quasi 2D method was found to be the worst, with turbulence being generated at the interface and thus significantly skewering the results downstream. This is not to be surprised that as the linear quasi 2D method is not recommended for these applications. The second worst method with respect to the turbulence was the distance weighted method. This did not actively produce turbulence at the interface, however at the extreme's artefacts were noticed along with randomly occurring turbulence not just at the forward bow interface, but also along the sides and bottom interface. This is likely the cause of the large deviations seen at around 50 and 54 seconds in Figure 4-16, while mostly meshing closely with the linear and least-squares method. Both the linear and least-squares method never appeared to show any consistent turbulence generation, with only the least-squares showing a few cells throughout the entire runtime having turbulence directly interface. The turbulence was monitored through a specific field function then applied only three cells deep into the overset region excluding the aft and free surface areas. This allowed the exact

number of cells experiencing unintended turbulence to be counted. Based on these results the linear method for overset interpolation is applied throughout the future simulations. This is checked periodically to ensure this is the best method to being used.

Along with an interpolation method study, a study to find the best volumetric shape the overset region was also conducted at the same time. Based on the roll decay studies mentioned above, as well as research conducted by (Lungu, 2019), potentially a cylindrical overset mesh would be more suitable for this research application. Therefore, a sensitivity study focusing on the shape of the overset region has been conducted. This was also conducted based on initial preliminary simulations using the KCS hull which noted issues with the flow entering the overset region. This study was used alongside the mesh optimisation to address these issues.

For the study three volumetric shapes is considered, the first are the standard rectangular volume matching the method put forward by Shen, et al. (2015). The final two volumes wilare based off the research conducted by Lungu (2019), using a cylindrical volume with one having domed ends. The addition of the domed ends was to ensure perpendicular flow into the overset region was maintained while the vessel is rotating. Figure 4-17 shows the cylindrical region with domed ends and the standard rectangular overset region box, the other cylindrical region is simply have flat ends. As seen from Figure 4-18, the domed ends are very subtle and only add a minor bulge to the overall volume. However, the subtle shape change may have a noticeable impact on how the overset region compares to the towing tank tests, and thus must be investigated.

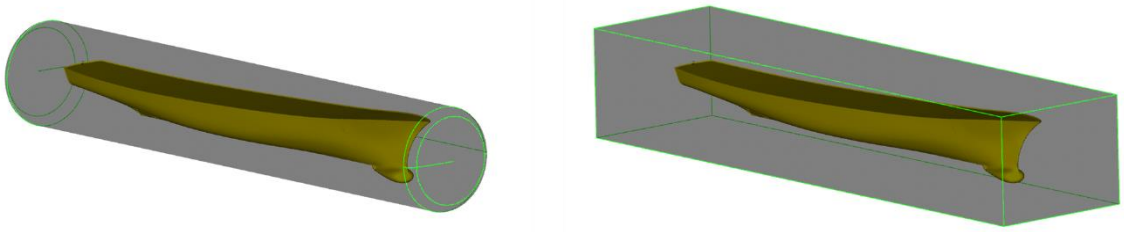

Figure 4-17 Cylindrical with domed ends and rectangular overset region

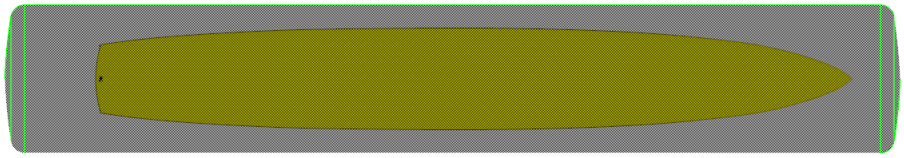

Figure 4-18 Cylindrical region with domed ends top view

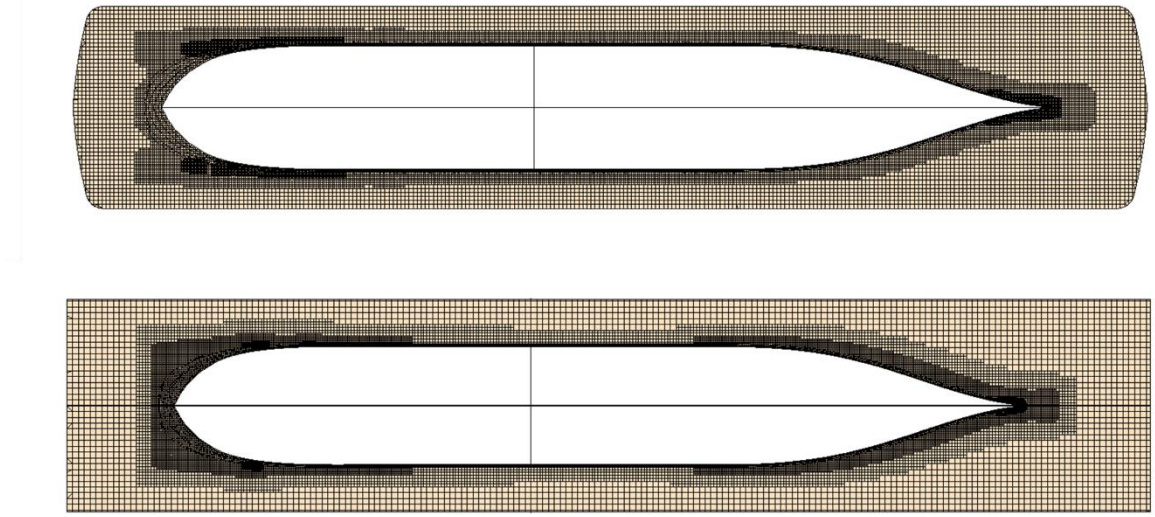

Figure 4-19 Top view of overset mesh region for cylindrical (top) and rectangular (bottom) region

Due to a consistent size needing to be maintained around the entire hull a larger diameter is required than its counterpart rectangular region. The cylindrical region with domed ends has a cell count in the overset region of 1.5 million, with reduction of around 10,000 cells for the flat ends, compared with 1.25 million for the standard rectangular region. This equates to a total of 5% increase in cell numbers when moving from the standard rectangle to cylindrical domed. This in turn would equate to a minimum of 5% increase in runtime, however it is likely to be slightly higher as there are greater number of cells in the overset region to resolve. The final runtime increase was 6.35% compared with the standard rectangle, with an even larger increase when simulating waves.

Figure 4-19 highlights a further drawback to using a cylindrical domain with or without domed ends. As can be seen from the top cross-section, the domed ends cause the trimmer mesh to become triangular. This is the same around the whole of the cross-section. Due to this rapid change in cell volume there is likely to be some potential calculation error. This triangulation can be seen in greater detail when looking at Figure 4-20, along with extra unintentional refinement at the interface at the free surface due to the free surface refinement. All of which causes hull numbers to increase as well as causing issues for the meshing outside the overset region. As a minimum requirement for using an overset mesh is to ensure the cells inside the overset region match those outside the region. Due to these meshing artefacts extra refinements outside the overset region would be required, this would even further increase the overall cell

numbers as well as complicate the parametric model even further. All of which add an extra step which may cause errors in the simulation.

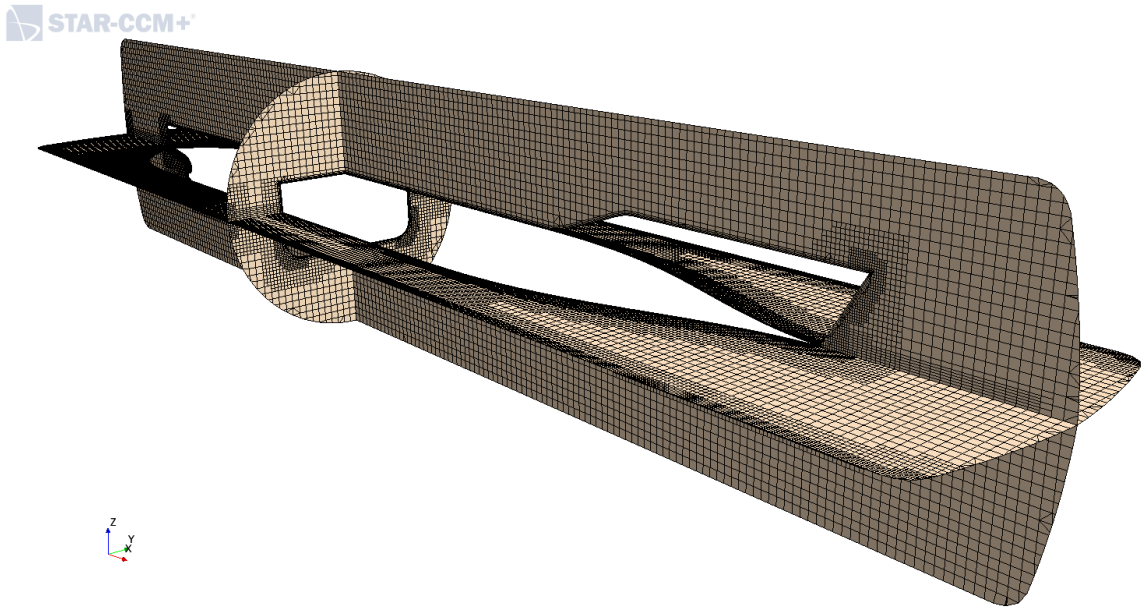

Figure 4-20 Cylindrical domain mesh cross sections

It is important to note however that all these limitations may be outweighed by the benefits of the accuracy achieved by using a cylindrical region. As previously mentioned only the DTMB towing tank tests are suitable for validating against simulations, as the KCS tank tests also have a rudder and rotating propeller included. Thus, only the DTMB is used to investigate the accuracy. The 3 different regions were tested against two different PMM tests in calm water. Equating to a total of 6 simulations ran for this specific study. The breakdown of the PMM towing tank values is given in Table 4-8, with the observed error for Y why force and moment around the z-axis given in Table 4-9 and Table 4-10.

Table 4-8 Overset volume study PMM and wave setup values

	V (m/s)	*PMM Amp (m)*	*PMM Period (s)*
Test 1	2.57	0.4323	4.78
Test 2	1.55	0.6428	8.55

Table 4-9 Observed Y force error percentage

Y Force	*Test 1*	*Test 2*
Rectangular	3.55 %	3.65 %
Cylindrical flat ends	7.12 %	7.18 %
Cylindrical domed ends	7.2 %	7.65 %

Table 4-10 Observed Z axis error percentage

Z Moment	*Test 1*	*Test 2*
Rectangular	3.24 %	3.75 %
Cylindrical flat ends	7.25 %	6.98 %
Cylindrical domed ends	7.18 %	7.32 %

When evaluating the PMM towing tank tests both the Y Force and z-axis moment need to be considered, all simulations were conducted without roll. Two velocities were tested as well as varying amplitude and PMM frequencies. This allowed for a small overview of how the overset mesh performs in varying conditions. These results were compared to the experimental data.

When comparing results to the Y force it can be seen in Table 4-9 that the standard rectangular overset region falls under 4% when compared with the towing tank tests. This error increases when the rectangular region is converted to cylindrical shape, as seen from Table 4-9, the error increases from close to 4% to over 7% for both tests. In addition to this, there was a slight increase in error when comparing the flat ended and domed ended cylinders. For test one this is less than 0.05% error but nearly increases to 0.5% for test 2. It is unclear as to what is exactly causing this slight deviation between the two simulations; however, it is likely due the irregular cell shapes caused by the trimmer mesh attempting to account for the overset shape and corresponding curvature. This is most noticeable where the domed ends move into the cylinder. This also causes unplanned for changes in cell size as noted above. All these attributes combined are likely the cause for these error deviations.

Like the Y force, the z-axis moment also has a noticeable error increase when moving from the standard rectangular region to either of the cylindrical regions. Both tests for rectangular region maintained an accuracy below 4% error, while the cylindrical regions were around the 7% error. The error increase was less consistent between regions compared with the Y force results but was overall lower than the Y force. The domed ends cylinder performed better with respect to the z-axis moment, seen in Table 4-10, when compared with the ever seen from Y force.

Based on these results it can be concluded that the circular region is not suitable for the rest of this study. It is likely only suitable for a specific rotation-based simulation, such as roll decay, and not suitable when other degrees of freedom are introduced like heave and pitch as well as

a forward velocity when using a trimmer mesh. This method may be more suitable when coupled with a non-trimmer, i.e. a polyhedral or tetrahedral meshing model. Due to the need of having a trimmer mesh to resolve the free surface the combination of these models would be the optimum setup. The combination of these models however is not possible in the current versions of Siemens Star CCM+.

4.4.3. Turbulence model systematic study

As mentioned in Chapter 4.3.1.2, the K-Omega model is used throughout this research. This is based on the recommendations presented by Siemens Star CCM+ (2020-A). To ensure this is the best model different turbulence models is evaluated for stability and accuracy. These include modified versions of the K-Omega model, along with the classic and modified K-Epsilon models commonly used for marine CFD.

Each model evaluated against a single PMM towing tank test. The highly evaluated DTMB setup is used rather than the last generation of the KCS simulations. As mentioned previously the KCS is not suitable for the next steps in the study due to it having a rudder and rotating propeller. The simulations however were vital in developing the model and the process that allowed for a highly accurate PMM simulation to be created. The percentage error observed for this turbulence systematic study are shown in Table 4-11.

Three K-Epsilon models is evaluated, these include the standard K-Epsilon, Realizable K-Epsilon and Realizable K-Epsilon two-layer models. Two K-Omega models are evaluated as well, the standard K-Omega and the SST K-Omega. All simulations are identical except for the turbulence model. The DTMB simulation chosen has total mesh number of 5.15 million cells. The PMM test values are the same as those used for test one in the overset shape systematic study, as shown in Table 4-8. All simulations were running for 24 hours on the Archie-WeST HPC, a total of 160 cores at 2.0GHz per processor, rather than specific simulation time cut off. This meant the efficiency of the turbulence model could be seen more clearly and quickly when comparing the simulations.

Table 4-11 Turbulence model error percentage and iteration count

Turbulence Model	*Y Error %*	*Z Mom Error %*	*Iteration Count*
Standard K-Epsilon	3.89	4.12	50,575
Realizable K-Epsilon	4.15	4.55	50,150
Realizable K-Epsilon Two-layer	3.25	3.11	49,950
Standard K-Omega	3.55	3.24	53,325
SST K-Omega	3.79	4.1	51,275

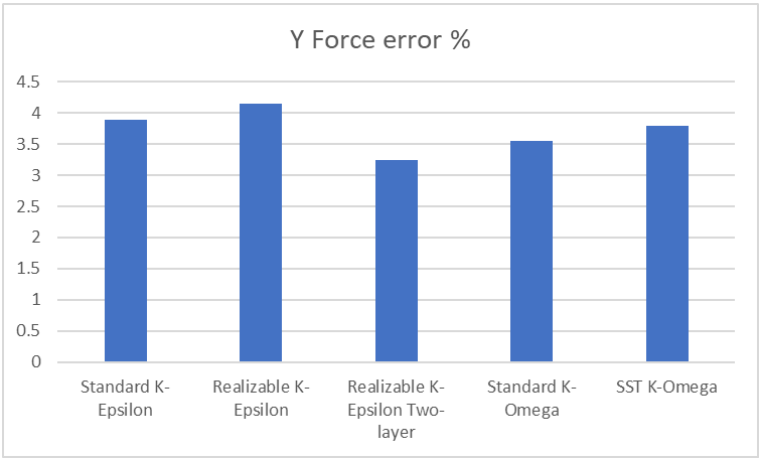

Figure 4-21 Bar chart showing the error percentage for the different turbulence model simulations for Y force

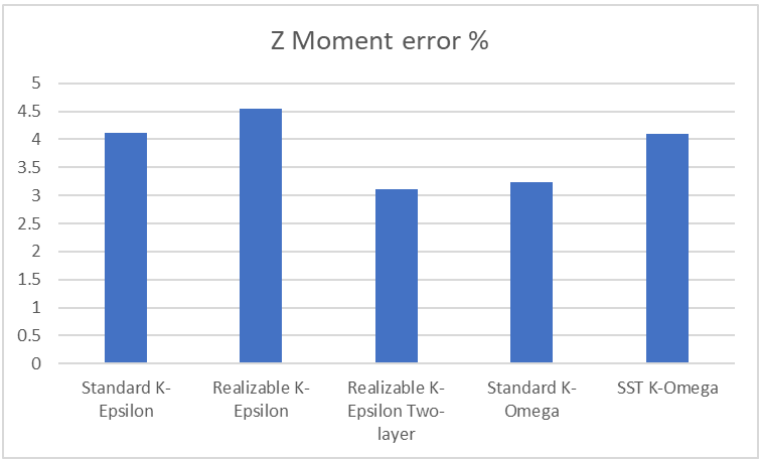

Figure 4-22 Bar chart showing the error percentage for the different turbulence model simulations for Z moment

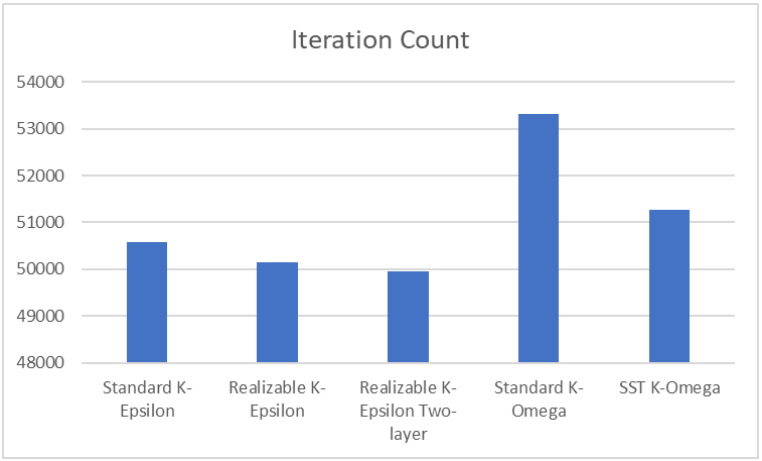

Figure 4-23 Bar chart showing iteration count for each turbulence model simulations

Based on preliminary results focusing on the error percentage compared with the towing tank, the Realizable K-Epsilon two-layer model proved to be the most accurate, with an error margin

close to 3% for both the Y force and Z moment. Following this the two K-Omega models performed better than the other K-Epsilon models. All models fell under the minimum desired accuracy 5%, therefore the runtime and stability must now to be considered. Comparisons between the turbulence models to the Y force and Z moment are seen in Figure 4-21 and Figure 4-22, respectively.

All simulations remained stable for the entire 24 hours of runtime, with no simulations diverging or having any noticeable stability issues. Both the Realizable K-Epsilon and SST K-Omega had less consistent trends with minor divergence at random points throughout this relation. This however never built up to cause a complete simulation failure but rather brought back into stability within a few time steps. This happened most notably at the maximum Y velocity points along the PMM path, i.e. where the path crosses the x-axis. Based on this these two models would not be considered for future simulations after the study.

The final evaluation of this study is to compare the total number of iterations over the 24-hour runtime. The total number of iterations for each turbulence model is shown in Figure 4-23. The higher the value the more efficient the simulation and turbulence model were. As seen from the bar chart the standard K-Omega model proved to be the most efficient, with a total of just over 53,000 iterations. The next model was the SST K-Omega model with over 51,000 iterations. However, as mentioned above the SST K-Omega model lacks the desired stability, so is no longer be considered for future work. The standard K-Epsilon model was the most efficient out of K-Epsilon trio, with the two-layer model being the least efficient and most accurate. Based on these results the best model that ensured consistent accuracy as well as efficiency was the standard K-Omega model. This is the model used throughout all future simulations.

4.4.4. Validation and verification study

Within this section as described validation and verification of the simulations are presented. The methodology used here is the same as that used in chapter 10.3.

The numerical uncertainty for the simulation was calculated, U_{SN}, along with the numerical errors, δ_{SN}. The numerical errors are assumed to be composed of three elements, the iterative convergence error (δ_I), grid-spacing convergence error (δ_G) and time-step convergence error (δ_T). These, in turn, defines equations (10-17) & (10-18) as proposed by Stern et al (2001) for the numerical error and uncertainty within the simulation. As mentioned previously the iterative uncertainty is not included in this validation and verification study. Therefore only the grid spacing (U_G) and time step (U_T) is presented.

This study like the previous study uses the grid convergence index (GCI) Roache (1998). For each study the uncertainty being investigated was systematically varied by a specific value. For the time step uncertainty study the finest mesh is used for all three of the simulations. The mesh convergence is the inverse, i.e. the smallest time step is used with the grid being coarsened throughout the whole domain by a specific value.

Equations (10-19), (10-20) and (10-21) define the convergence ratios used to specify the different convergence condition. The four convergence conditions are noted as follows: (i) monotonic convergence ($0<R_k<1$), (ii) oscillatory convergence ($R_k<0$; $|R_k|<1$), (iii) monotonic divergence ($R_k>1$), and (iv) oscillatory divergence ($R_k<0$; $|R_k|>1$) Stern, et al. (2006). The generalised Rirchardson extrapolation is used to predict the uncertainties and numerical error in condition (i). To obtain the uncertainties for condition (ii) a further step must be applied, this is seen in equation (10-22).

Following the same procedure as used in chapter 10.3 a uniform refinement ratio (r_G) is used for the grid convergence study. As in previous work this value is set at $\sqrt{2}$, with the boundary layer around the hull form adapting to this new mesh size. This is vital to ensure that the Y+ value around the hull form is consistent between the free simulations.

Table 4-12 Grid convergence cell numbers for the DTMB validation and verification study

Mesh Configuration	*Cell Base size*	*Cell Number*	*Channel Cell Count*	*Overset Cell Count*	*Average Y+*
Fine	9 m	3,871,092	3,046,066	825,024	275
Medium	12.72 m	1,811,133	1,373,846	437,287	281
Coarse	18 m	981,710	619,046	362,664	271

Table 4-12 shows the breakdown for the 3 simulations used for the grid convergence study, with the cell count overset and channel along with the average Y+ value acting on the wetted surface area of the hull. This Y+ value was set to be 290, but due to the oscillating nature of the PMM path, the variation in velocity causes a decrease in the average Y+ on the hull.

As multiple values have been calculated for these simulations, namely the Y force and the Z moment, a combined average for each simulation is taken for the study. However, these independent values are checked to ensure they are following desired path i.e. monotonic convergence. To speed the analysis up, the procedure presented by Stern, et al. (2001) was converted into a function within friendship framework by colleague Maarsch (2017). This function was integrated into the fully parametric setup to create a fully closed analysis loop.

This can also be defined as an optimisation goal. This was not done in this validation and verification study however, the procedure has been inbuilt to allow for this analysis to be conducted to help find the most accurate possible simulations.

To improve accuracy and stability minor changes were applied to varying relaxation factors in the simulation due to the different systematic studies discussed above.

Table 4-13 Grid convergence error percentages for Y force, Z moment and combined

Mesh Configuration	*Combined Error %*	*Y Force Error %*	*Z Moment Error %*
Fine	4.325	4.1	4.55
Medium	7	6.9	7.1
Coarse	11.98	12.21	11.75

The error percentages for the three grid convergence simulations are shown in Table 4-13. As can be seen fine mesh with nearly 4 million cells achieves accuracy close to 4%. As the cell numbers decrease the convergence condition follow monotonic convergence pattern. This along with the corrected and uncorrected numerical uncertainty with respect to the experimental data is shown in Table 4-14.

Table 4-14 Calculated validation and verification values for grid convergence study for the DTMB hull

	Y Force	*Z Moment*	*Combined*
S1	4.12 %	4.55 %	4.325 %
S2	6.90 %	7.11 %	7.00 %
S3	12.21 %	11.75 %	11.98 %
ε_K21	2.8	2.55	2.675
ε_K32	5.31	4.65	4.98
Convergence condition Rk	0.52731	0.54839	0.53715
Numerical error WRT EFD	2.8 %	2.55 %	2.675 %
Uncorrected			
Numerical uncertainty	3.7575 %	4.1893 %	3.9632 %
Validation uncertainty	4.513 %	4.8789 %	4.686 %
Comparison error	-4.1 %	-4.55 %	-4.325 %
Corrected			
Numerical uncertainty	0.3930 %	0.5411 %	0.4530 %
Validation uncertainty	2.531 %	2.558 %	2.541 %
Comparison error	-1.3 %	-2 %	-1.65 %

Along the grid convergence the time step convergence was also calculated using the method above. These results are shown in Table 4-15, with the error being slightly smaller than that observed in the grid convergence study. The time steps used for this study were as follows 0.0125, 0.01767 and 0.025 seconds, which used a multiplying base of $\sqrt{2}$.

Table 4-15 Calculated validation and verification values for time step convergence study for the DTMB hull

	Y Force	*Z Moment*	*Combined*
S1	3.89 %	3.77 %	3.83 %
S2	5.65 %	6.12 %	5.885 %
S3	9.87 %	10.13 %	10 %
ε_K21	1.76	2.35	2.055
ε_K32	4.22	4.01	4.115
Convergence condition Rk	0.417	0.586	0.499
Numerical error WRT EFD	1.76 %	2.35 %	2.055 %
Uncorrected			
Numerical uncertainty	2.2608 %	5.2804 %	2.2551 %
Validation uncertainty	4.1667 %	6.3351 %	4.1636 %
Comparison error	-3.89 %	-3.77 %	-3.83 %
Corrected			
Numerical uncertainty	0.5008 %	0.9768 %	0.2050 %
Validation uncertainty	3.5357 %	3.6338 %	3.5060 %
Comparison error	-2.13 %	-1.42 %	-1.775 %

As seen from Table 4-14 & Table 4-15 both studies found monotonic convergence based on the calculated convergence condition Rk being within zero and positive one. The grid convergence study, although having slightly larger errors, was found to have a smaller corrected numerical uncertainty with a finer difference between the Y force and the Z moment. Although having small errors it appears that the time step has a more dominant influence on the uncertainty and therefore must be carefully calibrated to ensure future simulations do not diverge.

$$U_v^2 = U_D^2 + U_{SN}^2 \tag{4-4}$$

$$|E| < U_v \tag{4-5}$$

To ensure the validation has been successful a comparison error E must be compared to the validation uncertainty error. The comparison error must, calculated from the equation (4-4),

be smaller than validation uncertainty error, equation (4-5), Stern, et al. (2006). The modulus of the comparison error |E| is taken. All validation uncertainty error percentages for the uncorrected grid convergence study are greater in the modulus of the comparison error, with the closest comparison being observed for the uncorrected Z moment with a difference of 0.3289.

As seen above all studies conducted from time step also achieve the desired validation based on Stern, et al. (2006) approach. For the time step convergence study, the closest comparison is seen to be the uncorrected Y force, with a difference of 0.2767.

Based on the results above it can be concluded that the base simulation is valid to be taken forward for further analysis. This is includes an extra degree of freedom, namely roll, an introduction of waves while the PMM tests are being conducted.

4.4.5. Roll decay systematic study

Before moving on to the next level simulations a final systematic study to validate the accuracy of the CFD setup is conducted. As future simulations include roll, it is vital to test the current simulation setup's ability to capture the roll characteristics of the vessel. To do this a roll decay study is completed, which are compared to the research conducted by Lungu (2019). Lungu (2019) used a specifically designed simulation to model and replicate experimental data for the DTMB 5415 while undergoing a roll decay towing tank test at varying angles.

The systematic study aims to achieve a satisfactory level of accuracy compared to both the CFD and EFD results by using the standard setup used in the validation and verification study. It is unlikely the standard setup is able to achieve the accuracy level produced by Lungu (2019), as the CFD simulation setup used in their research used a cell count of around 35 million, compared to just under 4 million for this study. The purpose of this study is to focus on the motions and not the specific flow details around the hull. In addition to the work presented by Lungu (2019), research conducted by Gao & Vassalos (2011) is also be used as a reference point for this analysis. This is primarily due to the lack of speed data used for simulations, whereas Gao & Vassalos (2011) present the Froude number used for the computations. Therefore, this is the primary source used to compare the accuracy. However, Lungu (2019) use nondimensionalised data with respect to the speed and length of the vessel, which in turn can be compared with the data presented by Gao & Vassalos (2011).

As presented by Gao & Vassalos (2011), the model is travelling at a Froude number of 0.138. This equates to a model speed of 0.86467 m/s. This data was inputted into the automatic boundary layer function, which in turn gave the required settings to maintain a Y+ over 250.

An initial roll angle of 10° was defined to match the test conducted by Gao & Vassalos (2011) and Lungu (2019).

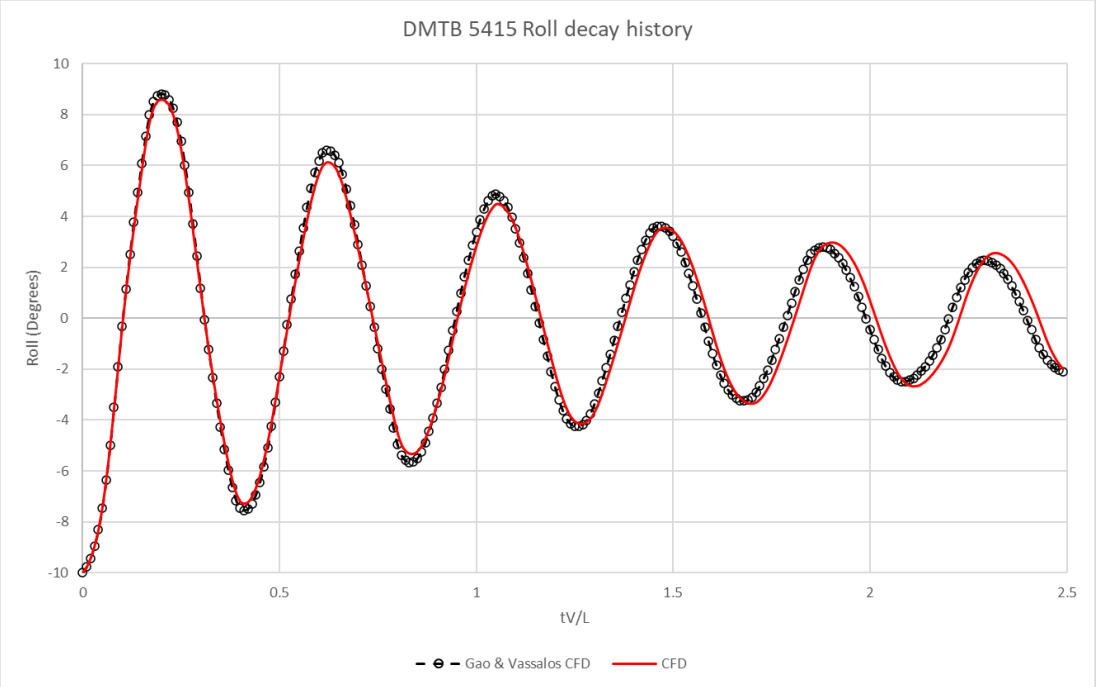

Figure 4-24 DTMB 5415 Roll decay history comparison

As can be seen from Figure 4-24, the simulations are in good agreement with the results presented by Gao & Vassalos (2011). There is an initial effect of greater dampening at the higher roll angles, with the rate of decay increasing compared to Gao & Vassalos (2011), whereas at around 3.5° the rate of decay decreases in comparison causing a slower roll decay with a minor increase in the period. This is noted to be less than 2.5% increase in the period length, as well as less than 6% increase for the final period when compared with Gao & Vassalos (2011) results. Overall, the result exceeded expectations as this simulation is not specifically geared towards such low Reynolds numbers. Based on this, it is with confidence that this simulation setup can be taken forward to evaluate how the roll effect influences the forces and dynamics and the PMM test cases. It is also a confidence that the motions of the vessel are accurately captured based on the systematic studies.

4.5. Additional degree of freedom comparison with SIMMAN towing tank tests

Within this section the simulations replicating various towing tank simulations ran for SIMMAN 2014 are presented. This mainly represent the accuracy that can be achieved using the model presented, as well as laying the foundation for adding an extra degree of freedom

for the simulations. The tests being replicated in the CFD simulations are given in the Table 4-16. Three different Froude numbers is simulated along with up to 4 different lateral amplitudes. These tests were selected to give the broadest overview of all the tests conducted for SIMMAN 2014 on bare hull DTMB 5415. A full table of all towing tank tests conducted is provided in the appendix.

Table 4-16 SIMMAN 2014 DTMB PMM Towing tank test input data (SIMMAN, 2014)

Test Number / *FN 0.138*	*Period (s)*	*Max Y (m)*	*X Velocity (m/s)*	*1/Period (hz)*
1067	14.96	0.1597	0.865	0.066865
1069	14.96	0.6383	0.865	0.066865
1070*	12.02	0.5103	0.865	0.083179
1155	14.96	0.3190	0.865	0.066865
FN 0.210				
1126	8.56	0.6428	1.755	0.116883
1158	8.56	0.1667	1.755	0.116883
1160	8.58	0.4283	1.755	0.11658
FN 0.410				
1131	4.78	0.4323	2.57	0.209303
1143	4.80	0.2883	2.57	0.208334

The corresponding Froude numbers, shown in Table 4-16, equate to 10, 15 and 30 knots, respectively. All simulations and tests have heave and pitch free, with surge, sway and yaw being controlled by the PMM mechanism. The PMM inputs were ran through the parametric modelling setup ensuring that every simulations setup would correspond accurately to the carriages speed and oscillation. In addition, the corresponding boundary layers were calibrated to ensure a Y+ value over 250 is maintained.

In addition to monitoring the Y force and Z moment, the sinkage and trim on the vessel is also monitored to compare with the towing tank tests. As CFD allows for difficult flow phenomena to be visualised easily, the flow and turbulence acting around the hull is also be monitored and visualised. This is key to understanding how key aspects of the hull affect the performance of the vessels manoeuvring characteristics. This is where numerical simulations outperform the standard and classical towing tank tests, in addition to allowing rapid iterations to be tested, for example the shape and position of the bilge keels.

To visualise the vorticity and flow produced by the hull and the bilge keels while undergoing a PMM test a couple of specific steps are required. Initial step is to define a volumetric threshold, this is simply a region which is defined by a scalar field function, this can be an inbuilt field function like turbulent viscosity or a user-defined function. An example of a user-defined function may be the underwater area of the hull or the relative Froude number along the hull. Once the volumetric threshold has been defined some cross sections can be created from this volume, these cross sections can then be used to visualise specific flow which is in the bounds and define the volume and region. Therefore, vortices created from the bulb or bilge keels can be clearly and easily visualised.

As highlighted above the simulations used in this study have a lower mesh than those used by Gao & Vassalos (2011). This allowed the simulations to have a shorter run time, however when comparing the simulation results with the towing tank tests presented in Table 4-16, the low-speed simulations had a greater error with respect to the Y force compared with the verification study results. This is likely due to the high Y plus used for these simulations. This increase in error is not noticed when comparing the moment around the z-axis. The error results for the towing tank tests are given in Table 4-17.

Table 4-17 Y force and Z moment percentage error comapred with SIMMAN 2014 tank data

		Y Force %	*Z Moment %*
FN 0.138	***1067***	7.52	24.34
	1069	10.63	6.439
	1070*	7.47	10.64
	1155	7.75	10.88
FN 0.210	***1126***	5.50	6.59
	1158	4.22	1.84
	1160	8.35	6.05
FN 0.410	***1131***	7.27	7.89
	1143	5.58	7.26

As mentioned, the Y force error observed the lower speed simulations is noticeably greater than that of the high-speed. Not only this but the tests with the smallest lateral amplitude have the greatest error. This error however falls within reasonable bounds, as well as below the maximum potential error from towing tank tests. The uncertainties calculated for the DTMB 5415 FORCE hull form are given in Table 4-18, Simonsen (2004). As can be seen when comparing Table 4-17 & Table 4-18, the uncertainty and error decreases as the velocity of the

PMM carriage/Froude number increases. Further to this, Table 4-19 presents the uncertainty for the moment around Z axis, yaw moment, which in turn also follows the same pattern of reducing error as speed increases. The error observed for the towing tank with respect to the yaw moment is lower than that of the presented CFD simulation at the maximum speed.

Table 4-18 Uncertainties and bias limits related to the Y-force, where r = rmax (Simonsen, 2004)

	Fr=0.138	Fr=0.280	Fr=0.410
r_{max} [rad/s]	0.065	0.132	0.193
B_{F_Y} [N]	0.433	0.954	1.175
F_Y [N]	-16.200	-73.236	-155.433
B_{F_Y} in % of F_Y [%]	2.7	1.3	0.8
$B_{Y'}$ [--]	0.00174	0.00094	0.00056
$P_{Y'}$ [--]	0.00057	0.00025	0.00018
$U_{Y'}$ [--]	0.00183	0.00097	0.00059
Y' [--]	-0.01155	-0.01759	-0.01704
$U_{Y'}$ in % of Y' [%]	15.8	5.5	3.5

Table 4-19 Uncertainties and bias limits related to the yaw moment, where r = rmax (Simonsen, 2004)

	Fr=0.138	Fr=0.280	Fr=0.410
r_{max} [rad/s]	0.065	0.132	0.193
B_{M_Z} [Nm]	0.750	1.762	1.771
M_Z [Nm]	-10.217	-56.129	-162.448
B_{M_Z} in % of M_Z [%]	7.3	3.1	1.1
$B_{N'}$ [--]	0.00074	0.00043	0.00024
$P_{N'}$ [--]	0.00008	0.00011	0.00009
$U_{N'}$ [--]	0.00075	0.00045	0.00026
N' [--]	-0.01025	-0.01348	-0.01821
$U_{N'}$ in % of N' [%]	7.3	3.3	1.4

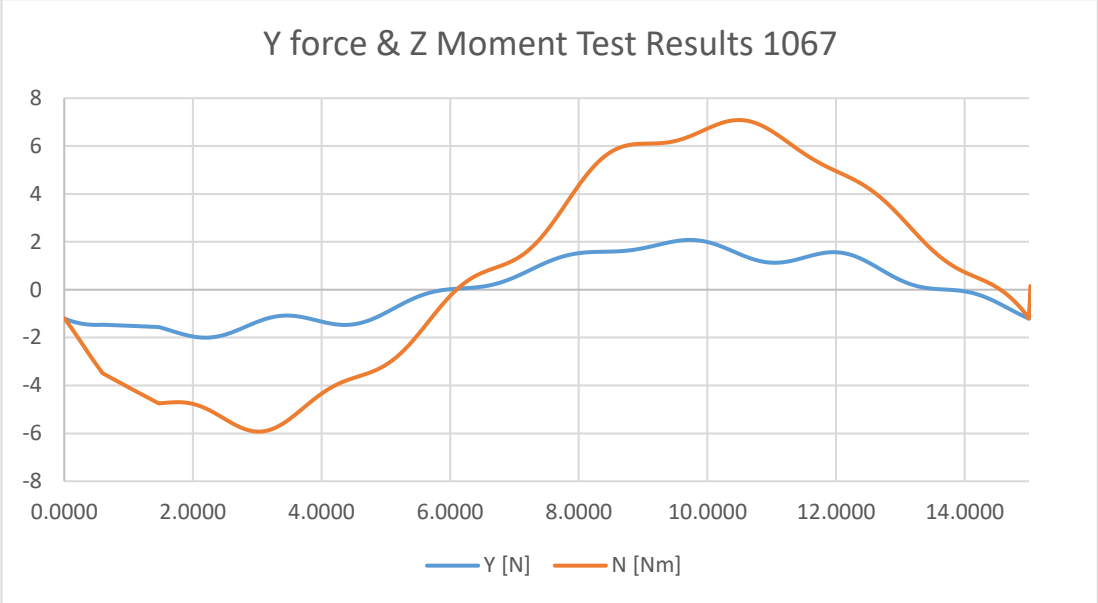

Figure 4-25 Graph showing towing tank results data for Y Force and Z Moment for test 1067 (SIMMAN, 2014)

An example of the towing tank data provided by SIMMAN 2014 is shown in Figure 4-25. The results shown are from the test which had the lowest speed, longest oscillation, and smallest lateral amplitude. Thus, having the smallest possible oblique flow acting around the hull. Due to the slow flow characteristics the results observe an oscillatory fluctuation for both the Y force and moment around Z axis. This is not observed for the CFD simulations, as the mesh and time step are tailored to each simulation.

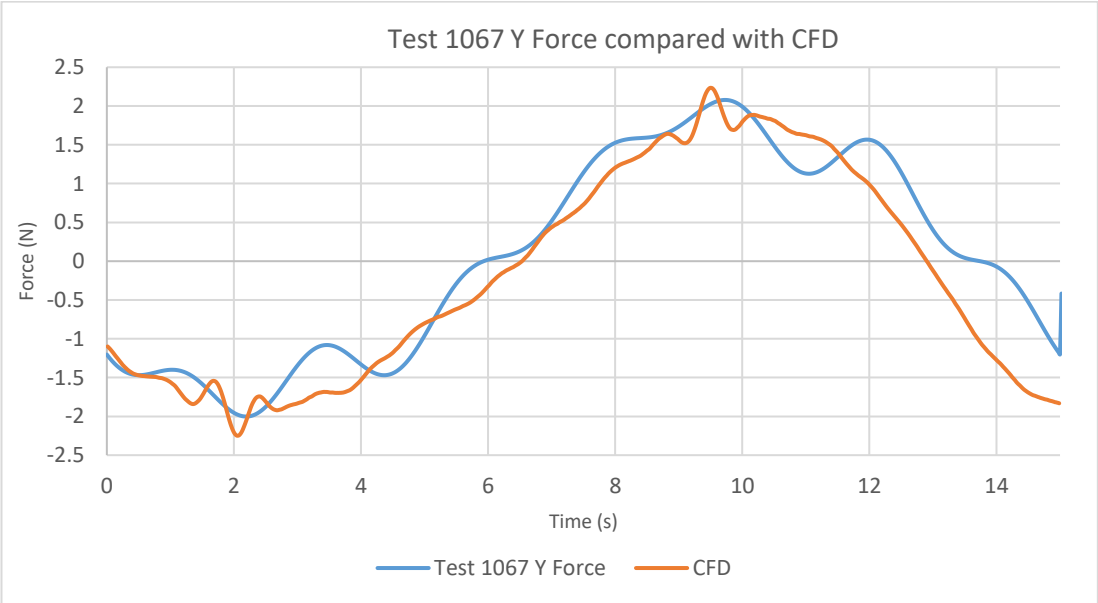

Figure 4-26 Graph shown a comparison between towing tank test 1067 Y force and CFD computed Y Force

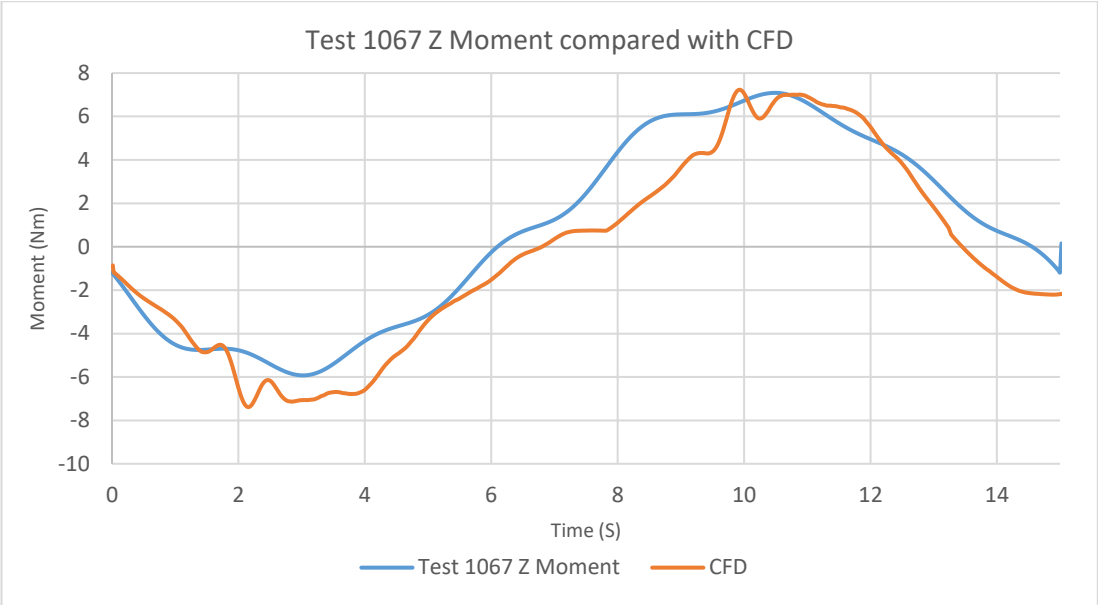

Figure 4-27 Graph shown a comparison between towing tank test 1067 Z Moment and CFD computed Z Moment

As seen from Figure 4-26 and Figure 4-27 the CFD results follow the towing tank tests path within reasonable accuracy. Due to the oscillatory error occurring in the towing tank data there are periods when a CFD significantly deviates from the towing tank data. However, the key regions namely the maximum and minimum closely match the towing tank data. The CFD results also have an improved symmetry along the x-axis compared with the towing tank. This is particularly noticeable when looking at Figure 4-27, as both the maximum and minimum of the CFD are around ±6.5 Nm respectively, whereas the towing tank varies from -6 to positive 6.5 Nm. It is unclear the exact cause however it is most likely due to the oscillating effects being observed at this low speed and low amplitude. These results are least accurate compared with the towing tank data, as well as having the greatest uncertainty for the towing tank data but enabled analysis of how the parametric method developed above performs.

Further to this, the low-speed runs help to highlight key regions within the overset domain which may require finer mesh refinement to improve the simulation accuracy. These regions were focused around the bulbous bow and bilge keels along the hull.

For an improved comparison, the nondimensional manoeuvring coefficients are presented for both the towing tank and CFD simulations, rather than the pure forces and moments in graphical form. The standard nondimensional equations for static tests are presented in equations (4-6), (4-7) & (4-8) (Simonsen, et al., 2012).

$$X' = \frac{F_{x\,measured}}{0.5\rho U^2 T_m L_{BP}} \tag{4-6}$$

$$Y' = \frac{F_{y\,measured}}{0.5\rho U^2 T_m L_{BP}} \tag{4-7}$$

$$N' = \frac{M_{z\,measured}}{0.5\rho U^2 T_m L_{BP}^2} \tag{4-8}$$

As the PMM tests are a dynamic test more complex nondimensional equations must be used. As dynamic tests include inertial forces due to exhilaration, these inertial contributions must be subtracted to get the hydrodynamic part, these inertial accounted for equations are shown in equations (4-9), (4-10) & (4-11) (Simonsen, et al., 2012), with the difference in distance between the pivot point and centre of gravity used in these equations. These equations are not required as they only account for any measurable distance between the centre of gravity and the point of rotation in longitudinal and transverse directions, *X* and *Y*.

$$X' = \frac{F_{X\,measured} + M\left(\dot{u} - rv - \dot{X}_G r^2 - Y_G \dot{r}\right)}{0.5\rho U^2 T_m L_{BP}} \tag{4-9}$$

$$Y' = \frac{F_{y\,measured} + M(\dot{v} - ru - Y_G r^2 - X_G \dot{r})}{0.5\rho U^2 T_m L_{BP}} \tag{4-10}$$

$$N' = \frac{M_{Z\,measured} + I_Z \dot{r} + M\left(X_G(\dot{v} + ru) - Y_G(\dot{u} + rv)\right)}{0.5\rho U^2 T_m L_{BP}^2} \tag{4-11}$$

A comparison between the nondimensional factors calculated for the experimental and CFD results are given in Table 4-20. Both the maximum and minimum nondimensional factors and the corresponding percentage error is provided in this table. As noted above, the smallest errors are observed in the Fn 0.28 and 0.41 tests, with the smallest errors occurring for test 1158.

Table 4-20 Calculated nondimensional factors for Y force and Z moment for peak values of EFD and CFD

	EFD		*CFD*			
	Y'	*N'*	*Y'*	*N'*	*Error %*	
1067	-0.0077	-0.0057	-0.0087	-0.0071	-12.35	-24.34
	0.0080	0.0068	0.0086	0.0067	-7.52	1.40
1069	-0.0350	-0.0253	-0.0382	-0.0237	-9.19	6.44
	0.0325	0.0264	0.0359	0.0248	-10.63	5.92
*1070**	-0.0512	-0.0362	-0.0543	-0.0385	-5.95	-6.21
	0.0454	0.0360	0.0488	0.0398	-7.47	-10.65
1155	-0.0158	-0.0116	-0.0171	-0.0128	-7.75	-10.88
	0.0155	0.0126	0.0167	0.0127	-7.73	-0.70
1160	-0.0397	-0.0248	-0.0427	-0.0251	-7.57	-0.90
	0.0383	0.0246	0.0351	0.0261	8.35	-6.05
1158	-0.0210	-0.0112	-0.0203	-0.0110	3.68	1.81
	0.0195	0.0118	0.0203	0.0120	-4.23	-1.85
1126	-0.0307	-0.0224	-0.0324	-0.0209	-5.50	6.59
	0.0324	0.0238	0.0336	0.0224	-3.64	5.75
1131	-0.0331	-0.0298	-0.0331	-0.0321	0.06	-7.89
	0.0357	0.0313	0.0331	0.0319	7.30	-1.94
1143	-0.0200	-0.0186	-0.0203	-0.0200	-1.55	-7.26
	0.0211	0.0200	0.0200	0.0200	5.59	-0.21

Following these results an investigation was conducted to evaluate the effect of rolling while conducting a PMM test. The experiment result provided by SIMMAN 2014 were limited to heave and pitch motions only, therefore additional simulations includes roll. Six out of the nine tests are evaluated. The three tests excluded from this investigation was due to the erratic and noisy experimental results data. This noisy data and lack of consistency primarily occurred at low speeds with tests 1070 and 1155 being excluded, with test 1158 also being excluded. Although test 1158 has the smallest error compared with the experimental for peak values, the overall comparison between the experiment and CFD paths were relatively noisy. On the other hand, the other six tests or maintained the minimum level of noise in the simulated results.

The results comparing the nondimensional Y force and Z moment between 2 DOF (heave and pitch) and 3 DOF (heave, pitch and roll) are shown in Table 4-21, with the peak forces given in Table 4-22.

Table 4-21 Nondimensional factors for Y force and Z moment comparing 2 DOF and 3 DOF CFD simulations

	HP		*HPR*			
	Y'	*N'*	*Y'*	*N'*	*Error %*	
1067	-0.0087	-0.0071	-0.0084	-0.0068	3.00	4.03
	0.0086	0.0067	0.0084	0.0066	2.00	2.10
1069	-0.0382	-0.0237	-0.0392	-0.0260	-2.75	-9.50
	0.0359	0.0248	0.0362	0.0270	-0.75	-8.78
1160	-0.0427	-0.0251	-0.04	-0.0254	6.44	-1.55
	0.0351	0.0261	0.0363	0.0265	-3.65	-1.24
1126	-0.0324	-0.0209	-0.0341	-0.0231	-5.15	-10.70
	0.0336	0.0224	0.0351	0.0246	-4.50	-9.80
1131	-0.0331	-0.0321	-0.0336	-0.0325	-1.50	-1.22
	0.0331	0.0319	0.0340	0.0326	-2.71	-2.41
1143	-0.0203	-0.0200	-0.0205	-0.0203	-1.20	-1.50
	0.0200	0.0200	0.0204	0.0207	-2.40	-3.50

Table 4-22 Comparison between peak results for Y force and Z moment for 2 DOF and 3 DOF CFD simulations

	HP		*HPR*			
	Y'	*N'*	*Y'*	*N'*	*Error %*	
1067	-2.249	-7.370	-2.182	-7.073	3.00	4.03
	2.235	6.989	2.190	6.843	2.00	2.10
1069	-10.826	-26.892	-11.123	-29.447	-2.75	-9.50
	10.184	28.145	10.261	30.615	-0.75	-8.78
1160	-45.446	-106.799	-42.521	-108.455	6.44	-1.55
	37.349	111.437	38.713	112.830	-3.65	-1.25
1126	-37.299	-96.173	-39.220	-106.464	-5.15	-10.70
	38.670	103.321	40.410	113.446	-4.50	-9.80
1131	-79.614	-308.941	-80.811	-312.712	-1.50	-1.22
	79.529	306.627	81.683	314.005	-2.71	-2.41
1143	-47.430	-187.035	-47.999	-189.841	-1.20	-1.50
	46.708	187.433	47.829	193.993	-2.40	-3.50

From these results in Table 4-21 and Table 4-22 a correlation between vessel speed PMM amplitude can be seen. As the speed increases both the Y force and Z moment increase as the vessel rolls. However, for lower speeds and smaller amplitudes, tests 1067 and 1071, the effect of vessel rolling was a small reduction in both the measured forces. This is most likely due to

the magnitude of roll. For both tests 1067 and 1071 the maximum roll angle is less than 3°, whereas all other tests have significantly greater maximum roll angle is. It is noted by (Liu, et al. (2018) that roll-coupled forces should not be ignored as they may have a noticeable effect.

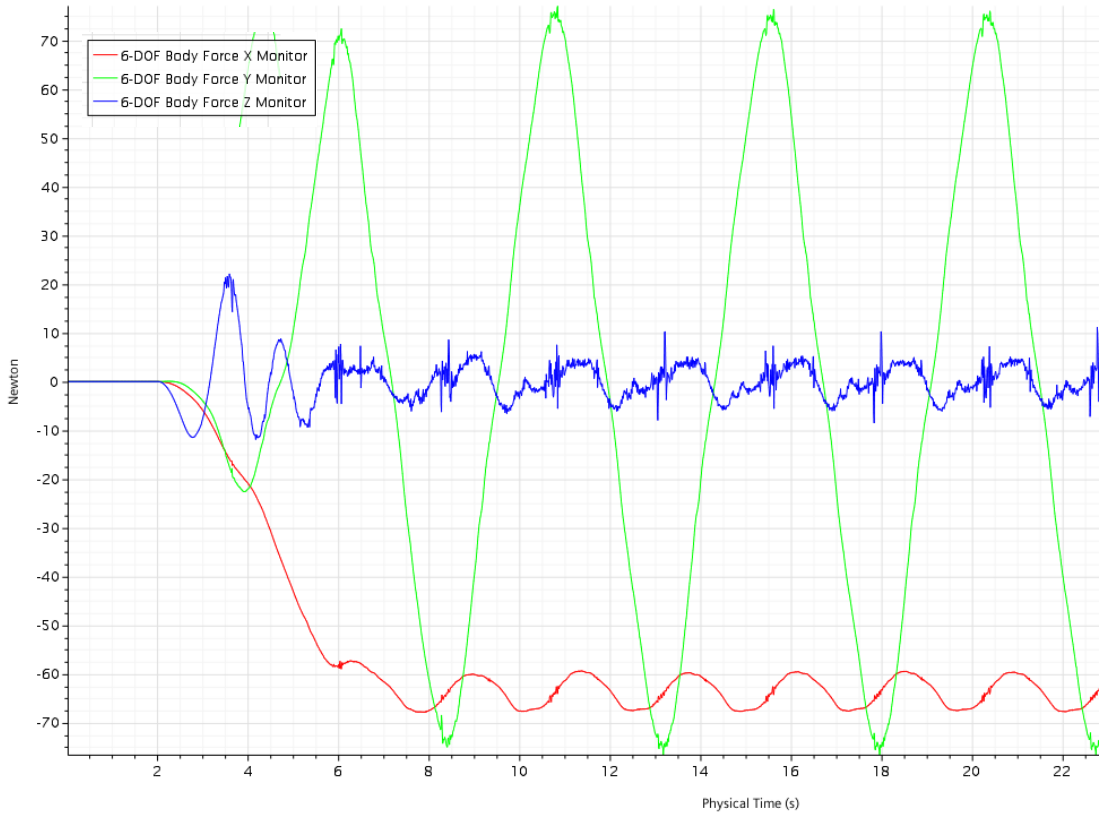

Figure 4-28 DFBI CFD forces results for heave and pitch simulation

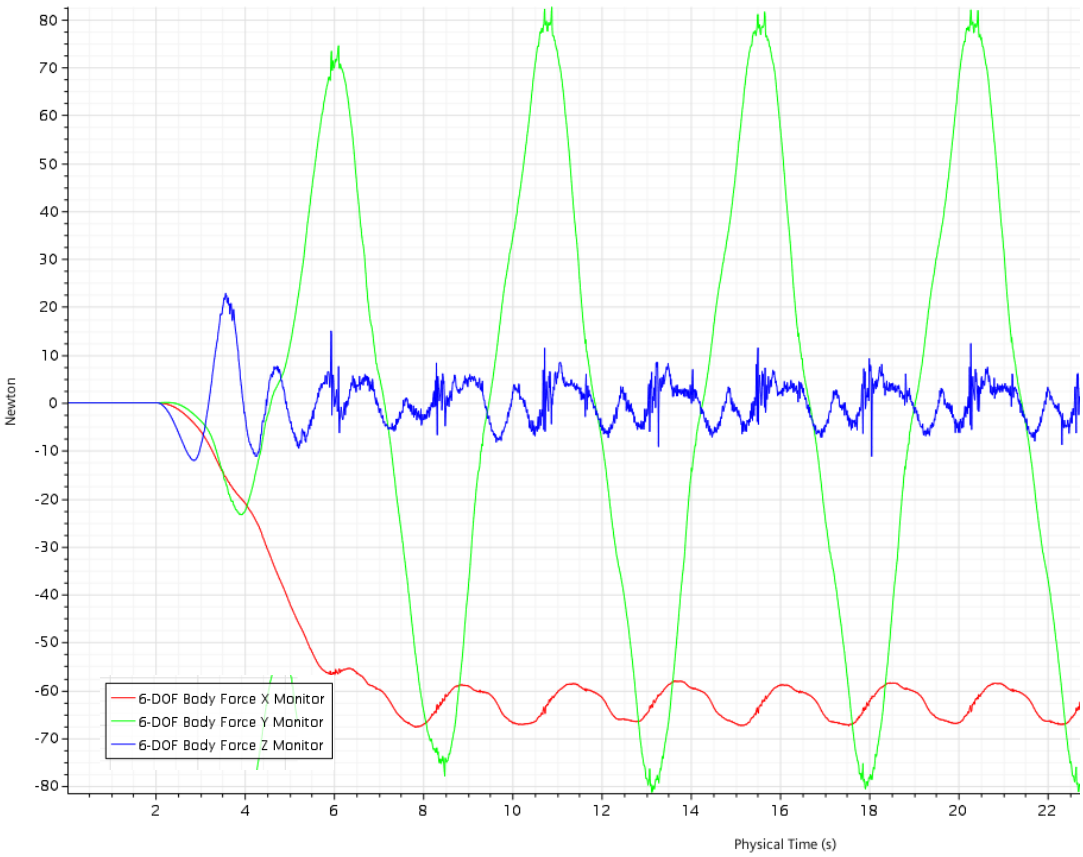

Figure 4-29 DFBI CFD forces results for heave, pitch and roll simulation

Along with the nondimensional peak forces given in Table 4-21 and Table 4-22, the raw data form the CFD simulations are shown in Figure 4-28 and Figure 4-29. This not only shows Y force but also the X force and Z force. They can be seen that at the peak of the PMM oscillation there is a lifting force. In addition to the visualised raw data, images showing the free surface along with the dynamics of the hull are given in Figure 4-30 and Figure 4-31. From these images it can be seen that with the addition of roll the trim/pitch angle reduces and amplitude as well as inverting its pattern. As the vessel achieves its maximum roll angle, pitch flattens out and then oscillates while the vessel traditions from peak PMM amplitudes. Though, when the vessel does not roll, the pitch angle decreases between peaks, opposite to that observed when rolling. This pitching is also the likely cause for the difference in generated vortices from the bulb which are visualised in Figure 4-32 and Figure 4-33. Both images were taken from the exact same time and position along the PMM test. The vessel without roll has a tendency to nose up when reaching the peak amplitude of the PMM oscillation, which in turn induces a noticeable turbulence aft of the bulb seen in Figure 4-32. However, the HPR hull tends to nosedive at the peak of the oscillation amplitude, this reduces the turbulence close to the bow

but increases the turbulence at the aft. The sinkage of the vessel is only slightly affected, with the range between peak and trough becoming slightly greater.

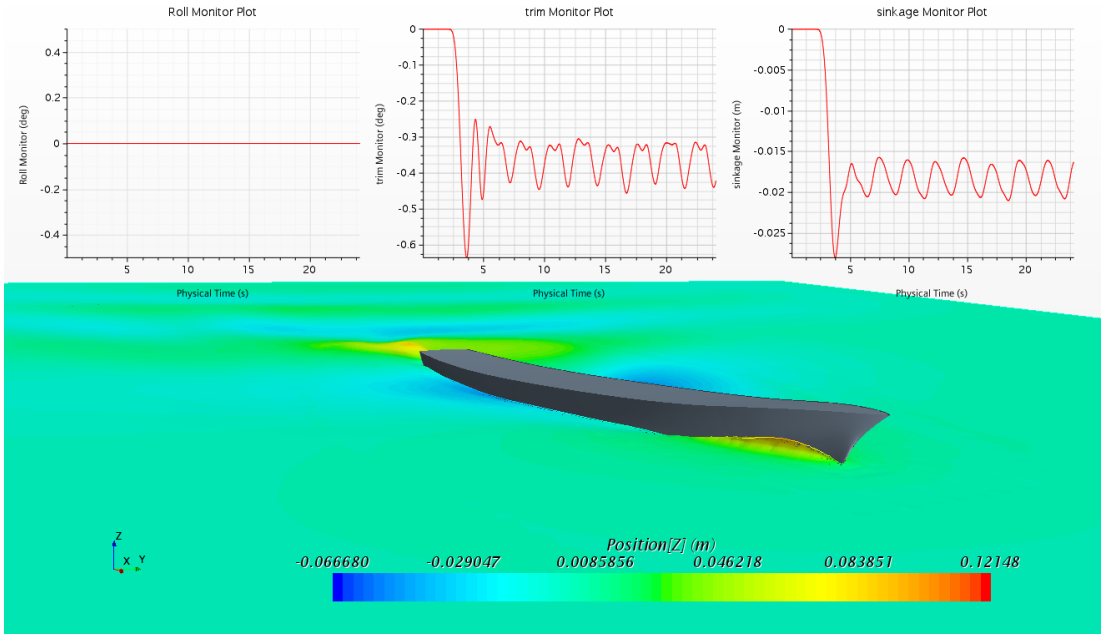

Figure 4-30 DTMB 5415 Hull conducting virtual test 1131 with free heave and pitch monitors, along with the visualised free surface

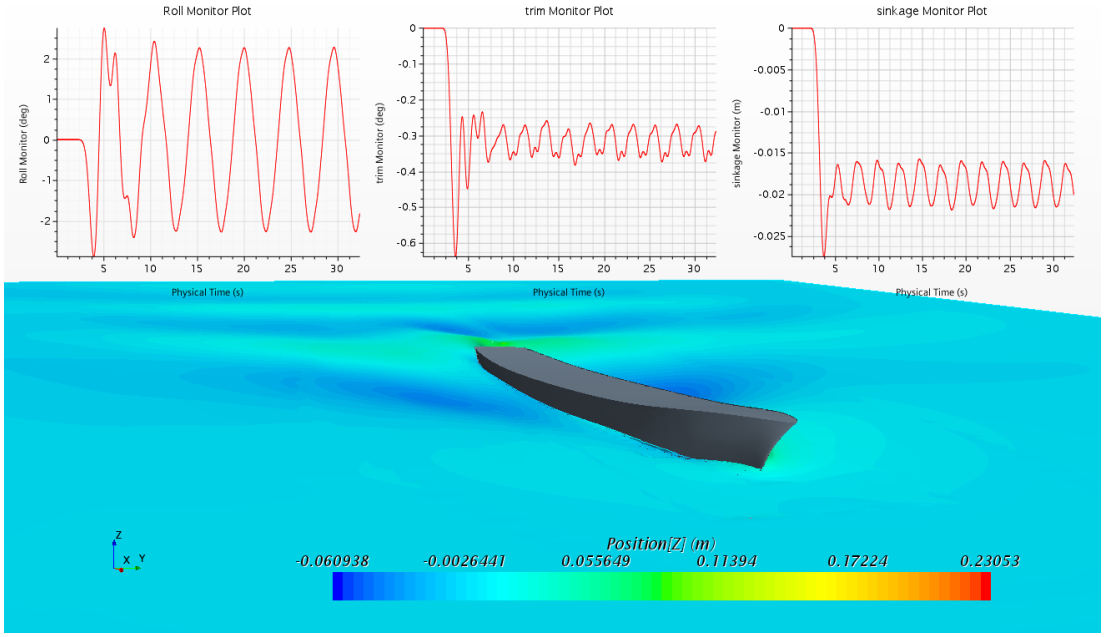

Figure 4-31 DTMB 5415 Hull conducting virtual test 1131 with free heave, pitch and roll monitors, along with the visualised free surface

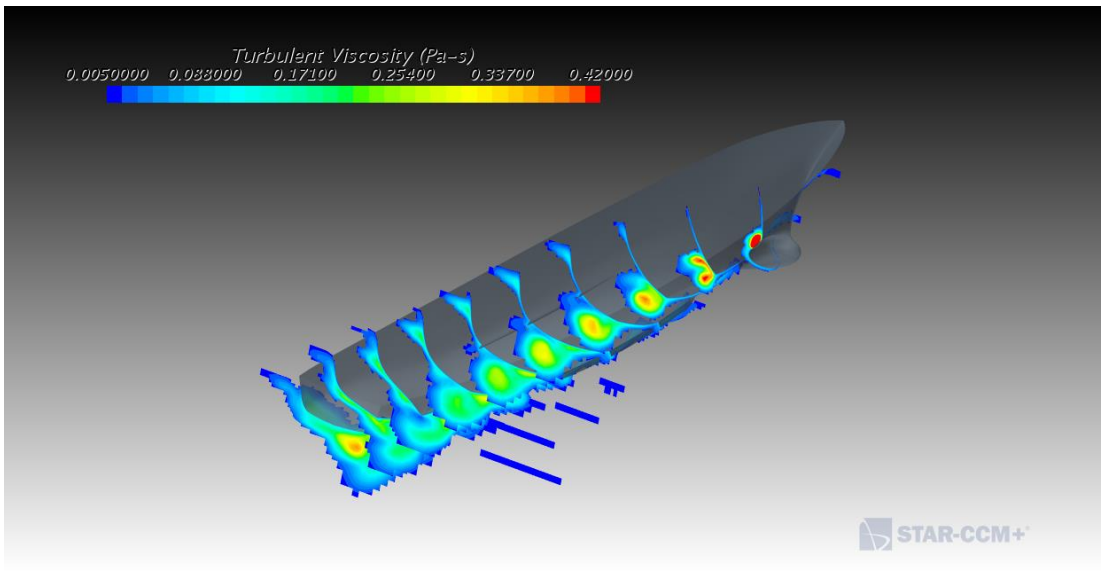

Figure 4-32 Visualised turbulent viscosity of heave and pitch hull prior to peak PMM amplitude

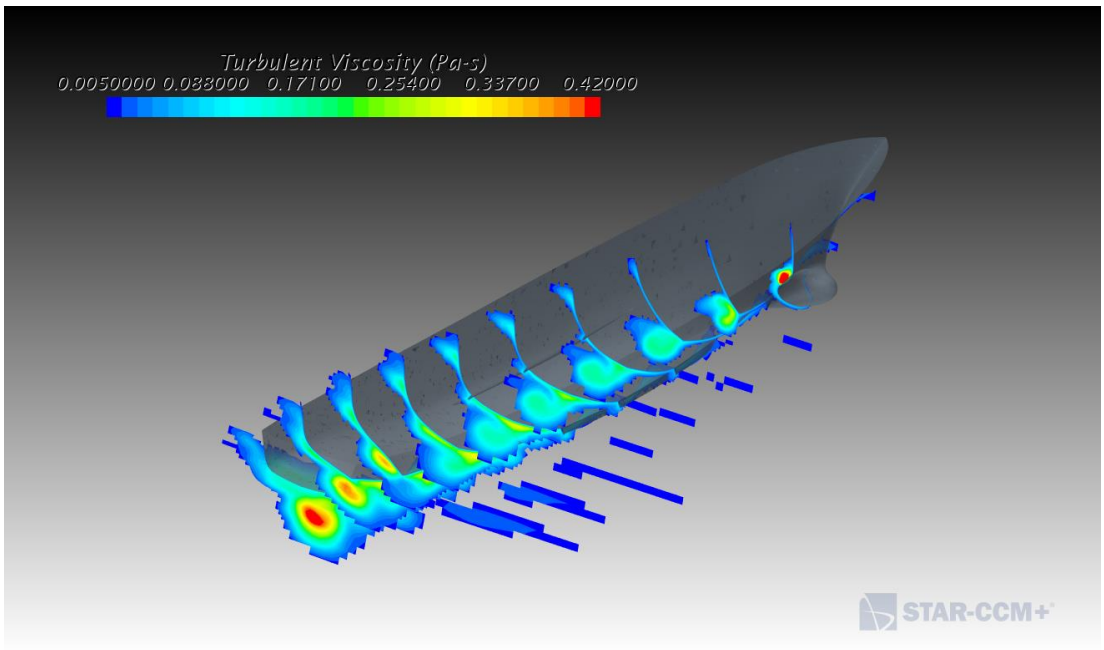

Figure 4-33 Visualised turbulent viscosity of heave, pitch and roll hull prior to peak PMM amplitude

Following this investigation, a study investigating the effects of wave induced forces on the DMTB 5415 hull is conducted focusing on a single PMM test setup, in this case test 1131.

4.6. PMM Simulations with waves

Unlike other investigations, this study systematically investigates the effects of wave induced forces at specific points along the PMM path, and a point along the vessel turn. This study investigates five wavelengths and corresponding positions, and four different wave heights. Each of these tests is further evaluated for different degrees of freedom, with three out of four

wave heights having no free motion. These help to provide the baselines for how the waves are affecting the forces and motions of the hull.

Before conducting the test two prior tasks are completed. First the wavelength and period for the waves are calculated. These parameters need to be calculated for a specific encounter frequency with respect to the PMM frequency. To quickly simplify the task visual code was created in grasshopper for Rhinoceros 3DM. This code generates the input parameters, wavelength and wave period, for a specific factor of the PMM oscillation. This code is visualised in Figure 4-34. The second task is to test and modify the base CFD simulation to include waves.

Initial tests highlighted inconsistent wave height readings from the two different wave probes included in the simulation. The problem was originally considered to be linked to the MRF PMM motions. However, this was not the case as a calm water test was conducted and it was found that the free surface probes produce an inconsistency that matched the irregularity seen in the wave heights. These elevation plots are shown in Figure 4-35 and Figure 4-36, which included a combined wave height and calm water profile which matches the desired wave height. This therefore shows the true simulated wave height matches the input.

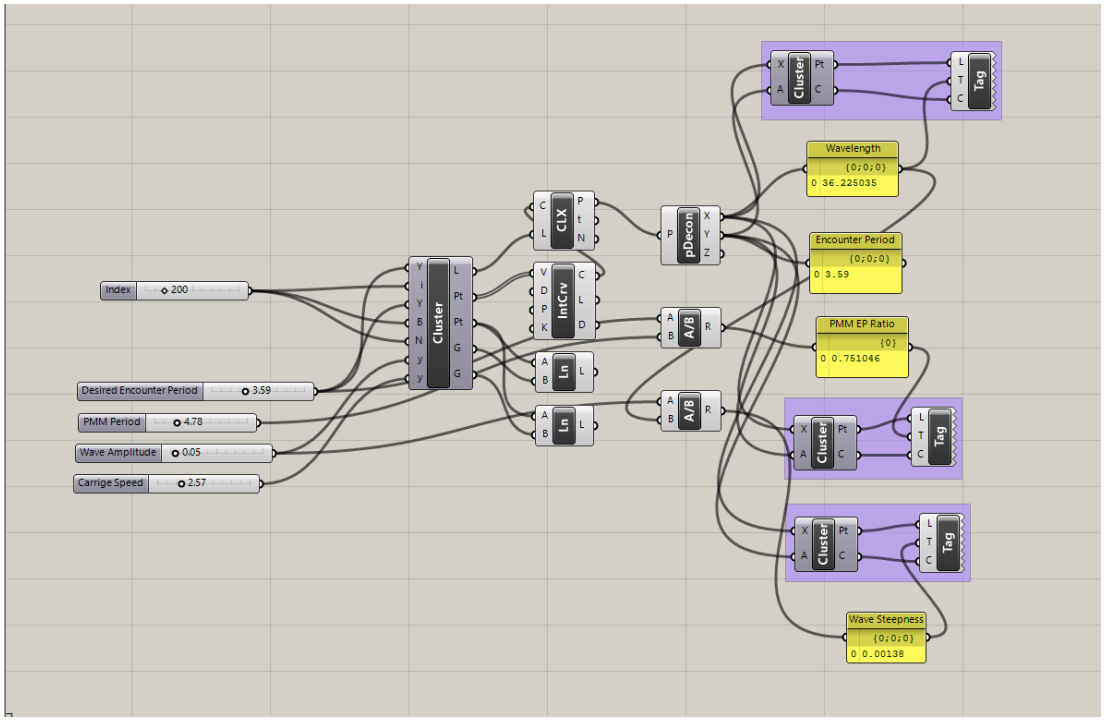

Figure 4-34 Visual code for generating input data for specific encounter wave

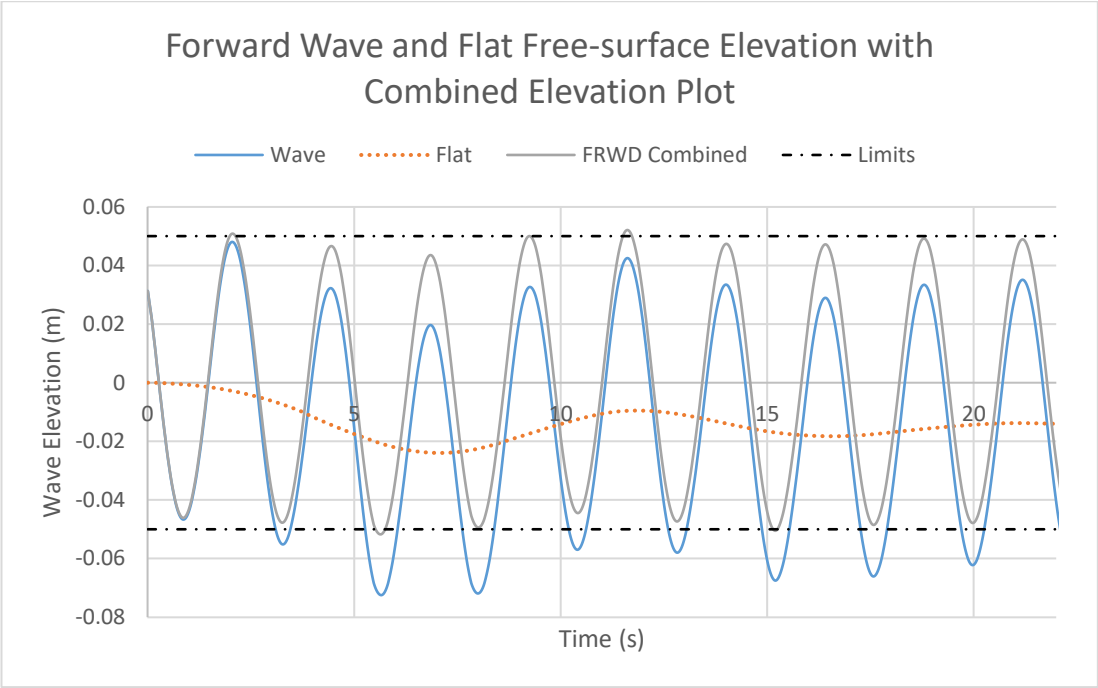

Figure 4-35 Graph showing the forward wave probe free surface elevation output for 0.05 m waves and calm water, along with a plot of these two combined

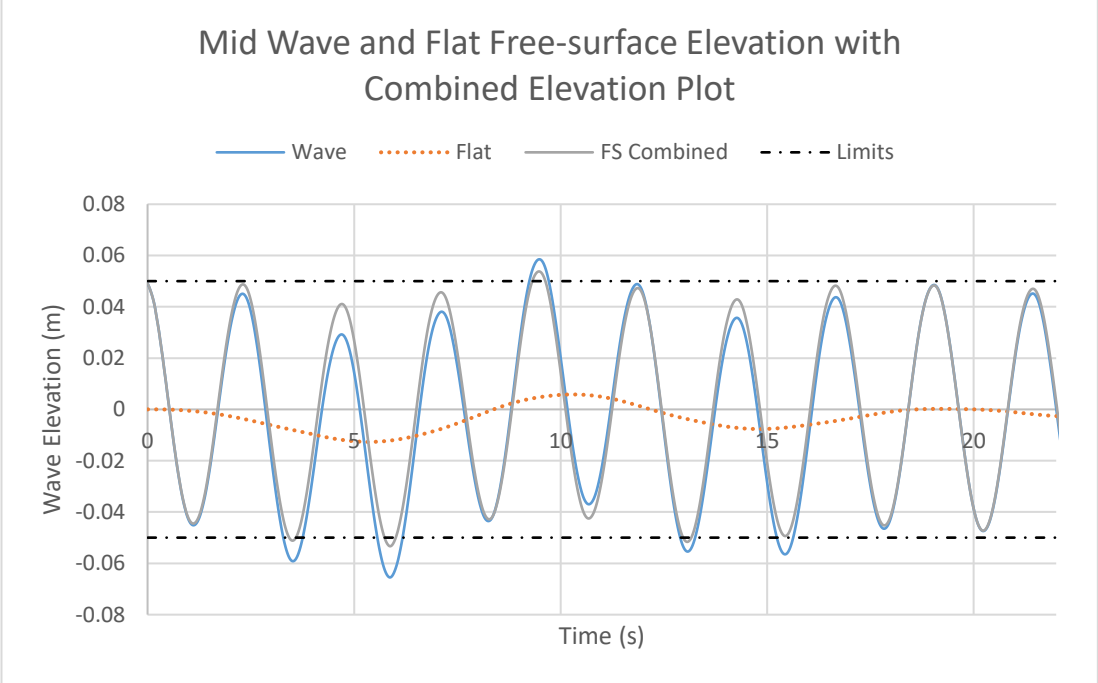

Figure 4-36 Graph showing the mid wave probe free surface elevation output for 0.05 m waves and calm water, along with a plot of these two combined

The corresponding factors that are evaluated, along with the calculated wave periods and lengths are provided in Table 4-23. This table also highlights the advantage of using CFD over the towing tank tests due to the wavelengths required. Along with the five wavelengths, four

wave heights is investigated, 0.1, 0.15, 0.2 and 0.25 m. A requirement was that no wave should exceed linear theory and have wavelength over height ratio less than 40. These wave lengths and periods are defined based on a factor of the PMM oscillation period.

Table 4-23 Factors of PMM period with corresponding wave period and length

Factor	*Period (s)*	*Wavelength (m)*
0.5	2.39	19.24
0.75	3.59	36.23
1.0	4.78	57.62
1.25	5.98	83.75
1.5	7.17	114.14

4.6.1. 0.1 m Wave height results

The maximum and minimum calculated Y forces and Z moments for wave height of 0.1 m are presented in Table 4-24. In addition to this, graphs showing the single PMM oscillation for both HPR and 0 DOF are shown in Appendix vi. Y force graphs shown in Figure 15-2, Figure 15-4, Figure 15-6, Figure 15-8 and Figure 15-10, with Z moment shown in Figure 15-3, Figure 15-5, Figure 15-7, Figure 15-9 and Figure 15-11, respectively.

The first thing that can be observed from Table 4-24 is that for wave factor of 0.5 there is a small reduction in Y force but a noticeable increase in the Z moment. This is due to the wave interacting with the hull at the peak amplitude of the PMM path. This interaction amplifies all motions, as well as causing the wave to additionally force both the bow and aft of the vessel around. This is consistently the most dangerous period for all tests, as the vessel is pivoting on the crest of the shortest wave. However, a wave factor of 1.25 has the smallest Y force with only a minor increase in the Z moment compared to the base calm water result. A factor of 0.75 and 1.0 were found to have the closest results matching the base hull with, with around 5.5% and 1.7% for 0.75 and 5.7% and 0.4% for 1.0 Y force then Z moment, respectively. The largest observed increase occurs for a factor of 1.5 and Z moment, this equates to 11% increase over the baseline. This increase occurs when the maximum amplitude of the PMM fall just for both the peaks of wave, as seen in Figure **15-11**.

In comparison to this the 0 DOF hull form exceeds the baselines Y force consistently along with the Z moment except for factor 0.5. The phase combination between the wave and the PMM oscillations do not greatly occur for the HPR (heave, pitch, and roll) simulation, however they are significantly more noticeable for the 0 DOF simulation. This interaction is most notable for factors are 0.5, 0.75 and 1.0, as the wavelength increases the interaction for both hull forms becomes less noticeable with only slight inflections seen for factor 1.5 in the

Y force for both combinations. These interactions can be seen in Figure 15-10, with the greatest inflections observed around the trough of the wave, which also corresponds to the point with the largest transverse flow passing over the hull.

Overall, there is no excessive distortion by wave height of 0.1 m, with the greatest fluctuations observed around the peaks and troughs for both the PMM and wave oscillation.

Table 4-24 Maximum and minimum observed Y force and Z moment table for wave height of 0.1 m for HPR and 0 DOF simulations

		Y Force Min (N)	*Y Force Max (N)*	*Z Mom Min (Nm)*	*Z Mom Max (Nm)*
Base	*HPR*	-79.614	79.529	-308.941	306.627
0.5	*HPR*	-77.524	77.246	-313.419	325.166
	NM	-95.360	100.649	-309.216	305.350
0.75	*HPR*	-81.008	84.806	-307.209	305.619
	NM	-105.960	94.165	-345.619	318.961
1	*HPR*	-80.136	75.388	-303.582	307.567
	NM	-100.361	93.146	-322.228	321.548
1.25	*HPR*	-73.598	74.840	-318.119	316.039
	NM	-98.194	112.058	-356.656	330.864
1.5	*HPR*	-79.278	84.484	-323.844	344.252
	NM	-102.281	106.391	-375.300	336.393

4.6.2. 0.15 m Wave height results

Following on from the initial wave height of 0.1 m, the next investigation focuses on 0.15 m waves with no 0 DOF simulations conducted. These results can be observed in Table 4-25. As with the previous wave height there is a relatively small variations from the baseline, excluding factor 0.75 which appeared to encounter harmonically induced motions. It is unclear if these motions are due to simulation error or genuine harmonic/parametric motions. Therefore, this simulation and results is considered separate from the group.

Overall, there is consistently less than 6% increase in Y force due to waves for all factors, except for factor 1.5 which had a peek increase of 32.6%. This fluctuation can be seen in Figure 15-20, where there is a clear reduction of Y force as the vessel enters a trough of the wave. This causes a drastic increase in the Y force as the vessel moves out of the trough towards the peak PMM amplitude. Outside of this significant increase, there is a relatively minimal inflections with only factor 0.5 skewing the Y force. This scheme causes a drastic decrease in Y force when moving from the maximum PMM amplitude to the minimum, with the Y force suddenly increasing after reaching the minimum PMM amplitude. All other Y forces, excluding factor 0.5 and the aforementioned point at 1.5, follow more closely to an

exaggerated sinusoidal path. This exaggerated shark tooth pattern can be more clearly seen in Figure 15-12.

The increase in Y force for factor 1.5 only equates to a 13.8% increase in the Z moment, seen in Figure 15-21. This is closely followed by 9.4% increase for factor 0.5, Figure 15-13. As noted above the trend that the factor 0.5 has the largest increase in Z moment also follows here, except for that single point of factor 1.5. Following this trend as the wave height increases the moment on the hull steadily increases as well, with Y force being minimally affected except for key points of interaction. This is seen more clearly through Figure 15-12, Figure 15-14, Figure 15-16, Figure 15-18 and Figure 15-20 for Y force, with Z moment being presented in Figure 15-13, Figure 15-15, Figure 15-17, Figure 15-19 and Figure 15-21.

Table 4-25 Maximum and minimum observed Y force and Z moment table for wave height of 0.15 m for HPR simulations

		Y Force Min (N)	*Y Force Max (N)*	*Z Mom Min (Nm)*	*Z Mom Max (Nm)*
Base	*HPR*	-79.614	79.529	-308.941	306.627
	0.5	-80.489	81.189	-330.022	335.387
	*0.75**	-198.229	200.149	-511.910	506.158
	1	-79.342	75.906	-312.646	315.508
	1.25	-76.028	78.738	-327.487	319.390
	1.5	-84.216	105.477	-327.157	349.031

4.6.3. 0.2 m Wave height results

The minimal increase observed for both the Y force and Z moment for wave heights 0.1 m and 0.15 m is not observed for 0.2 m waves. Unlike the wave height of 0.1 m where the 0 DOF had the highest Y force and Z moment, this is no longer the case. As the wave height increases the interaction between the short wavelengths becomes more significant. This is most prominent for factor of 0.5, as there is an increase of 86% over the baseline for Y force. This is primarily due to the vessel rotating over the peaks and troughs of the wave, this is seen very clearly in Figure 15-22, with the corresponding moment shown in Figure 15-23. As observed from Figure 15-22, the maximum spikes in Y force are directly when the peaks or troughs are encountered. This pattern alternates between the PMM amplitudes, i.e., after there is a spike at the maximum PMM amplitude the following trough has a lower decrease than what would be expected. This pattern continues to alternate, with the 0 DOF maintaining a consistent force throughout all wave interactions. Although there is a significant interaction between Y force and waves, this does not equate to an equivalent pattern observed for the Z moment, Figure

15-23. This wave interaction becomes less significant as the wavelength increases, with spikes in either the maximum or minimum only being observed when the vessel is at its maximum rate of turn while on a crest or trough of the wave, Figure 15-24, Figure 15-26, Figure 15-28 and Figure 15-30. These interactions do not correlate to excessive moments, as the Z moment remains consistently below 10.5% compared to the baseline, except for factor 1.5 when it increases to just over 28% deviation, derived from Table 4-26. The corresponding graphs can be visualised in Figure 15-25, Figure 15-27, Figure 15-29 and Figure 15-31.

This cannot be stated to be the same for the 0 DOF simulations, as these consistently exceed 20% increase over the baseline except for factor 0.5. This highlights that the dynamic motions may cause a slight increase in calm conditions but enable significant reductions in regular wave conditions. This is primarily due to the hull maintaining a parallel position to the free surface.

This increase in Y force can cause the vessel to have a wider turning circle, with the rate of turn due to moment not being significantly affected. This causes the vessel to have erratic behaviour, tending towards sudden bow movements, both around the z and y-axis. This can cause the vessel to turn perpendicular to the wave, which is commonly observed in real world conditions.

Table 4-26 Maximum and minimum observed Y force and Z moment table for wave height of 0.2 m for HPR and 0 DOF simulations

		Y Force Min (N)	*Y Force Max (N)*	*Z Mom Min (Nm)*	*Z Mom Max (Nm)*
Base	*HPR*	*-79.614*	*79.529*	*-308.941*	*306.627*
0.5	*HPR*	-149.897	148.201	-340.236	335.396
	NM	-129.429	130.260	-313.530	313.806
0.75	*HPR*	-81.934	101.445	-325.874	309.365
	NM	-119.792	120.465	-379.224	371.174
1	*HPR*	-116.223	73.968	-333.053	318.835
	NM	-121.329	94.498	-376.464	339.117
1.25	*HPR*	-83.320	92.354	-337.623	325.883
	NM	-128.842	126.180	-381.732	383.634
1.5	*HPR*	-91.968	97.173	-364.932	392.666
	NM	-121.880	135.462	-405.059	439.067

4.6.4. 0.25 m Wave height results

Unlike the previous wave height simulations, 0.25 m investigates not only HPR (heave, pitch, and roll) and 0 DOF, but also heave and pitch (HP) along with heave (H). The breakdown of the results are shown in Table 4-27. This test is to investigate the effects of extreme wave heights on the vessel, with an equivalent full scale wave height of 8.87 m or nearly 1.5 times the draft. Although this is a tall wave, factor 1.5 equates to a length over wave height ratio of 456.56, with factor 0.5 equating to 76.96. This provides a broad range of extreme wave conditions, from tall and steep to an extreme swell. With this in mind the additional degrees of freedom were evaluated to help highlight the key contributing factors.

When evaluating the Y force with respect HPR, the greatest increase was observed for factor 0.5, seen in Figure 15-32. This increase equated to over 100% the base calm water simulation observed. This increase reduced for factor 0.75 to just below 61%, with factor 1.0 observing the smallest increase of 47%. This was closely followed by factor 1.25 with an increase of 48.6%, where finally the second highest increase was observed for HP (heave and pitch) for Y force coming from factor 1.5 at 64.25%. The various interactions can be seen from Figure 15-32, Figure 15-34, Figure 15-36, Figure 15-38 and Figure 15-40.

This U-shaped decrease centred around factor 1.0 is not observed for the heave and pitch results (HP). The greatest increase in the Y force was seen for factor 0.75, the increase equated to 74.4%. This is close to 15% increase over the HPR result, suggesting that roll helps to mitigate Y force. These peak values occurred in each period of greatest yaw rate and wave trough; this is seen in Figure 15-34. In contrast the corresponding wave peaks have a slight reduction compared to the baseline HPR with respect to Y force. For both factors 1.0 and 1.25 there is an increase of around 47% over the baseline HPR, with factor 1.5 having an increase of 65%. Although factor 0.75 for HP increased compared to HPR, the range between the maximum and minimum errors is around 27%, whereas for HPR this is around 52%.

The Y force for pure heave has an error range of 37%, with the highest values observed for factors 1.25 and 1.5. Factor 0.5 is an overall increase of 83%, around 12% of the heave and pitch, with factor 0.75 reducing the force by 5% compared with heave and pitch. This increase in Y force is closely matched by factor 1.0. Factor 1.25 observed the same pattern of Y force increase when the vessel has greatest yaw rate while in a wave trough, seen in Figure 15-40. This is not observed for factor 1.5, as the maximum Y force is observed upon the crest of a wave.

The largest differences between the base simulation and why force and those seen for the 0 DOF setup. The smallest increase in Y force was observed for factor 0.5, followed by factor 1.25, 1.0 and 0.75. Factor 1.5 had a significant increase of over 215%. This occurred when the vessel had the highest yaw rate while on the crest of the wave. All other spikes are observed in wave troughs and maximum yaw rates.

Unlike the Y force, the Z moment does not have as greater differences between the various factors and degrees of motion, except for 0 DOF. These percentages are visualised in Figure 4-37, with the raw Z moment data presented in Figure 15-33, Figure 15-35, Figure 15-37, Figure 15-39 and Figure 15-41. From Figure 4-37 it can be seen that the factors are 0.75, 1.0 and 1.25 there is an increase in Z moment as the degrees of freedom reduces. In addition to this, the maximum percentage observed for any free moving vessel is 47.4% for factor 1.5 and heave only. These results highlight that although waves do affect the moment around the z-axis, they have a significantly lower impact than the Y force. The HPR simulation has a maximum percentage increase of only 31%, compared to the 101.5% seen for Y force. This matches the observations seen for smaller wave heights, which also suggests that large swells have greater impact on the vessel's moment than short steep waves. This is further supported by the greatest increase in the Z moment for the 0 DOF occurring for factor 1.5.

These results also complement the conclusions made earlier that there is an inverse relationship between increase in Y force and Z moment and the wave steepness. The greater the wave steepness the higher the difference between the Y force and Z moment, with the percentage difference of around 90% for 0.25 m waves. However, for large swells the difference between Y force and Z moment percentage is significantly lower, around 30% for wave height of 0.25 m. These fluctuations in force and moment can cause two noticeable motions. Firstly, steep waves due to the increase in Y force with minimal increase in Z moment the vessel tends to rapidly rotate while still maintaining its original course, causing significant drift. Secondly, for long swells the moment becomes the dominant factor causing vessels to turn rapidly and bleed off forward speed.

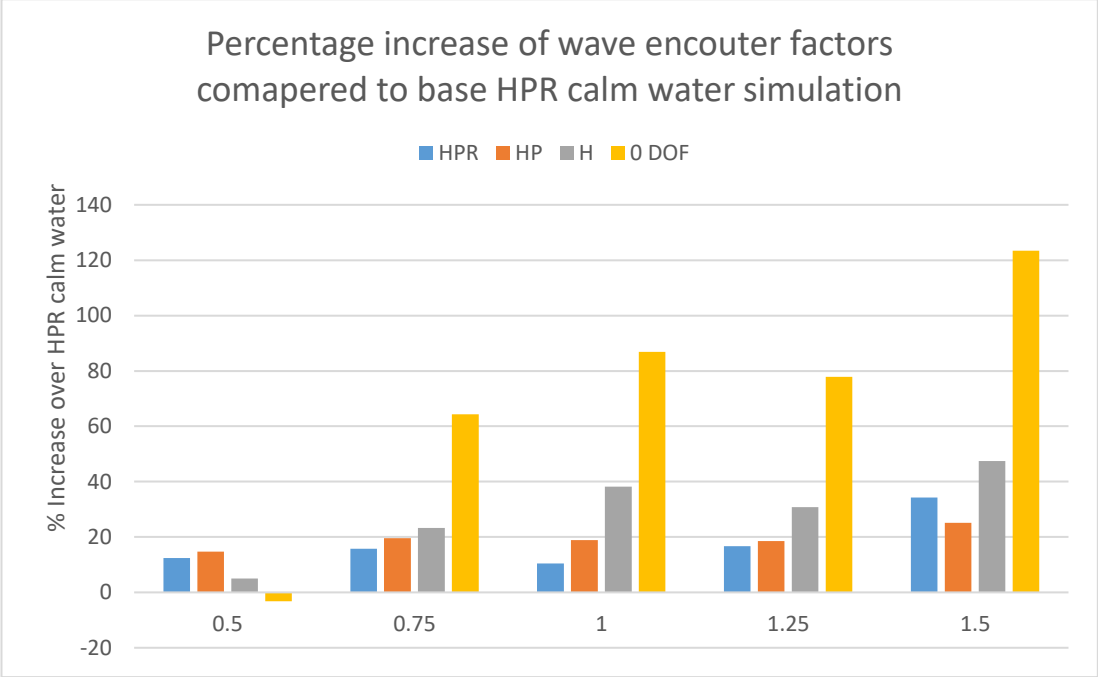

Figure 4-37 Percentage increase over base calm water HPR simulation

Table 4-27 Maximum and minimum observed Y force and Z moment table for wave height of 0.25 m for HPR, HP, H and 0 DOF simulations

		Y Force Min (N)	*Y Force Max (N)*	*Z Mom Min (Nm)*	*Z Mom Max (Nm)*
0.5	*HPR*	-160.437	155.491	-347.376	343.257
	HP	-133.130	136.741	-354.398	351.336
	H	-144.104	145.717	-320.861	321.933
	NM	-92.767	94.492	-299.006	298.582
0.75	*HPR*	-128.176	128.027	-339.688	354.985
	HP	-138.873	136.697	-344.855	366.748
	H	-113.026	133.671	-368.962	377.913
	NM	-151.728	155.081	-507.755	479.473
1	*HPR*	-117.063	72.869	-341.316	324.164
	HP	-116.338	75.828	-367.308	322.384
	H	-132.471	95.577	-427.050	351.257
	NM	-77.273	143.625	-145.315	572.903
1.25	*HPR*	-90.071	118.206	-360.387	333.601
	HP	-89.247	117.734	-366.345	354.814
	H	-156.856	146.021	-404.109	388.900
	NM	-126.585	106.000	-549.514	447.543
1.5	*HPR*	-127.052	130.629	-332.081	411.775
	HP	-128.373	131.787	-333.196	383.628
	H	-158.901	148.578	-403.764	452.119
	NM	-251.353	201.822	-689.453	685.119

4.7. Concluding remarks and summary

Throughout this chapter the methodology developed to simulate captive model tests has been presented. The chapter provides techniques used within parametric modelling software to enable rapid and accurate simulation setup. From here a detailed description of the CFD simulation setup was discussed followed by key systematic studies aimed at advancing the accuracy being obtained. Throughout all these studies methodology was able to maintain a high level of accuracy, which was confirmed by a detailed validation and verification study.

Upon completing this validation and verification study, the research aimed at continuing and then exceeding the studies conducted for SIMMAN 2014. This initially started by focusing on additional degrees of freedom, namely roll, and how these effects the manoeuvring abilities of the DTMB hull. From these results can be seen that when the vessel's manoeuvring at high speed or in tight turns the Y force and Z moment both decrease with roll. However, when the vessel's manoeuvring at low-speed and large turn radius's, there is a slight increase in Y force and Z moment.

Following this, the research focused on how different wave interaction criteria would affect the Y force and Z moment. From this investigation some key conclusions can be drawn. Firstly, for small wave heights independent of the wave steepness there is a relatively minimal variation due to waves for Y force and Z moment, with the greatest variation occurring when the wave peak and trough is in phase with the PMM path. This is most noticeable for the wave crest. For a wave height of 0.1 m the Y force is more greatly affected than the Z moment, whereas for 0.15 m the opposite is true with the Z moment being more greatly affected. Once the wave height has exceeded the nominal draft of the vessel, the results significantly change. Four wave height of 0.2 m wave steepness becomes a key factor, with the greatest difference between the calm water results being observed for the steepest wave for Y force. However, the Z moment follows an inverse path with the greatest difference being observed for the longest wavelength. Finally, for a wave height of 0.25 m a similar pattern as observed, the Y force is greatly affected for the steepest waves with the greatest difference between the calm water results being observed for the steepest wave. As with the previous wave height, the Z moment becomes ever more greatly affected as the wavelength increases. Additionally, this wave height investigation provided insight into the effects of degrees of freedom on the vessel, as well as their impact on the Y force and Z moment.

Secondly, this investigation highlighted the effectiveness of the simulation methodology developed in this chapter. Both to obtain high level of accuracy for harmonic captive tests, as well as the flexibility to simulate complex wave simulations. It can also be concluded that the

use of high Y+ techniques provide adequate accuracy for fast simulation analysis for such investigations. This may not however be the case when evaluating more complex appended hull forms with propellers and rudders.

5. Fully parametric hull modelling.

5.1. Introduction

Within this chapter the development and workflow of the creation of a fully parametric hull form is presented. To ensure the greatest flexibility when evaluating the manoeuvring of a vessel in an optimisation a fully parametric hull is considered the best option. This is due to a fully parametric hull surface being able to be completely changed based on input parameters and user defined constraints. This is a significant improvement over partially parametric or morphing techniques, as these methods are based of a predefined hull and all future variants follow the base design of this hull. This can be useful for optimisation with respect to specific hull regions, however this creates a limitation in the variation and in turn the potential gains that can be achieved through manoeuvring optimisation. This is due to the direct partnership between geometric shape and manoeuvring, as discussed in chapter 4.

5.2. Selection of the hull type

Throughout this research the choice of the final hull type for the optimisation has not been specified. This selection is key to ensuring the validation and verification on the numerical model used later achieves the desired accuracy that can be applied to a final optimisation. A specific hull type which has had a significant amount of research conducted on it is ideal to act as the base of the parametric hull. Based on this, the NPL hull form lends itself perfectly, an example of such research was conducted by Elhadad, et al. (2014) and Haase, et al. (2012). In addition, a partial focus of this research is aimed towards smaller high-speed craft used in the offshore industry acting as CTV's, which in turn matches the profile commonly associated with the NPL hull form.

Before defining key characteristics of the NPL hull that is used as the base, a small investigation is conducted to find upper and lower limits of these characteristics for similar offshore vessels in the desired size range. This investigation does not focus on any of the specific design variables, such as cross-sectional parameters or block coefficients, but rather on the length beam and draft, along with the displacement of these hulls. The research is likely to significantly limit the selection pool, however the investigation still ensures that the base hull for the parametric modelling falls within the limits of CTV hulls. However, it is important to note at this point the parametric hull is not only be limited to CTV hulls, but is created to have the capacity to manage larger displacement vessels.

Through this investigation, it was found that a vessel whose length fell between 15 and 25 m would encompass around 65 to 70% of the mono hull vessels in use for CTV's, whereas the

beam and draft of the vessels had a much greater variation for the hulls in use. This meant that both the beam and draft are more influenced by the NPL hull selection than matching to real-world vessels. From here the NPL characteristics used in the research conducted by Bailey (1976) are taken and used in partnership with the NPL equations to generate the geometric points for the hull. The characteristics for the parent hull, along with sectional lines plan and centreline profile are shown in Table 5-1, Figure 5-1 & Figure 5-2 respectively. This hull is converted into a 3D model, created in Rhinoceros 3DM, that is used as a reference geometry when building the fully parametric hull. This enables accurate tuning, as well as flexible creation of the parametric model.

Table 5-1 NPL Parent hull specifications (Bailey, 1976)

Lwl (m)	2.54
B (m)	0.4064
T (m)	0.14
Disp. (kg)	57.33
Cb	0.397
Cp	0.693
Cm	0.573
Lwl/B	6.25
B/T	2.9
Froude length Constant	6.59
Froude wetted surface constant (M)	7.17

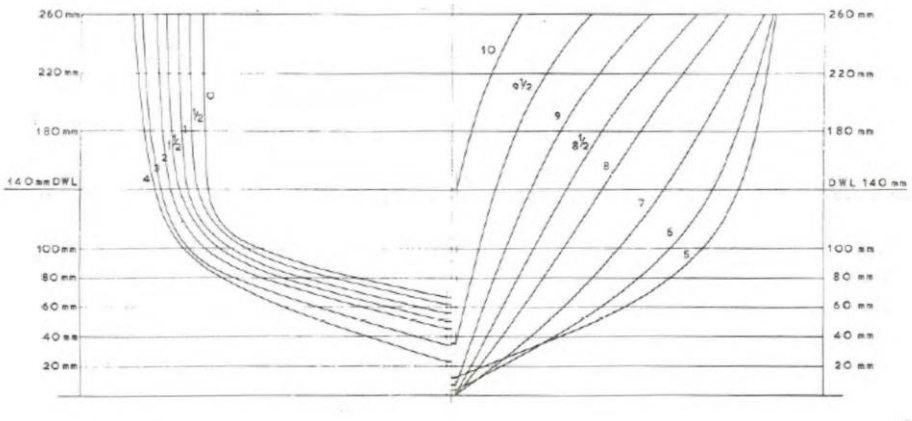

Figure 5-1 NPL Parent hull sectional lines plan (Bailey, 1976)

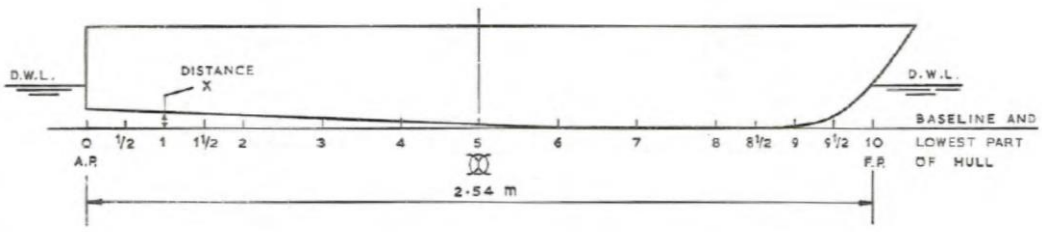

Figure 5-2 NPL Parent centreline profile (Bailey, 1976)

Now that the hull geometry has been selected, along with a reference 3D model, the fully parametric model for the vessel geometry can begin to be worked on.

5.3. Development of the fully parametric geometry

The NPL hull acts as a starting point for the parametric hull, in addition to the starting point for many of the optimisations. This in turn means that the parametric geometry must be stable enough to be able to have significant variation applied to it. Further to this, the geometry must also be able to accurately deform in key regions.

As discussed above in the literature review there are multiple methods on developing a parametric geometry. For this research it was found that the best method would be to utilise the meta-surfaces used in Friendship Framework software CAESES. It is noted that "meta-surfaces are parametric sweep surfaces, when the surface generation process is efficiently controlled by a set of function graphs" (CAESES, 2019), this has multiple advantages over other parametric modelling techniques along with disadvantages. As meta-surfaces are based upon a group of function curves, or a curve engine, there are no inherent geometric limitations that commonly occur with direct modelling techniques. This in turn allows for range in variation between surfaces that are created using these function curves, when focused on original designs. However, this technique is also very useful for focused geometric design, due to its base being built upon function curves, which can be set to match any other geometric 3D curve. This in turn lends itself perfectly to parametric optimisation as a large range of original and potentially unconventional surfaces can be rapidly created but can also be carefully controlled for specific optimisation aims.

However, the largest and most obvious drawback to this method is lack of control over a very specific point on the surface, which would normally be controlled through direct modelling techniques. It is possible to accurately manipulate a small region utilising this method, however this involves fine control over multiple function curves. This also highlights another drawback to this technique, that to achieve a specific hull type or to replicate a design, many

function curves are used. This can create a complex and messy design workflow. This is a common problem that occurs with any parametric modelling, particularly for fluid surfaces such as hull forms and marine vehicles. Therefore, the hull being modelled uses more than 10 functional curves to create the surface.

A comparative study was conducted by Katsoulis (2019) looking at alternative methods for parametric modelling of ship hulls, with a focus on using T-Splines in a NURBS based parametric modeller called TshipPM. The method used by T. Katsoulis is a hybrid between direct modelling and parametric modelling, this is because the parameters used within the parametric modelling control specific points on the NURBS surface. The study compared this method with the NURBS based parametric modelling in CAESES, which creates 3D surface based on sectional lines rather than functional curves. Both methods are limited in comparison to the use of meta-surfaces and functional curves to create the hull surface. This is because both surfaces are constrained by the construction method due to most of the parameterisation being done post modelling, whereas the functional curves for meta-surfaces are intrinsically parametric. This further highlights the advantage of using meta-surfaces for this parametric hull, as there are very few constraints to apply to the hull, and this greater variation and flexibility is needed. The study concludes that the T-splines based model produces fewer control points, but CAESES produces more accurate planar areas and sectional area curves. This is also vital to the parametric hull, as the sectional area curves are a key step in the final optimisation and thus greater accuracy in calculating theses curves are key. Along with the calculation of these sectional area curves the software also has inbuilt hydrostatic calculations based on these curves. This removes any extra processing there may be required when using direct modelling.

Although the aim for the parametric hull is to be as flexible a model as possible, realistic aims need to be set. These are key to developing and planning the parametric hull. For example, it is common for NPL hull have a chine line running along the hull, not an abrupt stepped chine, this chine line can be easily implemented on the meta surface through the addition of extra function curves. However, more complex chine lines may have to be discarded in addition to multiple chine lines. Multiple chine lines are not be considered for the parametric hull, this is not because NPL hulls variations or even CTV vessels do not have multiple chine lines, but rather the complexity in modelling and their effect on the manoeuvring characteristics of the vessel. As this study aims to cover a broad range of manoeuvring characteristics, not solely focused on pure vessel manoeuvring, but also on resistance and wave interaction behaviour, a more complex hull causes difficulties in narrowing down key aspects affecting key vessel

behaviours. The simpler the hull the greater the accuracy when developing the analysis methodology for the final optimisation. This is another reason why the NPL hull form was selected as the base hull.

The base NPL hull statistics are given in the table below, Table 5-2. These focus on key factors such as a length between perpendiculars, length overall, beam and draft. Displacement of the hull is also given to provide a comparison with the other CTV hulls. The vessel speed is also provided; however, this is matched to an analysis conducted by Bailey (1976). The speed is only be considered when the CFD model is being developed.

Table 5-2 Full-scale NPL hull characteristics compared with parent NPL hull

	NPL Parent	*NPL Full-scale*
LWL (m)	2.54	20
B (m)	0.4064	3.2
T (m)	0.14	1.1
Disp. (t)	0.05733	28.7
Cb	0.397	0.397
Cp	0.693	0.693
Cm	0.573	0.573
Max section	*40% from transom*	8
LCB	*43.6% from transom*	8.72
L/B	6.25	6.25
B/T	2.9	2.9
M	6.59	6.6

As can be seen from Table 5-2, the waterline length has been selected 20 m long. It has been chosen to match the majority of CTV and offshore working vessels. This is, therefore, the starting point for the entire creation of the parametric hull.

The hull surface is described by a defined section curve with the input parameters describing this curve controlled through the previously mentioned function curves. This first sectional curve is defined as a NURBS curve within a feature definition. This curve is created on the YZ plane and is mathematically describes the surface in the longitudinal direction. Once the sectional curve has been created, functional curves are used to control the sectional curves input parameters through a certain range, i.e., the overall length.

5.3.1. Cross sectional curve creation

As mentioned above the first step in creating a fully parametric hull using meta-surfaces is to describe the base sectional curve. This sectional curve is defined within a feature definition. A feature definition is a system created within CAESES that encapsulates multiple modelling procedures to streamline the workflow. There are three key procedures which are used in a feature definition:

- Arguments: the input data for the future, these can be values, points, strings, curves, surfaces etc.
- Create function: a sequence of commands which are defined by the user that use the given input data
- Attributes: simply the output, i.e., the resulting object which can be a curve or an equation for example

It is at this point design and complexity of the hull form must be initially laid down. It is not impossible to add extra complexity to a base sectional curve, however this is not simple and is likely to add error into the parametric workflow. Therefore, it is best just like with any 3D modelling software to have an initial design/concept created before advancing. It is this which meant it was vital to already have selected a hull form for to base this design on.

The future curves which control the shape of the sectional curve do not only control specific positions of points along this curve but also the weights of the points. Point weights are vital in helping to reduce the total number of points used to define a complex curve. As the sectional curve is defined by a NURBS curve, the weighting of the points can be considered like a gravitational force acting from the point. As the weight of the point increases curve is drawn closer to the point, and vice versa when the weight is reduced. This can be seen in Figure 5-3, where the exact same five-point NURBS curve is shown with only a variation of weight acting on the 3rd/mid-point along the curve.

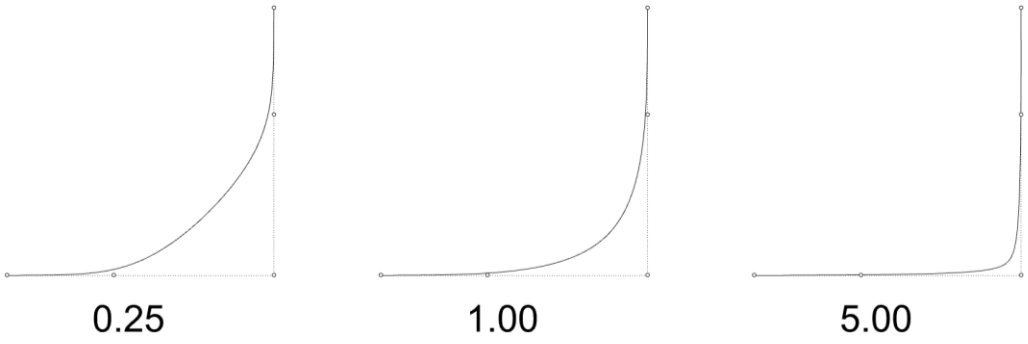

Figure 5-3 Comparison between different point weights acting on an identical NURBS curve

As can be seen, as the weight reduces the curve moves away from the points as well as becoming mathematically simpler. Whereas, as the weights increases curve moves closer to the point as well as becoming more complex. It is possible to create this geometric form by using additional points moving closer to the midpoint, however this adds a minimum of an extra two functional curves but realistically four for the desired accuracy. It is therefore more efficient to systematically select key points along the base curve to have an extra function curve describing the points weights along the longitudinal axis. This technique is particularly effective at creating chine lines as well as complex concave hull geometry. The equation for a NURBS curve is shown in Equation (5-1), where p is the order, $N_{i,p}$ are the B-Spline basis functions, P_i are control points and w_i the weight.

$$C(t) = \frac{\sum_{i=0}^{t} N_{i,p}(t) w_i P_i}{\sum_{i=0}^{t} N_{i,p}(t) w_i} \tag{5-1}$$

The generated sectional curve from a feature definition is created from five points, however there are a total of 14 input arguments used to describe this curve. To simplify the complexity of the curve, some points are linked by mathematical relationships. For example, the two points nearest the deck have their transverse position controlled in relation to the deck beam, with the point below the deck being controlled by a user-defined angle rather than a specific distance. This allows the user to directly input a desired bow flare angle. Along with this, the position of the keel point is also set up such that a flat keel can be easily modelled. Through this setup any possible curve can be created at a high fidelity, in turn leading to exceptional control over the hull surface. An example of a basic NURBS curve along with the input values are shown in Figure 5-4.

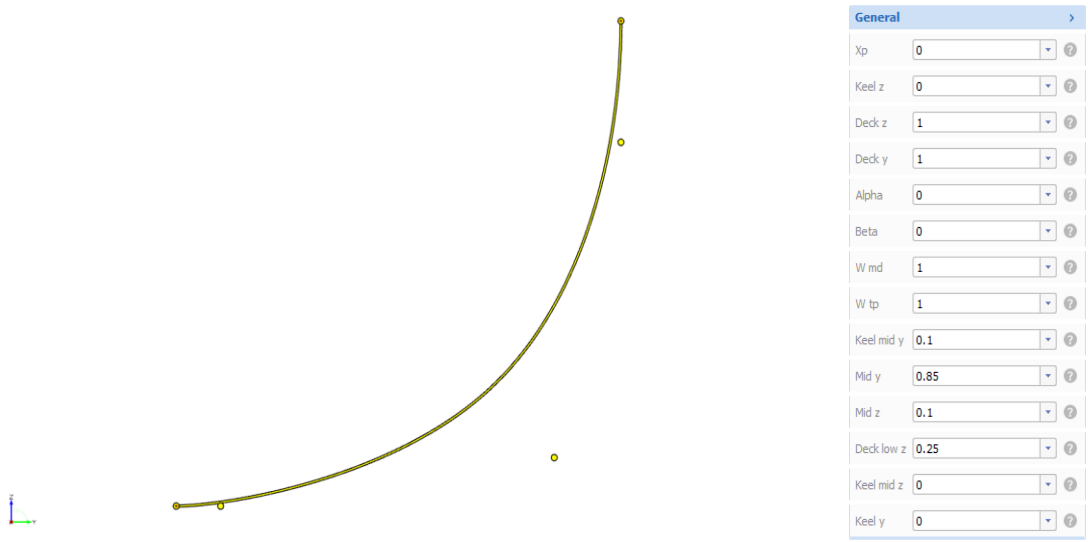

Figure 5-4 Generated parametric NURBS spline and input arguments

Further below in Figure 5-5, 10 random sectional curves created using this method are presented. A large amount of variation can be seen, thus leading to a very versatile parametric hull. The sectional curve is created using a function, base curve and input dialog shown in Figure 5-4. Variations to this base curve is presented in Figure 5-5, with the function describing the curve based on the input parameters given in Figure 5-6. Each variable defines either a Y coordinate or Z coordinate for the different points, the different mathematical additions can also be seen in lines 3 and 4.

Figure 5-5 Example of 10 random sectional curves

```
1  point p1(xp,keel_y,keel_z)
2  point p2(xp,keel_mid_y,keel_mid_z)
3  point p3(xp,(mid_y*deck_y),mid_z)
4  point p4(xp,(deck_y-(deck_z*deck_low_z)*tan(alpha)),(deck_z-deck_low_z))
5  point p5(xp,deck_y,deck_z)
6
7  nurbscurve section([p1,p2,p3,p4,p5])
8  section.setWeights([1,1,w_md,w_tp,1])
9
```

Figure 5-6 Sectional curve function definition

Before defining the different function curves, a length parameter, or in this case the overall length of the vessel, must be defined. This value is vital in completing the meta surface that represents the hull.

5.3.2. Functional curve creation

For each input variable another curve is created. This curve describes the variable's value throughout the longitudinal length of the vessel. It is by controlling the shape of these curves through the movement of the control points that the surface geometry can be controlled and changed, and in turn the hull geometry. Just like the sectional curve each functional curve is created from five points. Each longitudinal position of the point is defined as a factor of the overall length. This allows specific control over key areas, such as the midship. Most of the function curves are split equally along the length of the vessel, however certain functions have extra control added to allow for greater refinement in key regions, i.e., the bow region. The function curves for Z/vertical components are shown in Figure 5-7. The Y/transverse function curves are depicted in Figure 5-8, with Figure 5-9 showing the weight and longitudinal position function curves. The hull form created from these functions is purely an example does not match an NPL hull, this example hull is shown in Figure 5-10.

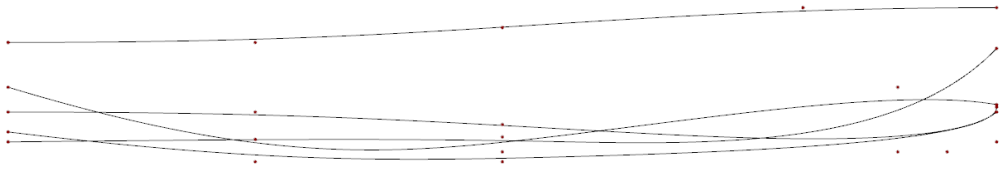

Figure 5-7 Function curves for Z/vertical components for curve engine

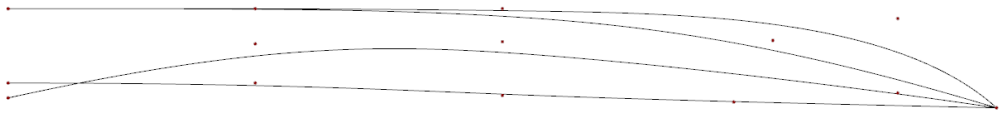

Figure 5-8 Function curves for Y/transverse components for curve engine

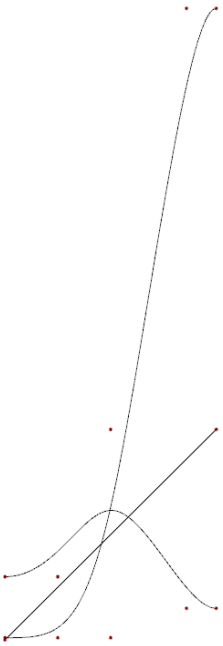

Figure 5-9 Function curves for point weight and longitudinal position components for curve engine

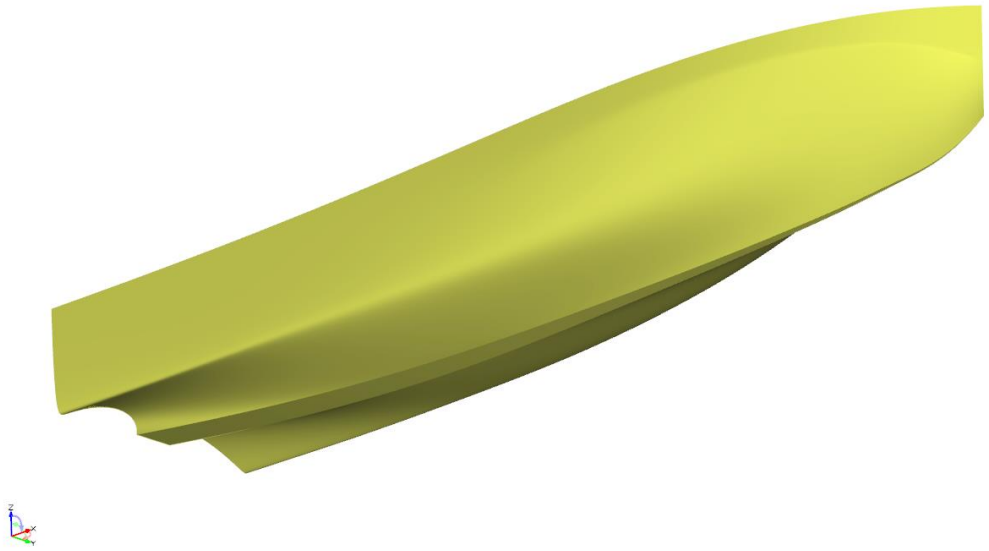

Figure 5-10 Non-NPL parametric hull example based on function curves shown in Figure 5-7, Figure 5-8 & Figure 5-9

Once the function curves have all been created these can now be integrated into a curve engine. This curve engine consolidates all the various function curves such that a meta surface can then be created. This meta surface can then parametrically be modified or manipulated from normal CAD methods. It is through these CAD methods that the draft and even the trim can be set. It is also possible within this parametric setup to define a model scale value to switch

between a full and model scale simply and quickly. This is used in conjunction with the NPL research conducted by Bailey (1976) for the validation and verification.

To complete the creation of the parametric hull, the key point values for the function curves must be parameterised. As can be seen there are 14 function curves, each with five points, leading to a total potential of 70 input parameters. This is simply to greater number to be feasible for any rapid optimisation. Therefore, certain regions along with certain points are linked and controlled through further mathematical functions, helping to significantly reduce the total number of input optimisation parameters, but this also reduces and limit the flexibility meta surface.

A two-tier system for the optimisation parameters is implemented. A primary set of parameters directly control the various point movements for the function curves, with a secondary set of parameters controlling the various mathematical functions. It is by using the secondary functions along with optimisation constraints that a specific hull form theme can be set for the optimisation.

5.3.3. NPL Hull Comparison

As noted above the NPL hull is used as the starting point for the fully parametric optimisation. Before moving on to developing the optimisation methodology, the fully parametric hull must be configured to match the NPL parent hull developed by Bailey (1976). The parent hull's sectional curves are compared with the generated parametric hull's sectional curves to give a deviation percentage to determine the fidelity of the surface.

To speed the process of matching and faring the parametric hull, an accurate 3D model of the NPL hull is imported into the CAESES software. This is used both to tune the input parameters visually and mathematically before having the sectional curves compared. The fairness and continuity of the hull surface is mathematically tuned.

Figure 5-11 shows the comparison between the parametric hull and the parent hull. The parent hull is represented by the black lines with the parametric hull variation shown as the blue lines. An enhanced view focused on the bilge region of the aft half of the vessel is also shown, this is used as there is minimal deviation from the parent hull lines.

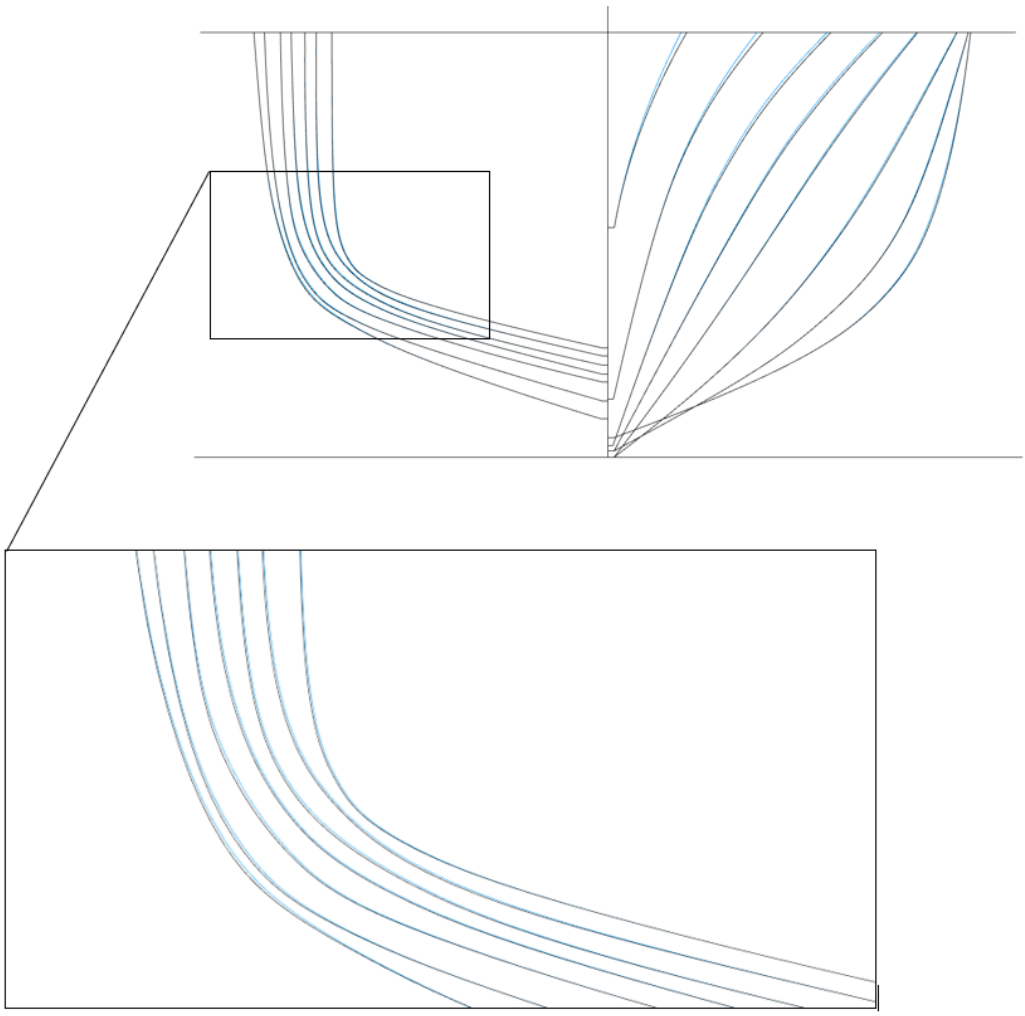

Figure 5-11 Comparison between parent NPL hull section lines (black) and parametrically created hull (blue).

The parametric hull was modelled in model scale to match the exact parent hull provided. This would then be simply scaled to a full-scale 20 metre hull by reverting the model scale back. The initial ship length in the parametric setup is based off 10 m, therefore the model scale input parameter was set to 0.254. This factor is then be set to 2 for the full-scale hull.

The initial step in modelling and accurately replicating the NPL hull was by starting with the keel shape. This was easily mapped to the drawings and schematics as the function curve directly represents the users geometric position. The keel has a small width which is inputted through a parameter. Upon accurately replicating the keel the next reference point is the deck position with respect to Y. This position is allowed to vary slightly compared with the NPL lines, as the primary focus for the parametric hull is the underwater region. Therefore, to allow as precise representation of the underwater region some flexibility is given to the deck shape. This flexibility can be seen in Figure 5-11 when looking at the most forward bow sections of

the lines plan. To ensure the bow curvature was met, the bow at the deck had to be made slightly finer than the parent hull, however this is less than 3% and does not continue down below the waterline.

The deviation around the bilge region, shown in Figure 5-11 enhanced view, is likely due to a reduced number of function curves acting as control points failing to create the desired accuracy. This slight deviation can be corrected through the addition of extra function curves; however, this would increase the total number of control parameters even further and may even fail to achieve the increased accuracy. Therefore, this slight deviation below the waterline was considered acceptable. This would equate to a less than 1% variation in the hull displacement. The final hull mesh is shown in Figure 5-12 for final check and preparation validation and verification study in Rhinoceros 3DM.

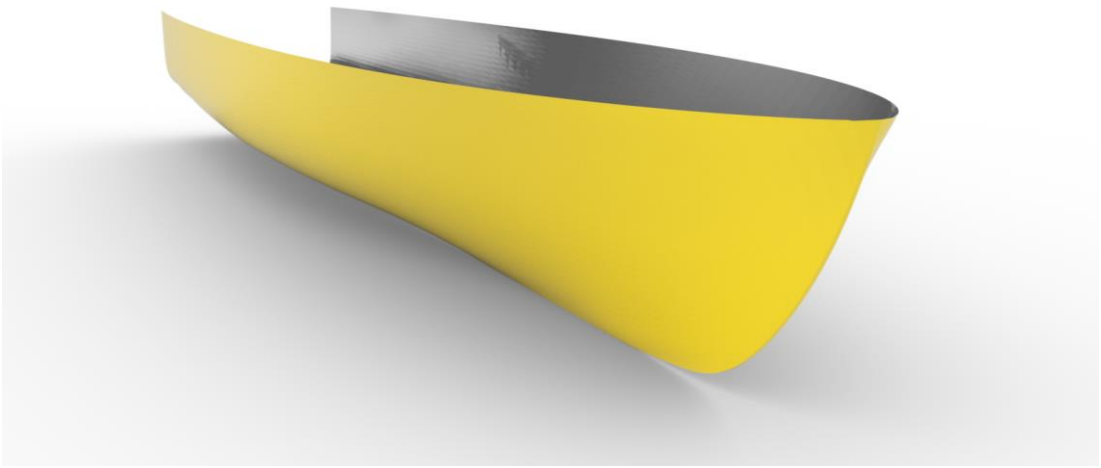

Figure 5-12 Exported parametrically modelled NPL hull mesh

5.4. CFD validation and verification

The accuracy of the manoeuvring methodology developed in Chapter 4, with respect to the NPL hull is also tested. As no PMM or manoeuvring coefficients are presented by Bailey (1976) for a bare hull, the accuracy of the model is validated by comparing the resistance and motion dynamics for straight-line resistance tests, which are comprehensively presented. This allows for high-level of accuracy to be drawn when moving to simulating PMM tests both captured and dynamic.

The validation and verification study is conducted in full-scale with the assistance calculation based off the NPL resistance calculations put forward by Bailey (1976). In addition, the

sinkage and trim has also been calculated based on these calculations. These results can be seen in Table 5-3.

Table 5-3 Calculated NPL full scale resistance, trim and sinkage results for calm water

		10 Knots	*20 Knots*
Total Resistance of Hull	*L/B*	6.250	6.250
*Pe = Rt*V*	*Fv*	0.939	1.877
Rt = Rf + Rr	*M*	6.590	6.590
Residuary Resistance	*L/B*	*Rr/disp.*	*Rr/disp.*
fig.6	3.33	0.225	0.635
fig.7	4.55	0.185	0.565
Interpolated	6.25	0.129	0.467
Aw (m^2) model scale from fig.3		1.675	1.675
Aw (m^2) full scale scaled up		103.850	103.850
Rr (kN)		3.710	13.416
*Rn (V*L/viscosity)*		86.6 e6	173 e6
delta Cf (default value)		0.000	0.000
Cf (ITTC '57)		0.002	0.002
Cf		0.003	0.002
Rf (kN)		3.563	13.123
Rt (kN)		7.273	26.539
Running Trim by Stern (degrees)	*L/B*	*Running Trim*	*Running Trim*
fig.16	3.33	0.350	2.300
fig.17	4.55	0.450	2.650
Interpolated	6.25	0.589	3.138
Sinkage at LCG	*L/B*	*(Rise or Fall/Lwl)*100*	*(Rise or Fall/Lwl)*100*
fig.21	3.33	-0.200	0.400
fig.22	4.55	-0.225	0.000
Interpolated	6.25	-0.260	-0.557
	Rise or Fall	-0.052	-0.111

As noted from the end of Chapter 4, the overall mesh can be coarsened carefully while still maintaining the accuracy required. It is based on this concept that the mesh used for the NPL resistance validation and verification study would have less than 1 million cells. This significant reduction in the number of cells is due to 2 main factors. Firstly, the relative speed and in turn the Reynolds number is lower closer to the hull therefore requiring a smaller prism layer mesh. The prism layer mesh was one of the key influencing factors in the cell numbers, and thus reducing this complexity significantly bringing the overset mesh numbers down. As presented and discussed in Chapter 4, the higher Y+ methodology for the prism layer tended to be more accurate per CPU hours compared with the standard low Y+ techniques. Therefore, the high Y+ technique is used for this mesh in this validation and verification study.

Secondly, vessel geometry is significantly less complex than the DTMB with bilge keels. Due to this reduced geometric complexity, less volumetric refinement regions is required in the overset region which in turn allows for a larger relative mesh cell size in the overset region to be used. However most notably, due to the squatter form of the NPL hull compared with the DTMB hull the overall domain size is noticeably smaller relative to the hull form.

Through these changes to the overset regions mesh was able to be reduced to just below half a million cells. These changes within the overset region also have a knock-on effect in the outer domain and the free surface refinement. The outer domain now also have a significantly lower mesh with a cell count close to half a million as well, creating an even split between the overset in the outer domain. It was also found that a faster growth rate in the outer domain can be used compared with the mesh for the DTMB hull analysis.

The results for these studies were calculated using the same calculation techniques shown in chapter 4.4.4, namely the grid convergence index (CGI) developed by Roache (1998) and the generalised Richardson extrapolation presented by Stern, et al. (2006). Unlike the previous validation and verification studies in both chapters 10.3 & 4.4.4, which excluded an iterative investigation, the study can include an iterative analysis.

Table 5-4 20m NPL mesh numbers and break down

	Fine	*Medium*	*Coarse*
Domain	571,366	254,794	118,072
Overset	373,530	254,826	140,044
Total	944,896	509,620	258,116

Table 5-4 gives the breakdown of the mesh numbers for both the overset and outer domain along with the final used in this validation and verification study. As noted, there is a significant reduction compared with the DTMB simulations. This is primarily due to the outer domain, as the finest mesh for the DTMB had a cell count in the overset region above 800,000 compared with the current mesh of just under 400,000. Due to the change in geometry as well as overall base size this is an acceptable variation between the two simulations, whereas the outer domain varies from 3 million+ cells for the DTMB hull and just under 600,000 for these simulations. This reduction is primarily due to the squatter shape of NPL hull, along with the increase in growth rate. The free surface mesh is shown in Figure 5-13, along with the growth rate and mesh seen clearly in Figure 5-14.

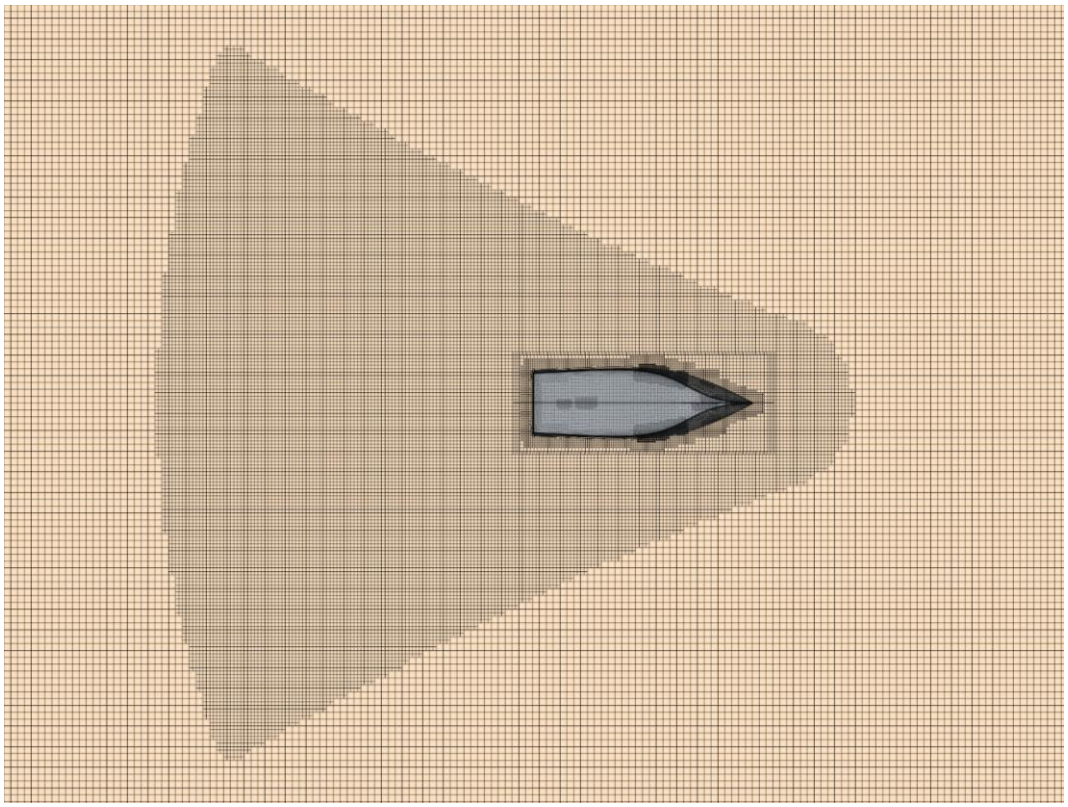

Figure 5-13 NPL Parent hull free surface mesh scene

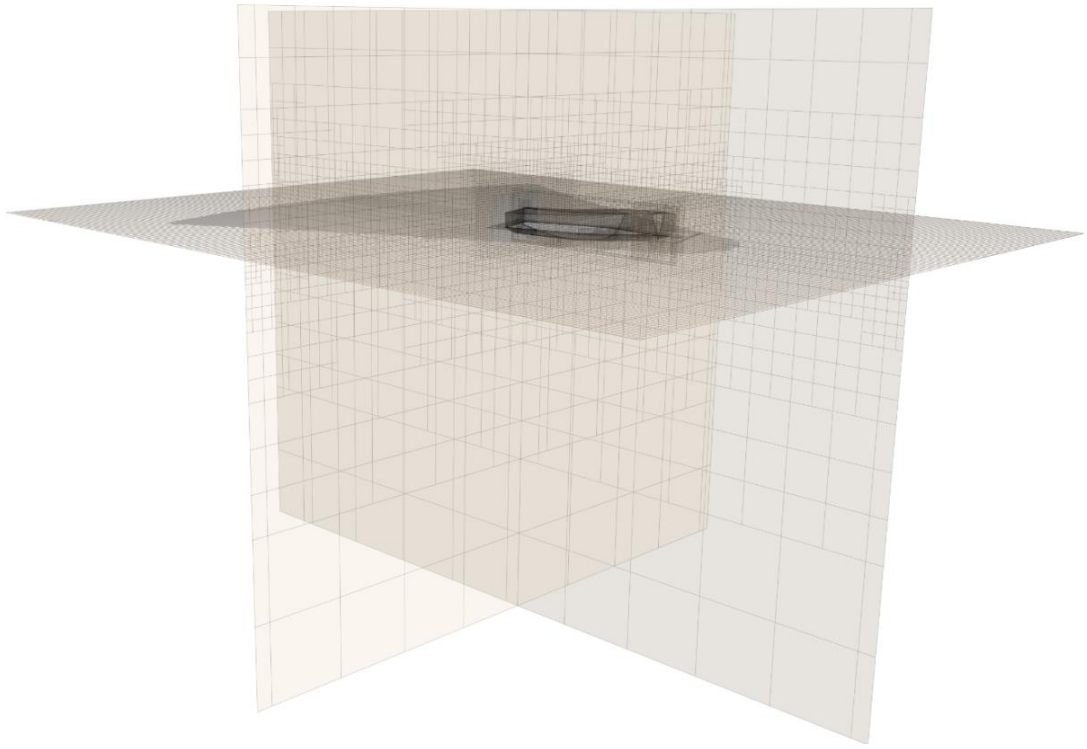

Figure 5-14 NPL fine mesh for validation and verification

Table 5-5 Calculated validation and verification values for grid convergence study for 20m NPL hull at 10 Knots

10 Knots	*Drag %*	*Trim %*	*Sinkage %*
Fine	1.27	2.43	1.88
Medium	5.65	7.85	6.13
Coarse	18.77	21.11	17.98
ε_K21	4.38	5.42	4.25
ε_K32	13.12	13.26	11.85
Convergence condition Rk	0.334	0.409	0.359
Numerical error WRT EFD	4.38%	5.42%	4.25%
Uncorrected			
Numerical uncertainty	6.57%	7.09%	6.12%
Validation uncertainty	7.03%	7.52%	6.61%
Comparison error	-1.27%	-2.43%	-1.88%
Corrected			
Numerical uncertainty	2.19%	1.67%	1.87%
Validation uncertainty	3.32%	3.01%	3.12%
Comparison error	3.11%	3%	2.37%

Table 5-6 Calculated validation and verification values for grid convergence study for 20m NPL hull at 20 Knots

20 Knots	*Drag %*	*Trim %*	*Sinkage %*
Fine	1.87	2.35	3.55
Medium	4.16	4.75	6.87
Coarse	11.35	13.56	17.57
ε_K21	2.29	2.4	3.32
ε_K32	7.19	8.81	10.7
Convergence condition Rk	0.318	0.272	0.310
Numerical error WRT EFD	2.29%	2.40%	3.32%
Uncorrected			
Numerical uncertainty	3.51%	3.90%	5.15%
Validation uncertainty	4.31%	4.63%	5.72%
Comparison error	-1.87%	-2.35%	-3.55%
Corrected			
Numerical uncertainty	1.22%	1.50%	1.83%
Validation uncertainty	2.78%	2.92%	3.10%
Comparison error	0.42%	0.05%	-0.23%

The results for the grid convergence validation and verification study are presented in Table 5-5 and Table 5-6. Based on these results, for both 10 kn and 20 kn a monotonic convergence can be observed for all three factors being tested for the grid convergence studies. However, initial simulations showed significant deviation from the calculator values for the NPL hull. This turned out to be the positioning and location of the attachment point for the DFBI setup. Upon correctly positioning the attachment point to be located at the centre of gravity the results fell more into line, and in turn able to be systematically studied.

The drag and the trim were found to be more closely correlated to the calculated values at the higher 20 kn speed between the different base sizes, while the sinkage showed greater accuracy for the slower speed. Overall, these results fall within the minimum level of accuracy desired.

Table 5-7 Calculated validation and verification values for time step convergence study for 20m NPL hull at 10 Knots

10 Knots	*Drag %*	*Trim %*	*Sinkage %*
0.005 (s)	1.27	2.43	1.88
0.01 (s)	3.63	3.13	2.953
0.02 (s)	7.99	6.21	5.65
ε_K21	2.36	0.7	1.073
ε_K32	4.36	3.08	2.697
Convergence condition Rk	0.541	0.227	0.398
Numerical error WRT EFD	2.36%	0.70%	1.07%
Uncorrected			
Numerical uncertainty	3.60%	1.19%	1.44%
Validation uncertainty	4.38%	2.77%	2.88%
Comparison error	-1.27%	-2.43%	-1.88%
Corrected			
Numerical uncertainty	0.43%	0.49%	0.36%
Validation uncertainty	2.54%	2.55%	2.53%
Comparison error	1.09%	-1.73%	-0.81%

Table 5-8 Calculated validation and verification values for time step convergence study for 20m NPL hull at 20 Knots

20 Knots	*Drag %*	*Trim %*	*Sinkage %*
0.005 (s)	1.87	2.35	3.55
0.01 (s)	2.27	3.71	4.87
0.02 (s)	5.61	6.333	7.005
ε_K21	0.4	1.36	1.32
ε_K32	3.34	2.623	2.135
Convergence condition Rk	0.120	0.518	0.618
Numerical error WRT EFD Uncorrected	0.40%	1.36%	1.32%
Numerical uncertainty	0.75%	1.68%	3.77%
Validation uncertainty	2.61%	3.01%	4.53%
Comparison error	-1.87%	-2.35%	-3.55%
Corrected			
Numerical uncertainty	0.35%	0.16%	0.82%
Validation uncertainty	2.52%	2.51%	2.63%
Comparison error	-1.47%	-0.99%	-2.23%

This time step convergence study used the finest mesh setup along with a factor of 2 for the refinement value, unlike the grid convergence study that used a factor of √2. The results for the time step convergence study are shown in Table 5-7 and Table 5-8. Like the grid convergence study, the time step study also follows monotonic convergence. The error margins for the time step are smaller between the different factors, which shows that the grid has a greater effect on the simulation accuracy rather than the time step.

From these results it is also seen that the trim on sinkage have a greater accuracy than the drag when the time step is increased. This is likely due to the high Y plus prism layer being implemented which can be susceptible to fluctuations in time step. Although convergence has been observed, it is possible that any greater increases in time step may have an impact on the simulation stability. As this simulation is used for greatly varying designs, simulation stability is vital, therefore, the time step must be carefully monitored.

Table 5-9 Calculated validation and verification values for iterative convergence study for 20m NPL hull at 10 Knots

10 Knots	*Drag %*	*Trim %*	*Sinkage %*
20 (inner iteration count)	1.27	2.43	1.88
14 (inner iteration count)	2.33	3.59	3.89
10 (inner iteration count)	4.56	5.614	6.924
ε_K21	1.06	1.16	2.01
ε_K32	2.23	2.024	3.034
Convergence condition Rk	0.475	0.573	0.662
Numerical error WRT EFD	1.06%	1.16%	2.01%
Uncorrected			
Numerical uncertainty	1.16%	8.03%	7.82%
Validation uncertainty	2.75%	4.41%	8.21%
Comparison error	-1.27%	-2.43%	-1.88%
Corrected			
Numerical uncertainty	0.12%	0.40%	1.94%
Validation uncertainty	2.50%	2.53%	3.16%
Comparison error	-0.21%	-1.27%	0.13%

Table 5-10 Calculated validation and verification values for iterative convergence study for 20m NPL hull at 20 Knots

20 Knots	*Drag*	*Trim*	*Sinkage*
20	1.87	2.35	3.55
14	2.13	2.98	4.76
10	3.75	3.897	7.11
ε_K21	0.26	0.63	1.21
ε_K32	1.62	0.917	2.35
Convergence condition Rk	0.160	0.687	0.515
Numerical error WRT EFD	0.26%	0.63%	1.21%
Uncorrected			
Numerical uncertainty	0.47%	3.37%	1.45%
Validation uncertainty	2.55%	4.20%	2.89%
Comparison error	-1.87%	-2.35%	-3.55%
Corrected			
Numerical uncertainty	0.21%	0.91%	0.14%
Validation uncertainty	2.51%	2.66%	2.50%
Comparison error	-1.61%	-1.72%	-2.34%

As this is relatively basic resistance and vertical motion simulation being performed, an iterative convergence study can also be conducted alongside the time step convergence studies. This is the first of this test within this overall study. The study focuses on the inner iterations count for each time step. The initial step count is 10, with an increase in increment based on the factor of √2. The initial step is slightly higher than the minimum that may be normally seen when conducting a basic resistance simulation. This is based off the reasoning that this simulation is used for a greater more complex PMM simulation, and therefore if low and iteration count show stability the higher number is sufficient for the PMM. It is also based off the theory applied when running the wave-based simulations. This theory has been described in greater detail in both chapters 10 & 4 when waves have been simulated.

Although this increase in iteration count significantly slows the simulation, the simulation stability is key to ensuring a stable platform to build off when running the optimisation analysis. It is therefore important to ensure that the simulation is stable without any user input while it is running, as a slower simulation is better than a failed simulation. It is also to be noted that these simulations can be physically sped up by increasing the core count when running on the remote high-performance computer Archie-WeST.

The calculated study results are presented in Table 5-9 & Table 5-10. As like the previous studies, these results follow monotonic convergence pattern. This is expected, as the iterative steps are already larger than would normally be considered for such a simulation. The iterative study shows the best convergence rates between the different speeds and convergence factors. With the drag and the trim having the lowest error changes between the different steps in refinement ratio's, while the sinkage has the largest change. This is observed for both 10 kn and 20 kn, which in turn shows good simulation stability when moving between different speeds.

These three studies show that the simulation attains the minimum required accuracy to be taken forward for the PMM simulations, along with a consistent stability for all different levels. This allows for a greater level of confidence in the final simulation using the finest mesh, the smallest time step, and the largest number of inner iterations.

5.5. Concluding remarks

This chapter presented the methodology used to develop and model a fully parametric hull. The methodology is based around a monohull form for all speed variants, which can be used for a single symmetrical catamaran hull as well. This method utilised the meta-surfaces to control surface curvature and position by varying control curves. The model can be scaled directly in the parametric setup allowing for rapid switching between model in full-scale. This model is then integrated into the parametric CFD setup developed above in chapters 10 and 4, to create a fully parametric hull form and CFD setup that can be easily tailored to any simulation criteria.

Upon completing this integration, the parametric hull was modelled to match an existing hull form that was used extensively in experimental tests. This allowed a basis for validating the fully parametric setup within CFD. This validation and verification study found good agreement with the experimental data supporting this simulation setup. Not only this the parametric hull was able to match the NPL geometry within a good degree of accuracy. This allows for the simulation and parametric hull to be utilised for optimisation research.

6. Development of manoeuvring evaluation equation

6.1. Introduction

Throughout this study there has been a primary focus on optimising and reducing the complexity of CFD simulations with the aim of using these simulations in an optimisation capacity. In addition to speeding up the CFD simulations, automated and parametric modelling techniques have been employed to slipstream the process from concept to result in a single workflow. This workflow has led to accurate results for both replicating towing tank simulations, as well as matching calculated vessel dynamics and resistance.

Based on these foundations the next stage utilises this workflow to develop and present a methodology for optimising vessel manoeuvring characteristics based purely on the geometric characteristics of a given hull. This moves away from the standard methods for analysing a vessel's manoeuvring characteristics, i.e., manoeuvring coefficients, and put forward new geometric coefficients that have been found to consistently influence how a vessel manoeuvres.

By utilising such coefficients an equation that is independent of any physical or computer testing for the user can be created. To create such an equation extensive CFD simulations are used to analyse the design space for a parametric hull that has a base hull design starting from the NPL parent hull. Throughout this testing a wide range of radical parametric hull's are coupled with the methodologies presented in chapters 10, 4 & 5. During this research extra and more complex geometric coefficients are developed to refine and strengthen the proposed equation to ensure greater flexibility in the hull design. This is vital as this equation should not be solely restricted to NPL hull styles, this of which may be a potential problem with this methodology, however it is hoped by acknowledging the potential for a problem at this stage avoids this error becoming baked into the equation.

The theory for each of the geometric coefficients, as outlined below, which enables the development of the preliminary equation and in turn the methodology for developing the equation further. This methodology also presents key aims and objectives in the development process. The final equations and workflow presented in this chapter is a completely novel and unique approach to manoeuvring optimisation, as well as a fresh perspective on how an optimisation may be conducted.

6.2. Outline of methodology

Throughout this study the primary focus has always been around a bare hull analysis. Although in key chapters bare hull analysis has been modified to include bilge keels, the overall process has excluded appendages, such as rudders and propellers. Due to this focus on bare hull analysis a significant understanding of the key characteristics affecting vessel motions has been acquired. It is based on this understanding that unique coefficients are created to be used in the ranking manoeuvring equation. The key aspects in developing this equation are shown below, along with key objectives that must be obtained to have a suitable equation.

Key equation objectives must:

- focus primarily on the Y force and Z moment.
- solely focus on geometric properties and not be dependent on prior simulation or tests.
- be able to be used with any mono hull type.
- focus primarily on low dynamic motions, i.e., no planing hulls.
- account for multi-degrees of freedom.

To develop such a flexible equation, multiple generations of hull designs as well as equations are used. Each generation improves the accuracy without compromising the flexibility of the equation. This is achieved by either modifying the equation or modifying the geometric coefficients. Modifying the equation may include additional variables added relating to the hull, i.e., the block coefficient, or purely mathematical changes. Whereas, modifying the geometric coefficients may involve creation of new coefficients, removing coefficients or combining coefficients together to create new coefficients.

Each generation is re-evaluated in comparison with a selection of key hull forms that were created as the initial generation. This initial generation, or GEN-0 known hereafter, has a seed hull based on the NPL parent hull. There is a limited number of parameters that can be changed for this hull from, along with a few constraints to reduce excessive geometric change and therefore complicate the development of the geometric coefficients. It is important at this stage control as many variables as possible to isolate the key factors influencing the manoeuvring forces.

GEN-0 is comprised of around 100 hull forms, all of which are simulated in CFD using the fully parametric PMM methodology developed in chapter 4. The hull forms that are created based off a Sobol pattern to ensure even spread across the design space. These hull forms are ranked with respect to the Y force and Z moment, and then evaluated to find re-occurring

geometric patterns. The geometric patterns are developed into the initial geometric coefficients which in turn are developed into the first manoeuvring equation.

Upon developing this first equation a separate generation of hull forms are created based on a new set of input parameter values and limits, as well as different parametric constraints. This generation again utilises the Sobol pattern to fill the design space, however this is entirely new design space compared with GEN-0. There are two main reasons for this, firstly to test the initial equation and geometric coefficients, and secondly to ensure random hull variation is continuously being tested against and worked into the equation. This ensures greater versatility for the equation. This initial parallel generation is fully analysed in CFD, compromising of around 100 hull forms.

This full design space analysis in CFD is not continued in future generations, but rather key regions and the design space are taken to be analysed in CFD. This is again due to 2 main factors, firstly the time required to run and evaluate over 100 designs within CFD, and secondly future generations become significantly larger to help refine the geometric coefficients, future generations include thousands of designs.

Each new generation of the modified equation have a parallel Sobol design space created to test and refine the model. Each new Sobol design phase has a completely new set of potential designs ensuring the model can account for the versatile range of hull forms. Once the model has been refined to the desired accuracy level optimisations are run, after a constraint sensitivity study has been conducted.

This constraint sensitivity study focuses on a completely new design which do not start from the NPL parent hull, but rather a set of key specific requirements and may be given by potential client. These include a specific displacement, specific beam, draft or even twin propeller tunnels. The study initially utilises the Sobol analysis to evaluate the design space, while in parallel a full optimisation to find the pareto frontier is conducted. This sensitivity study helps to clearly evaluate the flexibility and accuracy of this methodology before running the final optimisation on the NPL hull form. If this study finds problems with the accuracy, the model is re-evaluated and again retested.

A flowchart representing the process involved in creating the equation is shown in Figure 6-1. This depicts the process described in detail above. It highlights the feedback loops which are required to refine and ensure versatility of the equation. Each time one of these feedback loops is completed a new generation of equation is created and in turn evaluated, both with the original design space and the new parallel design space.

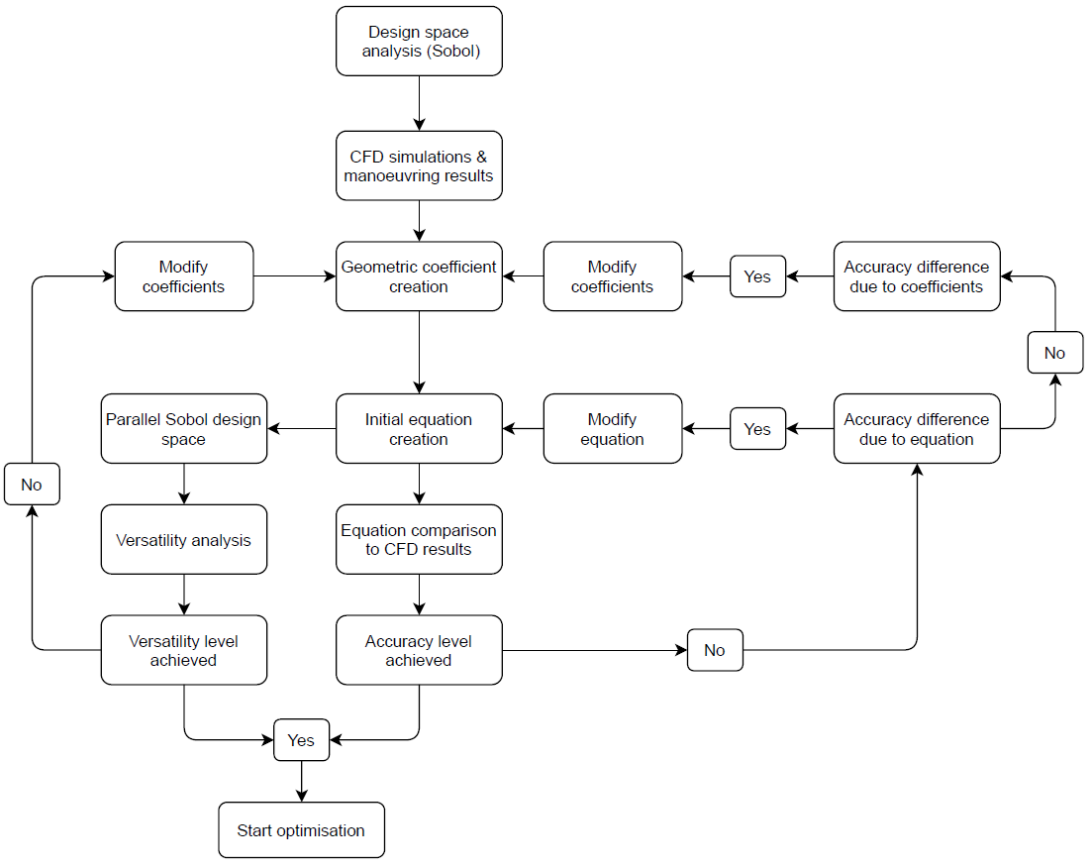

Figure 6-1 Equation development flowchart

6.3. Initial Sobol analysis with CFD results and preliminary geometric coefficient creation

This section breaks down the initial Sobol analysis acting as the foundation for developing the preliminary geometric coefficients. The creation of these geometric coefficients is based on external research along with personal research experience. It is hoped that an efficient analysis of key geometric factors highlight a pattern with respect to the Y force and Z moment of a given hull form.

As mentioned before, the Sobol sequence is used to evaluate the design space prior to developing the geometric coefficients. The Sobol sequence is an example of a quasi-random low discrepancy sequence, meaning that the design space is evenly distributed between a given number of designs. In this initial case 100 designs are used. This ensures that the hull forms generated have the greatest possible variation for the given number and input parameters.

For these 100 designs the limit for the input parameter values are set to 25% variation from those used to create the parent hull. The draft, waterline length and beam are constrained to match the NPL parent hull. The displacement of the hull is constrained for these initial designs,

the constraint are set to 10% plus or minus that of the parent hull. Although this reduces the total number of viable hulls that can be simulated in this initial run, it ensures that the main factors influencing the change in fluid forces are those created by the geometry, and not merely an entirely new hull form. Unlike an optimisation algorithm, the Sobol sequence does not ignore or stop at a design which breaks the defined constraints. This is useful for two main reasons, firstly, as this sequence algorithm can create extremely large design ranges that can be evaluated. Secondly, as CAESES allows for each design run to be evaluated based on the individual input parameters, the key parameters which caused various hull forms to break the constraints can be highlighted. This significantly helps to tune and refine the limits for each input parameter so as not to create invalid designs. A comparison of a design space created based on pseudo-random vs quasi-random numbers (Sobol) is shown in Figure 6-2 (Savine, 2018). The same population value is used for both design spaces, with the right design space being filled using a Sobol algorithm.

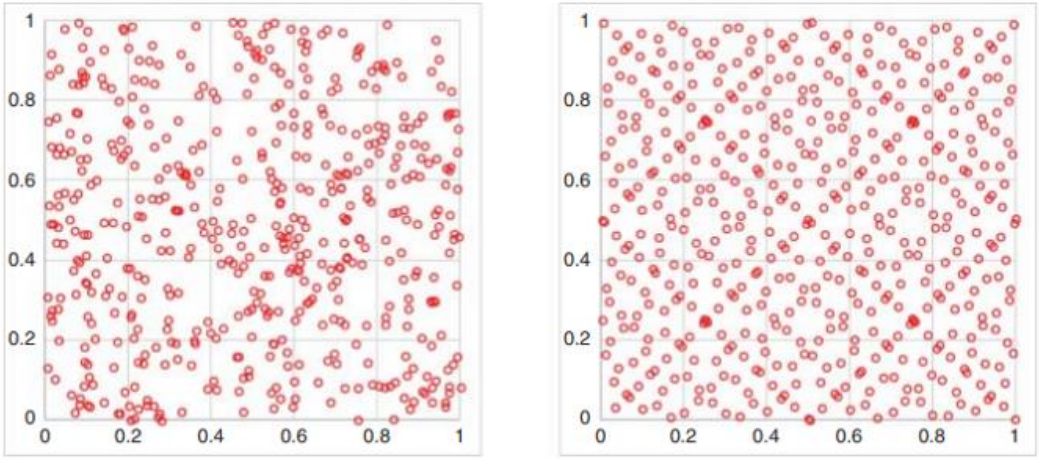

Figure 6-2 Comparison of pseudo-random and quasi-random (Sobol) generated design space (Savine, 2018)

As each design does not vary the overall length, beam or draft of the vessel, the volumetric refinements for the PMM simulations does not vary. This simplifies the creation of the simulations, as the only variables to change from simulation to simulation is the hull geometry and the corresponding hull characteristics. These design a closed STL file and CSV file is exported providing both the hull geometry and new centre of gravity details. It is assumed throughout all the simulations that the pivot point for the PMM simulation act directly above the centre of gravity by a specified amount.

A simple Java macro has been recorded in Star CCM+ that imports the new geometry, replace old geometry, define it as a region and specify as a DFBI body. Once in the DFBI body has been specified the pivot point can be modified to match that hull form. In addition, the new

displacement can also be inputted. Once these steps have been completed the mesh is generated and the simulation initialised.

To further speed this initial analysis, the forces acting upon hull also have a moving average applied to it. This was found to be highly effective at reducing the noise in the results without reducing or negatively impacting the key values.

Along with the respective forces acting upon the whole, key images of the hull and the fluid regions is also be saved to later be converted to short videos. This helps to visualise and understand the key characteristics effecting the flow around the hull. One such key visualisation, as used for the DTMB hull, is the turbulent flow generated from the turns.

Based on the initial constraints a total of 34 hull forms were valid from the original 100. The hull forms were run through the import procedure and simulated on the HPC Archie-WeST. Each simulation took around 18 hours to reach a point of convergence. The hulls were then ranked with respect to both Y force and Z moment. The free hull forms with the maximum and minimum Y force and Z moment were exported into Rhinoceros 3DM where they could be overlaid and easily compared visually and geometrically to one another. This is the first stage in developing the coefficients as well as bringing forward the theoretical knowledge built up throughout the previous chapters.

The initial equation coefficients focus on one singular equation combining both the Y force and Z moment. This would eventually be split into two separate equations, one for the Y force and one for the Z moment. This does not happen however until at least the fourth generation.

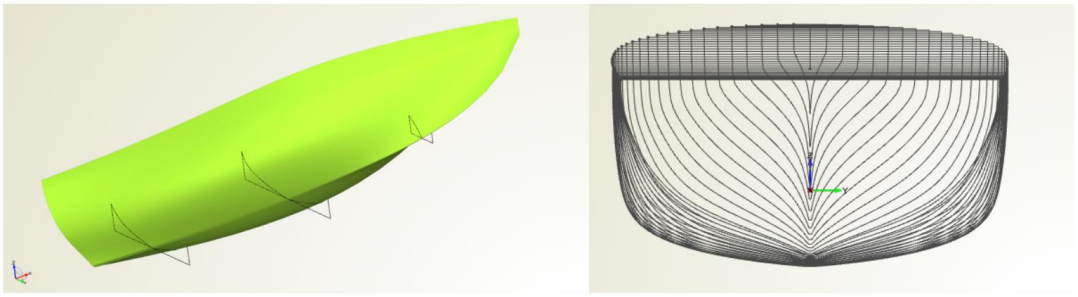

Figure 6-3 Hull form and sectional lines for hull 1 with minimum Y force and Z moment

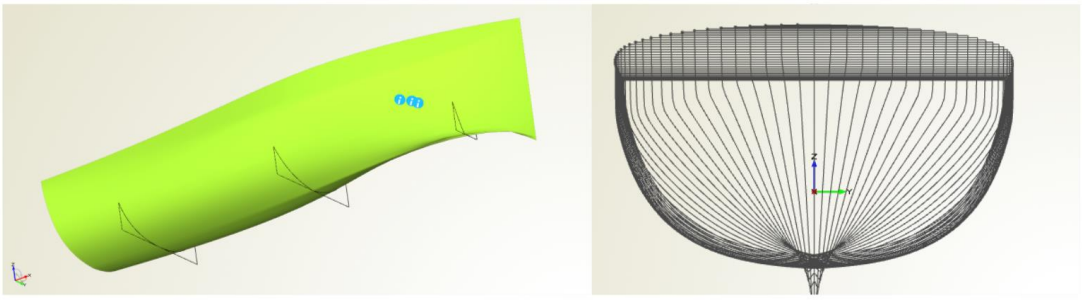

Figure 6-4 Hull form and sectional lines for hull 34 with maximum Y force and Z moment

An example of the two extremes of the results spectrum can be seen in Figure 6-3 and Figure 6-4. A few quick conclusions can be drawn from merely viewing the respect of hull forms.

- hull 1 has the smaller longitudinal sectional area out of the two
- hull 1 has minimal radical hull curvature
- the bow of hull 34 extends below the keel line

Based on these observations, two initial geometric coefficients are be conceptualised. This is first the longitudinal cross-sectional area of the hull below the waterline running along the centre line. This gives an immediate numerical value to the area that greatly affect the Y force of a hull form. This coefficient is simply modelled directly into the parametric modelling workflow, giving an immediate evaluation upon the creation of any hull form.

The second geometric coefficient is based off the longitudinal sectional area however this focuses on the area's centroid. As mentioned above the pivot points is acting the centre of gravity which is directly above the centre of buoyancy, i.e., the volumetric centroid of the underwater volume. The second coefficient considers both vertical and longitudinal difference between the longitudinal sectional area's centroid and the centre of buoyancy. This coefficient has a greater bearing on the moment, as it highlights in simple terms the moment arm acting on the underwater volume. In addition to this, the coefficient also highlights the displacement distribution for a given hull. For example, hull 34 has a large difference between longitudinal sectional area centroid and the centre of buoyancy, this is primarily due to the wave piercing vertical bow. The forward section of the hull is very slender in comparison to the aft two thirds, causing the majority of displacement to be found aft of the midship, whereas there is a relatively even distribution across the length of the hull for the longitudinal area. This combination causes a significant moment to occur, not only due to the large longitudinal area but also due to the change in hull slenderness between the bow and the aft. Although this is a simple coefficient, it is highly effective in highlighting multiple key factors that influence a hull forms manoeuvring capability.

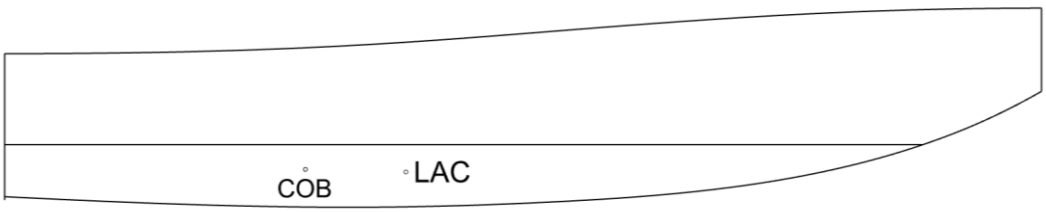

Figure 6-5 Longitudinal area coefficient diagram with highlighted centre of buoyancy

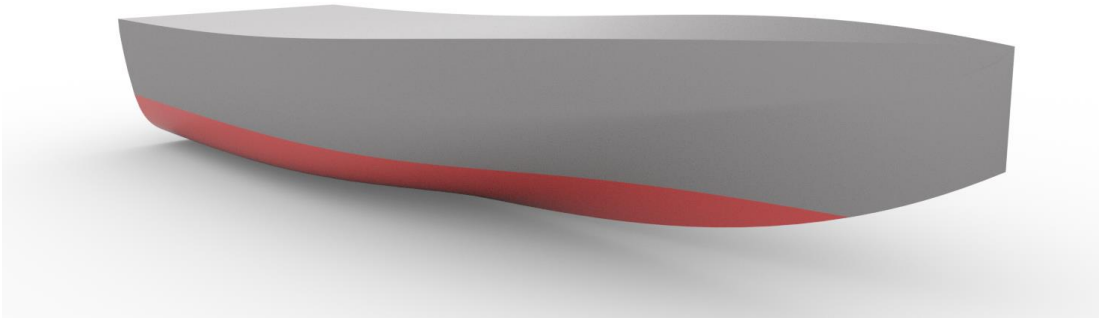

Figure 6-6 Hull form represented in Figure 6-5

Longitudinal area coefficient is visually represented in Figure 6-5, with the respective hull is shown in Figure 6-6, this is not the NPL parent hull but rather a hull with a slighter bow to help differentiate between the centre of buoyancy and longitudinal area coefficient.

With these initial geometric coefficients, a preliminary equation could be written, this equation had an overall trend matching the results obtained through CFD but was failing to achieve any accuracy towards the ends of the results. This therefore meant the addition of either coefficients obtained from the standard hull characteristics or the creation of extra geometric coefficients. The results were compared with the key characteristics, such as block coefficient or water plane area coefficient, however none of these coefficients compensate for the initial accuracy error.

Therefore, a new coefficient is created. Although the standard hull characteristic coefficients were unable to compensate the error, the block coefficient did have a slight tendency to improve the result compared to other coefficients. Due to this information the new coefficients is based off the idea and concept of the block coefficient.

For almost all fluid-based optimisations, when aiming to reduce drag and improve motion through the fluid, smooth surface curvature is key. This is a cornerstone to resistance optimisation for marine vessels and in turn plays a vital role in minimising lateral forces.

Therefore, a geometric coefficient that helps to numerically distinguish the surface curvature and key points help in the development of this equation. The concept usees four slices evenly spaced along the underwater hull; the slices have a two-dimensional block coefficient calculated. This coefficient roughly helps to evaluate the surface curvature at this specific section. By combining these four sections an idea of the overall underwater hull surface curvature can be obtained. This is particularly important when focusing on concave surfaces, such as the bow in this example. This phenomenon is discussed in greater detail by Muck (1985), who discuss that concave curvature has a destabilising effect on turbulent flow compared with convex.

The coefficient is calibrated by simply creating the ratio between the area of the section and the corresponding bounding box around each section, thus a two-dimensional block coefficient. This coefficient, however, is altered such that the upper limit is moved to 2 rather than 1. With one representing a sectional area equalling exactly 50% of the bounding box. This ensures that any sectional area which has a greater proportion than 50% as a cumulative effect.

After adding these coefficients to the initial equation, it was found that 4 sectional cuts were too many and in the incorrect positions. The number of sectional cuts was reduced to 3, with the middle cut positions at the midpoint. The two end sections were then initially placed 10% from the most fore and aft positions. This position is later refined through a focused systematic study to help improve the overall equation accuracy. The sectional cuts can be seen in Figure 6-7 along the hull with Figure 6-8 showing a detailed view of the free sectional cuts and boxes.

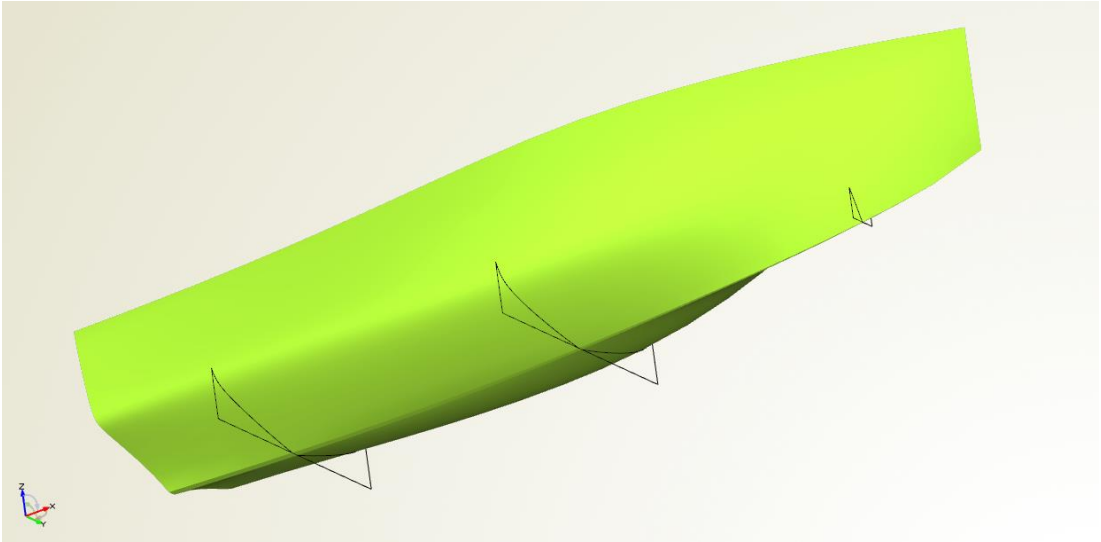

Figure 6-7 Hull 18 with sectional cuts and corresponding bounding boxes

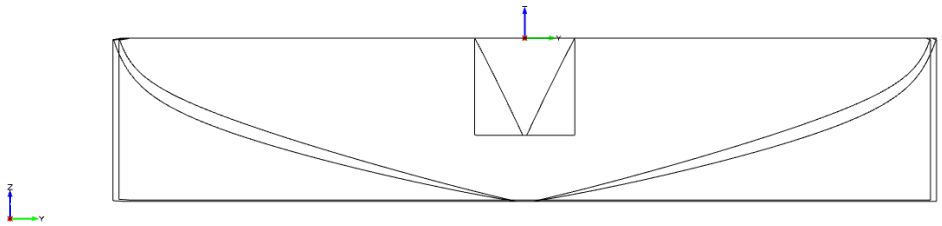

Figure 6-8 Detailed view of hull 18s sectional cuts and bounding boxes

These coefficients coupled with the longitudinal area coefficient help to clearly describe the hull curvature from the bow to stern. This is in essence the key and base of this equation. Based on these coefficients a preliminary equation was written. This equation was then tuned with an Excel sheet and the initial Sobol CFD simulations. This initial tuning did not satisfy the accuracy desired; therefore more generations and more model refinement are required.

The initial equation for both the Y force and Z moment for hull ranking is given in equation (6-1). To improve the accuracy as well as the flexibility of the equation, each coefficient and factor of the equation had a power applied to it which could be quickly varied in the Excel sheet. This allowed for rapid tuning, as well as quick isolation of the impact of different coefficients.

$$\left\{\left(\left|\left(\frac{\Delta Z}{10}\right)\right|^{N1}+\Delta X^{N2}\right)+\left(SAC_{Aft}^{N3}+SAC_{mid}^{N4}+SAC_{Frwd}^{N5}\right)^{N6}\right\}^{N7}=Hull\ Ranking \tag{6-1}$$

A breakdown for definition of each coefficient as well as the various power values used in this initial equation are shown in Table 6-1 and Table 6-2. As can be seen the lateral area was discarded from this first iteration of the equation.

Table 6-1 Initial equation coefficient breakdown table

ΔZ	*Vertical difference in height between central buoyancy and longitudinal area centroid*
ΔX	*Lateral difference in height between central buoyancy and longitudinal area centroid*
SAC_{Aft}	*Aft sectional area coefficient*
SAC_{Mid}	*Midpoint sectional area coefficient*
SAC_{Frwd}	*Forward sectional area coefficient*

Table 6-2 Initial ranking equation values for each power

N1	1
N2	3
N3	1
N4	1
N5	1
N6	0.6
N7	1.25

The output from the initial manoeuvring ranking equation for 25 hull forms is shown in Figure 6-9 against the simulated Y force. The calculated output from the equation shown in Figure 6-9, shows a clear stepping between the hull forms, but most importantly in a close matching between the maximum and minimum of the simulated CFD. This becomes a key focus for the future equations in maintaining this pattern- accuracy. This equation is also compared to the Z moment in Figure 6-10. As can be seen from both graphs the maximum and minimum regions are accurately estimated, however the region in the middle deviates significantly from the simulated results. Further to this, designs 6 through to 10 are significantly overestimated through this equation, while some values are lower than the first of five designs. This is particularly noticeable for Z moment shown in Figure 6-10.

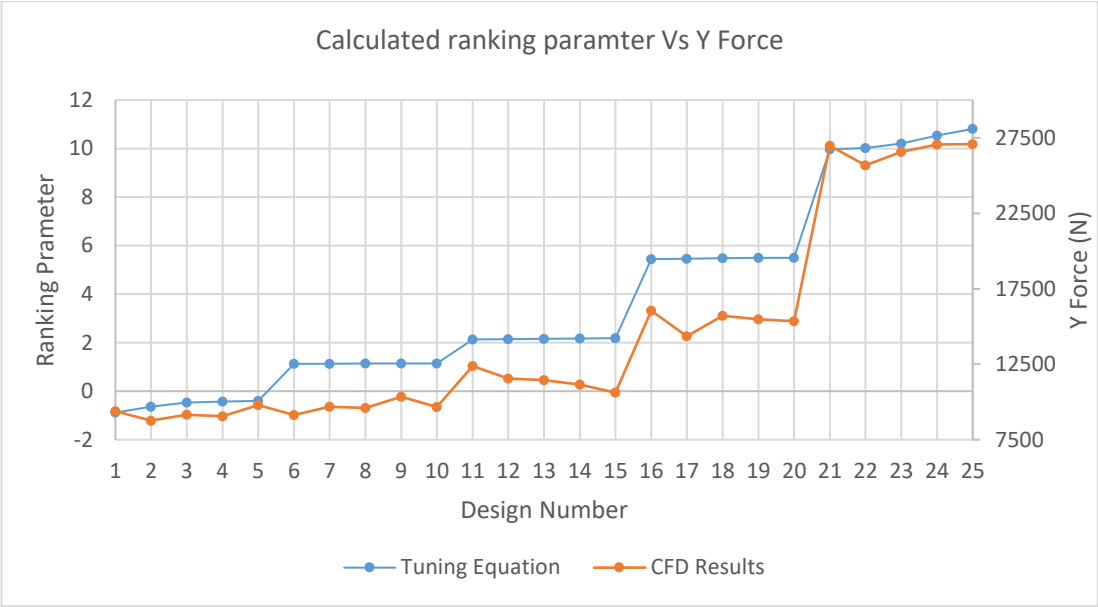

Figure 6-9 Graph comparing the initial manoeuvring ranking equation outputs vs the Y force of each hull form

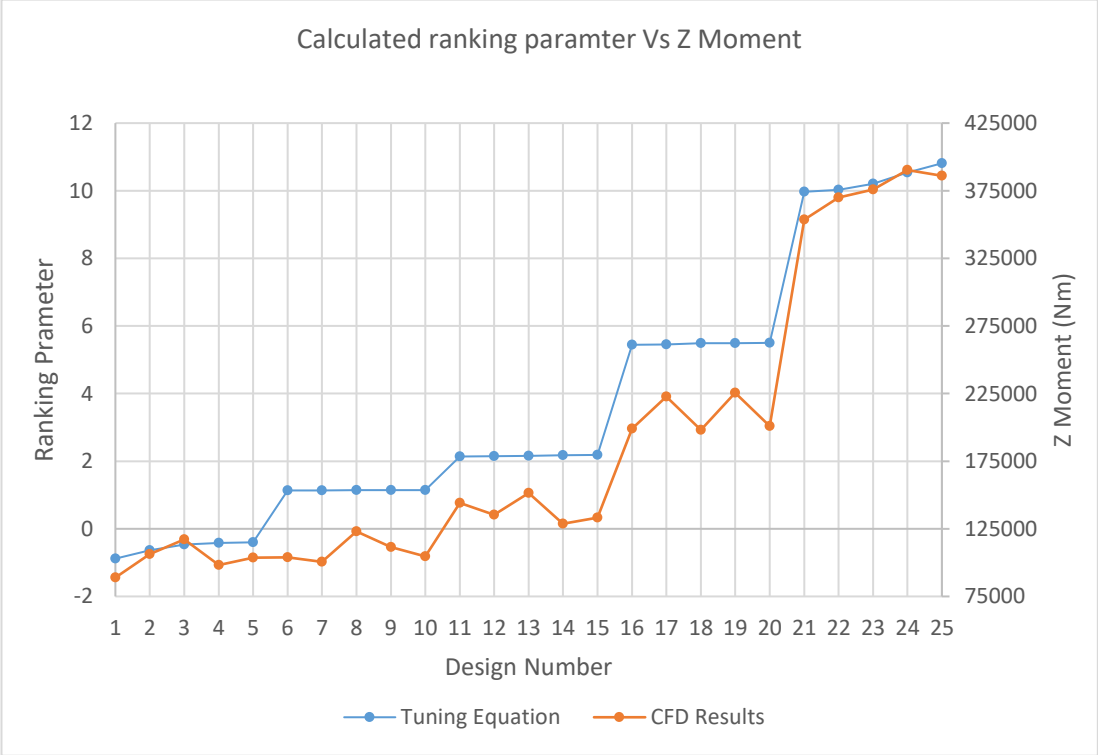

Figure 6-10 Graph comparing the initial manoeuvring ranking equation outputs vs the Z moment of each hull form

Although it is noticeable that there is a relationship between the Y force and Z moment, it is not impossible to have one singular equation they can be used to optimise for both. Therefore, a second equation is written for the Z moment from this point on. This initial secondary equation is modified by changing the values of the different powers shown in Table 6-2.

This failed to significantly improve the equation for the Z moment. Thus, leading to the creation of the first entirely new equation generation.

6.4. Model evolution

The next stage involves refining and iterating the current equation to improve the accuracy level. As highlighted in the end of Chapter 6.3, there is now two equations that are used for the optimisation, one for the Y force and the other for Z moment.

To have the greatest flexibility for tuning and refining the equations an Excel workbook is created. This Excel workbook is based off the analysis of 25 hull forms from each generation. These 25 hulls are selected at key intervals from the valid Sobol designs. These 25 designs are split into five individual groups consisting of five designs each. The position of each group can be visualised in Figure 6-11, with the five groups evenly spaced across the design range. A total of 25 designs for analysis were chosen to both save computational simulation time as well as giving a macro view at each point where a group is located. This helps to both visualise the overall pattern as well as a detailed view between the individual holes in each group.

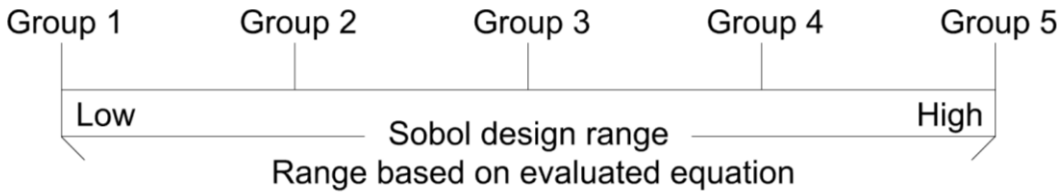

Figure 6-11 Group distribution Sobol design range

By using the Sobol algorithm rather than an optimisation algorithm, i.e. a T-search, there is greater variation between the five designs in each group. This is key to evolving and improving the overall equation accuracy. It is understood that if an optimisation algorithm has too many variables, the true optimum design may not be found as the algorithm may follow a specific path but may have missed another path in doing so. This is where an algorithm such as the Sobol proves to be more effective. This analysis approach is applied to the parallel generations when testing versatility on the current equation.

6.4.1. Model iterations

Each generation the maximum number of designs are increased to minimise the variation between the individual designs. This approach is hoped to improve the individual accuracy of the equation. The route taken to reach the final equation is shown in Figure 6-12. This diagram shows the point at which each generation inherited the equation, for example generation 3 directly inherited the base equations from generation 2, however generation 7 did not form

directly from generation 6 but rather parallel generation 4. This is due to the equation needing to be modified to account for the results obtained in parallel generation 4. There are only two instances when the parallel generation caused a change in the equation, these are generation 6 and generation 10.

In addition to the overall path depicted in Figure 6-12, the number of designs for each Sobol analysis is also shown for each generation. They can be seen the parallel generations never exceed a maximum number of 350 designs. This is due to greater focus on the overall pattern matching rather than the fine individual accuracy, which is principally focused on in the primary generations. As can be seen from Figure 6-12, generation 1 started with 100 designs which increased to a maximum design count of 8500 for generation 6. In addition to the overall design count the valid design count is also shown. Based on these generations' results the limits for each parameter were tuned, therefore allowing an increase in viable designs. This is not the case for the parallel generation, as these generations are designed to be completely independent from previous generation and therefore no parameter tuning is possible.

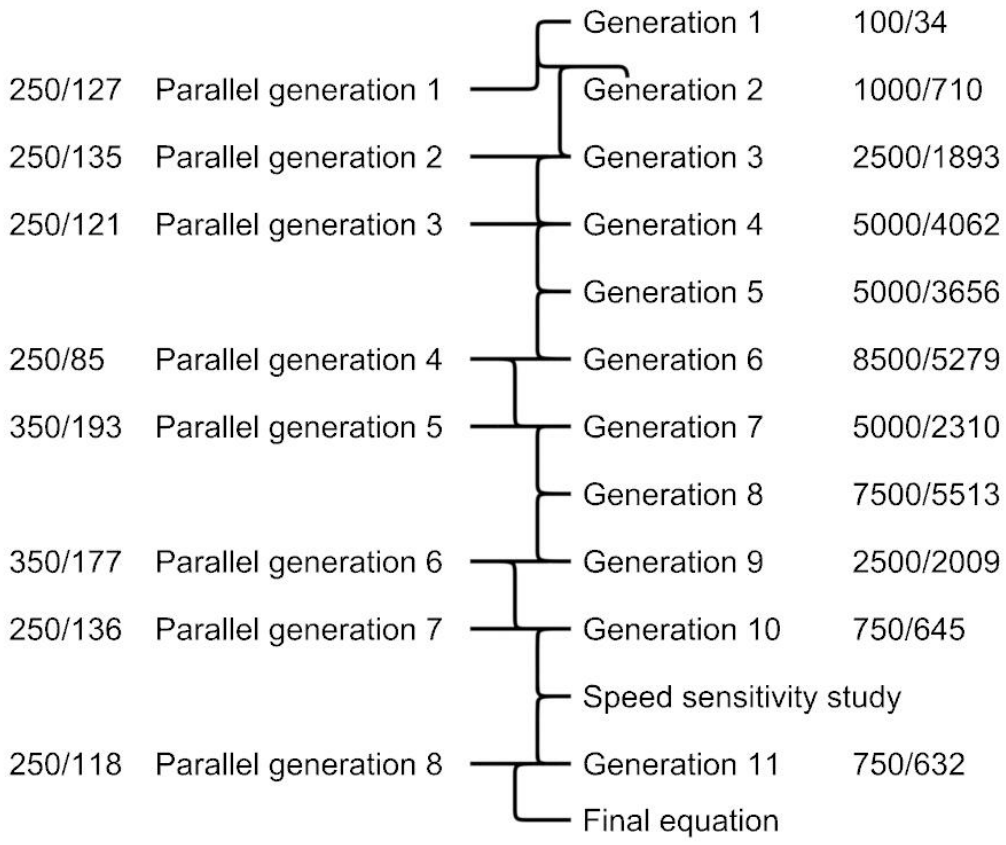

Figure 6-12 Diagram showing the route taken with each generation to reach the final equation

It is also noted that as the generations increase the number of designs follows closely to a bell curve, this is because when generations, generations 5, 6 and 7, primarily focused individual desired accuracy which caused a lack of accuracy for the overall equation. Therefore, the latest generations have reduced number of designs to retune for the overall path accuracy.

This was a consistent issue of balancing and refining the equations, as it followed closely to an oscillatory convergence pattern. Upon reaching generation 10 the accuracy for both the overall pattern and individual design had achieved an acceptable level. It is possible that the equations can be further improved through the addition of extra coefficients or more complex powers, however the equation had already reached a significantly greater level of complexity than the original and was becoming less and less user-friendly. Although it is not specifically stated, the user-friendliness of this equation is key as it should be simple and easy to apply to any hull form.

Further to this, a total of 275 hull forms from the primary generations were set up for simulation, however only a total of 187 were simulated. This was due to common designs reappearing throughout the different generations and therefore not requiring to be simulated again. This equated to around 3 ½ generations being saved from needing to be simulated, which in turn allowed for more generations than originally planned.

6.4.2. Speed and amplitude sensitivity study

Once generation 10 had been completed and the level of accuracy achieved, speed and amplitude sensitivity studies were conducted. Up to this point all the CFD simulations used the same carriage velocity and PMM oscillation amplitude. However, to ensure three versatile and stable equation the effect of these factors on the equation should be investigated.

Four studies are conducted, an increase and decrease for both the speed and oscillation amplitude from the baseline. This shows the stability of the equation all conditions. It is hypothesised that there is no significant change to the equation, this is due to 2 main reasons. Firstly, the speeds being tested at do not create any significant dynamic motion, and therefore the underwater geometry does not vary greatly between the different speeds. This leads to the second point, that these equations are based upon the geometric characteristics of the hull and are independent of the flow field. However, this is not sufficient for the optimisation, thus these extra studies are conducted.

Each systematic study evaluates the exact same 25 hull forms. The only factors that change from simulation to simulation is the mesh to compensate for the change in speed and amplitude. Each test 25 hulls are ranked according to the proposed equation, these is then

compared with the simulated results to evaluate both the overall and individual pattern accuracy.

A breakdown for all the tests along with the baseline PMM tests is presented below in Table 6-3 and Table 6-4. Due to the flexibility of CFD-based manoeuvring tests, the velocities and oscillation amplitudes can be higher than that normally seen in the standard towing tank. However, to mitigate any unwanted dynamic lift the Froude number does not exceed 0.475.

Table 6-3 Speed sensitivity study test case breakdown

Test case	*Base*	*Speed Increase*	*Speed Decrease*
Froude number	0.36	0.46	0.25
Oscillation Amplitude (m)	5 m	5 m	5 m
Velocity	5 m/s	6.5 m/s	3.5 m/s
Speed knots	9.72 kts	12.636 kts	6.804 kts

Table 6-4 Amplitude sensitivity study test case breakdown

Test case	*Base*	*Amp Decrease*	*Amp Increase*
Froude number	0.36	0.36	0.36
Oscillation Amplitude (m)	5 m	2.5 m	10 m

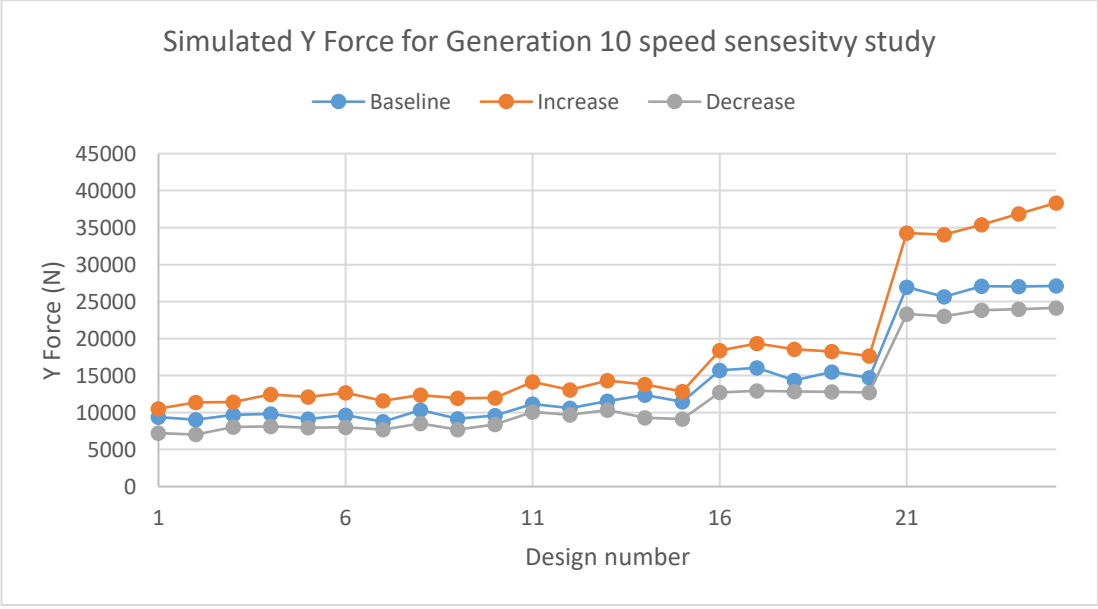

Figure 6-13 Comparison of Y force results for speed sensitivity study

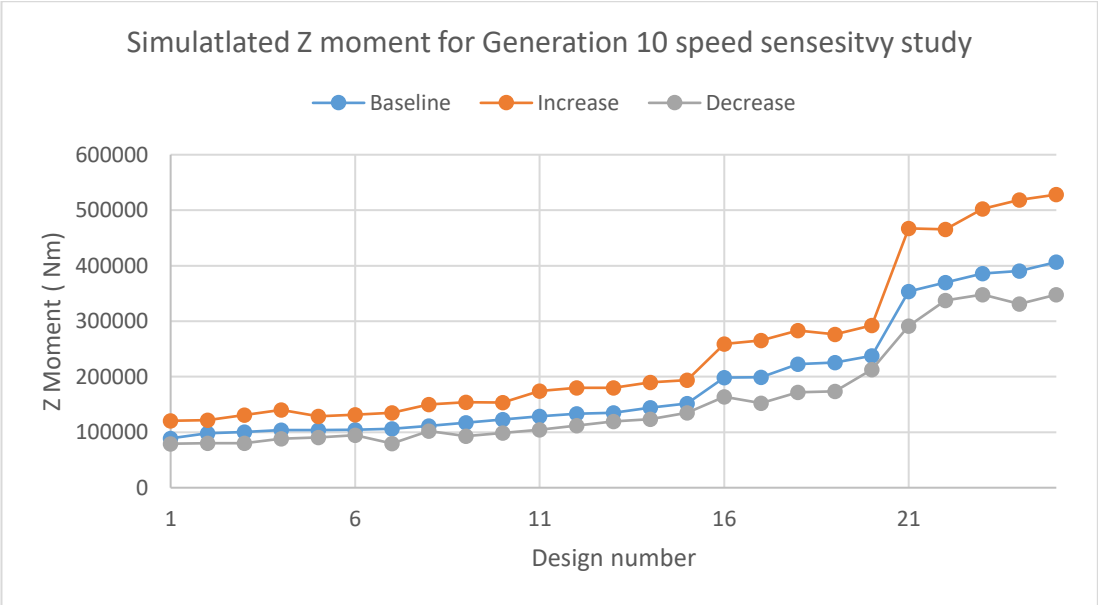

Figure 6-14 Comparison of Z moment results for speed sensitivity study

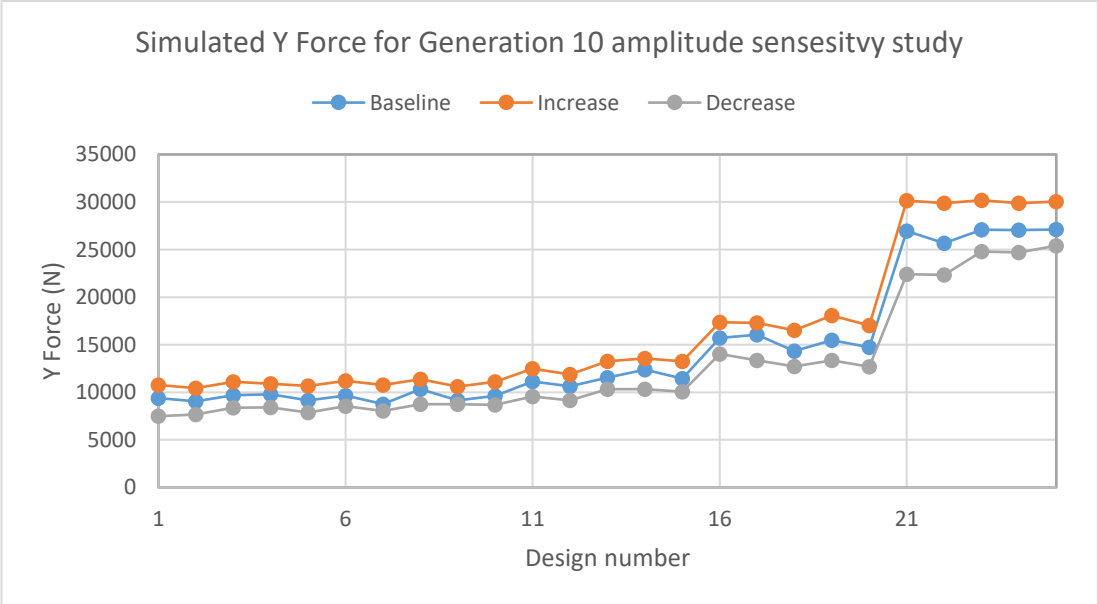

Figure 6-15 Comparison of Y force results for amplitude sensitivity study

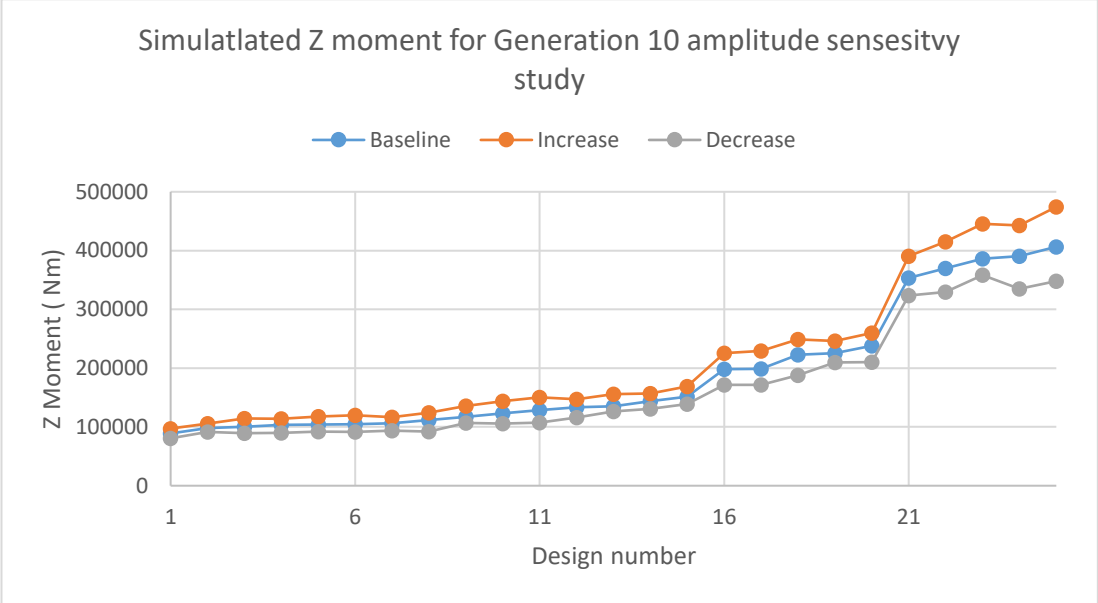

Figure 6-16 Comparison of Z moment results for amplitude sensitivity study

It can be seen from the results presented in Figure 6-13, Figure 6-14, Figure 6-15 & Figure 6-16, that both the Y force and Z moment follow the same trend as the baseline results, merely with a slight increase or decrease on the results. Based on these results the final 10th generation equation does not need to be modified, as this equation follows the trend predicted by both sensitivity studies. This is also due to the equation being independent of the forces and moments, and therefore possible to be scaled.

There was a greater increase and decrease in the results for the speed variation study compared with the amplitude variation. The increase in the oscillation amplitude did not equate to an equivalent increase in velocity, compared with the velocity change of the sensitivity study.

More research on the effects and repercussions of varying speeds and amplitudes are considered for future work, but at this point equations generated through this multigenerational process are believed to be sufficient for the future optimisation.

6.5. The final model equation

Upon completing the evolution of the equations the final equation ispresented here along with a description of the key aspects focused upon in each equation. The initial equation is given again below for easy comparison, equation (6-2).

$$\left\{\left(\left|\left(\frac{\Delta Z}{10}\right)\right|^{N1}+\Delta X^{N2}\right)+\left(SAC_{Aft}^{N3}+SAC_{mid}^{N4}+SAC_{Frwd}^{N5}\right)^{N6}\right\}^{N7}=Hull\ Ranking \quad (6\text{-}2)$$

The equation calibrated to predict the Y force acting on the hull based on the key geometric coefficients are presented first. This equation, equation (6-3), is the simpler out of the two equations. This is primarily due to the dominating factor being the lateral area of the underwater hull.

$$\frac{\left[Lateral\ _{Area}+\frac{1}{\Delta X}+\frac{\Delta Z}{10}+\left(SAC_{Aft}^{1.1}*SAC_{Frwd}\right)\right]^{3.8}}{190} = \text{Y Ranking} \quad (6\text{-}3)$$

As can be seen from equation (6-3), there is only one addition to the original base equation. The lateral area of the underwater hull is now added to the equation. The lateral underwater area becomes the dominant component in the equation, with no factors or powers reducing its overall effect. The next most notable change is the removal of the sectional area coefficient for the midpoint of the underwater hull. This proved to add no additional value to the equation, whereas the forward and aft sectional area coefficients found to contribute greater, with the aft coefficient slightly more than the forward.

The difference in longitudinal distance between the centre of buoyancy in the centre of lateral area, or ΔX, was found to vary greatly throughout the different generations, for example from 0.1 m to 3.75 m. Due to this extreme variance, as well as a noticeable pattern between the smaller values of ΔX and lower values of Y force, a factor of 1/ΔX was found to match more closely with the individual Y force results. It is also intended to reduce the impact of the larger values of ΔX. The change in vertical height, ΔZ, between the centre of buoyancy and centre of lateral area was kept at the same factor. This factor is more important when considering manoeuvring in waves and the effect of vessel rolling. However, the effect of waves is not considered in these equations but is a key consideration for future work.

Along with these additions the overall equation is divided by 190. This factor can be changed to account for variation in speed or oscillation amplitude. It is recommended that this factor be only reduced to a maximum of 100 should not be increased. As this causes the pattern to be compressed and lose the level of accuracy achieved through this multigenerational evolution.

This equation in relation to the original 23 designs analysed for generation 1 is shown in Figure 6-17. As can be seen the predicted pattern matches very closely, and within 5%, of the CFD results. The only noticeable deviation from the CFD is the medium range which falls outside the 5% markers. This was considered acceptable as this equation is intended for only use in an optimisation methodology, and therefore key focus on the lower end was of higher priority.

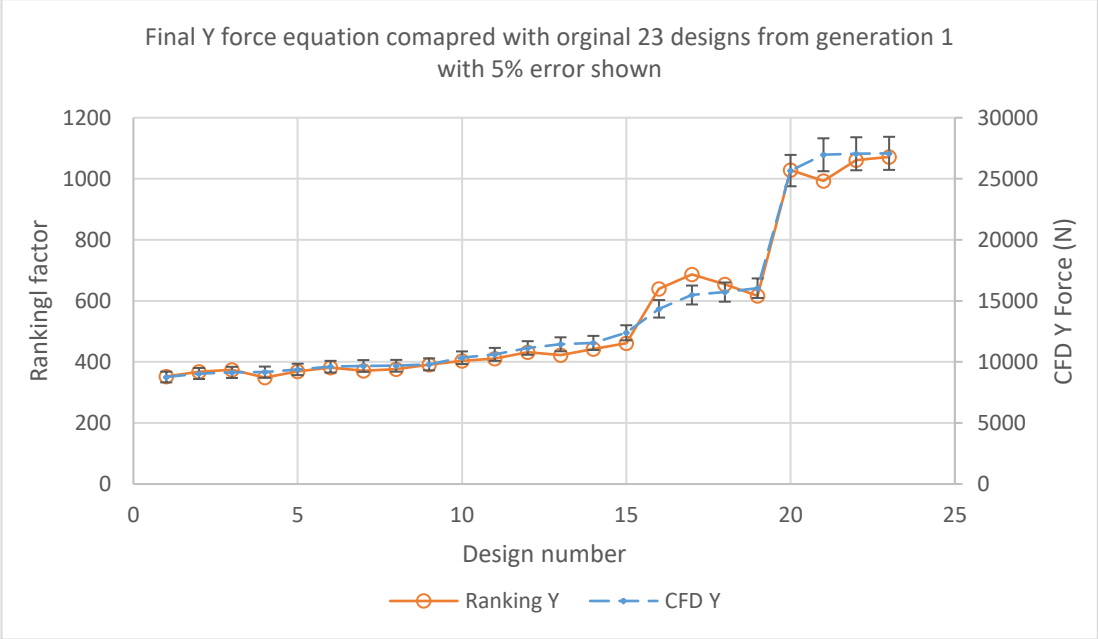

Figure 6-17 Graph comparing the final Y force equation with the original 23 designs from generation one

Unlike the Y ranking force equation, the moment around the z-axis was significantly more complex to match. The final equation to predict how the Z moment of the hull is comapred to other hulls is shown in equation (6-6). This final equation is split into two other equations to simplify the presentation, with equation (6-4) primarily focused on the forward half of the hull and equation (6-5) was primarily on the aft. It can be seen from these three equations that along with the addition of lateral area, LAT_{Area}, th distance from the aft perpendicular to the central buoyancy, LCB_x, on the length between perpendiculars, LBP, is also now included.

Along with these changes there is also a noticeable reduction in the use of powers throughout the overall equation. Based on the powers that have been included in this equation the sectional area coefficients play a minor role in the overall pattern prediction, with the mid-sectional area coefficient, SAC_{Mid}, being significantly reduced.

$$\left(SAC_{Frwd}^{0.8} + \frac{1}{SAC_{Mid}^{8}}\right) * LAT_{Area} = \alpha \tag{6-4}$$

$$\left(\Delta X - \frac{1}{SAC_{Aft}}\right) * \left(\frac{5 * LCB_x}{LAT_{Area}}\right) = \beta \tag{6-5}$$

$$(\alpha + \beta)^{2.6} * \frac{LBP}{LAT_{Area} * 1000} = Ranking\ Moment\ Z \tag{6-6}$$

As in the ranking Y equation, (6-3), there is a factor of 1000 acting as a scaling effect to match the CFD results pattern. This is well can be varied slightly to account for changes on PMM speed and oscillation amplitude. As in equation (6-3), this should only be increased rather than decreased and lose design accuracy. It is recommended that this value does not exceed 1200, as this equation is more susceptible to fluctuations in accuracy.

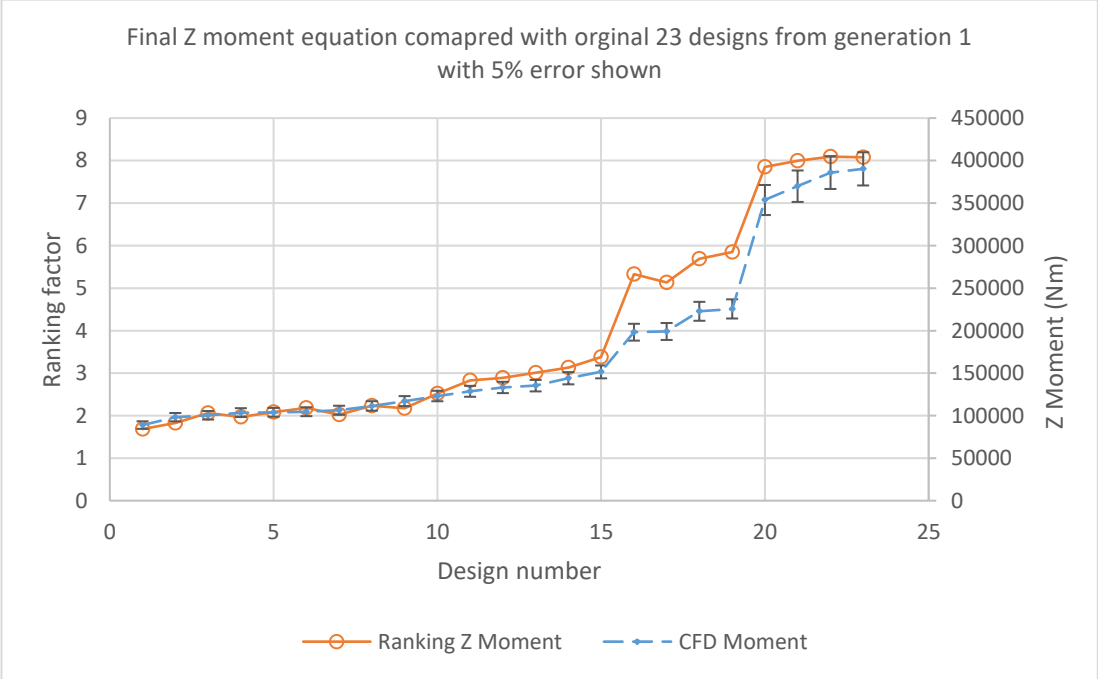

Figure 6-18 Graph comparing the final Z moment equation with the original 23 designs from generation one

Figure 6-18 shows a graph comparing the original 23 hull designs from generation one compared with the final version of the said moment ranking equation. As with the equation for Y force there is a primary focus on the lower end of the spectrum, due to its primary function for use in an optimisation algorithm. Like in Figure 6-17, the mid-region is least accurately predicted with a noticeable deviation for the largest results.

This deviation is not as significant a drawback as it may first seem, as these equations are merely a means of ranking designs of similar styles for an optimisation. The optimum designs predicted for these equations are then run through a higher fidelity solver such as CFD to truly evaluate vessel performance. This is the aim of the next section, to utilise these equations to optimise a hull form which can then be evaluated in CFD. This initial optimisation is again based off the parent NPL hull. However, a secondary optimisation is conducted using these

equations with the hull form that has no direct resemblance to the NPL hull and is significantly anthonyconstrained to match a real-world hull design problem.

6.6. Concluding remarks

Throughout this chapter there has been a steady development of an independent geometric equation that provides a means of ranking hull forms with respect to Y force and Z moment. The primary aim for these equations was to be able to quickly evaluate a vessel geometry and rank the hull form with respect to Y force and Z moment, independent of weight characteristics. Through this study key characteristics influencing these factors were determined, as well as unique and novel geometric evaluation techniques. These techniques can be applied to any monohull vessel.

To develop such equations extensive simulations were used in combination with the fully parametric setup described above in chapters 10, 4 and 5. Along with continuously evaluating and validating these equations, random geometric variation was intentionally instigated to improve equation stability. This intentional geometric variation ensures that these equations can be used within the industry and the early design stage to rapidly rank a selection of hull forms. Along with this computational effort required to solve these equations is minimal ensuring fast evaluations.

This chapter coupled with the previous chapters can be considered the most novel area of this research, with no research the authors knowledge having ever been conducted with this methodology in mind. These equations were specifically written with optimisation in mind, and therefore should only be considered for such a workflow. This workflow can be used for all non-dynamic lifting monohull vessels with little to no modification required, such as ferries and large passenger vessels. These equations have shown exceptional agreement with the simulated results, supporting this methodology and workflows accuracy.

7. Manoeuvring optimisation

7.1. Introduction

Within this chapter, the methodology and techniques used for optimising a specified hull form is presented. The optimisation utilises the equations developed in chapter 6. This optimisation also has a primary focus on the manoeuvring characteristics of the vessel. The optimisation uses Dakota optimisation software preinstalled into friendship framework CAESES.

Multiple optimisations are conducted to test the accuracy of the equations developed in chapter 6, however this is a secondary objective compared with the primary of optimising the parent NPL hull form for manoeuvring. Upon completing the NPL parent hull optimisations a new hull form is optimised using the same methodology and techniques discussed in the previous chapters. This hull form is a highly constrained and follows a specific hull theme. This is to present the effectiveness of the methodology for real world applications. This secondary hull form is also optimised three times for different objectives.

Upon completing these optimisations, the techniques and algorithms used are discussed along with the results and patterns observed. To ensure the validity of the optimised hulls, all optimised hull forms are analysed in CFD, along with several designs local to this optimum hull. This ensures that the equations developed in chapter 6 have found the best hull design, along with the level of accuracy that is able to be obtained through this methodology.

7.2. Optimisation overview

For this optimisation study, a total of six optimisations are run. These are split into two groups of three. The first group has a the starting hull form set as the parent NPL hull, with the second group having a completely new and undefined hull form. The second hull form is loosely based off mono hull CTV style hull forms, with a greater focus on the dimensional constraints than any specific geometric feature.

Each group is optimised for the Y force, Z moment and finally a combination of the two. This helps to evaluate the methodology as well as the restrictions observed based on the optimisation goal. These redesigns are likely to differ significantly. More complex and elaborate combinations are feasible however are not considered for this study, these can include optimising for Y force initially and then continuing a Z moment optimisation from the final Y force hull.

To perform the optimisations, the preinstalled Dakota optimisation suite is used within CAESES. This suite provides the user with multiple analyses techniques that can be selected,

ranging from gradient and non-gradient based optimisation algorithms, uncertainty quantification, and sensitivity/variance parameter studies. The various potential algorithms that can be used within CEASES is discussed in greater detail, with examples of these types presented below. These varying algorithms can be used by themselves or can be coupled to create more advanced strategies, these can include surrogate-based optimisation and optimisation under uncertainty, as well as other more comprehensive strategies. By combining this advanced optimisation suite with a highly flexible parametric hull, developed in chapter 5, and the equations developed in chapter 6, an extremely large and comprehensive design analysis can be conducted in a very short period.

Before running the final optimisations two test optimisations are run. These are used to evaluate the stability of the current setup as well as highlight any potential issues with the defined constraints. These two test runs are based off the combined Y force and Z moment factor, allowing for this combined factor to be tuned. It is also through these tests that the correct input values are selected for the optimisation algorithm that is used for the final runs.

The various algorithms that are included in CAESES and in Dakota is discussed below. This includes a brief discussion on the theory for various algorithms and how these can be best implemented for this optimisation analysis.

7.3. Optimisation Theory

Throughout this research the programme CAESES has been an integral part of the process. This integration has been vital to ensure flexibility and connectivity between CFD analysis, parametric modelling and finally optimisation algorithms. The suite within CAESES comes with a selection of optimisation algorithms along with the Dakota optimisation suite. The various optimisation algorithms are discussed briefly here along with a more detailed overview of the final algorithm used for the final stages of this research.

7.3.1. Brent

The Brent algorithm uses a one-dimensional minimisation methodology to find the minimum value function based on a single free parameter. Purely based on the single parameter limitation this is unsuitable for the final optimisations, however this algorithm was put into use within this overall methodology as it lends itself perfectly towards solving geometric optimisation tasks CAESES (2020). These tasks may include finding the shortest distance to a point or in the case of this research finding the length of a curve. This algorithm was prevented to find the length of the wake refinement region outer edge based on a given ship length factor.

The Brent algorithm uses a golden section search when the objective function fails to achieve the minimum and in turn switches to an iterative parabolic interpolation scheme. This is an incredibly fast algorithm when used for a simple geometric optimisation, as mentioned above. This in turn allows itself to be integrated seamlessly with complex optimisation algorithms without compromising either one.

7.3.2. Simplex Models

Within CAESES there are two simplex models that can be used for optimisation, both models are a single objective algorithm compatible with inequality constraints. The first simplex model is the Nelder-Mead algorithm, it is a downhill search algorithm that only requires the evaluation of the function then on the derivatives of this optimisation function. This room is known to be relatively inefficient with respect to the number of function evaluations that is required CAESES (2020). However, this lack of efficiency ensures it is a highly robust methodology for relatively low computationally demanding evaluations which need to be conducted quickly.

The second simplex model simply referred to as Simplexer, this algorithm applies are repetitive linearisation to non-linear objective function and corresponding constraints to allow them to be solved using the standard linear simplex method CAESES (2020). The model used in the software CAESES is a two-phase algorithm that requires the design variables to remain positive throughout the analysis. Phase 1 estimates a feasible domain for the minimum, with phase 2 calibrating the minimum of the objective function in that domain. Due to this, this methodology is used in two phases, with the initial phase guessing an initial feasible domain there is a likelihood that the minima for the objective function lies outside the bounds of this initial guess. This in turn gives a chance than the minimum for this model is not the true minimum of the overall design domain. In addition, due to this method applying a linearisation to potentially a non-linear problem it is possible that the linear minima do not match the minima of the non-linear function. Due to these drawbacks these simplex models are not considered for the final or future work optimisations.

7.3.3. Tangent search (TSearch)

The tangent search methodology uses a single objective organisation algorithm aimed towards small scales problems using inequality constraints. The primary aim of the tangent search methodology is to detect the descent direction in the solution space. Initially the algorithm conducts an exploratory search along the variable axes then move the descent search stage of the algorithm. If a constraint bound is approached on a descent or in an exploratory move the

algorithm moves tangentially to fall back within the feasible domain and continue the search. This methodology is commonly coupled with a preliminary Sobol analysis of the design space, at which point the best design from this analysis is taken as a starting point for the tangent search algorithm.

Although being a highly reliable tool, the lack of compatibility with equality constraints means that it is not useful for this optimisation. In addition, due to the highly complex parametric model there is a chance that this methodology unsupervised fail to find the global minima in the design space but rather a local minimum.

7.3.4. Newton Raphson algorithm

The Newton Raphson algorithm is like the tangent search methodology, in that it is closely related to a gradient based method. The algorithm utilises local quadratic approximations of the objective function, these approximations are created through second order partial derivatives, such as a Hessian matrix of the objective function CAESES (2020). This algorithm is both a single objective method as well as an iterative one. This method, although more complex than the Brent algorithm can be considered similar, in that it is not geared towards complex optimisation problems but rather simpler geometric of mathematical optimisation tasks.

7.3.5. NSGA-II

The NSGA-II design engine is a multi-objective optimisation algorithm, that is known for being a fast-sorting multi-objective genetic algorithm. It can be considered that the NSGA-II method can be split into six steps, these are quickly described below Yusoff, et al. (2011):

- Step 1: the population is initialised based on the design variables and constraints
- Step 2: the population is sorted based on a non-domination criterion
- Step 3: upon completion of the sorting the population individuals are given a crowding distance
- Step 4: population individuals are then selected through a tournament-based search using the crowding distance or crowded comparison operator
- Step 5: before the different generations can be created genetic operators must be calibrated to account for binary crossover and polynomial mutation
- Step 6: new generations are created to locate the optimum design

Within CAESES there are multiple input parameters for this design engine which control the number of generations, population size, the mutation probability along with crossover

probability CAESES (2020). This is a commonly used algorithm for complex optimisation problems that have multiple, as well as conflicting objectives that need to be minimised. This method is less complex than the final method used known as the global optimisation algorithm included in the Dakota suite.

7.3.6. MOSA

This design engine has similar capabilities to the previous method, NSGA-II, where multiple objectives need to be considered as well as potentially minimised. Like the NSGA-II, this design engine supports inequality constraints.

This design engine is a dominance based Multi-Objective Simulated Annealing (MOSA) algorithm. It is theoretically based on the process of annealing metals to slowly form a crystalline structure. Through this process slowly reducing the temperature in developing these theoretical crystals a minimum can be found. The process evolves like that of the NSGA-II, but rather than new generations being created, new crystalline structures are formed through the reduction of temperatures step by step. Each reduction in temperature causes a variation in a random design variable. Each variation is based on a Laplacian distribution. As mentioned before, this method follows a very similar process to the NSGA-II design engine but is still less advanced than the global optimisation algorithm that is used.

7.3.7. Efficient global optimisation

For the final optimisations, the efficient global optimisation design engine within the Dakota suite is utilised. This section presents the methodology and theory behind this model as well as the key advantages of using such a design engine for this analysis.

Efficient global optimisation (EGO) is focused on the minimisation unconstrained complex implicit response functions. The model is built on a multi-iterative process, with the initial iteration building a Gaussian model to act as a global surrogate for the sponsor function. With the following iterations adding extra samples into a new Gaussian model. These samples are intelligently selected centered around how much of an improvement they make on the iteration, and in turn the optimisation solution. Upon reaching a point where the improvements difference is negligible it can be drawn that global optimum solution has been found.

The first presentation of the efficient global optimisation model was presented byJones, et al. (1998), this model has been adapted into other global optimisation models which are built on the same theoretical base. The sequential kriging optimisation (SKO) model was proposed by Huang, et al. (2006), this model's primary difference from EGO is the formulation of the expected improvement function (EIF). This function is also the main feature that differentiates

both the EGO and SKO models from other global optimisation techniques. The EIF is the method in which the new starting point for a Gaussian iteration is calculated, this function attempts to maximise the improvement seen in the overall objective function. The main theory behind the EIF is to balance the positioning and calculation of the new point in relation to the overall objective function between the known region of good solutions in the design space, with regions where there is less overall information and greater uncertainty. The objective function could be improved if the new points predicted effect on the objective functions value is superior to the current best solution, or if the uncertainty in its prediction gives the probability that a better solution may be produced.

This overall process can be broken down into three steps, these are as followed Dalbey, et al. (2020):

1. "Build an initial Gaussian process model of the objective function.
2. Find the point that maximizes the EIF. If the EIF value at this point is sufficiently small, stop.
3. Evaluate the objective function at the point where the EIF is maximized. Update the Gaussian process model using this new point. Go to Step 2."

7.3.7.1. Gaussian process model

Unlike other surrogate models, the Gaussian Process (GP) does not only give a predicted value for a specific point but also provide a variance prediction estimate. This estimated variance provides an indication of the uncertainty for the GP. This is based on the concept that input points located closely to one another have outputs that strongly correlating. Therefore, the uncertainty around points located closely with the initial input points is small, but as this distance increases and new points are generated further from the initial points or training points the uncertainty increases.

The base Gaussian equation that assumes the true response function $G(\mathbf{u})$ for this methodology was proposed by Cressie (1991), this equation is given in equation (7-1).

$$G(\mathbf{u}) = h(\mathbf{u})^T * \beta + Z(\mathbf{u}) \tag{7-1}$$

With $\mathbf{h}()$ describes the trend of the model, $\boldsymbol{\beta}$ is the coefficients trend vector, $\boldsymbol{Z}()$ is a stationary Gaussian process with zero mean which describes the change of the model from its based trend. The model can be described as any function, however taking as a constant is sufficient. With the trend assumed constant and $\boldsymbol{\beta}$ taken as the mean of the response surface for the

training points, the covariance between two points, point **a** and point **b**, can be described in equation (7-2).

$$Cov[Z(\boldsymbol{a}), Z(\boldsymbol{b})] = \sigma_Z^2 R(\boldsymbol{a}, \boldsymbol{b}) \tag{7-2}$$

The factor σ_Z^2 describes the process variance, and *R*() describing the correlation function. This function can be described in many forms, the most commonly as the square exponential function, this function are shown in (7-3).

$$R(\boldsymbol{a}, \boldsymbol{b}) = \exp\left[-\sum_{i=1}^{d} \theta_i (a_i - b_i)^2\right] \tag{7-3}$$

Within equation (7-3), *d* represents the number of random variables, θ_i defines a scale parameter that represents the correlation between two points within dimension *i*. From here the expected value μ_G() the variance $\sigma^2{}_G$() of the GP model prediction appoint **u** are described in equation (7-4) and equation (7-5).

$$\mu_G(\boldsymbol{u}) = \boldsymbol{h}(\boldsymbol{u})^T \boldsymbol{\beta} + \boldsymbol{r}(\boldsymbol{u})^T \boldsymbol{R}^{-1}(\boldsymbol{g} - \boldsymbol{F}\boldsymbol{\beta}) \tag{7-4}$$

$$\sigma_G^2(\boldsymbol{u}) = \sigma_z^2 - [\boldsymbol{h}(\boldsymbol{u})^T \;\; \boldsymbol{r}(\boldsymbol{u})^T] \begin{bmatrix} \boldsymbol{0} & \boldsymbol{F}^T \\ \boldsymbol{F} & \boldsymbol{R} \end{bmatrix}^{-1} \begin{bmatrix} \boldsymbol{h}(\boldsymbol{u}) \\ \boldsymbol{r}(\boldsymbol{u}) \end{bmatrix} \tag{7-5}$$

The factor **r**(**u**) is a vector containing the covariance between **u** and each of the **n** training points, described in equation (7-4), **R** is an n × n matrix containing the correlation relationship between each pair of training points, ***g*** is the vector of response outputs at each of the training points, and **F** is an n × q matrix with rows $\mathbf{h}(\mathbf{u_i})^{\mathrm{T}}$ (the trend function for training point ***i*** containing *q* terms; for a constant trend *q*= 1). This form of the variance accounts for the uncertainty in the trend coefficients ***β,*** but assumes that the parameters governing the covariance function ($\boldsymbol{\sigma_z^2}$ and $\boldsymbol{\theta}$) have known values Dalbey, et al. (2020).

Estimations based on maximum likelihood are used to determine the factors $\boldsymbol{\sigma_z^2}$ and $\boldsymbol{\theta}$. To do this the log of the calculated probability for the response values ***g*** based on the matrix **R**. This is shown in equation (7-5).

$$\log[p(\boldsymbol{g}|\boldsymbol{R})] = -\frac{1}{n}\log|\boldsymbol{R}| - \log(\hat{\sigma}_z^2) \tag{7-6}$$

With |**R**| describing the determinant of **R,** and $\hat{\sigma}_z^2$ is the optimal variance value based on an estimate of $\boldsymbol{\theta}$ based on the equation (7-7). By maximising equation (7-6), the value of $\boldsymbol{\theta}$ can provide the estimate the maximum likelihood, which allows $\hat{\sigma}_z^2$ to be calculated.

$$\hat{\sigma}_z^2 = \frac{1}{n}(g - \boldsymbol{F\beta})^T \boldsymbol{R}^{-1}(g - \boldsymbol{F\beta}) \tag{7-7}$$

7.3.7.2. Acquisition functions

The next stage in optimising the given function requires calculation of the acquisition functions. These functions are used to establish the location for next sampling point/refinement points. By maximising this acquisition function equation (7-8) can be written.

$$\boldsymbol{u}^* = \underset{\boldsymbol{u}}{\arg\max}\, a\,(\boldsymbol{u}) \tag{7-8}$$

7.3.7.2.1. Expected improvement acquisition function

The expected improvement acquisition function identifies the location where new training points should be added. It is by definition, that the EIF provides a point in the search area that has a better solution than the current best solution based on the predicted values and variances calculate by the GP model. As mentioned previously EIF is defined such that it creates a careful balance between the good solutions that have been found in the design regions where there is greater uncertainty. The equations defining the EIF are noted below, along with the various factor definitions.

$$\hat{G}(u) \sim \mathbb{N}\,(u_G(\boldsymbol{u}), \sigma_G(\boldsymbol{u})) \tag{7-9}$$

$$EI\left(\hat{G}(\boldsymbol{u})\right) \equiv E\left[\max\,(G(\boldsymbol{u}^*) - \hat{G}(\boldsymbol{u}), 0\right] \tag{7-10}$$

$$EI\left(\hat{G}(\boldsymbol{u})\right) = \int_{-\infty}^{G^*} (\hat{G} - G)\,\hat{G}(\boldsymbol{u})\,dG \tag{7-11}$$

$$EI\left(\hat{G}(\boldsymbol{u})\right) = (G^* - \mu_G)\,\Phi\left(\frac{G^* - \mu_G}{\sigma_G}\right) + \sigma_G \varphi\left(\frac{G^* - \mu_G}{\sigma_G}\right) \tag{7-12}$$

$$\alpha_{EI}(\boldsymbol{u}, \{\boldsymbol{u}_i, y_i\}_{i=1}^N, \theta) = \sigma(\boldsymbol{u}) \cdot (\gamma(\boldsymbol{u})\Phi(\gamma(\boldsymbol{u})) + \varphi(\gamma(u))) \tag{7-13}$$

$$\gamma(\boldsymbol{u}) = \frac{G^* - \mu(\boldsymbol{u})}{\sigma(\boldsymbol{u})} \tag{7-14}$$

The Gaussian distribution as described in equation(7-9). $G(u^*)$ describes the current best solution chosen from the various true function values and the different training points. To compute the expectation and integral is taken of equation (7-10) to determine (7-11). This integral can be further described analytically in equation (7-12), where G is a realisation of $\hat{G}$. By further simplifying this equation and understanding that μ_G and σ_G are a function of **u**, equation (7-13) can be written. Equation (7-14) describes the expected improvement acquisition function for unknown **u**.

Each time the EIF is maximised a new training point is created and in turn a new GP model is built around this point. This circular pattern continues until the EIF achieves the maximum value falls within a given tolerance. To find a point at which the EIF has achieved a maximum value in the Nelder-Mead simplex model is used. This, however, can be inefficient and computationally expensive as the EIF is quite often multimodal. To account for the multimodal characteristics of the EIF Jones, et al. (1998) applied a branch and bound technique for maximising the EIF, this was also found to be expensive to run to full convergence. To this effect, the DIRECT global optimisation method discussed in Gablonsky (2001) is utilised.

The EIF leads towards optimal solutions based on equation (7-12), as this equation highlights the objective functions value and X is expected to be lower than the current best solutions prediction. Due to the GP model providing a Gaussian distribution at each point, an expectation of this point performance can be calculated. A point is known to be exploiting when it is expected to have the values and small variance, whereas exploration points may have potentially poor values but large variance.

To account for the inclusion of equality constraints within the optimisation the addition of the expected feasibility function is required. This is due to EIF being inappropriate, as the response functions no longer appears on the objective but rather the constraint, which in turn requires the feasibility for each point to be calculated.

7.3.7.2.2. Probability improvement acquisition function

The probability of improvement acquisition function applies the same base theory as the expected improvement function, namely the GP prediction of a Gaussian distribution. However, it is found that the expected improvement better than the probability improvement (PI) function. The equation for the probability improvement is shown in eq. (7-15).

$$\alpha_{PI}(\boldsymbol{u}) = \Phi(\gamma(\boldsymbol{u})) \tag{7-15}$$

7.3.7.2.3. Lower-confidence bound acquisition function

In addition to the previous two acquisition functions, the lower-confidence bound (LcB) is another method to calculate the acquisition function. This technique was proposed by Srinivas, et al. (2012) and has been seen to perform well, shown in equation (7-16).

$$\alpha_{LcB}(\boldsymbol{u}) = -\mu(\boldsymbol{u}) + k\sigma(\boldsymbol{u}) \tag{7-16}$$

The factor *k* describes the exploitation-exploration balance. It is considered best when *k* = 2 for optimisations, however it is possible to have a function describing *k* per iteration Daniel, et al. (2014). The function for *k* shown in equation (7-17) along with the respective factors, eith *d* representing the dimensionality of the problem and $\delta \in (0, 1)$, (Srinivas, et al., 2012).

$$k = \sqrt{v\gamma_n} \qquad v = 1 \qquad \gamma_n = 2log\left(\frac{N^{\frac{d}{2}+2}\pi^2}{3\delta}\right) \tag{7-17}$$

7.4. Test optimisations

Before running the final optimisations on the NPL hull and the constraint hull, test optimisations is run. These test optimisations uses the current set up for the NPL hull, however the generated hull forms and optimum designs are not analysed in CFD or have the equations tested. The primary focus of these two tests is to evaluate the stability of the parametric hull and develop improved constraints that may not have originally appeared obvious. This is to ensure that when the final optimisations are conducted no potential loopholes or errors are found and exploited by the organisation algorithm. The secondary focus of these tests is to gauge the computational time required to run a specific number of generations and in turn designs. This test is benchmarked to provide a constant value for the time per design evaluation.

Along these key aims for these tests the output files generated for each design also need to be tuned and tested. These files not only include the respective data for each design input value, as well as the designs constrained values and the equation values, but is also includes diagrams and geometric data. These diagrams includes a 3D view of the hull, sectional lines plan and pictorial representation of the sectional area coefficients, as seen in Figure 6-8. These are used to quickly compare the different designs, as well as being used to generate a video showing the optimisation progression.

To enable quick CFD evaluation of the hull form, 3D geometric data is also required to be exported for each design. Originally an IGES file was used, however as required manual conversion to a mesh file and finally exporting into a CFD solver, therefore creating and in turn exporting the mesh file direct from the parametric modeller was considered better. Each hull form is converted into an STL mesh file, that is pre-tuned to capture the details of the hull while still maintaining a low face count. This pre-tuning is vital to maintaining a quick evaluation of each hull form, as a highly detailed STL file of the hull form may require many seconds to even dozens. This time significantly adds up when evaluating multiple thousands of designs. Therefore, prior to running these optimisation tests a tri-mesh of the hull form was created in the parametric setup. This tri-mesh focused on maintaining the key service edges and angles while minimising the face count in low curvature regions. This meant that an exported STL required 2 to 5 seconds to be completed.

The export of an STL file setup for an additional line of code inputted into the pre/post-processing command line built into the optimisation design engine, this commandline is shown in Figure 7-1. This line of code found the tri-mesh of the current designs hull form, found the reference number of that design and in turn found the folder relating to that design. Upon finding this folder an STL file are exported and saved in the location. This significantly saves manpower when finding the optimum designs and in turn the geometric data for the hull. Although it is possible to simply open that design within CAESES from the design engine, as can be very slow and potentially cause the program to crash due to the vast numbers of designs, plus a manual export of an STL file is then required. It is therefore considered better and safer to export the geometric data at the same time the design is created and evaluated.

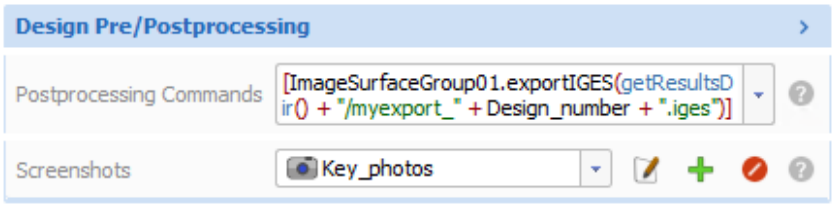

Figure 7-1 Example of pre/post processing commands for exporting an IGES file to a referenced design folder

The initial test focuses on constraints, loopholes, and overall optimisation stability, the second test conducts a multi-objective analysis to test its stability while also evaluating the changes made this based on the initial test findings.

For these tests, an upper limit of 7500 designs are set to guarantee a reasonable runtime as well as a diverse enough design space to test the parametric setup. As these optimisations utilise

the EGO model in the Dakota suite an initial population size is required as well as the number of generations. These tests have an initial population size of 100 and a maximum of 20 generations. These have been selected so as not to be too small or too large as to create excessive number of designs per generation.

7.4.1. Results and discussion

This section briefly discusses and presents the results obtained from these two test optimisation runs. It also presents the changes made in creating stable constraints and improving optimisation stability.

The NPL hull was said to be constrained in a few different ways. As the final analysis takes the optimised hull forms and simulate a turning circle manoeuvre with them, it is key that the region where the rudder and propeller are located are maintaining consistency between the different designs. The specific rudder and propeller design for this hull form is taken from Bailey (1976). Based on information provided in Bailey (1976), the aft most key point does not exceed 90% of the overall ship draft. This ensures that the rudder does not hang fully below the keel. As this hull is to remain within the NPL bounding box in essence the beam, draft and overall length is constrained to match the full-scale NPL hull modelled in chapter 5. The next key constraint based on these values is the displacement of the hull. As mentioned previously this is calculated for every new design iteration, therefore this can be defined as a parameter which in turn can have a specific constraint applied to it. For these tests, the hull should not go above or below a 10% margin from the parent hulls base displacement.

These were the key constraints that were applied to this initial optimisation test. It is also important to note that the input parameters for each design variable of the parametric hull can have an upper and lower limit. These limits become constraints within their own right. Based on this, these design variables are carefully chosen to allow for extreme variation while still maintaining reasonable and logical limits. This can become an unforeseen problem when running such a lightly constrained optimisation. Therefore, these limits were set such that there remained within the NPL bounding box, with the only exception being the bow region to allow extreme wave piercing/vertical bows to be possibly modelled.

At this point a warning must also be brought forward, as prior design influence may cause unintentional design bias. Due to the stages of equation iteration and model simulations, an unintended bias towards the key design characteristics which improve the manoeuvring characteristics may appear. Therefore, the bounding box surrounding the parent NPL hull became the key factor in where the design variables could be located. This could be subject to

unintentional constraint breaking, primarily due to the factors influencing point weight. To account for this, none of the geometric design variables could extend beyond the bounding box, except for the forward 25% which could only extend below the draft.

The initial test generated a total of 3953 designs, with 1234 designs remaining within the constraints and staying valid. This equates to 44.66% of the overall designs being within the constraints, with a large portion of these failed designs being created towards the start of the optimisation.

The complete optimisation results can be seen in Figure 7-2, which shows the valid designs, or designs which remained within the constraints as black and the invalid designs as red crosses. There is a greater number of invalid designs than valid, this is due to limits for each input parameter being too large and allowing the hull to break the displacement constraint primarily. Although a significant majority of the design iterations were invalid, the organisation algorithm began to refine and discover the limits that not only led to better designs but also a reduction in invalid designs. This observation can be graphically seen in both Figure 7-3 and Figure 7-4. Figure 7-3 shows a greater density of valid designs within the final 1000 design iterations compared with invalid. This is backed up by Figure 7-4 which shows an overall decreasing trend in invalid designs as the optimisation continues, with the initial stages of the optimisation producing around 85 to 90% invalid designs, whereas the final stages producing around 50% to 60% are invalid.

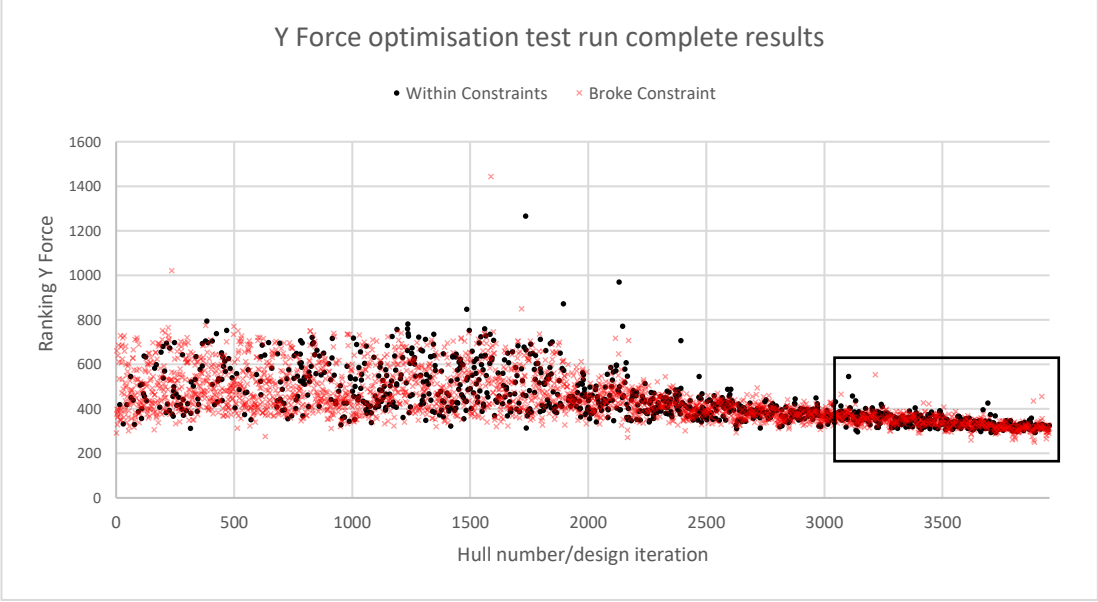

Figure 7-2 Optimisation results for initial test run focused on Y force

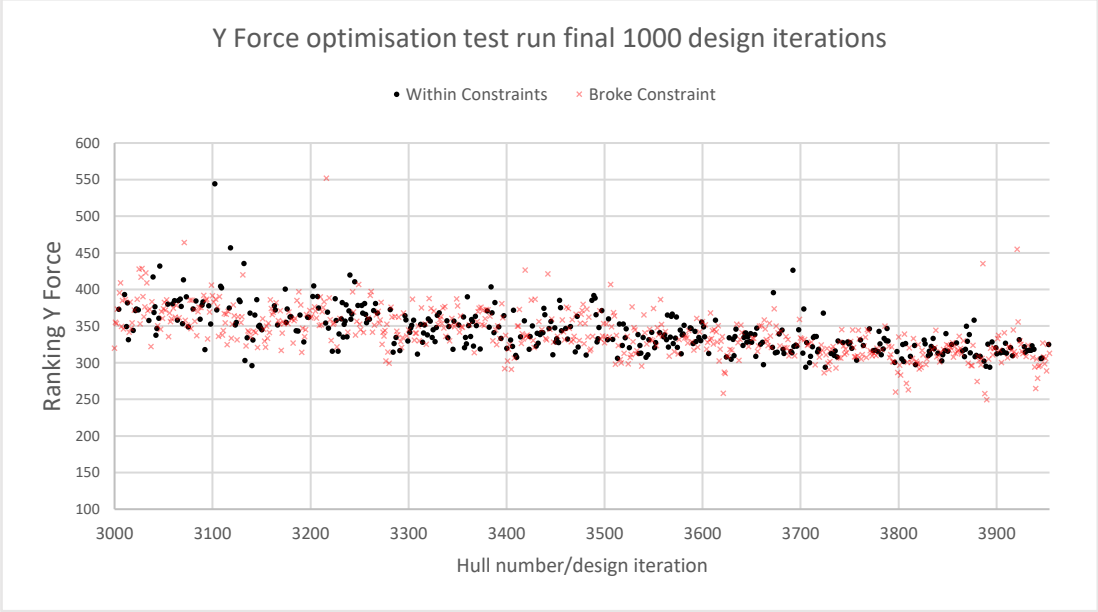

Figure 7-3 Detailed view of final 1000 designs for Y force optimisation shown in Figure 7-2

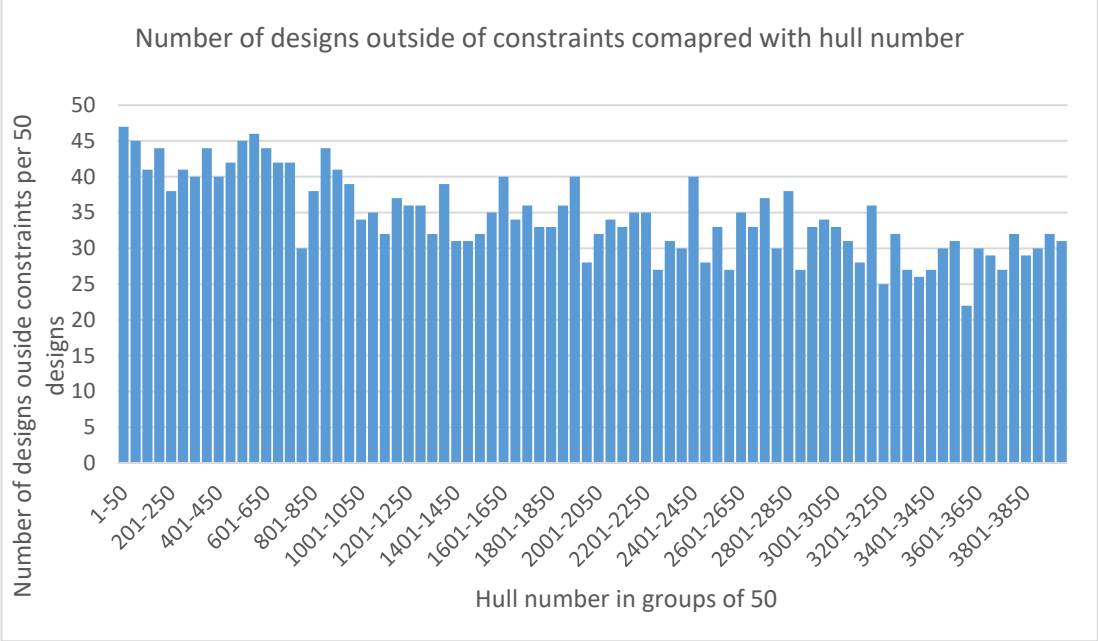

Figure 7-4 Graph showing the number of invalid designs per 50 design iterations as the optimisation progresses

To analyse, model and export around 4000 designs, the total runtime from start to final export to a total of 11 hours 58 minutes. This in turn equated to around 2.5GB of design data, which included separate folders for each design with the specific designs input parameters and calculated outputs noted, as well as the geometric export.

As mentioned previously the export is set as a STL mesh, however, to ensure an extra level accuracy with all CFD simulations an extra stage to the geometric import into a CFD

simulation file is included. This stage involves importing the geometric file into Rhinoceros 3DM, where a more accurately controlled mesh can be generated for STL import. In addition to this, the key characteristics can be doublechecked to ensure the hydrostatic's have been calculated correctly. By including this extra step there is no need for the parametric model to generate the mesh, therefore a simple IGES file can be exported and in turn significantly reduce the time required to export each file. Through this simple switch a decrease in the evaluation time of around 65% per iteration was observed, which in turn equated to the run time of 11 hours and 58 minutes.

Within these 4000 design iterations a total of 27 designs failed to compute, these were simply discarded by the optimisation algorithm but highlighted that there is an issue either with the evaluation technique or modelling technique. These designs were checked to find a primary cause of them failing. This evaluation found that for certain designs the evaluation of the sectional area cuts, presented in chapter 6.3, would fail to be calculated and in turn cause the equation to fail. This was rectified by modifying the geometric techniques used to create these cuts, and in turn improve the stability. With this new technique the 27 designs were evaluated again to test the stability, which found that this modification cured the instability.

The second optimisation test is conducted with a focus on multi-objective optimisation along with the influence of the modifications. In addition, minor changes to the input parameter limits have been set with a view toreducing the number of invalid designs being created. These were very minor changes as these changes could significantly limit the design pool and in turn remove a valid design which may be a contender for the best design. It is possible within CAESES to quickly generate graphs representing each design parameter and another variable such as valid or invalid designs. By using these key parameters causing the greatest number of invalid designs were found and slightly modified.

The results for both the Y force and Z moment are shown in Figure 7-5 and Figure 7-7 respectively, with detailed views highlighted by the box shown in Figure 7-6 and Figure 7-8. A total of 3953 design iterations were completed, of these designs 2807 were invalid equating to just under 30% valid designs. It is unclear to the primary cause of this; however it can be speculated this is most likely due to the multi-objective nature of this optimisation which in turn required greater variation between each design and thus pushing the limits. Although there is a greater percentage of invalid designs, there is a noticeable decrease in invalid design density as the optimisation progressed. With an initial density more than 90% and a final density at 40%. This can also be seen when viewing the detailed views of the final 1000 designs for both the Y force and Z moment in Figure 7-6 and Figure 7-8 correspondingly.

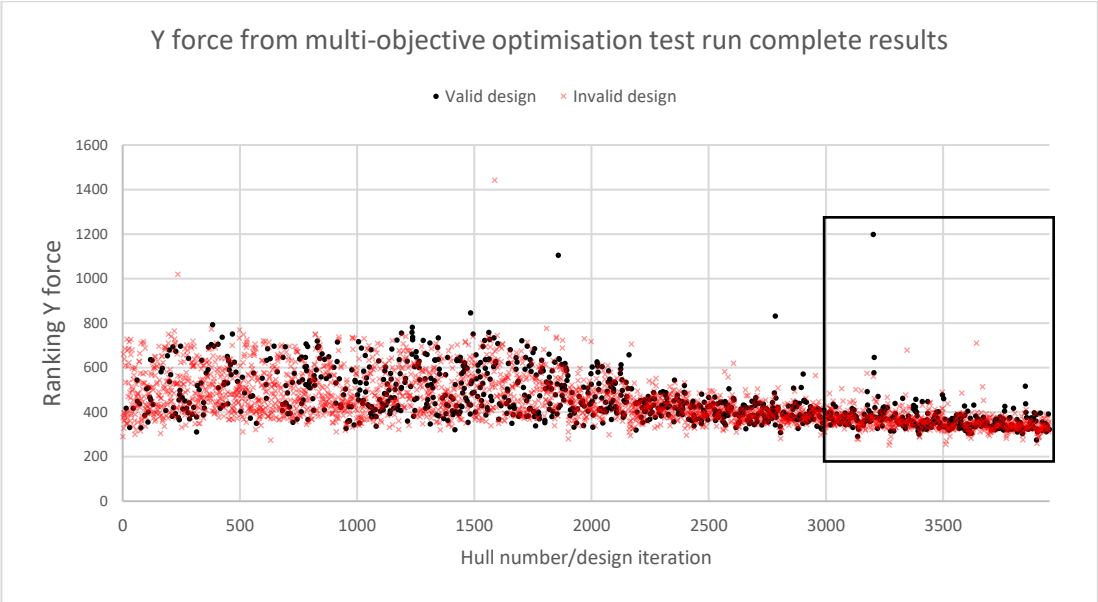

Figure 7-5 Complete results from the Y force in equation for the multi-objective optimisation test run

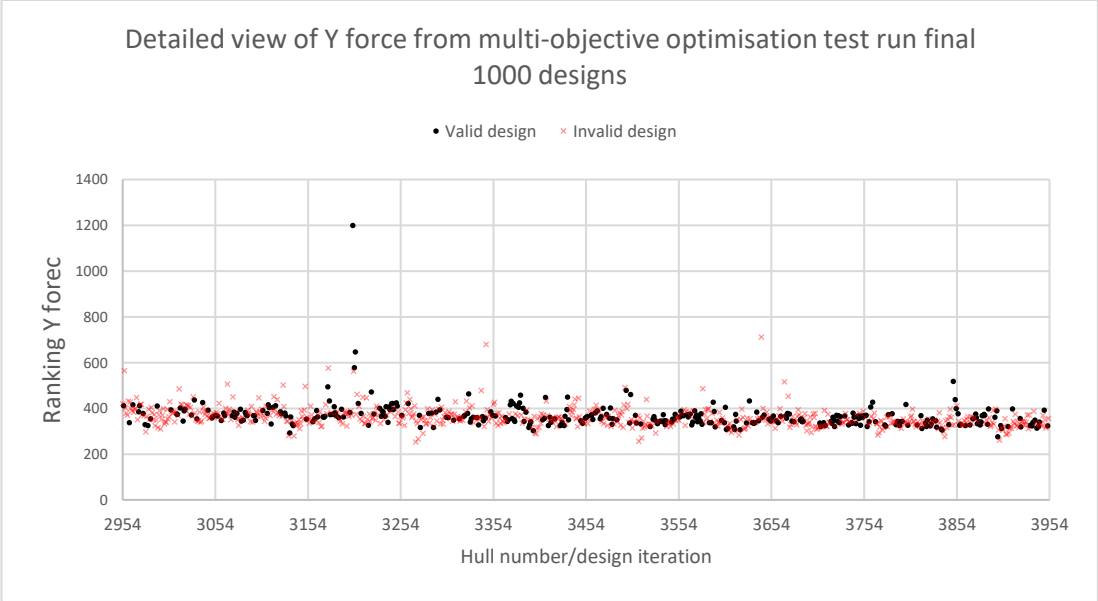

Figure 7-6 Detailed view the final 1000 designs shown in Figure 7-5

The modifications made to the sectional area cuts coefficients, there were no failed designs with all designs being successfully calculated. This optimisation took a total of 17 hours and 23 minutes to complete. This accounted for a 45% increase in overall run time compared with a single objective optimisation.

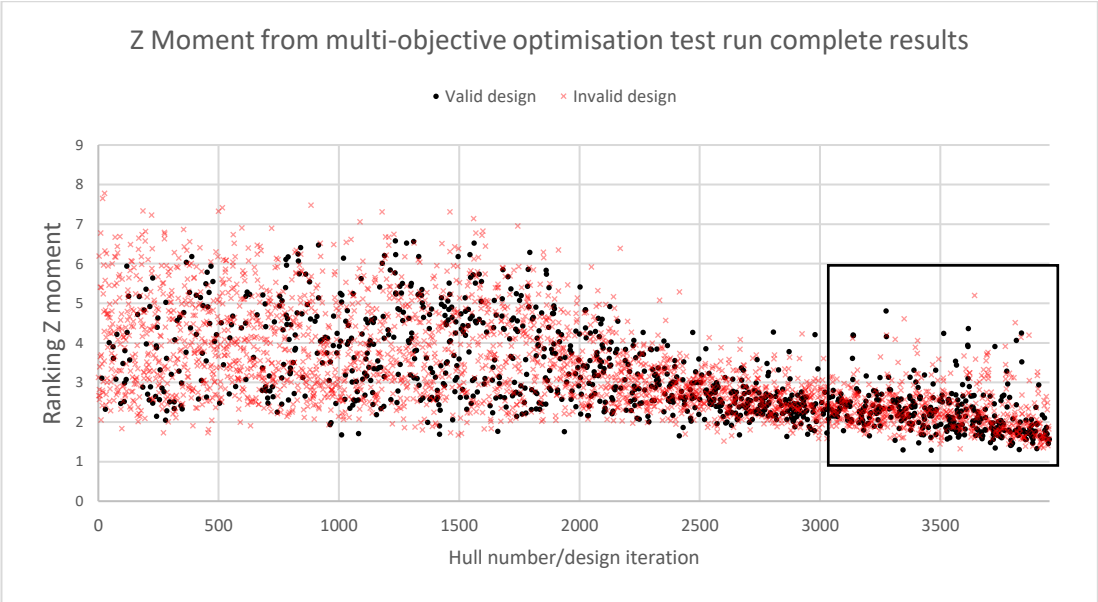

Figure 7-7 Complete results from the Z moment equation for the multi-objective optimisation test run

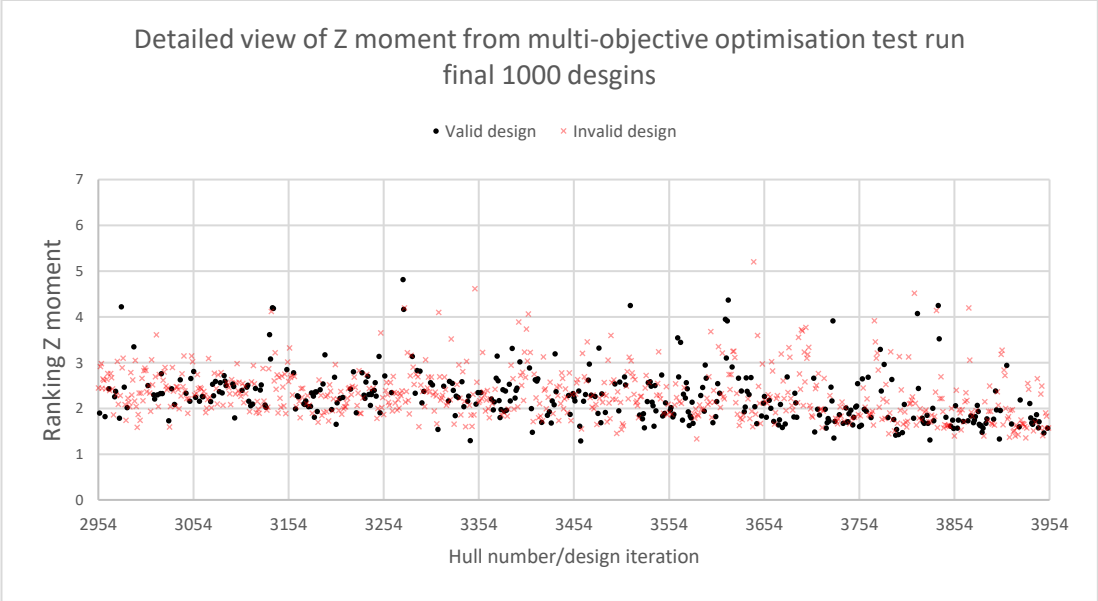

Figure 7-8 Detailed view the final 1000 designs shown in Figure 7-7

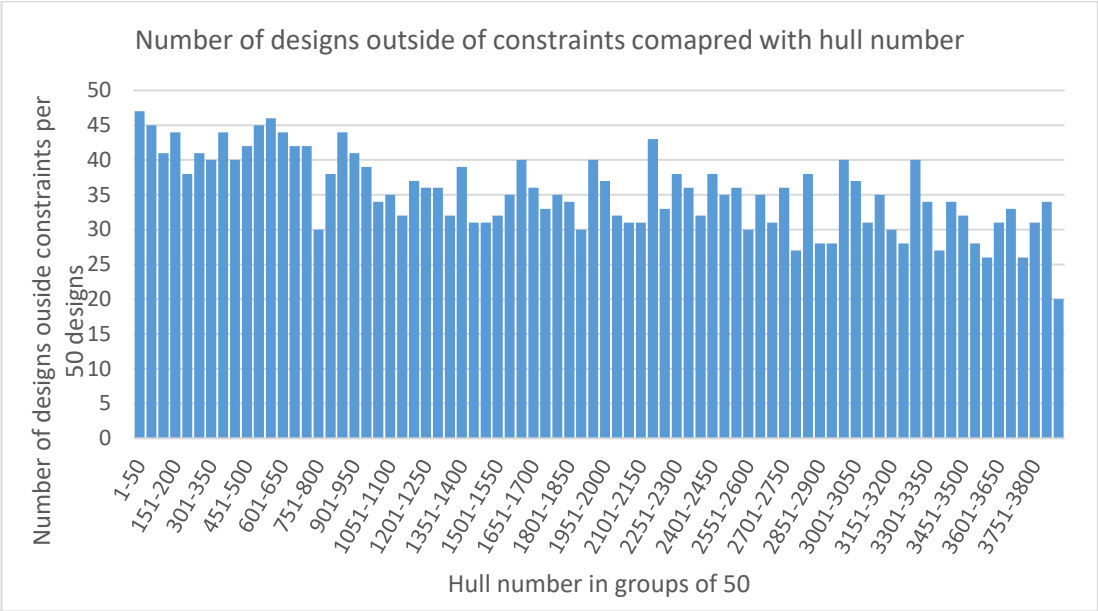

Figure 7-9 Graph showing the number of invalid designs per 50 design iterations as the optimisation progresses for the multi-objective optimisation

These results show good stability in the optimisation setup as well as the parametric model. Based on these results a fully focused NPL optimisation can now be conducted. As noted in section 7.3.7, increasing the initial training population gives improved results in later populations. Therefore, these optimisations have an initial population of 750 to 1000, as is hoped to improve the density proportion between valid and invalid designs later in the run, as seen in Figure 7-9.

7.5. NPL hull optimisation Case Study 1

This section briefly outlines methodology used for this optimisation, present the results from the optimisation, and finally move in quantifying these results through CFD simulations. The parent NPL hull is used for all three optimisation runs as the initial starting point. The NPL hull is optimised for Y force, the moment acting around the vertical axis and a multi-objective optimisation using both these functions as the objectives.

By optimising separately and then together is expected that the key factors influencing these components can be isolated and discussed in greater detail. It is also expected that the multi-objective optimisation creates a clear Pareto frontier that complements the results obtained through the single objective optimisations.

7.5.1. Optimisation setup

The optimisation for the NPL hull usees the global optimisation algorithm provided in the Dakota suite for these evaluations. Both the Y force and Z moment evaluations have a maximum of 15,000 design iterations based off 30 generations. The multi-objective optimisation have the same upper limit for design iterations; however, the number of generations is increased to 45. This increase in generations account for the greater number of design iterations that may be required. All these evaluations have an initial population size of 750.

Preliminary optimisation runs based around the NPL hull form with the initial four constraints, found that the algorithm find loopholes to overcome these constraints while also minimising the evaluation equation. An example of such a hull form can be seen in Figure 7-10. To overcome this extreme deformation two extra constraints are included. These control the aft keel heights in relation to the centre line keel, such that the beam keels do not extend to such extremes below the aft keel. These have been included to ensure the hull forms follow a more practical form.

Figure 7-10 An example of a loopholed NPL design iteration (test optimisation hull 6250)

7.5.2. Y-Force optimisation for the NPL hull

Within this section the results for the optimisation with respect to the Y force equation is evaluated, in addition to the patterns and the geometric features of the optimum hull compared with the baseline. After this the optimum hull form is evaluated in CFD to validate its performance improvements over the parent NPL hull.

7.5.2.1. Results and discussion for Y force optimisation

Following the methodology used in the test optimisations, this optimisation usese the global optimisation algorithm. This optimisation was completed in 6537 design iterations, with the optimum design being found at iteration 6495. The number of iterations only encompass 43.58% of the total allowable iterations. To complete these 6537 designs, the optimisation took over 27 hours to complete.

The complete optimisation results can be seen in Figure 7-11, these include all the designs which failed to stay within the design constraints. From this figure can be seen there is significantly larger density of invalid designs compared with the test optimisations, as seen in Figure 7-2. Most of the designs which broke constraints failed to achieve the displacement constraint. From Figure 7-11 the optimisation follows a traditional downward gradient, with minimal design explorations. The majority of the exploratory designs are found in the final stages of the optimisation. These exploratory designs are created by the design algorithm increasing the value the of expected improvement acquisition function. These designs of located in the final 1000 iterations, this is their calculated ranking results significantly exceed that of the surrounding designs. These exploratory designs can be seen in greater clarity by comparing Figure 7-11 and Figure 7-12. Steady increase of the expected improvement acquisition function can be taken as an indicator that the algorithm is trending towards an optimum design. Although the exploratory designs do not appear to significantly vary from natural trend, by viewing these designs from the perspective of Figure 7-12, they deviate from the natural trend in density by over 100%. For example, between designs 6000 to 6200 the natural trend does not vary more than 20 for the calculated ranking Y force, whereas the exploratory designs in this region deviate from the maximum by over 35, equating to a deviation of 175%.

In addition to this macro analysis, Figure 7-12 also shows a flattening and increasing in design density towards the latter half of the 1000 designs. It is from this region where the optimum design is found. By also comparing Figure 7-11 and Figure 7-12 with Figure 7-13, the overall trends of the optimisation algorithm show that initially there is a domination of invalid designs which then reduces throughout the midregion of the run, to finally reach a near steady state of invalid designs to valid designs. This density equates to 63.15% of the total number of invalid designs being evaluated in the initial 36.71% of the design iterations. On the other hand, the final 52% of the design iterations account for only 21.5% of the total proportion of invalid designs.

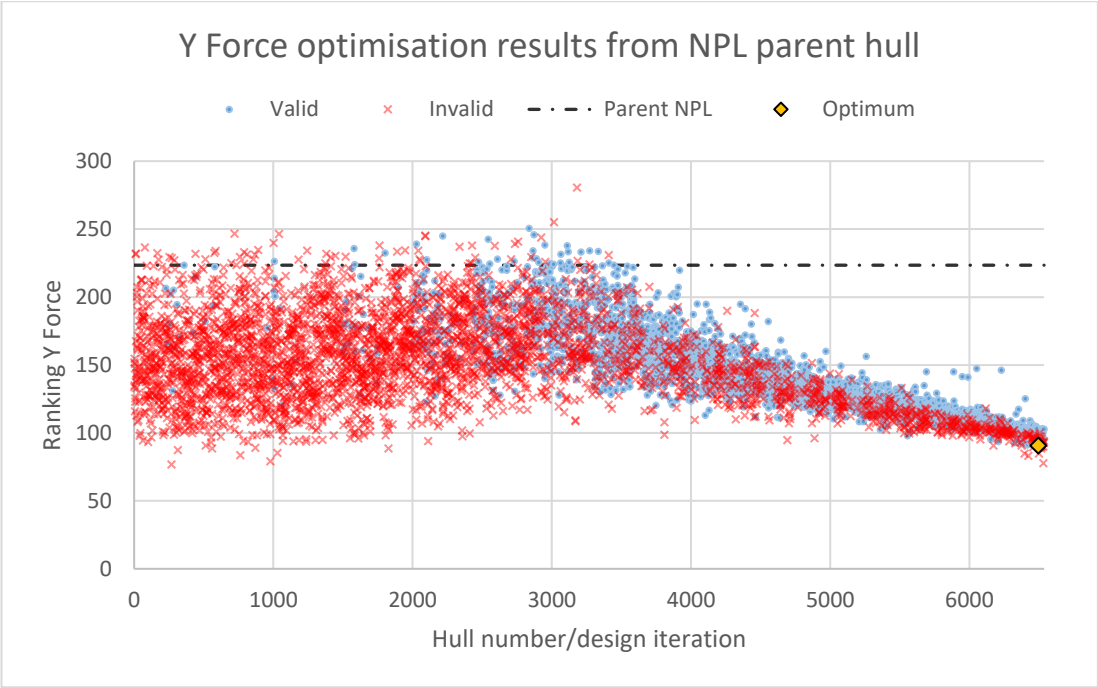

Figure 7-11 NPL parent hull Y force optimisation results with respect to design iteration

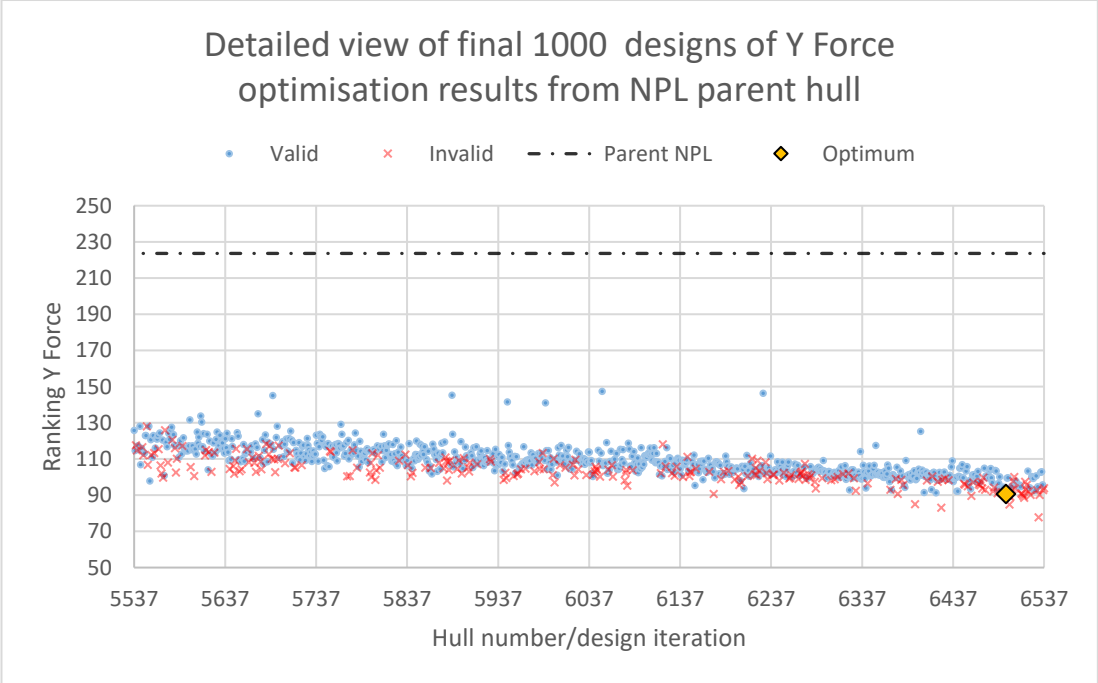

Figure 7-12 Detailed view of final 1000 iterations for the Y force optimisation on the NPL parent hull

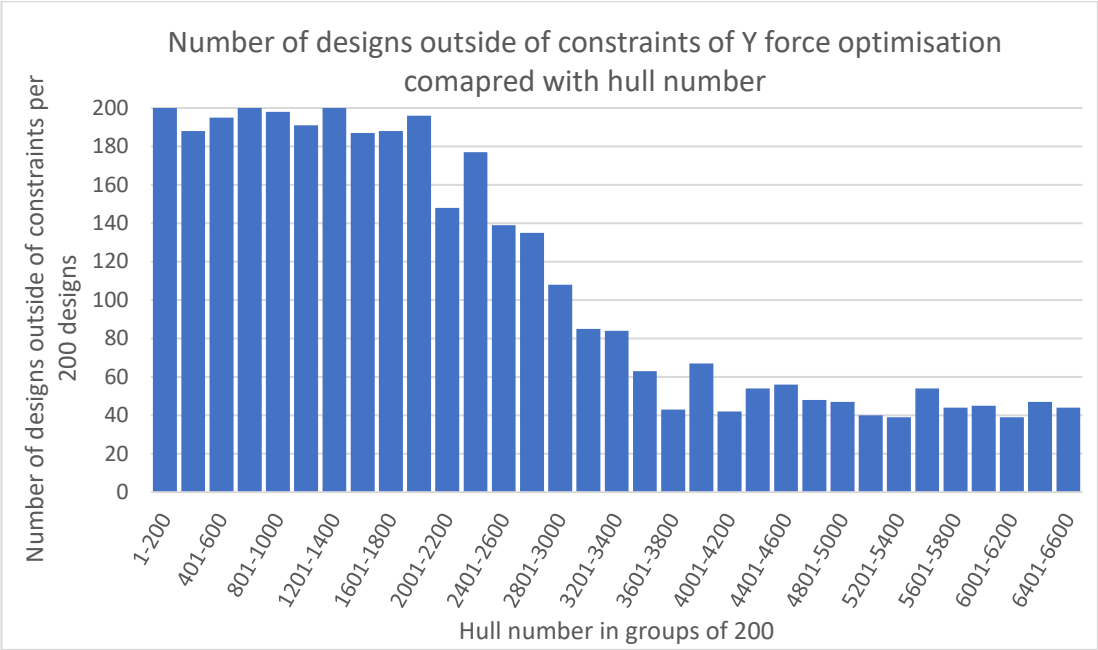

Figure 7-13 Bar chart showing the density of invalid designs per 200 design iterations for Y force optimisation of NPL parent hull

The key numerical differences between the optimised Y force hull (hull 6495) and the parent NPL hull are given in Table 7-1. From this table it can be seen that the displacement has reduced by 2.757 tons, which is equivalent to 9.61%. This reduction is 0.39% away from the maximum allowable reduction in displacement. This is a common theme throughout these optimisation runs, as this proximity to displacement constraint is also seen in the optimisation for the Z moment. This reduction was matched in the block coefficient.

The most notable change however is the movement of the longitudinal centre of buoyancy. Unlike what the initial hypothesis would predict, the LCB has moved 0.104 m aft. Throughout the process of developing the evaluation equations, chapter 6, a commonly observed trend for both the Y force and said moment was to have the LCB close to the midship. This hull form however contradicts this by moving the LCB aft 1.19%. That only has the LCB moved aft, but the centre of lateral area along the centre line moved forward creating a 1.95 m gap between them. Initially this would suggest poor Y force performance by purely evaluating these two factors.

Table 7-1 Comparison between NPL parent and 6495 hull key characteristics

	NPL Parent	*Hull 6495*
LWL (m)	20	20
B (m)	3.2	3.2
T (m)	1.1	1.1
Disp. (t)	28.7	25.943
Cb	0.397	0.360
LCB (m from aft)	8.72	8.616
Ranking Y Force	223.5458	90.7585
Ranking Z Moment	3.496	2.775

It is therefore key to evaluate other hull form characteristics with respect to the geometry to be able to state whether the hull form has outperformed the parent hull. From initial observations of both Figure 7-14 and Figure 7-15, the optimum hull (6495) appears to have relatively minor geometric changes compared with the NPL parent hull. By more closely evaluating Figure 7-14 they can be seen that the bow region has become finer as well as moving safely aft for the lowest point. The most significant change can be seen in the sectional lines plans. There has been a large reduction in the bilge keel curvature, in addition to an increase in the aft beam and underwater curvature. Unlike the parent NPL hull, the transom is significantly boxier with only a minor curvature towards the centre line. This simpler geometric form should theoretically allow smoother flow than that of the parent NPL. This further squaring can also be seen in Figure 7-15 when evaluating the water lines plans.

These plans in Figure 7-15 further help to show how hull 6495 outperforms the NPL parent. Unlike the parent NPL hull, hull 6495 is very simple geometry aft of the midship which helps to dissipate any turbulence or large vortexes generated from the bow. It can therefore be concluded that although hull 6495 is largely similar to the NPL parent hull at first observations. The simpler aft geometry allows for greater performance with respect to the Y force, but not the Z moment primarily due to the increase in distance between the LCB and the centre of lateral area along the centre line. Therefore, it is paramount that this hull form be evaluated carefully in CFD to truly gauge its performance improvements.

Figure 7-14Comparison between sectional and buttock lines plans for hull 6495 and NPL parent hull

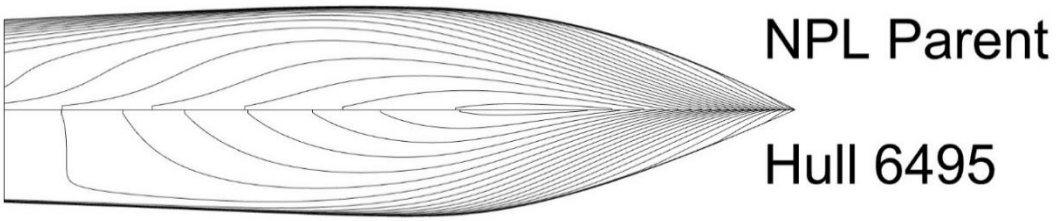

Figure 7-15 Comparison between waterlines plans for hull 6495 with NPL parent hull

7.5.2.2. CFD Evaluation

To obtain the two-level of improvement over the NPL parent hull with respect to Y force, hull 6495 is evaluated in CFD using the methodology developed in chapter 4. As noted in chapter 5 each hull form generated in the parametric model has an exported IGES or STL file for the geometry. This geometry can be directly imported into the CFD base simulation, however for this analysis the geometry is first checked in Rhinoceros 3DM for geometric continuity and any potential points where meshing may encounter errors. At this point the hulls displacement, LCB and moment of inertia are also verified against the parametrically calculated values. All values fell within 3% of the initial calculations.

Upon completing the geometric analysis, the hull was converted to a mesh and then imported as an STL file into Star CCM+. Once the geometry successfully imported into the CFD software a further geometric continuity check was conducted in Star CCM+, which included highlighting key geometric curves that helps to ensure as accurate a volume mesh is created. The mesh was then defined as a wall region in the overset domain. After this region have been fined key factors influencing the vessel's motions can be inputted into the corresponding DFBI model.

The volumetric mesh for the outer and overset domains were generated giving a total mesh count of 1.06 million cells, compared with the 948,896 cells used for the NPL parent hull. These additional cells were generated in the overset domain due to the increased curvature rate of the hull in the aft region, as well as a small additional refinement at the forward perpendicular.

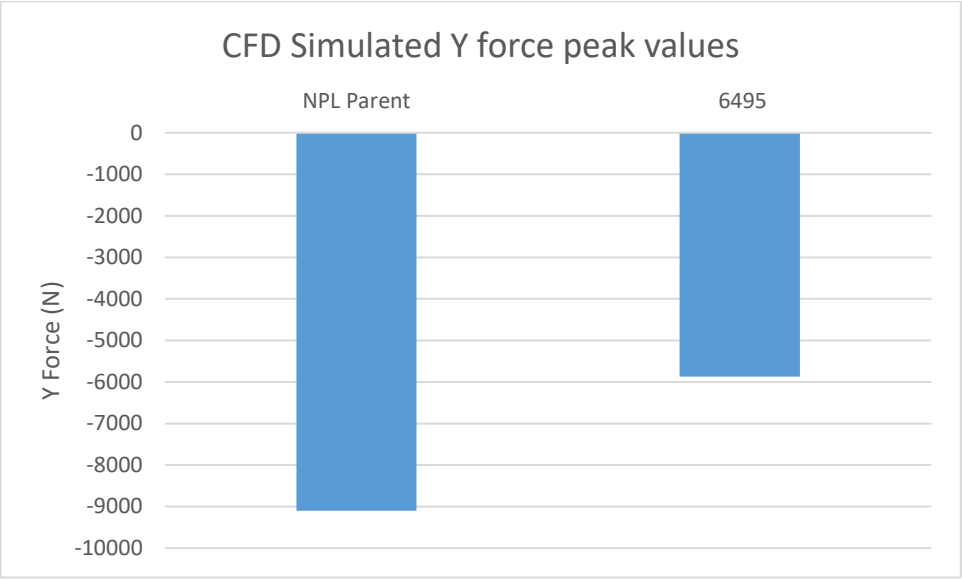

Figure 7-16 Bar chart comparing the simulated Y force comparison between the NPL parent and hull 6495

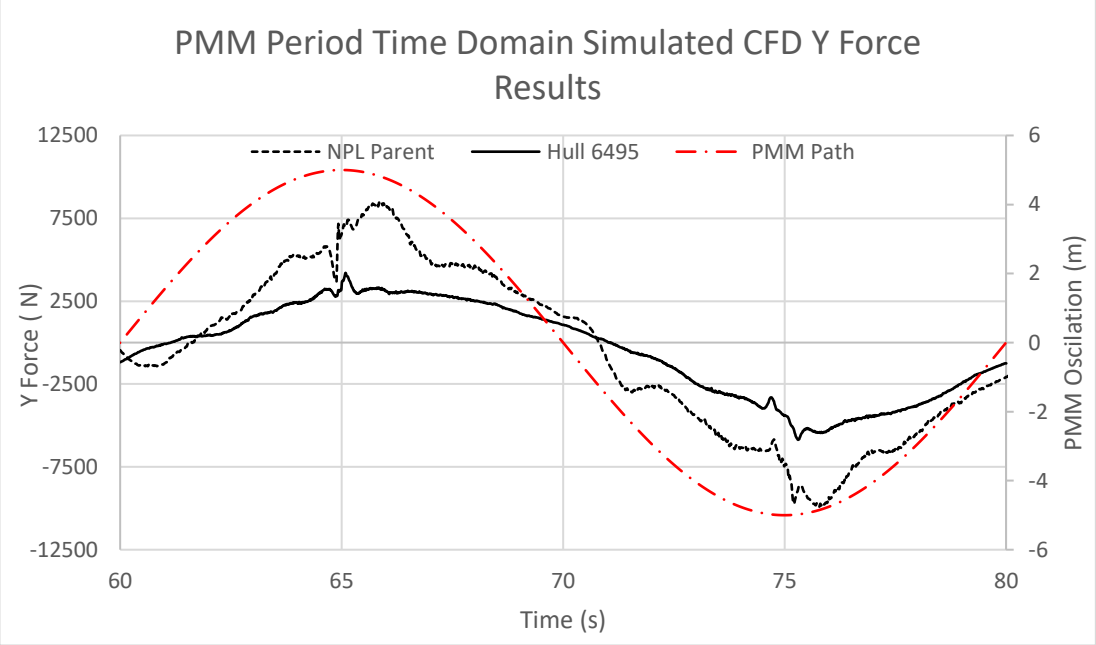

Figure 7-17 Y Force time domain results comparison for NPL parent with hull 6495

The CFD results are shown in Figure 7-16 and Figure 7-17, respectively. From Figure 7-16 hull 6495 reduced the lateral Y force by 3229 N from the NPL parent hulls 9096.99 N. This is an overall reduction of 35.495%. This peak value is taken at 75.3 seconds, or 15.3 seconds into the PMM oscillation.

Unlike the moment, the Y forces peak is delayed until after the maximum amplitude of the PMM oscillation has been achieved. This delay of 0.3 seconds equates to a phase angle of 5.4 degrees from the PMM oscillation. From Figure 7-17 can be seen that the NPL parent hull has

a spike at the same point as hull 6495, however the maximum Y force does not come until 0.845 seconds later which in turn accounts to phase angle of 15.21°. Not only has a phase angle moves closer to the peak amplitude of the PMM oscillation, but the overall Y force acting on the hull has been smoothed out significantly, as seen from Figure 7-17.

In addition to the reduction in Y force, there was also a reduction in both the vessel dynamics. The vessel trim pitch was reduced by 27.43%, there was a similar reduction of 21.25% of the maximum roll angle. The pitch was reduced due to the movement of the LCB aft while also increasing the water plane area in the aft region for hull 6495. This added greater restoring moments around the y-axis and thus reducing pitch. This increase in the water plane area also help to reduce the maximum roll angle. By reducing both these dynamic motions the vessel maintained the smoother and more stable position while moving through the water, and thus smaller vortices were generated helping to reduce the Y force, and slightly the Z moment.

This smoothing and reduction of overall noise is primarily due to the smoother aft region of hull 6495. This is corroborated when viewing Figure 7-18, the viscosity in the aft region is primarily peaking around the tighter bilge keels. However, the vortex generated by the bow is significantly dissipated. Not only is the vortex smaller but the turbulent viscosity has also been reduced, this can be seen from Figure 7-19 of the NPL parent hull's turbulent viscosity.

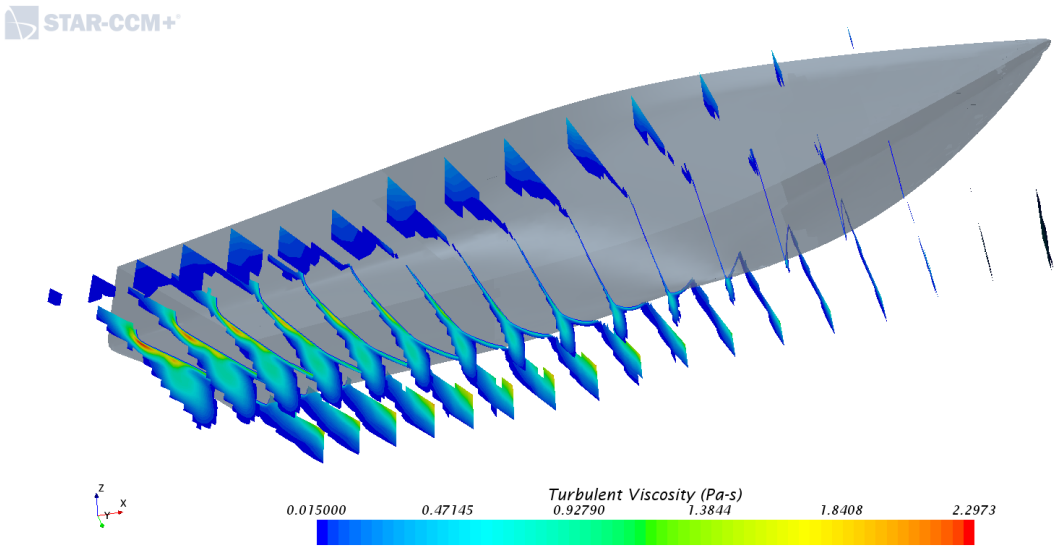

Figure 7-18 Visualised turbulent viscosity from CFD simulation for hull 6495

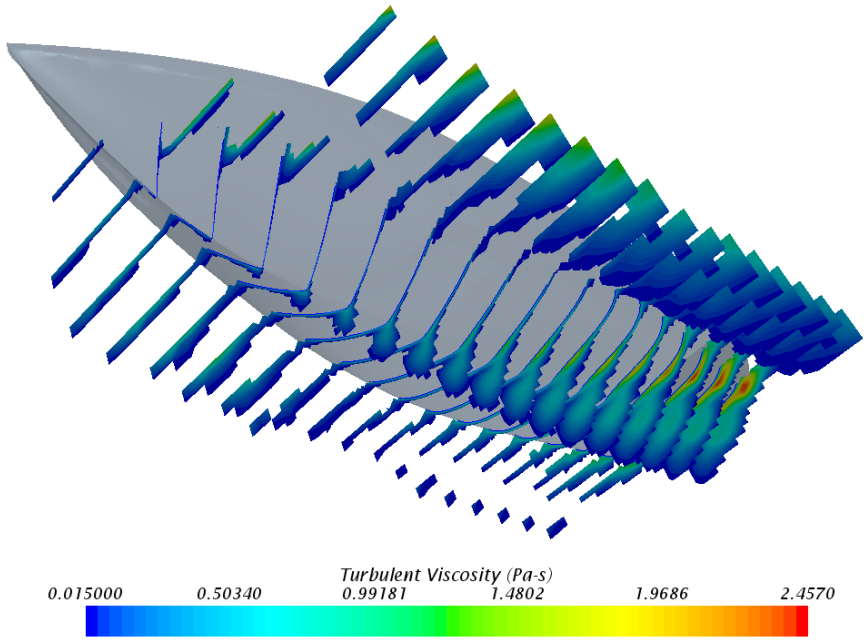

Figure 7-19 Visualised turbulent viscosity from CFD simulation for NPL Parent Hull

In addition to the turbulent viscosity, the fluid streamlines on the hull also highlight how the changes have improved the flow. By comparing Figure 7-20 to Figure 7-21, can be seen that hull 6495s flow has fewer variations in streamlined direction from bow to stern compared to the NPL parent. Hull 6495's flow initially follows that of the NPL parent hull but after the midship flow maintains its move curvature, unlike the NPL parent hull where the flow begins to move back towards the centreline. This suggests grid instability and lower pressure for the NPL parent hull, with squarer and bulkier aft region of hull 6495 helping to reduce these additional forces.

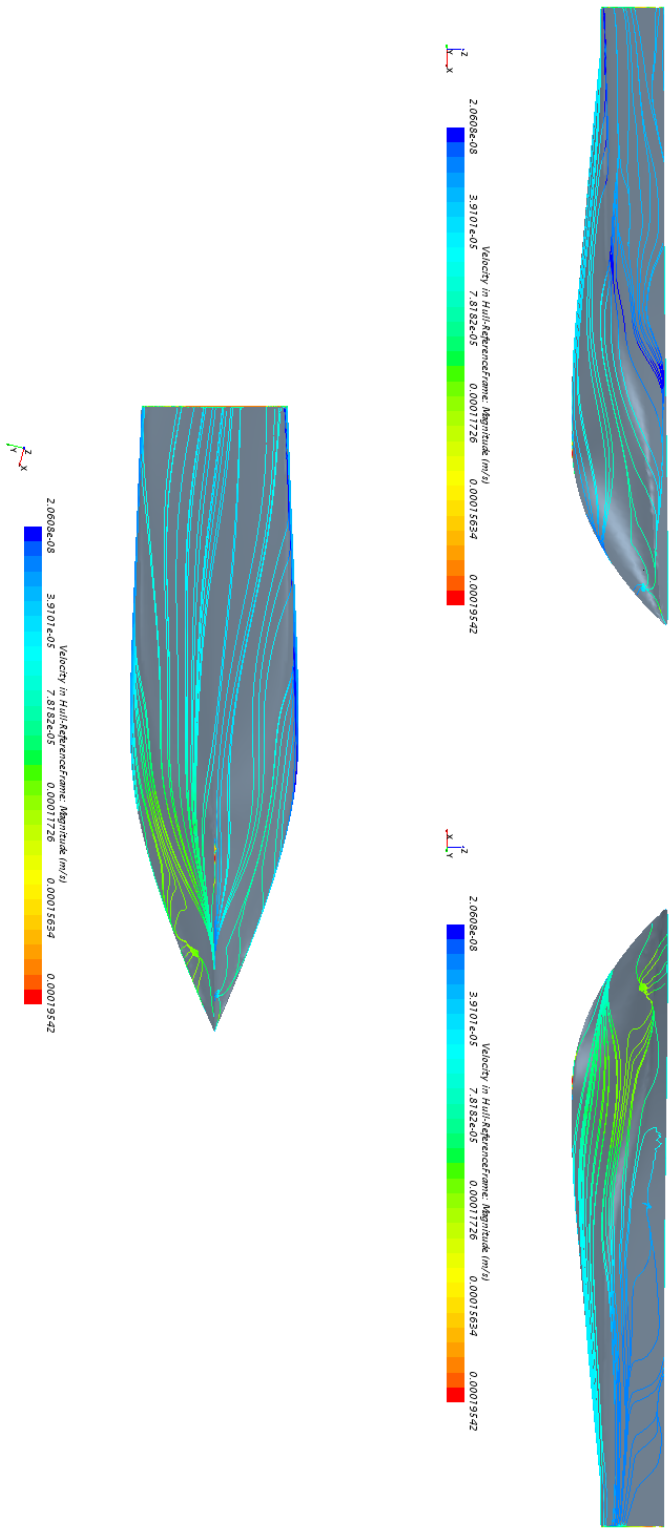

Figure 7-20 Visualised streamlines for hull 6495

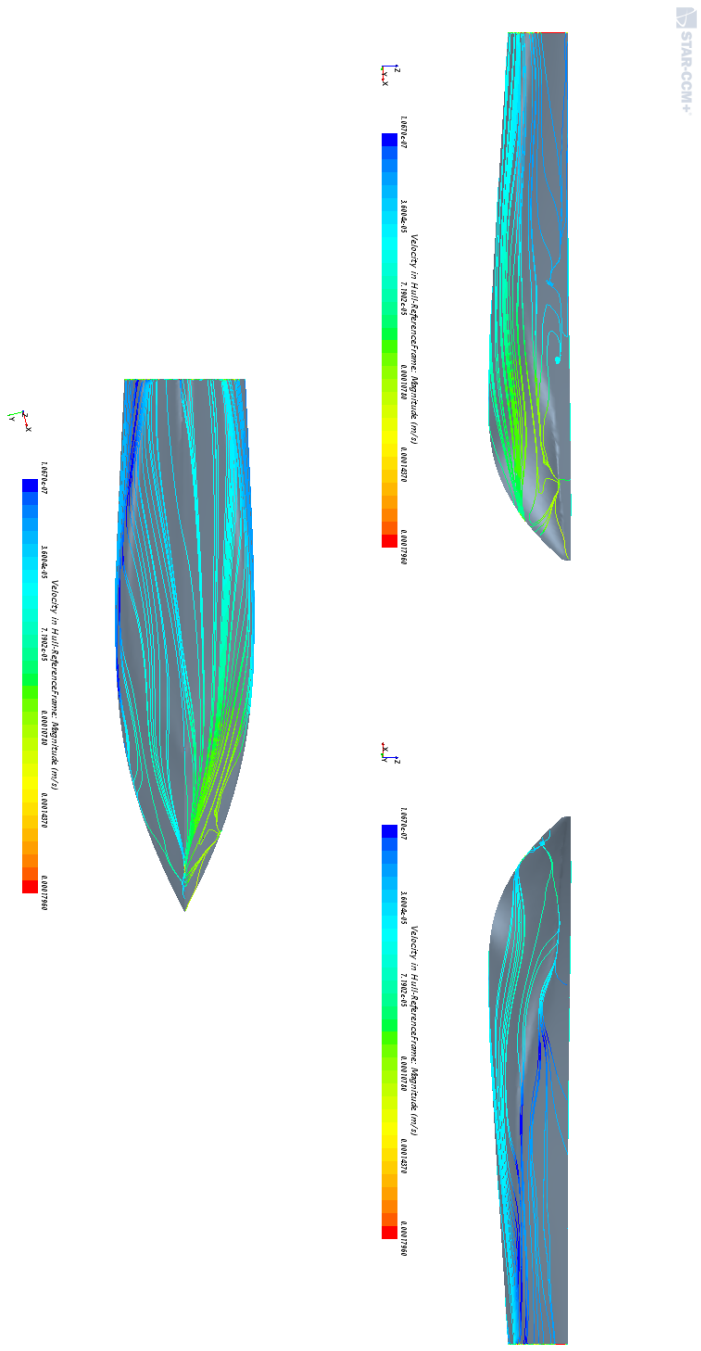

Figure 7-21 Visualised streamlines for parent NPL hull

For this optimisation although it would first appear that only minimal geometric changes have occurred, these minor changes have significantly helped to reduce and improve the optimum hulls Y force performance. These improvements have also helped to produce a more stable hull while dynamically moving. All these factors help with improving the vessel manoeuvring characteristics in real world conditions.

7.5.3. Z Moment optimisation NPL hull

Within this section the results for the optimisation with respect to the Z moment equation is evaluated, in addition to the patterns and the geometric features of the optimum hull compared with the baseline. After this the hull form is evaluated in CFD to validate its performance improvements over the parent NPL hull.

7.5.3.1. Results and discussion for Z moment optimisation

The optimisation for the Z moment follows the exact same setup with a maximum design iteration limit of 15,000, however, the optimum design was found at iteration 6475. The optimisation ran up until iteration 6537, or 43.6% on the design iteration limit.

The complete optimisation results for the Z moment are shown in Figure 7-22. From this graph can be seen that the initial starting generations both fail to meet the constraints while also evaluating the design space to find the feasible design route. Upon finding the feasible route the optimisation follows a traditional downward trajectory and eventually plateaus around the optimum design. This plateauing can be clearly seen in Figure 7-23, which shows the final 1000 design iterations in greater detail. From Figure 7-23 two things can be observed, firstly the plateauing and increased density of design iterations from design iteration 6337 onwards. The increase in density is characterised by many designs, including invalid, been calculated between one and 1.354 ranking Z moment. With only nine designs being outside of these limits. Secondly, by comparing Figure 7-22 to Figure 7-23 it is observed that the optimisation algorithm is beginning to further test the less obvious and more obscure designs by altering the expected improvement acquisition function. From Figure 7-22 there is a noticeable decline in invalid designs outside of the optimisation route between 5300-5900 iterations. However, after this region there is a sudden increase in invalid designs, as well as their deviation from the valid designs, all of which characterises a point at which an optimum may be found.

From the total 6537 designs, 3447 failed to meet the constraints, this equates to 52.7% of the total designs. Most of these invalid designs were due to the tight restrictions on the displacement variation. This majority of these invalid designs are found in the first 3000 design iterations. This is backed up when Figure 7-24 is considered. It can be seen from Figure 7-24 and for the first 2000 design iterations only 57 designs fell within the constraints. This accounts for 56.4% of the total number of invalid designs. This proportion of invalid designs is then steadily brought down over the next 1500 iterations to a point where the final 3000 designs encompass less than 17% of the invalid designs. An additional note can be made when

evaluating Figure 7-22, from around iteration 3000 to just over 5000 there is a noticeable delineation between generations as there is a sudden increase in the density of invalid designs.

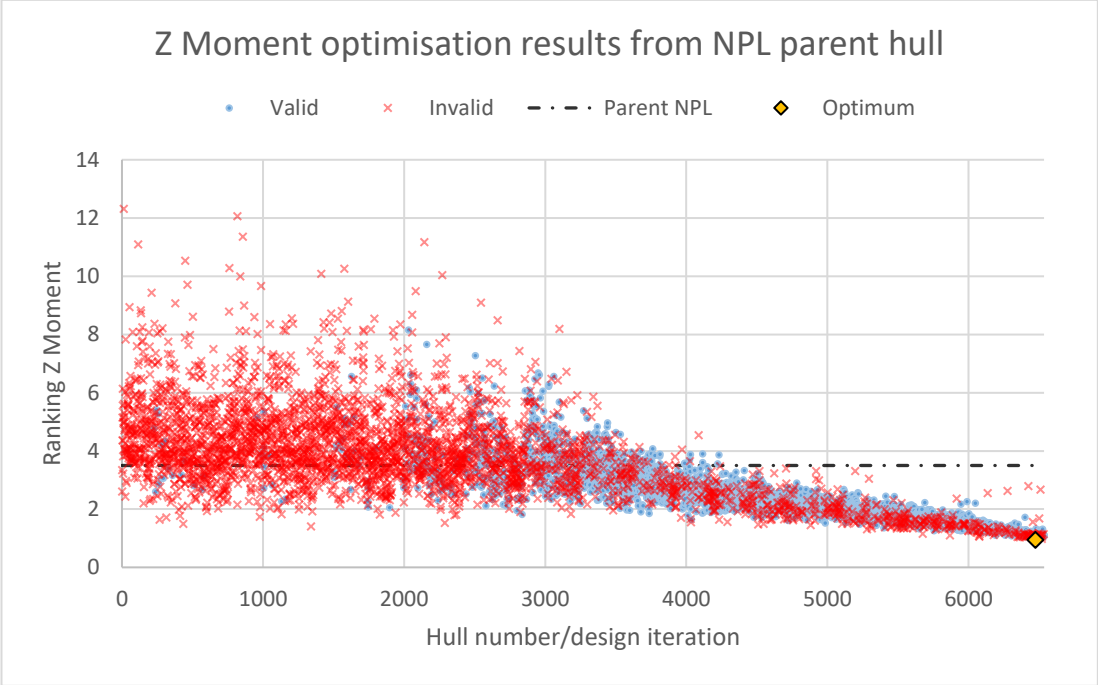

Figure 7-22 NPL parent hull Z moment optimisation results with respect to design iteration

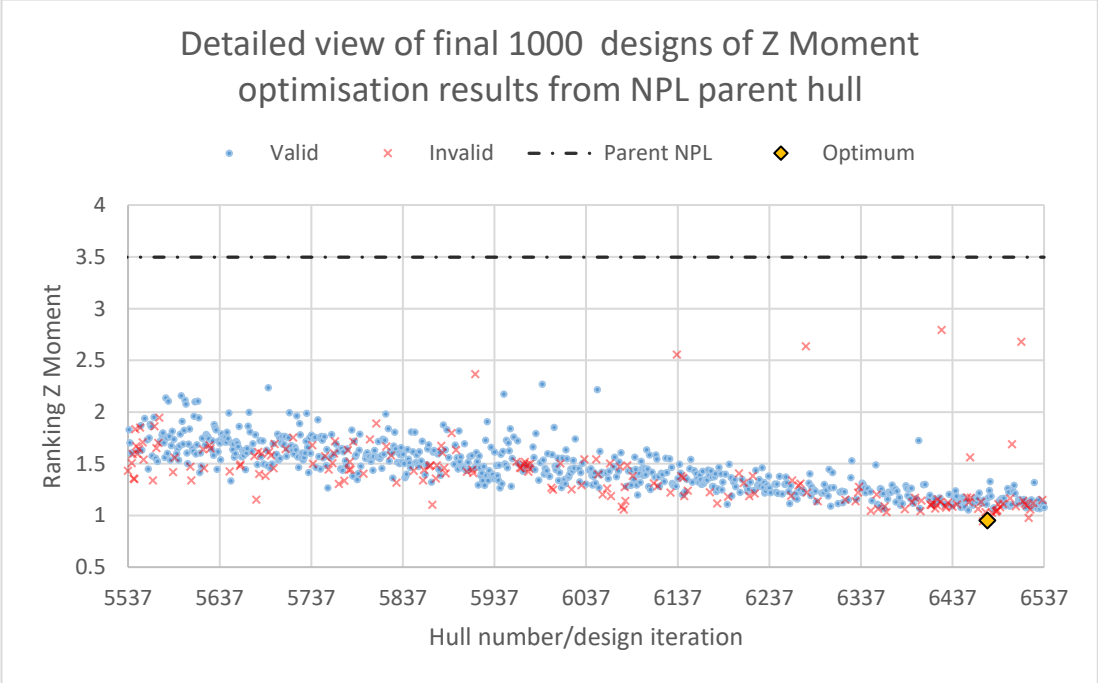

Figure 7-23 Detailed view of final 1000 iterations for the Z moment optimisation on the NPL parent hull

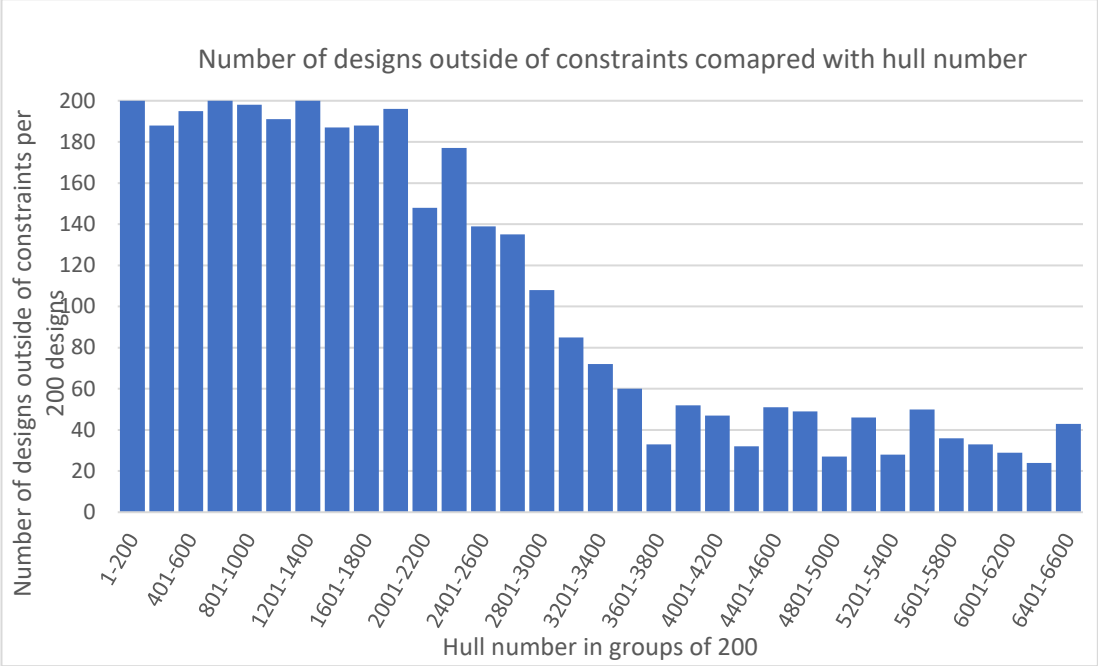

Figure 7-24 Bar chart showing the density of invalid designs per 200 design iterations for Z moment optimisation of NPL parent hull

The optimum hull form is shown in comparison with the NPL parent hull in Figure 7-25 and Figure 7-26, the optimum hull is hereafter known as hull 6475. In addition, some of the key characteristics are given in Table 7-2. It is through this table and figures the key factors allowing hull 6475 to outperform the NPL parent hull with respect to Z moment can be drawn.

First two key observations can be observed from Table 7-2. The displacement for hull 6475 has reduced by 2.814 tons, equating to a 9.8% reduction which is close to the upper limit of 10% for the optimisation constraints. The longitudinal centre of buoyancy has moved forward close to 1.6 m, which in turn is around an 8% increase with respect to the overall length of the vessel. This has moved the centre buoyancy closer to the midship, which in turn is a characteristic highlighted as helping to minimise the moment around the z-axis.

Table 7-2 Comparison between NPL parent and 6475 hull key characteristics

	NPL Parent	*Hull 6475*
LWL (m)	20	20
B (m)	3.2	3.2
T (m)	1.1	1.1
Disp. (t)	28.7	25.886
Cb	0.397	0.3655
LCB (m from aft)	8.72	10.312
Ranking Y Force	223.54579	132.94935
Ranking Z Moment	3.4960017	0.953367

Hull 6475 had some significant geometric changes from the NPL parent hull. These changes may be seen when comparing the various lines plans depicted in Figure 7-25 and Figure 7-26. By first comparing the sectional lines plans shown in Figure 7-25, the obvious rounding to the overall hull form can be seen. This rounding is primarily focused on the bilge region, this change has also noticeably reduced the beam at the waterline compared to the parent NPL hull. This rounding has also continued forward towards the bow region. Although the bow region maintains a concave bow flare, the region about the centre line clearly transitions from perpendicular to the centreline to the smooth concave bow flare. This is done through a significantly round and smooth transition. This rounding helps to reduce turbulent flow at the bow in comparison when rotating.

Further to this the aft region is considerably different, with the aft more closely resembling a region of a bow. This change allows for greater symmetry about the midship, and thus minimising the opposing moment forces. This change in the aft transition into the water is also noted for reducing the transoms beam. This is noticeable when comparing both the section and waterline plans in Figure 7-25.

Figure 7-26 helps to highlight the more rotund nature of hull 6475. As well as the bow overall becoming less sharp and having a greater volumetric weight towards the bow tip than the NPL parent hull. Although there have been many changes, an interesting similarity between the two hull forms is the angle from the deepest point of the hull to the transom staying nearly identical between the two hull forms. This is due to hull 6475 moving its volumetric weight forward as well as slightly reducing the draft at the transom.

Overall, hull 6475 has become substantially rounder within an inverse rounding at the aft. This has created greater symmetry between the aft and bow. Combine these features with the reduced displacement and forward movement of the longitudinal centre buoyancy, noticeable reduction in the Z moment should be observed.

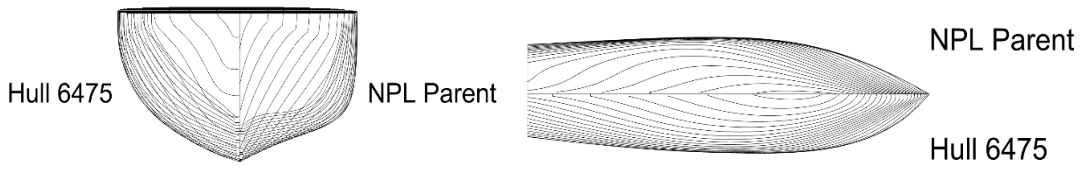

Figure 7-25 Sectional lines (left) and waterlines plans (right) comparison between hull 6475 and NPL parent hull

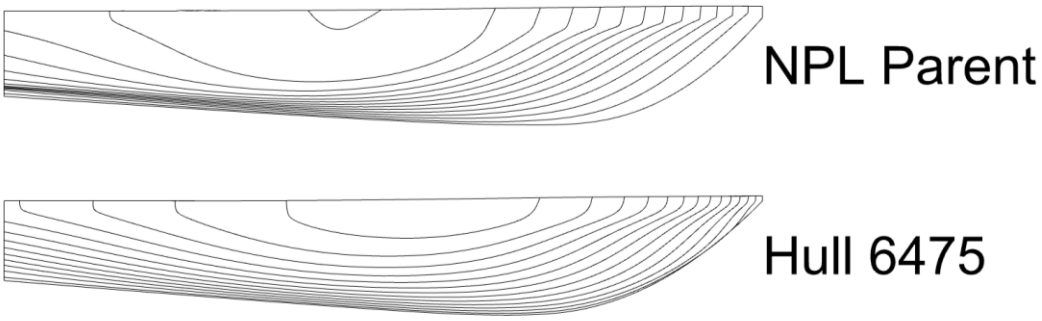

Figure 7-26 Buttock lines plans comparison between hull 6475 and NPL parent hull

7.5.3.2. CFD Evaluation

This section presents the results and methodology used to evaluate the optimally ranked hull form in comparison to the NPL parent hull in CFD. To ensure as accurate a simulation as possible, the simulation is based off the setup developed in chapter 5.4.

As mentioned in the Y force optimisation CFD analysis, although the exported hull geometry can be imported directly in to the CFD simulation, an extra step of evaluating and repairing any geometric deficiencies is added. This is merely to ensure no problems may be caused from the geometric data. Although the methodology developed through chapters 4 & 5 allows for complete parametric creation of all volumetric refinements, including the overset box. These refinements are not required as the PMM values and hull bounding box does not vary from those used in chapter 5.4.

Upon importing the hull geometry into the simulation, the imported mesh was evaluated and prepared within Star CCM+, with the key curves being highlighted for meshing. While the model was being checked before import, the calculated moment of inertia, longitudinal centre buoyancy and displacement were also verified to match those calculated parametrically. These values were then imported over into the DFBI model.

The simulation had a total mesh count of 1.12 million cells, this is a slight increase from the NPL CFD setup which had a cell count of 948896, as shown in Table 5-4. The slight increase is due to additional refinement regions located in the located in the fore and aft regions close to the waterline. These refinements were intended to improve free surface resolution due to the varied hull form.

Each simulation was run for a minimum of five PMM oscillations, with the first three oscillations not being considered for the results and analysis. This ensures the greatest level of the simulation stability as well as results convergence.

Through the CFD simulations the Z moment for hull 6475 was found to be 45,537.6 Nm. This is a reduction of 40,318.3 Nm from the NPL parent hull. This reduction equates to 46.96% off the NPL parent hull. These results can be seen in Figure 7-27, with the real-time Z moment results shown in Figure 7-28.

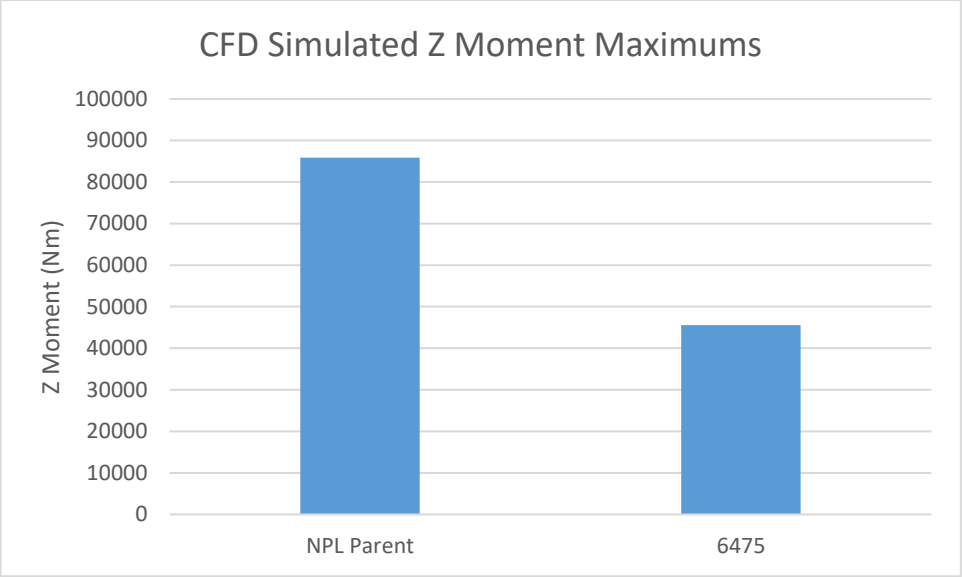

Figure 7-27 Bar chart comparing the simulated Z moment comparison between the NPL parent and hull 6475

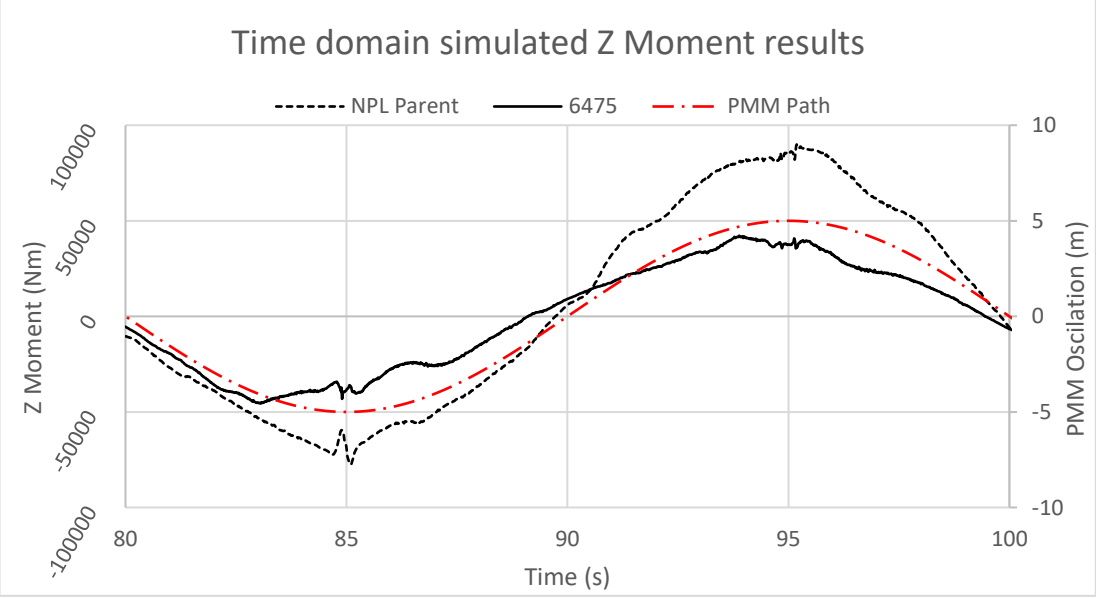

Figure 7-28 Z moment time domain results comparison for NPL parent with hull 6475

By more closely evaluating Figure 7-28, at the peak amplitude of the PMM path both hull forms experience spikes in the Z moment. With hull 6475s spike occurring in the opposing direction to the NPL parent hull. These spikes are observed at the maximum angle of roll, with

hull 6475 having an increase in roll angle throughout the whole of the PMM path, whereas the parent hulls roll follows a more aggressive oscillation. Although hull 6475 has an increase of 11.37% for the maximum roll angle, the roll acceleration is lower than that of the NPL parent hull. This is primarily due to the rounder hull form, which in turn reduces the induced bow vortex.

In addition to the moment spikes, the maximum observed moment force does not occur at the spikes but rather to seconds prior for hull 6475. This peak value occurs around 10% earlier or 2 seconds along PMM oscillation.

7.5.4. Multi-objective optimisation based of parent NPL hull form

In addition to the optimisations for Y force and Z moment, another optimisation was conducted with both factors being used as an evaluation in a multi-objective optimisation. This helps to provide an insight into which methodology, single or multi-objective, provides the best results. It is also expected that this multi-objective optimisation may provide differing design branches from single evaluation optimisations.

7.5.4.1. Results and discussion for multi-objective optimisation

This section provides a brief overview of the results obtained from the multi-objective optimisation and how they differ from the single objective runs. The graphs showing the optimisation results with the highlighted optimum designs with respect to the Y force and design iteration can be seen in Figure 7-29 and Figure 7-30. The corresponding graphs with respect to Z moment are shown in Figure 7-31 & Figure 7-32, with density distribution of invalid designs for the overall multi-objective optimisation depicted in Figure 7-33.

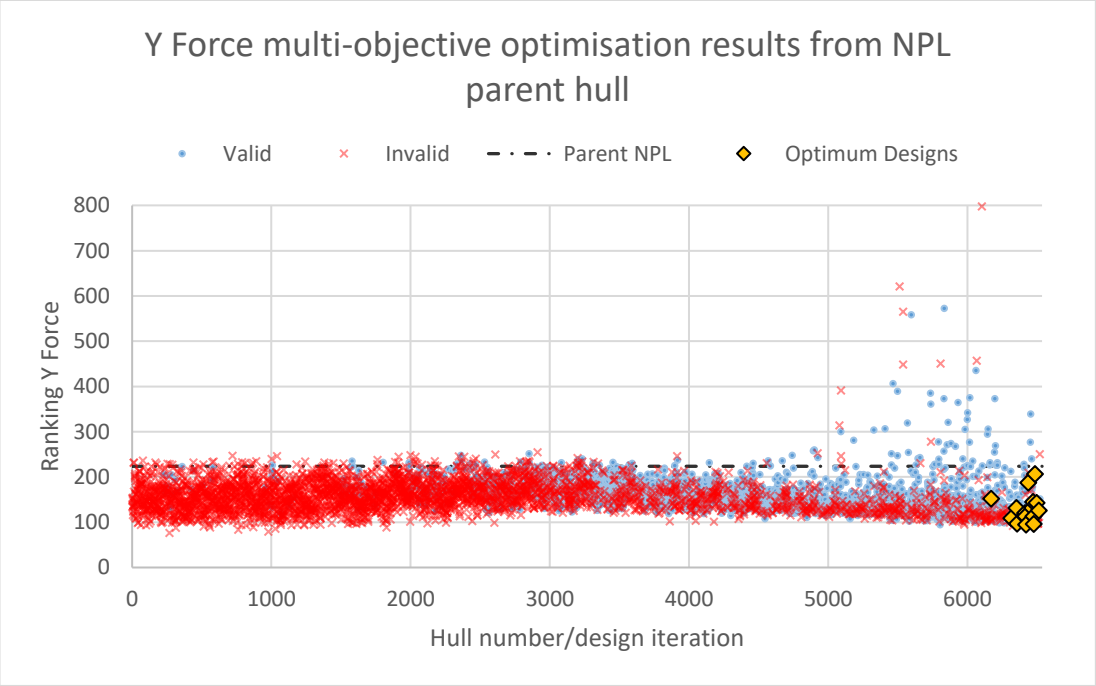

Figure 7-29 NPL parent hull multi-objective optimisation results with respect to Y force and design iteration

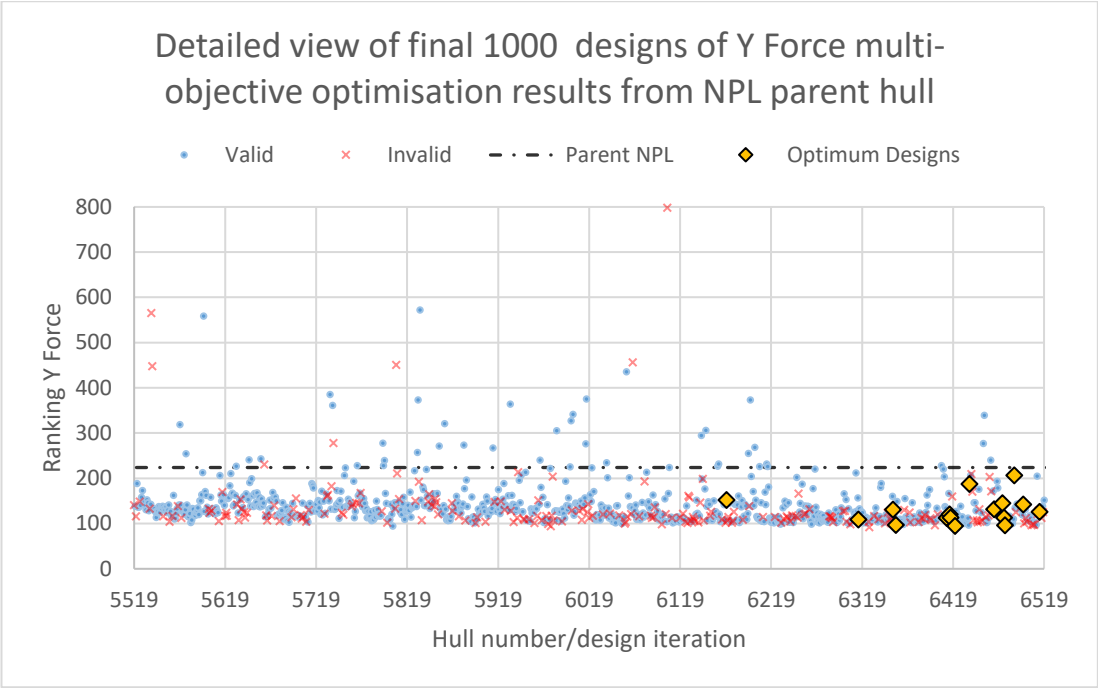

Figure 7-30 Detailed view of final 1000 iterations for the multi-objective optimisation on the NPL parent hull with respect to Y force

Unlike single objective optimisation for Y force, the multi-objective optimisation does not have this noticeable downward gradient as the design iteration count increases, this is seen when comparing Figure 7-11 with Figure 7-29. Although there is a slight downward trend, the greatest difference between Figure 7-11 and Figure 7-29 as the final few thousand design iterations. Unlike in the single objective optimisation variation in the final few thousand designs do not greatly exceed that of the natural trend and high-density path, as discussed in chapter 7.5.2.1. From Figure 7-29, after around design iteration 4500 there is a noticeable increase in the number of designs exceeding the main downward trend, as well as an increase in the range between these designs. This increase can be accounted for with an increase in the value for the expected improvement acquisition function in these later generations. This increase in design spacing and results range is not observed when evaluating the results with respect to the Z moment, shown in Figure 7-31.

From all the graphical representations of the results of the multi-objective optimisation, there are multiple optimum designs rather than a single optimum for each evaluation. This is due to difficulty of a multi-objective optimisation and the corresponding Pareto frontier. It is therefore up to the user to select the optimum design for their respective design.

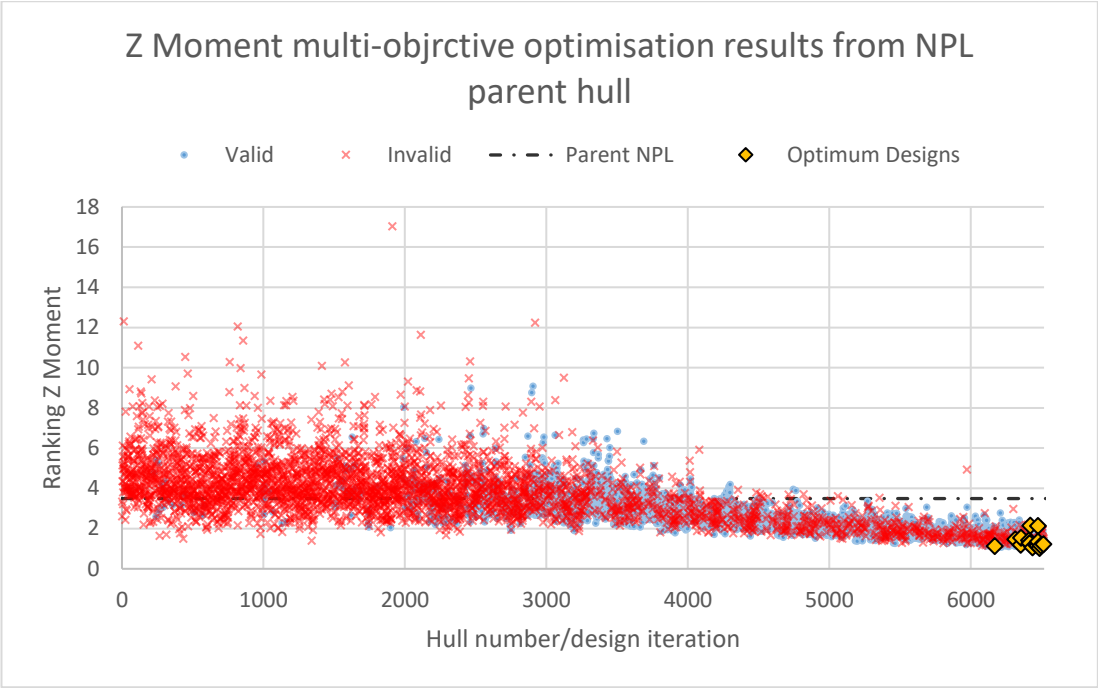

Figure 7-31 NPL parent hull multi-objective optimisation results with respect to Z moment and design iteration

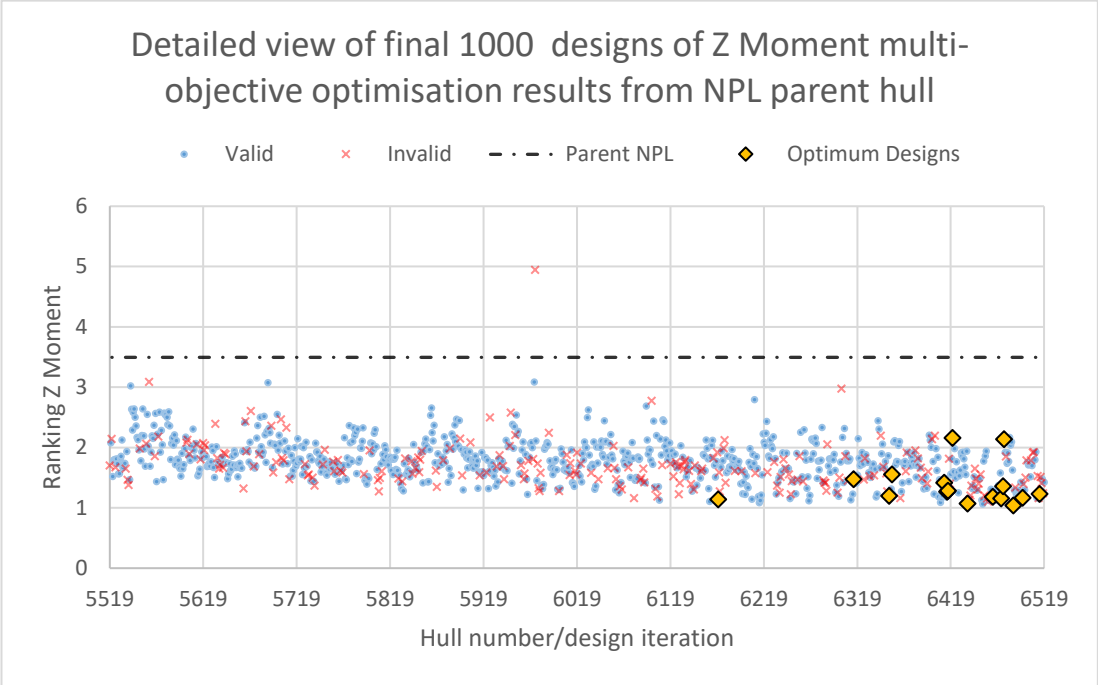

Figure 7-32 Detailed view of final 1000 iterations for the multi-objective optimisation on the NPL parent hull with respect to Z moment

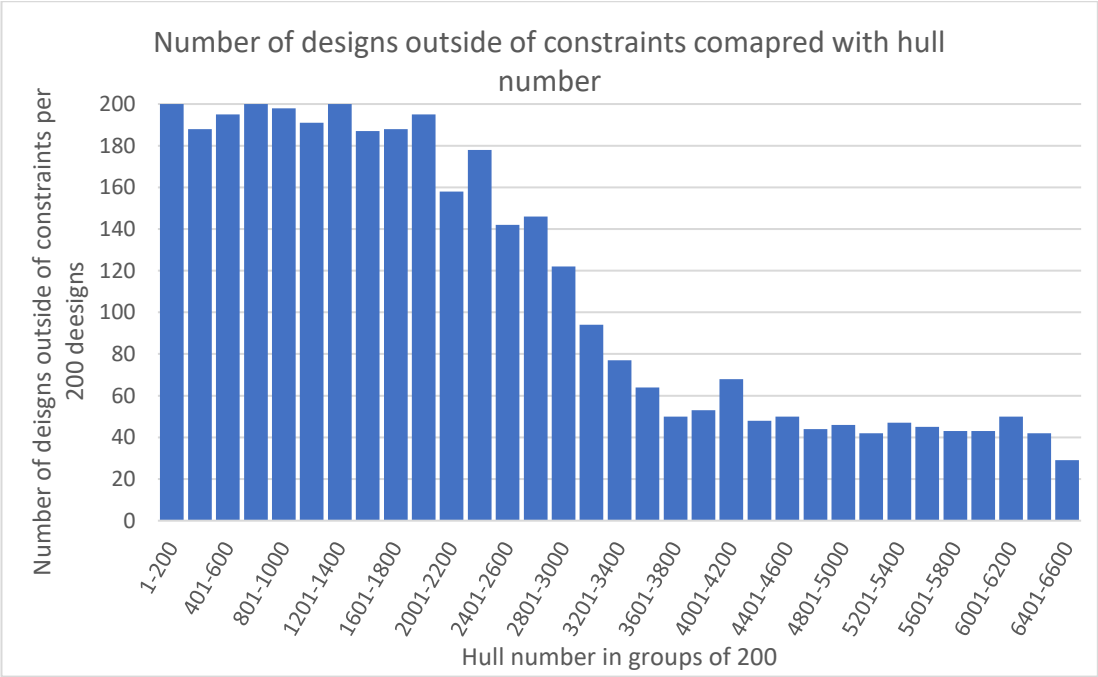

Figure 7-33 Bar chart showing the density of invalid designs per 200 design iterations for multi-objective optimisation of NPL parent hull

The graphs shown in Figure 7-31 and Figure 7-32 give the optimisation results with respect to Z moment and the design iteration. Unlike the results depicted with respect to the Y force, Figure 7-29, Z moment results initially start off with a significantly greater range than that of the Y force. This range begins to taper and refine, such that there begins to be a noticeable downward trend towards where the final optimum designs are located. Unlike in Figure 7-29, there was no significant increase in design variation towards the final few thousand designs due to the expected improvement acquisition function. This is particularly noticeable when comparing Figure 7-30 with Figure 7-32, with Figure 7-32 maintaining a nearly perfect oscillatory pattern between a range of 1 to 3.1. This oscillation also helps to delineate the various generations, as well as showcase how the optimisation algorithm attempts to find optimum designs for multiple objectives. This oscillation is less visible in Figure 7-30.

As with the previous optimisations around 56% of design iterations were invalid. As can be seen in Figure 7-33, the invalid designs follow a similar trend to that seen in both the Y force and Z moment optimisations. By further evaluating Figure 7-33, it is noted that 62.87% of the invalid designs occur within the first 36.8% of the design iterations. From here there is a steady downward trend to where the invalid design density which is a near steady state. This steady state account for 44.78% of the design iterations but only 19.321% of the total number of invalid designs.

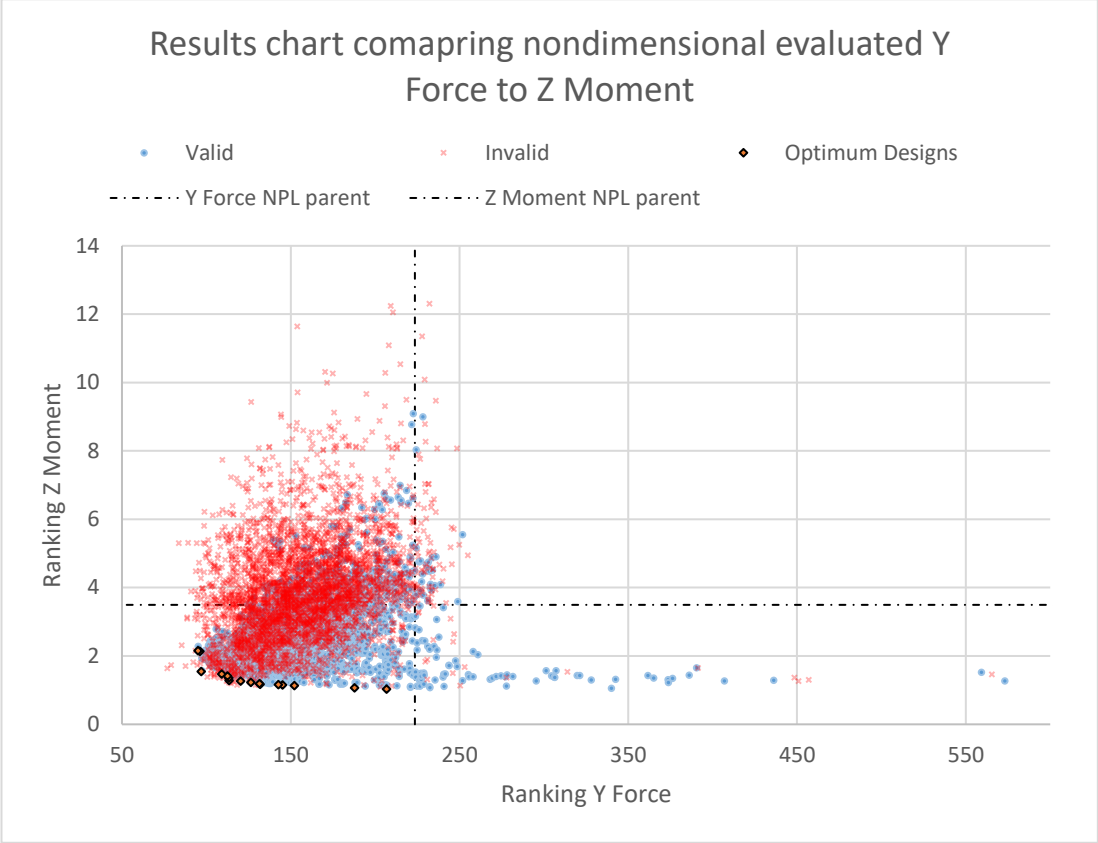

Figure 7-34 Results graph comparing Y force and Z moment for multi-objective optimisation

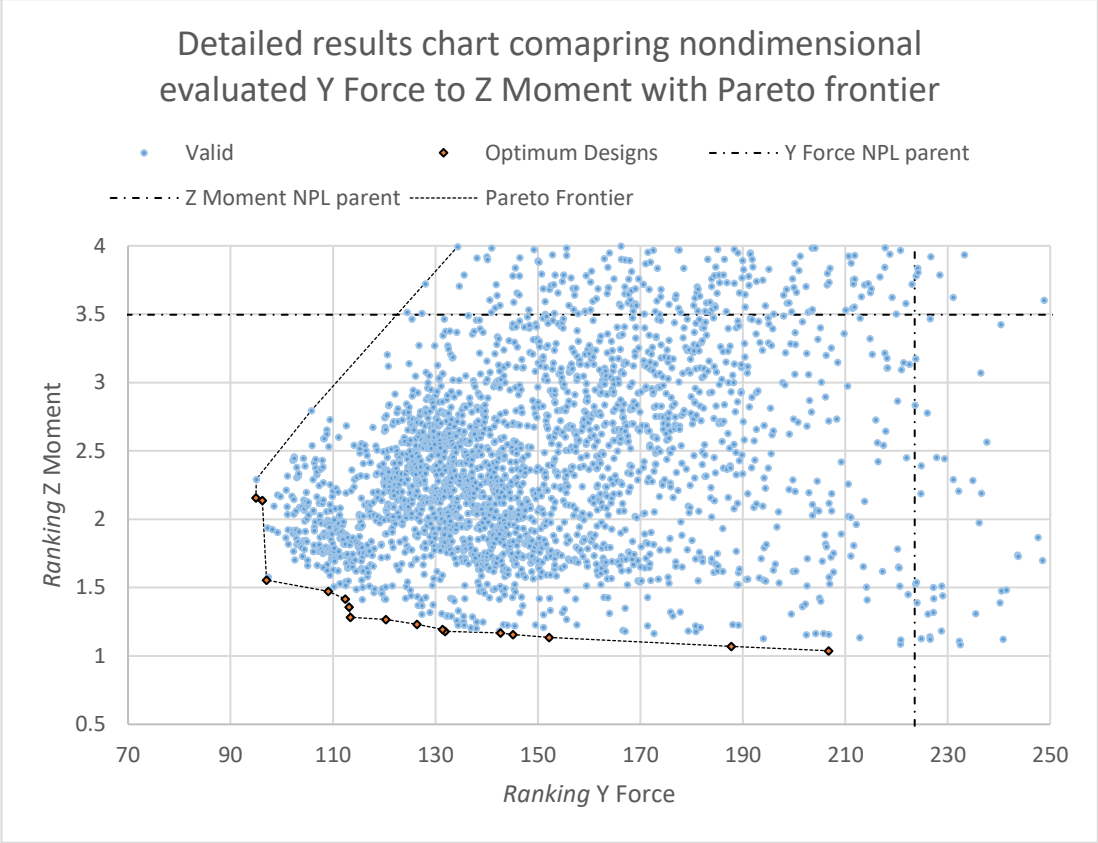

Figure 7-35 Detailed view of results graph comparing Y force and Z moment for multi-objective optimisation including Pareto frontier

The final two results graphs, Figure 7-34 and Figure 7-35, for the optimisation run show a comparison between the two objective functions with additional key data. Figure 7-34 shows the complete results including all the invalid designs with the optimum designs highlighted, additionally lines delineating the NPL parent hull results are also shown. From Figure 7-34 the majority of all results fall below the calculated ranking Y force for the parent NPL hull. This equates to 96.89% of the total number of designs being improvement over the parent NPL hull, whereas there is a significant proportion of designs which exceed the parent NPL hulls calculated ranking Z moment, as proportion accounts for 39.63% of total number of designs. This also highlights the importance to differentiate between an optimisation focused on Y force or Z moment.

Purely based on these observations it can be said that the parent NPL hull naturally has poor Y force characteristics. This is corroborated by the parent NPL hull relatively large lateral area, as well as poor for sectional area coefficients. However, due to the relatively close LCB to the midship and a small difference between the LCB and the lateral area centroid (ΔX), the parent NPL hull starts with acceptable Z moment performance.

Figure 7-35 shows the Pareto frontier along with position of the optimum designs along this front. This figure also highlights in greater detail the various improvements gained over the parent NPL hull. In addition to the Pareto front, this more detailed view of the valid designs also highlights key areas of density differences. These bands of low-density are not filled with invalid designs, but is rather be due to the limitations of the design variable limits and in turn the hull form.

Table 7-3 Optimum hulls and parent NPL hull key hull characteristics and evaluated results

	Ranking Y Force	*Ranking Z Moment*	*Disp. (t)*	*LCB (m)*
Parent	223.546	3.496	28.70	8.720
6170	152.209	1.137	25.05	10.087
6315	109.071	1.474	25.87	9.844
6353	131.407	1.195	25.41	9.998
6356	97.024	1.554	26.15	9.588
6412	112.415	1.417	25.31	9.819
6415	120.322	1.267	25.42	9.953
6416	113.383	1.283	26.18	9.897
6421	94.968	2.157	25.46	9.184
6437	187.731	1.070	25.32	10.182
6464	131.925	1.180	26.20	10.046
6473	145.160	1.157	25.69	10.125
6476	96.213	2.138	25.99	9.216
6486	206.746	1.038	25.22	10.272
6496	142.691	1.168	25.55	10.050
6514	126.404	1.231	25.37	9.967

Table 7-3 provides an overview of all the optimum hull forms, focused on the calculated evaluations as well as the displacement and LCB. In addition to Table 7-3, there is a 3D render and sectional lines plan for each optimum hull provided in Appendix vii. These are used to compare the results with respect to the geometric characteristics of the various hull forms.

By evaluating Table 7-3 no optimum design outperforms the designs found for the single objective optimisation. Although no multi-objective design outperforms the single objective optimum hulls, some of the designs listed in Table 7-3 fall very closely. By comparing the best performing hulls, with respect to Y force and Z moment from Table 7-3, with the previous optimum hulls key differences and influencing factors may be observed.

Before evaluating the various geometries shown in Appendix vi, three key designs need to be highlighted, these represent the optimum designs with respect to Y force, Z moment and combined. The optimum Y force is hull 6421, which is shown in Figure 16-15 and Figure 16-16. The optimum Z moment hull as 6486, shown in Figure 16-25 and Figure 16-26. For the

combined hull form, Figure 7-35 was used in partnership with Table 7-3 two select hull 6356. Hull 6356 as the most obvious hull form that does not fall within the nominal range but is rather an outlier as seen from Figure 7-35 being the abrupt angle along the Pareto frontier. Hull 6356 3an be seen in Figure 16-7 and Figure 16-8 of Appendix vi. Another hull form may be considered to represent the combined hull would be hull 6416, due to itself falling as a potential outlier in the Pareto front.

Hull 6421 can be seen to follow the same dominant characteristics as observed in chapter 7.5.2. Further to this the calculated ranking Y force for hull 6421 is 97.024, compared with 90.7585 for the single objective Y force optimisation, hull 6495. When comparing the two hull forms obvious similarities can be observed, the aft portion of the hull form follows the boxy shape with a smoother shave bow region. In addition, the displacement for both hull forms is very similar, with hull 6421 being slightly lower hull 6495. Although similar geometric properties can be seen, the LCB for hull 6421 has moved forward compared with aft movement for hull 6495. This aft movement is likely due to the more subtle geometric differences between the two hull forms.

As noted, at initial glance the hull forms appear very similar, however, hull 6421 as a narrower transom with an overall flatter keel. On the other hand, hull 6495 has a wider beam at the transom as well as a slightly deeper draft at this point, along with a concave curvature of bilge keel is to the centre line keel. These additions the slightly greater increase and displacement and thus the aft movement of the LCB. Additionally, the bow region of hull 6495 is more concave than that of Hull 6421, this can be seen when comparing Figure 7-14 and Figure 16-16, respectively.

Similarities between the multi-objective and the single objective optimum for Z moment can also be seen. Similarities between the two hull forms is less than that observed for the Y force, however the base characteristics follow the same trend. The most notable similarity between the two hull forms, comparing hull 6486 in Figure 16-26 with hull 6475 in Figure 7-25, is the increased displacement towards the bow causing a rounding along the centreline. As with the multi-objective optimum for Y force, the Z moment optimum also has a lower displacement than its equivalent for the single objective. The greatest difference between hull 6486 and hull 6475 is the aft region and transom of the hulls. For the multi-objective optimum the beam at the transom is slightly greater than that of hull 6475, this however is mainly due to the overall boxy form of the transom of hull 6486. In addition to the increased block coefficient in the aft region, hull 6486 also maintains the appearance of two propeller tunnels unlike hull 6475. The

slightly lower displacement in the forward region contributes to the slight movement aft in LCB for hull 6486.

As both the hull forms, with respect to the Y force and Z moment, follow similar trends to those observed in the single objective optimisation, it is of interest to see how the compromised hull form compares with these trends. As mentioned, hull 6356 has been selected to represent the multi-objective optimum.

Unlike the previous hull forms, hull 6356 has the third highest displacement out of the optimum designs. The displacement has reduced by 2.55 tons, whereas the optimum designs that performed better with respect to a single objective have a further reduction of 0.8 to 0.9 tons. This equates to nearly 3% when considered in comparison to the parent hull form. The slightly smaller reduction in displacement is also noted for hull 6416. Both potentially combined optimum hull forms have an LCB closer to the midship than the parent hull. Hull 6356 has a forward LCB movement of 9.95% with hull 6416 having 13.19%, these movements fall between for 6421 and 6486.

Hull 6356 is more closely related to the Y force optimum for the multi-objective optimisation, as it has a slightly tapered transom a flatter stern. However, unlike hull 6421 bow has become fuller as well as having an increased rounding along the centre line at the bow. By rounding the bow and increasing the volumetric displacement there is a slight increase from the ranking Y force while having a significant decrease for the ranking Z moment. This rounding can also be seen more clearly in Figure 16-8. These minor changes reduce the ranking Z moment from 2.157 to 1.554 for hull 6356, and a reduction of 0.874 for hull 6416. This greater reduction in ranking Z moment is due to the even greater rounding of the bow along the centre line as seen in Figure 16-14. In addition, hull 6416 also has a rounder midship with a less tapered transom, these factors help to improve Z moment performance, while not overly negatively impacting Y force.

It is due to this subtle and fine differences between the group of optimum hulls from the multi-objective optimisation that an accurate CFD tool is required to truly evaluate these designs. All designs are evaluated in CFD using the methodology used in the evaluations of the optimum hull forms for the single objective optimisations.

7.5.4.2. CFD evaluation

This section focuses on presenting the results for the group of optimum designs discovered in the multi-objective optimisation. Each design is evaluated with respect to both Y force and Z

moment such that they can be clearly evaluated between one another as well as with respect to the NPL parent hull.

For the evaluation, the same methodology and setup used for the single objective optimisations is utilised. The methodology and setup have been discussed in both chapter 7.5.2.2 and 7.5.3.2, refer to these chapters for greater detail and reference. All simulations were run to a minimum simulation time of 100 seconds, upon which the final two PMM oscillations were taken to evaluate results.

The results for the CFD simulations are shown below in the various bar charts. Following the same pattern above the Y force results is discussed first followed by Z moment. For both these evaluations there is a relatively wide spectrum of results for the group of optimum designs, which in turn is matched by CFD simulations.

The simulated results for the Y force are shown in Figure 7-36, as can be seen the optimum design with respect to the simulated CFD results matches that of the ranking evaluation equations. In addition, the CFD also validates each ranking for the various designs. These results also highlight that the ranking has no direct correlation to the potential Y force reduction. This can be seen when considering hull 6421, this hull form had a ranking Y force of 94.968 and the simulated 6109.945 N. When considering the ranking Y force there was a reduction of just over 57%, however, this reduction only correlated to a 32.84% in the simulated Y force. This pattern continued for all hull forms in the optimum group, with hull 6486 having the closest correlation between evaluated equation and the simulated Y force. Hull 6486 had only a 3.75% reduction in simulated Y force, while the ranking Y force and a reduction 7.515%. Figure 7-36 highlights the overall performance gains achievable by using the equations developed in chapter 6. However, for greater detail with respect to the key designs Figure 7-37 presents the simulated Y force for these four designs compared with NPL parent hull.

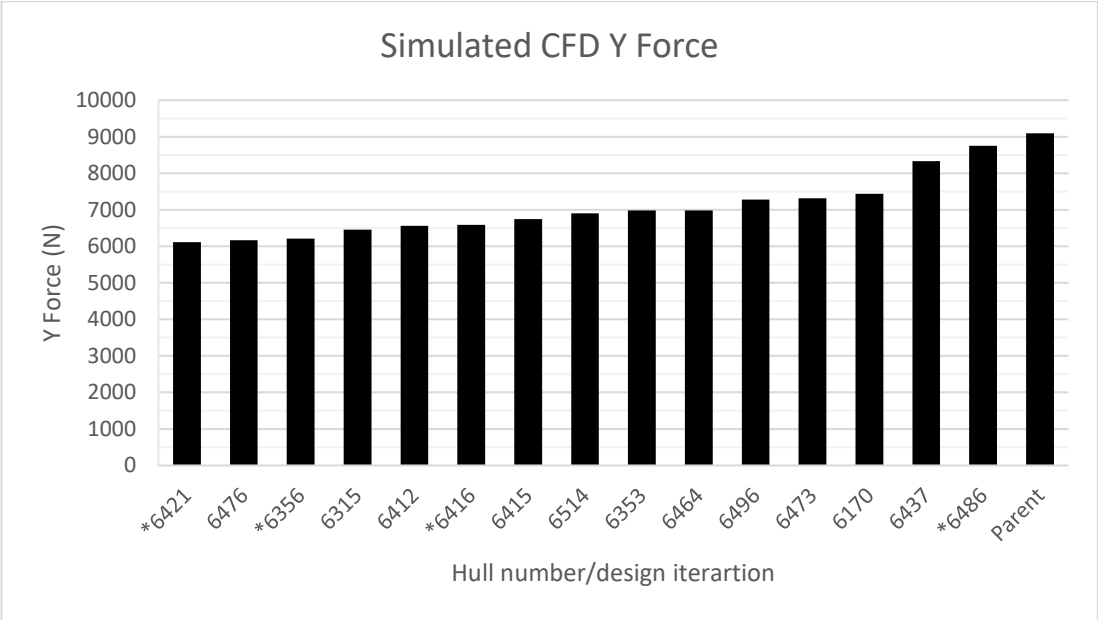

Figure 7-36 Bar chart presenting the simulated Y force for each hull form from the multi-objective optimisation

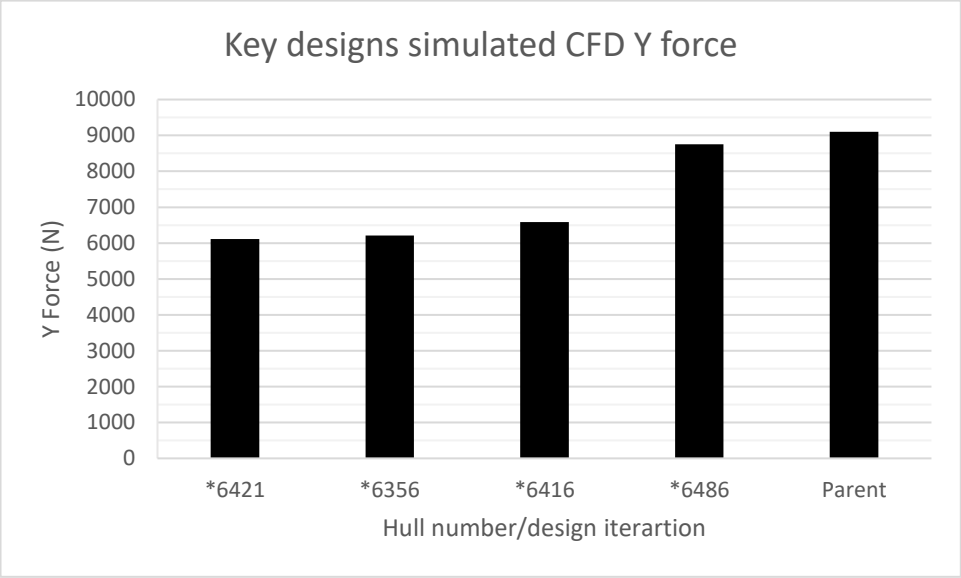

Figure 7-37 Bar chart showing the simulated Y force for the four key designs compared with the NPL parent hull

As mentioned above, hull 6421 achieved a reduction of 32.84%, the rest of the key designs numerical results and percentage improvements can be seen in Table 7-4. From this table they can be seen that all key designs achieve some level of improvement over the NPL parent hull. However, the two key designs that should be focused on the hull 6356 and 6416. These two hull forms can be considered to be a compromise on either of the evaluation factors. Hull 6356 achieves a reduction of Y force of 31.75%, with hull 6416 achieving 27.56%. All results were

taken from the maximum peak value observed along the final two PMM oscillations, these peaks were observed and spikes like those seen and discussed in Figure 7-17.

The three spikes for hulls 6421, 6356 and 6416 occurred between 0.235 and 0.411 seconds after the peak of the PMM oscillation. The smallest phase angle occurred for hull 6356, with angle of 4.23° and time difference of 0.235 seconds. Hull 6421 had a time difference 0.337 seconds equating to a phase angle of 6.066°, with hull 6416 having the largest phase angle of 7.398° due to the 0.411 seconds. These all fall significantly below the phase angle of 15.21° for the NPL parent hull.

Table 7-4 Key design results with respect to Y force

Hull	*6421*	*6356*	*6416*	*6486*	*Parent*
Ranking Y	94.97	97.02	113.38	206.75	223.55
CFD Y Force (N)	6,109.945	6,208.937	6,589.840	8,755.852	9,096.987
% Improvement	32.84	31.75	27.56	3.75	-

The results for the simulated Z moment are visualised in Figure 7-38. As with the ranking Y force, the ranking Z moment equation effectively predicted the position of each of the hull forms with respect to one another and the NPL parent hull. Unlike the ranking Y force, where hull 6486 fell closely to the NPL parent hull for example, the ranking Z moment was considerably improved for all hull forms. This is particularly noticeable in Figure 7-38 where there is significant drop from the NPL parent hull to the worst performing hulls in the group.

From Figure 7-38 it is observed that there is a clear improvement in the initial 3 to 4 designs, however after this there is a noticeable decline in improvement from design to design. In addition, unlike the ranking Y force and the accompanying simulated results, not all hull forms in the inexact ranking position calculated by the ranking equation. This is most noticeable for hull 6514, which has an increase of around 600 Nm over hull 6415 with was predicted to perform 6514. Along with hull 6514, hull 6473 was also predicted to be slightly better than hull 6496, however hull 6473 only had an increase of 190 Nm or 0.2%. These variations fall well below the numerical uncertainty predicted for the simulation setup in chapter 5.4.

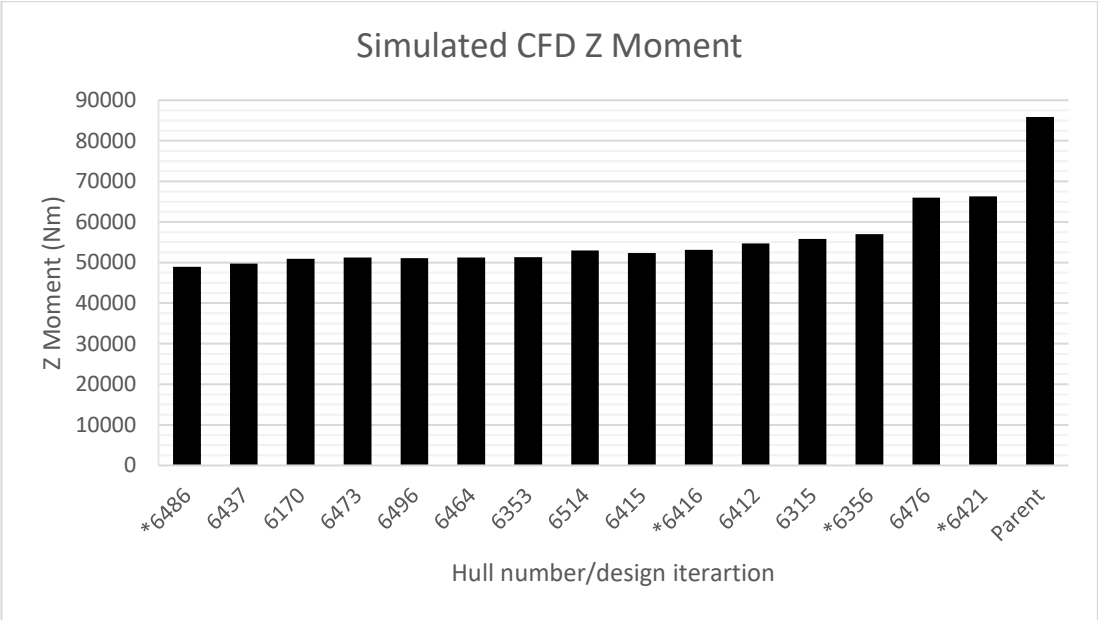

Figure 7-38 Bar chart presenting the simulated Z moment for each hull form from the multi-objective optimisation

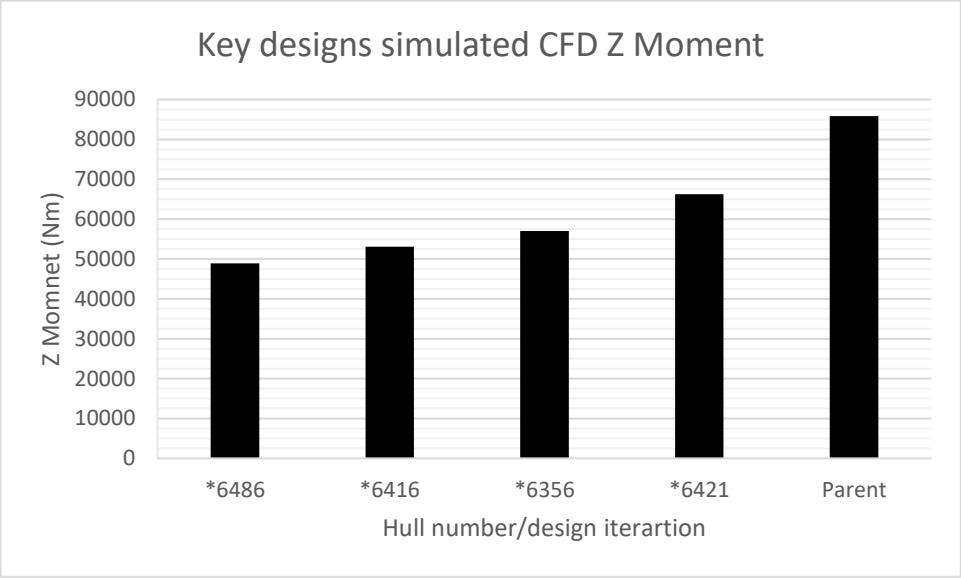

Figure 7-39 Bar chart showing the simulated Z moment for the four key designs compared with the NPL parent hull

As with evaluating the simulated Y force, the simulated Z moment is provided a good overview in Figure 7-38 with Figure 7-39 providing a more detailed view in comparison of the results for the four selected key designs. Based on these results 6486 achieved a 43% reduction in the Z moment compared to the NPL parent hull. As originally stated, the two hull forms which were considered best to represent the multi-objective optimisation were selected based on their positioning on the Pareto front. These positions trended towards the lower end of the ranking Y force, therefore for the ranking Z moment and in turn the simulated results,

these hull forms performed significantly more poorly and were found more closely to the NPL parent hull. These key designs have been visualised with a star in front of the hull number in Figure 7-38 and Figure 7-39, which in turn helps to visualise the positioning of these hull forms with respect to all others and the parent hull.

Although these hull forms did not achieve a greater reduction as hull 6486, there were still able to achieve between 38% and 22% in reductions for the Z moment. These percentages and corresponding reductions in moments can be seen in Table 7-5. From this table they can be seen that hull 6416 achieved a reduction of 38.12% or 32,730 Nm. Following this hull form, hull 6356 has a 33.6% improvement over the NPL parent hull the worst performing, hull 6421, achieving a reduction of 22.79%. As mentioned previously, the ranking Z moment had a much larger reduction in ranking Y force. This can be seen when comparing Figure 7-31 to Figure 7-29, as the Z moment results show a clearer downward gradient towards the optimum designs, Figure 7-31, whereas the ranking Y force as a much smaller gradient.

As with the results for the single objective optimisation, the greatest moment force did not occur at the peak amplitude of the PMM oscillation but rather 1.75 seconds before. This closely matches the behaviour seen in the single objective optimisation as both hull forms follow very similar geometric characteristics. This large phase angle is not observed for the other key hull forms, as they follow more closely with the NPL parent hull. These hull forms do observe a slight deviation from the normal gradient between 1.5 and 0.6 seconds prior to the PMM peak, however none of these deviations end up achieving the maximum observed Z moment.

Table 7-5 Key design results with respect to Z moment

Hull	*6486*	*6416*	*6356*	*6421*	*Parent*
Ranking Z Moment	1.04	1.28	1.55	2.16	3.50
CFD Z Moment (Nm)	48921.0	53125.3	57003.2	66288.4	85855.9
% improvement	43.02	38.12	33.61	22.79	-

For all the four hull forms not only was there improvement in Y force and Z moment but also improvement in the vessels motion dynamics. All four hull forms had a reduction in the maximum observed pitch angle, as well as a reduction in roll for hulls 6421, 6356 and 6416. For hull 6486 the maximum roll increased by 9.75%, whereas the other free hull forms an introduction in peak roll angle closer to 19%. Hull 6416 had the largest reduction in peak roll angle of 18.97%, with hull 6421 following closely with 18.45% and hull 6356 having 18.13%. The reduction in roll appears to be mainly due to the increased beam width at the transom, whereas the hull 6486 transoms beam reduces while also having less abrupt variations in curvature from midship to aft.

7.6. Twin screw CTV optimisation Case Study 2

Within this section the global optimisation algorithm within the Dakota suite is used for multiple evaluation runs on a completely novel hull form. This hull form is roughly based on key dimensions that represent a standard mono hull CTV. However, to add an extra dimension of complexity to test the evaluation methodology developed above, the hull form is required to maintain a twin-screw capability. Unlike other hull forms that may use twin screws, these propeller tunnels are designed directly into the hull form. This greatly complicates the fluid flow around the aft region of the hull form.

Three optimisations are conducted, the first focuses on the lateral Y force, the second the moment around the z-axis and finally a multi-objective combining the two. Each run compromises of thousands of design iterations with each run being highly constrained to maintain a specific set of requirements desired by the imaginary owner.

7.6.1. Hull design and limitations

The hull form is based loosely off a 25 m mono hull CTV vessel dimensions designed by Incat Crowther (Incat Crowther, 2020). The details of both vessels are given in Table 7-6. The parametric hulls displacement was predicted based on other similar vessels, as well as allowing for small volumes of cargo be transported.

Table 7-6 Comparison of parametric and real-world hull dimensions for twin screw CTV hull (Incat Crowther, 2020)

	Parametric Hull	*Incat Hull 18001*
LOA (m)	25	25
LWL (m)	25	21.7
Beam (m)	6	6
Draft (m)	1.59	1.2-1.7
Depth (m)	3.75	3
Disp (T)	151.693	N/A
Cb	0.52	N/A
Prop Config	Twin Screw	Twin Screw

Along with the twin propeller tunnels the hull form also has two other constrained features. These are a vertical wave piercing bow and a specific aft keel width, although not directly specific to any CTV operation of these characteristics are set to complicate the optimisation design space. It is the primary aim of this group of optimisations to evaluate the methodology on a more complex and less conventional hull form.

The baseline hull geometry for the initial start point for each optimisation is visualised in Figure 7-40. The distinctive colouring as a method commonly used to highlight geometric curvature known as an environmental map. This has been selected to allow quick comparison between the various hull forms that may only have subtle geometric differences, which in turn can be difficult to see in a standard geometric render. In addition to the environmental map representation, the lines plans and Gaussian curvature distribution are shown in Figure 7-41. These visual reputations on the hull forms used to highlight key features which have influenced the optimisations as well as the key characteristics influencing the overall vessel manoeuvring characteristics.

Figure 7-40 The baseline hull form visualised with an environmental map to highlight hull geometric curvature for greater ease of comparison

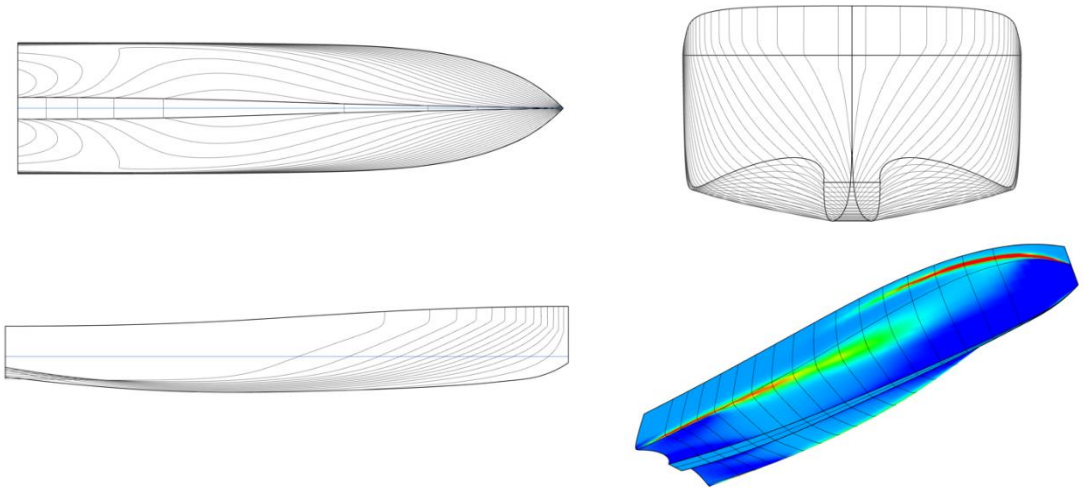

Figure 7-41 Twin screw baseline hull forms lines plans and Gaussian curvature distribution

As highlighted in the NPL optimisation focused on Y force, it is possible for the equation developed in chapter 6 to be subverted. By combining a constraint on the vessel's

displacement, as well as having one of the key geometric coefficients focused on the lateral area along the centre line, the optimisation algorithm can find an optimum design based on the equation which in fact does not perform at that level. This is due to the aft keel being brought closer to the water line, while the beam regions of the hull are lowered to compensate for the reduced displacement. Therefore, the parametric hull has a further geometric monitor that tracks the change in draft between the centre line keel and the beam keels. This ensures that this loophole is not used by the optimisation algorithm.

The final additional constraints applied to the optimisations is on the position of the longitudinal centre of buoyancy, and the displacement of the hull form. Like the NPL optimisation, the displacement of the hull form is constrained within predetermined percentage bounds. This is set to ±20% of the baselines.

Other key hull features include a constant beam width from aft to midship, this has been set to simulate the requirement for the maximum aft deck area to be maintained for cargo. Moving from the aft to the bow, to improve desired performance in rough sea conditions a vertical bow was chosen. In addition, the forward deck area cannot be significantly reduced to create a finer bow shape, this is to maximise the overall deck area for both cargo and the superstructure.

Due to the highly constrained nature of this geometry, additional design variables are included in the optimisation compared with the NPL hull. As mentioned in Chapter 5, there are two layers of design variables, the first directly influences the position of the geometric points controlling the NURBS curves, with the second controlling less influential values. The second layer includes the design variables to ensure the maximum variability.

7.6.2. Y-Force optimisation

This section presents the setup, results and discussion surrounding the optimisation of the twin screw CTV hull for reduction in lateral Y force. The baseline hull form has been created, as well as the corresponding constraints and design variable limits. Before running the optimisation using the global optimisation algorithm, a Sobol design space analysis is run to ensure no illogical designs are considered feasible, in addition to finding any potential loopholes that may be taken advantage of by the optimisation algorithm.

The Sobol analysis is based off 5000 design iterations with all constraints applied. Upon concluding this analysis no loopholes or illogical designs were found, thus the true optimisation can be run.

7.6.2.1. Set up

The optimisation utilises the global optimisation algorithm within the Dakota suite. The maximum number of designs is set to 12,500, with a total of 20 generations and an initial population size of 750. These parameters ensure a diverse range of designs that can be evaluated, particularly in the initial population. With an initial population that is relatively large, the algorithm is able to evaluate multiple potential routes for the optimisation, as well as highlight certain key design variables which may have a greater weighting towards the optimum design or braking constraints.

For each design iteration in the image for the 3D geometry, sectional area coefficients and sectional lines plan is created and saved into the corresponding design iteration folder. In addition, each geometry is exported as an IGES file that is used later for CFD evaluations.

7.6.2.2. Y Force optimisation results and discussion

Although the optimisation was able to have a total of 12,500 design iterations, the optimisation algorithm completed after 6304 design iterations. In comparison to the NPL optimisation there are significantly fewer designs which broke constraints. Out of the 6304 designs only 155 exceeded the constraints. This is primarily due to the carefully controlled design variable input limits. This ensured a greater efficiency for the optimisation algorithm, as fewer failed designs would have to be evaluated and in turn their effects on the manoeuvring equation accounted for by the algorithm.

A graph showing the calculated ranking Y force for a hull number/design iteration can be seen in Figure 7-42. This graph also highlights the designs within constraints and the failed designs. A more detailed view of the final 1300 design iterations is shown in Figure 7-43. The optimum design in Figure 7-42 and Figure 7-43 is visualised as the golden marker.

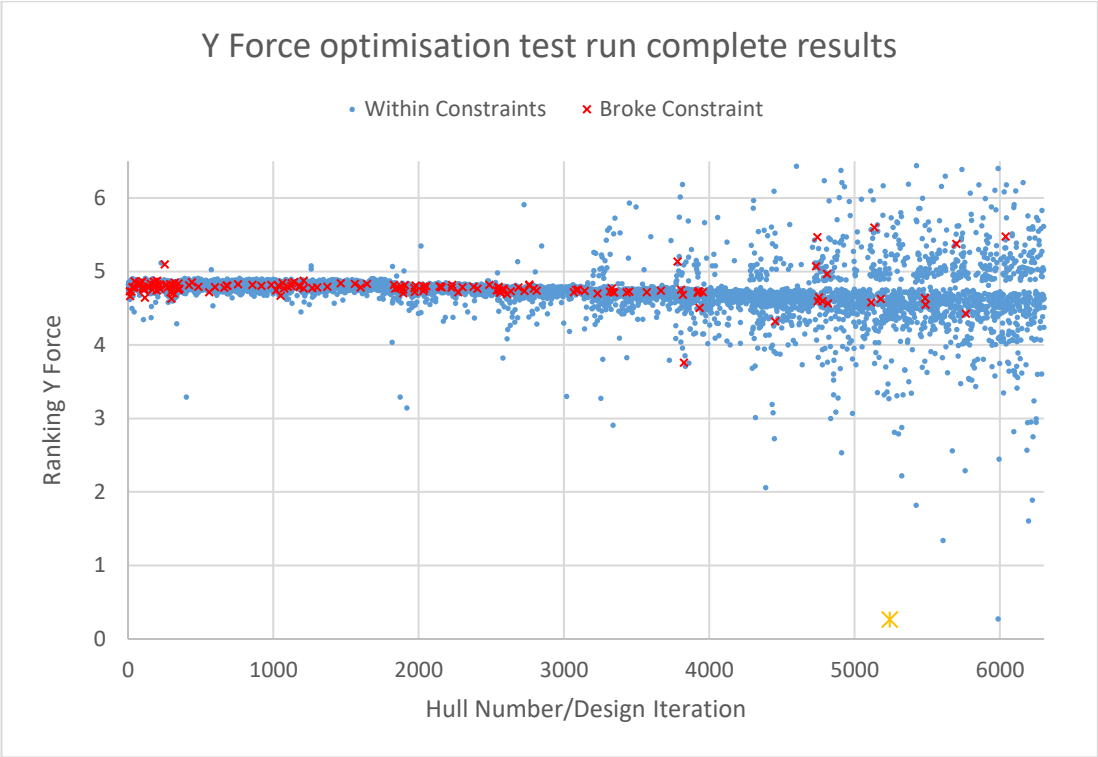

Figure 7-42 Graph comparing the calculated ranking Y force with the hull number/design iteration for the twin screw CTV optimisation (complete results)

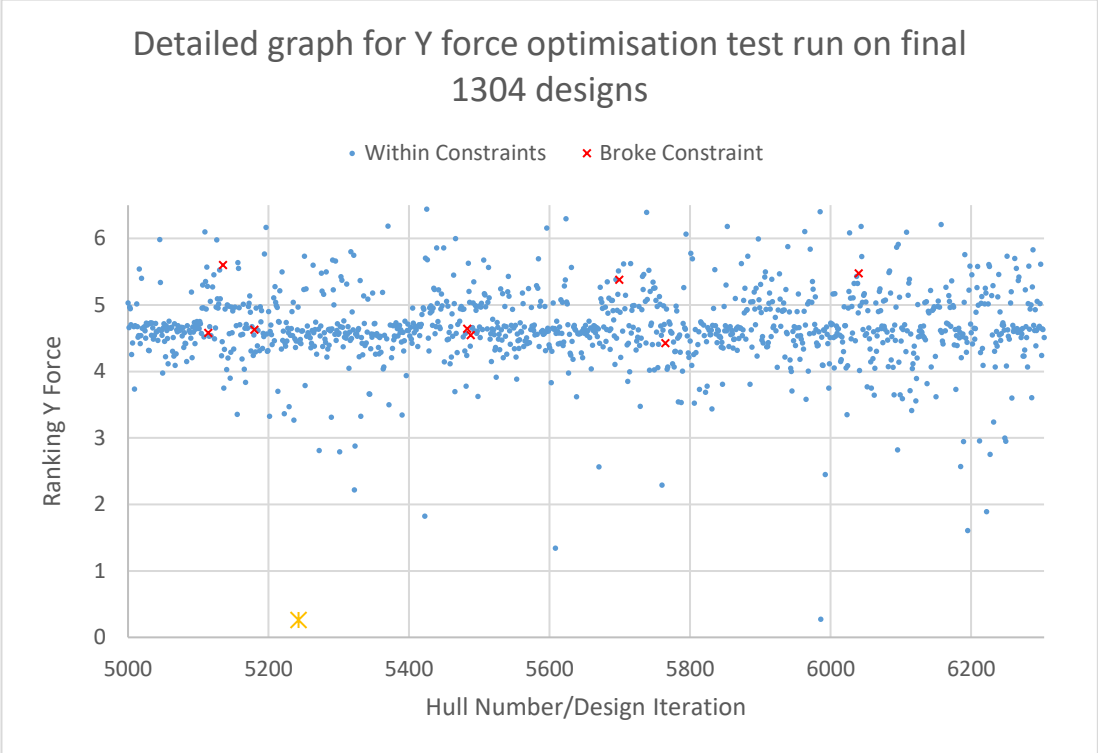

Figure 7-43 Graph comparing the calculated ranking Y force with the hull number/design iteration for the twin screw CTV optimisation (Detailed view of final 1304 design iterations)

It can be seen from Figure 7-42 that as the algorithm continues through the optimisation process fewer and fewer designs which break the constraints are evaluated in the later generations. This pattern is shown in greater clarity in Figure 7-44. This bar chart shows a natural trend in a reduction of density in invalid designs for later generations of the optimisation process. It can also be observed that the density of valid designs is significantly lower than that seen for the NPL optimisation runs. This is primarily due to the greater flexibility in vessel displacement, as this was the primary constraints broken for the NPL optimisation.

In addition to seeing a reduction in invalid design density, it is also seen that a greater range of calculated Y force is being observed in the later generations. This ties directly back to the theoretical basis of the global optimisation algorithm discussed in chapter 7.3.7. As stated in this chapter, as the optimisation moves into later generations the algorithm attempts to push the limits of the expected improvement acquisition function. It is because of this acquisition function that the current optimum design was found. Without this additional function the designs which remained within the high-density regions (between around 4 and 5.5 for the ranking Y force) would have been the region where the optimum design would have been drawn from. However, as the optimisation progressed the expected improvement acquisition function also increased, until the extreme limits had been tested. Resulting in optimum design.

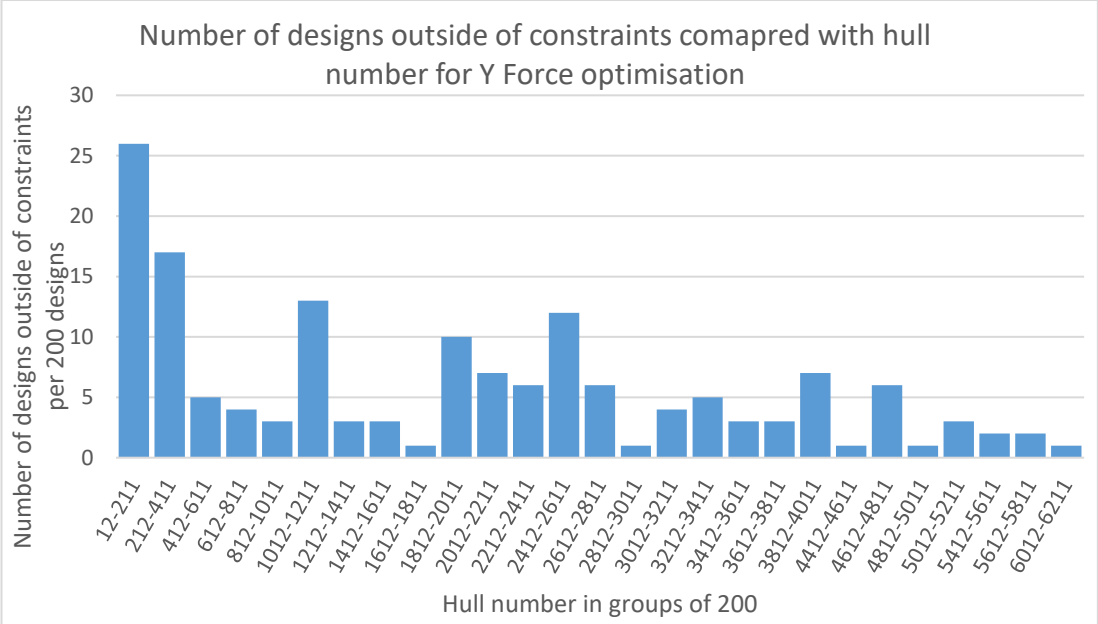

Figure 7-44 Bar chart comparing the density of invalid designs per 200 design iterations for Y force optimisation

As can be seen from Figure 7-42 and Figure 7-43, the optimum design was found at design iteration 5243, hereafter referred to as hull 5243. The hull form can be seen in Figure 7-45,

with the various lines plans shown in Figure 7-46. Table 7-7 shows a comparison between some of the key geometric features for the base hull and hull 5243. It can be seen from Table 7-7 that hull 5243 had a calculated ranking Y force of 0.261 compared with the base hulls 4.751.

From this table they can be seen that the optimum hull has had a reduction in displacement by 2.55%, which in turn led to a reduction in the block coefficient. Although the LCB is constrained for this optimisation study, the optimum hulls LCB move forward 1.46% when compared to the base hull LOA. This forward movement in the LCB equated to positioning the centre of buoyancy closer to the midship position. This is a key characteristic with vessels which have relatively low lateral force when manoeuvring. This is due to the hull's displacement being equally distributed fore and aft of this point.

Table 7-7 Key hull feature comparison table between base hull and hull 5243

	Base Hull	*Hull 5243*
LOA (m)	25	25
LWL (m)	25	25
Beam (m)	6	6
Draft (m)	1.59	1.59
Depth (m)	3.75	3.75
Disp (t)	151.693	147.912
Cb	0.52	0.507
LCB (m frm aft)	9.529324	9.89499
Ranking Y Force	4.750769	0.261029
Ranking Z Moment	14.9524	12.992

In addition to the forward movement of centre of buoyancy, there is also a reduction in the difference between the central buoyancy and centre of lateral area along the midship. The base hull had an initial ΔX (delta longitudinal centre of buoyancy and the centre of lateral area) of 1.51288 m, whereas hull 5243 reduced this down to 1.3016 m. Although only a slight reduction of 0.2113 m, this also highlights that along with the LCB moving towards the midship there has been an equalising of both the lateral area and volumetric displacement fore and aft.

Along with these key numerical changes in the geometric characteristics, there have been some significant changes to the overall geometric features that can be observed visually. When comparing Figure 7-40 and Figure 7-45, there are a few key features that can be seen to have changed. Moving from the aft to the forward of the hull these are as follows.

Firstly, the aft bilge keels have become less pronounced while still maintaining the desired twin tunnel configuration. This reduction in the extreme curvature change meant that the aft

sectional area coefficient increased slightly from 1.66 to 1.758. This may at first seem likely to increase the Y force, however, due to the twin tunnel feature of the aft, a closer value to the maximum of two is in this case be positive. It can also be seen that the overall depth the propeller tunnels has been reduced, again helping to reduce turbulent flow in this region.

Secondly, the midship of the vessel has also become more rectangular compared with the baseline hull. This would also initially be assumed to hinder the reduction in the Y force, however this increase may relate more to the volumetric displacement distribution. By increasing the block coefficient in the midship centre of buoyancy is also move towards a midship which is the most preferable position with respect to the Y force.

Thirdly and finally the greatest geometric change can be observed in the forward bow geometry. When comparing Figure 7-40 and Figure 7-45, it can be seen there has been a significant increase in both volumetric displacement and convex curvature in the forward region, Figure 7-46 helps to clearly view the increased convex curvature at the bow. When comparing Figure 7-41 and Figure 7-46, it can be observed that the whole forward section of the hull form has moved from a more traditional concave bow shape to a convex bow shape. This is particularly noticeable when comparing the water lines of the two hull forms, whereas the buttock lines do not help to highlight this change. The sectional lines clearly show that the forward bow region of hull 5243 has changed from a more extreme wave piercing convex shape, as well as a knife edge at the keel, to a rounded convex shape at the keel, as well as increasing bow width. This transition from concave to convex can also be clearly seen when comparing the Gaussian curvature distribution of the hulls in Figure 7-41 and Figure 7-46, with hull 5243 having a much smoother transition from the midship to the bow, with only the convex curvature at the keel being noticeably extreme.

It is also through Figure 7-41 and Figure 7-46 sectional lines plans that the change in the propeller tunnel can be visualised even more clearly. The propeller tunnels of hull 5243 become significantly rounder as well as being more geometrically symmetrical around the assumed propeller axis. It is also noted that the aft keel of hull 5243 has become lower than that of the baseline.

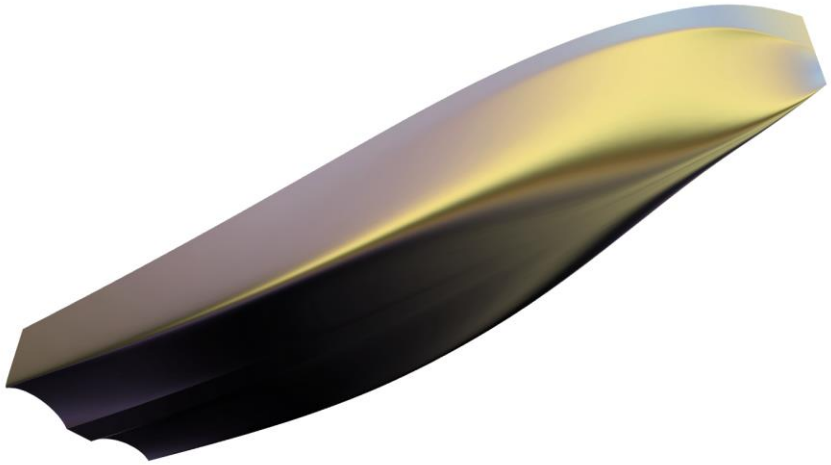

Figure 7-45 Visualised geometric hull form for optimum Y force of twin screw optimisation (hull 5243)

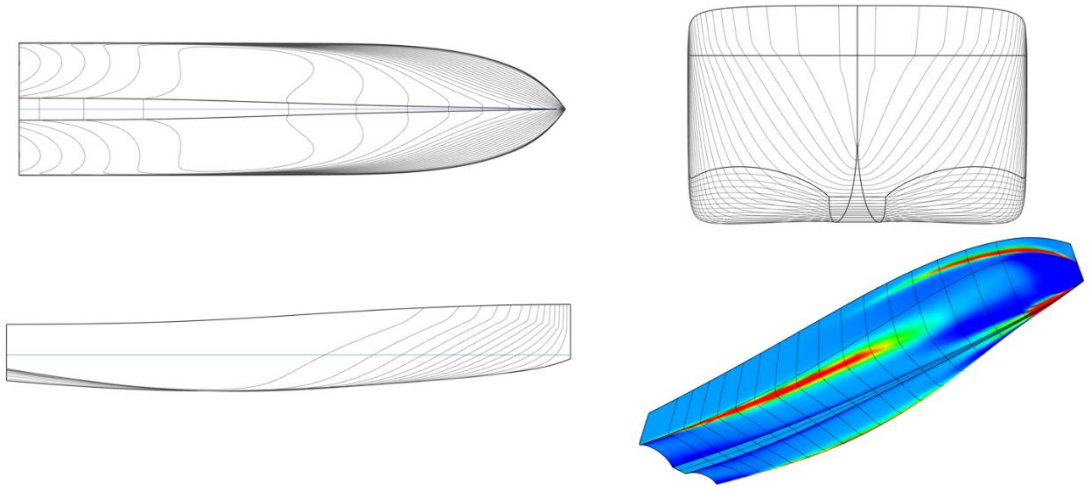

Figure 7-46 Lines plans for the optimum hull form and Gaussian curvature distribution for minimised Y force for twin screw hull

As discussed in chapter 6, the manoeuvring equations do not provide a scale on which the optimised parameter have been reduced by. It has also been presented in chapter 6 that there is a high level of confidence with the accuracy of these equations and therefore would require no further analysis, however for this study these hulls are evaluated at each stage within CFD to validate the optimisation, in addition to providing a quantitative value of the optimisation.

7.6.2.3. CFD Results Y force optimisation

Within this section both the baseline hull and hull 5243 are evaluated in CFD to determine the forces acting on the hull. This primarily focuses on the evaluation of the Y force, however the moment acting around the vertical axis is also assessed. This extra step in the hull evaluation highlights the importance of two independent manoeuvring equations.

Using the methodologies developed in chapters 4 and 5, the saved hull geometry for both the baseline and hull 5243 are imported into the NPL PMM CFD base setup. This base setup is purely used to speed up defining the physics and overset mesh settings. All other features are required to be reimported as the overall length of the vessel has changed compared to the 20 m NPL. In addition to the length and overall size of the hull, the speed at which the PMM manoeuvres are run at is also been increased. This increase is to account for the increase in the operational speed profile of the vessel. The NPL hull was evaluated at a Froude number of 0.36, with this hull series being evaluated at a Froude number of 0.48, which corresponds to around 15 kn.

As both the ship length and carriage velocity has increased, all the refinement regions and the outer domain had to be reimported to match the base simulations geometric factors. All these imports were parametrically created instantly when the vessel length and PMM velocity was modified in the parametric model file. The mesh for the CFD simulations can be seen in Figure 7-47 & Figure 7-48. The mesh count using recalculated base sizes for the speed change came to 1.75 million cells. The boundary layer used the high Y plus methodology discussed in chapter 4 from Peric (2020).

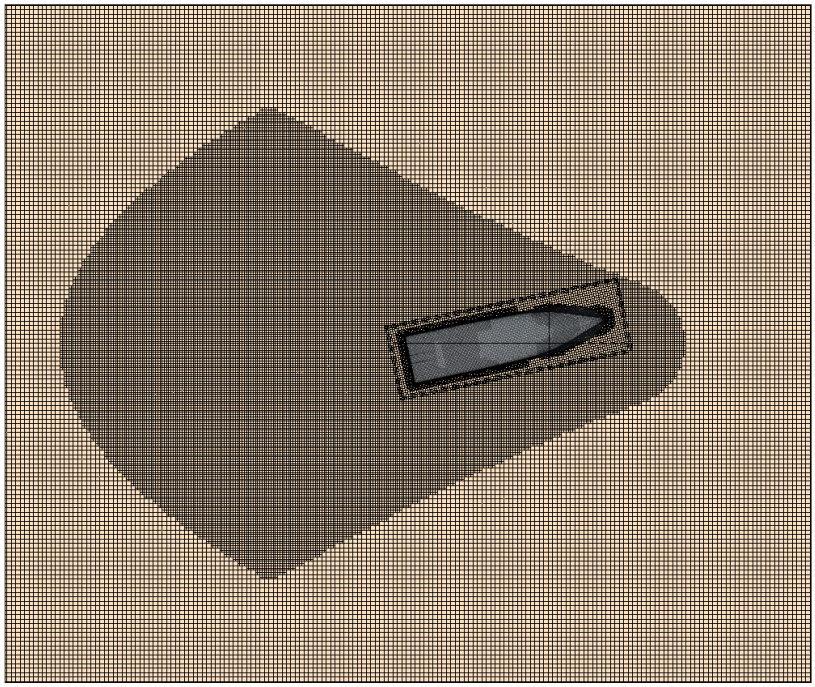

Figure 7-47 Top view of twin screw CTV mesh for Y force optimisation analysis

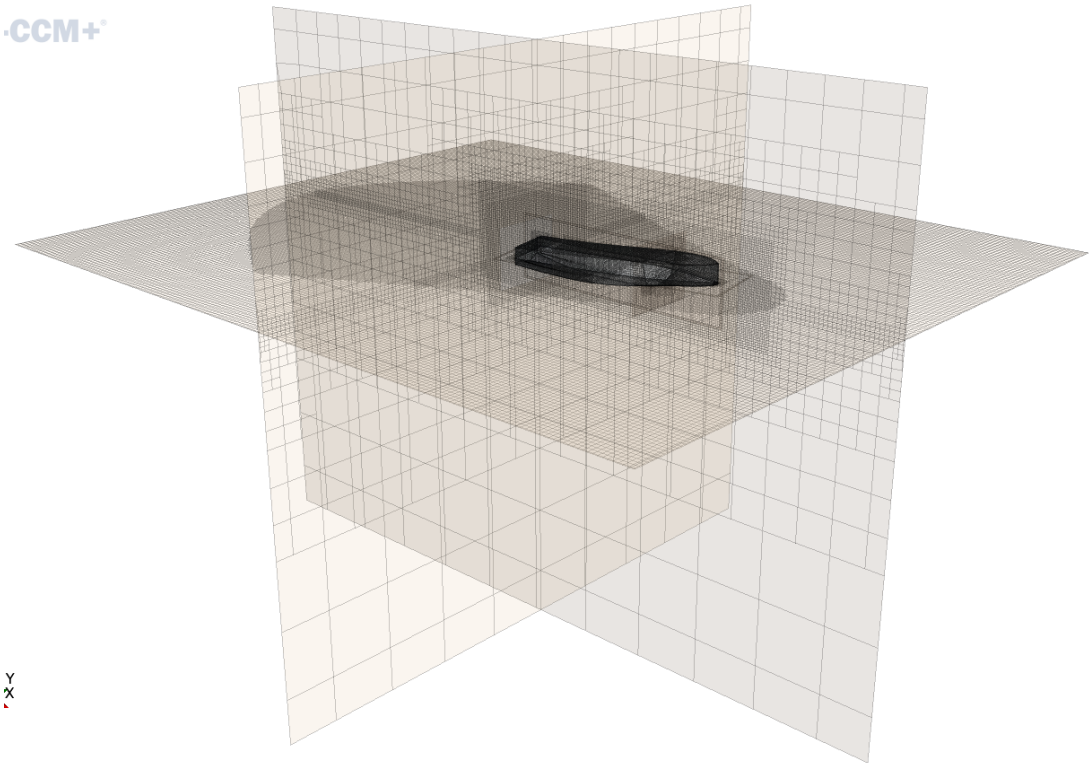

Figure 7-48 Perspective view of twin screw CTV mesh for Y force optimisation analysis

To ensure as accurate results as possible extra editing was done by the user to ensure key features, such as the sharp edges and extreme curvature in the propeller tunnels, was maintained. This was completed by manually highlighting key edges that would be considered when the meshing algorithm was running. In addition, an extra region of volumetric refinement was placed in the aft region to improve cell resolution. The surface mesh for hull 5243 can be seen in Figure 7-49.

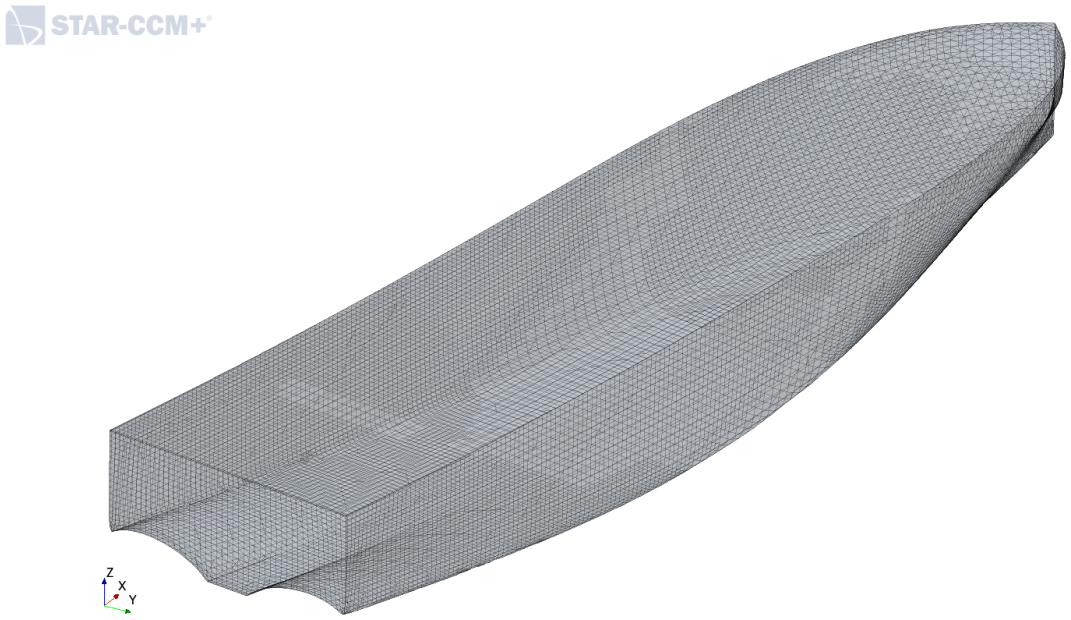

Figure 7-49 Hull 5243 surface mesh within Star CCM+

For hull 5243 simulation was run for a total of 97.5 simulated seconds, equating to 4.875 PMM oscillations. The results were taken from the final oscillation which showed only a 3% difference from the previous oscillation.

The simulated Y force can be seen in comparison to the baseline simulated Y force through CFD in Figure 7-50. The baseline hull form had a simulated lateral Y force of 26,000 N, whereas hull 5243 had a lateral Y force of 20,010 N. This reduction of 5990 N equates to 23.03% reduction in lateral Y force acting on the centre of gravity. As noted previously, reductions in Y force directly reduces the turning radius of the vessel while allowing the vessel to maintain a higher speed.

In addition to a reduction of Y force, hull 5243 had a 7.23% reduction in maximum roll angle at the peak point of rotation. The base hull had a maximum roll angle of 2.275 degrees with hull 5243 seeing a peak of 2.11 degrees from the DFBI monitored CFD results. This is primarily due to the increased squareness of the bilge keels, as well as a more evenly distributed displacement around the central buoyancy.

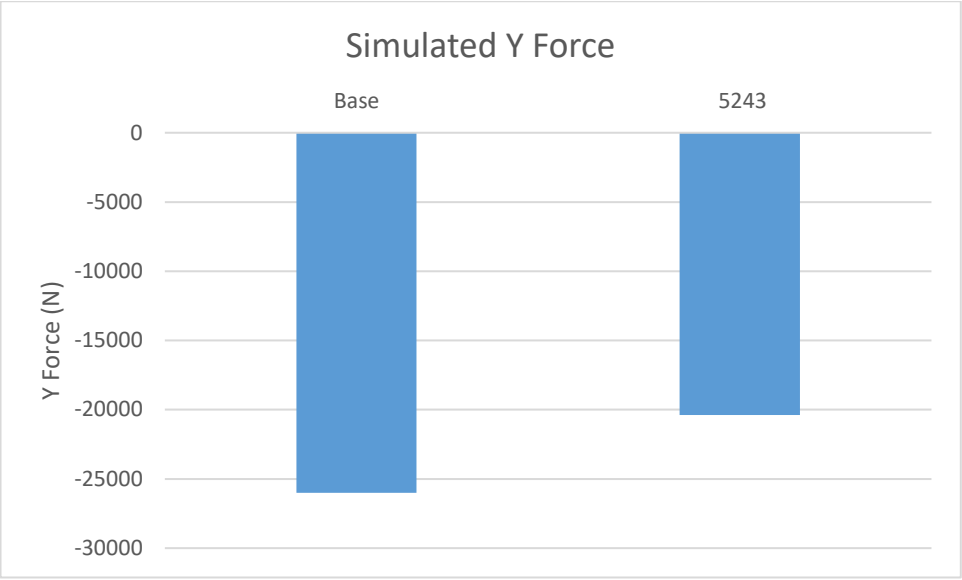

Figure 7-50 Bar chart comparing the optimised hull for Y force (hull 5243) with baseline hull in CFD

In addition to the pure lateral Y force, further comparisons between the baseline and hull 5243 were conducted. By comparing Figure 7-51 and Figure 7-52, hull 5243 reduced the peak height of the aft wake along with the wave breaking directly behind the hull. There is however a slight increase in the height of the bow wave/spray compared to the baseline. This increase is likely due to the increased displacement and rounding at the bow keel region. All visual comparisons were taken on a constant iteration point all simulations.

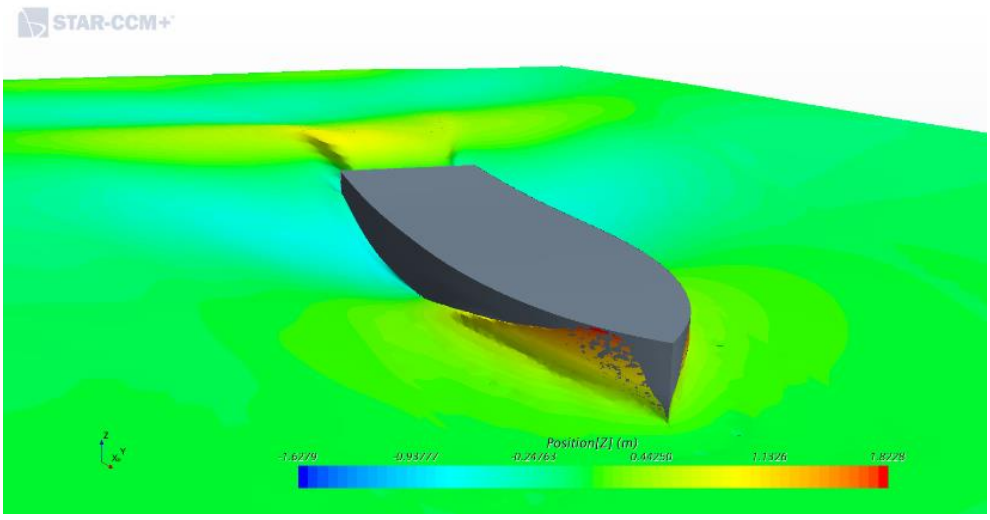

Figure 7-51 Free surface visualisation for design base hull (Fn 0.479)

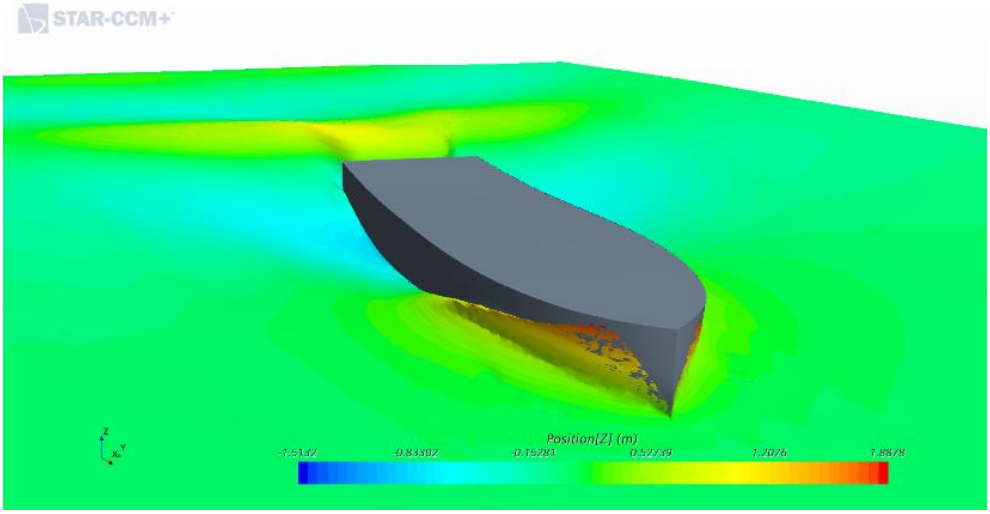

Figure 7-52 free surface visualisation for design 5243 (Fn 0.479)

Along with a visual comparison of the free surface, streamlines visualising the flow velocity and direction have also been compared. The most notable difference between the baseline hull's streamlines, depicted in Figure 7-53, and the hull 5243's streamlines, shown in Figure 7-54, is the change in flow velocity and direction in the aft region. Viewing Figure 7-53, it is noted that the flow moves away from keel line from the bow to the midship but then changes direction to move towards the keel line in the aft. This flow also significantly slows to achieve this change in direction, all of which contribute to an increased lateral Y force. Unlike the baseline streamlines, the streamlines for hull 5243 seen in Figure 7-54 have a significantly smoother flow as well as having a lesser change in velocity the aft. It is due to this smoother flow that the hull can move more smoothly and efficiently when in a dynamic manoeuvre.

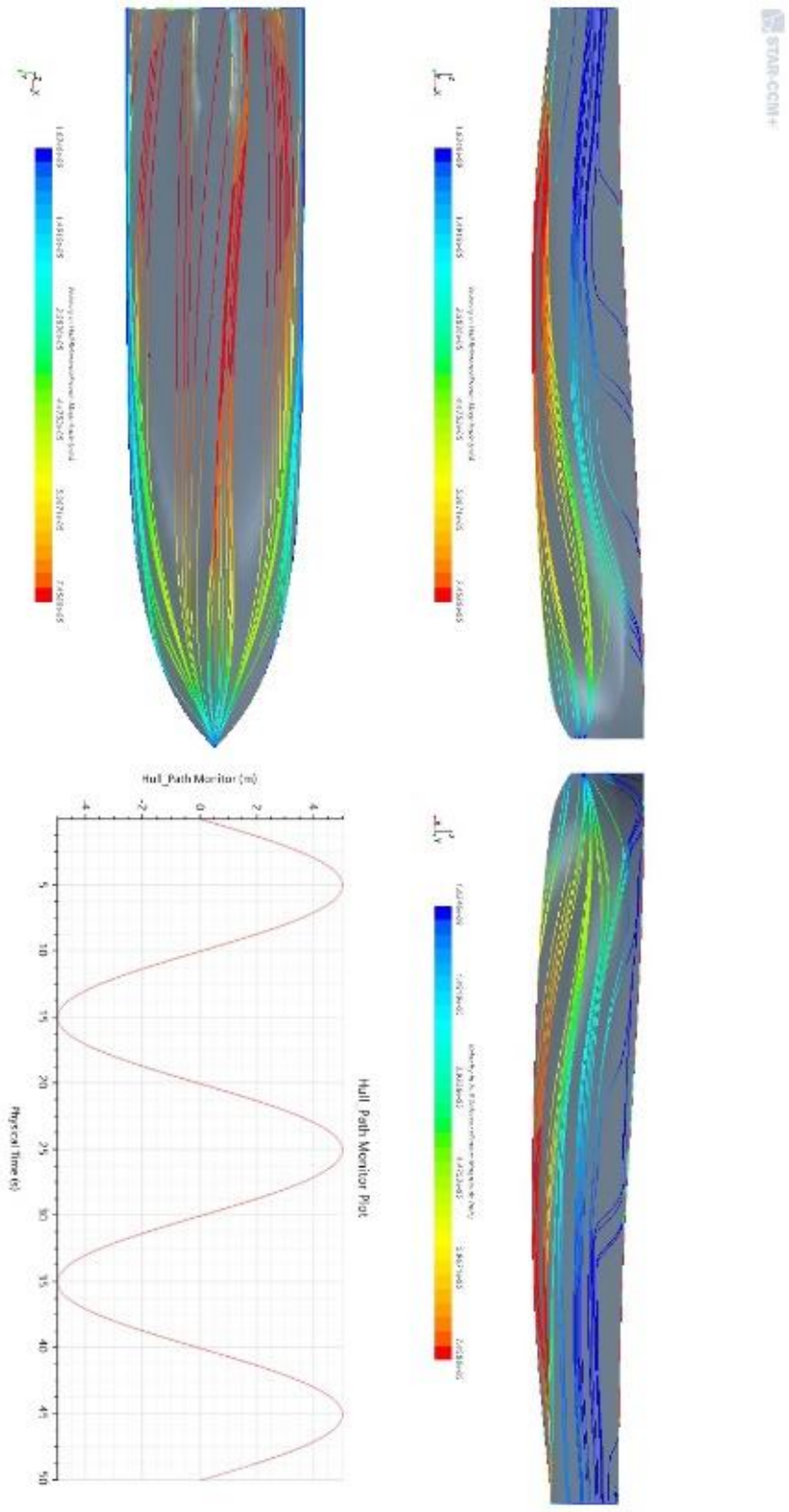

Figure 7-53 Visualised streamlines along hull for base hull

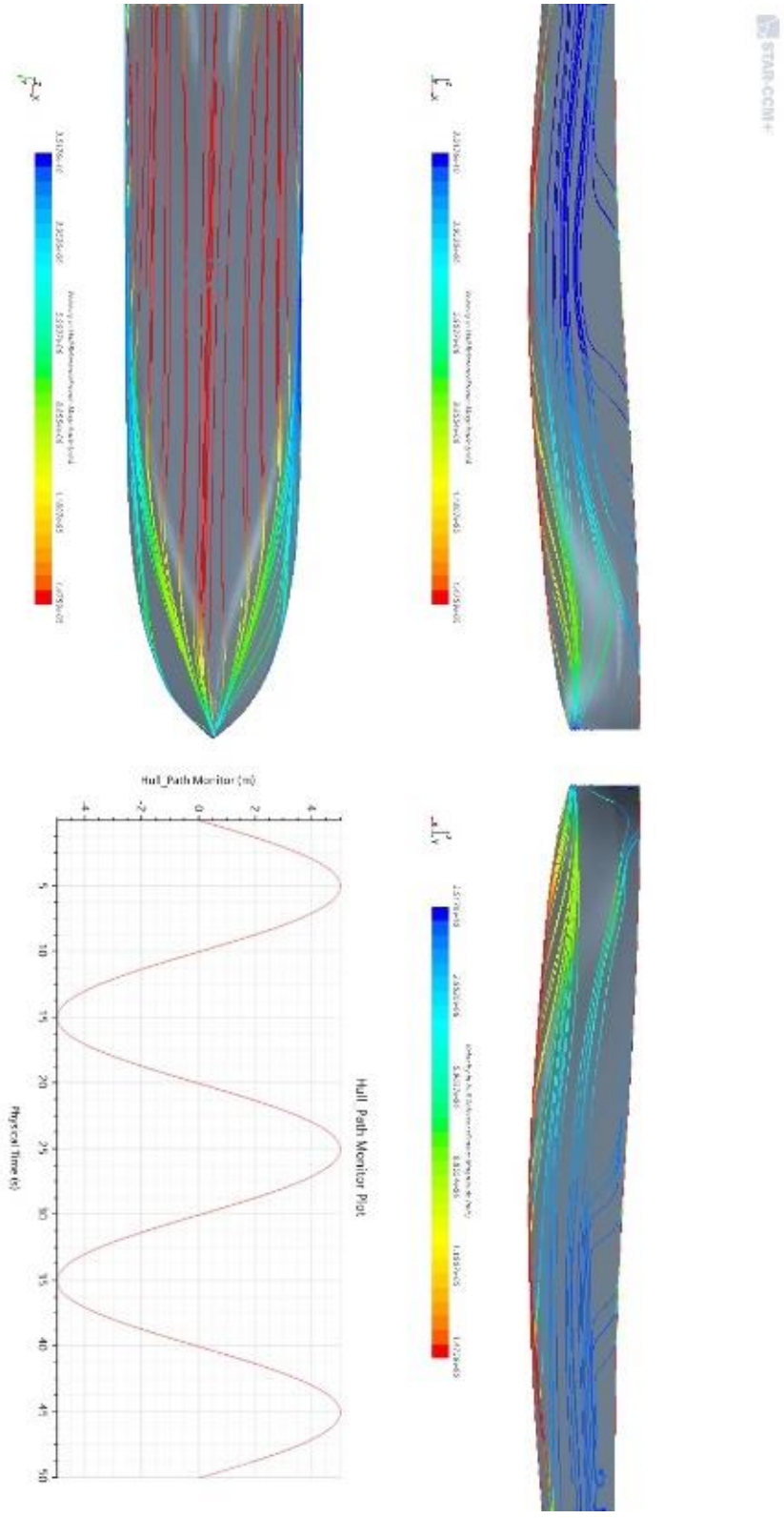

Figure 7-54 Visualised streamlines along hull for 5243

7.6.3. Z-Moment optimisation

The optimisation for the Z moment is presented below. To speed the process up for each optimisation both the Y force and Z moment can be inputted within the optimisation interface with only one being selected to be evaluated. This ensures that all the design variables remain within the exact same limits for each optimisation, as well as ensuring the constraints are consistent.

The optimisation follows the same procedure as laid out in chapter 7.6.2.1, with the maximum population size of 12,500 initial population of 750 and 20 generations.

7.6.3.1. Z moment optimisation results and discussion

For the moment optimisation a total of 7869 designs were evaluated, with 200 breaking constraints. Using the global optimisation algorithm, design 7828 was found to be the optimum hull form with respect to the moment acting around the z-axis at the centre of gravity.

The key hull characteristic data is given in Table 7-8, along with the calculated ranked Y force and Z moment. The ranked Z moment was reduced from 14.952 for the base hull to 6.248 hull 7828.

This optimum came later in the design iterations compared with the Y force optimisation. The optimum design for the Y force was found that around 83% of the way through the total number of iterations, whereas hull 7828 was found to be the optimum at around 98.2%. This is possibly due to the more traditional optimisation shape when observing complete results in the overall design trend of the algorithm. This trend along with the overall distribution of results compared with the design iteration can be seen in Figure 7-55.

In comparison to the Y force optimisation, Z moment optimisation has the greatest range of results at the start rather than the final designs as in the Y force optimisation. It can be clearly seen in the global optimisation algorithm initially tests the overall design space to find the key variables which help to reduce the optimisation aim. Although not clear it is possible to see that it takes around 3 to 4 generations before all design iterations fall below the baselines result. This appears to happen at around design iteration 1800, with each generation being delineated due to the abrupt reduction in ranking Z moment, Figure 7-55. As the optimisation continues each generation becomes more difficult to be visualised from the previous, however as a new generation started there is a sudden spike in invalid designs due to the algorithm testing the limits of the design variables and constraints. This is supported when comparing both the detailed graph on the final 1000 design iterations including the optimum design, Figure 7-56,

and the bar chart in Figure 7-57 showing the invalid design density throughout the optimisation.

Observations drawn from Figure 7-56 show that there are no invalid designs in the final stage's optimisation, in addition to a significant density of designs around the optimum design point. Only in the final 1000 designs does the algorithm achieve a ranked Z moment below 6.5. Moreover, even when the algorithm attempts to test the extreme limits to find a potential optimum, these designs still fall significantly below baseline. 90% of these final designs fall between 7.5 and 6.25.

From Figure 7-57 over 75% of the invalid designs had occurred before the halfway point of the optimisation, and over 22 ½% of these were found in the first generation. Unlike the Y force optimisation, the expected improvement acquisition function appeared to have a lesser impact on the overall optimisation. This pattern is evaluated when multi-objective optimisation for both Y force and Z moment is conducted.

The optimum design, hull 7828, as shown as the golden marker in Figure 7-55 and Figure 7-56.

Table 7-8 Key hull feature comparison table between base hull and hull 7828

	Base Hull	*Hull 7828*
LOA (m)	25	25
LWL (m)	25	25
Beam (m)	6	6
Draft (m)	1.59	1.59
Depth (m)	3.75	3.75
Disp (t)	151.693	123.83
Cb	0.52	0.424
LCB (m frm aft)	9.529324	10.13913
Ranking Y Force	4.750769	4.625708
Ranking Z Moment	14.9524	6.248314

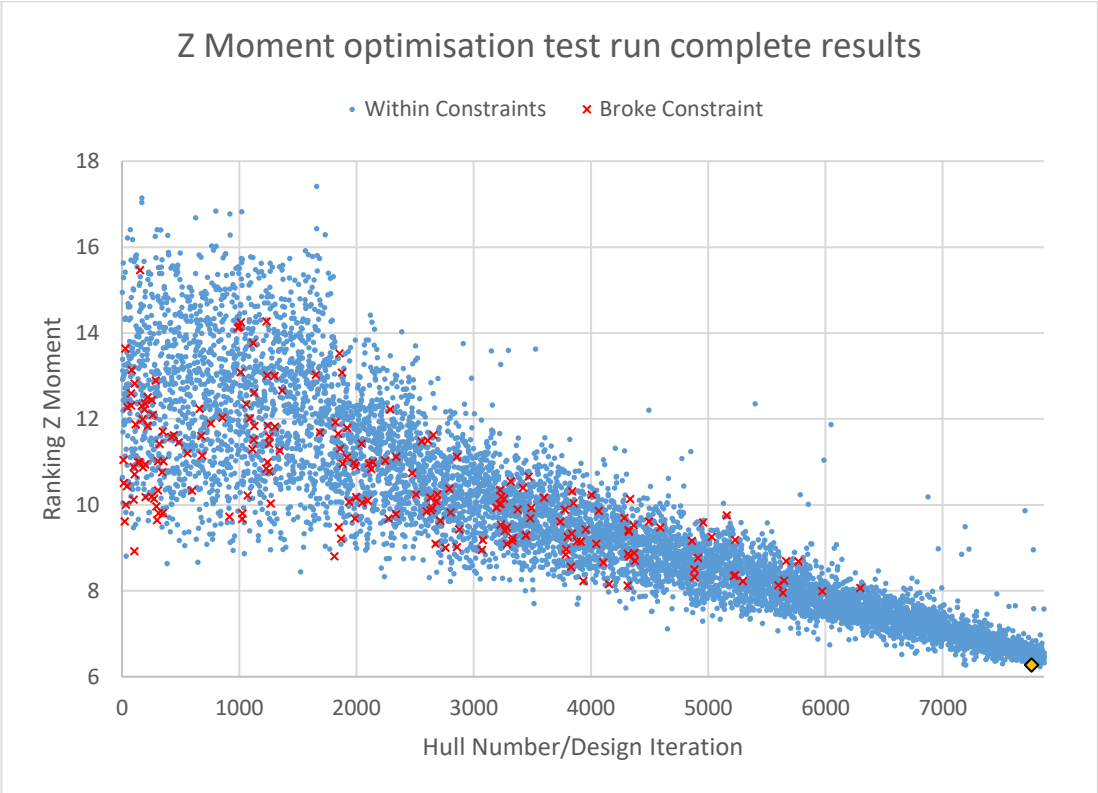

Figure 7-55 Graph comparing the calculated ranking Z moment with the hull number/design iteration for the twin screw CTV optimisation (complete results)

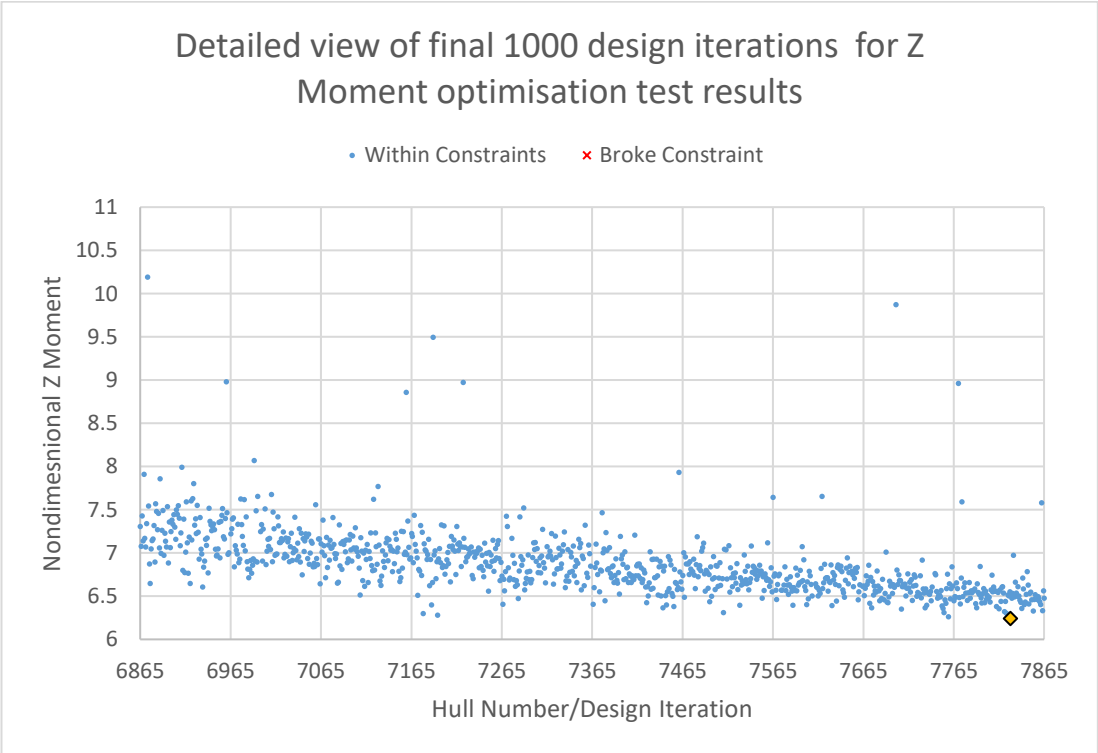

Figure 7-56 Graph comparing the calculated ranking Z moment with the hull number/design iteration for the twin screw CTV optimisation (Detailed view of final 1000 design iterations)

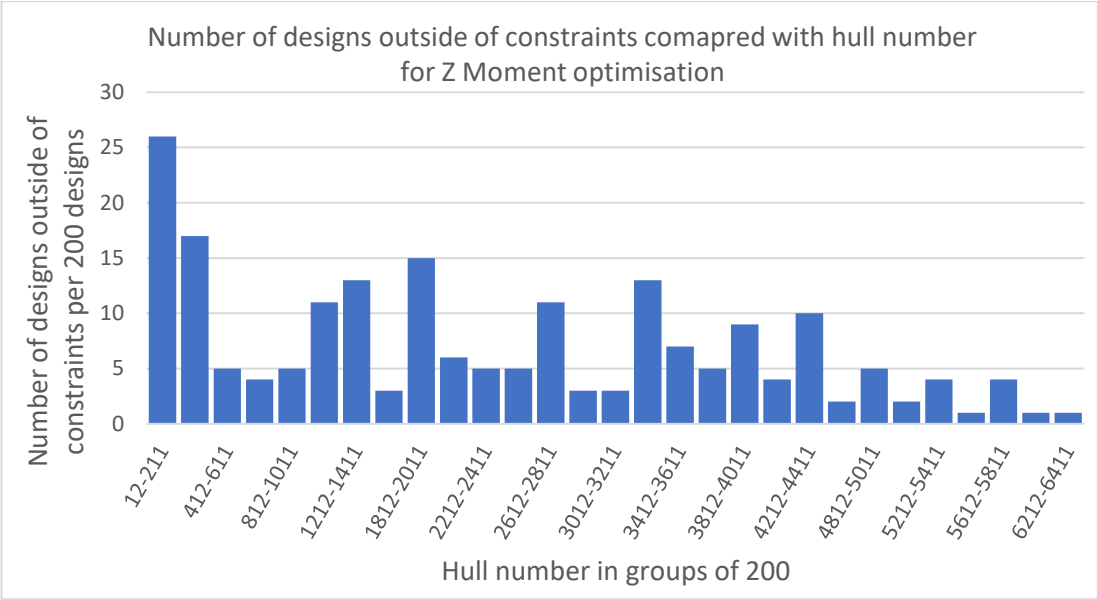

Figure 7-57 Bar chart comparing the density of invalid designs per 200 design iterations for Z moment optimisation

This optimum has been achieved for the change of some of the key characteristics of the hull form. One of the first and most notable differences between hull 7828 and the base hull is the significant reduction in displacement. This has been reduced from 151t to 124t, which is a reduction of 27 tons and the maximum allowable under the given constraints. This voluntary displacement is primarily focused at the fore and aft regions of the hull, with the most significant being the aft propeller tunnels. As described above key design feature for this hull as there should be two propeller tunnels to allow for twin screws, this feature did not specify whether these tunnels should extend above the waterline. In the case of Hull 7828 these propeller tunnels extend above the waterline. This is only a very small region which extends above the waterline and the very point of the propeller tunnels, however due to the increased height as well as the increased tunnel width a significant reduction in displacement happens here.

This increased propeller tunnel width and height may appear counterintuitive at first glance with the aim is to minimise forces which combine to account for the moment, however these changes need to be considered with respect to the entire hull. Unlike the Y force, the moment acting around the z-axis is equally affected by the balancing of forces between the fore and aft of the hull. As can be seen from Table 7-8, the longitudinal centre of buoyancy and in turn the position of the centre of gravity has moved forward 2.44% of the vessels LOA. This forward movement of the LCB allows for simpler force balancing between the fore and aft regions as the pivot point moves closer to the midship.

Like hull 5243, the midship has become the dominant volumetric region with respect to displacement, as well as becoming significantly more block like. This can be seen when comparing Figure 7-40 and Figure 7-58, as a drastically sharper bilge keel can be seen the hull 7828. This ensures that a large proportion of the displaced volume is located around the centre of gravity and buoyancy. This very blocky region can also be seen to be further aft than the baselines, seen in Figure 7-40, to be closer to the pivot point.

In addition to the increase in the block coefficient amidship, the keel has also become more prominent along the full length of the vessel. This is primarily due to the algorithm attempting to balance the two regional forces fore and aft. The increase in keel prominence can be clearly seen in Figure 7-58, also in Figure 7-59s Gaussian curvature visualisation. The midship is very similar shape to that of hull 5243 which allows for even and smooth flow across the hull at varying angles.

The bow, unlike hull 5243, is significantly more concave and like that of the baseline. This is seen most clearly when comparing the sectional lines plans for Figure 7-41 (baseline), Figure 7-46 (hull 5243) and Figure 7-59 (hull 7828) respectively. This is a clear symmetry with the aft region of the optimum Z hull. The symmetry is also clearly seen when evaluating the buttock lines in Figure 7-59. There is a smooth continuous curve going from aft to the bow, with the lowest point located closely to the longitudinal centre of buoyancy. All of these factors varying the geometry around the LCB allow for a clear pivot point for the hydrodynamic forces to act around.

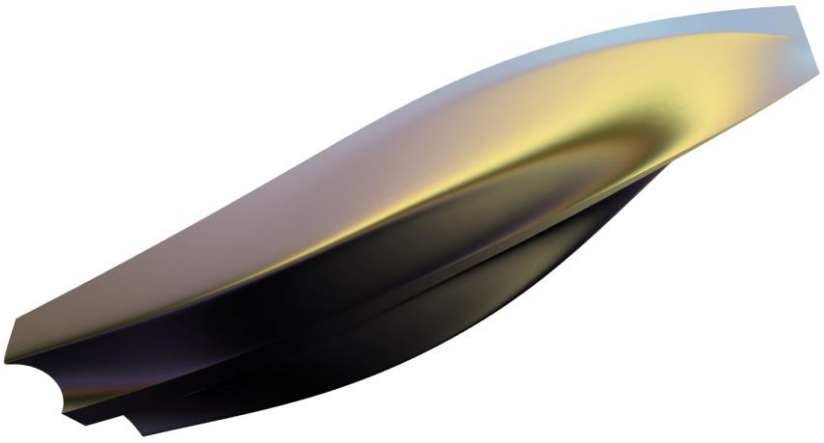

Figure 7-58 Visualised geometric hull form for optimum Z moment of twin screw optimisation (hull 7828)

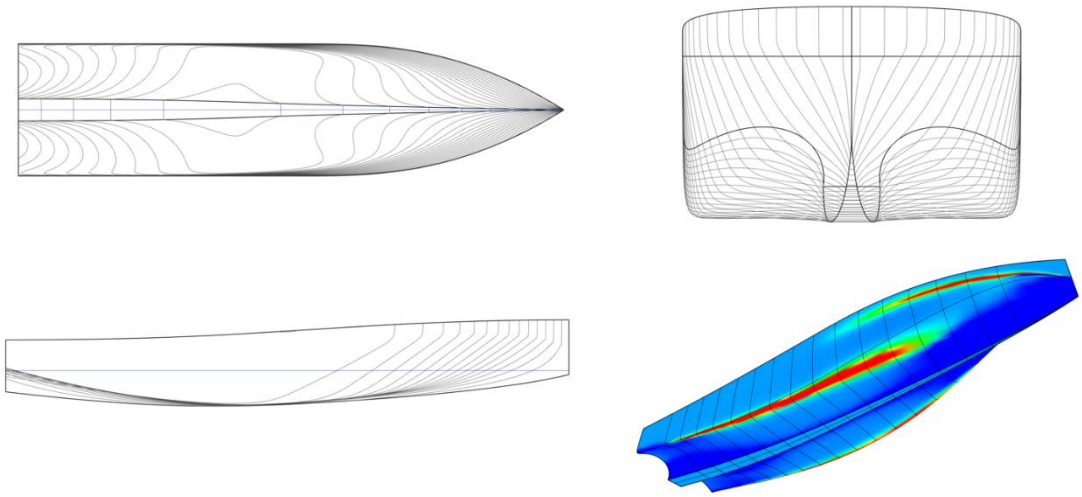

Figure 7-59 Lines plans for the optimum hull form and Gaussian curvature distribution for minimised Z moment for twin screw hull (7828)

Unlike the lateral Y force, the moment acting around the vertical axis allows for significantly greater turn rates, as well as smaller turn radii. This would appear to be better for the manoeuvring of the vessel and purely the Y force, however these two combined can cause manoeuvring instability and therefore may make the vessel less predictable while manoeuvring. It is therefore vital that when optimising the Z moment with given equations an evaluation in CFD must also be conducted to ensure the vessel performs in a stable condition.

7.6.3.2. CFD Results for Z Moment optimisation

This section presents the results for the CFD comparison between hull 7828 and the baseline. The CFD simulations follows the same setup methodology as discussed and presented in chapter 7.6.2.3. As mentioned in Chapter 7.6.2.3, the base NPL CFD simulation has been modified using the fully parametric regions and simulation domains to account for increased ship length and speed.

The volumetric mesh for hull 7828 can be seen in Figure 7-60 and Figure 7-61, which shows a mesh with 1.77 million cells. The same procedures for adding additional detail as well as maintaining key features was also applied to hull 7828, the surface mesh for the hull geometry is presented in Figure 7-62. This visualisation also further highlights the additional height and curvature in the aft propeller tunnels, in addition to a significantly sharper bow shape both along the waterline and the deck.

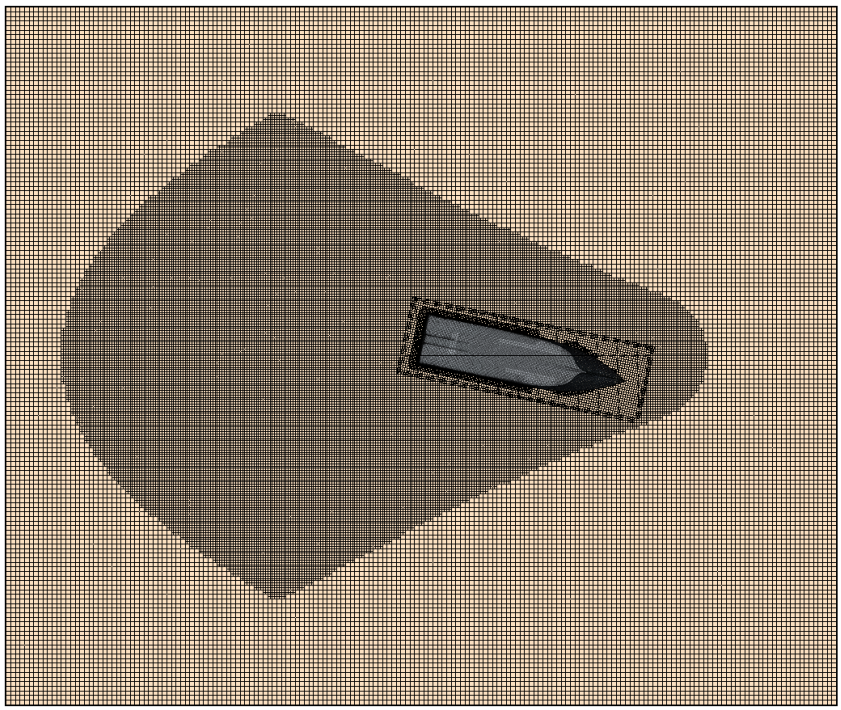

Figure 7-60 Top view of twin screw CTV mesh for Z moment optimisation analysis

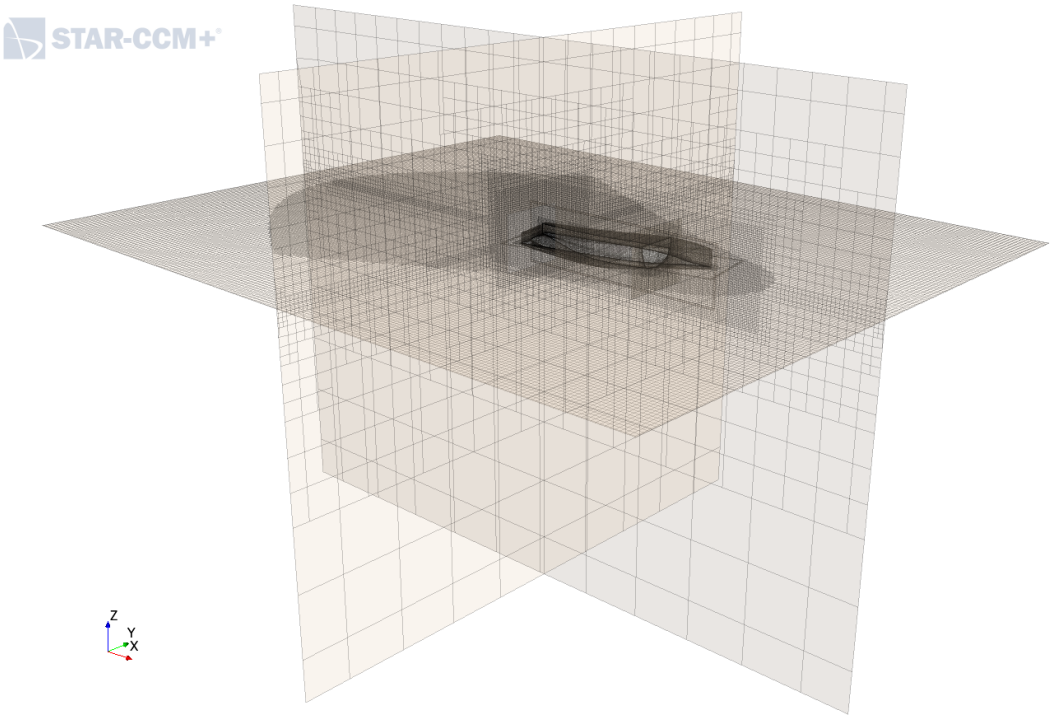

Figure 7-61 Perspective view of twin screw CTV mesh for Z moment optimisation analysis

Figure 7-62 Hull 7828 surface mesh within Star CCM+

Due to the minor increase in cell count, the simulation ran up until 94.5 seconds, equating to 4.725 PMM oscillations. The simulation was also slower due to more complex free surface flow at the aft due to the propeller tunnels.

Unlike the Y force, the Z moment simulations achieve better continuity much sooner. A 5% deviation from the previous oscillation was achieved at 2 ½ PMM oscillations, or around 50 seconds simulated time. Although the simulations stability was achieved much sooner, the results were taken from the last oscillation to ensure best flow stability, as well as ensuring the Y force had converged.

From Figure 7-63 the baselines Z moment is 492,219 Nm, whereas Hull 7828 reduced the Z moment to 306,881 Nm. This reduction equates to 37.65% off the baseline. This reduction dramatically increases the vessels rate of turn as well as reducing the turn radius at a given speed. However, as mentioned previously reducing the moment around the z-axis may also have negative impacts on the vessel stability. The vessel stability in this case was not compromised, however there was an increase in both maximum angle as well as maximum pitch angle. The role angle increased by 4.375%, with the pitch angle increasing to 27.263% above the baseline, which equates to an increase of 2.2°.

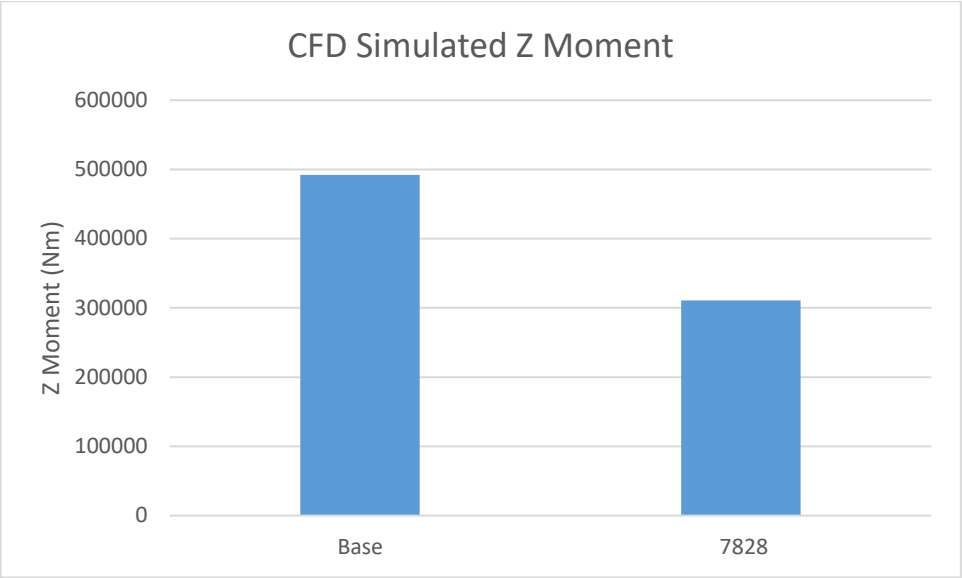

Figure 7-63 Bar chart comparing the optimised hull for Z moment (hull 7828) with baseline hull in CFD

Due to the slenderer shape and reduce displacement of Hull 7828 the overall drag resistance was lower than both the baseline and hull 5243. This can be visualised when comparing Figure 7-64 with Figure 7-51 and Figure 7-52. The significantly finer bow region around the waterline causes the bow wave to move further aft as well as be reduced in height. This height reduction is around 0.5-0.55 m for hull 7828. This aft movement of the bow wave had an impact further down the hull, the overall wake profile was moved further aft, in addition to also being reduced vertically. The lowest point of the induced waves was increased from -1.62 to -1.49 m for the base hull and Hull 7828, respectively. All these factors highlight that although the hull form has been optimised for reduced moments, there has also been a significant reduction in the wave making characteristics and drag resistance of the hull. The only noticeable draw back the free surface for hull 7828 is due to the increased height and the propeller tunnels. It can be seen when comparing Figure 7-64 and Figure 7-51, that the wake of the hull 7828 directly behind the transom has become more unsteady and turbulent due to the increased propeller tunnel size.

Moving from the free surface to the streamlines, there is a clear improvement in the transition from bow to aft for hull 7828. Although there is an increase in velocity change and direction in the propeller tunnels, the overall flow around the underwater region of the hull has become significantly smoother, as well as more closely following the contours of the hull.

It can therefore be concluded that Hull 7828 has been significantly more optimised to tailor the flow around the hull. These improvements for overall straight-line performance appear to be more closely related to the optimisation the moment rather than the Y force, as hull 7828

only had a reduction of 1500 N the lateral Y force. This also correlates closely with the calculated ranking Y force seen in Table 7-8. All these factors also highlight the importance of using a separate equation for each optimisation parameters.

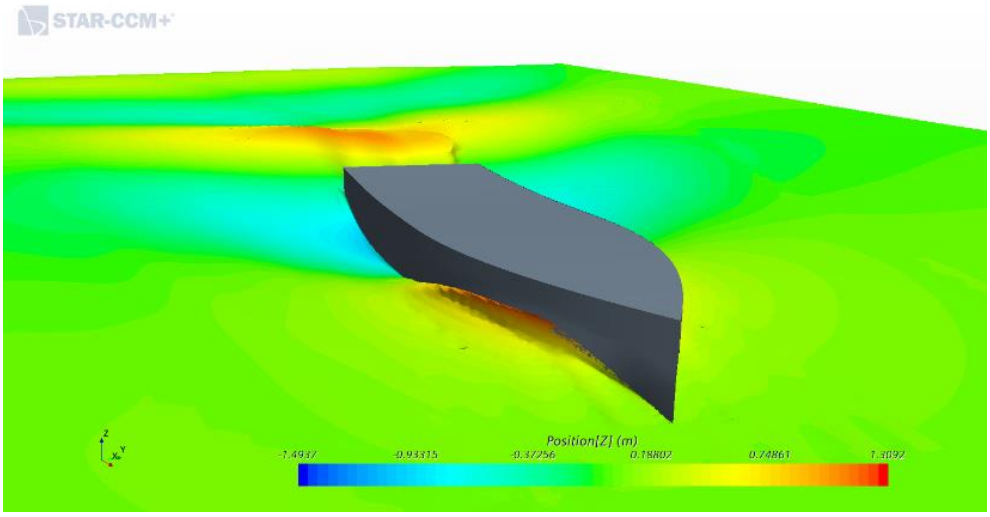

Figure 7-64 Free surface visualisation for design 7828

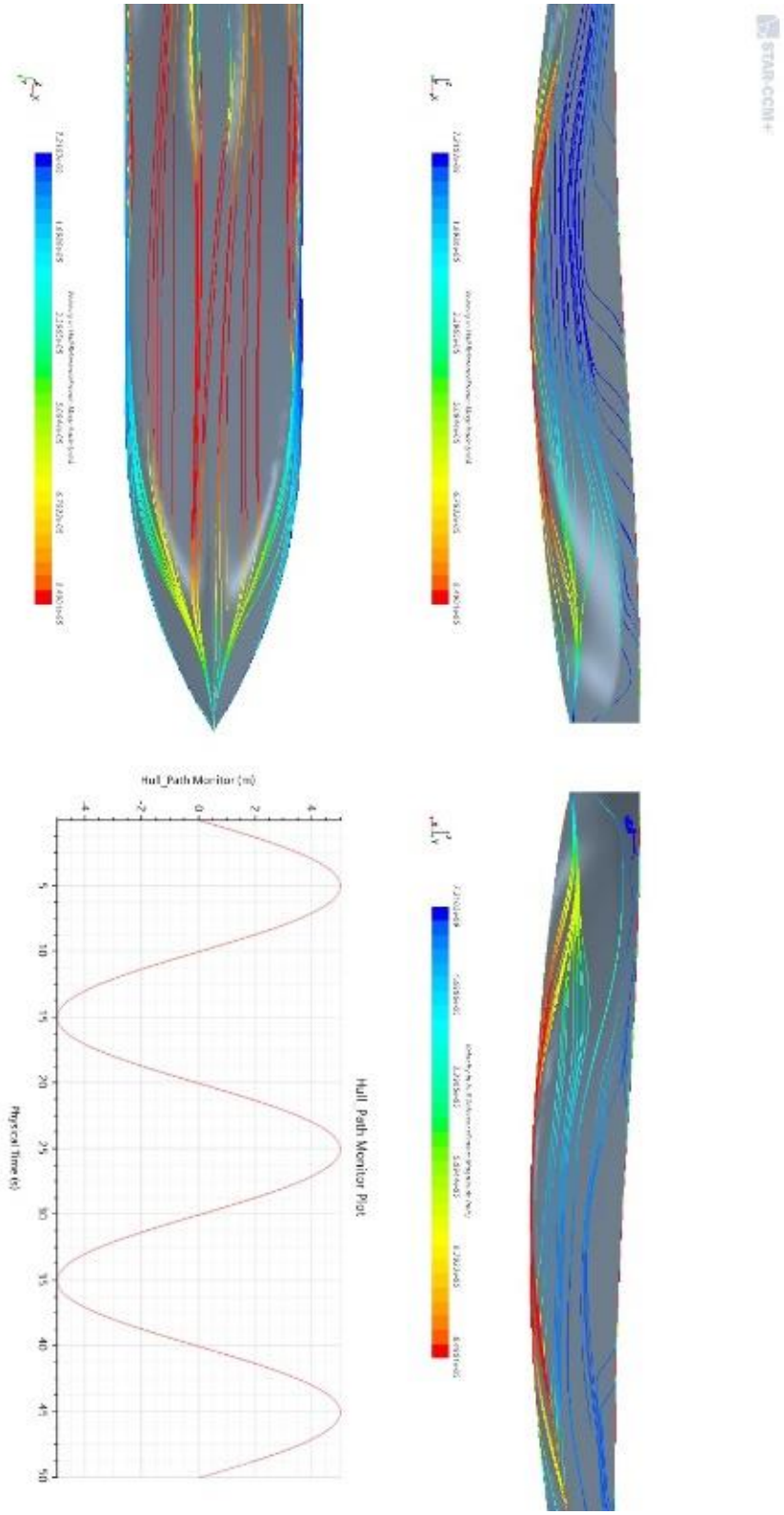

Figure 7-65 Visualised streamlines along hull for 7828

7.6.4. Multi objective optimisation

Upon completing the two individually focused optimisations, a third and final analysis is conducted. This analysis is a multi-objective optimisation that is used both the Y force and Z moment as the means of evaluation. This provides a compelling investigation into the various potential hull forms, as well as the various compromises that may be found. From this analysis there is a capacity for designs which outperform the individually optimised hull forms.

Unlike the previous optimisations, this optimisation can use the previous optimisations as an initial design pool to learn which variables tend towards the optimum. This historical learning also helps to potentially reduce the number of invalid designs. All other factors influencing the optimisation is kept consistent with the previous evaluations.

7.6.4.1. Multi-objective optimisation results and discussion

Unlike the previous evaluations the multi-objective optimisation does not give a singular optimum design, but rather a group of designs that the user has to personally evaluate to find the best design for that problem. For this analysis eight designs were found, the designs characteristics and calculated ranking values are given in Table 7-9. For ease of visualisation the ranking factors have been colour-coded to visualise the minimum and maximum values seen. This is key as there is no perfect design which minimises ranking factors. Therefore, the algorithm selects key designs that satisfy the evaluations.

Table 7-9 Top 8 designs compared to baseline hull for multi-objective optimisation

	Disp (t)	*Cb*	*LCB (m from aft)*	*Ranking Y Force*	*Ranking Z Moment*
Base Hull	151.693	0.52	9.529	4.751	14.952
*3198**	152.406	0.522	9.801	0.432	12.558
7416	139.767	0.479	10.011	1.118	7.139
7755	133.241	0.457	9.996	2.431	6.761
7827	126.49	0.434	10.291	4.574	6.443
*7905**	137.797	0.472	9.947	1.237	7.111
7922	133.378	0.457	10.109	4.157	6.717
7947	128.59	0.441	10.338	4.55	6.603
*7971**	124.759	0.428	10.264	4.628	6.374

The optimisation took just below 8000 iterations to complete. The ranking Y force and Z moment results in comparison to the design iteration are shown in Figure 7-66 & Figure 7-67. It can be seen from these two graphs that optimisation process followed a very similar pattern to the two previous optimisation runs.

The main difference when comparing, for example Figure 7-42 & Figure 7-66, is the density of results in the design space. Unlike in the focused Y force optimisation, multi-objective is significantly fewer outlying and exploratory design iterations. This is because of a greater density of designs in the main band region with fewer designs pushing the extremes. This density variation can also be seen in Figure 7-67, but a noticeable decrease in density, particularly in the later stages of the run. In comparison to the results seen in Figure 7-55, the results for the multi-objective optimisation are significantly more widely spread across the design space.

From these eight designs three user defined optimum designs have been highlighted. These designs are what is considered the optimum for the three potential cases. Hull number 3198 is considered the Y force optimum, as it has achieved the lowest value for the calculated ranking Y force. Hull number 7971 is considered the optimum for Z moment. With hull number 7905 being considered the compromised optimum. Hull 7905 does not have the lowest, or adjacent lowest ranking factors, but rather has the lowest this pairing. This would signify the most compromised and split hull form between the two optimisation evaluations out of the eight selected hull forms. These hull forms can be seen as separate icons in Figure 7-66 and Figure 7-67. In addition to being highlighted here, they have also been highlighted in Figure 7-69 and Figure 7-70 respectively.

In addition to the greater spread of results, there has also been an increase in invalid designs. This has not quite doubled, however has increased from around 150 to 230. With only four invalid designs in the final 1000 design iterations. The invalid design density for the multi-objective optimisation is shown in Figure 7-68.

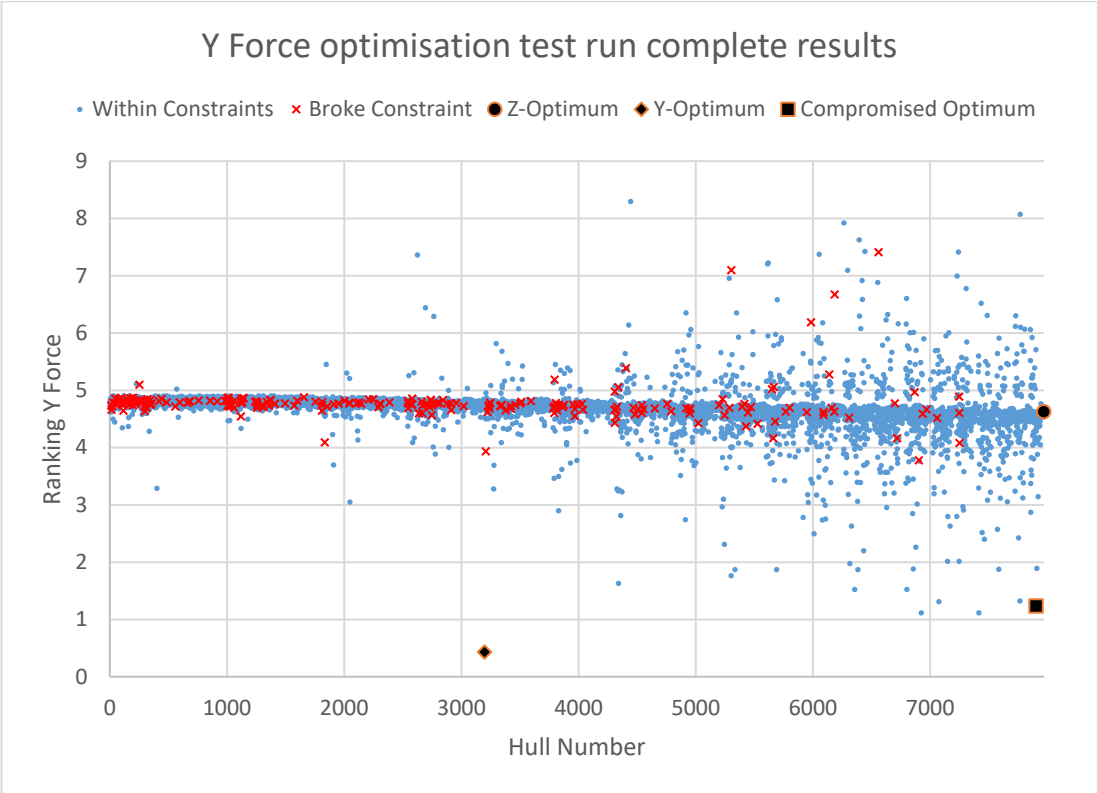

Figure 7-66 Multi-objective optimisation ranking Y force results plotted against design iteration

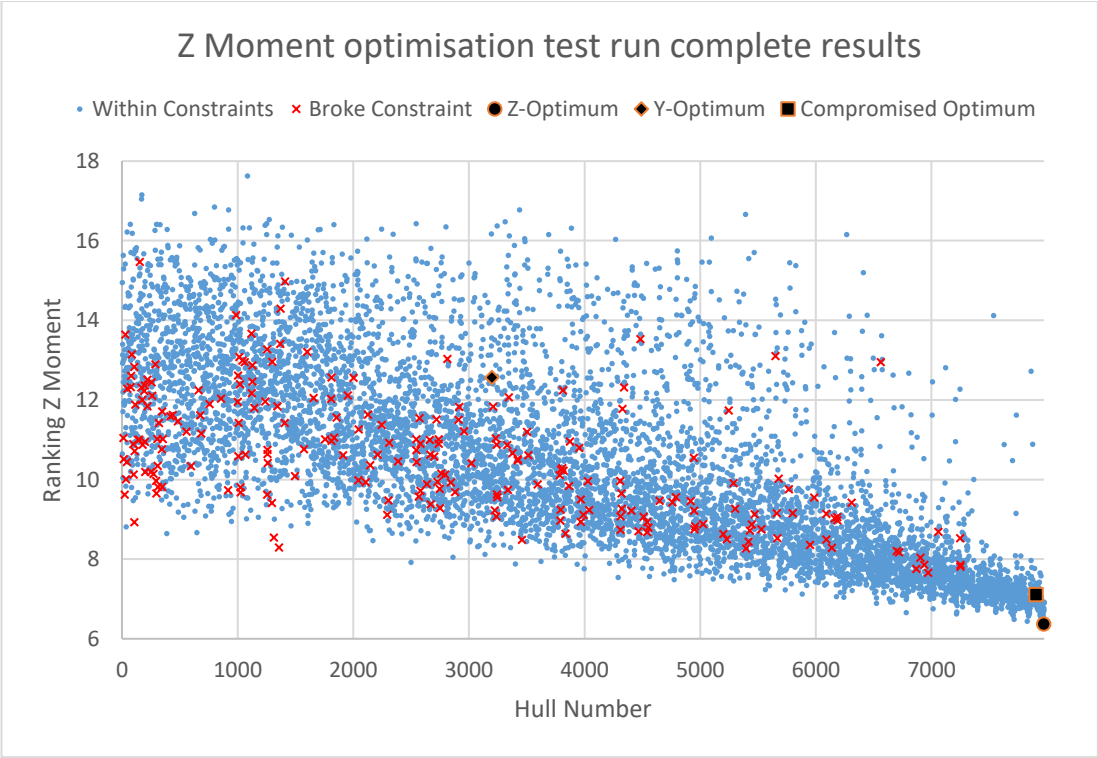

Figure 7-67 Multi-objective optimisation ranking Z Moment results plotted against design iteration

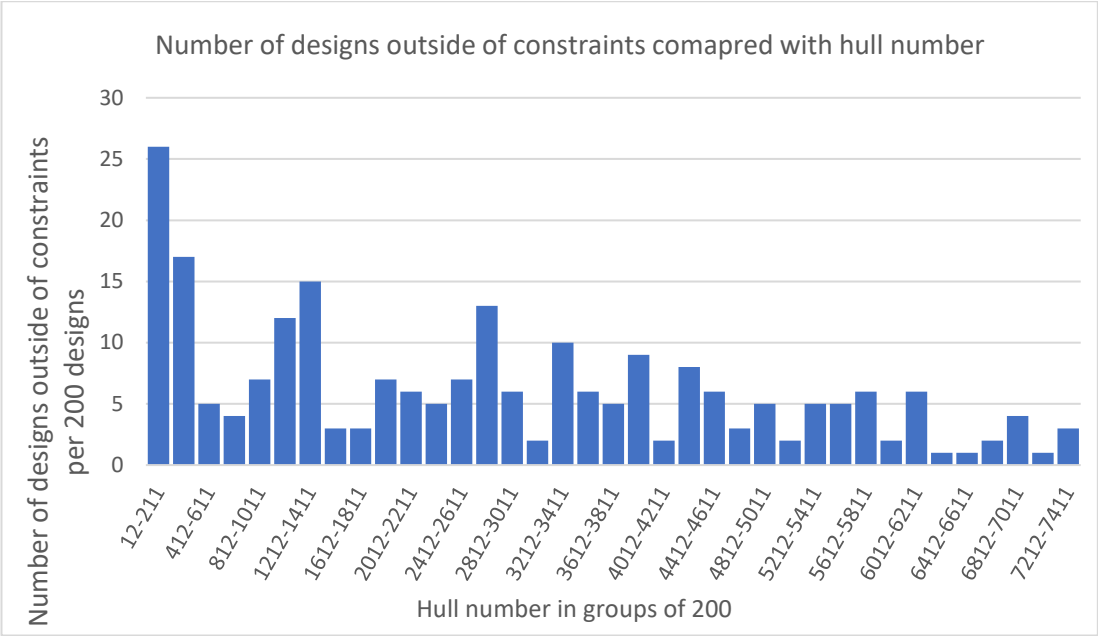

Figure 7-68 Bar chart comparing the density of invalid designs per 200 design iterations for the multi-objective optimisation

Focused comparison of the results for the individual ranking factors provides an interesting insight into the variation that occurred due to the multi-objective optimisation. However, the greatest and most effective method for evaluating the multi-objective optimisation is to compare the ranking results to one another. This provides a clear evaluation on the design space, and how the ranking factors influence each other.

The results shown in comparison to one another are visualised in Figure 7-69. This figure shows the design space generated based on the design variables, along with highlighting where the invalid designs fall. By evaluating Figure 7-69, there is a clear high-density band running in the X axis direction that makes a clear delineation between a large quantity of designs. This would appear to be a natural limit within this optimisation, given these design variables limits, however the designs north of this border appear mainly to be the exploratory designs. By using the global optimisation algorithm with the expected improvement acquisition function, these designs exceeded the potentially natural limit, and therefore may never have been evaluated using another algorithm. It is equally likely the designs at the most southerly regions of Figure 7-69 had high values for this expected improvement acquisition function.

When comparing two evaluation factors to one another it is possible to draw a Pareto frontier. This frontier draws a line between the feasible design space and the unfeasible. It is along this frontier that the optimum designs lie. It is then up to the user to select the design to be finally used. This Pareto front is visualised in Figure 7-70.

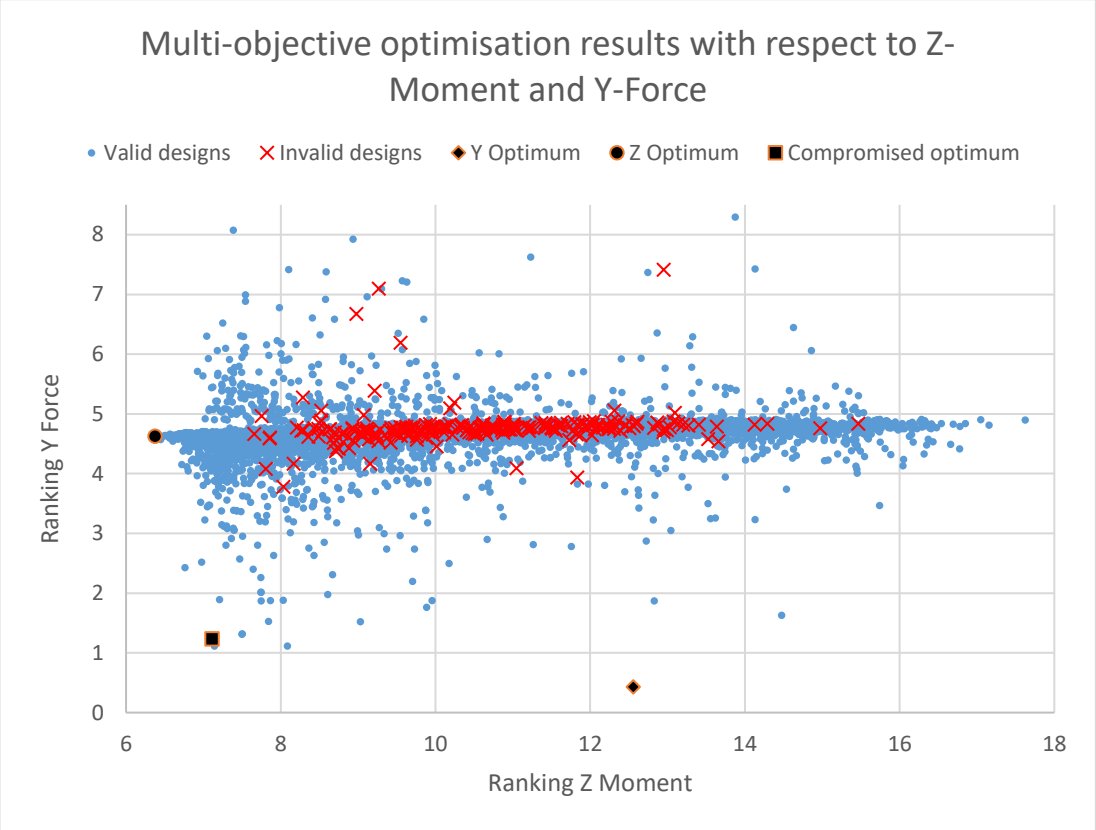

Figure 7-69 A graph showing the complete results by comparing ranking Z moment to Y force

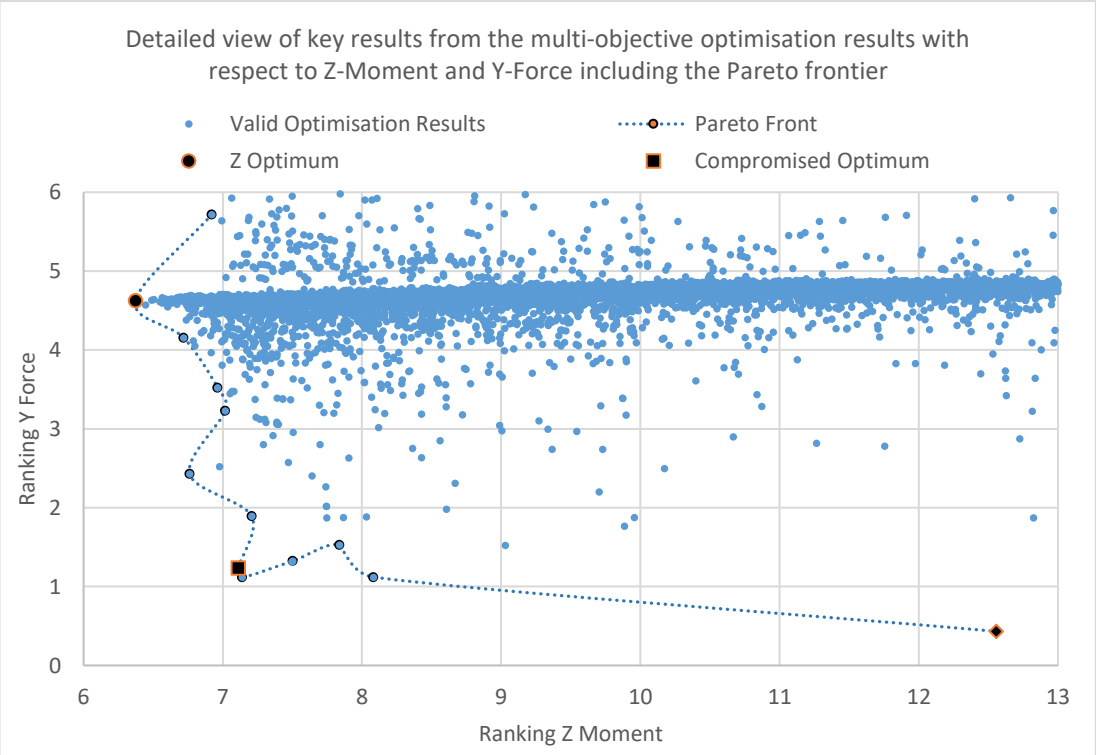

Figure 7-70 Graphical depiction of the multi-objective optimisation Pareto frontier when comparing ranking Z moment to Y force

As mentioned previously, the optimum designs can be drawn directly from the three different, as seen in Figure 7-70. From this graph the positioning of the compromise hull form, Hull 7905, can be clearly seen as the abrupt spike this in the lower left quadrant of Figure 7-70. This abrupt change in direction is often the clearest way to identify a result of the compromises between the multi-objective evaluations.

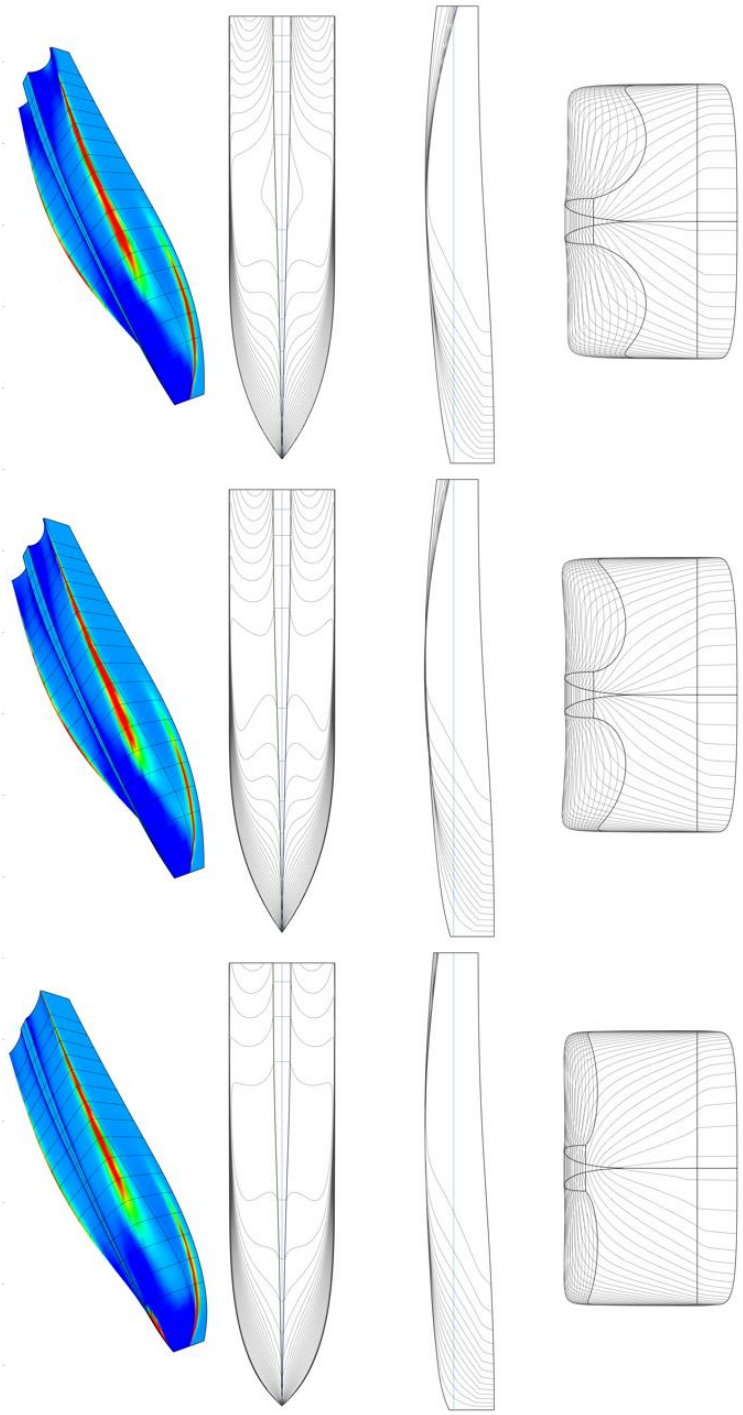

Figure 7-71 Lines plan comparison between multi-objective optimisation hulls: left to right hull numbers 7971 (Z moment), 7905 (compromised) and 3198 (Y force)

Figure 7-71 shows the three user defined optimum designs lines plans. By comparing these three designs, it is possible to see that the characteristics presented in both chapter 7.6.2.2 and 7.6.3.1 are continued with these hull forms. From Figure 7-71 a can be seen in the compromise hull form in the combination of the two other hull forms, to such a point that it appears that there is a clear metamorphism moving through the hull forms. This transitional behaviour can also be seen when comparing the displacements, block coefficients and the position of the longitudinal central buoyancy in Table 7-9.

The key geometric features that are influencing the ranking Y force also present in hull 3198. There is a slight, less than 0.5%, increasing displacement, as well as a forward shift in the longitudinal central buoyancy, 2.85%. In addition, the flattening of the propeller tunnels and the rounding of the bow region all contribute. These geometric details also observed for hull 7971. A reduction of 17.76% in the displacement and a forward movement of the longitudinal central buoyancy by 7.71%. Both these hull forms are following the same trends noted previously, while also being at the limit of the constraints, both for propeller tunnel height and displacement reduction with regards to hull 7971.

The compromised hull form, hull 7905, falls in between these two with regards to both the displacement and the longitudinal central buoyancy. The displacement reduction of hull 7905 puts it nearly equidistant from both hull 3198 and 7971. The change in longitudinal central buoyancy is not as equal, with an increase of 0.15 m from hull 3198 and a change of 0.32 m from hull 7971. These results can be seen from Table 7-9.

As this was a multi-objective optimisation, there was a potential that the singular optimums for an individual ranking factor may not achieve the same level of optimisation as the previous individual optimisation runs. By comparing the ranking factors calculated for the Y force and Z moment optimisation runs with the corresponding factors in this optimisation run, the individually focused runs achieved a greater level of optimisation. This could have been overcome through the addition of extra optimisation generations, however this would have significantly increased simulation time.

When comparing hull 3198 to hull 5243, the corresponding calculated factors are 0.432 compared with 0.261029, respectively. This is the same when comparing the Z moment factors, hull 7971s factor of 6.374 to 6.248 for hull 7828. Based upon these results the singular focused optimisations has achieved a greater performance improvement, however, to validate this the three used defined optimum hull forms are evaluated in CFD.

7.6.4.2. CFD results for multi-objective optimisation for the selected star hulls

This section presents the results obtained using the modified CFD setup that has been used for the previous optimisation runs. As with the previous optimisation runs in sections 7.6.2.3 & 7.6.3.2, the only steps required for evaluating a new hull form is to replace the old hull form, repair and mark key geometric curves on the hull, specify regions, and finally input the corresponding hull DFBI data. Upon completing these steps, the simulations were initialised and prepared for export to the HPC. All simulations kept a constant boundary layer mesh as well as the same time step.

This the generated surface mesh is for the free star hulls are shown in Figure 7-72, Figure 7-73 and Figure 7-74.

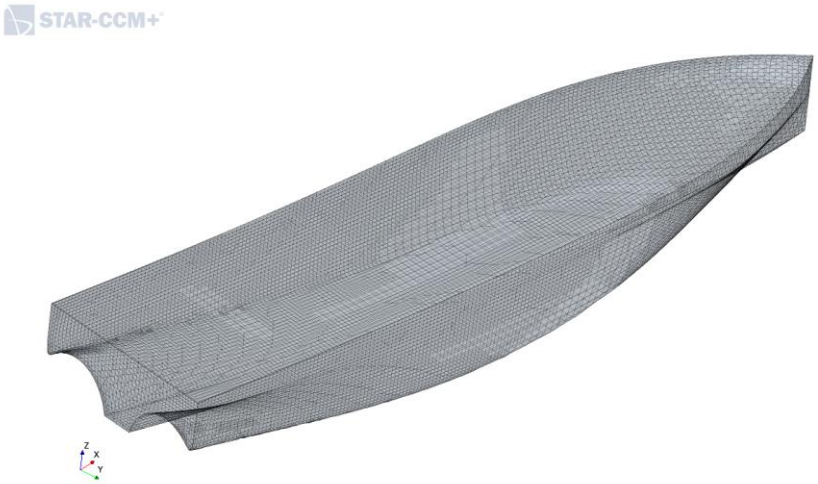

Figure 7-72 Hull 7971 surface mesh within Star CCM+

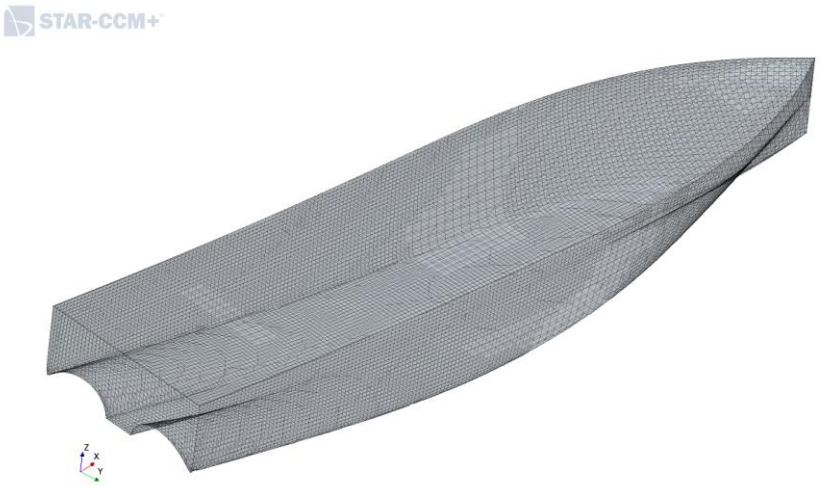

Figure 7-73 Hull 7905 surface mesh within Star CCM+

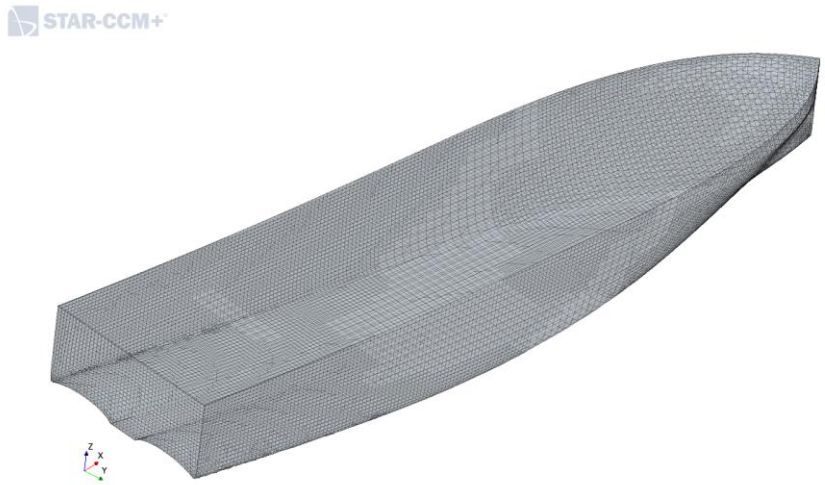

Figure 7-74 Hull 3198 surface mesh within Star CCM+

As mentioned previously, each simulation ran to around 100 seconds, with the results being obtained from the final PMM oscillation. Out of the three simulations, hull 7971 was the least efficient, this was due to an initial excessive trim that slowed the DFBI model. Due to this excessive trim the minimum PMM oscillation that could have been used to was at 3.5, instead of the previously aforementioned 2.5. The other two simulations achieved the minimum level of convergence more closely to the previous CFD simulations 2.5.

7.6.4.2.1. Y force optimisation

The results from the simulations are shown in the following graphs. The ranking factors are initially compared with the focused optimisation results and then compared with respect to the other star hulls from the multi-objective run.

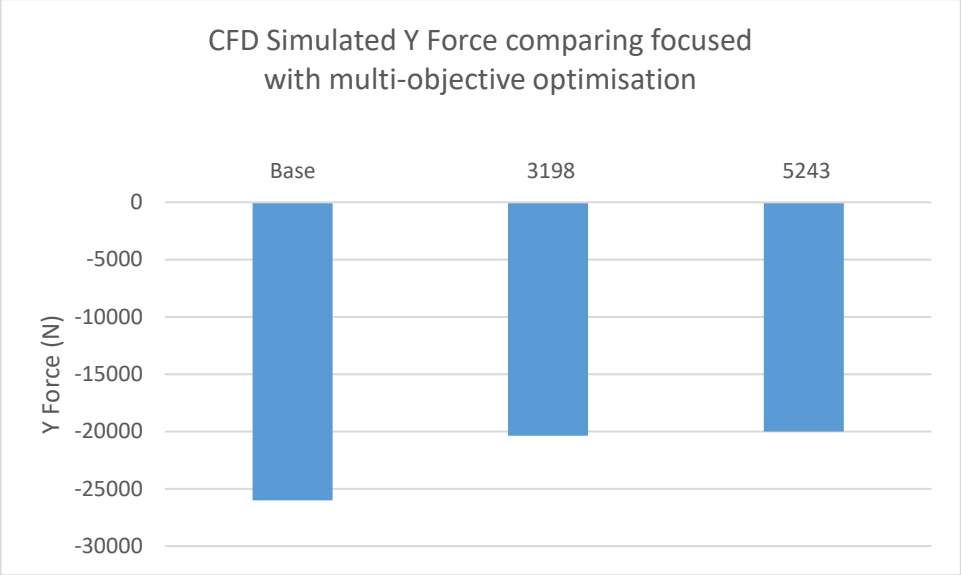

Figure 7-75 Graph comparing the CFD simulated Y force optimum for the multi and focused optimisations with respect to the baseline

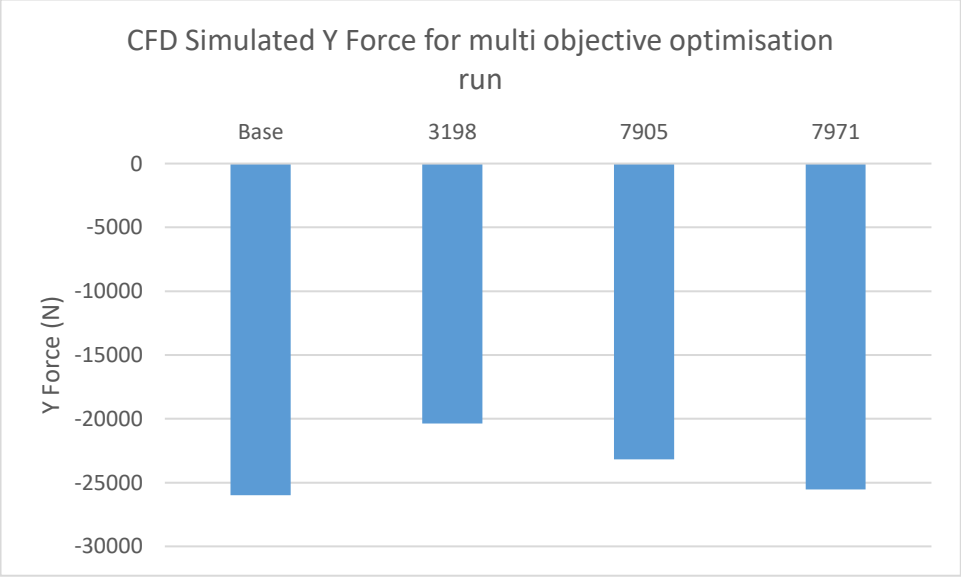

Figure 7-76 Graph comparing the three user defined optimum hulls from the multi-objective optimisation with respect to the baseline for Y force

By referring to Figure 7-75, the focused optimisation achieved a slightly lower Y force than the optimum hull for Y force in the multi-objective optimisation. With respect to the baseline, the multi-objective optimum achieved a reduction of 21.73% whereas the focused optimisation

achieved 23.03% drop. This equates to a 1.3% difference between hull 3198 and 5243. Along with this, all multi-objective optimums achieved an improvement over the base hull, as seen from Figure 7-76. The kinematics of the hull are not greatly varied between the two optimum hulls, this is simply due to the negligible geometric difference between the two hull forms. The minor geometric differences can be observed in Figure 7-77. The most noticeable difference between the two hull forms is the reduced curvature in the aft propeller tunnels and the more prominent keel line at the bow for hull 3198.

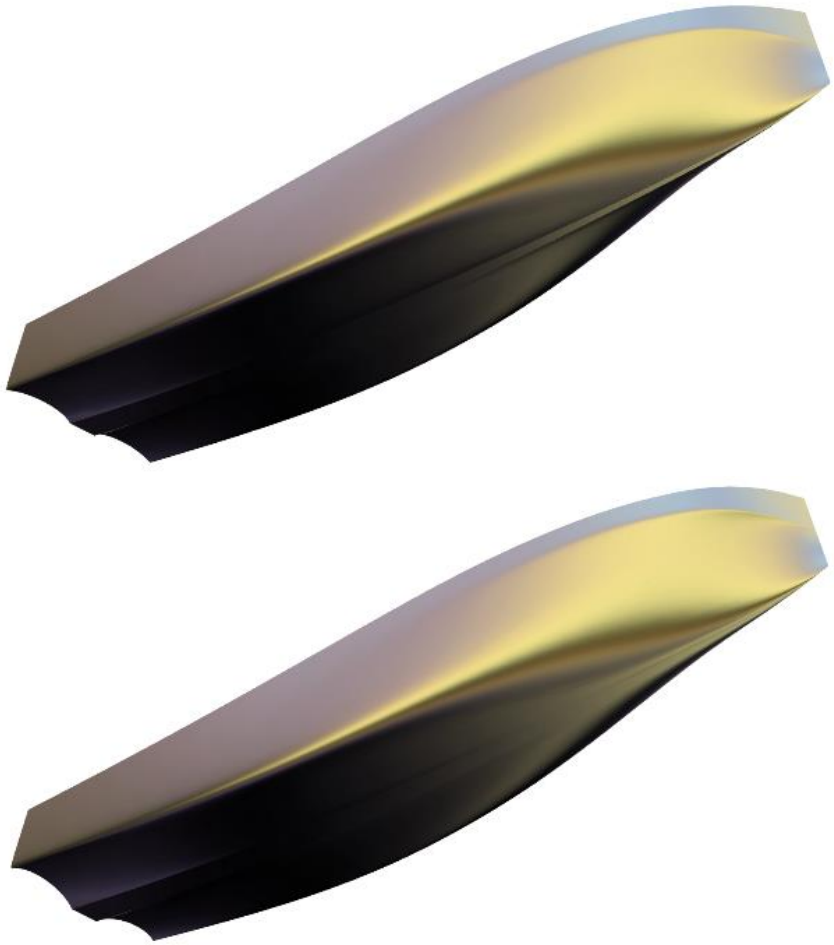

Figure 7-77 Visual comparison between hull 3198 (top) and hull 5243 (bottom)

Further to comparing to the focused Y force optimisation, the Y force for all three of the user defined optimums from the multi-objective optimisation were evaluated to validate the accuracy of the ranking equations. These results can be seen in Figure 7-76, with hull 3198 surpassing all with its reduction of Y force. Although both hull 7905 and hull 7971 achieve a noticeable reduction in comparison to the baseline as calculated from the ranking equations. It is important to note that although Hull 7905 lies closely to the midpoint between hull 3198

and 7971, which matches its position with respect to the ranking factors, this is not a consistent pattern.

The results validate that the ranking equations are capable of accounting for more complex hull geometry which may become more commonplace when optimising for reduced carbon emissions. Although this has not been discussed in greater detail within this chapter, an intrinsic aim for this research was to develop methodology that would help the industry achieve the future carbon emissions levels. Throughout this optimisation this discussion the focus has been on how the Y force reduces the turning circle radius, however this can also be seen in a different sense, namely maintaining the baselines turning circle at a lower power.

7.6.4.2.2. Z moment optimisation

As with the Y force, the results are initially compared with the focused optimisation and then with the other star hulls from the multi-objective optimisation. The results for the Z moment from the baseline, hull 7971, and hull 7828 are visualised in Figure 7-78. Through the two optimisations a reduction of 36.89% was achieved for the multi-objective optimisation, while the focused optimisation achieved 37.65%. This equates to a difference of 0.76%, or 3762 Nm. Similar to the Y force, the ranking factors for Z moment are very close, 6.374 to 6.248, respectively. This minor variation can be very clearly seen in the only minor deviation between the two hull forms.

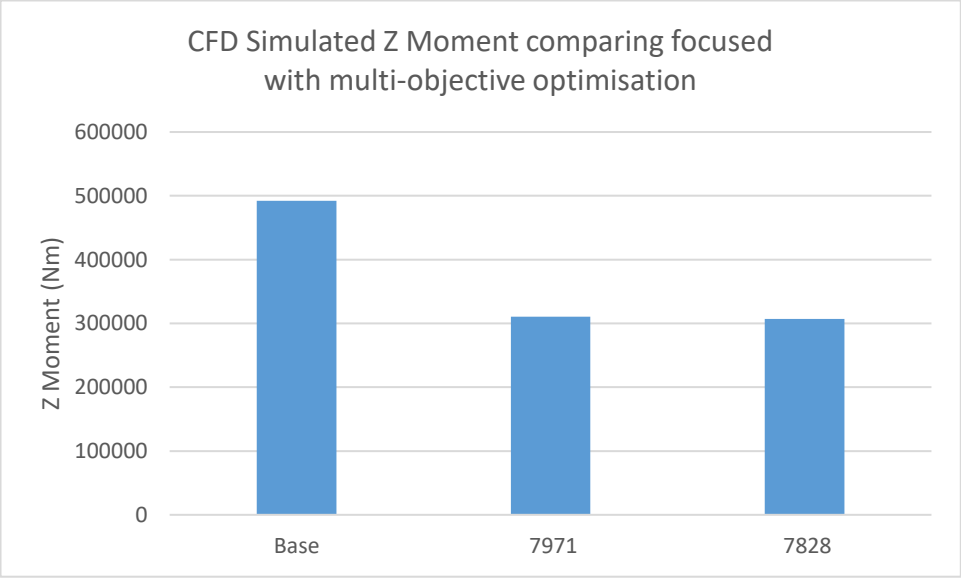

Figure 7-78 Graph comparing the CFD simulated Z moment optimum for the multi and focused optimisations with respect to the baseline

It can be seen from Figure 7-79 that the ranking factor for Z moment does not directly correlate to the simulated Z moment, but rather defines the vessel's ranking with respect to the factor.

This is particularly noticeable when comparing the upper pair (baseline and hull 3198) to the lower pair (Hull 7905 and 7971) with respect to the ranking factor and the simulated Z moment. The disparity between the Z moment difference and ranking factor difference ratio, and the same ratio for lower pair suggest more of a logarithmic increase than linear. This observation can be validated by evaluating a random hull that has a significantly greater value for the ranking Z moment. These results further validate the importance of taking the ranking factors more as a ranking methodology than a means to directly evaluate a vessel's manoeuvring capability.

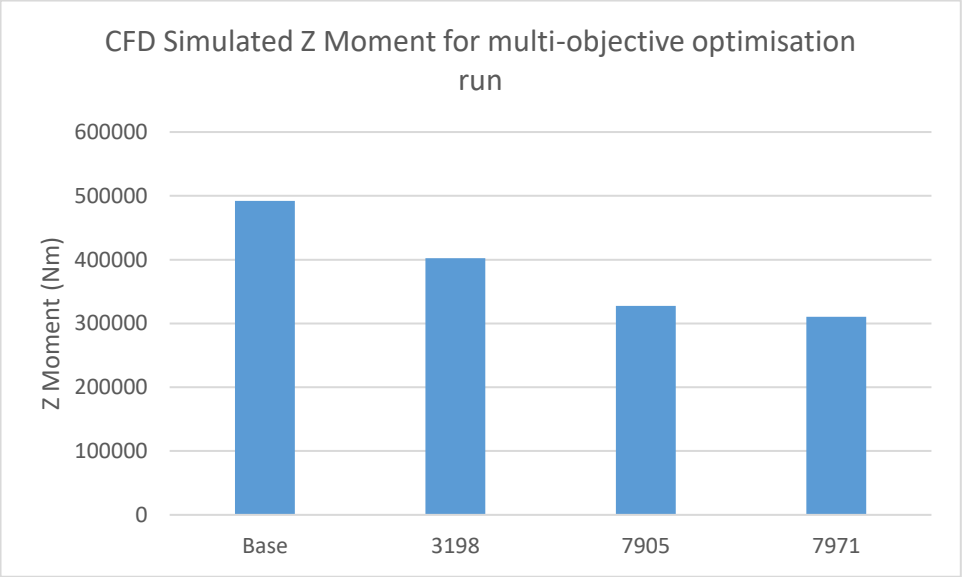

Figure 7-79 Graph comparing the three user defined optimum hulls from the multi-objective optimisation with respect to the baseline for Z moment

7.7. Concluding remarks

Within this chapter multiple optimisation runs and analyses have been conducted using both the equations developed in chapter 6 and CFD simulations to validate these results. The first two optimisation analyses focused on the NPL hull were found to have good agreement with the developed equations. In addition to the accurate results obtained through the CFD simulations, the test optimisations highlighted potential loopholes or errors that could be used by the optimisation algorithm. These loopholes in the parametric model were fixed and in turn led to exceptional results being observed for the NPL parent hull optimisation. Upon the success of the NPL optimisations an original untested hull form was created in the parametric model with differing geometric characteristics and highly specific constraints. This third optimisation analysis was conducted to test the evaluation equations respect hull form different from that used to develop the equations. This third optimisation analysis found the ranking manoeuvring equations to accurately predict the ranking of the original hull form. Throughout

these studies the displacement has been allowed to vary by a minimal percent. This is to ensure the parametric model can sufficiently vary within the design constraints, as noted for Case Study 1, with respect to Y force, only 45% of design iterations were valid, this percentage begins to significantly diminish as the displacement constraint becomes smaller. In addition, by allowing greater variation in the displacement the ranking scheme is tested more vigorously once compared with CFD.

Throughout these optimisation evaluations ranking equations developed in this research have been thoroughly tested and have led to exceptional results. These results highlight two key conclusions: firstly, these equations can be used on a significantly more complex hull form than the basic NPL hull form that was used to develop it. Secondly, these results further highlight the importance of using these equations either in an optimisation or a rapid design space evaluation that is purely based on a ranking scheme, rather than direct calculation of the factors. It is therefore based on these two conclusions that this technique implemented in a methodology for evaluating mono hull geometries numerically can be highly successful when used as a ranking tool.

From this it can be concluded that this methodology of combining ranking manoeuvring equations with an optimisation algorithm and a final validation analysis in CFD's highly successful and can be implemented on varying forms of monohulls and at differing speeds. Multihull vessels and dynamic lifting conditions have not yet been considered in this analysis; however, this work should be considered a good steppingstone to move on to the evaluation of these factors.

To fully understand the improvements obtained through these optimisation runs, a further study is conducted on a select number of the NPL optimised hull forms to analyse the turning circle abilities in CFD. This analysis helps to provide an understanding of how these factors can be linked to real world conditions.

8. Optimisation results applied to CFD self propulsion turning circle tests capability improvements

8.1. Introduction

This chapter presents the setup, results, and discussion for a six degree of freedom turning circle simulation to evaluate the real-world performance improvements gained from the optimisations conducted on the NPL parent hull in calm water. This also helps to provide greater insight into how the individual factors being optimised for influence the vessel in real world conditions.

For this analysis only the NPL parent hull optimums are evaluated. Each optimum found from the single objective optimisation is used, with a single hull form selected from key designs of the multi-objective optimisation is also evaluated. For comparison, the NPL parent hull is simulated to set the baseline and to observe how the dynamics vary between the hull forms.

8.2. Numerical Setup

For the simulation, an entirely new setup is required as there are a couple of key features needed to accurately model such a simulation. This includes the addition of a moving rudder, a virtual disc and full 6 degrees of freedom. Each point needs to be carefully modelled to ensure simulation stability. Although an entirely new simulation is created, the theoretical knowledge as well as some key points from methodologies developed for simulating vessels in irregular waves as well as PMM towing tank tests in both calm and wave conditions is used to create this simulation.

Unlike the previous CFD simulations there is no prior knowledge of the bounding box that encompasses the simulation area. For example, a simulated PMM towing tank test, the lateral movements are already be known, as well as the maximum rotational angle, rotational acceleration, and lateral acceleration to name a few. The vertical motions of the ship are also well predicted; therefore, a full towing tank domain can be created if required. However, due to the requirement of having the smallest possible simulation that may be used in a potential optimisation capacity, a full size virtual towing tank was not feasible. This lack of prior knowledge going into the turning circle setup requires a highly versatile and flexible simulation domain to be created such that any potential movement can be simulated and modelled for. It is based upon this key requirement that the use of the combined overset and region-based simulation is used. As highlighted in the previous chapters this methodology and technique has proven its accuracy and versatility.

The MRF setup for such a simulation does not only require two coordinate systems but a minimum of four coordinate systems. Initial two are with respect to the overset domain and the outer domain, with the overset domain being controlled by the DFBI motions. To model a turning circle simulation both the rudder and propeller is required to be modelled. Each of these components require its own individual coordinate system coupled to the DFBI model and subsequent coordinate system. As noted, there is not a physically modelled propeller in the simulation but rather a virtual propeller created using the virtual disc model in Star CCM+. Greater detail with respect to the virtual disc is presented below. Not only does the rudder require tone coordinate system but also a separate overset mesh to allow for rotational movement to be captured. Therefore, within the setup there are three overset mesh region's and four coupled coordinate systems.

For the simulation, the rudder geometry used by Bailey (1976) is modelled and used in these full-scale simulations. The rudder geometry that is used for the turning circle simulations are shown below in Figure 8-1. The rudder geometry was modelled in Rhinoceros 3DM, which is then also be used to model the various extra overset regions and the volumetric refinements that are required for the simulation. Although the geometry is created for the parametric model created in chapter 5, the corresponding parametric volumetric refinements are not suitable for this simulation. Details of the mesh setup are discussed below.

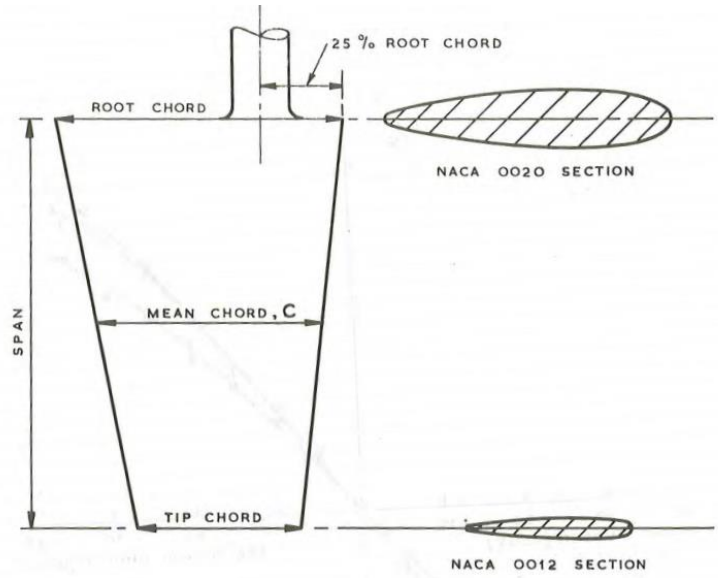

Figure 8-1 For the geometry used by (Bailey, 1976)

Unlike the rudder, the propeller used in Bailey (1976) is not suitable for the full-scale simulations, therefore an outside propeller was selected based on full-scale test data. The propeller data used was from the Princess Royal research vessel used by both Newcastle

University and the University of Strathclyde Cameron (2020). This was due to its accessibility and ease of open order test data, in addition to extensive CFD analysis within the department.

The position of the rudder with respect to the hull form is shown in Figure 8-2, along with a preliminary position and size for the virtual disc. The exact size and position is refined upon later. Figure 8-3 visualises the general position of each of the local coordinate systems:

1. Represents the global coordinate system for the outer domain
2. the local coordinate system around the centre of gravity, datum point for the DFBI model
3. local coordinate system for the rudder, the motion of this coordinate system is coupled to that of the DFBI model with additional input for the rotation around Z axis
4. the preliminary position of the local coordinate system for the virtual disc

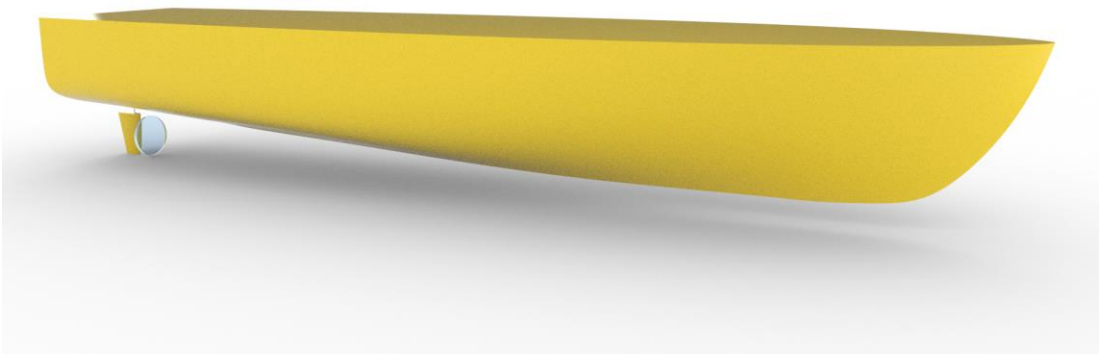

Figure 8-2 Parent NPL hull form with rudder (Bailey, 1976) and preliminary virtual disc

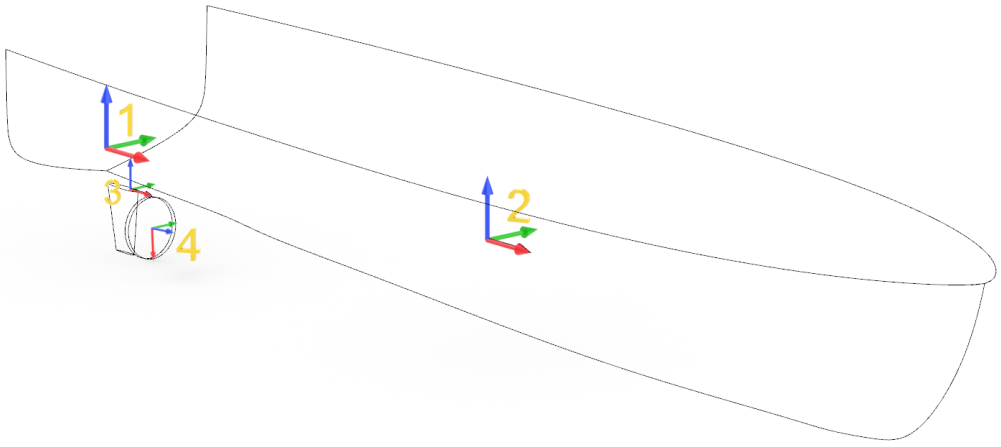

Figure 8-3 Perspective view visualising parent NPL hull silhouette and corresponding coordinate systems (x-axis = Red, y-axis = Green and z-axis = Blue)

After the initial determination of the position of each local coordinate system the various overset boxes and volumetric refinements can be modelled. To ensure the best performance for the overset box containing both the hull and the rudder, the initial dimensions used for the box in the previous investigations is increased. This ensures additional volumetric refinements is captured in the overset, as well as maintaining sufficient spacing between the rudder overset and the main overset boundaries. The sizes for the various overset boxes are given in Table 8-1.

Table 8-1 Overset boundary measurements

	X (m)/ LPP factor	*Y (m)/ LPP factor*	*Z (m)/ LPP factor*
Outter domain	140 m / 7	120 m / 6	100 m / 5
Hull Overset	31.59 m / 1.75	12 m / 0.6	10.5 m / 0.425
Rudder Overset	0.95 m	1.2 m	0.3 m

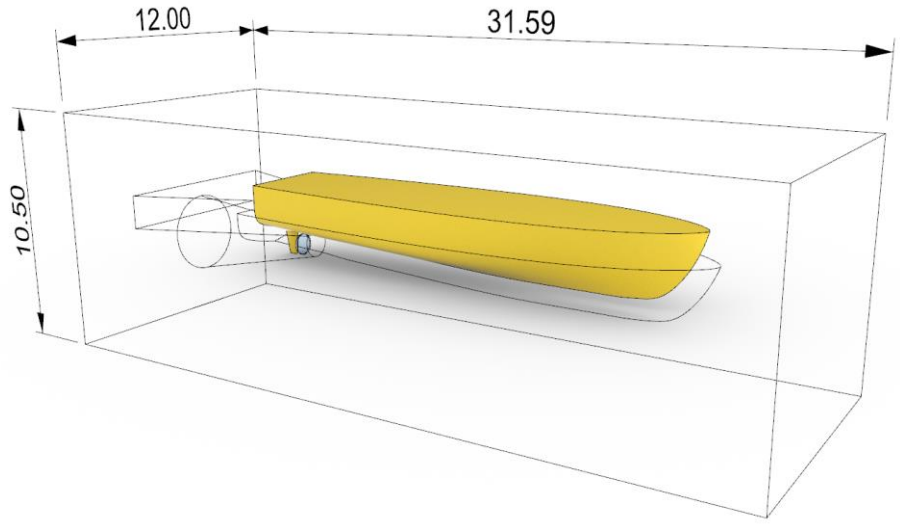

Figure 8-4 Parent NPL hull inside the overset box with key employment refinements shown, dimensions shown in meters

The additional volumetric refinements required for improved simulation stability are visualised in Figure 8-4, an additional free surface volumetric refinement is added but was shown to help more clearly visualise the more complex geometric refinements. These refinements are focused around the underwater hull to help capture vortex flow, a conical region to help resolve both downstream prop flow and rudder flow, along with an additional transom refinement region. These helps to resolve the even more complex flow conditions acting around the hull form.

One of the greatest differences between this simulation setup and all the PMM simulations is that the outer domain is also rotating with the hull. This is due to potential of reverse flow on the outlet when the vessel has rotated 180°. Preliminary simulations were conducted to test the

problems and repercussions that may occur due to rotating the outer domain. Although the simulations that did not use the rotating outer domain maintain simulations stability, there was a clear error that occurred when the vessel has rotated 180°. This problem was solved when the outer domain also rotated with the overset. This additional outer domain rotation did require a smaller time step to ensure simulation stability. This rotation also allowed for the refinement outside the overset region to be significantly reduced helping to reduce the mesh counts.

Another key difference is that there is no additional volumetric refinement for the wake of the vessel in the outer domain. The primary reason for this is that the rate of turn is unknown, and thus may add a potential error to the simulation if refined incorrectly. The secondary reason is due to the outer domain rotating and in turn the need to maintain minimal cell size variations across the free surface in the direction of flow. This led to a single full domain volumetric refinement being used for the free surface and wake region, this region would have a greater level of refinement than would be normally seen for a free surface region.

All these volumetric refinements and increased the main sizes equated to a final volume mesh count of 4.98 million cells for the NPL parent hull. A full breakdown for the different regional cell counts for the NPL parent hull simulation are shown in Table 8-2. The volume mesh is visualised in Figure 8-5, the ex-refinement the hull and stern of the vessel can be seen. From this figure around the far outer boundaries of the outer domain the cell size increases, this is to help with resolving flow direction entering the domain. This coarsening only works for calm water conditions.

Table 8-2 NPL parent hull turning circle mesh count breakdown

Domain	*Cell Count*
Outer Domain	3,054,064
Overset	1,903,408
Rudder	21,882
Total	4,979,354

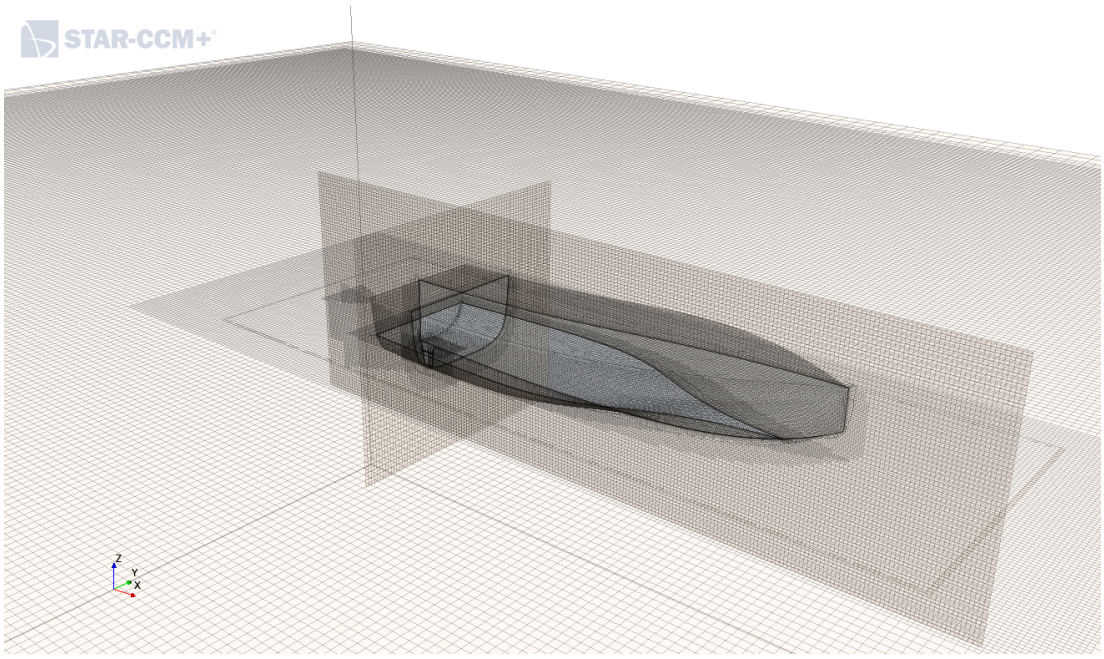

Figure 8-5 NPL parent hull volume mesh for turning circle simulation

The simulation uses the DFBI model to calculate the motions and translate these motions into the movements for both the overset and outer domain. Unlike the PMM simulations, the DFBI is set to multi body motion rather than the planar motion carriage. This not only allows for full 6 degrees of freedom movement, but also the inclusion of external forces and moments. In the case of the simulation this includes force generated by the virtual disc. Not only does this model allow for external forces but also the addition of other bodies on top of the hull, in this case the rudder. By allowing this addition there is no additional work by the user to ensure the rudder follows the hull form accurately, as well as transferring the forces seen on the rudder to the hull. The coordinate system specifically set up for the rudder is merely used to define the rotation of the rudder.

By including a rotational rudder in an overset mesh an extra level of overset interface is needed. For the previous PMM simulations there was only a single interface between the outer domain in the overset hull region. For the setup there needs to be an extra interface between the hull and overset region and the rudder overset. This adds to the computational demand needed to solve the simulation. Based off the studies conducted in chapter 4.4.2, the least squares method is applied for both these interfaces.

To instigate the turning circle manoeuvre a vessel starts by travelling at a constant speed at which point the rudder is turned to a specific angle and held at this point. To create this motion for the rudder, a rotational motion is defined in the superposing motions motion under the hull motions within the tools section of Star CCM+. There are multiple methods for defining the

rotation of the rudder, these include a JavaScript describing the rotational rate of the rudder and then calculating the start stop time from a desired angle, to simply inputting the rotational rate against time as a table. As this investigation is simply to validate the optimisation and show performance improvements in the real-world there is no direct need to script a potentially complex JavaScript. Therefore, the motion of the rudder simply described through the output of an Excel spreadsheet and corresponding table. The output of this table is given in Figure 8-6 with respect to time. It can be seen from this graph that the rotation does not start until 11 seconds into the simulation. This ensures that the hull has achieved an initial level of equilibrium between itself and the propeller.

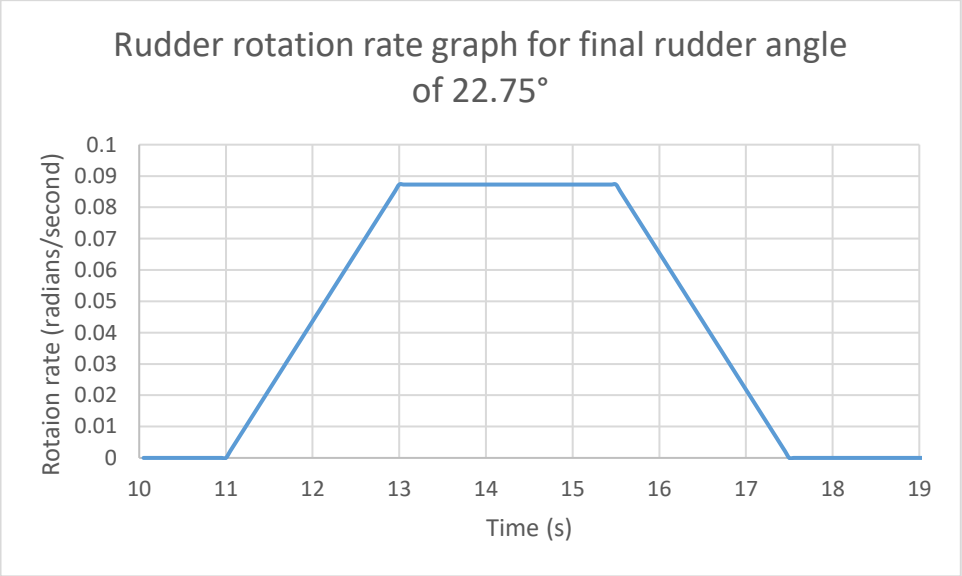

Figure 8-6 Graph showing the rotational rate of the rudder to achieve a final angle of 22.75°

8.2.1. Virtual Disk

This section presents a brief overview of the theoretical background as well as the key characteristics of the model implemented within the simulation. As noted previously a virtual disc is used in place of a fully modelled propeller. The virtual disc generates the correct rotational flow and thrust forces based upon the inputted propeller performance tables. This does not only push the vessel forward but also develop an accurate representation of the flow field around the rudder. The body for propeller method is used from within Star CCM+, this is specifically designed to model the flow interaction between the propeller and the hull on the ship (SIEMENS Star CCM+, 2021). This method allows direct influence between itself and all geometries connected to the hull form. It is important to note that complex flow characteristics such as cavitation or extreme velocity gradients is not and may not be modelled accurately respectively.

To further minimise simulation complexity a five bladed propeller that has been extensively tested and researched, both open water and CFD, within the Department was selected. This propeller is used on the research vessel Princess Royal, to which the Department has use, therefore allowing the propeller curves to be easily accessed.

This propeller does not match that used in the research by Bailey (1976) when model scale tests for turning circle performance were conducted. This therefore invalidates the results obtained by Bailey (1976) as a means of validation. In addition, the exact position of the propeller for these model tests is unknown, therefore the propeller and in turn the virtual disc must be manually positioned with respect to each hull form. The position between each hull form only varies in the Z axis to maintain a set distance between the hull, rudder, and propeller. The angle of the propeller is not varied between the different simulations. A 3D render of the five bladed propeller being used is shown in Figure 8-7.

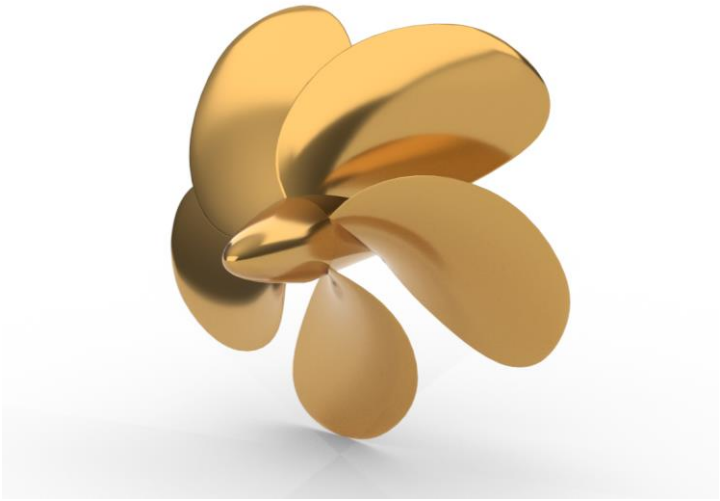

Figure 8-7 3D render of propeller used for turning circle simulations with data provided by Princess Royal research vessel (Carchen, et al., 2015)

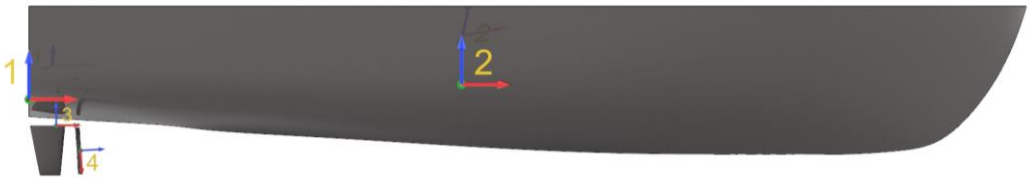

Figure 8-8 Visualised position of each corresponding local coordinate system for NPL parent hull

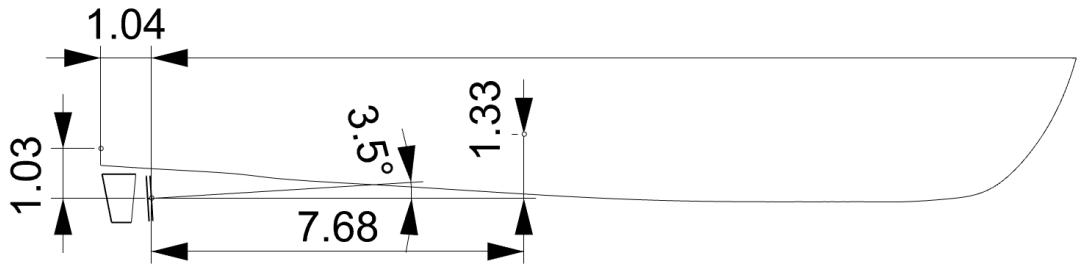

Figure 8-9 Position of virtual disc with respect to origin (1) and centre of gravity (2) in metres along with propeller inclination

The position and inclination on the virtual disc can be seen in both Figure 8-8 and Figure 8-9. The tip separation between the hull and virtual disc was maintained at 0.15 m all simulations. In addition to these figures the corresponding input data for the virtual disc is presented in Table 8-3, with the open water CFD performance curves shown in Figure 8-10, data provided by Cameron (2020).

Table 8-3 Geometric input data for virtual disc

	Virtual Disk Input	
Inner Radius/Shaft radius (m)	0.0715	
Outer Radius (m)	0.425	
Thickness (m)	0.07725	*(25% of propeller blade x distance)*
Inflow Plane Radius (m)	0.4675	
Inflow Plane Offset (m)	0.085	
Propeller Inclination (degrees)	3.5	

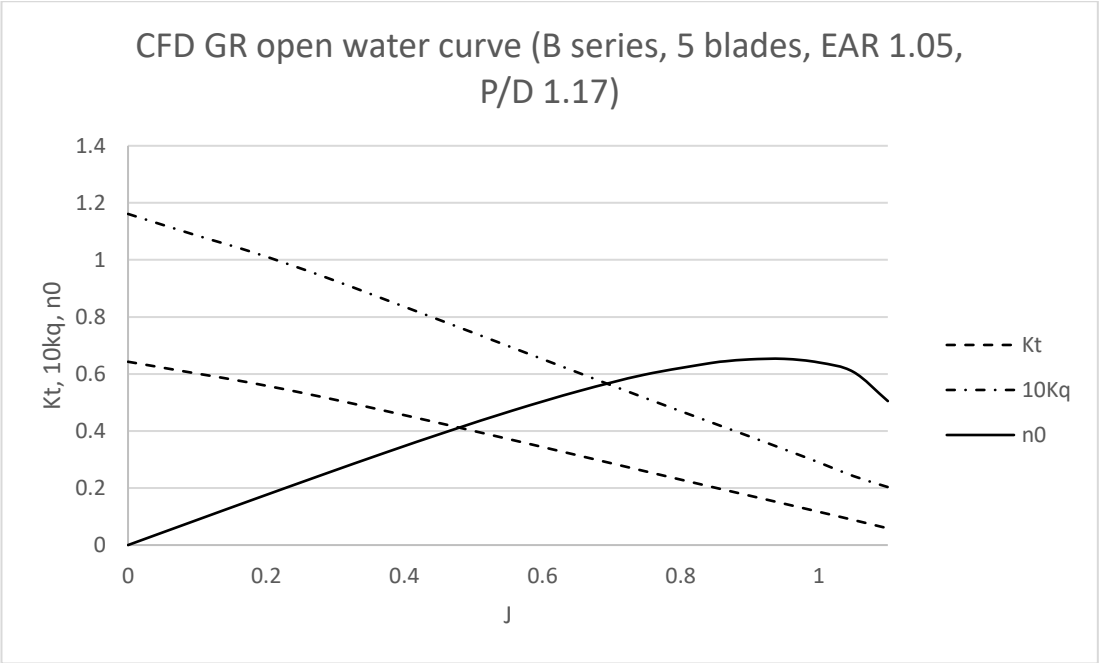

Figure 8-10 CFD Simulated propeller open water performance given for Princess Royal five bladed propeller (Cameron, 2020)

Upon inputting the virtual disc data, the final stage is to determine the correct propeller rpm for a given speed. The preliminary estimation can be made mathematically, however the most accurate method is to run a self-propulsion resistance test. This simply involves running the current setup with no rudder deflection, additionally lateral movement is constrained. A single simulation is run with an open-ended run time to allow the user to manually vary the propeller rpm once the virtual disks thrust reaches equilibrium with the hull's drag.

Upon completing an initial test run of this self propulsion simulations a simple JavaScript was recorded to automatically monitor the convergence between the virtual disks thrust and hulls drag. Once this convergence is maintained within a desired level of deviation for a desired number of iterations the rpm is increased by a specified amount. This provides a simple method to interpolate the corresponding ship speed and propeller rpm.

Through this simple investigation a preliminary 750 rpm was found to achieve the desired 12 kn or 6.173 m/s. This rpm is maintained throughout the entire turning circle simulation, as well as maintained on the other hull forms. It is highly likely that due to the modifications and variations applied to the optimised hull forms the initial cruising speed may increase. This is another factor that is evaluated in the simulations. Not only does the speed variations between the hull forms, but also the speed variation throughout the test is also assessed. It would also be possible to use the recorded JavaScript with advance modifications to develop a test where

the turning circle is conducted and a predetermined speed that is maintained throughout the turn. This is not added at this stage.

Upon finding the correct propeller rpm the turning circle tests can now be conducted to evaluate the performance improvements for the optimum hulls compared with the NPL parent hull. Each simulation is run open-ended for 72 hours on the Archie-WeST HPC.

8.3. Results

Within this section the results for the turning circle manoeuvring simulations are presented and discussed. As noted above there are four hull forms analysed within this section. This provides a clear side into how the characteristics optimised for directly affect the vessel performance in real world conditions. Not only are the pure turning circle paths evaluated, but also the various dynamic motions and velocities of each hull form are compared and discussed.

An initial comparison of the results obtained from the ranking equations is shown in Table 8-4. This table provides the baselines how the real-world results relate to the methodology developed in this research.

Table 8-4 Optimisation equation results for the four hull forms being evaluated in the turning circle simulations

	NPL Parent	*Hull 6495*	*Hull 6475*	*Hull 6416*
Disp. (t)	28.7	25.943	25.886	26.18
Cb	0.397	0.360	0.366	0.363
LCB (Frm. Aft [m])	8.720	8.616	10.312	9.897
Ranking Y Force	223.546	90.759	132.949	113.383
Ranking Z Moment	3.496	2.775	0.953	1.283

A comparison between the different simulated turning circles can be seen visualised in Figure 8-11. The first conclusion they can be drawn from this visualisation, as that all three optimised hull forms significantly outperform the parent NPL hull. In Figure 8-11 the parent NPL hull is shown as a dashed black line, this route surrounds all other turning circles.

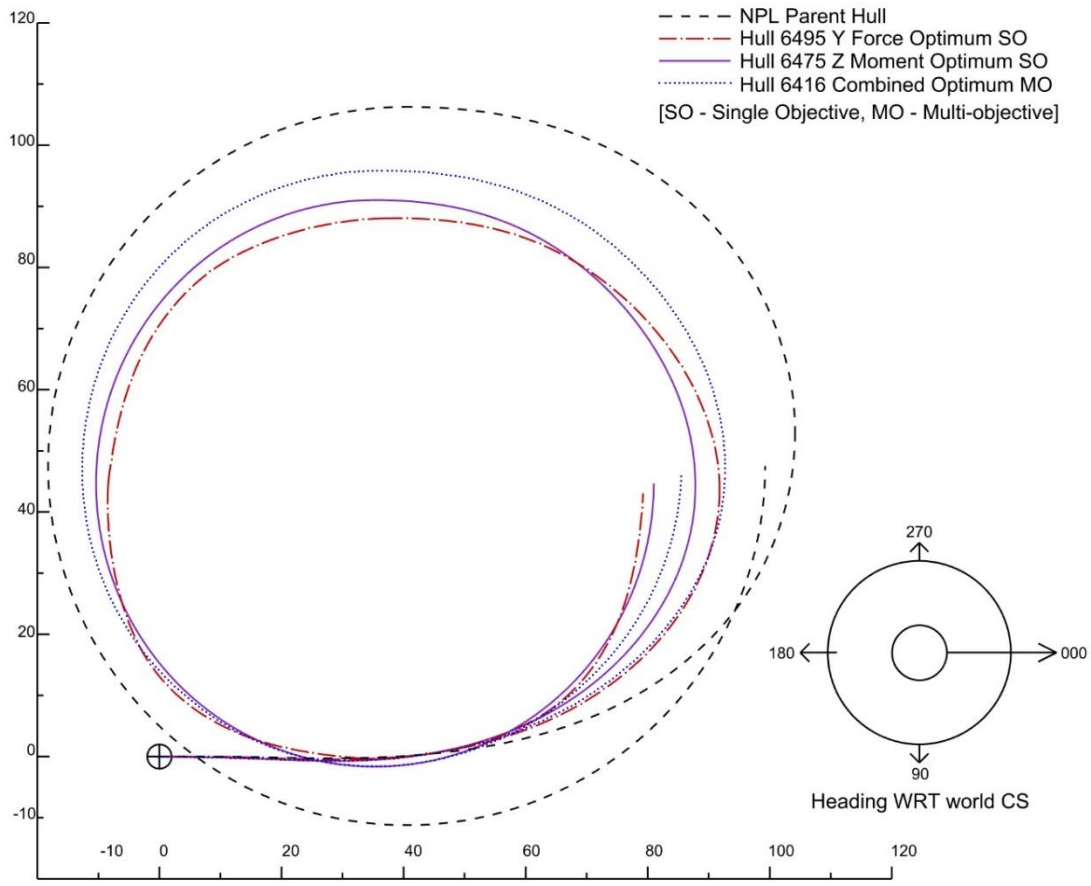

Figure 8-11 Turning circle path comparison between the selected four hull forms (axis representing distance in metres)

When evaluating the difference between the overall turning circle performance of the various hull forms the greatest deviation between the optimums and NPL parent is the initial turn rate. From Figure 8-11 the NPL parent hull has the slowest initial turn rate with the second slowest being the Y force optimum (hull 6495), followed by the multi-objective optimum (hull 6416), and finally the Z moment optimum (hull 6475) outperforming all with the fastest initial rate of turn. This initial rate of turn is maintained by hull 6475 for most of the remaining turning circle. However, hull 6495 has a sudden increase in turn rate between a heading of 90 and 180°, this causes the hull to move inside the turning radius of the Z moment. Hull 6416 follows a steadier rate of turn like that of hull 6475, with the overall yaw rate lower creating a smoother wider circle than that seen for the Z moment optimum.

All three optimum hull forms begin to converge close to a heading of 45°. This is also the point at which the parent NPL hull has the smallest deviation from the optimum hulls of just over 5.5 m. All three optimum hulls converge close to the point of initial rudder deflection. Prior to this the Y force optimum had been outperforming both the Z moment and multi-

objective, however, hull 6495 had a slight increase in its velocity between a heading of 90 and 30°, this caused its turning circle radius to slightly increase. This velocity increase eventually reduced such that hull 6495 would achieve the smallest final turning circle radius.

This final radius was 19.99 m less than that of the NPL parent hull, with hull 6475 (Z moment optimum) reducing its final radius by 18.26 m, with hull 6416 having the smallest improvement over the NPL parent hull with a reduction of 13.81 m. These measurements are a direct comparison between the different hull forms as measured from the initial starting position. Table 8-5 presents the radius of the final quarter turn of the turning circle simulations and the respective improvements between the hull forms. These improvements are lower than those taken with respect to the initial starting position. This table in turn presents the steady state turning capability of each hull form and in turn improvements gained through the optimisation. It can be seen from this table that the real world improvements do not directly match the reductions seen by the optimisation. An influencing factor can be the variation in speed seen between the hull forms. This speed variation can be seen in Figure 8-12, when velocity of the vessel is compared to the percentage of turning circle completed. For these simulations it is taken as one and ¼ revolutions as 100%, this is also where the graphical representation of the turning circle paths is stopped for comparison. This is due to all but one simulation running out of time before achieving one and ½ revolutions.

From the velocity results, the Z moment hull as the highest initial velocity going into the turn, which is then most significantly bled off through its initial turn phase. This velocity is then recuperated to the point at which it maintains the highest velocity out of all the hull forms. This velocity is maintained due to the high average roll angle maintained throughout the manoeuvre. As hull 6495 and 6416 are relatively similar they also have similarities with respect to the velocity and roll rate. It can be seen from Figure 8-12 that hull 6416 has the smoothest velocity which also correlates to the second most consistent turning circle after the NPL parent hull. This smooth velocity throughout the turning circle is mostly due to the compromises made to both the Y force and Z moment. Although the hull form of hull 6416 is like that of hull 6495, hull 6416 maintains a higher average roll angle as well as less erratic trim angles. These factors contribute to smoother turn with lower accelerations, therefore making it the best performing hull with respect to human factors.

Although the Y force optimum has some of the best numerical performance, its dynamic motions with respect to trim and roll are the worst. With erratic motions in both roll and trim, which in turn impact the ships performance with respect to human factors. This is also similar

to what is seen for the Z moment optimum. Unlike hull 6495, hull 6475 has minimal erratic motions but has the highest average roll angle out of all vessels.

Table 8-5 Comparison table of final radii for turning circle

	Final Radii (m)	*% Reduction*
NPL Parent	58.75	-
Hull 6495	45.270	22.945
Hull 6475	45.69	22.230
Hull 6416	50.14	14.655

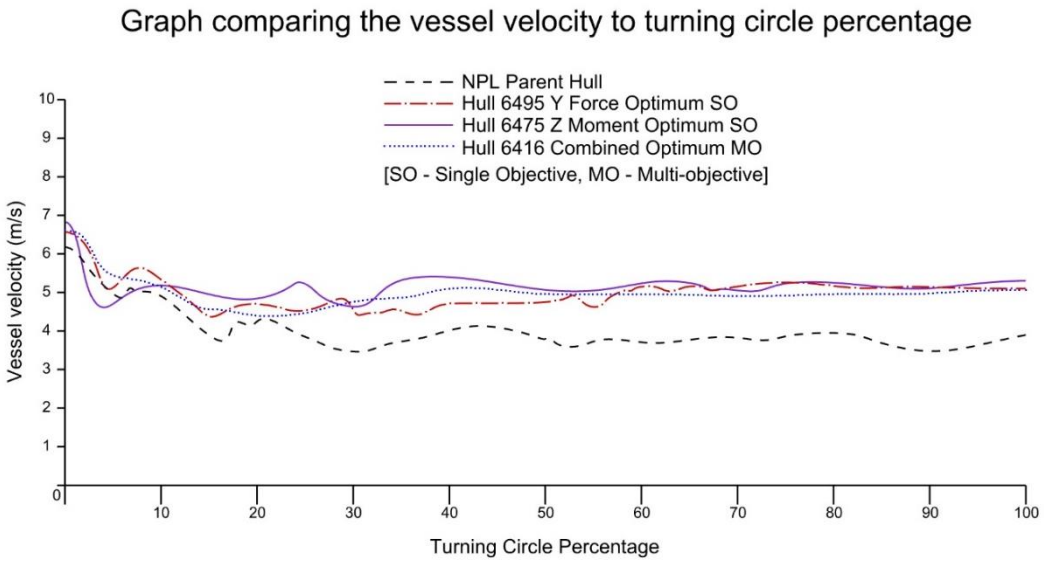

Figure 8-12 Graph showing the vessel velocity with respect to the percentage of turning circle completed

These vessel dynamics are also seen in Figure 8-13, which shows the initial movement of the hull latterly when the rudder is rotated to port, the paths have been amplified to improve visual comparison. From this figure can be seen in the parent NPL hull smallest lateral movement with the Z moment optimum (hull 6475) having the largest lateral movement. This large lateral movement, in comparison to the other hull forms, the primary cause for the velocity reduction and in turn the increased turn rate. This is also due to the greater rolling characteristics of hull 6475, whereas hull 6495 and 6416 both have relatively low roll angles which in turn helps to mitigate the lateral movement. These hulls however still have a significantly reduced lateral area compared to the parent NPL hull, which in turn allows for the hull to slew in the opposite direction.

Counterintuitively though, hull 6416 has the second soonest peak after the parent NPL hull even though it has the second highest speed entering the turn. Hull 6475 has a higher speed which in turn is bled off most quickly out of the hull forms, however this initial high-speed causes the peak lateral slew to occur furthest from the initial point for the rotation. Hull 6495 has a second farthest from starting point, it is unclear exactly the cause for this, however it could be related to the flat stern allowing the vessel to slide.

In addition to the initial lateral drift diagram shown in Figure 8-13, the advance and transfer lengths are given in Figure 8-14. From this figure can be seen that the Z moment optimum as the smallest advance length and the second smallest transfer length. This speaks to its ability to rapidly turn stably, however at the loss of vessel velocity. Both hull 6495 and 6416 have very similar advance lengths with hull 6495 outperforming all the others with respect to the transfer length. This performance is due to the vessels velocity reduction within the first 20%, as seen in Figure 8-12. These results seen in Figure 8-13 again verify that the Z moment optimum has the best performance for short aggressive turns.

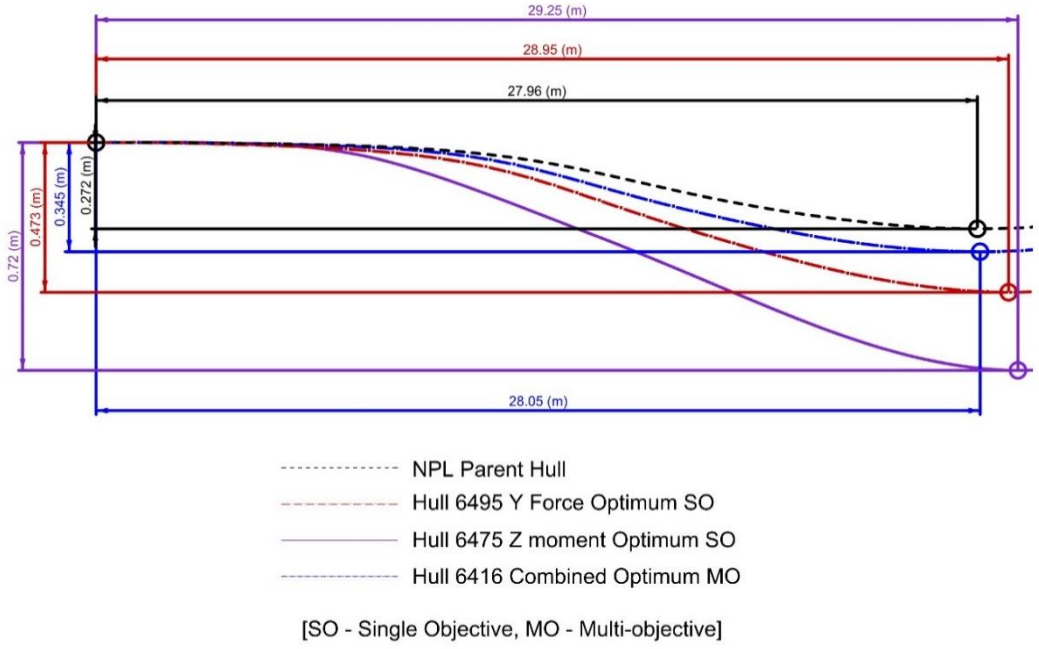

Figure 8-13 Amplified representation of initial inverse motion to rudder angle (not to scale)

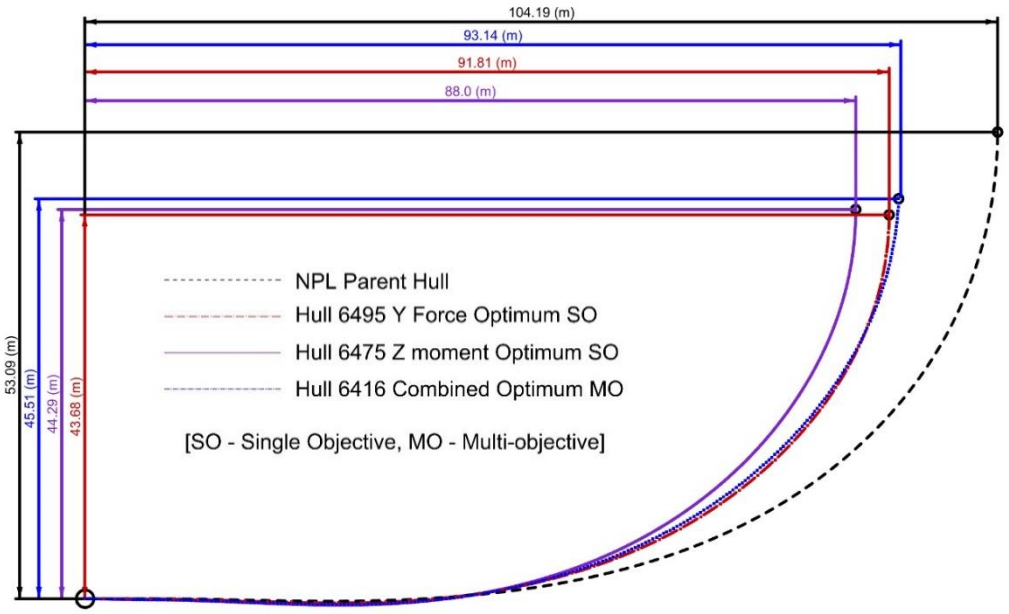

Figure 8-14 Visualised advance and transfer measurements for the various hull forms

8.4. Concluding remarks

From this investigation multiple conclusions can be drawn. First and foremost is the accuracy and ability of the ranking equations to predict which hull form performs best in real world conditions with multiple degrees of freedom. As noted previously there are limitations to this ranking evaluation methodology, however in terms of this optimisation these equations have been found to exceed initial expectations.

Secondly, the initial predictions of how the various key forces acting on the hull effect the performance in the real-world manoeuvre can be considered valid. As stated previously Z moment has a great effect with respect to the initial rate of turn. This hull form also has a greater tendency for large roll angles as well as the ability to bleed off velocity quickly. To contrast this the Y force was predicted to have the best steady-state and equilibrium. This was proven to be correct however, due to the aggressive stern motions of the vessel may not ensure the best performance in the real-world. It can be said then that the multi-objective optimum was found to have the overall best performance when considering real world conditions and in turn human factors. This hull form has exceptional steady-state turning capabilities while not compromising on the roll or trim characteristics.

It can then be finally concluded that the MRF overset CFD methodology developed throughout this research has again proven to accurately model advanced vessel manoeuvring. This methodology coupled with the irregular sea methodology allows for truly real-world

simulations to be modelled. The simulations however involve substantial computational resources which in turn may not be available for the next few years, therefore, highlighting the substantial benefits of using the ranking equations to speed up such an analysis process.

9. Conclusion and Future Research

9.1. Conclusion

As presented in chapter 3 there were three primary aim is for this research to achieve. The first aim is presented as follows:

Following this the second aim was achieved in chapter 4. The same was defined as such:

- *Develop a fully automated methodology for calculating key manoeuvring variables in CFD in various wave conditions*

As can be seen, the aim follows on from the previous work and objectives. By utilising the parametric methodology for controlling and defining the simulation domain, created in chapter 10, a preliminary base foundation was developed. This foundation was used to create a fully parametric methodology for simulating captive model manoeuvring tests. This methodology was broken down by the objectives outlined below:

a. Investigate the limitations of current literature surrounding CFD manoeuvring simulations, along with the main advantages to using CFD over other potential codes
b. Develop an adaptive MRF scheme that describes a combination of pure yaw, pure sway and static drift carriage motions
c. Develop an automated CFD domain generation tool, that generates all the key CFD volumes based upon the adaptive MRF variables
d. Develop an automated mesh scheme that is validated and adapted against multiple towing tank results conducted by SIMMAN 2014
e. Conduct tests to investigate various factors affecting manoeuvring variables, such as wave interference

A preliminary literature review was conducted to ensure that this research would be filling the gaps that have been left in the current literature. This fully parametric methodology was the foundation for the adaptive MRF scheme. This scheme was evaluated through multiple iterations, as well as key factors affecting CFD simulations in specific systematic studies. Upon achieving a stable simulation, an extensive validation and verification study was conducted against the SIMMAN 2014 experimental data. Upon finding good agreement with the EFD results studies to further evaluate factors affecting the key manoeuvring characteristics were conducted. This took the form of additional degrees of freedom and evaluating the effect of wave interference under PMM test conditions. These tests were

conducted systematically to evaluate specific points of interaction relating to the wave profile, wave steepness and the corresponding PMM path. It is to the author's knowledge there has been no study that has been conducted in such a systematic way. This provided detailed insight into key factors affecting manoeuvring, as well as the computational demand required for extensive manoeuvring CFD studies. This in turn leads to the final aim and to how this aim was achieved.

The final aim was focused optimisation and was presented as follows:

- *Conduct a fully automated optimisation on a parametric vessel for optimal manoeuvring*

As with the previous aims, this aim required multiple stages to be achieved, which was built up by chapters 5, 6, 7 and 8. Each of these chapters focused on a specific point of this aim. Chapter 5 focused on the development of fully *parametric vessel,* by using the software package CAESES from Friendship Framework. However, further analysis to develop it automated optimisation methodology required the validation and verification of the hull form created in this fully parametric setup. This hull form was chosen to be the NPL hull, which was evaluated using a technique developed for the second aim. Following this a method to find the *optimal manoeuvring* vessel was needed. To achieve such an objective two unique and novel equations were developed based upon the knowledge gained through the previous aims. This utilised a simple genetic growth methodology to find these equations that matched a large results ball of CFD simulations, while remaining flexible to varying geometry and accurate enough to be used in an optimisation. Upon finding these novel equations they were integrated into the fully parametric setup to create a *fully automated optimisation* setup. Upon achieving this automated setup, the NPL hull form was optimised for manoeuvring in three optimisation cycles. The first focused on Y force, with the second on Z moment, and the final a multi-objective of both. Although the optimisation used the unique equations developed in chapter 6, the optimum designs was re-evaluated in CFD to validate these results. These optimisations found substantial gains over the base parent NPL hull.

Following these optimisations, a further set optimisation cycles was conducted focused on a completely unique hull form. This optimisation utilises completely different constraints, along with a completely novel hull form to test the flexibility of the automated optimisation setup. These optimisation cycles found that the equations and methodology developed was both stable and accurate. This approach is considerably novel, as these equations purely rank the various hull iterations with respect to one another. This ability to rapidly evaluate these hull

forms significantly improve the flexibility at the early design stage to achieve ever greater low-carbon vessels.

The final stage for this aim was to apply these optimised hull forms in the real-world test. This test are fully free running turning circle tests to present the performance improvements obtained from the NPL hull optimisation. To conduct such a test completely new CFD setup was used, with key parametric volumes been generated from the previous aims. Along with this, the addition of a virtual disc and rudder would also be required to be included. This test results obtained through the optimisation, showing significant improvements of the baseline hull, not only with respect to manoeuvring but also in resistance. In addition to these improvements, this test validated the key dynamics affected by Y force and Z moment and how such factors influence a vessel in real world.

Overall, these simulations have matched the experimental data using novel and unique approaches. Further to this, this research has shown the capabilities of such methodology at the early design stage to gain significant improvements and flexibility for future vessels. Although multiple subjects have been evaluated throughout this research, at each point considerations for how this research may continue were noted. The research that was not selected is discussed and presented below future research.

9.2. Future research

This section provides an overview of how each key section of this research can be further researched and advanced in future work. Throughout this research there has been relatively large range of subjects researched, which eventually became more and more refined as the research progressed. At each key stage of the research there were options as how to progress further, this meant that some aspects of research were put on hold to be considered for future work and research. In addition to this, some aspects were briefly investigated to provide insight into how they would fit into the scope of this research. These investigations are lightly over viewed.

9.2.1. Fully parametric CFD manoeuvring tool

Following on from chapter 10, chapter 4 follows a similar trend for future research. As shown in chapter 4, the speed variation and regular waves were evaluated. To further this research methodology should be evaluated with respect to both shallow water and varying wind conditions. It is common practice for manoeuvring towing tank tests to be conducted in shallow water, therefore advancing this research with respect to shallow water would allow for towing tank validation.

Limited research has been conducted with respect to shallow water manoeuvring combined with waves. This would be a natural progression when evaluating shallow water simulations combined with prior wave-based investigations.

As the methodology developed in chapter 4 uses the MRF and overset method additional motions can be easily captured. These motions include additional roll due to extra wind forces being imposed on the hull form. The additional wind forces may not have great effect on pure hull simulation, however by adding the superstructure these forces can be more accurately captured. This addition of increased wind velocity was considered for this research, to the point where an accurate DTMB 5415 hull form with superstructure was modelled to match the MARIN model. Figure 9-1 shows a 3D render of the model ready to be imported into Star CCM+, with Figure 9-2 showing a photo of the constructed DTMB 5415 hull with superstructure and Figure 9-3 showing the general arrangement used to model the superstructure within Rhinoceros 3DM.

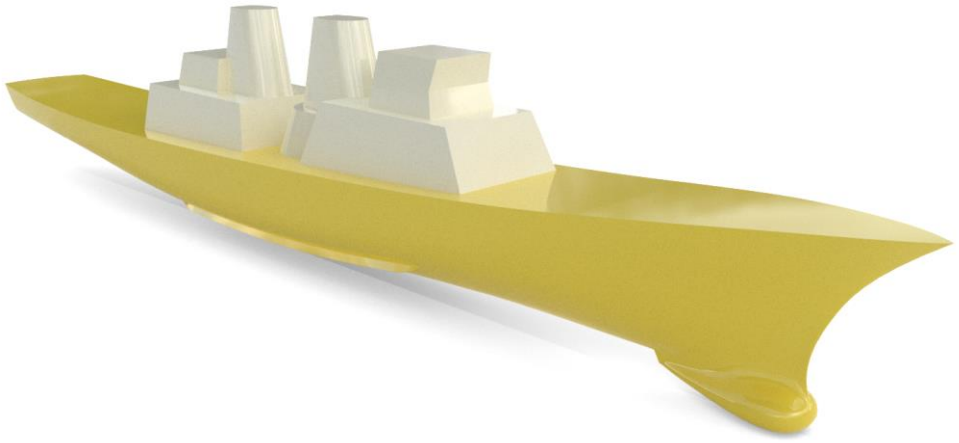

Figure 9-1 Rhinoceros 3DM 3D Render of DTMB 5415 with superstructure

Figure 9-2 DTMB 5415 Free running hull model with superstructure (Toxopeu, et al., 2008)

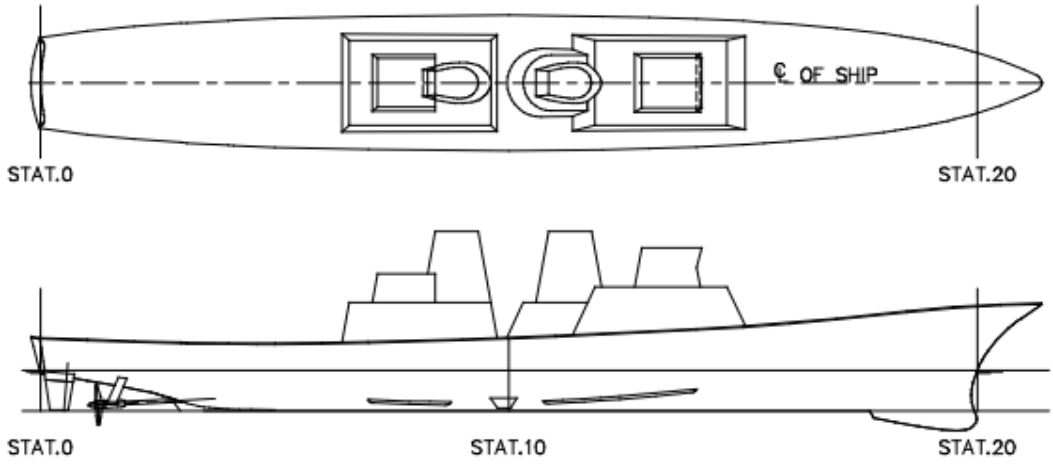

Figure 9-3 General arrangement lines plan showing superstructure used to model hull form shown in Figure 9-1 (Toxopeu, et al., 2008)

This additional research with respect to wind forces will have to be conducted carefully due to the different scaling effects for water and air. With any original hull forms having to be evaluated in full scale to negate any adverse complications unless towing tank data can be used validation.

9.2.2. Ranking Equations

The future work related to the ranking equations directly relates to the future work conducted for both irregular seas and advancements to the fully parametric CFD manoeuvring tool. This future work aims to integrate the results obtained from this future research to broaden the application for the ranking equations. It can be theorised that additional terms can be added or subtracted to account for waves, shallow water and windage. It is also hoped that by combining

research directly related to seakeeping with the prior ranking equations, that a ranking scheme can also be developed for the basic seakeeping characteristics of a given hull. This may be related to human factors or purely numerical simulations.

However, as with the equations for Y force and Z moment these future equations should only be focused on a ranking scheme that can be used in the overall optimisation methodology developed in this research, rather than a direct numerical estimation of its characteristics. This is due to one of the key factors surrounding these equations developed in chapter 6, that the ranking is purely developed on the simple vessel geometry and centre of gravity.

Further consideration for future research may include multihull vessels. This would be less complex when focused solely on seakeeping, however when considering manoeuvring with multi-degrees of freedom this is a considerable challenge. This research however provides further assistance towards the industry, primarily offshore CTV's.

9.2.3. Manoeuvring optimisation

Unlike the prior future work does not require additional direct research to find the results, but rather to expand the optimisation scope presented in chapter 7. This may involve greater variation between the hull forms or the inverse to evaluate the sensitivity and accuracy of the ranking equations. This additional work may also involve significantly expanding the limits of the optimisation, both with respect to the constraints and the input parameters for the global optimisation algorithm.

Additional research should be focused on pushing the boundaries of the variety of vessels that are studied in the optimisation, for example large container vessels or cruise ship hull forms. By evaluating these larger hull forms a greater understanding of how this methodology can be applied within the industry can be drawn. Inversely to this, optimisations focusing solely on a specific region of hull may also be considered for future research.

In addition, it should be considered to include additional manoeuvring tests to evaluate how these optimised factors effect these manoeuvring characteristics. This could include tests such as zig zag manoeuvre, Dieudonne spiral, crash stop and man overboard tests. These various tests help to highlight further the key geometric influencing factors.

10. Appendix i - Development of a CFD methodology for the numerical simulation of irregular sea-states

10.1. Introduction

It has been shown that over 90% of global trade is transported over the sea, thus highlighting the importance the shipping industry plays in a unified global economy (Rahm, 2015). Growing worldwide concern over the volume of emissions and particulate matter (PM) emitted from a ship impacts the brand and corporate responsibility of shipping companies. This is dominantly due to the shipping industry being highly dependent upon the use of fossil fuels to produce the required energy. Due to global use and hunger for fossil fuels, the level of CO_2 in the atmosphere has reached its highest in recorded history. This has led both international and regional organisations, such as the International Maritime Organisation (IMO) and the European Union (EU), to regulate shipping emissions more stringently.

Further to the release of CO_2, it has been estimated that the shipping industry accounts for 8% of global SO_x and 15% of global NO_x emissions annually (Rahm, 2015). It is also the leading industries in releasing dust and soot particles, due to the use of burning heavy fuels (Rahm, 2015). It estimated that global shipping's greenhouse gas (GHG) emissions will have doubled or tripled in the worst case scenario by 2050 (European Commission , 2013).

By accurately modelling a realistic non-linear sea, vessels and marine structures can be optimised with an aim to enhance their performance. This would result in a longer working life and thus an improved lifetime efficiency of the vessel or structure, helping to reduce the marine industry's global emissions. Two examples of utilising real sea way conditions are put forward below:

1. To reduce the added resistance and increase the accuracy of the calculated results for a large container vessel, with the aim of minimising emissions or enabling an alternate power source to be used.
2. To optimise the motion performance of small vessels vital in supporting offshore industries, thus enabling such vessels to continue working safety in ever more varied sea states (Offshore Wind, 2017).

As technology and computational power increases, the marine industry has begun to utilise Computational Fluid Dynamics (CFD) as a common means to evaluate vessel performance over the past few years. Due to the increasing demand on the industry to minimise GHG emissions, a significant focus has been drawn to evaluating vessels characteristics in real world

conditions. However, as technology has only recently allowed such CFD simulations to be conducted, the original benchmark utilised potential flow theories to evaluate such performance in regular or irregular waves. These potential flow methods are limited due to restrictions within these methods, and therefore are restricted in accuracy. Due to the increase in technology and cloud-based simulating, it is becoming ever more realistic for industries to consider running such real-world simulations. Such simulation have significant advantages over the commonly run regular and calm water simulations.

There is limited to no clear literature describing a methodology for simulating and modelling irregular seas with the aim of modelling non-linear sea ways seen in the real-world. It is, therefore, the primary focus of this study to provide a clear and accurate methodology for simulating a non-linear unknown sea way using CFD.

To the best of the author's knowledge, to date, no studies exist which provide and clear a precise methodology for simulating any irregular sea state within CFD, along with a discussion on the key factors affecting the accuracy of the simulation.

It has been highlighted by Shen et al. (2014-A) that the use of unsteady Reynolds-averaged Navier Stokes (URANS) CFD coupled with irregular seas can achieve accurate results with a limited number of simulations. Within Shen et al.'s (2014-A) work, a model scale vessel was simulated in long crested irregular seas, although a high accuracy relating to the results was achieved, the methodology and running time constrain the applicability of the research. As the research focused on long crested waves, a significant reduction in compatible hull designs is caused. This is due to long crested irregular seas being most commonly seen in the open ocean with a significant time required for such sea states to develop. In addition, the use of the superposition method to generate free surface limits the complexity that can be seen in truly non-linear sea ways. Ming et al (2013) applied a similar methodology while investigating oblique irregular seas in model scale to derive multiple transfer functions and obtain an even higher definition for the added resistance. Nevertheless, as both methods utilised the superposition method for modelling the free-surface, along with a limited time period and a predetermined free-surface cut, the ability to model a multi order sea way with the methods proposed within these papers fails to be applicable outside of such research.

Therefore, both Ming et al (2013) and Shen et al. (2014-A) show the advantages of running such simulations to achieve a greater overall picture of the vessels thrust requirements and motion characteristics in real sea conditions. However, both papers do not develop or propose a clear methodology that can be applied in modelling irregular seas and applied within the industry for advanced analysis with ease.

Hence, it is with this knowledge that this study aims at closing this gap and proposing a clear and accurate methodology, for multiple industries, to model and maintain any desired sea state within CFD. It is also hoped that the study will clarify the advantages and disadvantages in modelling irregular seas.

The study below is organised as follows. Section 10.2 covers the numerical setup for modelling irregular seas is provided, with a preliminary background into the statistical features of irregular seas and how they can be utilised to define the key features in the CFD simulations. From these values, the best practices and definitions for defining and modelling such simulations are provided for use in Star CCM+, along with other applicable CFD solvers. Following this, Section 10.3 provides a verification study conducted to investigate the ability of the numerical setup to maintain and model the desired sea state. Section 10.4 provides a discussion on three different sea state simulations, along with both the practical application of such simulations and application within a CFD code, this case being Star CCM+. Finally, Section 10.5 will provide the overall conclusions drawn from this study, providing an overview of the best practices for defining such simulations and a discussion on the applications within the industry. Future research using the methodology is put forward in this study will be proposed in the final sections of this paper 10.6.

10.1.1. Irregular Seas Literature Review

As advancements in technology and the ever-increasing concerns of achieving the efficiency aims put forward by the International Maritime Organisation (IMO) (IMO, 2021) draw closer, the need to accurately model and study ever more complex resistance models comes forward. It is therefore vital that knowledge of improving both performance and motions is easily at hand when in the early design stages. The seakeeping characteristics of a vessel can be obtained by numerical analyses, towing tank experiments with the model-scale ship and full-scale tests at sea. The literature offers a wealth of numerical techniques which can be utilised to assess both the seakeeping behaviour and added resistance of vessels.

As indicated by (Tezdogan, et al., 2014b), (Beck & Reed, 2001) estimate that in the early 2000s, 80% of all seakeeping computations at forward speeds relied on strip theory, due to its rapid solutions. It is commonly known that strip theory provides the advantageous of being applicable to most conventional ship geometries. However, (Newman, 1978) discussed that the traditional strip theory-based methods are subject to some deficiencies in long incident waves and at high forward speeds. (Tezdogan, et al., 2014c) highlighted that this is because of the evolution of forward speed effects and the treatment of the diffraction problem in such theories. (Faltinsen & Zhao, 1991) also state that strip theory is dubious when applied at high

Froude numbers, because it takes into account the forward speeds in a simplistic manner. Differences between strip theory and experiments for higher Froude numbers, or highly non-wall sided hull forms, have therefore motivated research to develop more advanced theories, such as the 3-D Rankine source panel method and CFD-based RANS methods (Beck & Reed, 2001).

(Simonsen, et al., 2013) highlight that the effects neglected in the potential flow theory such as breaking waves, turbulence and viscosity should be directly taken into account in the numerical methods when more accurate results are sought. Such effects become more pronounced in extreme sea conditions, such as large sea states and high Froude numbers. CFD-based RANS methods, for example, are very good alternatives to the potential flow theory since they can fully incorporate all the nonlinearities, including viscosity and free surface both in regular and irregular seas.

It is discussed by multiple sources that there is no clear and simple method for calculating added resistance in a sea way for all vessel sizes and types. As stated by (McTaggart, 1997)"*added resistance is the longitudinal component of the steady wave drift force. Since added resistance is a second-order phenomenon, it is significantly more difficult to predict than first-order phenomena such as ship motions*". As is commonly known within this area of research, numerical methods for calculating added resistance can be split into two main areas, 'Near-field' and 'Far-field'. 'Far-field' methodologies are based upon the momentum flux being evaluated across a vertical control surface of infinite radius encompassing the ship. Conversely, a 'Near-field' methods predict wave drift force by direct integration of the pressure distribution over the ships wetted surface. (Seo, et al., 2013) can be referred for a broad literature reviewing these two major approaches to predict added resistance in waves. However, both methods are flawed in accurately calculating the added resistance, as they are defined upon a 1st order basis. It is therefore becoming ever more common that added resistance calculations are being conducted within the area of CFD to begin accounting for greater nonlinearities seen in complex flow models.

As computational power increases and becomes ever more available, recent studies have investigated the added resistance problems of vessels using a CFD-based RANS solver. (Orihara & Miyata, 2003), for example, developed a CFD code, called WISDAM-X, to calculate the added resistance of vessels due to waves. They used overset mesh in order to simulate the interaction of the vessel with the incoming waves generated at inlet. The CFD tool was validated for a container ship against experiment and the motion and added resistance results were found in good agreement. They finally showed that the software package can be

used by naval architects as a ship design tool with adequate engineering accuracy. More recently (Tezdogan, et al., 2015) predicted the added resistance of a full-scale KCS ship in regular head seas using a commercial CFD-based software package (Star-CCM+) at typical design and slow steaming speeds.

The methods used by (Orihara & Miyata, 2003) and (Tezdogan, et al., 2015) applied a similar methodology for modelling and calculating the added resistance, in addition to validating the results using known vessel motions. However, it has been highlighted by (Bertram, 2016) that the process of estimating added resistance through motion validation may indeed be an inaccurate methodology. (Bertram, 2016) continues to discuss key factors that should be considered when aiming to accurately calculate added resistance, these include "transfer functions of added resistance" along with "arbitrary spectrum of natural seaway, able to represent wind sea, swell or combination of both" (Bertram, 2016), along with resistance affected by manoeuvring forces and considering both engine & propeller dynamics. Thus, stressing that although a result may be achieved through motion validation, the method fails to account for the second order nature seen in added resistance. It therefore further brings forward the question and validity of using multiple regular seas to accurately calculate the required coefficients that can be applied outside of individual simulations.

From this consideration, an interest in conducting such resistance simulations has changed focus towards using irregular seas to derive such coefficients. It has been highlighted by Shen et al. (2014-A)that the use of CFD URANS coupled with irregular seas can achieve accurate results with a limited number of simulations. Within (Shen, et al., 2014-A) work, a model scale vessel was simulated in long crested irregular seas, although a high accuracy relating to the results was achieved, the methodology and running time constrain the applicability of the research. As the research focused on long crested waves, a significant reduction in compatible hull designs is caused. This is due to long crested irregular seas being most commonly seen in open ocean with a significant time required for such sea states to develop. In addition, the use of the superposition method to generate the free surface limits the complexity that can be seen in truly non-linear sea ways. (Ming, et al., 2013) applied a similar methodology while investigating oblique irregular seas in model scale to derive multiple transfer functions and obtain an even greater definition for the added resistance. Nevertheless, as both methods utilised the superposition method for modelling the free-surface, along with a limited time period and a predetermined free-surface cut, the ability to model a multi order sea way with the methods proposed within these papers fails to be applicable outside of such research.

Therefore, both (Ming, et al., 2013) and (Shen, et al., 2014-A) show the advantages of running such simulations to achieve a greater overall picture of the vessels thrust requirements and motion characteristics in real sea conditions. However, both papers do not develop or propose a clear methodology that can be applied in modelling irregular seas and applied within the industry for advanced analysis with ease.

Hence, it is with this knowledge that this study aims at closing this gap and proposing a clear and accurate methodology, for multiple industries, to model and maintain any desired sea state within CFD. The study in Chapter 10.5 will clarify the advantages and disadvantages in modelling irregular seas.

10.2. Numerical Setup

Within this section, the key aspects and difficulties in accurately modelling, maintaining and simulating irregular seas will be discussed. In addition, a clear methodology for simulating truly non-linear irregular seas will be proposed based on the statistical and simulated analysis.

As seen from the literature, Computational Fluid Dynamics (CFD) has not yet been extensively used to estimate and model irregular seas for various types of investigations. Thus, the literature surrounding a methodology for such a simulation is significantly lacking.

The most commonly used approach to generating irregular seas in the current literature is to use the superposition method with a specified number of waves and respective periods to model a predetermined sea state. This was used to great effect by Shen et al. (2014-A). However these simulations only encompass a small time period and a prescribed wave pattern. It is therefore aimed with this methodology to provide a set of guidelines to address the issues faced when modelling for truly unknown non-linear irregular seas, and therefore enable a clear representation of real sea states to be modelled, these unknown sea sates can also be described as an undefined sea state. This lack of predefinition before simulating the waves ensure truly non-linear behaviour is being captured, and in turn real world conditions.

The diagram in, Figure 10-1, shows the overall path that is presented in this section, along with the outputs and required user inputs to model a stable simulation. The user inputs are displayed on the left hand side, with key outputs following the path down with only the potential error limits being presented on the right hand side, these will be discussed in greater detail in Chapter 10.2.1. The path described in Figure 10-1 is split into three key sections. The initial section focuses on using an in-house MATLAB code to generate a time history of a JONSWAP spectrum defined by the key variables, such as significant wave height (H_S) and peak period (T_P). The in-house code will continue to post-process the generated time history

and produce the key variables used further on in the methodology presented. The methodology described can be easily modified to be used for other spectrums. This analysis provides key wave data that is inputted into the second section which is the meshing and domain definition for the CFD. The final part is the running and monitoring of the simulation. These sections are further elaborated on below, with a primary focus on the two initial setup sections of the path.

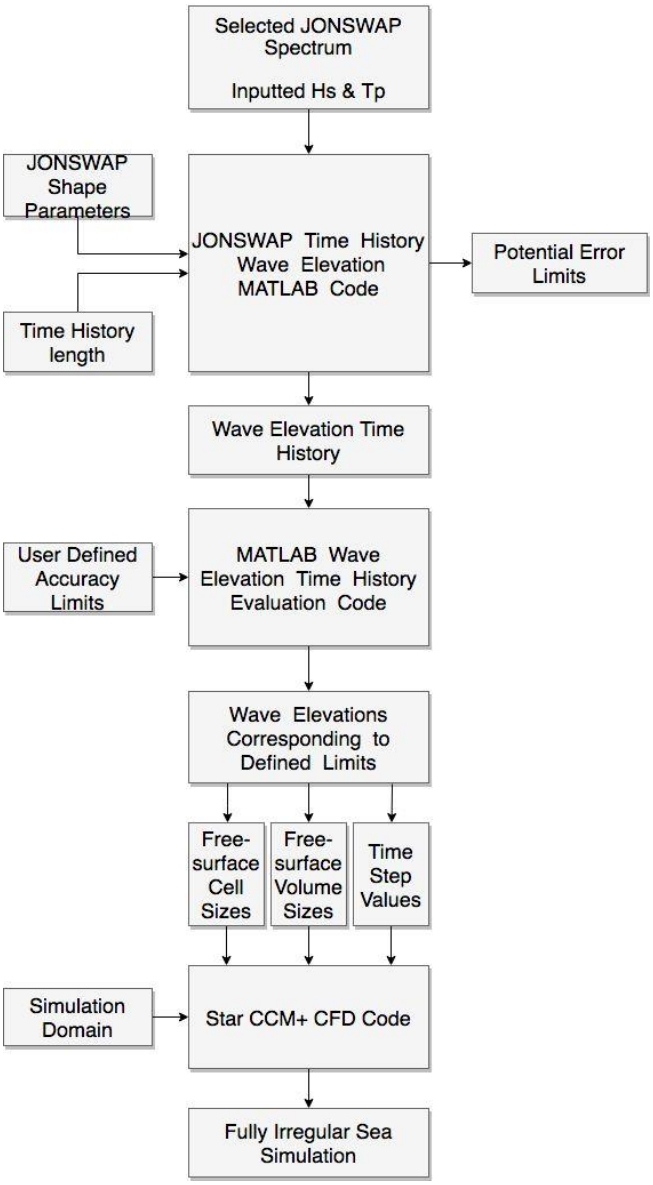

Figure 10-1 Irregular sea methodology path

10.2.1. MATLAB Time History Analysis

To successfully model and maintain a fully non-linear irregular sea state in CFD, an initial investigation into the observed wave elevations for a given sea state must be conducted. The investigation will provide key data that is used to calculate important input variables that can

be implemented into a CFD code later in the methodology. This section will offer a description of the schemes and the in-house MATLAB codes used to develop a time history for the JONSWAP spectrum, along with the approaches used to calculate the various cells sizes, volumes and time step.

As highlighted above, this investigation focuses on the JONSWAP spectrum (S_J). However the methodology discussed can be used with any other wave spectrum provided the key steps are followed, as shown in Figure 10-1. To successfully model an unknown sea state within CFD the range of wave elevations must first be found and analysed, this, in turn, will enable the best selection of cell sizes and volumes to be chosen. This is accomplished by coding the desired wave spectrum to produce a time history with respect to wave elevation.

The base equations for the code to define the spectrum were those used within Siemens PLM Star CCM+ CFD code for generating irregular seas, these definitions were selected to ensure the in-house code, and CFD codes match when generating the time histories, and thus remove a variable when evaluating the methodology discussed later. The basis Pierson-Moskowitz spectrum for the JONSWAP spectrum is given in equation (10-1), along with the angular spectral peak frequency in equation (10-2), with ω defining the wave frequency. The formulation for the JONSWAP spectrum used in this analysis is shown in Eq (10-3) (CD-Adapco, 2017b), with H_s defining the significant wave height in metres (m) and T_P defines the peak period in seconds (s). For which A_γ equation (10-4) is the normalising factor, with γ describing the non-dimensional peak shape parameter.

$$S_J(\omega_w) = A_\gamma S_{PM}(\omega_w)\gamma^{exp\left(-0.5\left(\frac{\omega_w-\omega_{wp}}{\sigma\omega_{wp}}\right)^2\right)} \tag{10-1}$$

$$\omega_{wp} = \frac{2\pi}{T_p} \tag{10-2}$$

$$S_{PM}(\omega_w) = \frac{5}{16}\left(H_s^2\omega_{wp}^4\right)\omega^{-5}exp\left(-\frac{5}{4}\left(\frac{\omega_w}{\omega_{wp}}\right)^{-4}\right) \tag{10-3}$$

$$A_\gamma = 1 - 0.287\ln(\gamma) \tag{10-4}$$

The in-house code is defined in three sections, the initial section establishes a range of angular frequencies, the second defines the wave spectrum in the frequency domain, in this case,

JONSWAP, and the final section converts the defined spectrum into wave elevation with respect to time history. The equations and methodology used to convert the spectrum into a time history are those used by (Branlard, 2010), equations (10-5), (10-6) & (10-7) show the conversions used, with $\eta(t)$ representing the amplitude with respect to time, A_j defining the amplitude at a specified frequency and ε_j the randomness factor. An example of a completed time history elevation plot is shown in Figure 10-2 along with the complete code is shown in Appendix ii. along with the graphical statistical output shown in Figure 11-1.

$$\eta(t) = \sum_{j=1}^{N} A_j \cos(2\pi f_i + \varepsilon_j) \tag{10-5}$$

$$A_j = \sqrt{2S_J(f)\Delta f} \tag{10-6}$$

$$\varepsilon_j = rand(0\,, 2\pi) \tag{10-7}$$

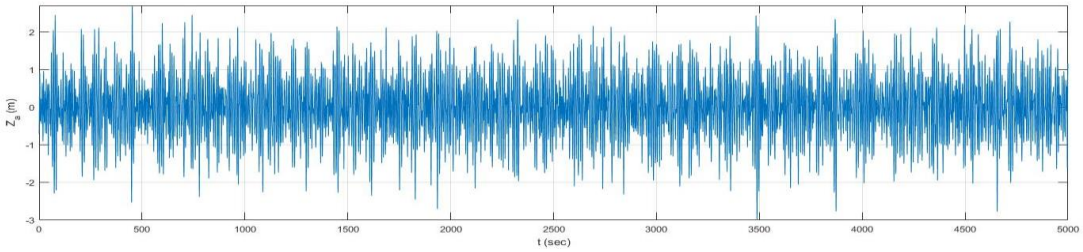

Figure 10-2 Time history wave elevation plot (Hs = 3.25 m & Tp = 9.7 s)

The raw wave data generated from the in-house code is evaluated in two ways. The first evaluation is applied through a second in-house function which uses the generated wave data, along with a further set of simulated time histories to produce upper and lower bounds of the theoretical potential error seen for a given length of time. This can be key to assessing the completed CFD simulations accuracy, as the simulation time may not correspond to a time history with a calculated significant wave height matching the inputted significant wave height. Figure 10-3 shows multiple runs of the second in-house function at various lengths of times and the theoretically calculated maximum & minimum observed error for 1000 sets of time histories. This figure also helps to highlight the importance of having a long simulation time to minimise any observed error, this is discussed in further detail below.

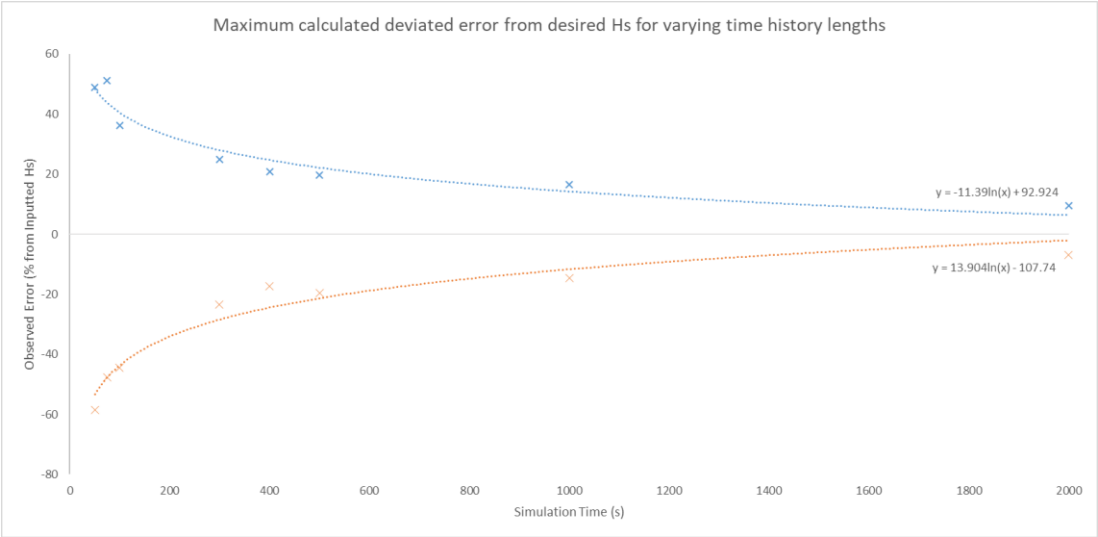

Figure 10-3 Theoretically calculated error limits from defined Hs with respect to simulated time (SS-5)

As seen from **Error! Reference source not found.**, combined with Figure 12-1, Figure 12-2, Figure 12-3, Figure 12-4 and Figure 12-5 in Appendix iii, the simulated time histories generated from the in-house code have a consistent pattern. As the theoretical time history length decreases, the maximum error observed increases. This is due to the reduced balance between large and small wave heights and wave lengths. This is a key factor to consider, as the shorter the observed time history for the simulation the greater the potential error will likely be when calculating the significant wave height. This however does not mean that the time history did not produce an accurate representation of the desired sea state, just that the time history was too narrower view to cover the whole significant wave height for that sea state. This point, produced through this evaluation, is one of the main reasons why this study will go on to use longer time histories to validate the methodology provided below, to ensure that lower run times will capture all the key characteristics of the simulated sea state.

The second evaluation provides a method to set upper and lower limits on the generated time history wave elevations. This is done by evaluating the distribution of the wave heights and understanding the providence of each wave and its overall effect on desired Hs. This step is the key for an engineer to be able to apply practical knowledge of the type of simulation, and the impact various factors have on the simulation. Based upon the inputs of the user, the upper and lower limits for wave elevation are calculated, these may be for example the maximum and minimum wave elevations observed in a defined irregular seaway, or the upper and lower 5% of wave heights seen in the time history. The lower limit will correspond to the minimum wave elevation being modelled within the simulation, while the upper limit will define the

maximum and minimum heights of the fine free-surface region for mesh generation, this is discussed in further detail below in the mesh generation section.

These limits allow the calculation of key CFD variables along with a further potential error limit within the simulation. An error exceeding the combination of these two evaluations implies that there is a greater problem with the overall simulation, and it must, therefore, be evaluated.

$$s_p = 2\pi H_s/(gT_p^2) \tag{10-8}$$

$$s_m = 2\pi H_s/(gT_z^2) \tag{10-9}$$

These limits are used in partnership with equations (10-8) & (10-9), which have been put forward by Arena et al. (2010) to estimate the wave steepness (S_P & S_m wave steepness factors with respect to peak period and zero mean crossing period) in an irregular sea based upon the either the peak period, T_p equation (10-8), or the respective zero-up-crossing mean period (T_z) to S_m for equation (10-9). These equations coupled with the recommendations put forward by (CD-Adapco CSP, 2017) and common best practices when modelling waves within CFD, both the Z and X lengths for the smallest cell in the free-surface region can be calculated. This is completed all at once within the second in-house code when the time history is being analysed, along with the estimations of various time steps as described in section 3.7. A worked example is shown in Appendix ii for Hs = 5 (m), Tp = 12.4 (s) with key calculated values highlighted in red.

Due to the complexity and non-linear characteristics of an irregular sea way, the mesh refinement volume which defines the smallest cell height should aim to encompass 95% of the waves, with the extra 5% covering the tallest waves. The second mesh size control volume has a cell height twice that of the previous volume, this ensures that the waves seen in this volume will be sufficiently refined for. The volume is set to encompass this region mainly due to the non-linearity seen in irregular seas, namely small wavelengths and wave heights are not limited to the mean free surface, this can be seen in Figure 10-4. It is therefore essential in maximising the accuracy of the simulation these waves must be modelled as efficiently as the smallest waves entering the domain. It is for this primary reason that the mesh control volume defining the minimum cell height aims to encompass 95% of the wave heights generated throughout the simulation, with the second region aiming to capture 99% of waves and the third domain 99.75%, respectively.

Figure 10-4 depicts a 2000m wave cut, from the simulation previously used as an example, with overlays calculated based on a significant wave height of 5m and a peak period of 12.4 seconds. As can be seen, the largest number of waves are encompassed within the first volumetric region, with only the highest waves exceeding the limits of the first region.

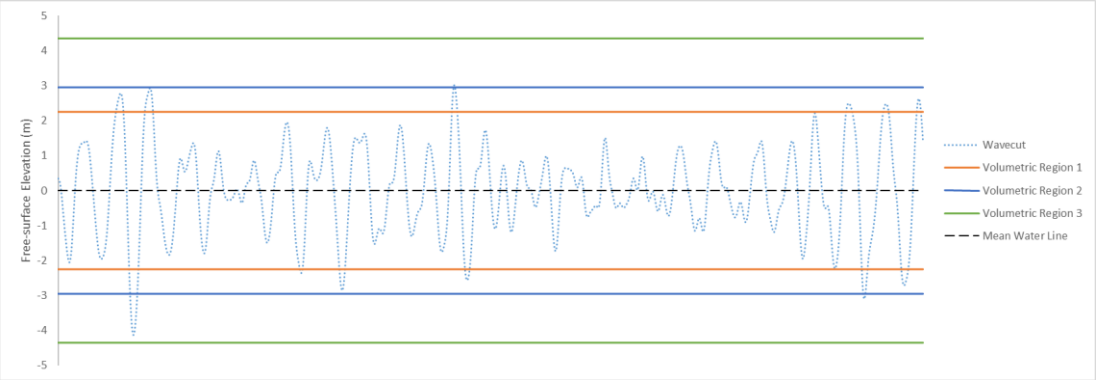

Figure 10-4 SS-6 Wave cut profile overlaid with calculated refinement volume Z heights, as calculated in Table 13-1

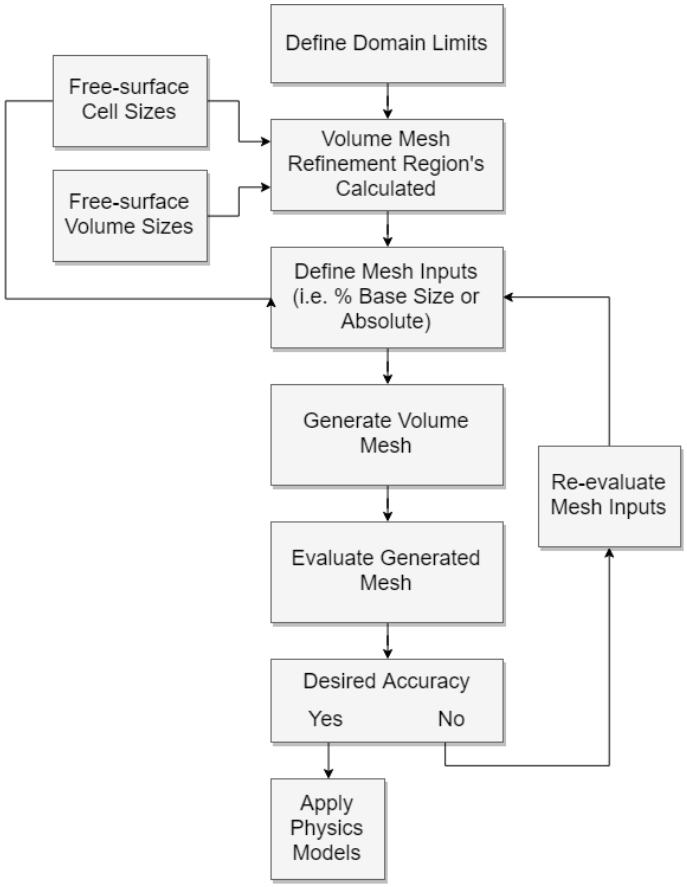

Figure 10-5 CFD Free-surface mesh setup path with calculated inputs from MATLAB code

10.2.2. Domain Size

To ensure stable simulations and only investigate the effects of varying the mesh strategies, the domain limits were defined by the recommendations proposed by ITTC (2011a). In addition to these recommendations, the best practices advised for use in Star CCM+ (CD-Adapco, 2017b) were also applied. However, it is recommended to apply variuos methods to achieve the best results. Further examples of such reccomendations are seen in Table 10-1**Error! Reference source not found.**.

Table 10-1 Boundary locations based upon regular wave simulations for vessels based upon the length between perpendiculars (LBP)

References	*Upstream*	*Down Stream*	*Up*	*Down*	*Transverse*
(Y.H. Ozdemir, 2014)	2 LBP	3 LBP	2 LBP	2 LBP	2 LBP
(C.D. Simonsen, 2013)	0.6 LBP	2 LBP	Undefined	Undefined	1.5 LBP

10.2.3. Mesh Setup

The mesh setup path for the free-surface is shown in Figure 10-5. This is in addition to the normal procedures used for modelling the desired mesh in Volume Of Fluid (VOF) CFD simulation while utilising a derivative of the trimmed mesh model.

To ensure an adequate mesh is generated, the trimmed mesh method should be employed. This method is commonly used for complex mesh problems, with a focus on VOF and free-surface interactions.

To accurately capture all waves to the minimum desired accuracy the cell height and length must be calculated to match the smallest waves that will be modelled. As highlighted above the Minimum Wave Amplitude (MWA) is defined as the lower limit for smallest wave amplitude to be modelled. Based upon the recommendations put forward by Star CCM+, a minimum of 12 cells (CD-Adapco CSP, 2017) should cover the full wave height, defined as the twice MWA. From both the recommendations coupled with the MWA value a minimum cell height can be calculated. Through this investigation, it was found that a minimum of 16 cells per wave height ensures improved stability, in addition to allowing an error margin for the smallest waves created.

The minimum wave height can be further coupled with Equation (10-8) to estimate the minimum wavelength. This wavelength is used to calculate cell values for both X & Y by applying both the ITTC (2011a), along with Star CCM+ recommendations. It was found that maintaining a constant cell value for both X & Y in the finest mesh refinement region significantly improved simulation stability along with overset mesh interaction. The transvers cell length, Y, may be increased to twice that of the longitudinal in the intervening mesh refinement volumes to reduce the total cell number, however, for best practice, it was found that maintaining a single value for both the longitudinal and transvers proved most effective.

Both the longitudinal and transverse cell lengths may be increased compared with the recommendations to reduce the total cell count. However a maximum aspect ratio between Z & X should not be considered higher than 15. As significant free surface instabilities will appear and create a diverging simulation.

As seen in Table 13-1 in Appendix iv, key parameters such as the overall domain size, along with the respective sea state characteristics are used to estimate the minimum number of cells within the free surface. By utilising equation (10-8) the average wave steepness for the specified sea state can be calculated. This coupled with the MWA value found through the preliminary post-processing analysis derives an estimated minimum wavelength. Both the minimum desired wave height to be modelled and the derived minimum wavelength allows a calculated absolute cell height and length (longitudinal and transverse) to be found. An initial mesh number within the first free surface refinement can be estimated based upon the total volume within that refinement and the respective cell volume defined by the calculated X, Y & Z lengths in the simulations Cartesian coordinate system.

As recommended by Star CCM+ (CD-Adapco, 2017b) a minimum of 8 cells in the Z height should be used when moving between the various mesh refinement volumes. However, it was found that 8 cells failed to allow complete coverage of a fully developed seaway. Therefore, as each free surface mesh refinement volumes cell height doubles with respect to the previous volume, the number of cells required in the Z direction to cover 99.5% of the propagating waves can be calculated. For the case shown in Table 13-1, the volumes upper bounds were defined as 4.35 (m) due to the post-processing data showing a wave amplitude of 4.25 (m) encompasses 99.65% of waves seen within the wave cut. This equated to an intermediate cell number of 16, twice that recommended by Star CCM+. It is vital to note that this value is subject to change depending on the spectrum defined and if any parameters, such as the peak shape parameter, are varied from the predefined JONSWAP spectrum.

As recommended by Star CCM+ along with (Jin, et al., 2017) the cell growth rate within the domain should be set to such that there are no abrupt or extreme changes in neighbouring cells, ensuring a steady progression from the free surface to the outer domain regions. This helps to mitigate any issues caused by freak waves or wave heights exceeding the limits of the produced in the post-processing of the in-house code.

10.2.4. Governing Equations

The averaged continuity and momentum equations may be written in tensor form and Cartesian coordinates for incompressible flows without body forces as shown below (Ferziger & Peric, 2002):

$$\frac{\partial\left(\rho\bar{u}_i\right)}{\partial x_i}=0 \tag{10-10}$$

$$\frac{\partial\left(\rho\bar{u}_i\right)}{\partial t}+\frac{\partial}{\partial x_j}\left(\rho\bar{u}_i\bar{u}_j+\rho\overline{u_i'u_j'}\right)=-\frac{\partial\bar{p}}{\partial x_i}+\frac{\partial\bar{\tau}_{ij}}{\partial x_j} \tag{10-11}$$

in which τ_{ij} are the mean viscous stress tensor components, as shown in Eq. (10-12)

$$\bar{\tau}_{ij}=\mu\left(\frac{\partial\bar{u}_i}{\partial x_j}+\frac{\partial\bar{u}_j}{\partial x_i}\right) \tag{10-12}$$

and p is the mean pressure, $\bar{u}_i$ is the averaged Cartesian components of the velocity vector, $\rho\overline{u_i'u_j'}$ is the Reynolds stresses, ρ is the fluid density and μ is the dynamic viscosity.

To model fluid flow, the solver employed uses a finite volume method which discretises the integral formulation of the Navier-Stokes equations. A predictor-corrector method is used to link the continuity and momentum equations within the RANS solver.

10.2.5. Physics Modelling

The turbulence model chosen for these simulations and investigations was the standard K-Epsilon model. This model is extensively used within the industry for multiphase flow and wave modelling, from regular, super position and irregular seas (CD-Adapco, 2017a).

To ensure accurate modelling of the multiphase flow the use of the ‘Volume Of Fluid’ (VOF) method has been applied. This method has been used to great effect in modelling both regular

and irregular superposition waves by (Tezdogan, et al., 2016) and (Shen, et al., 2014-A)respectively. The VOF model key assumption is that the same basic governing equations as those used for a single-phase problem can be solved for all the fluid phases present within the domain, as it is assumed that they will have the same velocity, pressure and temperature.

The second-order convection scheme was applied in all simulations to increase resolution between the interfaces of the different phases.

Although the simulations within this section have not applied any rigid bodies, such as vessels, these can be easily modelled though the use of the Dynamic Fluid Body Interaction (DFBI) model. The model enables full six degrees of motion to be captured through the calculations of the excitation forces and moments acting on the rigid body (CD-Adapco, 2017b).

10.2.6. Boundary Conditions

To ensure stable flow, along with the quickest flow solution, the boundaries must be defined and selected according to recommendations put forward by ITTC (2011a)for similar flow problems.

For flow entering the domain, the use of a velocity inlet over mass flow inlet is recommended, with the opposing boundary defined as a pressure outlet. The respective positioning of inlet and outlet is directly related to the apparent wave and flow heading, best practice relating to such positioning is defined by CD-Adapco (2017b).

Flow problems focused on either head seas or following seas. It is advised to use a symmetry plane (half domain) through the centre, due to the increased mesh numbers seen when meshing. For problems outside of such headings, a full domain should be used.

The top, bottom and outer side may be defined as multiple boundary types, such as velocity inlet, slip wall or symmetry plane. Advice relating to best practice may be seen in CD-Adapco (2017b).

Damping should be applied to both the Outlet and Side, with the application of ‘forcing’ being used at the Inlet, Side and Outlet boundaries (Royal Institution of Naval Architects, 2018). The lateral component should be forced to zero towards the Side boundaries, with the vertical component forced to zero at the Outlet, thus mitigating any wave reflections and over damping within the domain. Ensuring all wave energy is damped correctly on the pressure outlet and sides is key to maintaining accurate wave propogation and negating any negative wave reflections.

10.2.7. Time Step Calculation

Unlike pure resistance or regular sea simulations, the time step is over refined for the majority of the simulation to ensure the minimum wave modelled for is accounted for in the time step selection.

Multiple methods for calculating the time step are used. These are primarily based upon the minimum desired wave height, as used in the mesh generation.

Unlike most simulations conducted within this region of research, the Courant Number is not the primary method for estimating the simulations time step. This is not due to its lack of importance, it is due mainly to the time step being focused upon the smallest wave within the domain, and therefore the time step will be significantly lower than normally estimated.

Equation (10-13) uses the recommendations provided by ITTC (2011a) with an increased power to reduce the time step value to compensate for the smaller waves entering the domain. However, this method lacks accuracy relating to the specific sea state and the desired accuracy aimed for, as it is based upon regular sea simulations with an increase in power from the recommendation put forward by (ITTC, 2011a), with $T_{Min\,\lambda}$ defining the minimum wavelengths period. Therefore, in this work Equations (10-14), (10-15) & (10-16) were defined to maintain a relationship between a specific sea state and the accuracy desired for.

$$\Delta t_{\lambda} = \frac{T_{Min\,\lambda}}{2^9} \tag{10-13}$$

$$\Delta t_{H} = \frac{0.5 * T_{Min\,\lambda}}{2.5 * NZ_{Min\,\lambda}} \tag{10-14}$$

$$\omega_{E} = \frac{2\pi}{T_{Min\lambda}} - \left(\frac{4\pi^2 U}{{T_{Min\lambda}}^2 * g}\right) * Cos(\theta) \tag{10-15}$$

$$\Delta t_{fe} = \frac{2\pi}{\omega_E 2^9} \tag{10-16}$$

Equation (10-14) uses the advice provided by Star CCM+ (CD-Adapco, 2017b) to estimate the time step directly relating to the minimum desired wave height and the number of cells in the vertical direction. It is recommended that the free surface should travel no more than 40% of the cell height per time step. Assuming a constant vertical velocity across half the wavelength from peak to trough an estimated time step can be drawn up relating to the number of cells used for the minimum wave height ($NZ_{Min\,\lambda}$).

To ensure simulations can be accurately maintained in varying wave headings (with head seas defined as θ = 180), equations (10-15) & (10-16) are drawn up to calculate the time step based upon the angular encounter frequency (ω_E), which is calculated with respect to the vessel's speed (U). As in the previous time step calculations the frequency is based upon the minimum desired wave height.

Equations (10-13) to (10-16) highlight the minimum required to maintain a constant and stable free surface. However these time steps may be increased to reduce computational time. It is therefore recommended that a preliminary time step study should be considered.

The use of first-order temporal scheme is advised over second-order to discretise the unsteady term in the Navier-Stokes equations due to potential instability issues arising when coupled with overset regions.

10.2.8. Run Time Estimation

As highlighted above, it is recommended to have a minimum of 300 waves encountered, as defined by ITTC (2011b) for model scale tests and at least 1.5 hours' testing on sea trials. This ensures a large enough range of waves has been encountered to establish an accurate calculation of the significant wave height. As the number of waves encountered reduces, the accuracy of the calculated significant wave height begins to decrease, this can be seen in Figure 10-3 when comparing the lower and higher run times based on the theoretical margins. This selection of encountering 300 waves can equate to a significantly high run time, with a complex and high mesh number simulation.

This may not be feasible and therefore simulation time may be required to be reduced to become a practically possible. It has been discussed by (Mousaviraad, 2010) that it is possible to calculate a transfer function for a vessel in an irregular seaway using a single CFD simulation, as highlighted previously. Within the work conducted by (Mousaviraad, 2010), the time history used only encompasses around a 10-second period with predefined wavelengths and frequancies. However, by reducing simulation time and cutting the number of waves encountered there is a high potential for errors appearing in the calculated H_s, when limited to such low run times in irregular seas. For (Mousaviraad, 2010) to overcome the limited time history and calculate the transfer funtions, the application of Discrete Fourier Transform (DFT) was used. This enabled limited time history to be used and based upon to calculate the results.

Therefore, to ensure a stable sea state has occurred, along with the desired Hs, a minimum of 100 waves should be encountered when investigating non-linear irregular seas. This was the

minimum value selected for this study, however even a further reduced number of encounter waves may be specified if the mesh and time step definitions match those described above. The key factor to consider when running such low encountered wave simulations is the inaccuracy of the observed significant wave height from the recorded time history. The selection of lower run times should be considered with respect to the patterns observed in Figure 12-4 as an example.

10.3. Verification Study

In this study the primary focus has been on the free surface mesh refinement and optimising this region for irregular seas. To further verify the work conducted, along with the methodology proposed in the study above, a verification study utilising the methodology devised by Stern et al (2001) has been conducted. As there are no vessels within the study, the verification will focus solely on the free surface refinement and its ability to maintain the inputted significant wave height.

The domain for the verification study was created in mind of having a small vessel, around 25m overall length, within it. This is both for reducing the total number of cells required through minimising the domain volume, and verifying a similar sized domain as used in the case study later in this study. The domains length was defined as 1.5 λ (wave length) of a single regular wave with an equivalent wave height of the desired H_s. All boundaries were defined as stated above.

Each simulation was run with no current or wind, and solely focused on the waves transiting the domain due to their own speed. The simulations were running for a total of 1500 seconds, ensuring around 300 seen waves. Simulating over 300 waves ensures that the calculated Hs will not be distorted due lower run times, as can be estimated from Figure 12-4. Further to this, each simulation utilised the test setting in the Irregular Wave model within the CFD code, ensuring each simulation had the same incoming wave profile for each simulation. Thus, ensuring the only factor changing would be the grid spacing or time step.

Within this process, a verification study was conducted to investigate the numerical uncertainty with the simulations, U_{SN}, along with the numerical errors, δ_{SN}. The numerical errors are assumed to be composed of three elements, the iterative convergence error (δ_I), grid-spacing convergence error (δ_G) and time-step convergence error (δ_T). These, in turn, defines equations (10-17) & (10-18) as proposed by Stern et al (2001) for the numerical error and uncertainty within the simulation.

$$\delta_{SN} = \delta_I + \delta_g + \delta_t \tag{10-17}$$

$$U_{SN}^2 = U_I^2 + U_G^2 + U_r^2 \tag{10-18}$$

With U_I, U_G and U_T describing the uncertainties for iterative, grid spacing convergence and time step convergence errors respectively.

Due to the transient nature of the simulation, along with the inability to clearly define a point at which a steady state solution has been achieved, the iterative convergence error has been neglect, as it is not suitable for such a simulation and verification study.

From this, both grid spacing and time step convergence studies were conducted according to the Grid Convergence Index (GCI) study proposed by (Roache, 1998). As no fluid stucture interaction would be taking place within these simulations, turbulence model study was not considered. Further to this, other studies focusing on wave verification, such as (Lal & Elangovan, 2008), found no noticable effect on wave elevation due to turbulence model variation. This meant that only the grid spacing and time step variation would have the largest effect on the simulations, and thus are the key focus of this study.

The GCI method was performed with three solutions, each of which had a methodically refined grid spacing or time step. For each solution the primary parameter, i.e. the grid spacing or time step, was coarsened/increased by a specific value, while all other parameters were maintained at a constant value. For example, when conducting the time step convergence study the finest mesh was used for all three simulations and only the time step value was increased. The mesh convergence follows the inverse of this, namely that the smallest time step is used with the grid being coarsened throughout the whole domain by a specific value.

$$R_k = \frac{\varepsilon_{k21}}{\varepsilon_{k32}} \tag{10-19}$$

$$\varepsilon_{K21} = S_{k2} - S_{k1} \tag{10-20}$$

$$\varepsilon_{K32} = S_{k3} - S_{k2} \tag{10-21}$$

Equation (10-19) depicts the convergence ratio used to assess the various convergence conditions in the two studies described above. The top term (10-20) defines the difference

between the medium-fine solutions, while the lower term (10-21) defines the difference between coarse-medium solutions.

Four typical convergence conditions may be seen: (i) monotonic convergence ($0<R_k<1$), (ii) oscillatory convergence ($R_k<0$; $|R_k|<1$), (iii) monotonic divergence ($R_k>1$), and (iv) oscillatory divergence ($R_k<0$; $|R_k|>1$) (Stern et al., 2006).

The generalised Richardson extrapolation is used to predict the uncertainties and numerical error in condition (i). To obtain the uncertainties for condition (ii) a further step must be applied, this is seen in equation (10-22).

$$U_K = \frac{1}{2}(S_U - S_L) \tag{10-22}$$

S_U and S_L define the maximum and minimum found in the convergence study respectively. Finally, for cases (iii) and (iv), diverging conditions, the uncertainty or the error cannot be assessed (Stern, et al., 2006).

As used in similar studies to this work (Terziev, et al., 2018), a uniform refinement ratio (r_G) is used to in the mesh convergence study. In the case of this study, the value for r_G was defined as $\sqrt{2}$ throughout the whole domain and mesh continuum. The final mesh numbers for each of the mesh convergence cases are listed in Table 10-2.

Table 10-2 Final cell numbers for fine, medium and coarse mesh convergence studies

Mesh Configuration	*Min Z Cell Height*	*Cell Number*
Fine	0.0219	14,798,388
Medium	0.0309	5,565,638
Coarse	0.0438	2,105,162

Table 10-3 Simulated Hs and relative error from desired value in mesh convergence study

	H_s (metre)	*% Off Desired Hs*
Fine	5.05	0.9901
Medium	5.485	8.8423
Coarse	5.987	16.4857

Following the same method as the mesh convergence study, the time step convergence study used three cases, each of which has their time step increased from the calculated minimum value by a uniform refinement ratio (r_T) of 2. Using equations (10-13) & (10-14) a minimum time step of 0.0035 s was estimated. The fine mesh setup was used for the time step convergence study.

Utilising equations (10-19), (10-20) & (10-21), the Richardson coefficient is calculated for both the grid spacing and time step studies. The computed values for both the grid refinement and time step convergence studies can be seen in Table 10-4 & Table 10-5.

The relative errors because of the grid coarsening are seen in Table 10-3. This preliminary study begins to highlight the effects of grid coarsening upon the desired Hs and in turn the dependency that goes with it.

Table 10-4 Grid convergence study with respect to Hs

Parameter	r_g	Solutions			R_g	GCI		
		s1	s2	s3		GCI21	GCI32	GCIRatio
Hs	√2	5.050	5.485	5.987	0.870	72.058	76.257	1.058

Table 10-5 Time-step convergence study with respect to Hs

Parameter	r_t	Solutions			R_t	GCI		
		s1	s2	s3		GCI21	GCI32	GCIRatio
Hs	2	5.050	5.150	3.750	-0.071	0.190	2.614	13.728

As seen in Table 10-4, a monotonic convergence can be observed from the calculated R_g value of 0.87. This was to be expected as through this study it has been made clear that there is a distinct relationship between the sustained significant wave height and the inputted value. Table 10-4 further highlights that such simulations have a dependency upon grid spacing, which in turn directly relates to the predetermined accuracy level being aimed for.

In addition to this, the verification study has further highlighted a dominant part when attempting to maintain a stable free surface, namely the reliance on the time step. Although an oscillatory convergence was seen in the time-step convergence study, represented by R_t, the free surface failed to maintain a constant and stable surface. Further to this, Table 10-5 shows a significant dependency upon the time step in maintaining the desired significant wave height, along with a stable simulation. This is noted even further when comparing Figure 10-6 & Figure 10-7. Both scalar scenes show the free surface defined by the Volume Fraction of H_2O

in the fine mesh simulation. Figure 10-6 simulation uses the minimum defined time step, while Figure 10-7 simulation uses the maximum time step in time-step convergence study. As can be seen from Figure 10-7, a dominant region of the free surface has broken down and spread across a significant number of cells, causing the defined interface to be lost and trend towards a divergent solution. It is therefore paramount that the time step is selected carefully and only modified with caution.

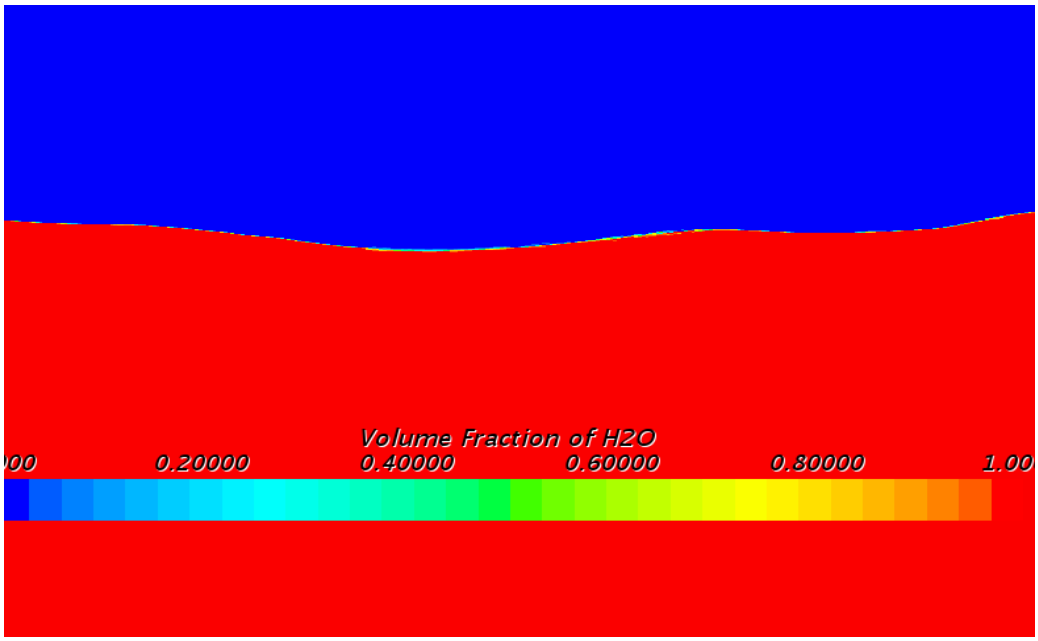

Figure 10-6 VOF Scalar scene depicting the free surface when Ts = 0.0035 s

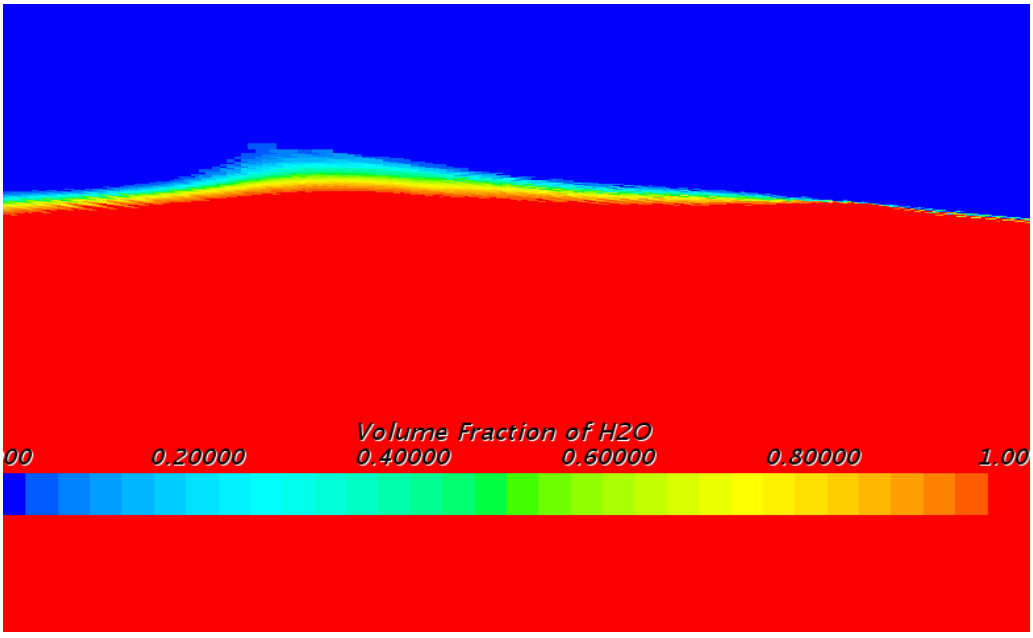

Figure 10-7 VOF Scalar scene depicting the free surface when Ts = 0.014 s

10.4. Results Section

10.4.1. Introduction

This section will present results and analysis obtained by using the methodology described above for three significant wave heights and mesh accuracy levels. This is carried out to compare the effectiveness of the methodology for various sea states, along with practical limitations of such simulations and methods.

10.4.2. Sea State 6

The initial seta state being discussed in this section will be that also used within the validation and verification section above. As shown above, a significant wave height of 5 (m) and a peak period of 12.4 (s) was selected. This has been chosen to show the methodologies accuracy in modelling large sea states that will likely be investigated in CFD for both added resistance and motion analysis.

Based upon these JONSWAP parameters, the initial mesh characteristics and time steps were calculated using the in-house code shown in Appendix v. The calculated mesh values are shown in Table 10-6. As can be seen, a minimum cell height of 0.022 (m) has been calculated, along with an upper limit of ±2.25 (m) from the mean water line for the first refinement region. It can also be seen from Table 10-6 that a minimum wave height of 0.35 (m) will be modelled within this region, based upon a 16 cell distribution in the Z height.

Table 10-6 Calculated cell heights and distributions for a Sea State 6 simulation

Sea State	6		
Hs	5 m		
Tp	12.4 s		
Spectrum	*JONSWAP*		
Av Wave Steepness	0.0208275		
Max Z height in +ve & -ve	2.25 m		
Min Wave Height	0.35 m		
Free Surface Refinement Region	*FrSf_1*	*FrSf_2*	*FrSf_3*
No of Cells per Wave Height	16		
Z cell Height	0.0219 m	0.0438 m	0.0875 m
		0.7 m	1.4 m
	16	2.95 m	4.35 m
Min Wave length	16.805 m		
No of Cells per L	60	4	4
X Cell Length	0.2801 m	0.5602 m	1.1204 m
Y Cell Length	0.2801 m		

Upon the calculation of the various volumes and cell sizes, the simulation was modelled and meshed. Although an initial cell size of 0.022 (m) had been calculated, the meshing scheme within the CFD code did not allow a cell of the calculated Z and X lengths to be generated. This led to the closest cell to be modelled having a Z height of 0.024 (m). Table 10-7 shows a comparison between the desired and generated dimensions, along with the potential observed error also being shown. This increased cell height meant that the minimum wave height was split between 15 cells in the Z height rather than the desired 16. Due to only a minor increase in cell height, the observed smallest wave was 30% smaller than the minimum wave height planned for, this can be seen in Figure 10-8. Figure 10-9 shows the full wave elevation compared with run time, this figure compared with Figure 10-10 also highlights the run time limitations as the number of observed waves is significantly lower than can be seen in Figure 10-9. This backs up the error margins discussed in section 10.2.1.

Table 10-7 Comparison of theoretical and generated mesh size (Z direction)

Calculated	*Generated*
0.022 (m)	0.024 (m)
Difference	9.09%
Number of cells per Min Wave Height	14.6 ~ 15

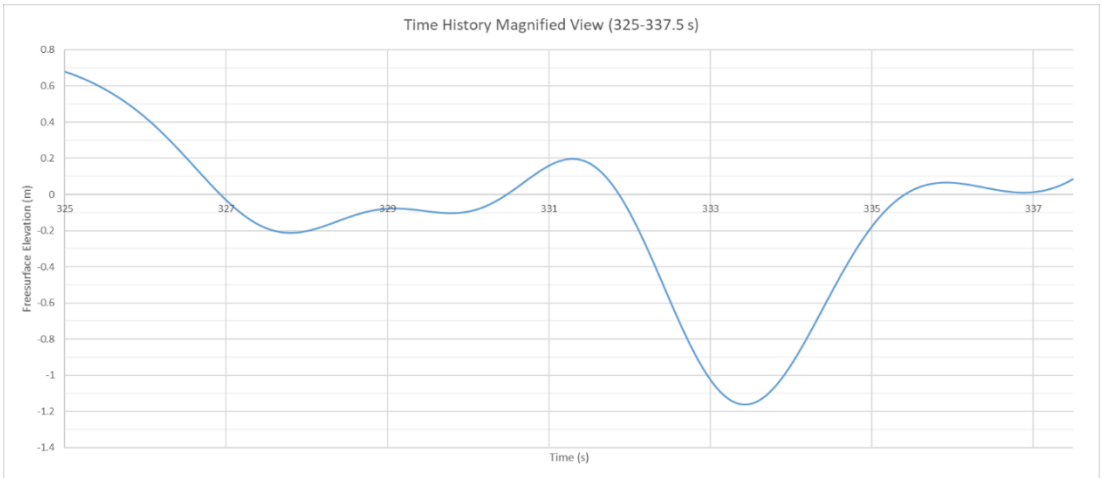

Figure 10-8 Magnified view of wave elevation between 325-337.5 seconds to view the smallest observed wave

As shown in the validation and verification study above, the mesh scheme developed in this paper achieved an error of less than 1%. This error margin is significantly below the estimates laid out above. This is due to two main reasons. Firstly, the mesh scheme and time step used were very close to the estimated optimal values, but predominately the second reason in the selection of simulation time. As the simulations in the V&V study used the test mode within the JONSWAP spectrum, a simulation time was selected to match the 300 encountered waves but also ensured the observed Hs matches within 0.5% of the desired value. This is significantly below the theoretical maximum potential error limit of -6.05% and 9.62% respectively, as estimated based upon the data from Figure 12-1. Further to this, the initial 300 seconds of the wave elevation were analysed to compare with the other sea states due to their reduced simulation time. The Hs error seen for 300 seconds increased from 0.5% to 2.43%. This value fits the observed pattern of error deviation seen in Figure 12-1 when compared with the error value found for 1500 seconds. As seen from Figure 12-1, the theoretical maximum potential error increases as the simulation time decreases, this increases is around 4.75 times from 1500 to 300 seconds. Based upon this observation, an estimated error of 2.375% at 1500

seconds, which is marginally lower than actual observed error. These values are both around 10 times lower than the calculated theoretical maximum limits from Figure 12-1 of around 30%. This is likely due to relatively consistent wave elevations over the 300 second period, as can be seen in Figure 10-10.

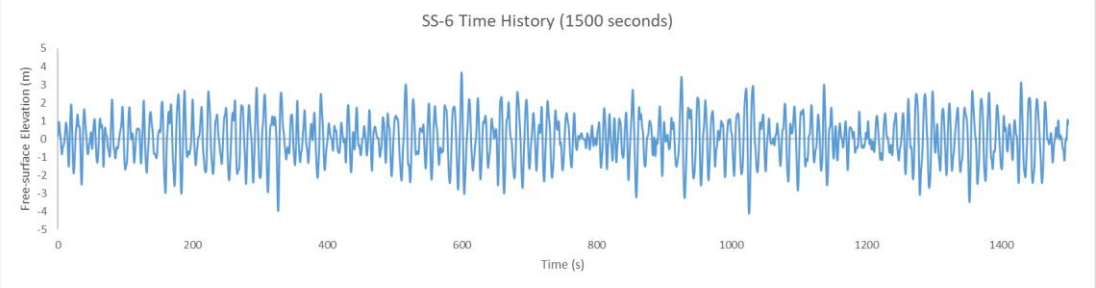

Figure 10-9 CFD free surface elevation for SS-6 over 1500 seconds

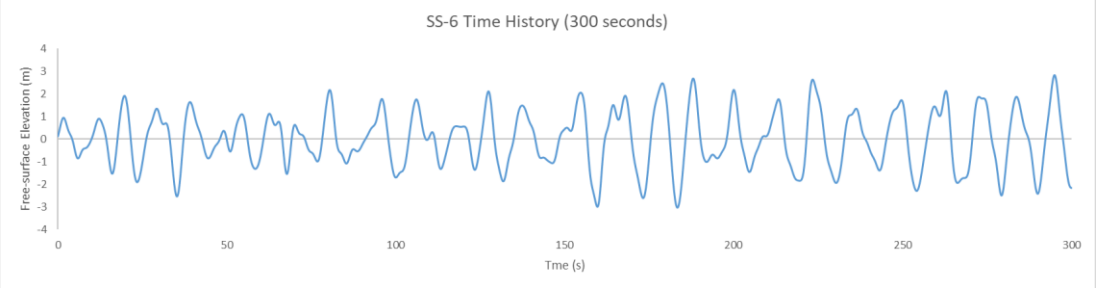

Figure 10-10 CFD free surface elevation for initial 300 seconds for SS-6

Due to the size and complexity of the simulation, the only practical way to run the simulation was through the use of an High Performance Computer (HPC, Archie-WeST). The simulation took in excess of to 675,000 CPU hours for 1500 second simulation time. This would have been reduced to 530,000 CPU hours due to the final period of the simulation running on a hardware updated HPC. This length was due to the simulation needing to model both small and large waves over the full range of Sea State 6 limits. This highlights the major drawback to such a simulation for practical applications at the current point in time.

10.4.3. Sea State 5

In addition to SS-6 (sea state), both SS-5 & SS-4 were also investigated to analyse the accuracy of the methodology and the running time for various sea states. For SS-5 the calculated mesh variables are shown in Table 10-8, along with the prospective errors. As can be seen, the minimum cell size is much smaller than with respect to the relative significant wave heights. In addition to the reduced cell size, the number of cells in the Z height for the first refinement region should remain constant, however when the mesh has been generated the smallest Z height that could be modelled was 18% larger than desired. Leading to a cell height of 0.0117

(m), this in turn, caused a reduction in the number of cells per minimum wave height from 16 to 13. This still remained within the limits advised by Star CCM+, however this meant that a much smaller margin of lower wave heights can be captured in the mesh. This was seen in the form of the smallest stable wave being only 0.1037 (m), a reduction of around 6% from the minimum modelled height of 0.1098 (m). This is a significant reduction compared with the 30% seen in SS-6.

Table 10-8 Calculated cell heights and distributions for a Sea State 5 simulation

Sea State	5		
Hs	3.25 m		
Tp	9.7 s		
Spectrum	JONSWAP		
Av Wave Steepness	0.0221		
Max Z height in +ve & -ve	1.3089 m		
Min Wave Height	0.11 m		
Free Surface Refinement Region	FrSf_1	FrSf_2	FrSf_3
No of Cells per Wave Height	16		
Z cell Height	0.0097 m	0.0194 m	0.0388 m
Min Wave length	4.9626 m		
No of Cells per L	60	4	4
X Cell Length	0.0830 m	0.166 m	0.332 m
Y Cell Length	0.0830 m		

Although the over cells sizes have been reduced, thus causing an increase in potential overall cell number, the overall cell number is slightly lower than SS-6 due to the reduction in overall domain size caused by the decreased maximum wave length. This trend is further seen in SS-4, suggesting smaller sea states become more computationally efficient. This however, does not make the simulations quicker at a similar rate, as the time steps required become smaller due to the reduced cell size. It is noted that although there is limited equalling effect of reduced

cell numbers and time step size, a SS-5 simulation ran around 10% quicker than an equivalent SS-6 simulation.

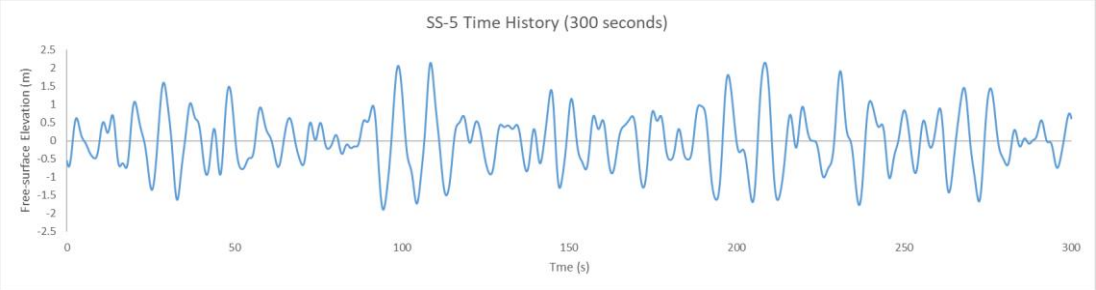

Figure 10-11 CFD free surface elevation for initial 300 seconds for SS-5

The calculated Hs derived from the simulated waves matched the desired Hs within 5%, which is still significantly below the error cone discussed on section 10.2.1, which highlighted a potential maximum observer error of 27% for a simulated time of 300 seconds. The observed time history is shown in Figure 10-11. This also highlights the increase in observed waves within the simulated time compared with SS-6.

Two reasons led to the reduced running time of 300 seconds, the first was practical hardware limitations and the second was to apply the simulations in a more practical simulated approach. Although practical applications may reduce the simulation even further, as mentioned in section 10.2.8, 300 seconds was chosen as the time allowed a large variety of waves to travel through the domain and thus produce a small but accurate snap shot of the irregular sea. The overall simulation required around 1.25e5 CPU hours to run. This further highlights the hard ware and software requirements of such a simulation.

10.4.4. Sea State 4

As mentioned above multiple sea states have been used to test the methodology put forward in this paper. However SS-4 was also testing the greater practicality of the methodology. As it is becoming a much greater interest to both research's and industry to test simulation in real world conditions, therefore SS-4 was selected as it represents a common extreme worked in by offshore industries.

The estimated cell sizes and time steps are shown in Table 10-9. Based upon these values, overall 20 million cells were used. A reduction of around 5 million cells compared with SS-5. As with the previous simulations, the generated cells varied slightly compared with the calculated values. The variation increased significantly for SS-4 in cell height, with a deviation of 20%. This caused the cells per minimum wave height to reach the minimum limit of 12, thus leading to no further reductions in simulated waves.

The simulated Hs for the 300 periods came to 1.724 (m) that equated to a deviation of 9.1% from the desired Hs of 1.88 m. The simulated wave elevation for SS-4 is shown in Figure 10-12. This error remained within the maximum potential limits of around 25%, as estimated in Figure 12-3 in Appendix iii.

This cell size increase was due to the meshing scheme within CFD code, as it failed to accurately match the desired inputs and aspect ratios, thus leading to a compromised mesh that did not allow for any smaller waves than the calculated minimum to be simulated. This also matched the previously mentioned trend of smaller wave height simulations having a much lower ability to model smaller waves than the calculated minimum wave height. This becomes a significant problem, as the cell numbers within a small simulation can become too large to be considered advantageous or practical.

Table 10-9 Calculated cell heights and distributions for a Sea State 4 simulation

Sea State	4		
Hs	1.88 m		
Tp	8.8 s		
Spectrum	JONSWAP		
Av Wave Steepness	0.0155		
Max Z height in +ve & -ve	0.7684 m		
Min Wave Height	0.0645 m		
Free Surface Refinement Region	FrSf_1	FrSf_2	FrSf_3
No of Cells per Wave Height	16		
Z cell Height	0.0054 m	0.0107 m	0.0215 m
Min Wave length	4.1457 m		
No of Cells per L	60	4	4
X Cell Length	0.0691 m	0.138 m	0.276 m
Y Cell Length	0.0691 m		

Minimal tweaking of the time step was required, in this case the time step was increased slightly from the calculated value without causing instabilities within the simulation. The increased time step led to further reduction in overall simulation time and CPU usage, with a

17% reduction in CPU hours used compared with a 20% reduction in cell numbers. The simulation used 1.1e5 CPU hours to reach 300 seconds. However, due to the smaller waves, a greater number of waves entered the domain compared with the previous simulations, this can be seen clearly in Figure 10-13, it is, therefore, possible to reduce the overall run time to account for the increased number of waves seen per minute.

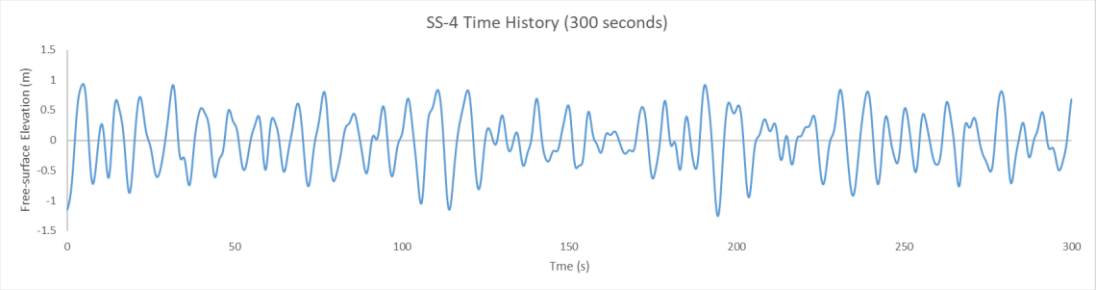

Figure 10-12 CFD free surface elevation for initial 300 seconds for SS-4

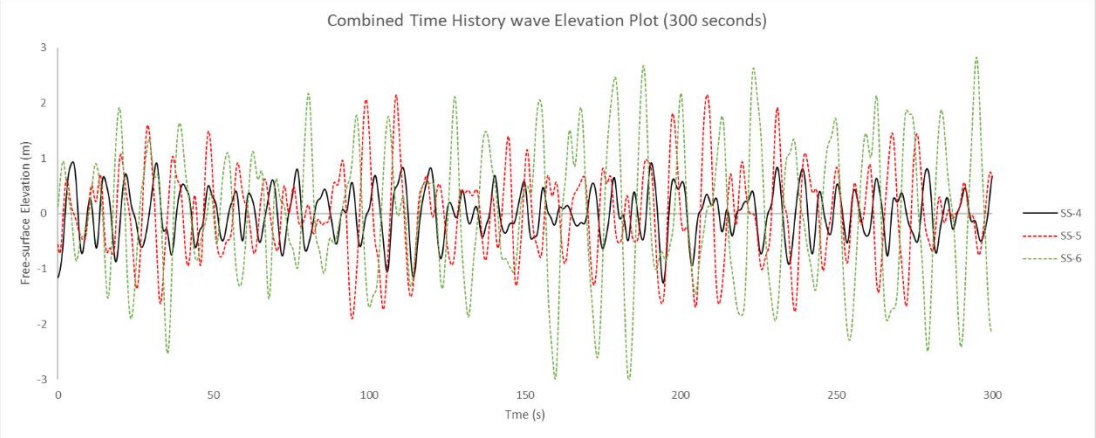

Figure 10-13 Comparison of CFD Time histories for simulated sea states

As can be seen from the discussions above, all the simulations fell well within the theoretical maximum error margins estimated through the in-house code and shown in Figure 10-3, Figure 12-1 and Figure 12-3 in Appendix iii. These graphs also show that as the Hs decreases, the theoretical error margin for smaller run times also decreases due to the reduced average wave period and thus an increase in a number of observed waves, this is shown clearly in Figure 12-5.

10.5. Concluding Remarks

This section will provide a final overview of the work conducted above, along with the key factors relating to the best practices for simulating unknown irregular seas.

Through the study looking at various sea states, multiple points can be drawn for both the results obtained, along with the overall methodology. Each simulation achieved a level of accuracy that satisfies the simulation time error, along with the additional mesh errors. This shows that the methodology of decomposing an irregular sea into key factors guarantees the ability to capture the desired sea state with respect to accuracy levels needed required that simulation. As noted above, these accuracy levels vary greatly with respect to the mesh density, estimated time steps, and overall simulation. Two examples of varying accuracy levels may be as follows:

1. A small wind and current device located in a minor harbour, such that all wave heights are vital to the operation of the system, thus a high mesh count and accuracy level is critical to ensuring valid simulation results
2. An ocean-going vessel, such as a large containership or anchor handling tug, experiencing a large sea state and variable wind conditions, to investigate vessel motions and performance limitations. Such a simulation may require a large full domain to allow variable wave directions. Thus the requirement for the smallest waves may be ignored, to a certain degree, due to the large moments and forces required to instigate motions, and thus helping to reduce cell numbers.

These examples highlight both the importance of the engineers understanding of the subject being simulated, along with an initial methodology to work off and vary based upon the simulation.

It can be seen from the results discussed throughout section 4, that the current values used and proposed in the creation of the simulations may be over refining the mesh density. This, in turn, causes the simulation to be slower than the required for the final desired accuracy level, this is most seen when comparing SS-6 and SS-4 simulations. Both achieve the desired accuracy level, with SS-6 being closer to the desired aim, while SS-4 Hs is only slightly less accurate but with a significant reduction in cell numbers comparatively. It is therefore advised that the initial mesh should aim to be over refined and then to coarsen the mesh. An initialisation of the free-surface within the domain will further help to identify if the mesh is over refined or at the correct level for the simulation.

The simulations maintained the desired accuracy, with the minimum wave captured travelling through the domain being below the desired smallest wave height according to the mesh coarsening. Therefore, although the mesh was coarsened, the relative error from the coarsening was reduced. Further to this, the methodology has proven accurate in modelling the desired time history. However such simulations are very dependent upon the simulated time and the respective time history error. In order to effectively analyse the time history error within a simulation, the simulated free-surface should have a Fourier analysis conducted to compare with the desired wave spectrum. This ensures that an observed error may be due to either the time history error margin or inaccuracies within the simulation. The second factor will require a reworking of the simulation.

The ability to accurately model such conditions will become invaluable when attempting to simulate ever more realistic ocean conditions for fatigue and motion simulations for offshore or coastal engineering projects. In addition to increasing the accuracy for estimating complex drag problems for both marine vehicles and structures.

As discussed and highlighted above, irregular sea simulations require a significant amount of computational power and time. It is therefore vital that any research or application within the industry conduct a preliminary statistical analysis of the desired sea state to be modelled. Not only does this provide a clear benchmark to later validate against, but provides the initial steps in defining the accuracy level desired for the specified work as seen in the case study section of this study.

From post-processing analysis of the modelled time histories, the key values relating to the minimum desired wave height, the maximum height for the fine refinement region, and the statistical maximum wave height can be drawn. These values can be used, as described in Section 2, to define the refinement volumes, along with the key cell length required to maintain the specified Hs. These can be calculated by using the equations defined by (Arena, et al., 2010) to determine the wave lengths, based upon the wave height and in turn the wave periods. These equations can be seen in section 10.2.1, defined as equations (10-8) & (10-9).

To further ensure simulation stability, the maximum aspect ratio for the cells within the free-surface refinement regions should not exceed 15 with respect to X & Z. It is possible to increase the cell length in the Y direction in the far field regions to reduce the overall cell numbers used in the simulation.

Upon the mesh reaching the desired accuracy and refinement level, the respective time step must be defined. Depending upon the simulation, the time step may be defined using the equations listed above in section 10.2.3, (10-13), (10-14), (10-15) & (10-16).

The overall simulation time must be selected, and as prescribed above a minimum of 100 waves should be used only when used with a Discrete Fourier Transform (DFT), as describeded by (Mousaviraad, 2010) and all other simulations should look to encounter a minimum of 300 waves or a simulation time of 1.5 hours.

As highlighted from Section 10.4, the numerical setup defined in Section 10.2 assumes an optimum setup and therefore may be tweaked to reduce cell numbers and running time. This, however, should be done with care to remain as close to the described best practices above as possible.

It can be concluded that such simulations come with a significant requirement for computational power and time. It can also be drawn that conducting such simulations in full scale can elevate any potential scaling issues when modelling the waves, as the mesh number will remain constant for the free surface region independent of model or full scale.

Further to this, this study has provided an initial baseline investigation for an alternate method other than the superposition methods currently in the literature. As highlighted above, this method aimed at improving the accuracy of modelling non-linear irregular seas at a greater accuracy than the commonly used superposition methods. The primary limitation of current superposition methods is the number and range of waves being modelled by the user, whereas the method developed above uses spectrum based data and thus has a significantly larger range of waves used to model the sea state. Due to the increased range, the wave interactions are modelled more accurately, and in turn the complex non-linear effects. Although the method described in this paper enables a more accurate simulation of non-linear waves, it is significantly more computationally heavy than the superposition method. This is most noticeable of short run time simulations, as both the simulation requires more computational power and there is no guarantee of achieving the desired Hs being modelled for compared with the superposition methods. However, for longer run time simulations the ability to model more complex wave interactions and non-linear effects the presented method becomes more appealing. Due to the need to increase the number of user defined waves in the superposition method, the advantages become negated while still producing limitations to the overall complexity of the sea state.

This study has provided the preliminary foundations for future CFD work relating to non-linear unknown irregular sea simulations to be worked upon. Such research should investigate the effects of varying wind conditions and the corresponding effect on the free surface, thus bringing CFD closer to full modelling of real-world conditions.

Further research should be conducted looking in to marine structure interactions and the effects on the described methodology by utilising this full domain rather than half domains with symmetry planes, with varying wave headings and the respective effect on added resistance and motions. It should also be considered in applying propellers and other appendages to investigate the effects of such sea states on these factors and how to improve complete vessel performance in irregular seas.

Further research should aim to investigate how optimisation using irregular seas can be achieved, and how this can be applied within the industry to reduce the GHG emissions of the marine industry. The research should focus on utilising transfer functions to validate vessel performance in such a method that the second order characteristics of added resistance are satisfied.

10.6. Future Work - Irregular seas

As seen in this chapter the developed tool achieved a high accuracy in simulating an irregular sea state with respect to the accuracy that is determined by the user. This irregular sea was solely focused on deep water and calm wind conditions. It is therefore considered for future work to evaluate how this methodology accounts for shallow water conditions and varying wind conditions.

As there is an ever-increasing interest in evaluating offshore structures focused on energy capture, these structures are required to be relatively close to the shoreline. Due to this the structures do not fall in the category of deep water or even a constant depth of water. Therefore, evaluating how the methodology captures shallow water waves, along with a changing water depth will provide exceptional situation capabilities for such an industry. The shallow water investigations can be further analysed to encompass shorelines and breakwater situations.

Along with how the methodology copes with shallow water conditions, the methodology should also be evaluated to account for various wind conditions. As this methodology allows for accurate representations of large sea states it is therefore additionally important to consider the wind conditions when evaluating vessel dynamics in such sea states. This will allow for example, greater evaluation of green energy devices retrofitted or designed onto vessels while in adverse conditions.

11.Appendix ii

Worked example of MATLAB code with key inputted values

```
Hs=5; % wave height significant (m)
Tp=12.4; % Peak period (s)


w=linspace(0.2,2.5,50);
delta_w = w(2)-w(1);
w = w + delta_w .* rand(1,length(w)); % random selection of
frequencies
w3=w;


% JONSWAP spectrum
gama  = 3.3;
fp    = 2*pi/Tp;
fac1  = (320*Hs^2)/Tp^4;
sigma = (w<=fp)*0.07+(w>fp)*0.09;
Aa    = exp(-((w/fp-1)./(sigma*sqrt(2))).^2);
fac2  = w.^-5;
fac3  = exp(-(1950*w.^-4)/Tp^4);
fac31 = exp(-5/4*(w/fp).^-4);
fac4  = gama.^Aa;
S     = fac1.*fac2.*fac3.*fac4;
%
%% JONSWAP Time history
skl  = 1;   % scale factor
tend = 5000; % time history length
sfr   = 100;   % sampling frequency (Hz)
t = [0: 1/sfr: tend]*sqrt(skl); % time vector
phi = 2*pi*(rand(1,length(w))-1); % random phase of ith frequency
A = sqrt(2*S.*delta_w); % amplitude of ith frequency


for i = 1:length(t)
    wave(i) = sum(A .* cos(w*t(i) + phi));
end
subplot(2,2,[1 2]);
plot(t,wave);xlabel('t (sec)');ylabel('Z_a (m)');grid;
axis([0 t(end) -inf*1.2 inf*1.2]);
```

```
HsCalc=4*std(wave); % Hs calculated from time history
error=(HsCalc/Hs*100)-100;
HsE=[HsCalc error] =

          5.1246 (m)    2.4921 %

% calculated Hs from time history and error margin off inputted value
dlmwrite('HsError',HsE,'delimiter',' ')
%dlmwrite('wave',wave,'delimiter',' ')
%% Peak and trough definitions
[Pks,locsPks,wP,pP]=findpeaks(wave,t);
[Trgh,locsTrgh,wT,pT]=findpeaks(-wave,t);
FPks=abs(Pks);
FTrgh=abs(Trgh);
SrtP=sort(FPks);
StrT=sort(FTrgh);


Elv=[Pks, Trgh]; % peaks and troughs
LocsElv=[locsPks, locsTrgh]; % location of peaks of troughs
SrtE=abs(Elv);
ELVmu=mean(Elv);
ELVsig=std(Elv);
%[h,stats]=cdfplot(SrtE);
ElvMu=mean(SrtE);
ElvSig=std(SrtE);
subplot(2,2,3);
pL1=5;       % lower bound percentage description
pU1=5;     % upper bound percentage description
mu=mean(wave);
sig=std(wave);
HL1=norminv((pL1/100),mu,sig)

      -2.1074 (m)

% wave elevation limit corresponding to lower bound (L1)

HU1=norminv((1-pU1/100),mu,sig)

      2.1072 (m)

% wave elevation limit corresponding to upper bounds (U1)

L1=[HL1,HU1]
```

```
      -2.1074 (m)    2.1072 (m)
      (lower and upper limits for initial free surface region)

[h,stats]=cdfplot(wave);
subplot(2,2,4);
probplot(wave);
MidP=5.5; % percentage limits of minimum wave heights been
considered for modelling
Plmid1=50+(MidP/2);
Plmid2=50-(MidP/2);
Hlmid1=norminv((Plmid1/100),mu,sig);
Hlmid2=norminv((Plmid2/100),mu,sig);
MinWaveElv=(Hlmid1+(abs(Hlmid2)))/2; % minimum wave elevation (1/2
wave height) to be modlled based upon Mid percent (MidP)
MinWaveHeight=MinWaveElv*2

      0.1768 (m)

%% Cell Caculations
g=9.81;
WSF=(2*pi()*Hs)/(g*(Tp^2))

      0.0208

% Wave steepness factor
MWL=(2*MinWaveElv)/WSF

      8.4871 (m)

% Minimum wave length
ZN=12; % Number of cells in Z height per wave
XN=60; % Number of cells per wave length
YFact=1; % Scaling factor for Y cell length, best practice -- 1 --,
may be used to reduce overall cell number by increasing value
MCZh=(MinWaveElv*2)/ZN

      0.0147 (m)

% Z input height for smallest cell
MCXl=(MWL/XN)

      0.1415 (m)

% X Input length for smallest cell
MCYl=MCXl*YFact

      0.1415 (m)
```

```
% Y Input length from smallest cell
AspectRatio=MCXl/MCZh
```

9.6027 < 15 therefore good size limits

```
% This aspect ratio factor should not exceed -- 15 --
FS1cN=ceil((abs(HL1)+HU1)/MCZh)
```

287

```
% estimated number of cells in initial free surface region
```

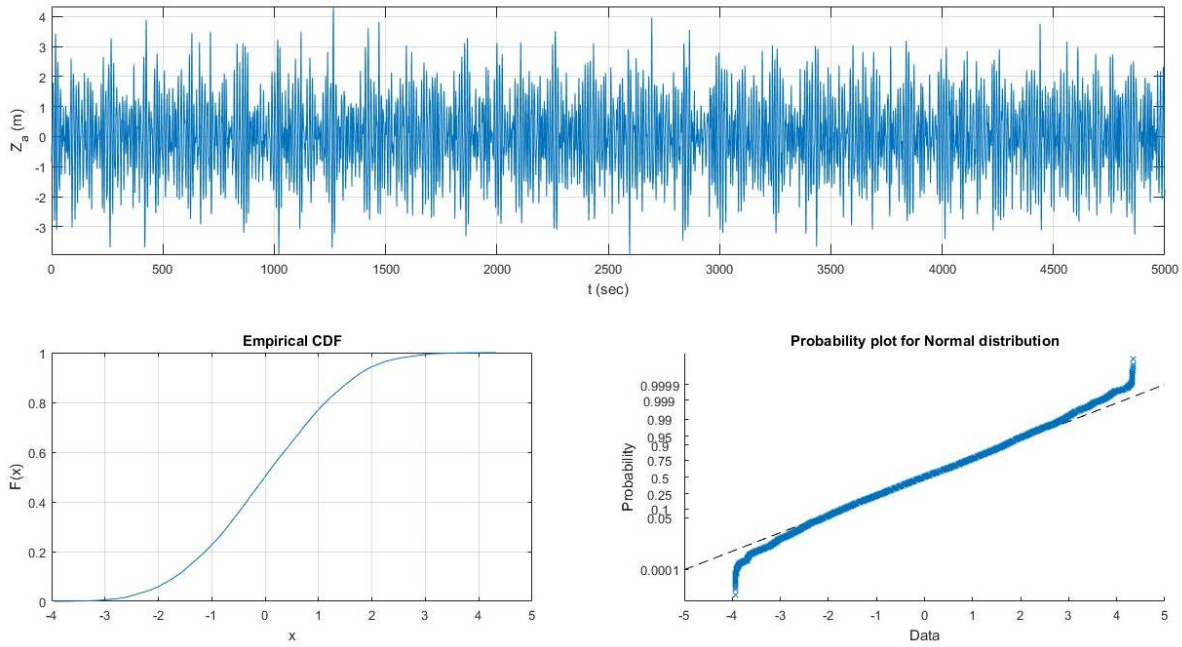

Figure 11-1 Graphical output from JONSWAP Matlab code for Hs = 5 (m), Tp = 12.4 (s) & T = 5000 (s)

12.Appendix iii

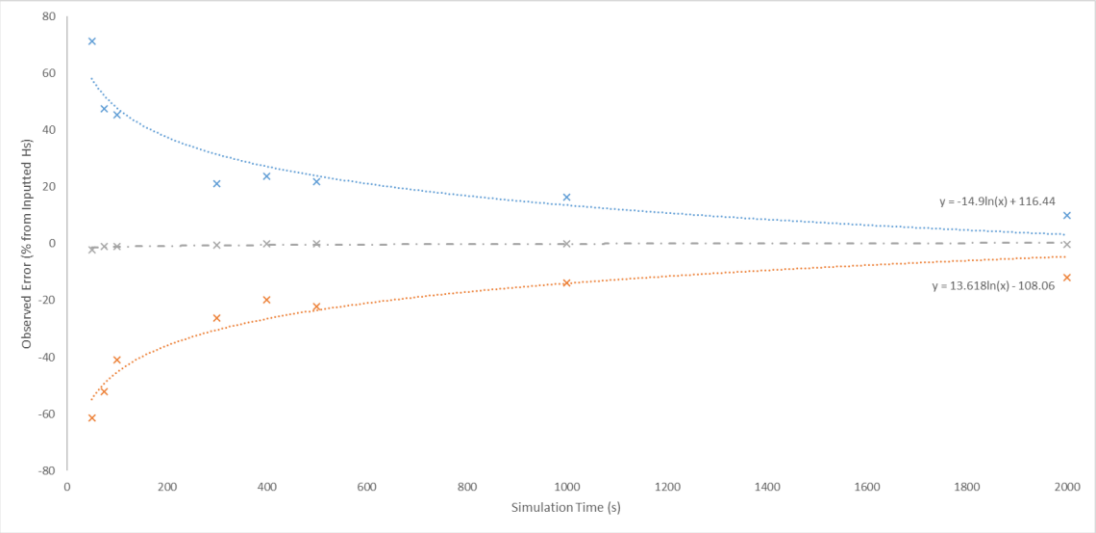

Figure 12-1 SS-6 Theoretical error margins with respect to MATLAB simulation time

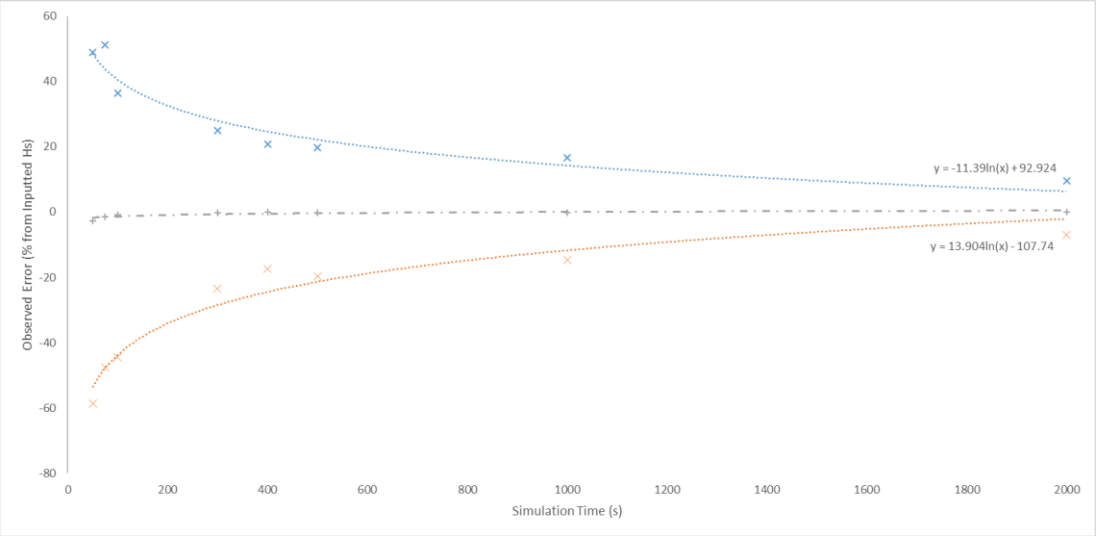

Figure 12-2 SS-5 Theoretical error margins with respect to MATLAB simulation time

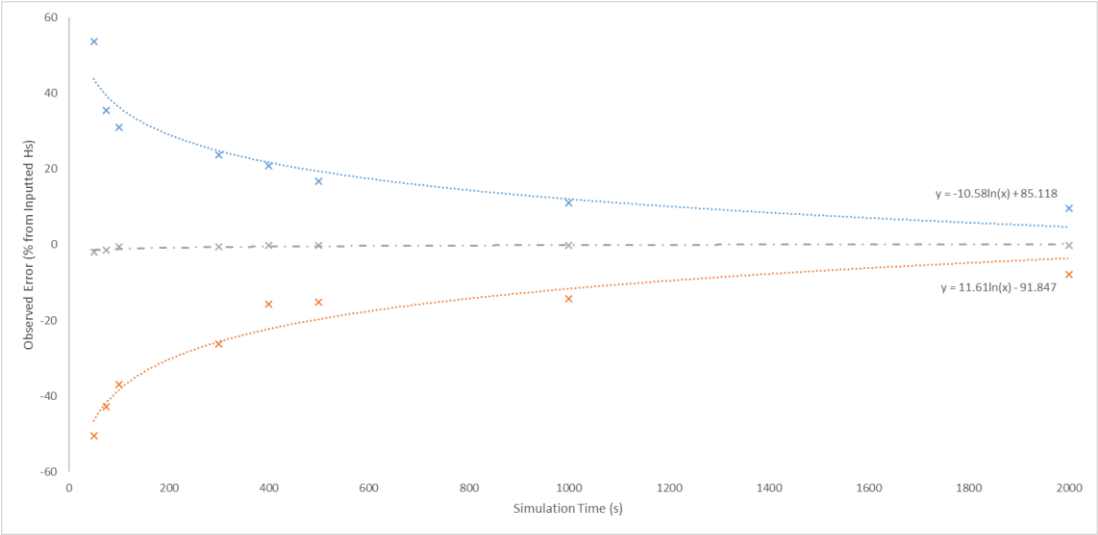

Figure 12-3 SS-4 Theoretical error margins with respect to MATLAB simulation time

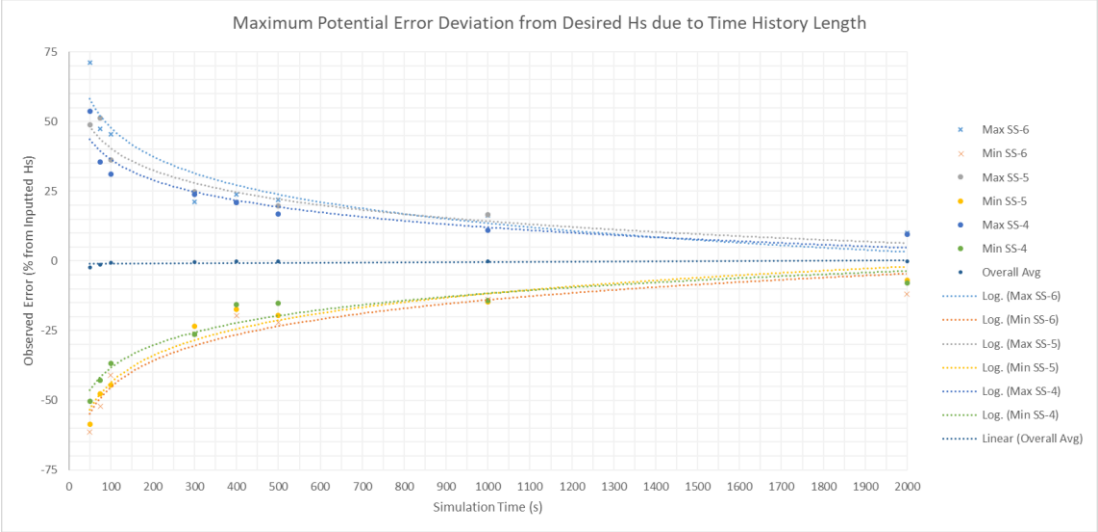

Figure 12-4 Combined theoretical error margin plot with respect to MATLAB simulation time

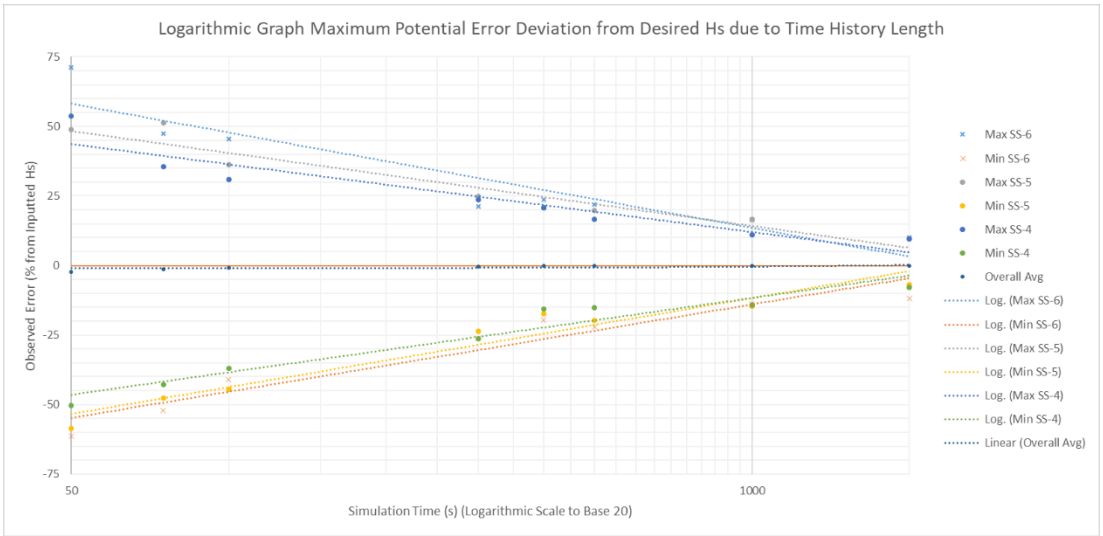

Figure 12-5 Logarithmic plot of combined theoretical error margins (SS-6, SS-5, SS-4) with respect to MATLAB simulation time

13.Appendix iv

Table 13-1 Mesh estimation scheme, sea state 6

LOA	
Domain X	100m
Domain Y	75m
Domain Z	75m

Sea State	6
Hs	5m
Tp	12.4s
Spectrum	JONSWAP

Av Wv Steepness	0.0208275
AWS	H/L

Max H	2.25m
Min H	0.35m

	FS_1	FS_2	FS_3
No of Cells per H	16		
Z cell Height	0.021875m	0.04375m	0.0875m
		0.7m	1.4m
	16	2.95m	4.35m

Min L	16.805m		
No of Cells per L	60	4	4
X cell	0.2801m	0.5602m	1.1204m
Delta Volume		2.2406m	4.4813m

Y cell	0.2801m

Volume Ratio X	0.85
Volume Ratio Y	1
Volume Ratio Z	0.8

Cell Volume FS1	0.00612m^3
Cell Volume FS2	0.00686m^3
Cell Volume FS3	0.02745m^3

volumes			
x	85m	87.240m	91.721m
y	75m	75m	75m
z	2.25m	3.65m	5.05m
volume	14343m^3	23882m^3	34740m^3
Delta Volume		9539m^3	20397m^3

No Z	102.857
No X	303.486
No Y	267.782

				Est Free Srf Cell Number
Total No Cells	8.36E+06	1389657	917901.6	1.07E+07

14.Appendix v

Raw JONSWAP spectrum time history, post-processing analysis and mesh value calculations.

```
close all;clear;clc;


Hs=1.88; % wave height significant (m)
Tp=8.8; % Peak period (s)


w=linspace(0.2,2.5,50);
delta_w = w(2)-w(1);
w = w + delta_w .* rand(1,length(w)); % random selection of
frequencies
w3=w;


% JONSWAP spectrum
gama  = 3.3;
fp    = 2*pi/Tp;
fac1  = (320*Hs^2)/Tp^4;
sigma = (w<=fp)*0.07+(w>fp)*0.09;
Aa    = exp(-((w/fp-1)./(sigma*sqrt(2))).^2);
fac2  = w.^-5;
fac3  = exp(-(1950*w.^-4)/Tp^4);
fac31 = exp(-5/4*(w/fp).^-4);
fac4  = gama.^Aa;
S     = fac1.*fac2.*fac3.*fac4;
%
%% JONSWAP Time history
skl  = 1;   % scale factor
tend = 5000; % time history length
sfr   = 100;   % sampling frequency (Hz)
t = [0: 1/sfr: tend]*sqrt(skl); % time vector
phi = 2*pi*(rand(1,length(w))-1); % random phase of ith frequency
A = sqrt(2*S.*delta_w); % amplitude of ith frequency


for i = 1:length(t)
    wave(i) = sum(A .* cos(w*t(i) + phi));
end
subplot(2,2,[1 2]);
```

```
plot(t,wave);xlabel('t (sec)');ylabel('Z_a (m)');grid;
axis([0 t(end) -inf*1.2 inf*1.2]);
HsCalc=4*std(wave); % Hs calculated from time history
error=(HsCalc/Hs*100)-100;
HsE=[HsCalc error] % calcuated Hs from time history and error margin
off inputted value
dlmwrite('HsError',HsE,'delimiter',' ')
%dlmwrite('wave',wave,'delimiter',' ')
%% Peak and trough definitions
[Pks,locsPks,wP,pP]=findpeaks(wave,t);
[Trgh,locsTrgh,wT,pT]=findpeaks(-wave,t);
FPks=abs(Pks);
FTrgh=abs(Trgh);
SrtP=sort(FPks);
StrT=sort(FTrgh);

Elv=[Pks, Trgh]; % peaks and troughs
LocsElv=[locsPks, locsTrgh]; % location of peaks of troughs
SrtE=abs(Elv);
ELVmu=mean(Elv);
ELVsig=std(Elv);
%[h,stats]=cdfplot(SrtE);
ElvMu=mean(SrtE);
ElvSig=std(SrtE);
% probplot(SrtE)
% PELmin=51;
% HLmin=norminv((PELmin/100),ElvMu,ElvSig)
% plot(LocsElv,Elv)
% TF=islocalmax( wave);
% TFm=islocalmin(wave);
%% Probabilty discriptions
subplot(2,2,3);
pL1=5;      % lower bound percentage description
pU1=5;    % upper bound percentage desciption
% pL2=1;      %      ---------""---------
% pU2=1;      %      ---------""---------
% pL3=0.1;    %      ---------""---------
% pU3=0.1;    %      ---------""---------
mu=mean(wave);
```

```
sig=std(wave);

HL1=norminv((pL1/100),mu,sig); % wave elevation limit corresponding
to lower bound (L1)

HU1=norminv((1-pU1/100),mu,sig); % wave elevation limit
corresponding to upper bounds (U1)

% HL2=norminv((pL2/100),mu,sig); % wave elevation limit
corresponding to lower bound (L2) skewing error due to extreme
limits, proceed with catution

% HU2=norminv((1-pU2/100),mu,sig); % wave elevation limit
corresponding to upper bounds (U2) skewing error due to extreme
limits, proceed with catution

% HL3=norminv((pL3/100),mu,sig); % wave elevation limit
corresponding to lower bound (L3) skewing error due to extreme
limits, proceed with catution

% HU3=norminv((1-pU3/100),mu,sig); % wave elevation limit
corresponding to upper bounds (U3) skewing error due to extreme
limits, proceed with catution

L1=[HL1,HU1]

% L2=[HL2,HU2];

% L3=[HL3,HU3];

% Lower=[HL1,HL2,HL3];

% Upper=[HU1,HU2,HU3];

[h,stats]=cdfplot(wave);

subplot(2,2,4);

probplot(wave);

MidP=5.5; % percentage limits of minimum wave heights been
considered for modelling

Plmid1=50+(MidP/2);

Plmid2=50-(MidP/2);

Hlmid1=norminv((Plmid1/100),mu,sig);

Hlmid2=norminv((Plmid2/100),mu,sig);

MinWaveElv=(Hlmid1+(abs(Hlmid2)))/2; % minimum wave elevation (1/2
wave height) to be modlled based upon Mid percent (MidP)

MinWaveHeight=MinWaveElv*2

%% Cell Caculations

g=9.81;

WSF=(2*pi()*Hs)/(g*(Tp^2)) % Wave steepness factor

MWL=(2*MinWaveElv)/WSF % Minimum wave length

ZN=12; % Number of cells in Z height per wave

XN=60; % Number of cells per wave length

YFact=1; % Scaling factor for Y cell length, best parctice -- 1 --,
may be used to reduce overall cell number by increasing value

MCZh=(MinWaveElv*2)/ZN % Z input height for smallest cell
```

```
MCXl=(MWL/XN) % X Input length for smallest cell

MCYl=MCXl*YFact; % Y Input length from smallest cell

AspectRatio=MCXl/MCZh % This aspect ratio factor should not exceed -
- 15 --

FS1cN=ceil((abs(HL1)+HU1)/MCZh) % estimated number of cells in
intial free surface region
```

15.Appendix vi

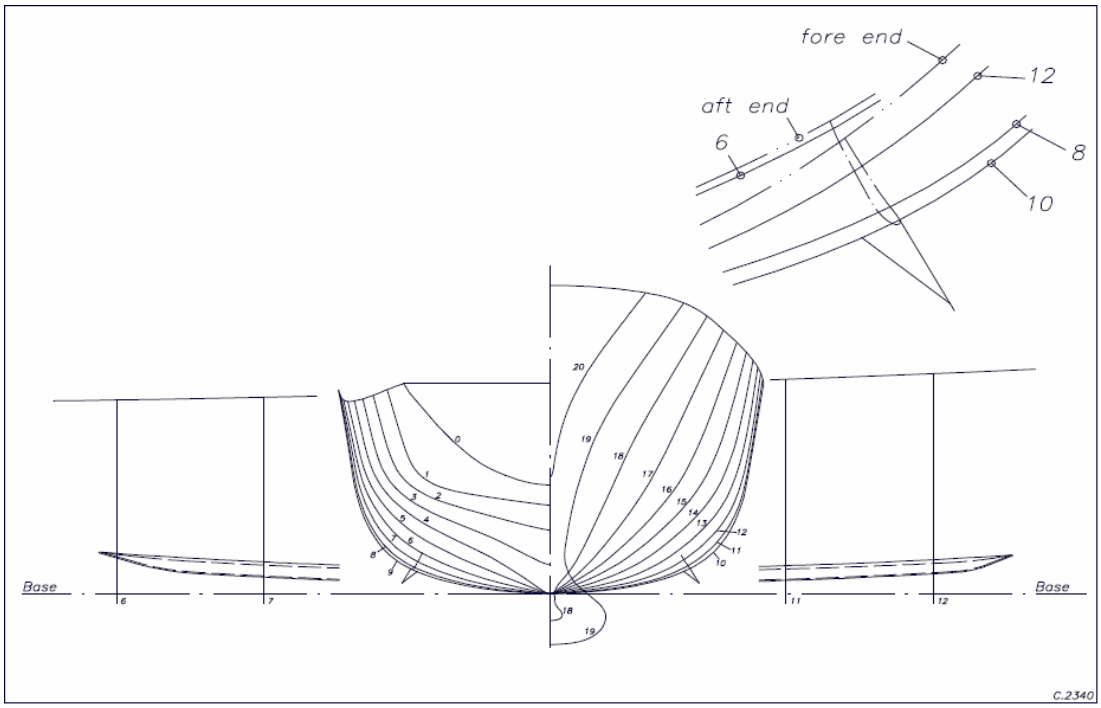

Figure 15-1 DTMB 5415 MARIN Hull 7967 bilge keel sectional lines

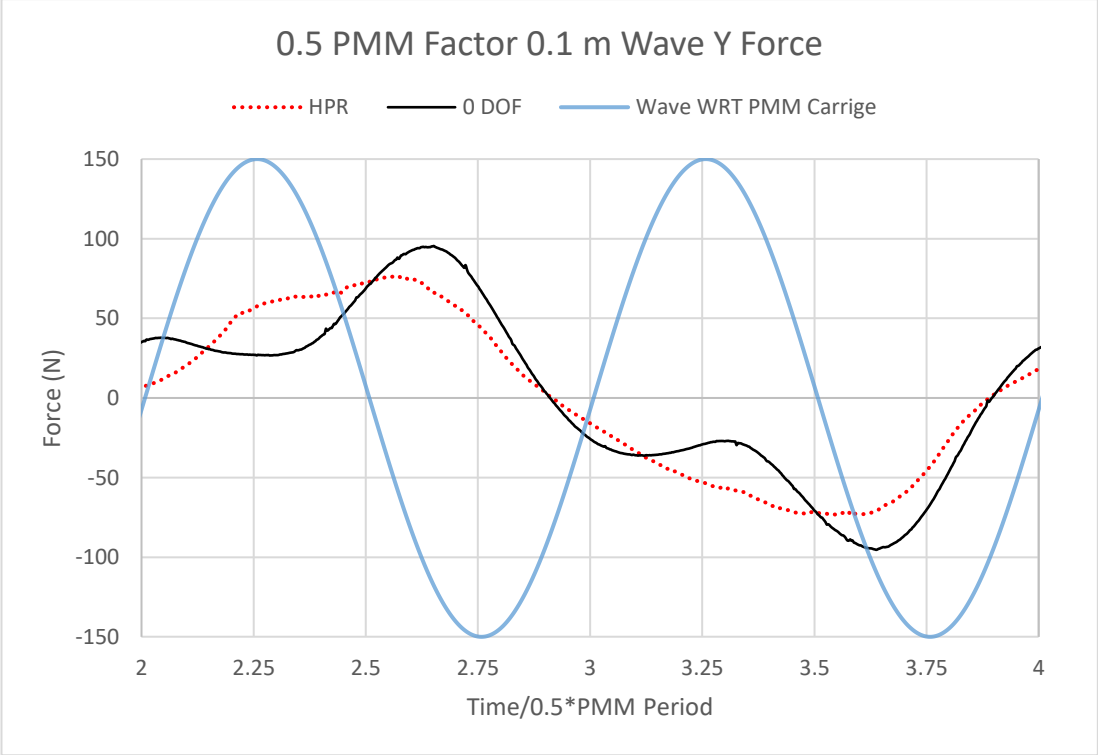

Figure 15-2 Graph showing Y force comparison between HPR and 0 DOF for 0.1m wave height 0.5 PMM period

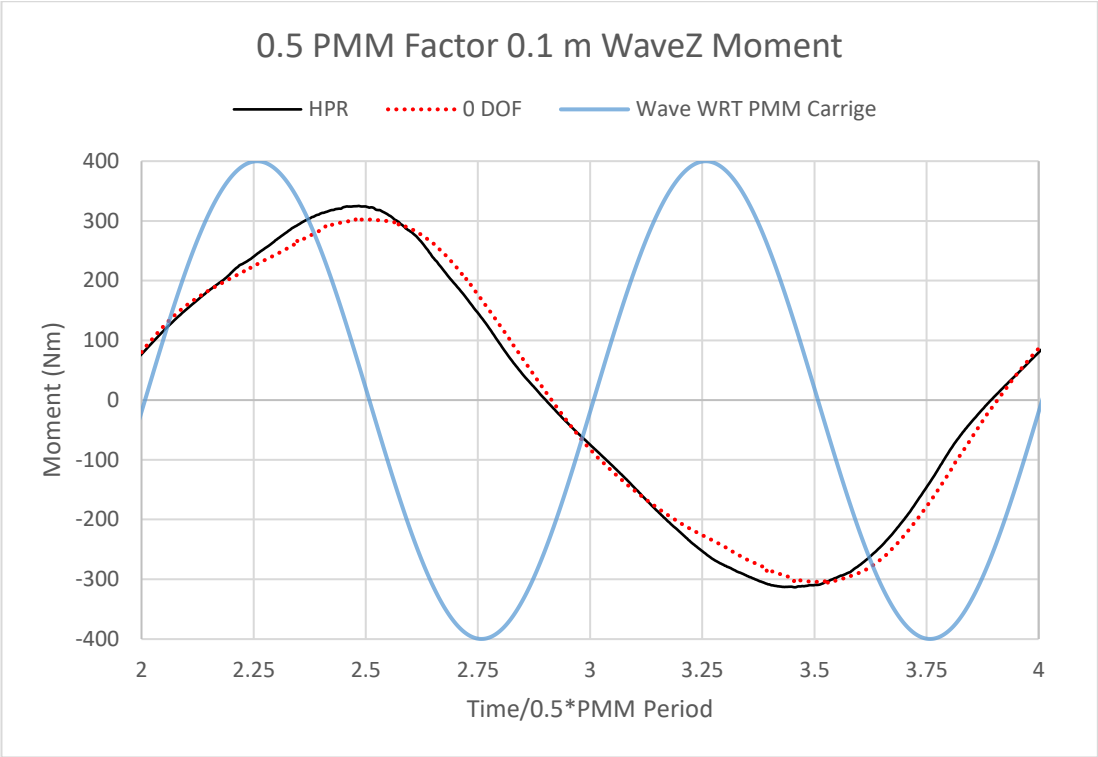

Figure 15-3 Graph showing Z moment comparison between HPR and 0 DOF for 0.1m wave height 0.5 PMM period

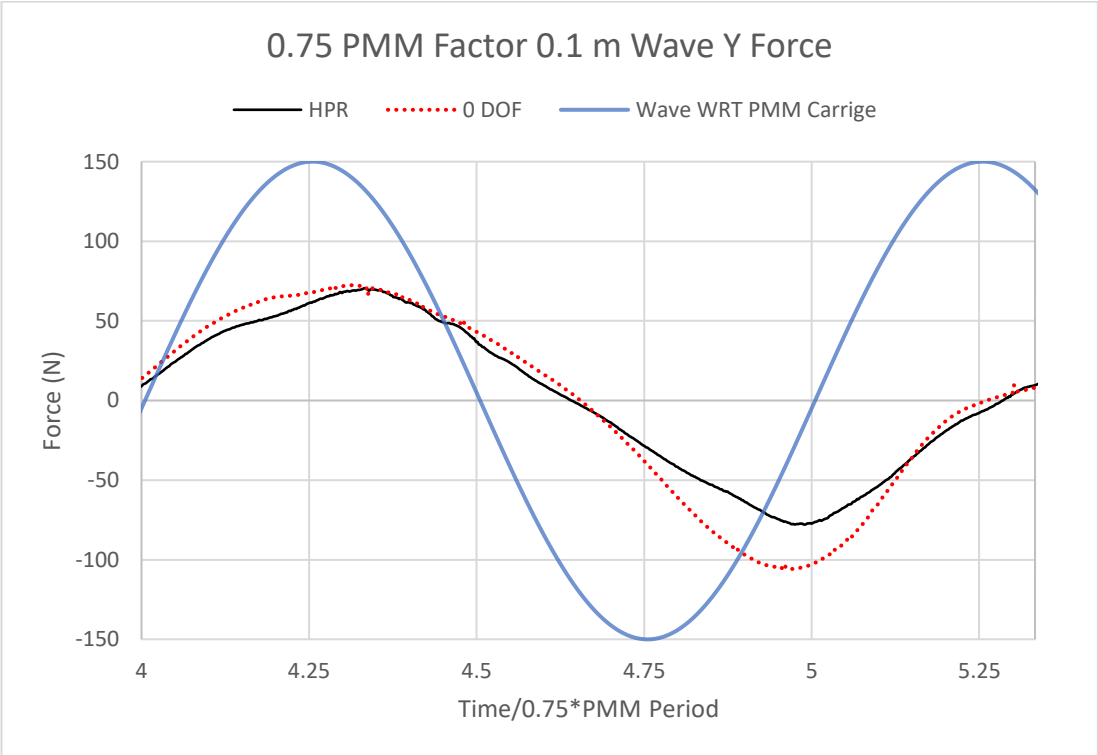

Figure 15-4 Graph showing Y force comparison between HPR and 0 DOF for 0.1m wave height 0.75 PMM period

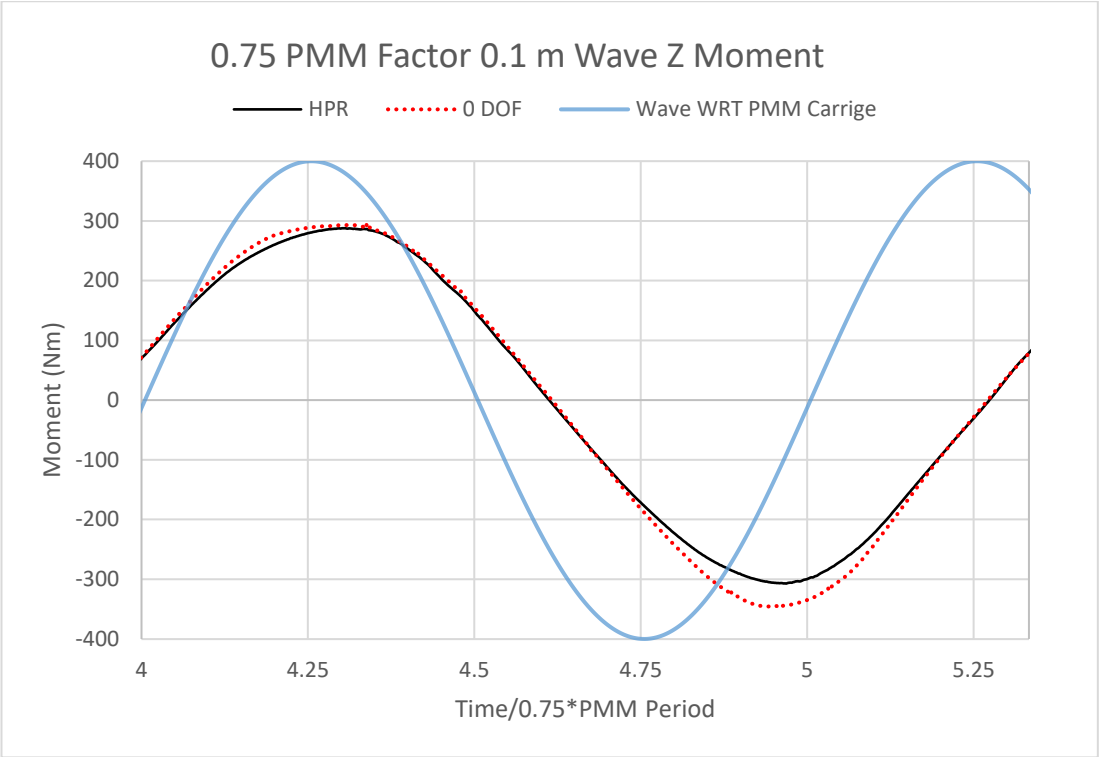

Figure 15-5 Graph showing Z moment comparison between HPR and 0 DOF for 0.1m wave height 0.75 PMM period

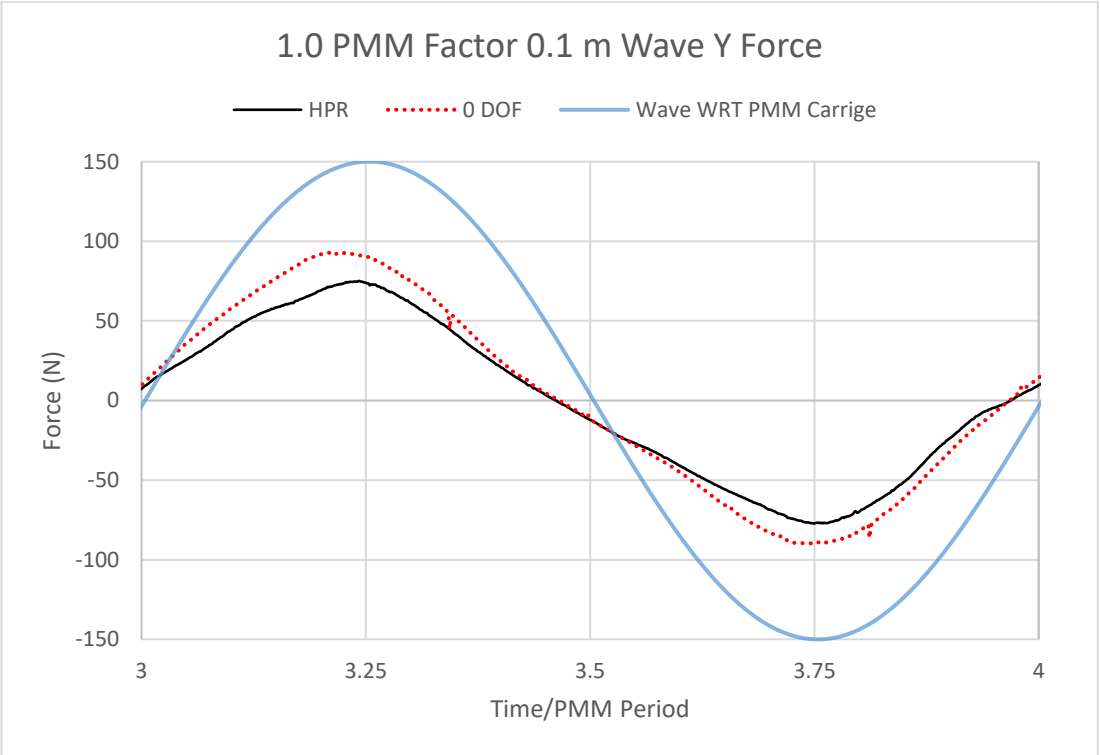

Figure 15-6 Graph showing Y force comparison between HPR and 0 DOF for 0.1m wave height 1.0 PMM period

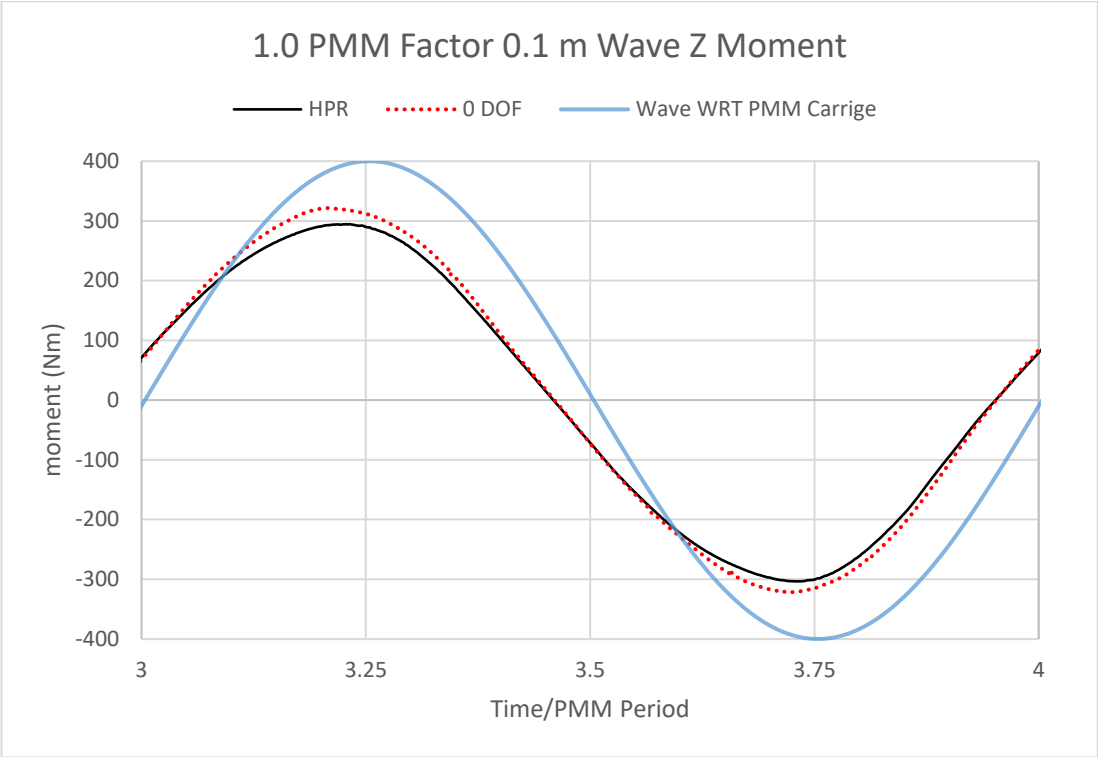

Figure 15-7 Graph showing Z moment comparison between HPR and 0 DOF for 0.1m wave height 1.0 PMM period

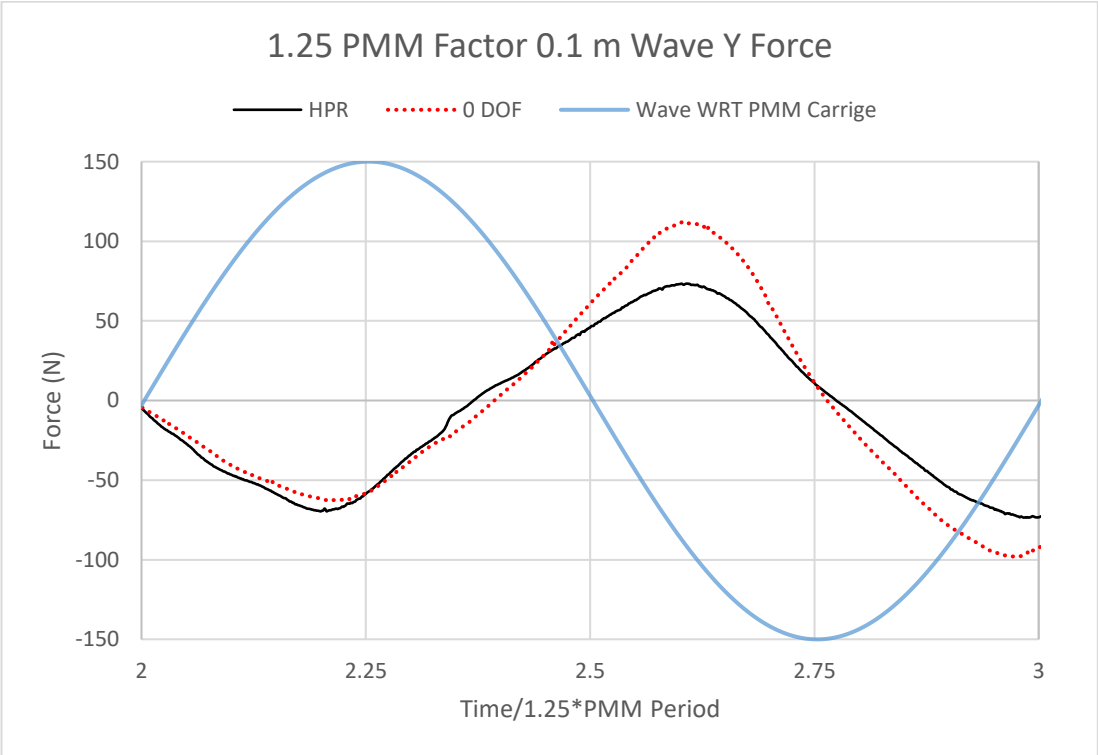

Figure 15-8 Graph showing Y force comparison between HPR and 0 DOF for 0.1m wave height 1.25 PMM period

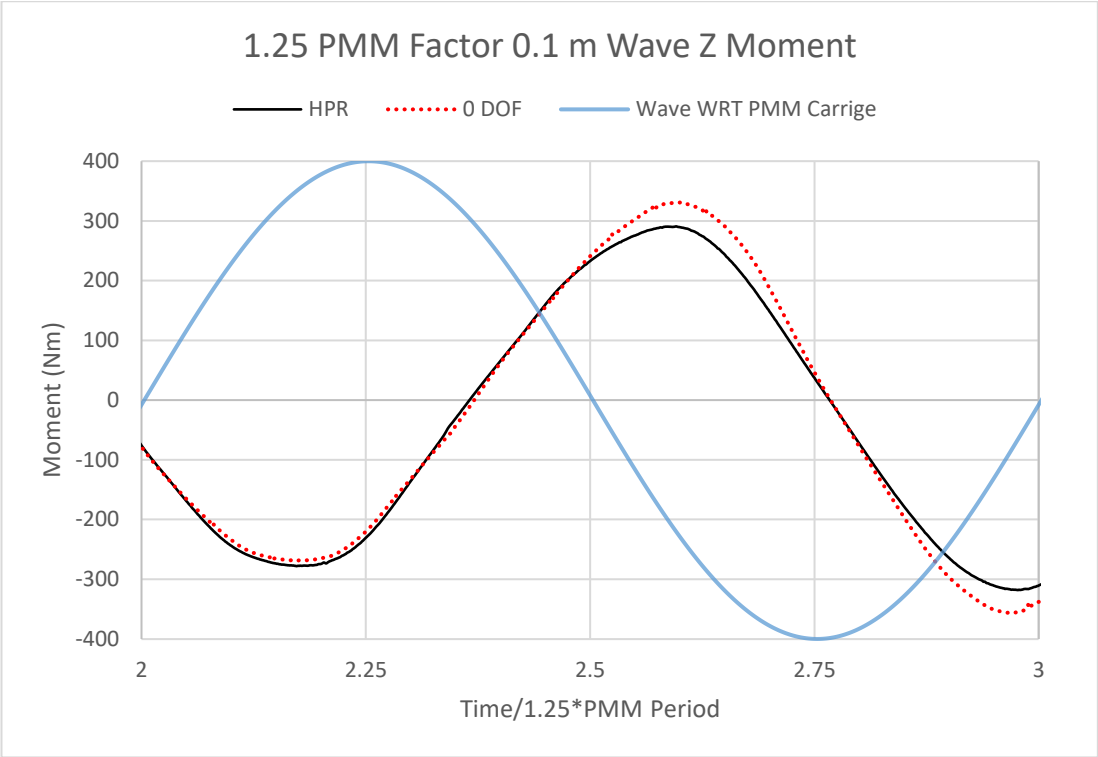

Figure 15-9 Graph showing Z moment comparison between HPR and 0 DOF for 0.1m wave height 1.25 PMM period

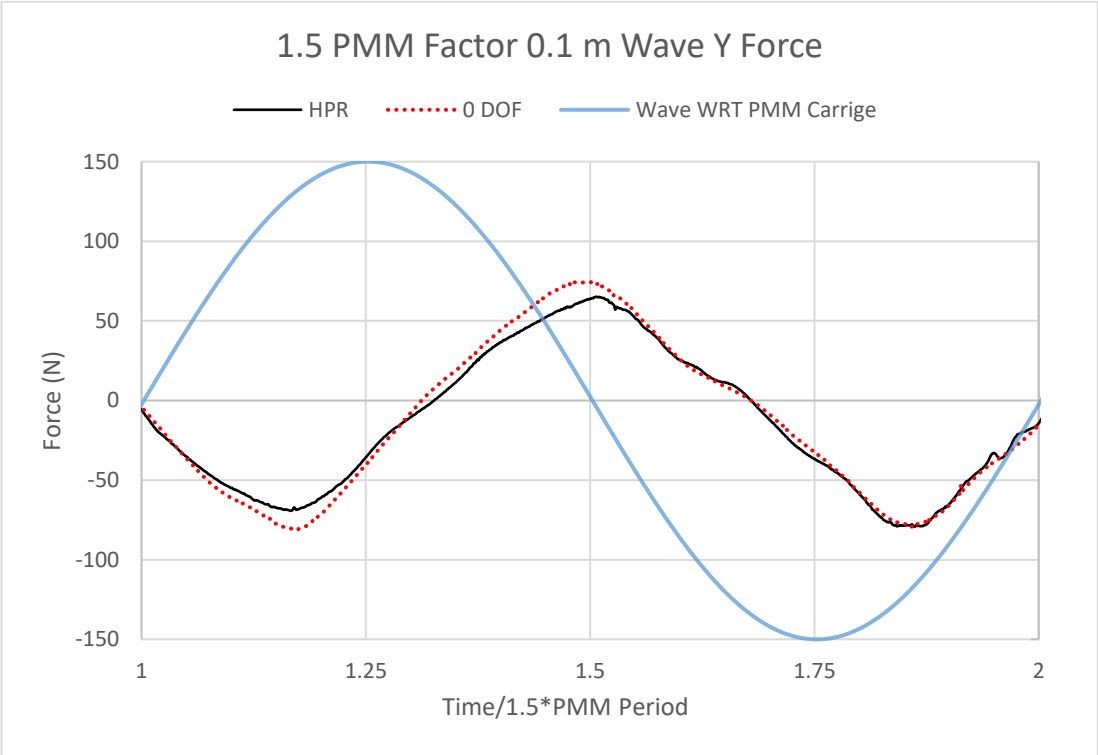

Figure 15-10 Graph showing Y force comparison between HPR and 0 DOF for 0.1m wave height 1.5 PMM period

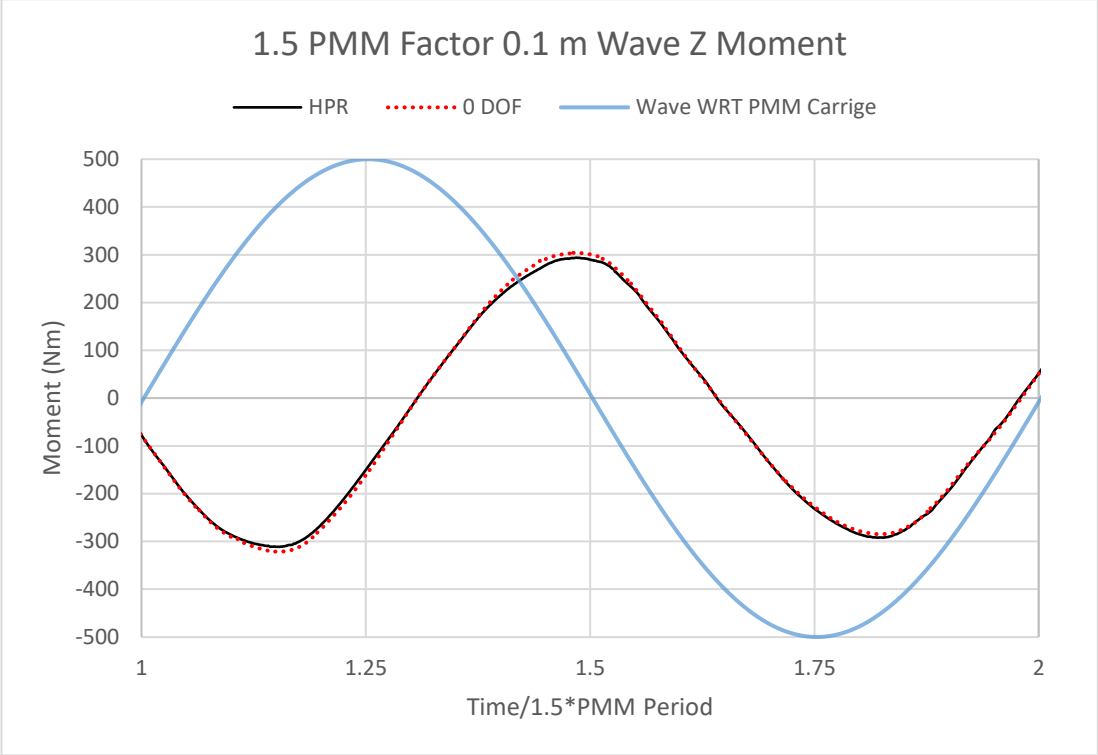

Figure 15-11 **Graph showing Z moment comparison between HPR and 0 DOF for 0.1m wave height 1.5 PMM period**

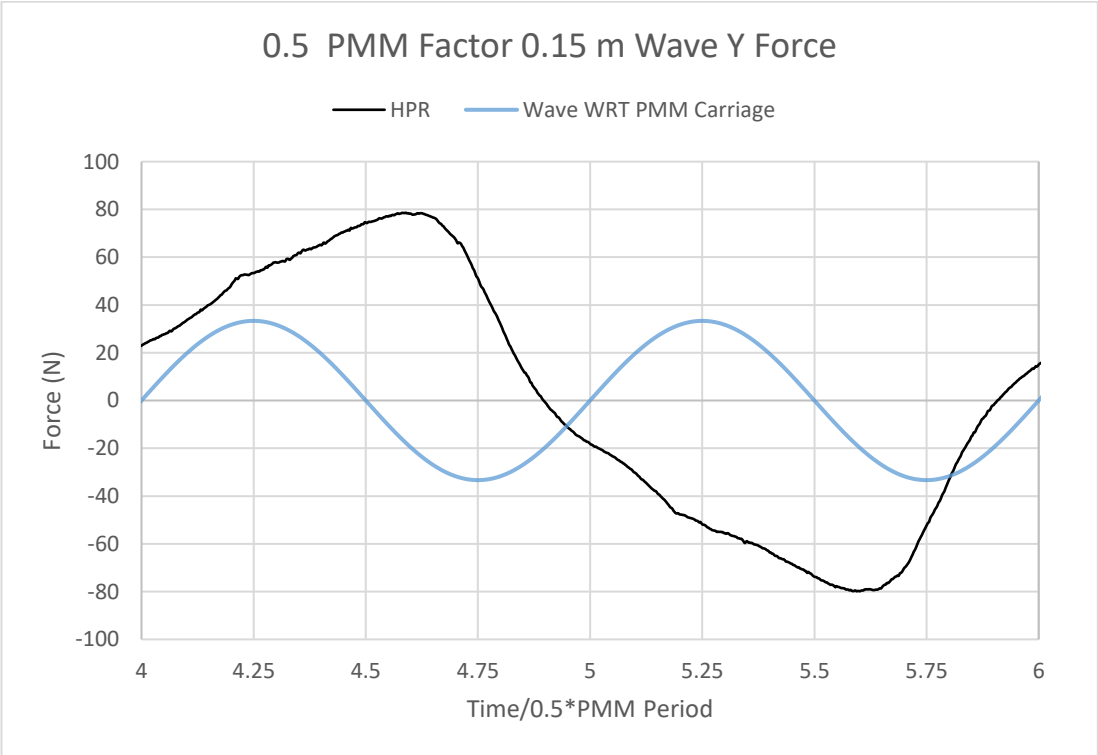

Figure 15-12 Graph showing Y force comparison between HPR for 0.15m wave height 0.5 PMM period carriage

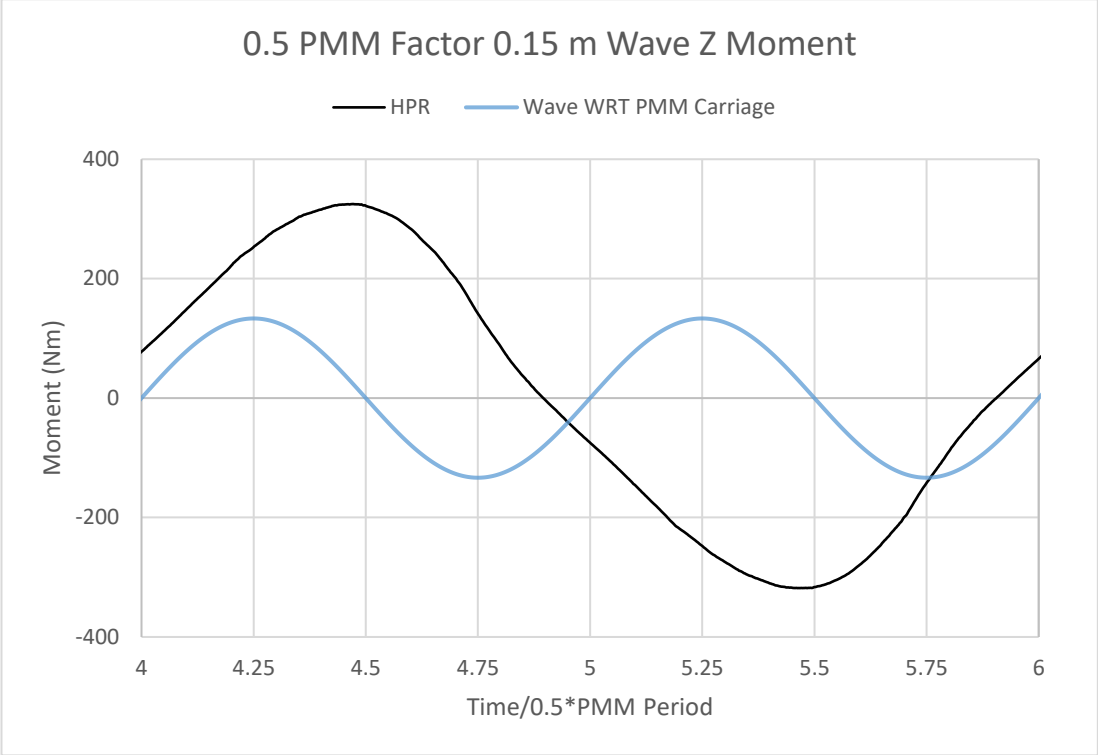

Figure 15-13 Graph showing Z moment comparison between HPR for 0.15m wave height 0.5 PMM period

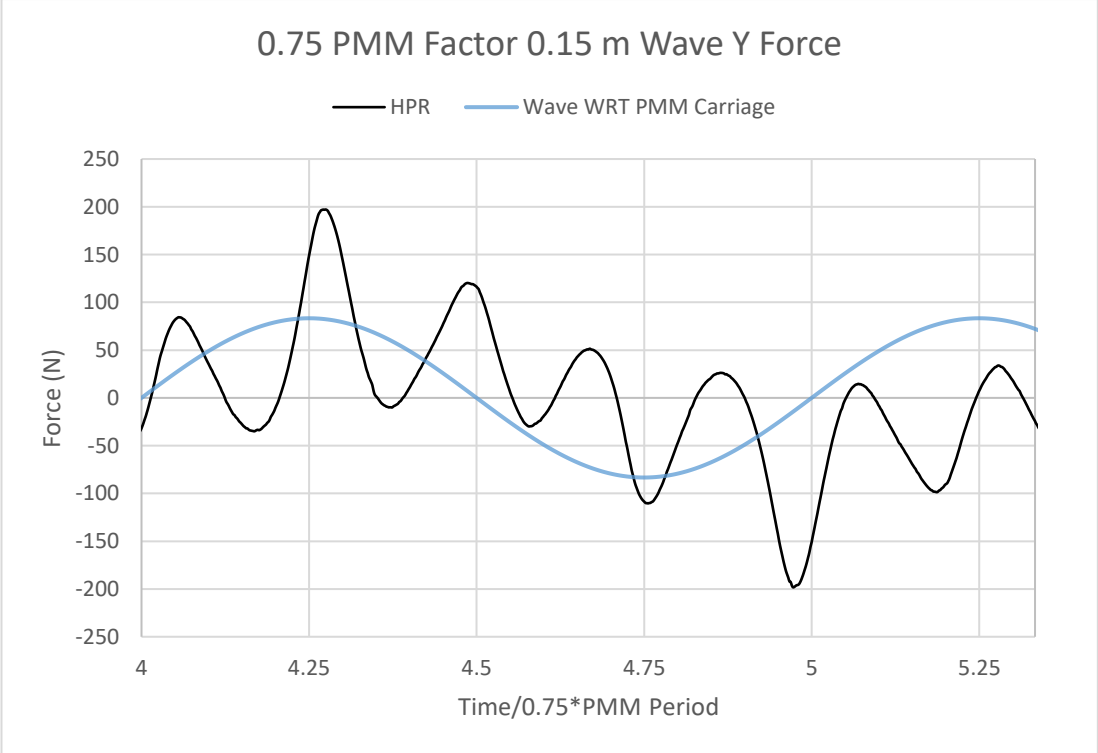

Figure 15-14 Graph showing Y force comparison between HPR for 0.15m wave height 0.75 PMM period

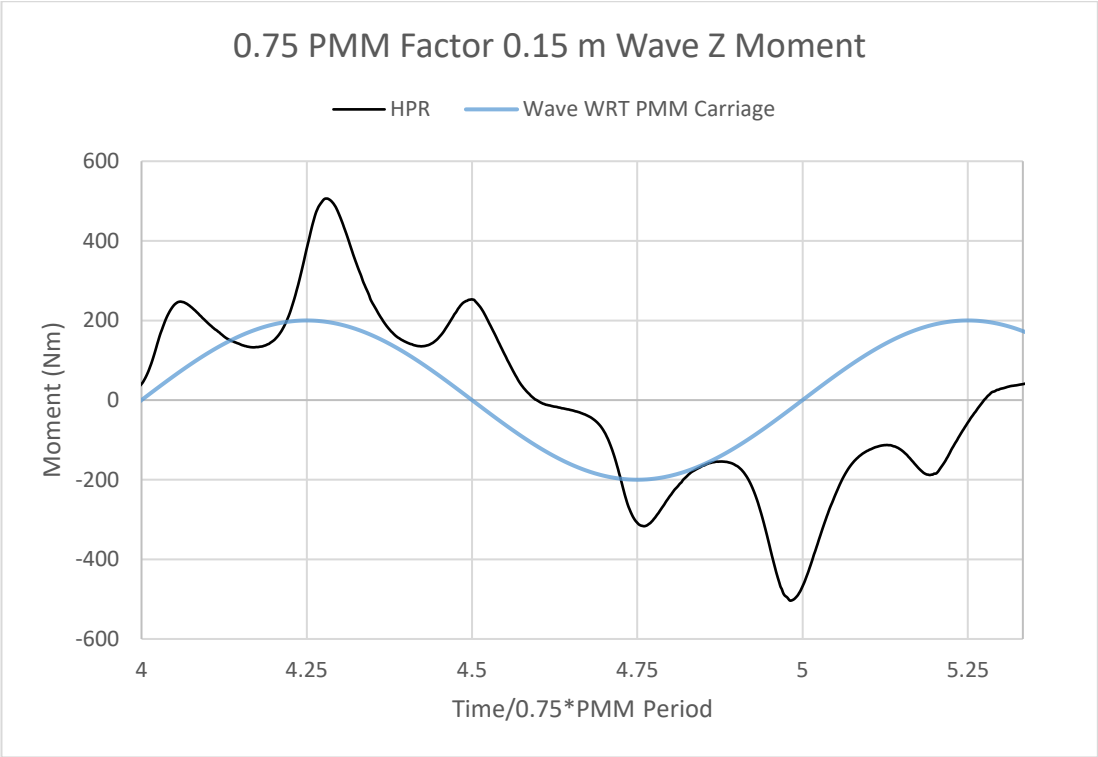

Figure 15-15 Graph showing Z moment comparison between HPR for 0.15m wave height 0.75 PMM period

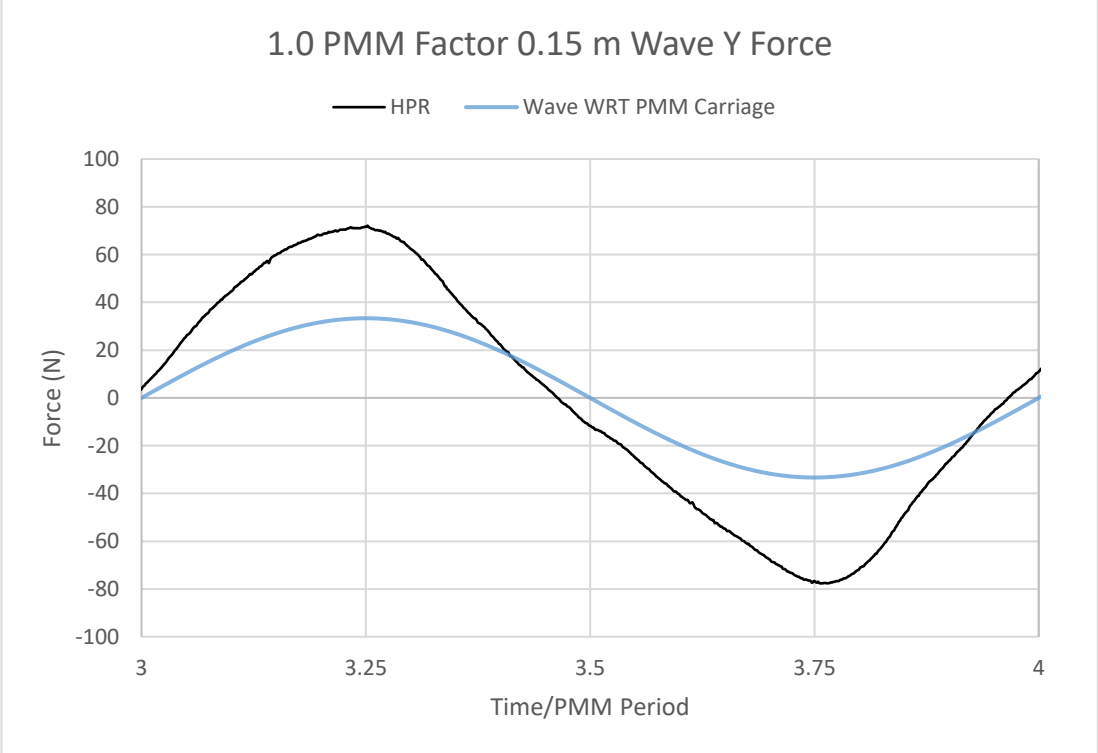

Figure 15-16 Graph showing Y force comparison between HPR for 0.15m wave height 1.0 PMM period

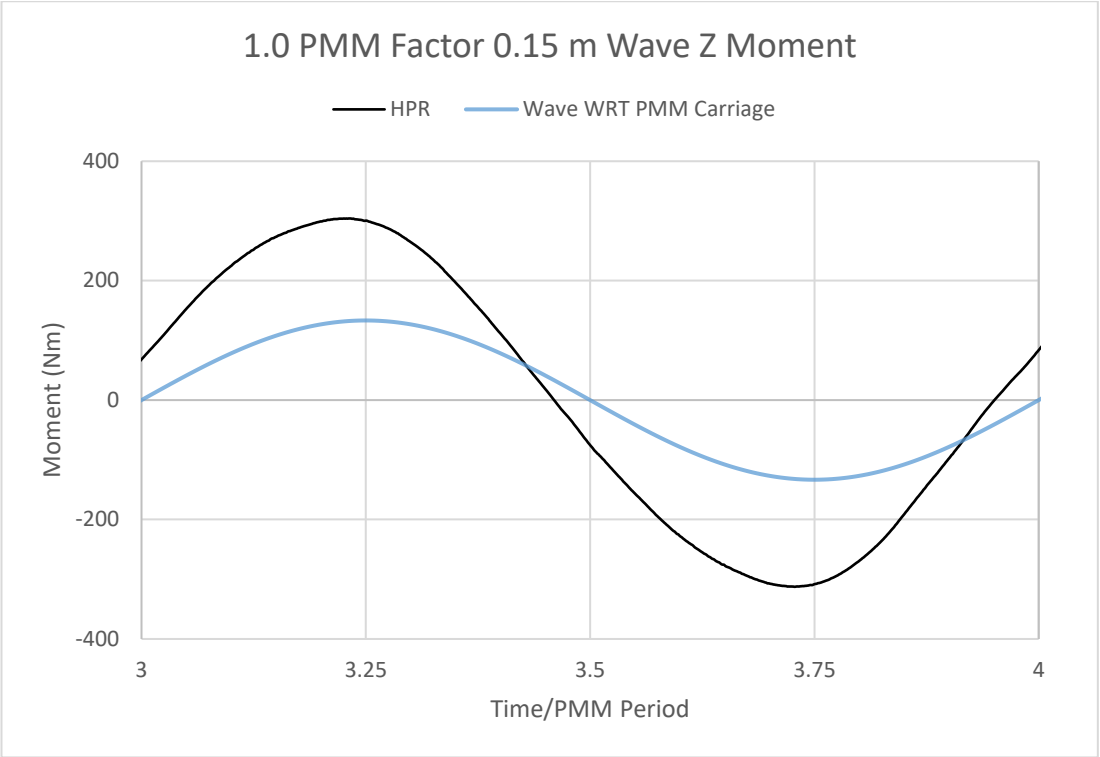

Figure 15-17 Graph showing Z moment comparison between HPR for 0.15m wave height 1.0 PMM period

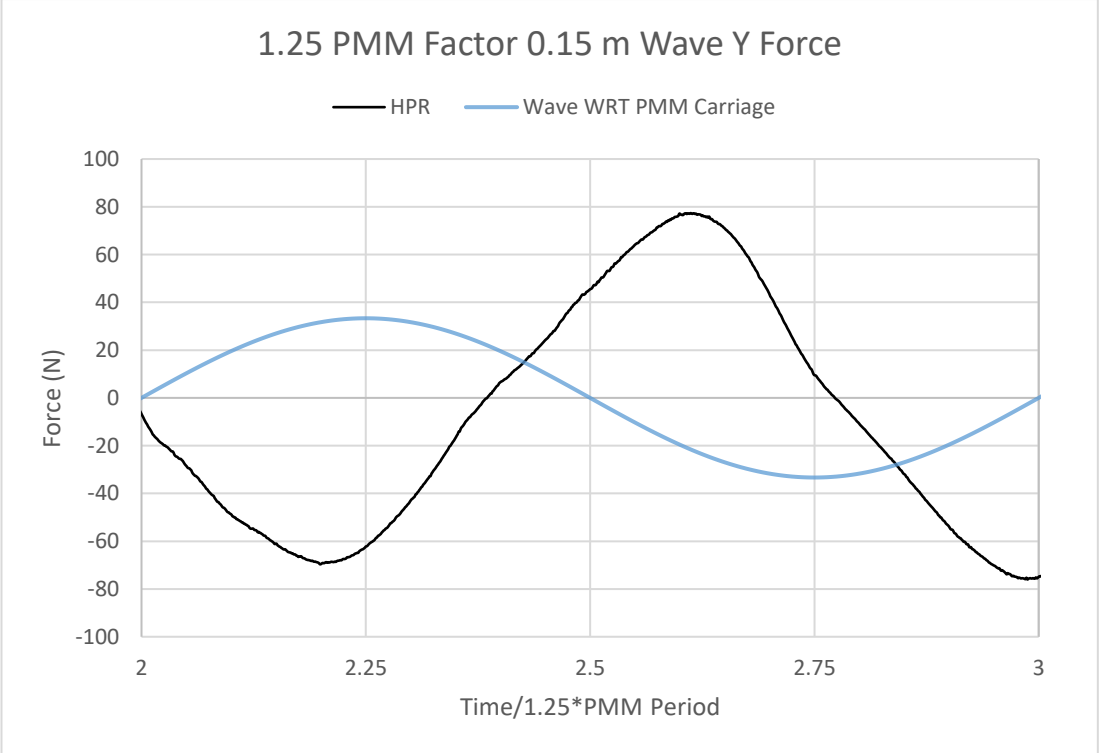

Figure 15-18 Graph showing Y force comparison between HPR for 0.15m wave height 1.25 PMM period

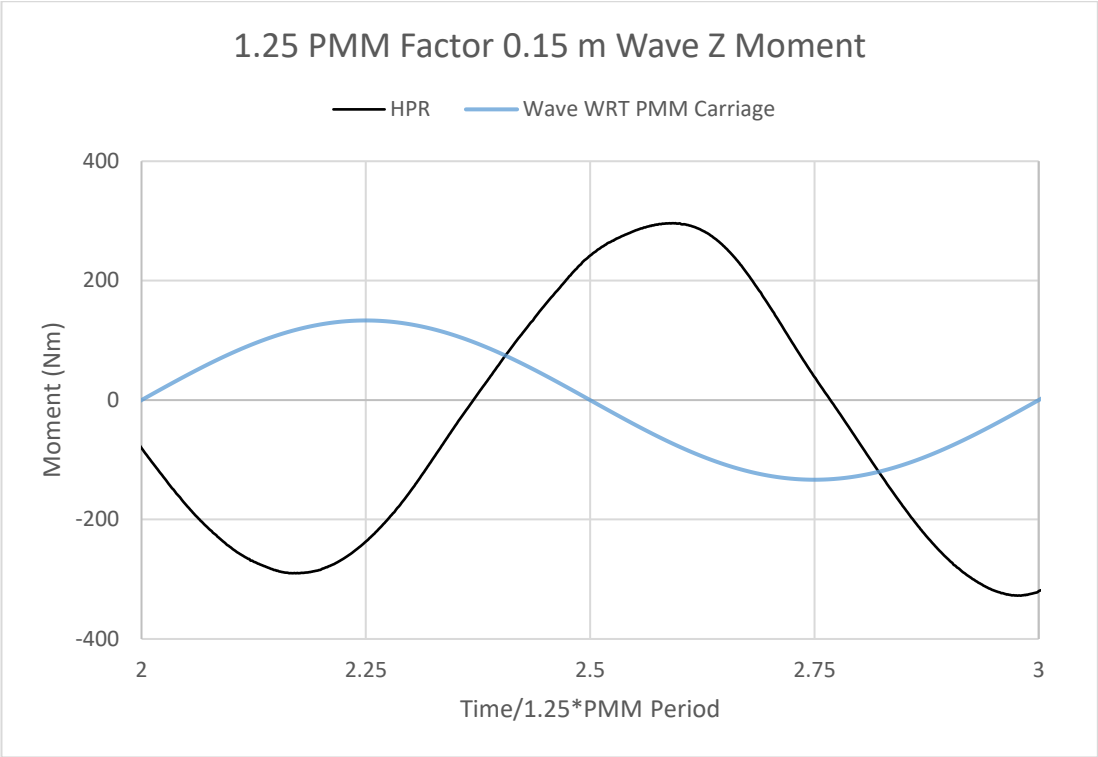

Figure 15-19 Graph showing Z moment comparison between HPR for 0.15m wave height 1.25 PMM period

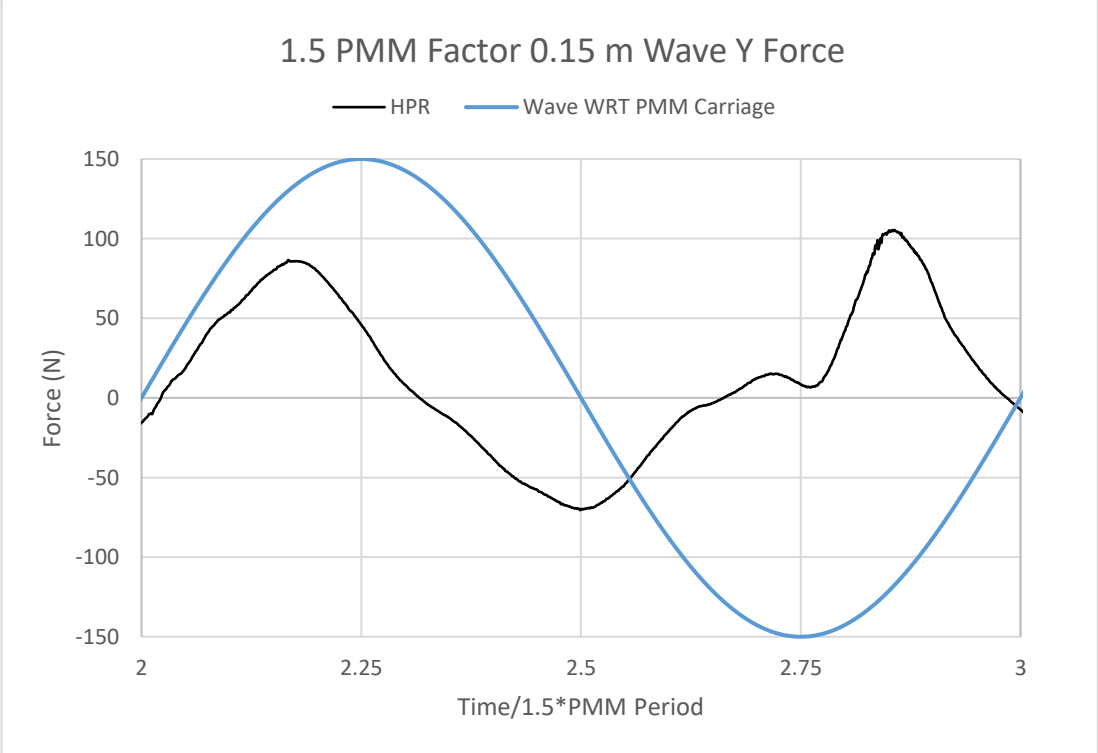

Figure 15-20 Graph showing Y force comparison between HPR for 0.15m wave height 1.5 PMM period

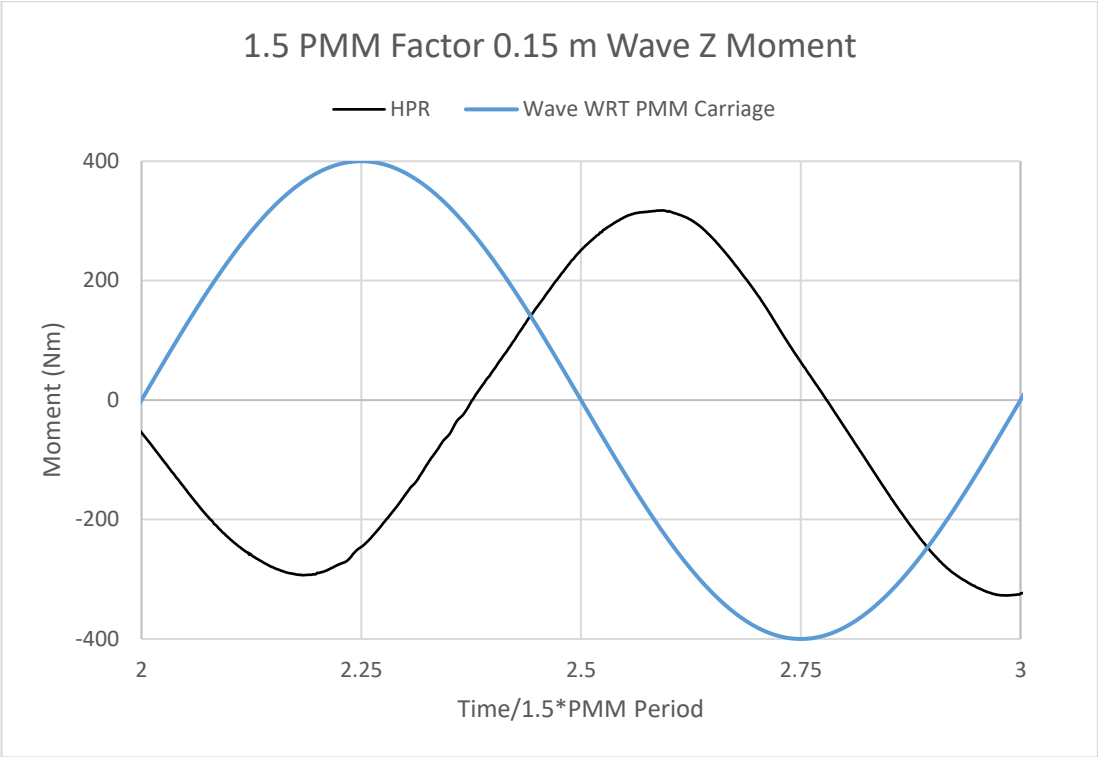

Figure 15-21 Graph showing Z moment comparison between HPR for 0.15m wave height 1.5 PMM period

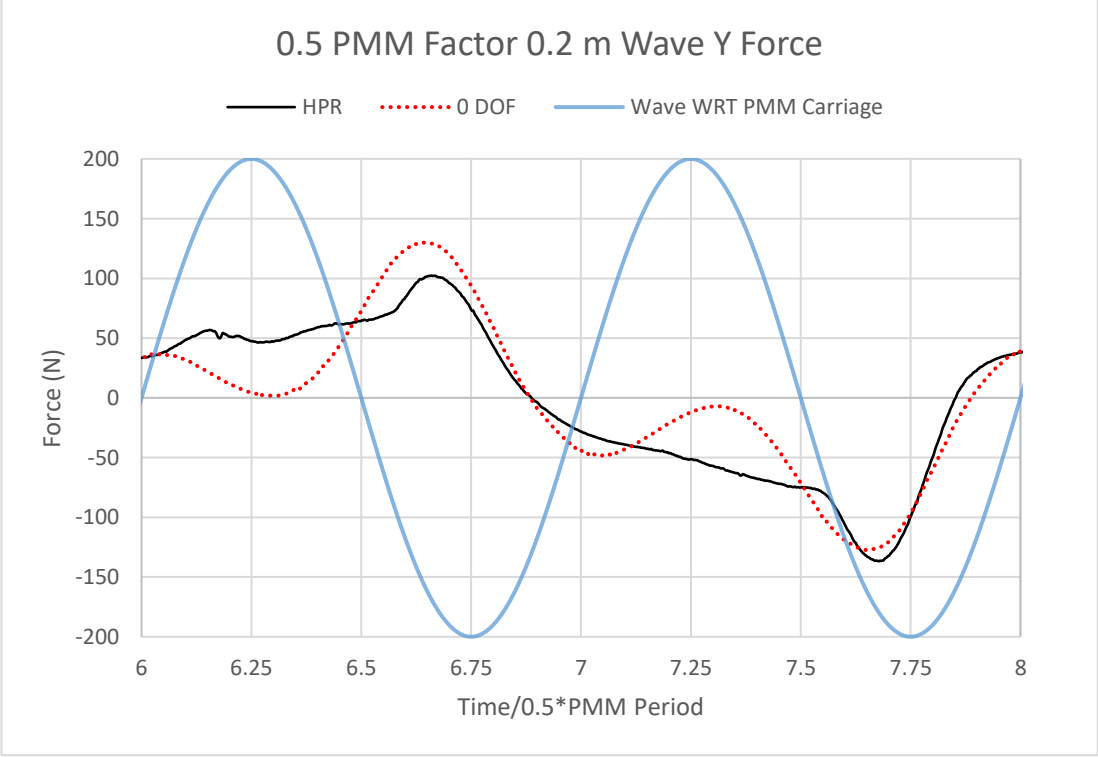

Figure 15-22 Graph showing Y force comparison between HPR and 0 DOF for 0.2m wave height 0.5 PMM period

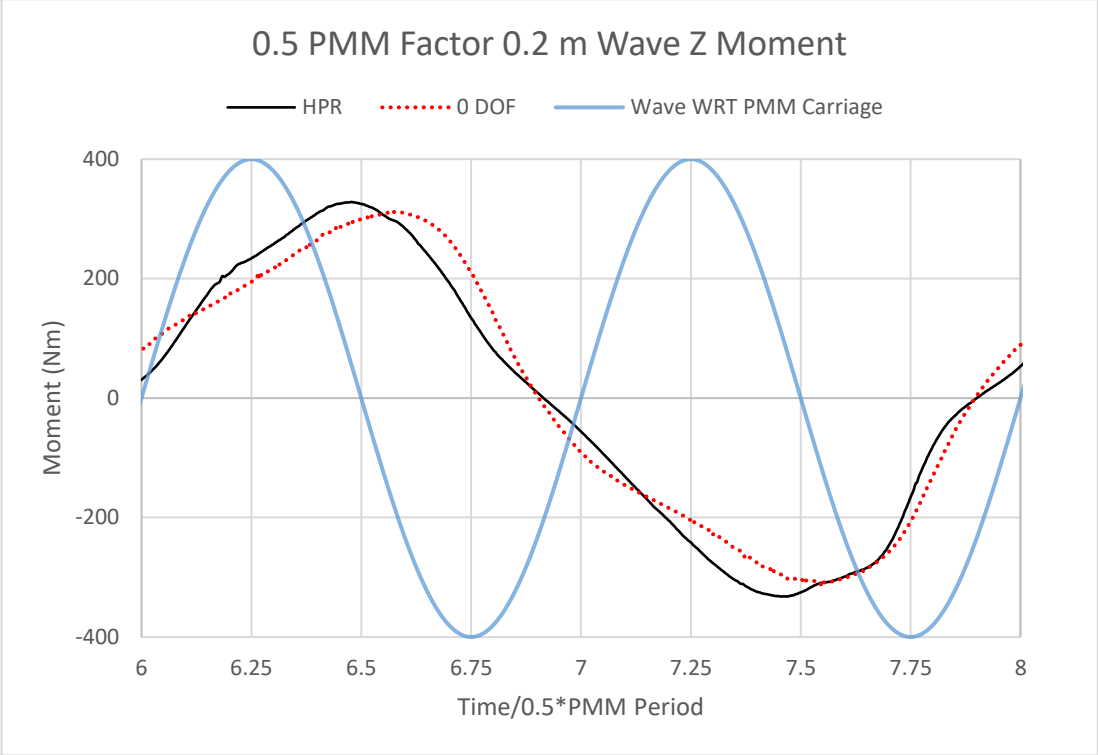

Figure 15-23 Graph showing Z moment comparison between HPR and 0 DOF for 0.2m wave height 0.5 PMM period

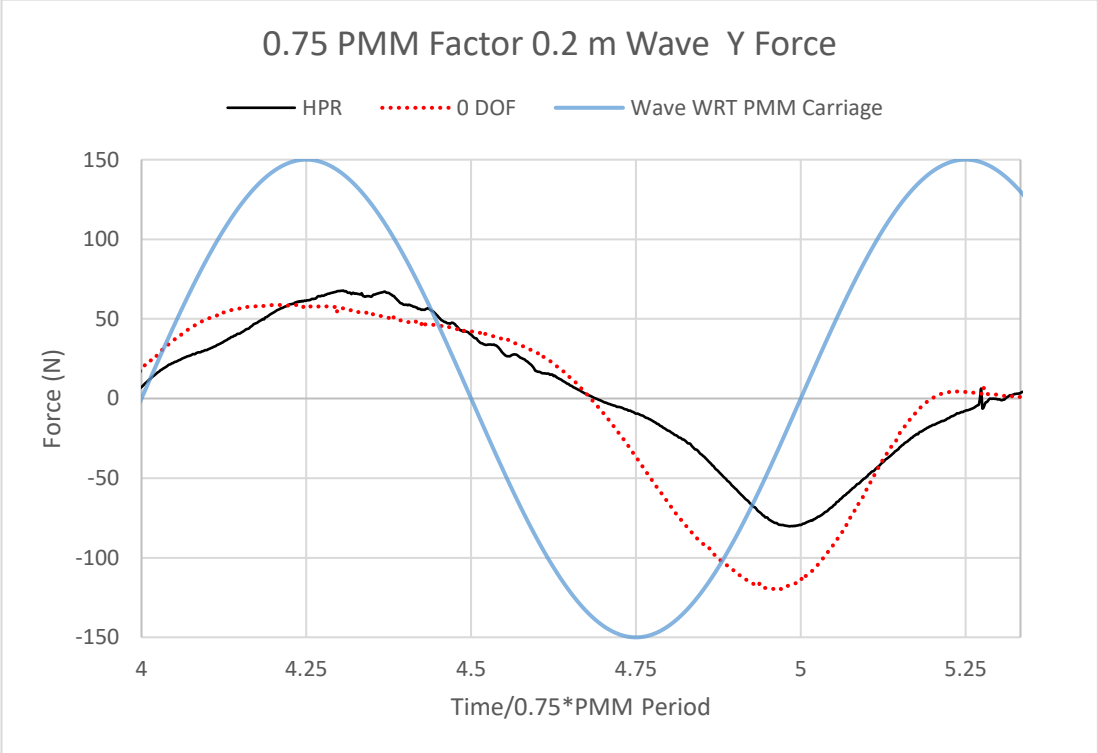

Figure 15-24 Graph showing Y force comparison between HPR and 0 DOF for 0.2m wave height 0.75 PMM period

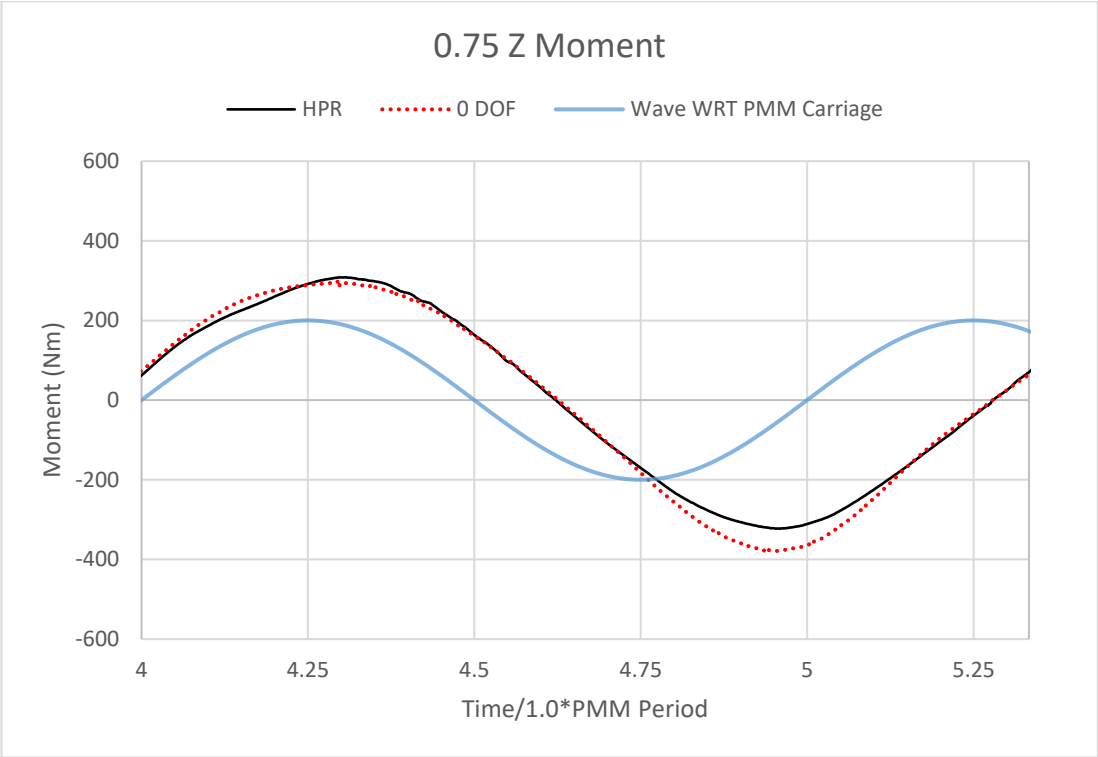

Figure 15-25 Graph showing Z moment comparison between HPR and 0 DOF for 0.2m wave height 0.75 PMM period

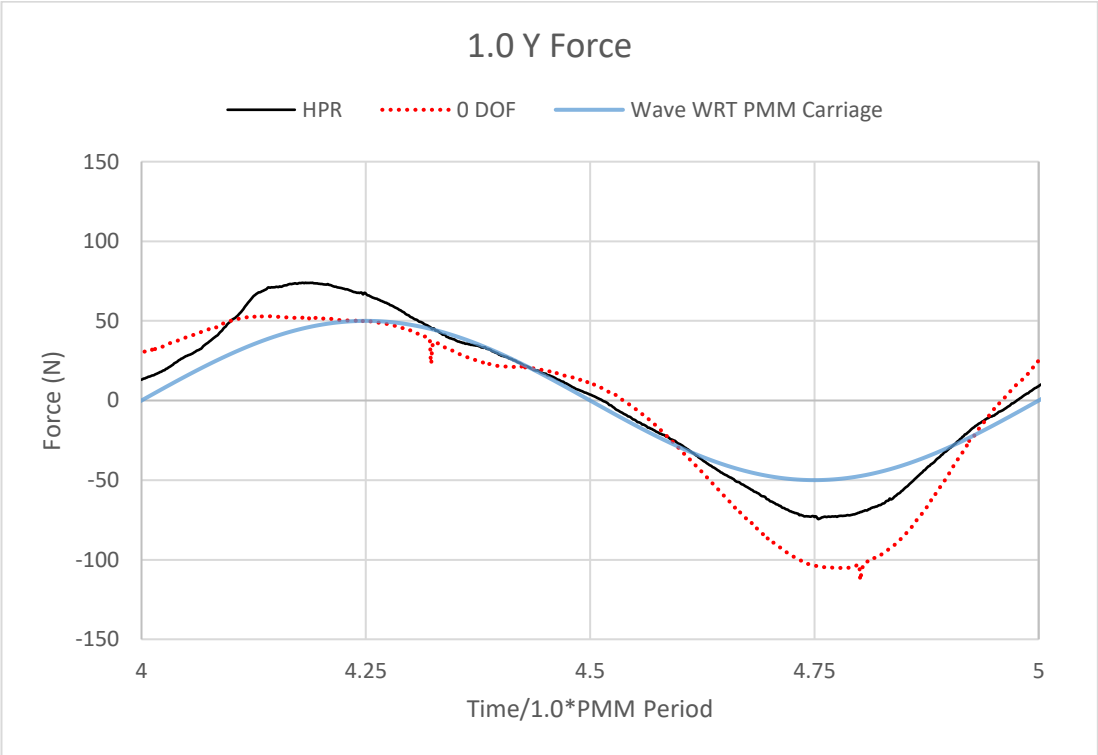

Figure 15-26 Graph showing Y force comparison between HPR and 0 DOF for 0.2m wave height 1.0 PMM period

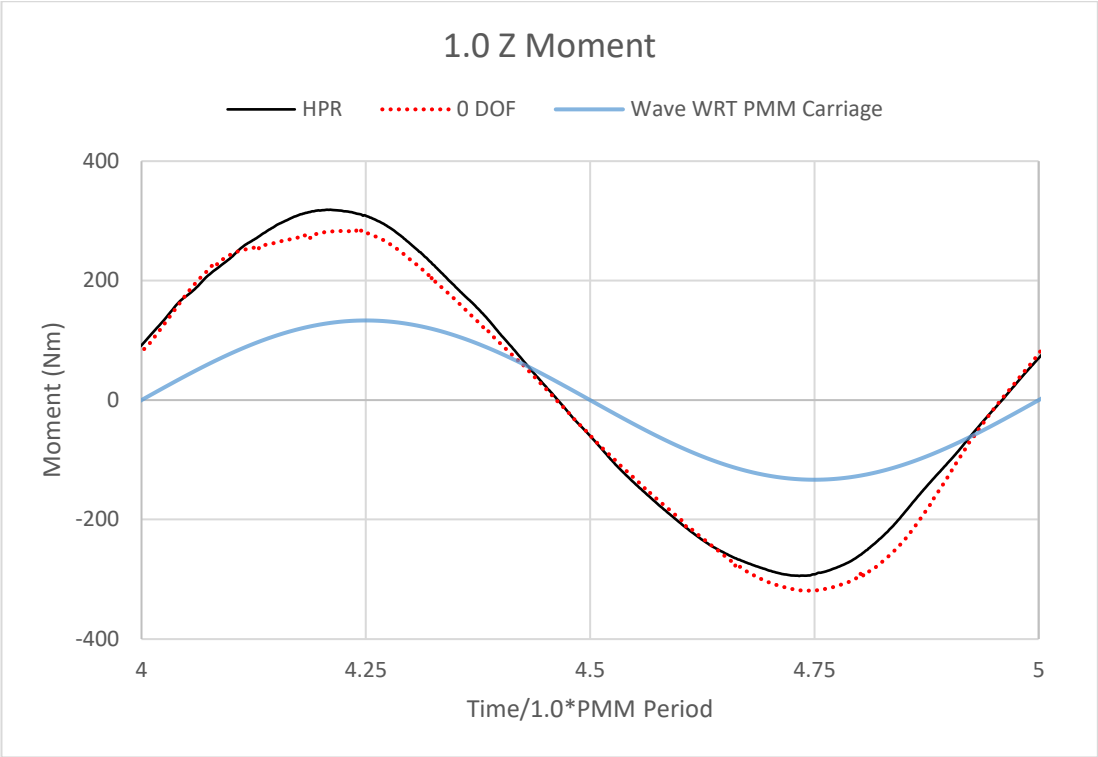

Figure 15-27 Graph showing Z moment comparison between HPR and 0 DOF for 0.2m wave height 1.0 PMM period

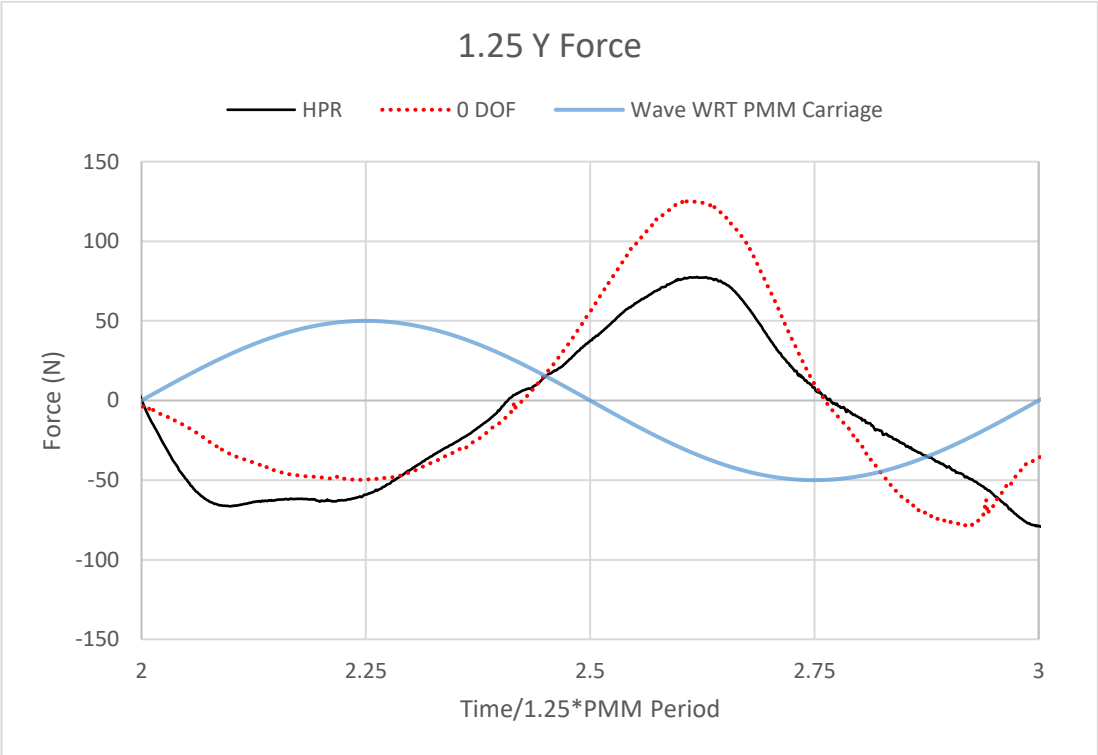

Figure 15-28 Graph showing Y force comparison between HPR and 0 DOF for 0.2m wave height 1.25 PMM period

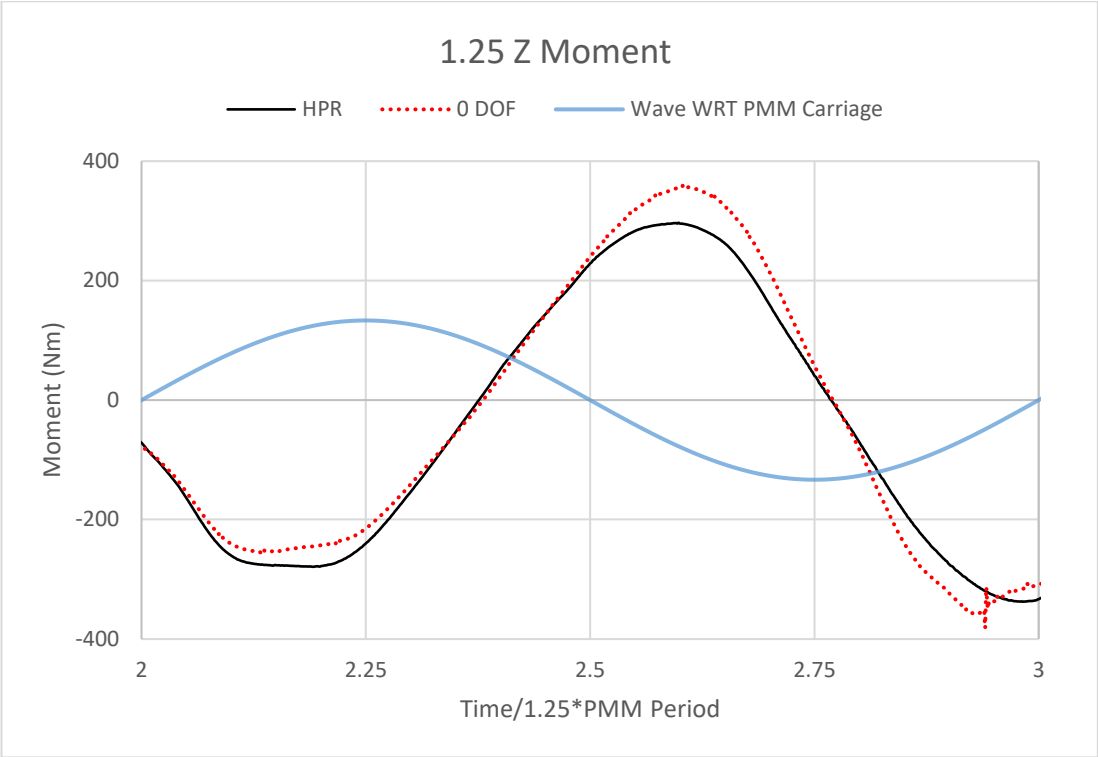

Figure 15-29 Graph showing Z moment comparison between HPR and 0 DOF for 0.2m wave height 1.25 PMM period

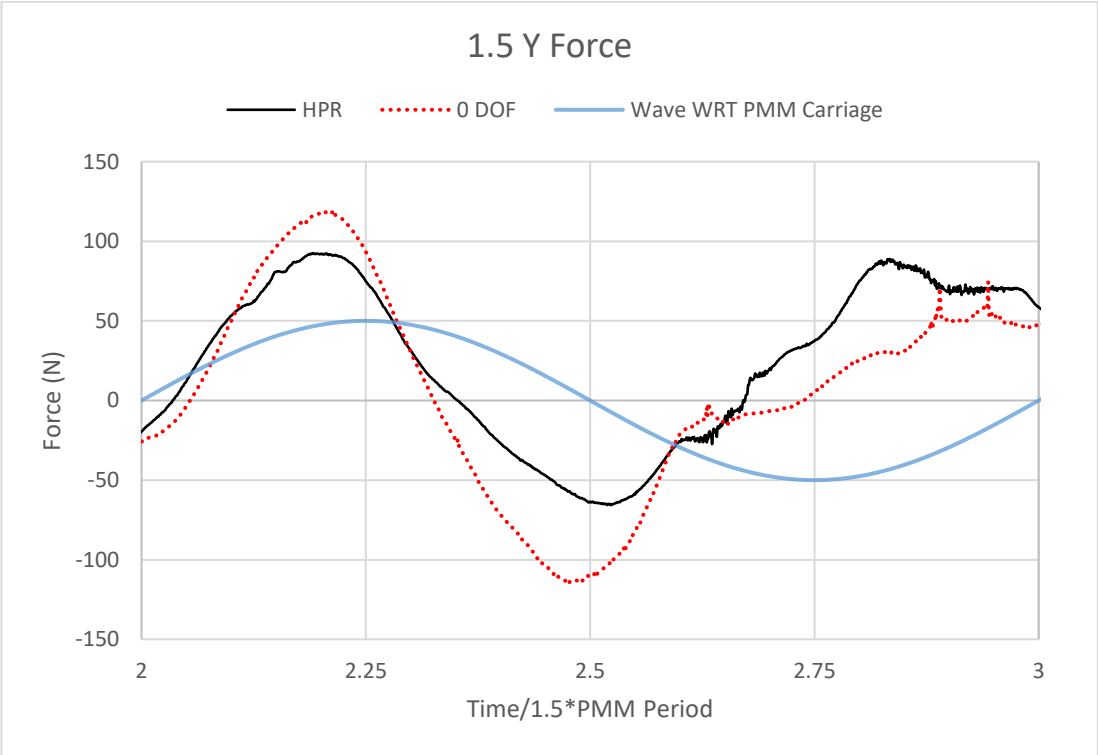

Figure 15-30 Graph showing Y force comparison between HPR and 0 DOF for 0.2m wave height 1.5 PMM period

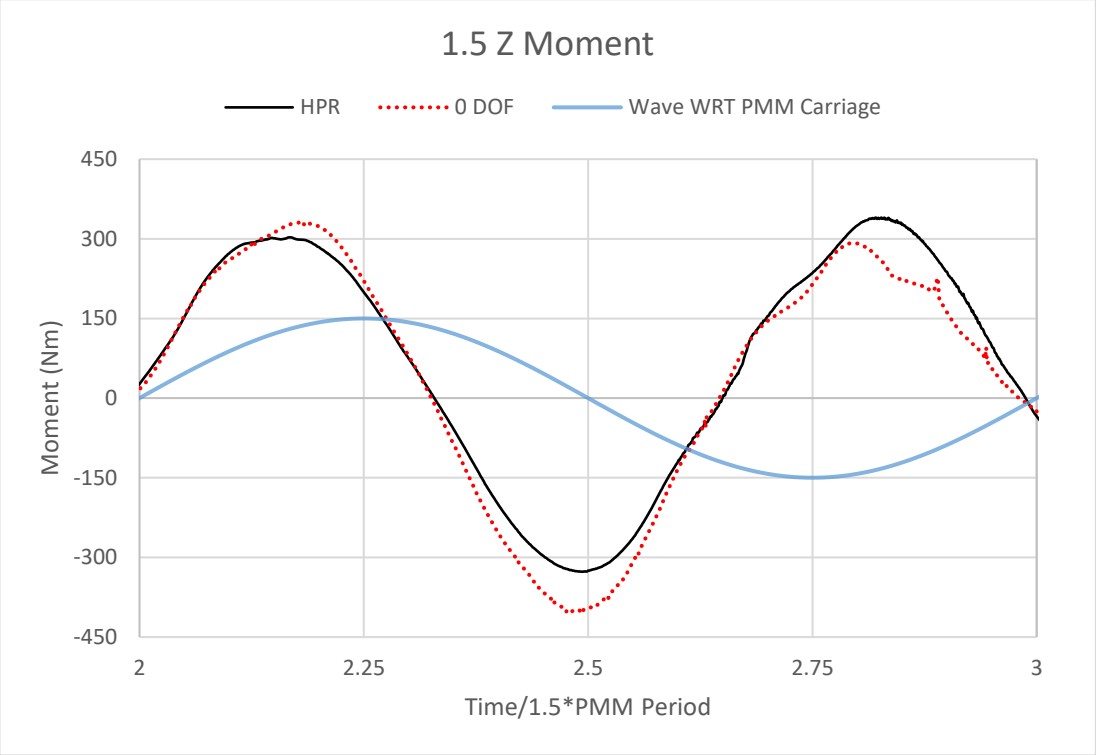

Figure 15-31 Graph showing Z moment comparison between HPR and 0 DOF for 0.2m wave height 1.5 PMM period

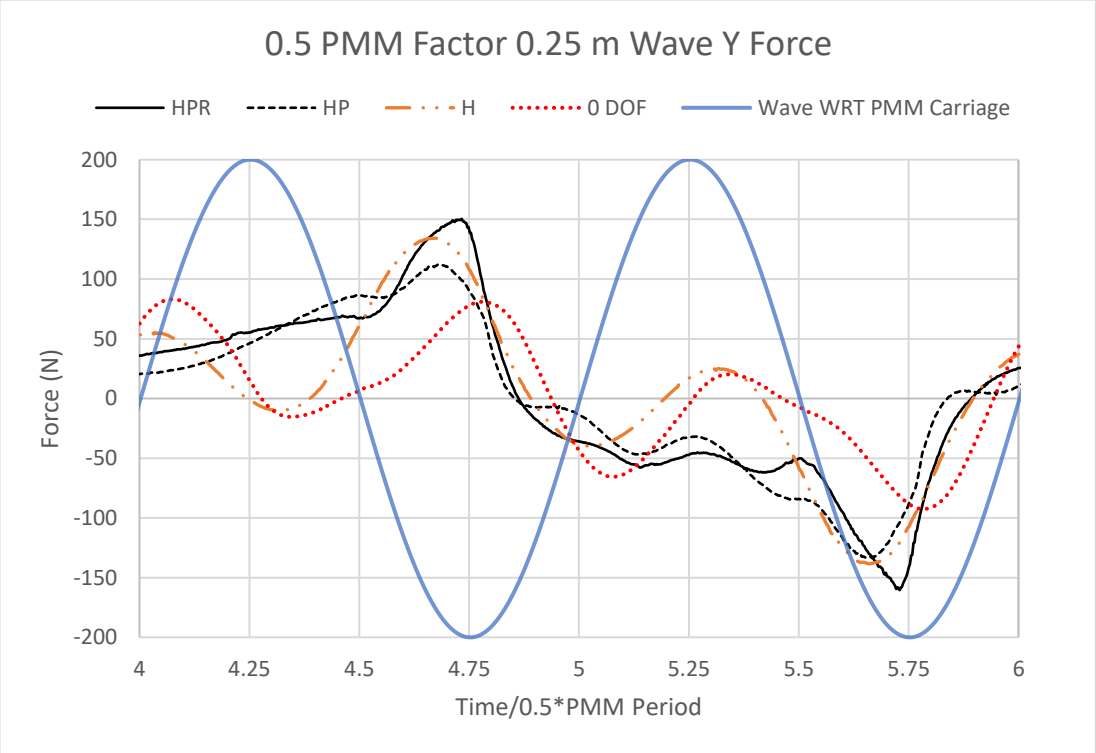

Figure 15-32 Graph showing Y force comparison between HPR, HP, H & 0 DOF for 0.25m wave height 0.5 PMM period

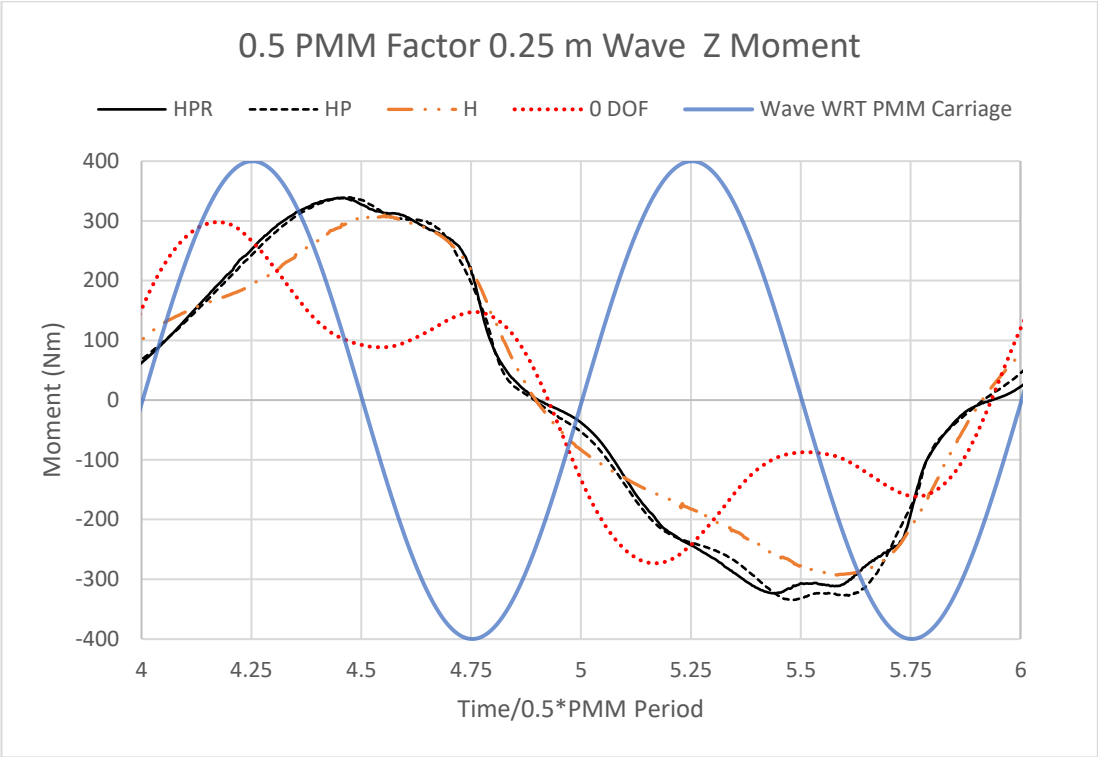

Figure 15-33 Graph showing Z moment comparison between HPR, HP, H & 0 DOF for 0.25m wave height 0.5 PMM period

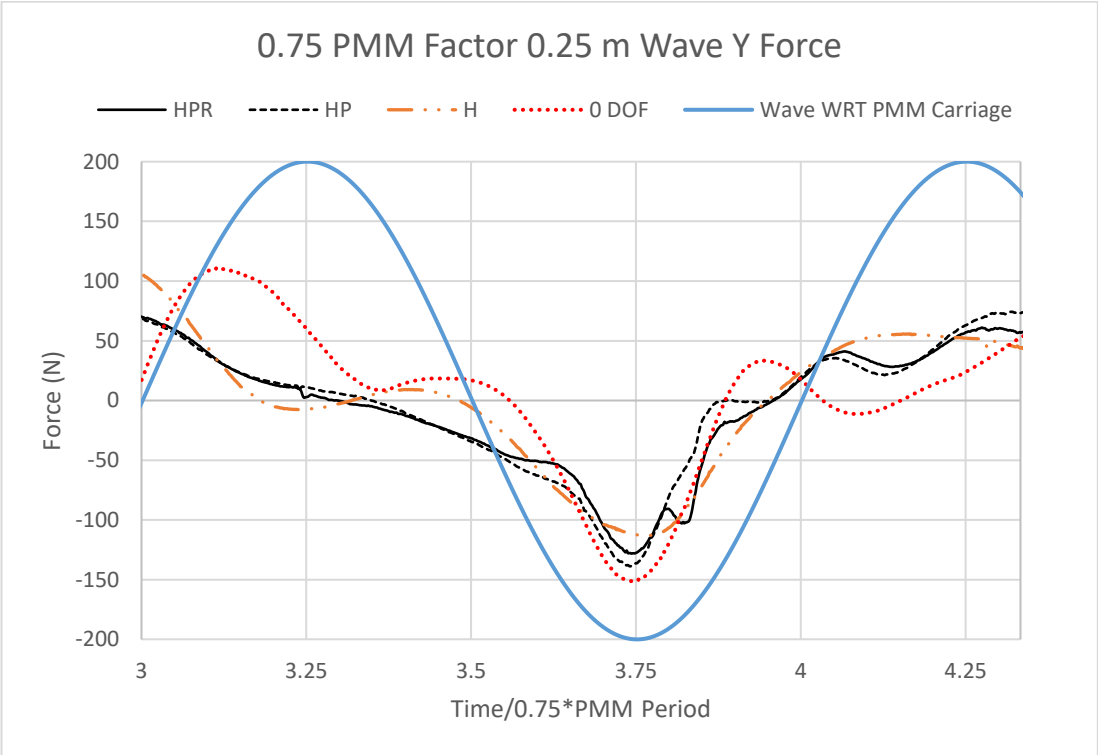

Figure 15-34 Graph showing Y force comparison between HPR, HP, H & 0 DOF for 0.25m wave height 0.75 PMM period

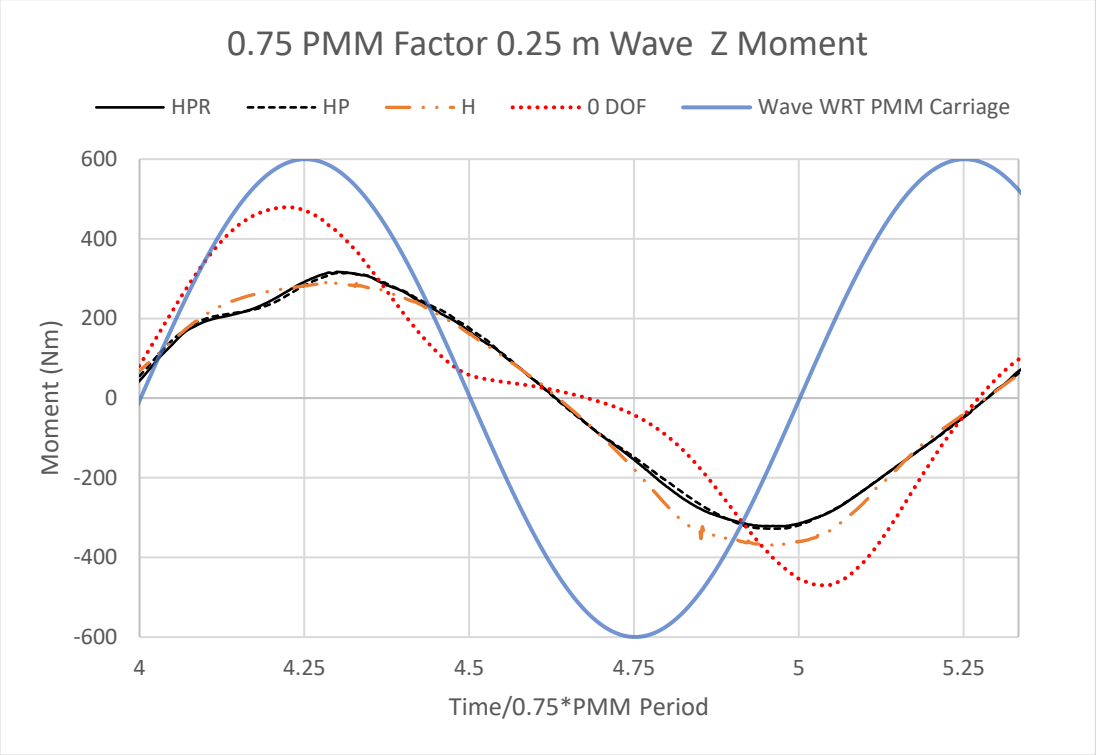

Figure 15-35 Graph showing Z moment comparison between HPR, HP, H & 0 DOF for 0.25m wave height 0.75 PMM period

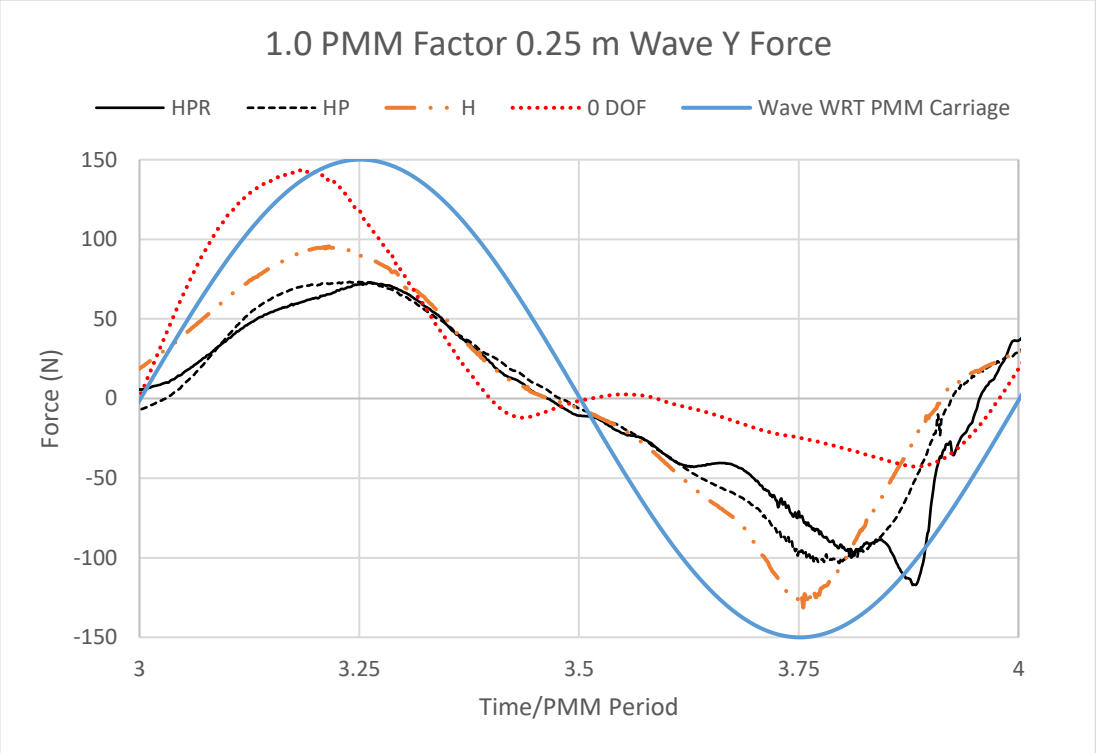

Figure 15-36 Graph showing Y force comparison between HPR, HP, H & 0 DOF for 0.25m wave height 1.0 PMM period

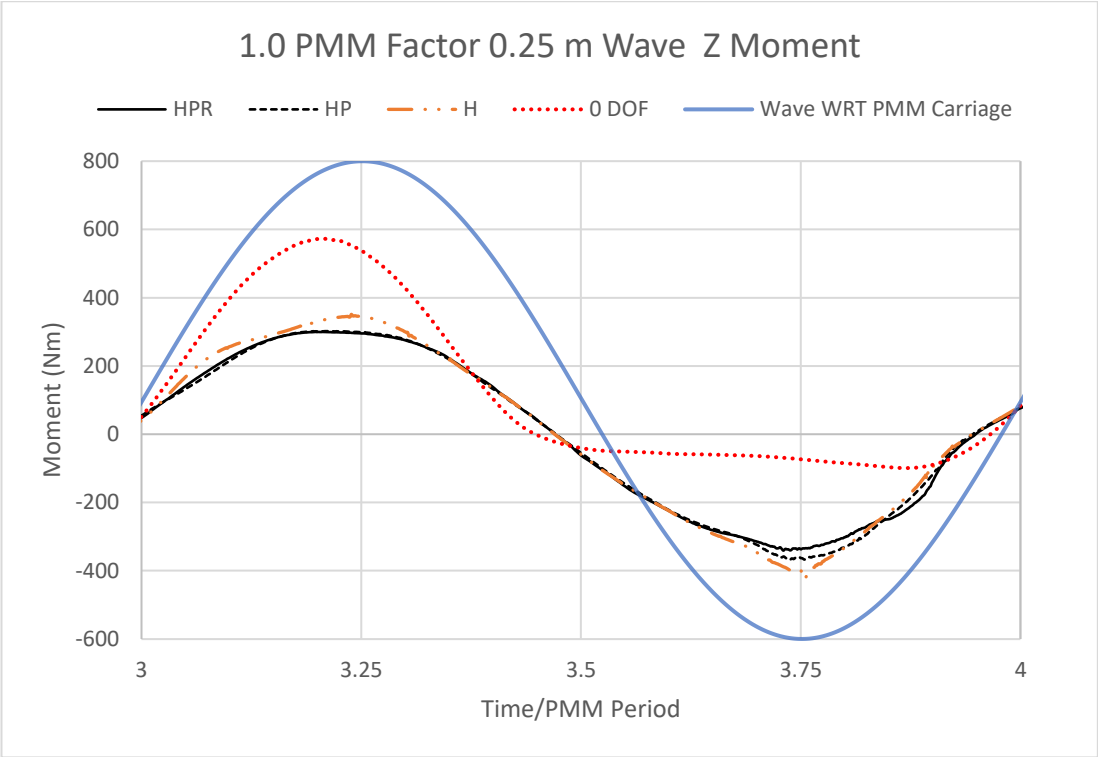

Figure 15-37 Graph showing Z moment comparison between HPR, HP, H & 0 DOF for 0.25m wave height 1.0 PMM period

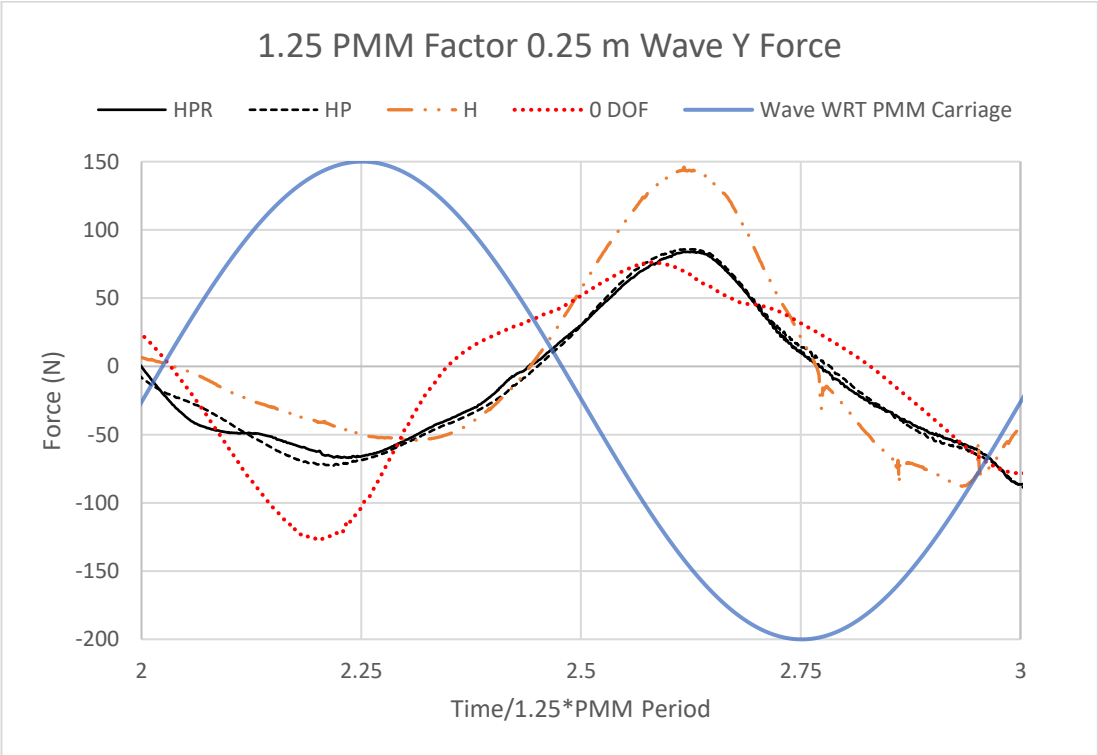

Figure 15-38 Graph showing Y force comparison between HPR, HP, H & 0 DOF for 0.25m wave height 1.25 PMM period

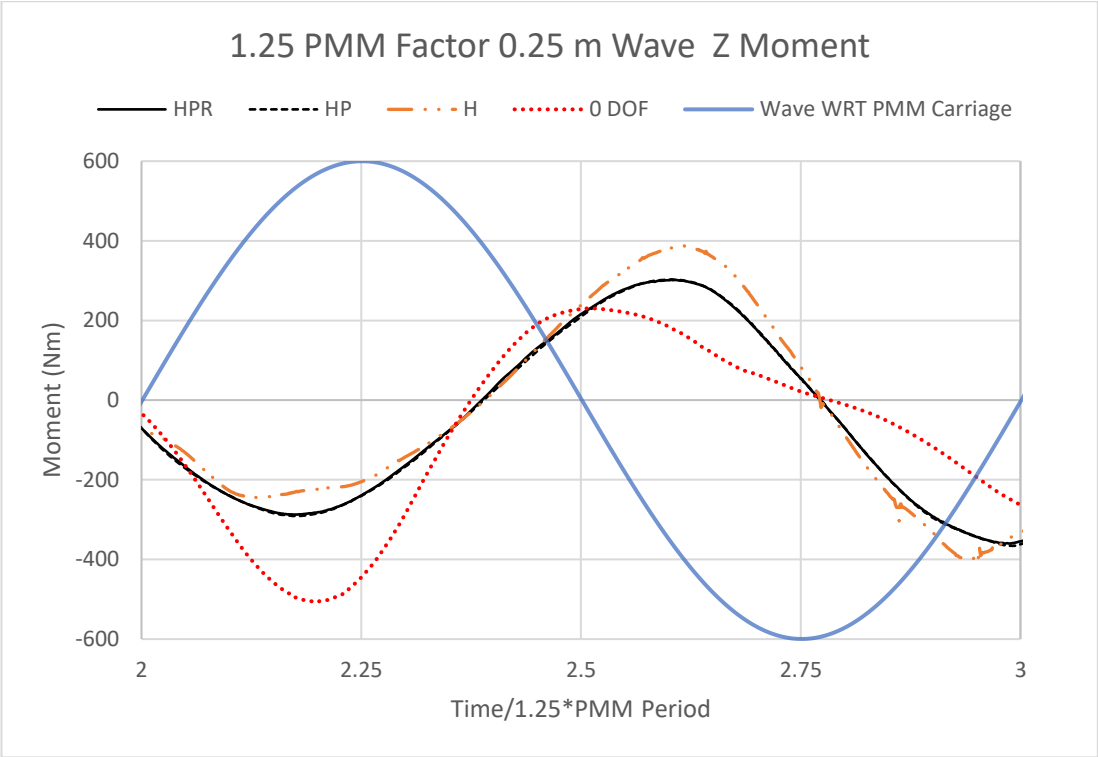

Figure 15-39 Graph showing Z moment comparison between HPR, HP, H & 0 DOF for 0.25m wave height 1.25 PMM period

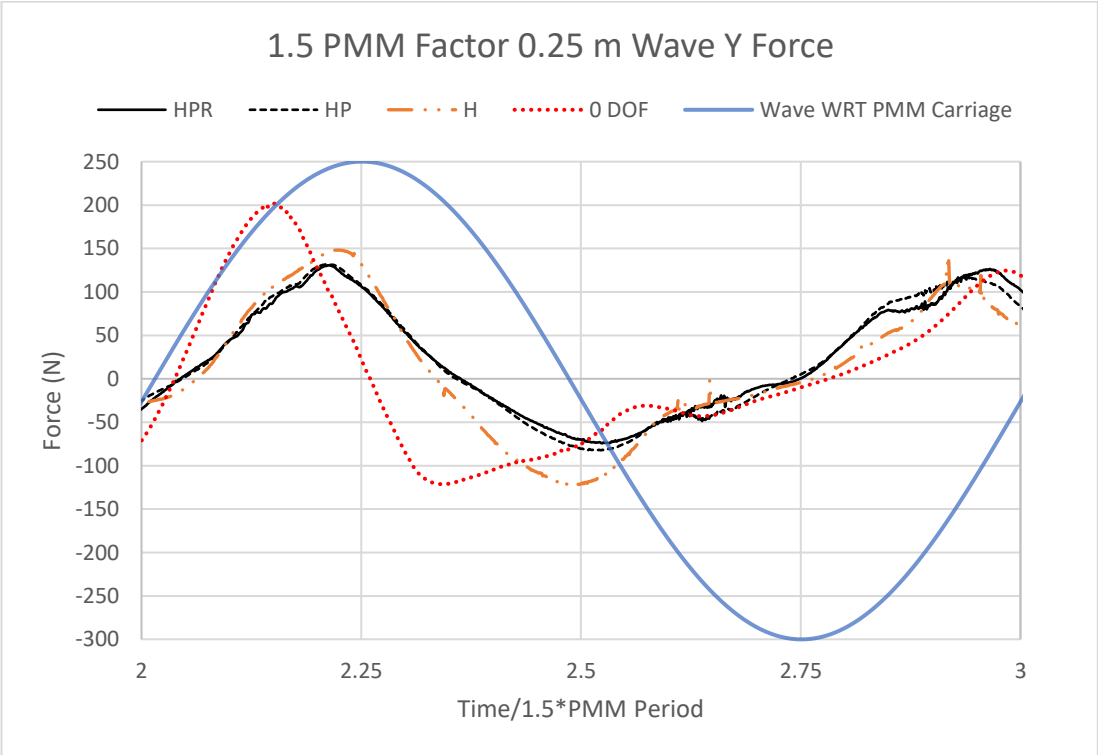

Figure 15-40 Graph showing Y force comparison between HPR, HP, H & 0 DOF for 0.25m wave height 1.5 PMM period

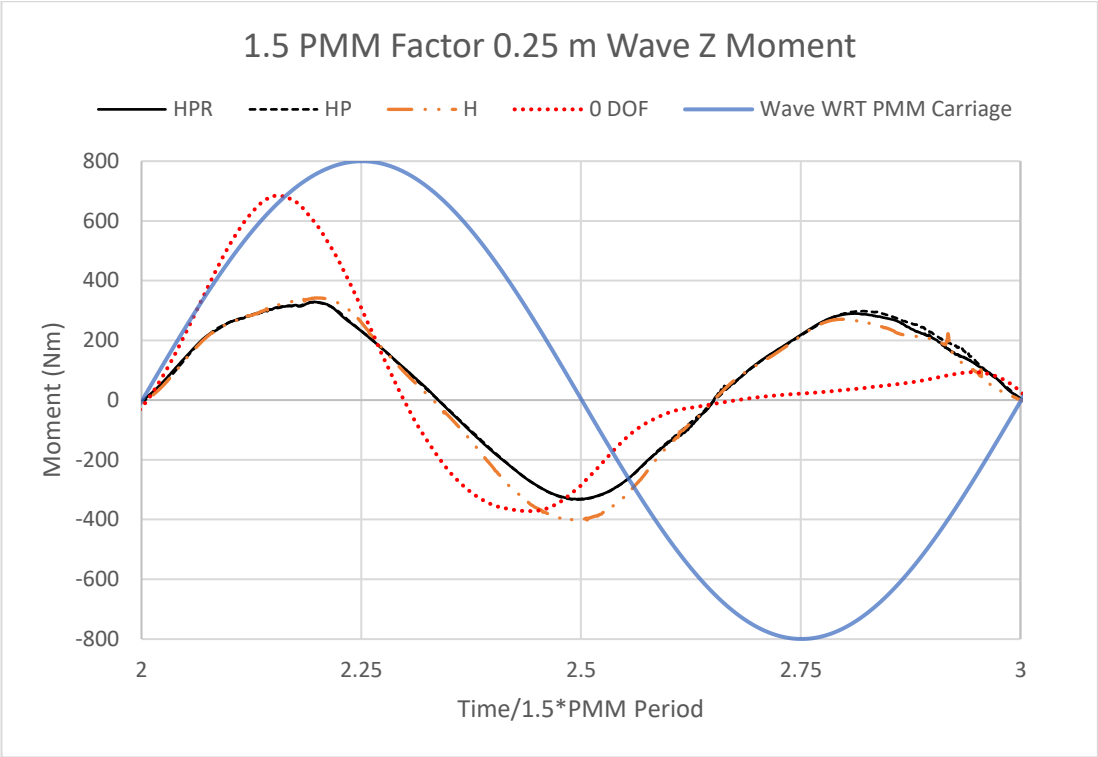

Figure 15-41 Graph showing Z moment comparison between HPR, HP, H & 0 DOF for 0.25m wave height 1.5 PMM period

16. Appendix vii

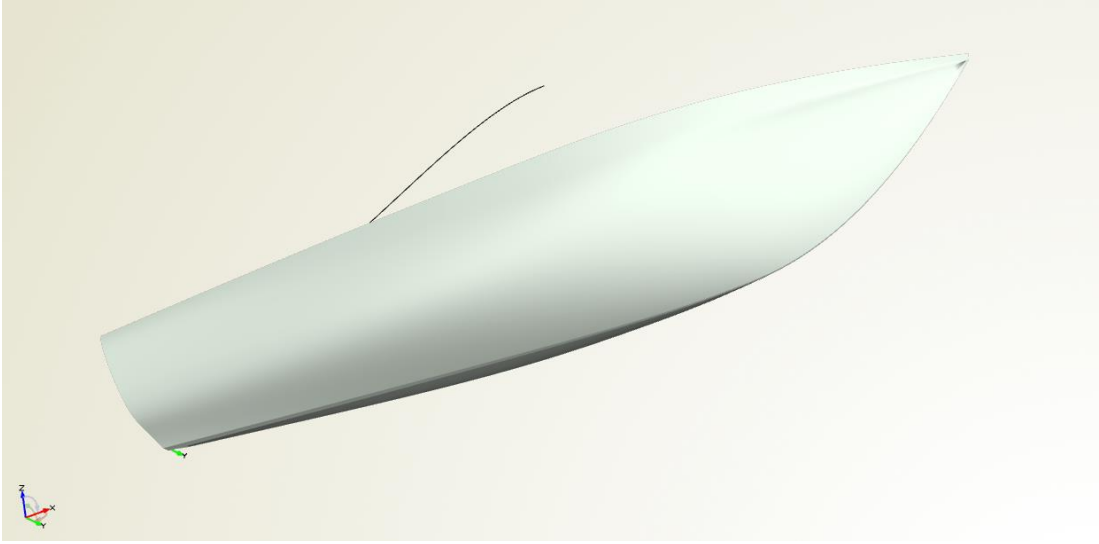

Figure 16-1 3D Render of hull 6170

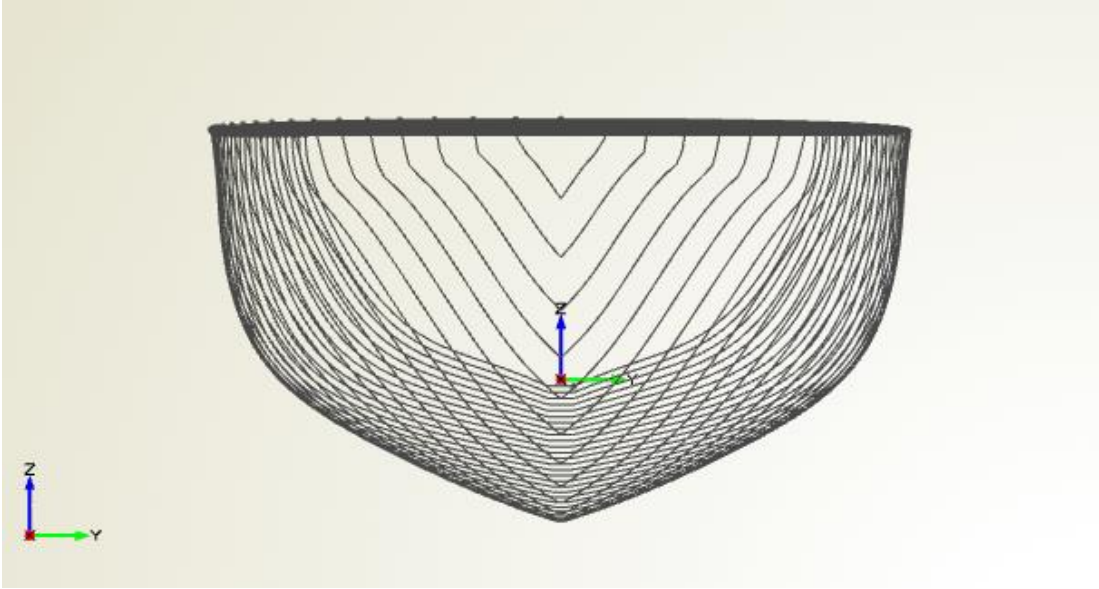

Figure 16-2 Sectional lines plan for hull 6170

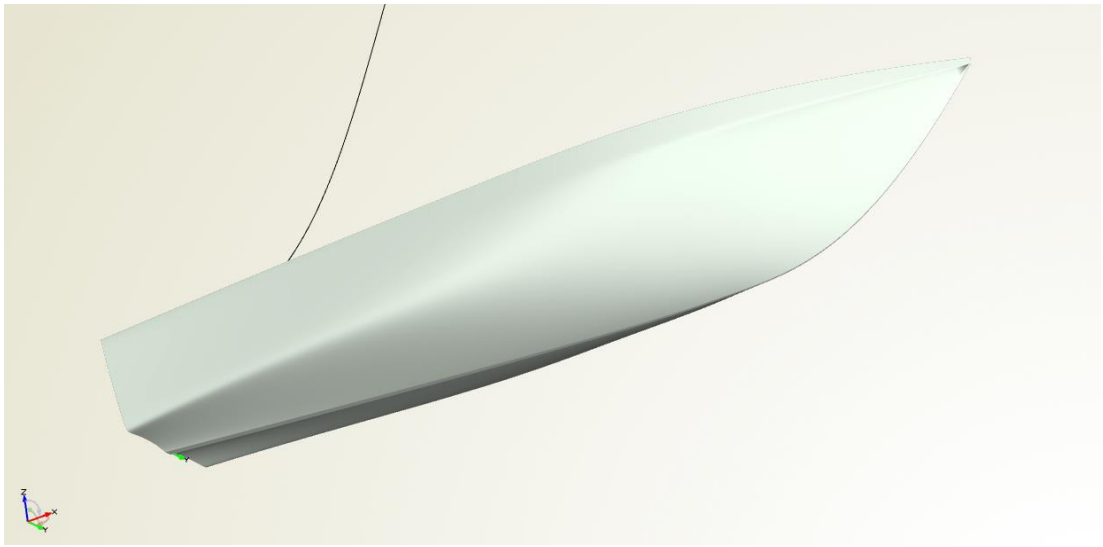

Figure 16-3 3D Render of hull 6315

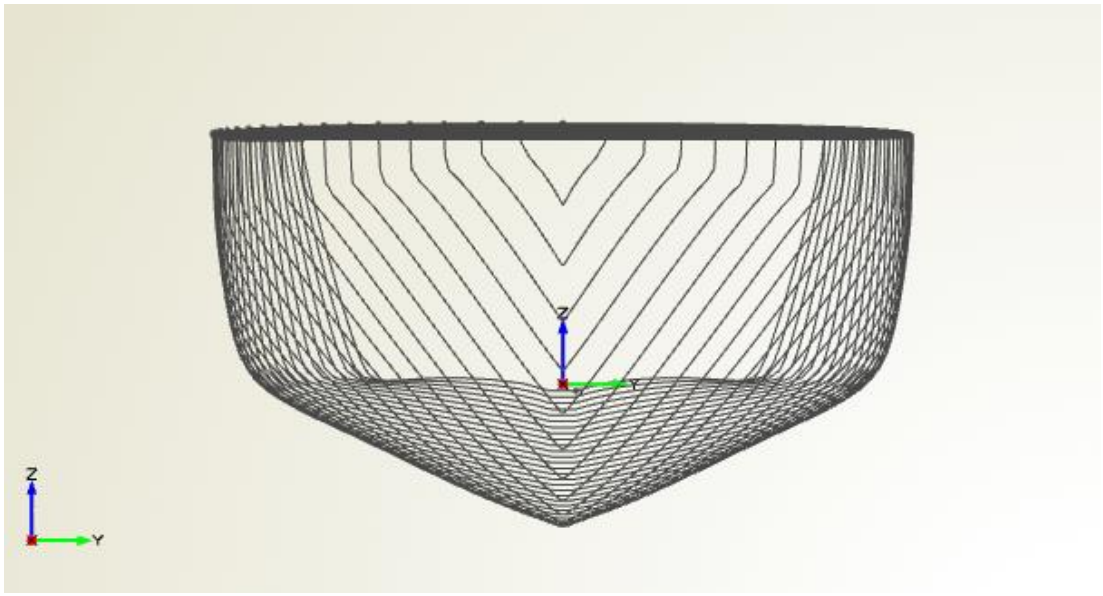

Figure 16-4 Sectional lines plan for hull 6315

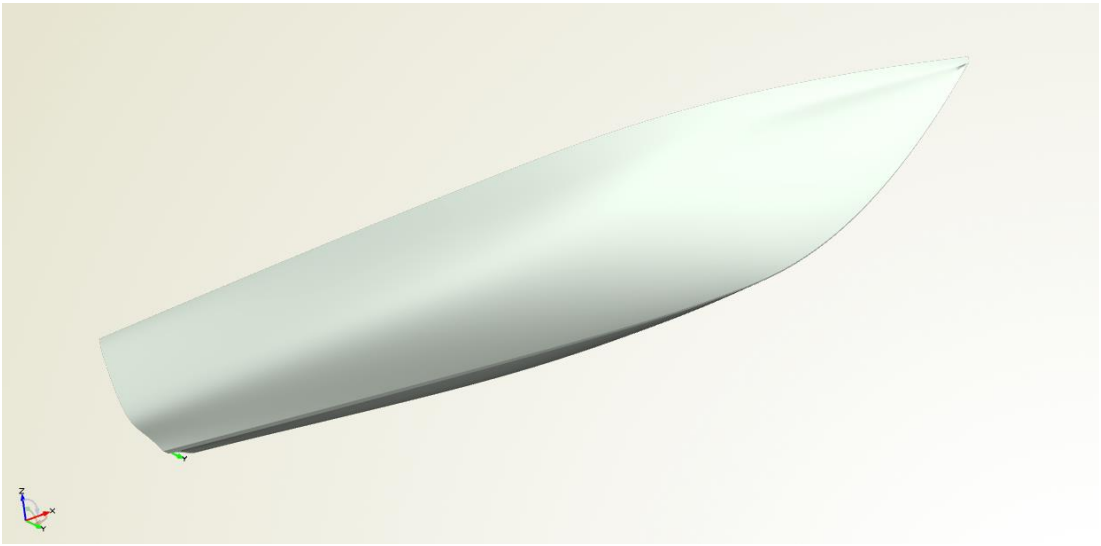

Figure 16-5 3D Render of hull 6353

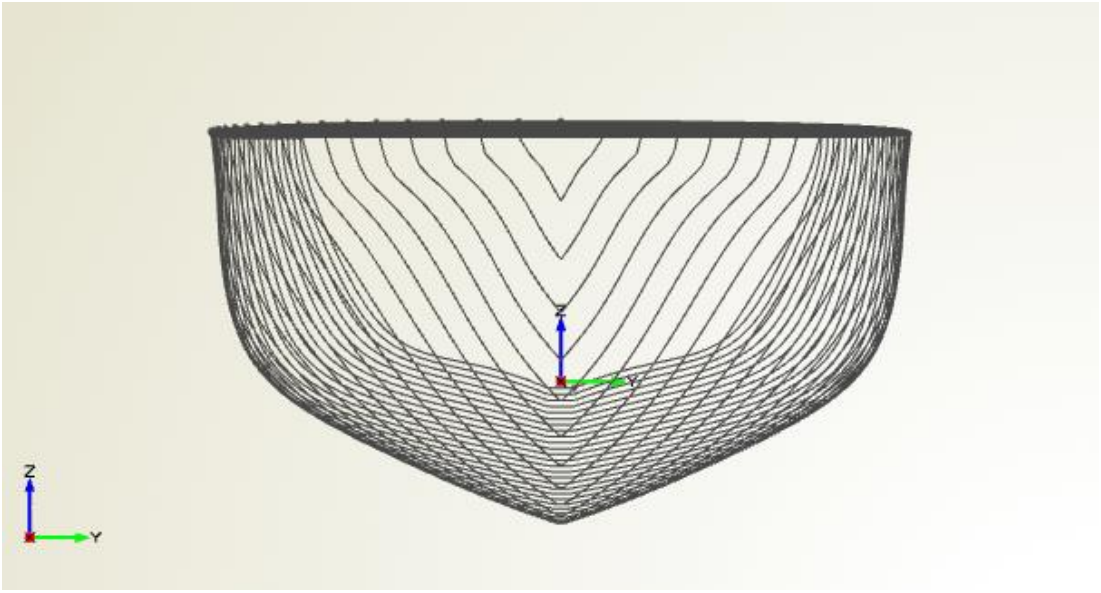

Figure 16-6 Sectional lines plan for hull 6353

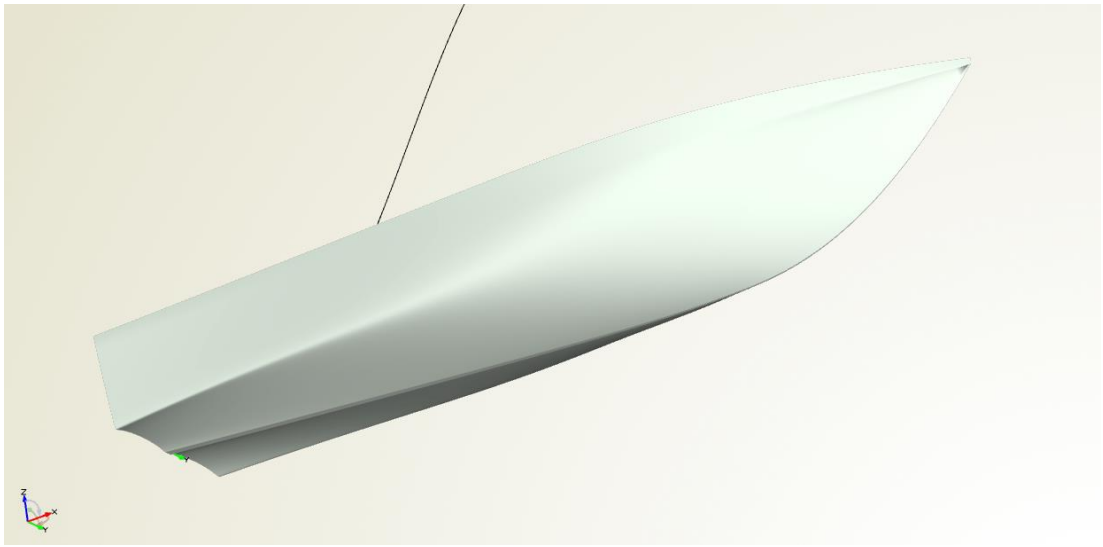

Figure 16-7 3D Render of hull 6356

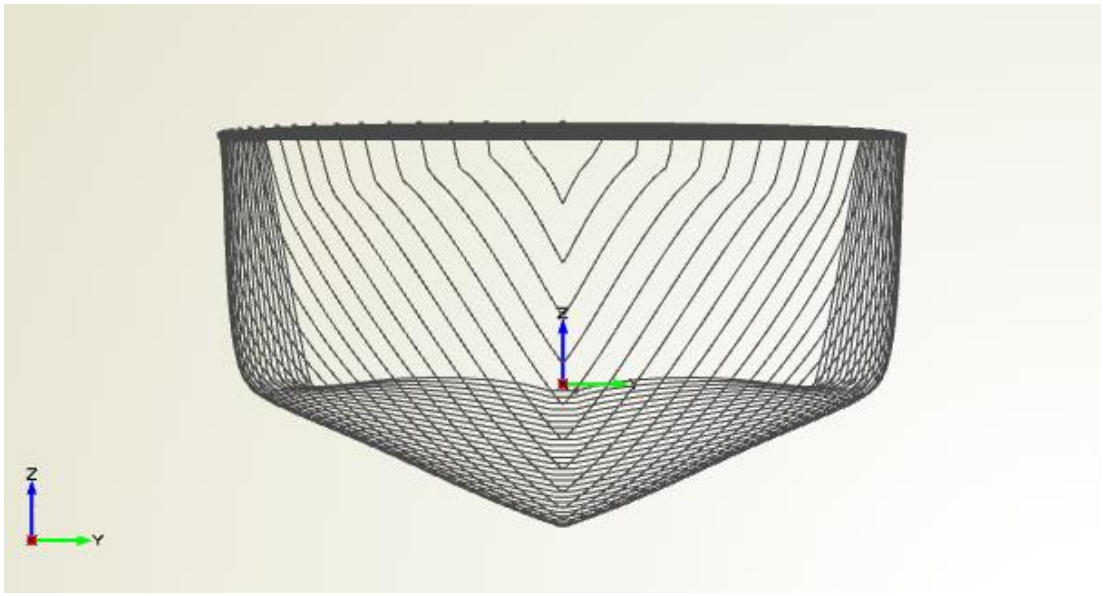

Figure 16-8 Sectional lines plan for hull 6356

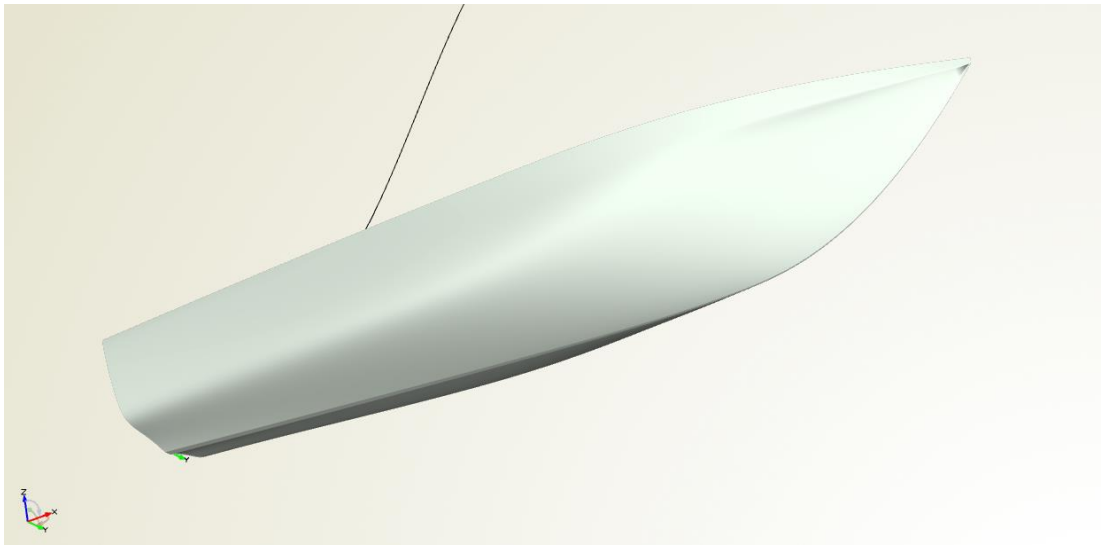

Figure 16-9 3D Render of hull 6412

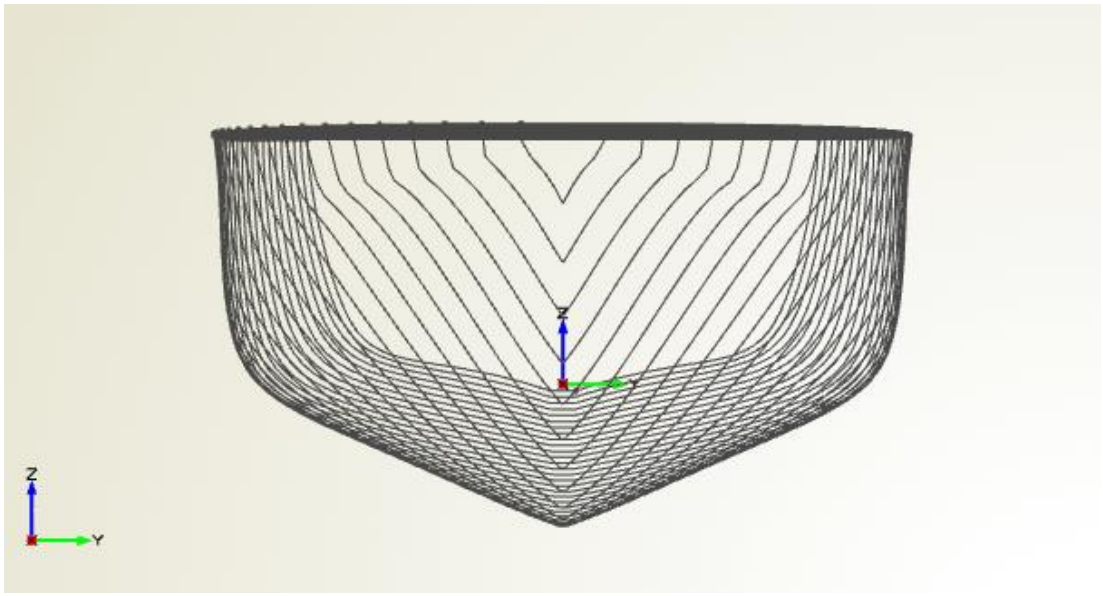

Figure 16-10 Sectional lines plan for hull 6412

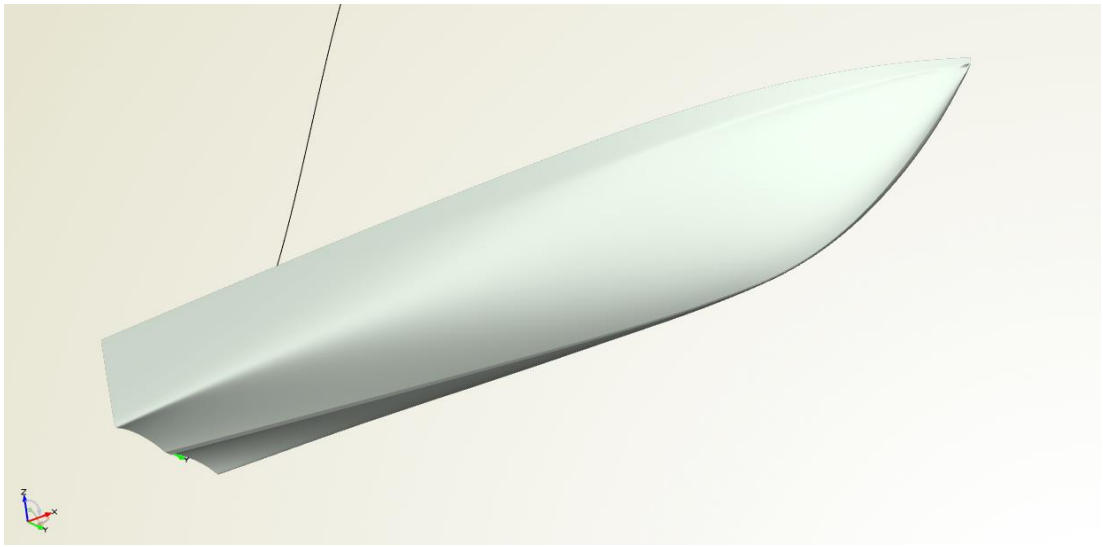

Figure 16-11 3D Render of hull 6415

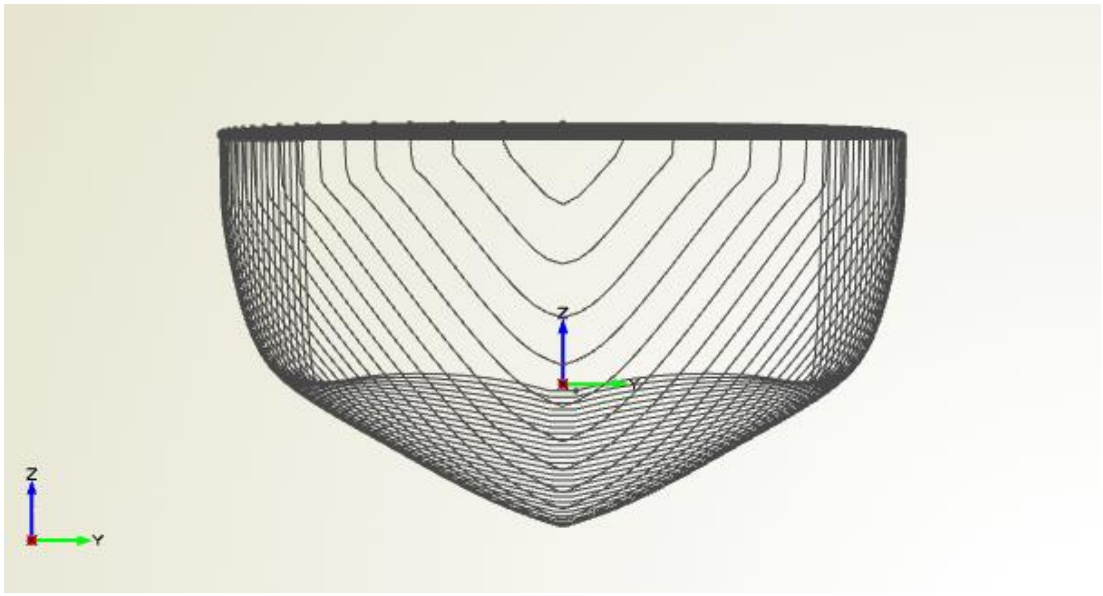

Figure 16-12 Sectional lines plan for hull 6415

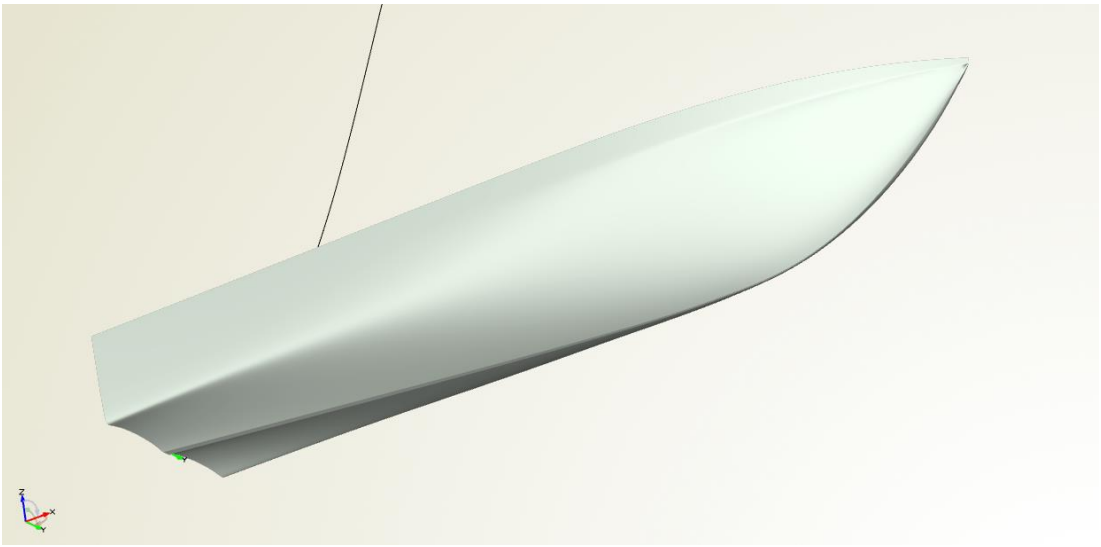

Figure 16-13 3D Render of hull 6416

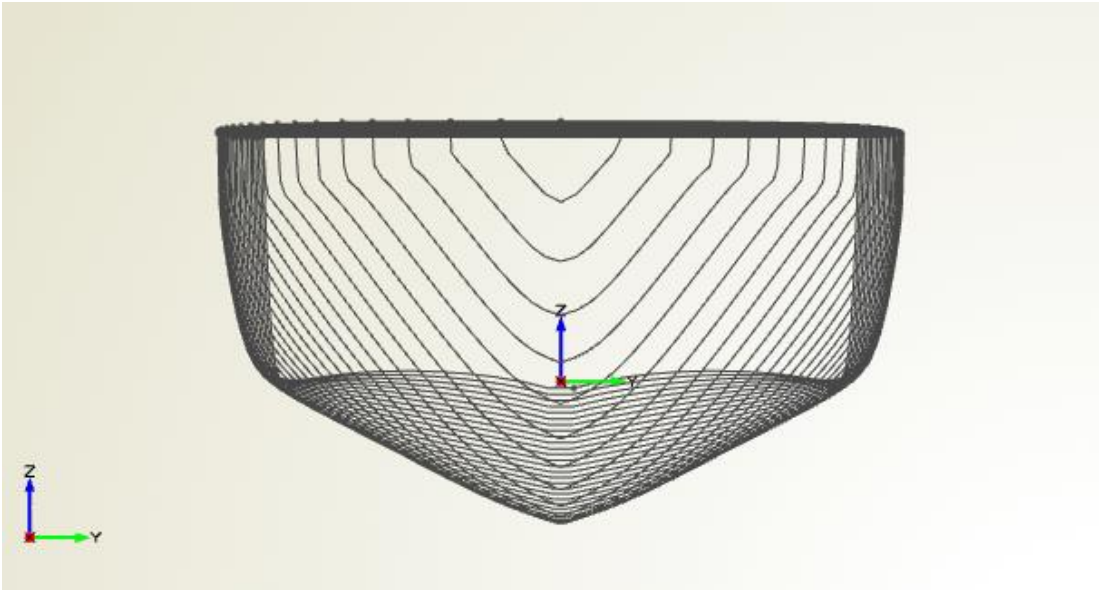

Figure 16-14 Sectional lines plan for hull 6416

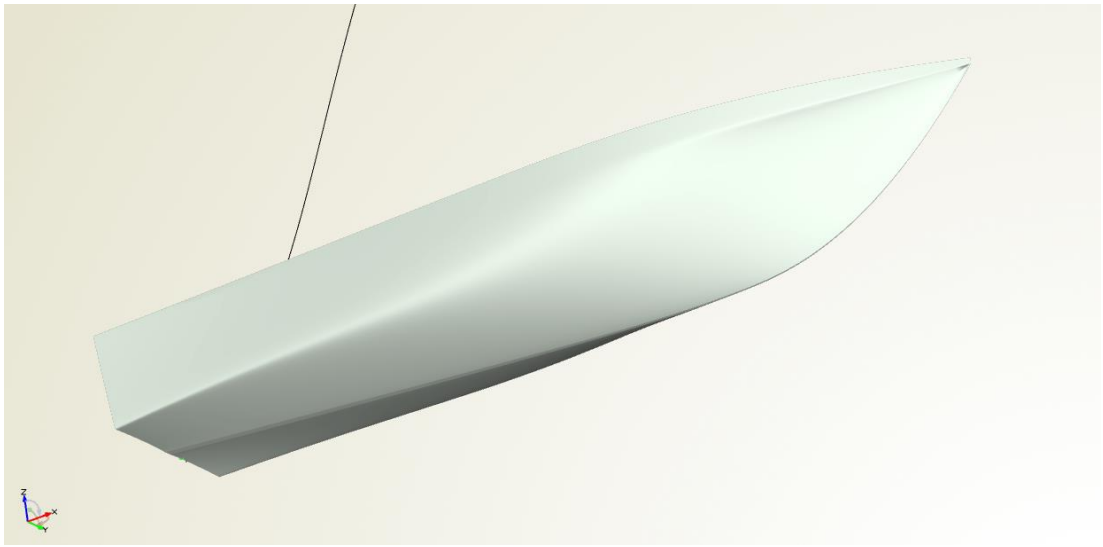

Figure 16-15 3D Render of hull 6421

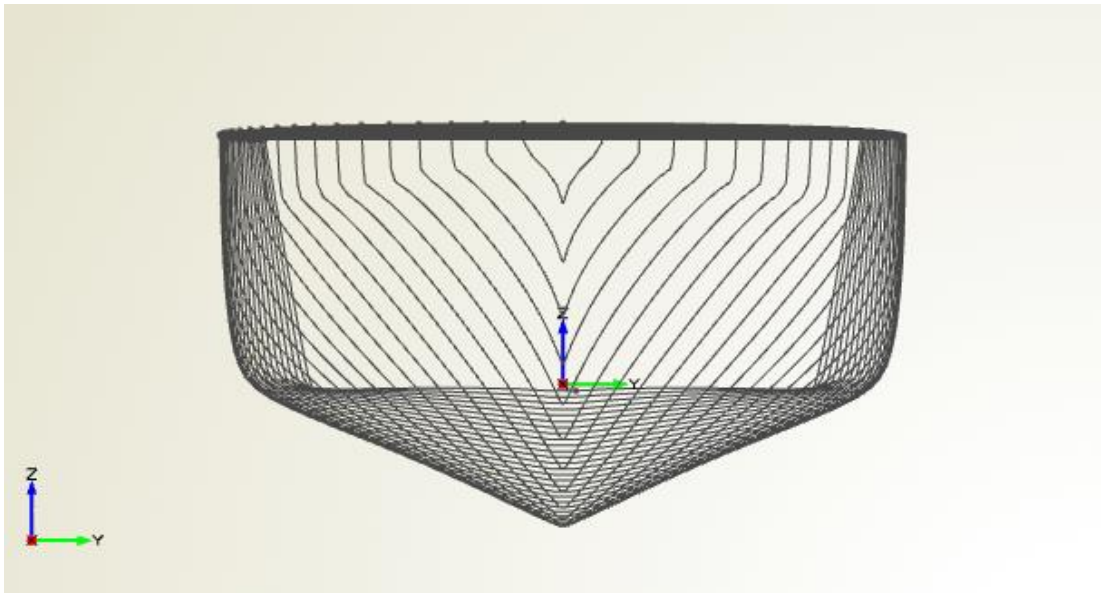

Figure 16-16 Sectional lines plan for hull 6421

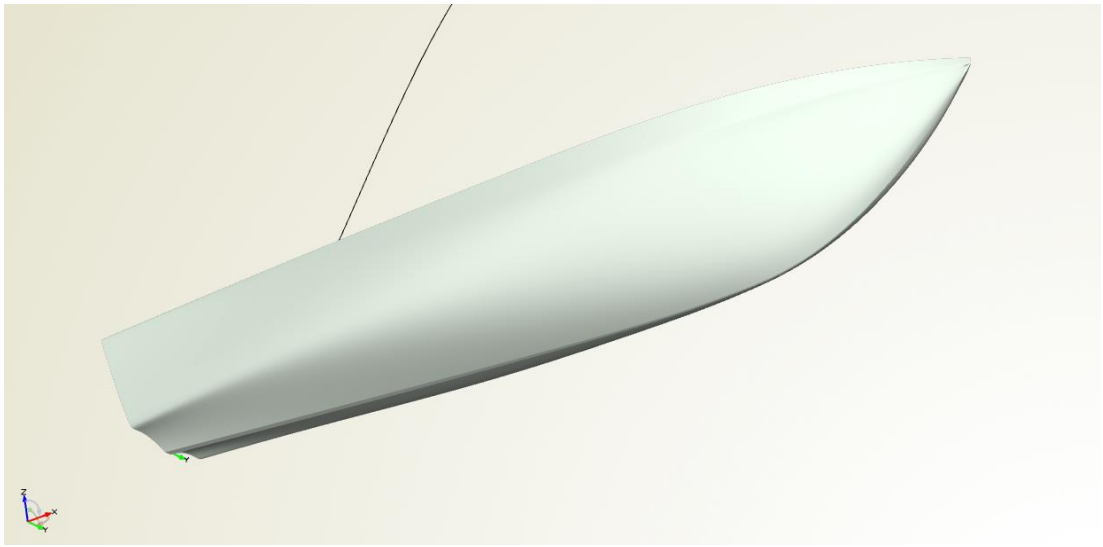

Figure 16-17 3D Render of hull 6437

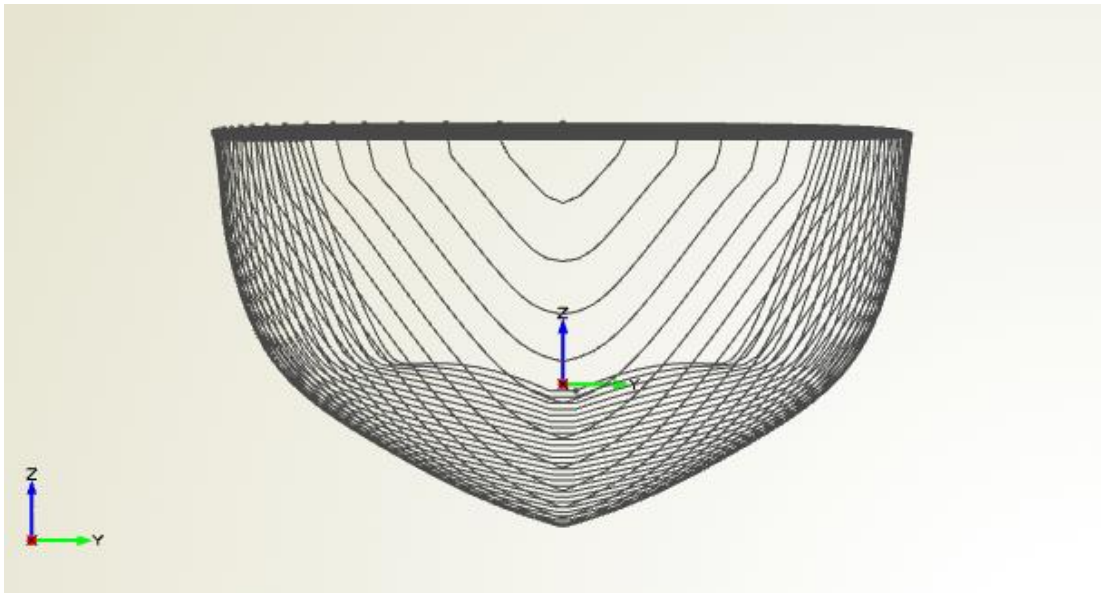

Figure 16-18 Sectional lines plan for hull 6437

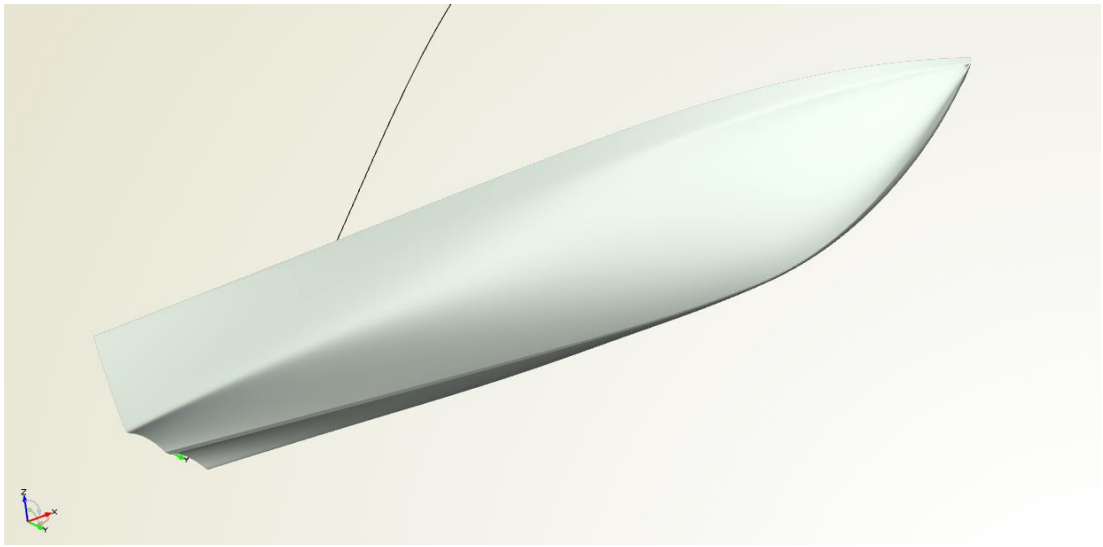

Figure 16-19 3D Render of hull 6464

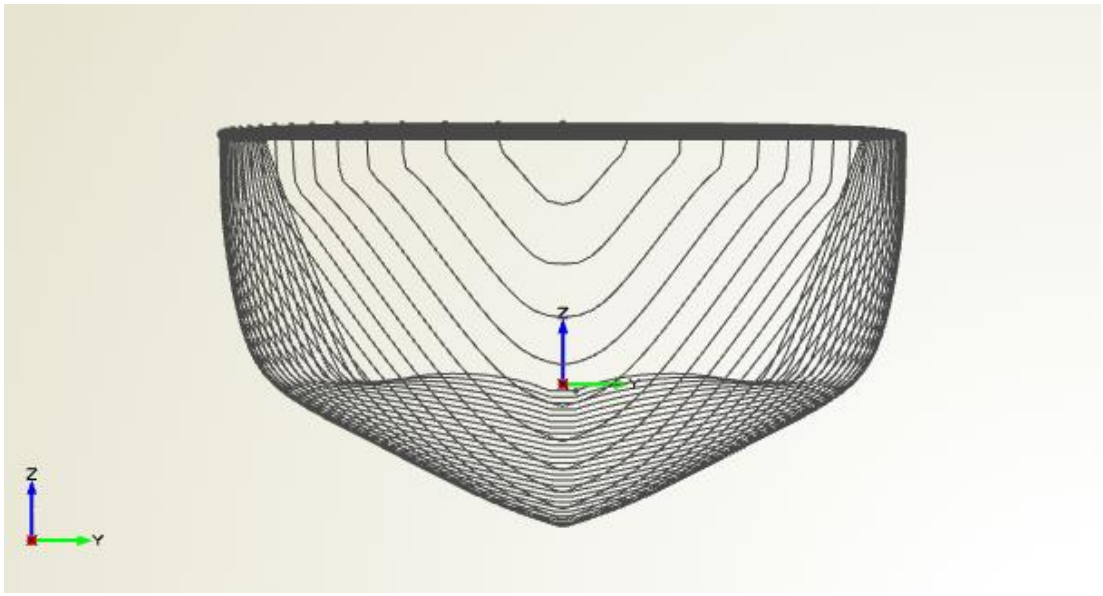

Figure 16-20 Sectional lines plan for hull 6464

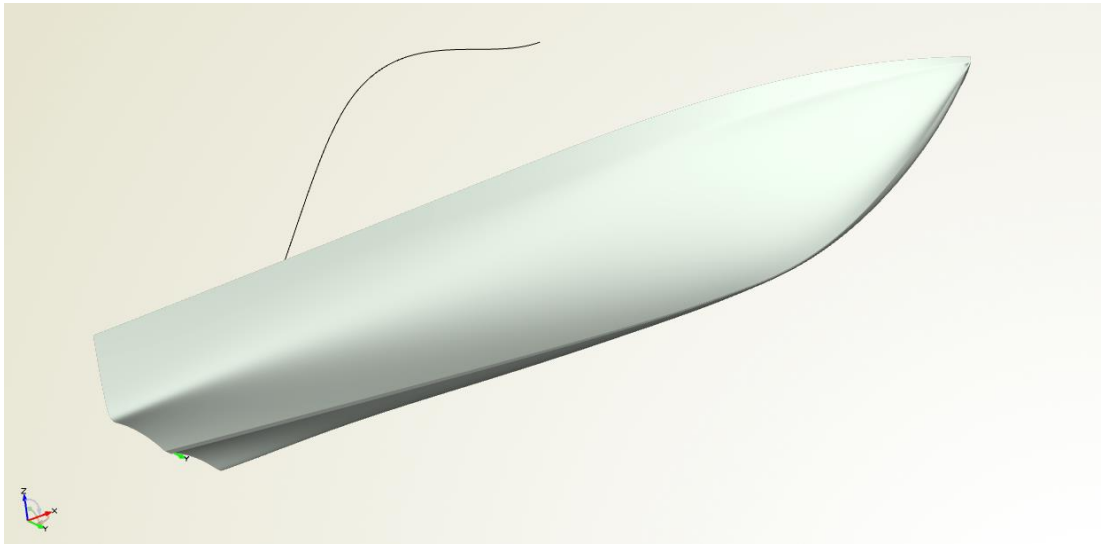

Figure 16-21 3D Render of hull 6473

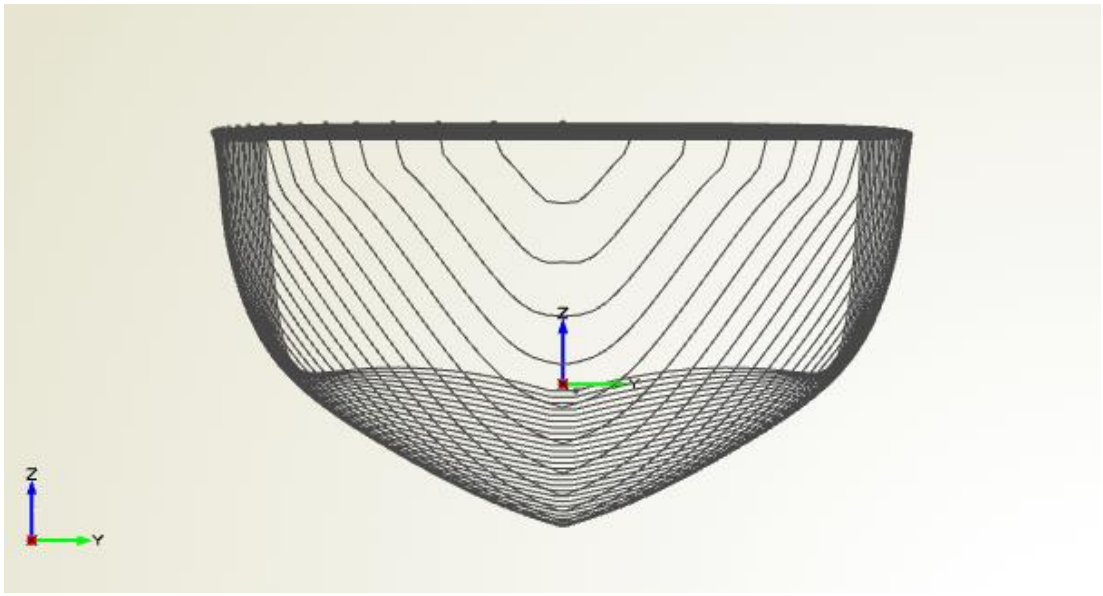

Figure 16-22 Sectional lines plan for hull 6473

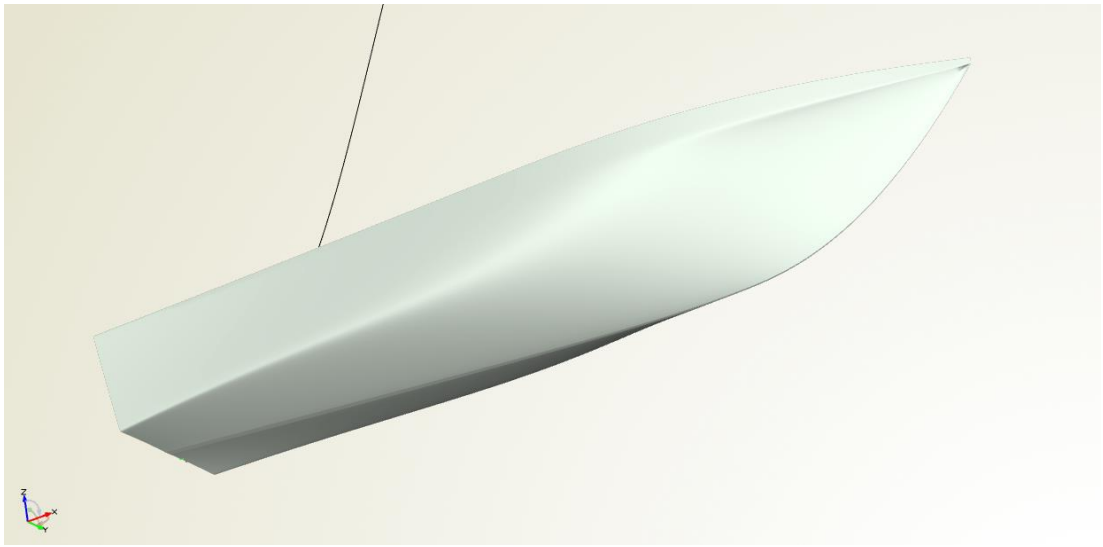

Figure 16-23 3D Render of hull 6476

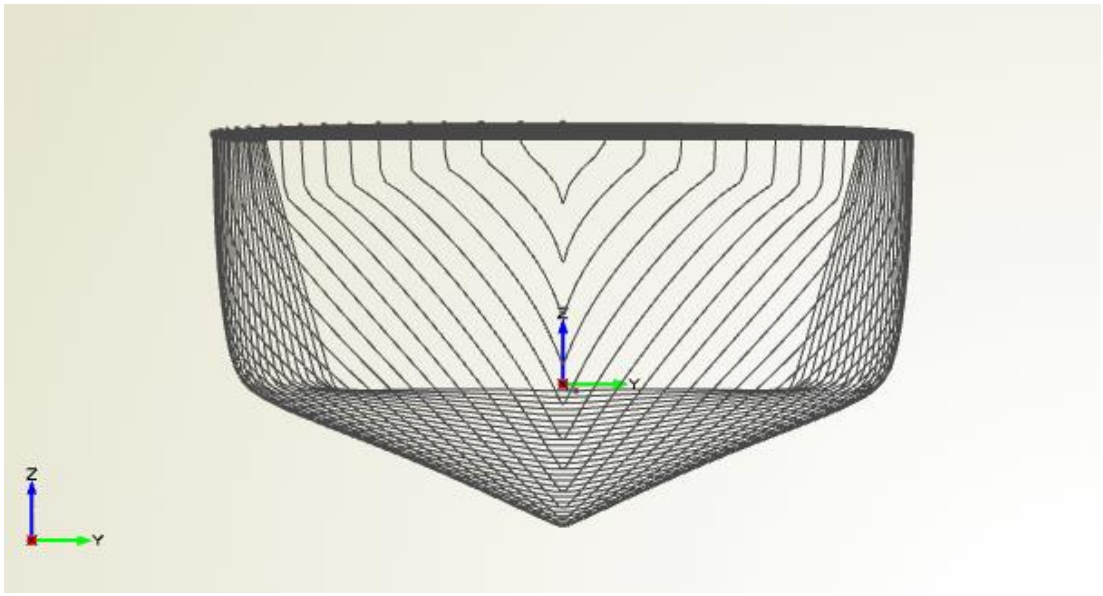

Figure 16-24 Sectional lines plan for hull 6476

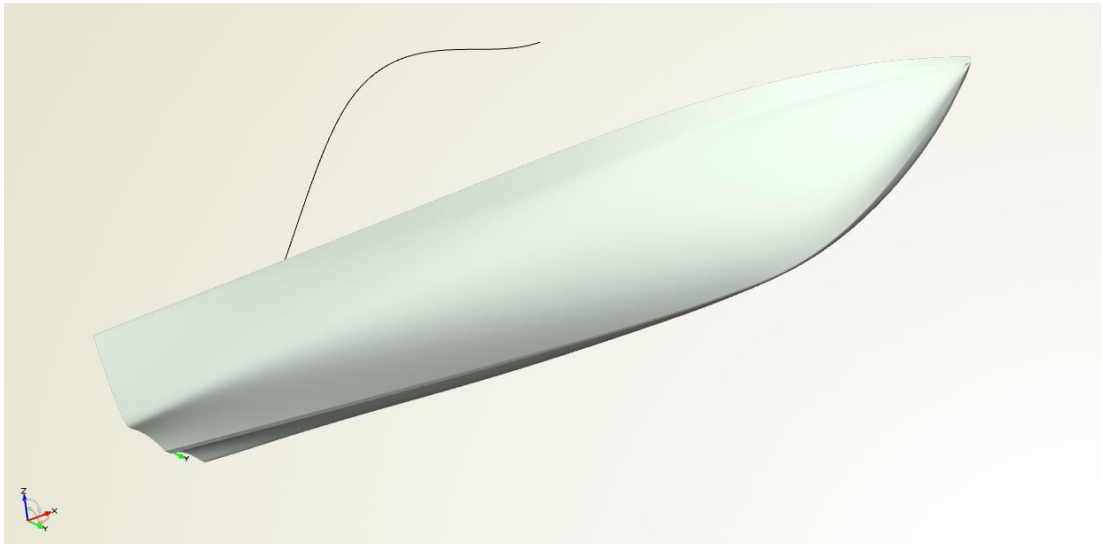

Figure 16-25 3D Render of hull 6486

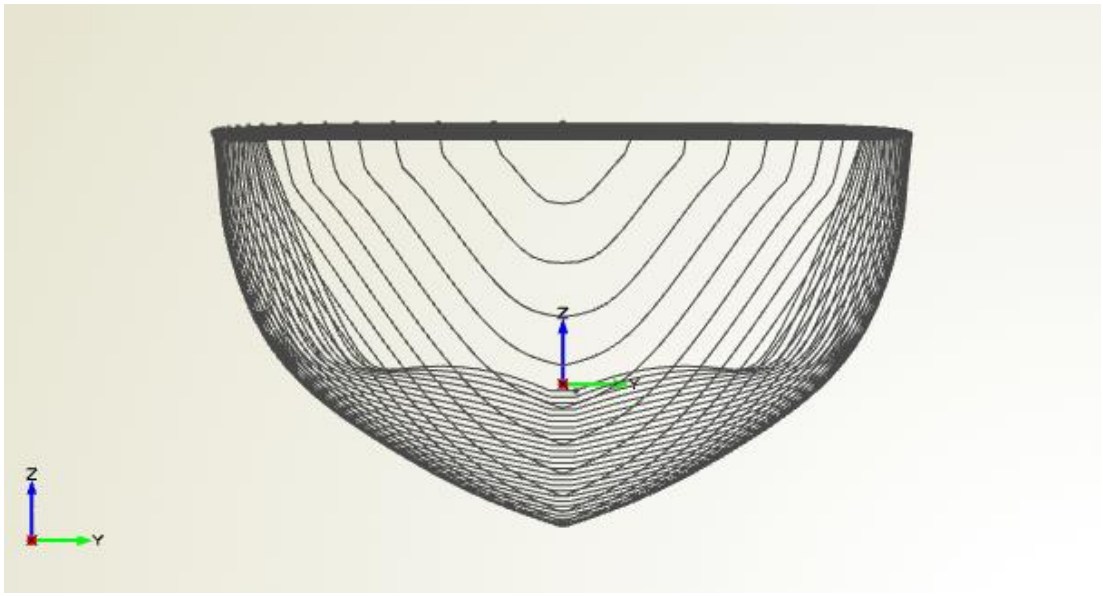

Figure 16-26 Sectional lines plan for hull 6486

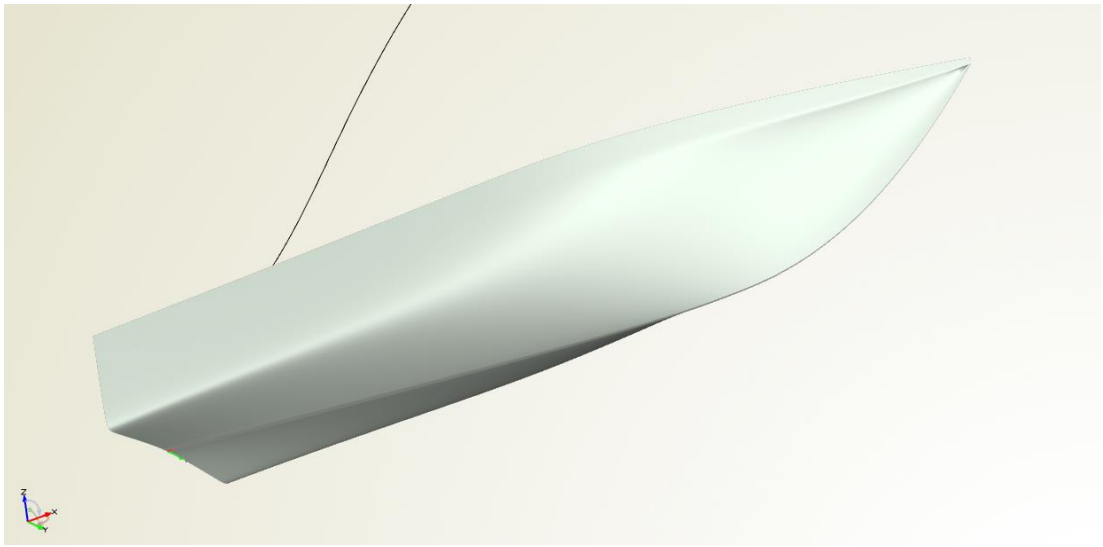

Figure 16-27 3D Render of hull 6495

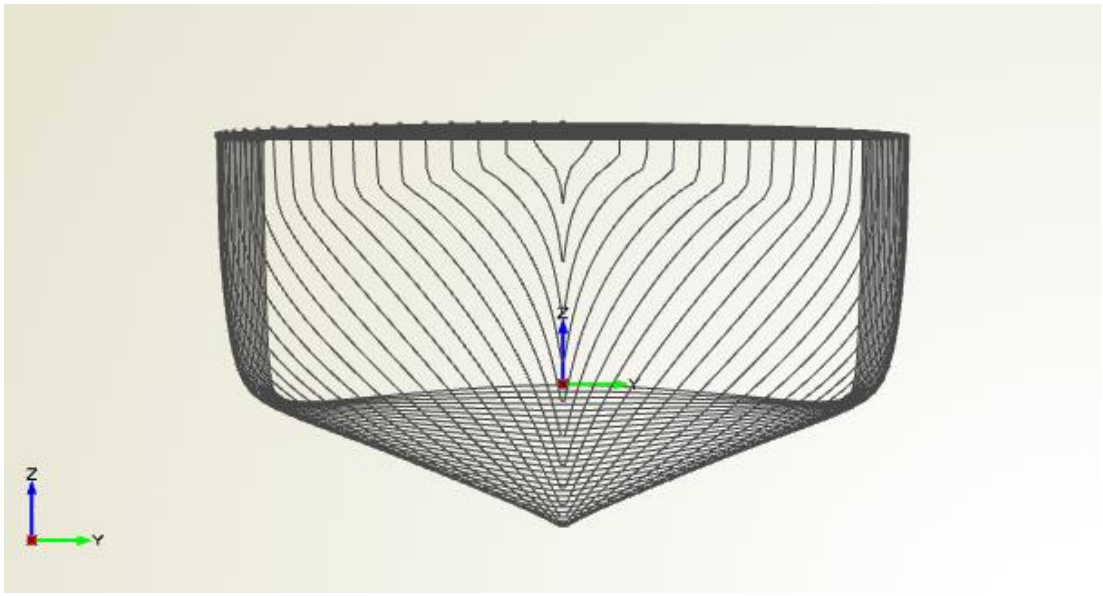

Figure 16-28 Sectional lines plan for hull 6495

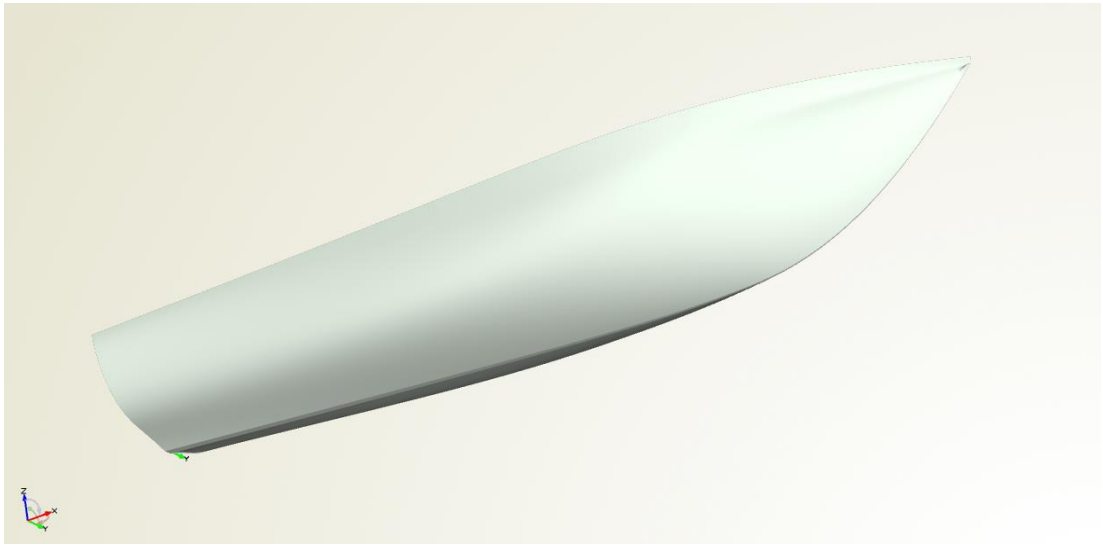

Figure 16-29 3D Render of hull 6496

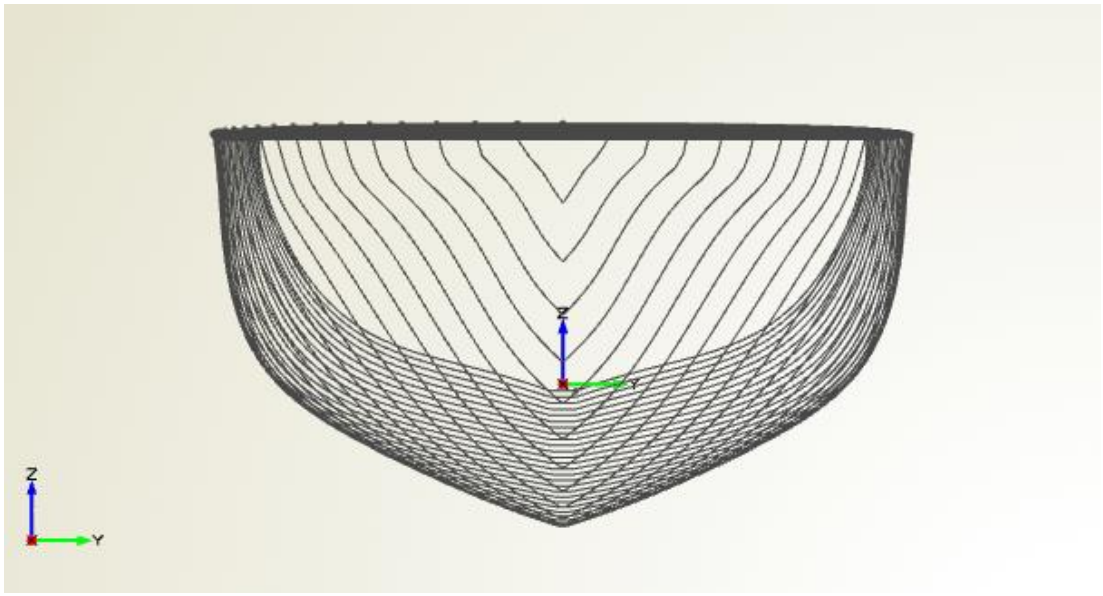

Figure 16-30 Sectional lines plan for hull 6496

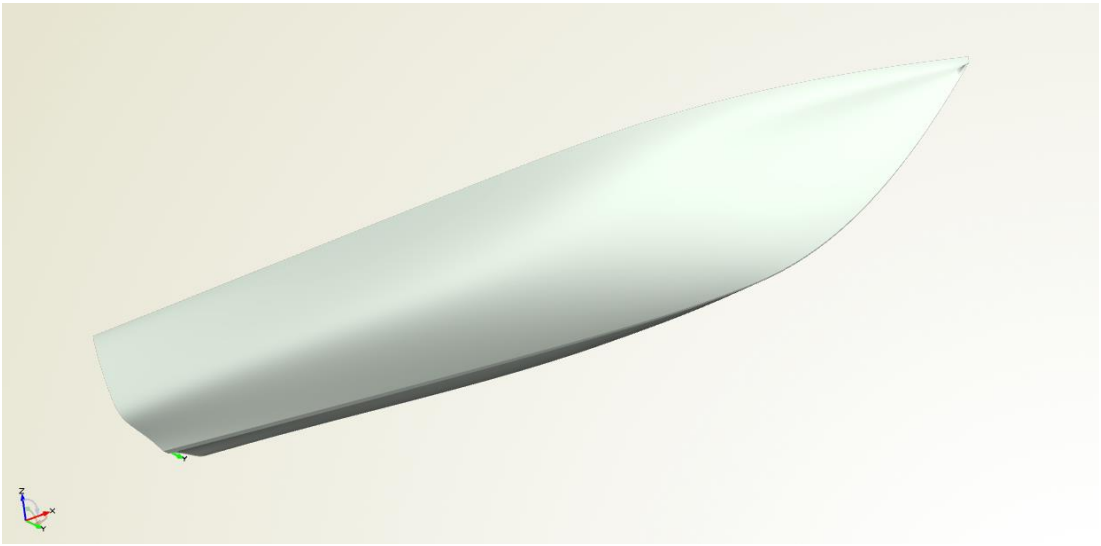

Figure 16-31 3D Render of hull 6514

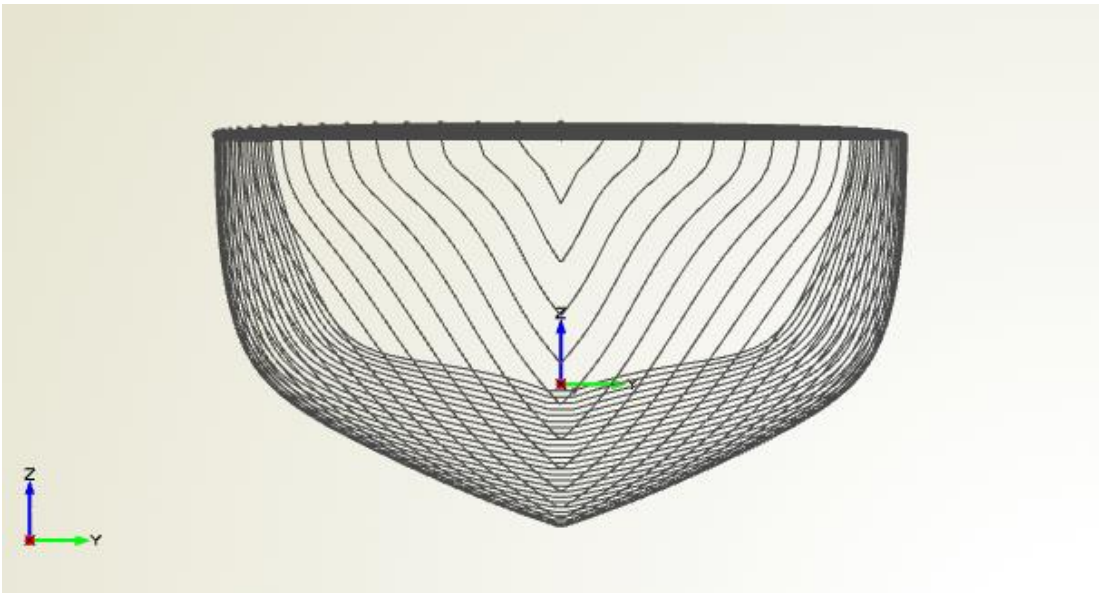

Figure 16-32 Sectional lines plan for hull 6514

References

Abt, C., Bade, S., Birk, L. & Harries, S., 2001. - *Parametric Hull Form Design — A Step Towards One Week Ship Design.* Shanghai, s.n., pp. 67-74.

Agdrup, K., 2004. *15 SIMMAN Model Test Report 4515 PMM Bare FORCE 2004,* s.l.: SIMMAN.

Almeida, R., 2020. *Operations and Maintenance Considerations to Increase Shipping Efficiency.* [Online]
Available at: https://gcaptain.com/part-operations-maintenance-considerations/?36627

Ang, J. H., Goh, C. & Li, Y., 2015. *Hull form design optimisation for improved efficiency and hydrodynamic performance of 'ship-shaped' offshore vessels.* Bremen, s.n.

ANSYS Inc, 2021. *Addressing the Challenges of the Design of Hypersonic Vehicles with Simulations.* s.l.:s.n.

Araki, M. et al., 2012. Estimating maneuvering coefficients using system identification methods with experimental, system-based, and CFD free-running trial data. *Ocean Engineering,* pp. 63-84.

Arena, F., Soares, C. G. & Petrova, P. G., 2010. *Theoretical Analysis of Average Wave Steepness Related to Peak Period or to Mean Period.* Shanghai, s.n.

Bailey, D., 1976. *The NPL high speed round bilge displacement hull series.* s.l.:Royal Institution of Naval Architects.

Beck, R. & Reed, A., 2001. Modern computational methods for ships in seaway. *Transactions - Society of Naval Architects and Marine Engineers 109.*

Bertram, V., 2016. *Added Power in Waves - Time to Stop Lying (to Ourselves),* s.l.: s.n.

Bertram, V. & Tasdemir, A., 2016. *A CRITICAL ASSESSMENT OF MEASURES TO IMPROVE ENERGY EFFICIENCY IN CONTAINERSHIPS.* s.l., s.n.

Beyer, H.-G. & Sendhoff, B., 2007. Robust optimization – A comprehensive survey. *Computer methods in mechanics and engineering,* pp. 3190-3218.

Birk, L., 2019. *Fundementals of Hydrodynamics: Fluid Mechanics, Ship Resistance and Propulsion.* s.l.:John Wiley and Sons, Ltd.

Bishop, R. E. D. & Parkinson, A. G., 1970. On the Planar Motion Mechanism Used in Ship Model Testing. *Philosophical Transactions of the Royal Society of London. Series A, Mathematical and Physical Sciences,* pp. 35-61.

Bitner-Gregerse, E. M., Soares, C. G. & Vantorre, M., 2016. *Adverse weather conditions for ship manoeuvrability.* s.l., s.n., pp. 1631-1640.

Bole, M. & Forrest, C., 2005. *Early Stage Integrated Parametric Ship Design*, s.l.: ICCAS.

Branlard, E., 2010. *Generation of tie series from spectrum: Generation of wind time series from Kaimal spectrum, Generation of wave time series from the JONSWAP spectrum.* Kongens Lyngby: Technical University of Denmark.

Broglia, R., Dubbiso, G., Durante, D. & Di Mascio, A., 2012. Simulation of turning circle by CFD: Analysis of different propeller models and their effect on manoeuvring prediction. *Applied Ocean Research,* pp. 1-10.

Broglia, R., Dubbiso, G., Durante, D. & Di Mascio, A., 2015. Turning ability analysis of a fully appended twin screw vessel by CFD. Part I: Single rudder configuratio. *Ocean Engineering,* pp. 275-286.

Bruinessen, T., Smulders, F. & Hopman, H., 2013. *TOWARDS A DIFFERENT VIEW ON SHIP DESIGN The development of ships observed through a social-technological perspective,* Delft: s.n.

C.D. Simonsen, J. O. S. J. F. S., 2013. EFD and CFD for KCS heaving and pitching in regular head waves. *J. Mar. Sci. Technol,* pp. 435-459.

CAESES, 2019. *Meta surface: An Introduction.* [Online]
Available at: https://www.caeses.com/blog/2019/meta-surface-an-introduction/

CAESES, 2020. *CAESES User manual,* Berlin: CAESES.

Cameron, P., 2020. *Princess Royal Propeller data* [Interview] (March 2020).

Carchen, A. et al., 2015. *Design and review of the new NPT propeller for The Princes Royal.* Istanbul, AMT15, Istanbul, September 2015 - Istanbul, Turkey.

Carrica, P., Mofidi, A., Eloot, K. & Delefortrie, G., 2015. Direct simulation and experimental study of zigzag maneuverof KCS in shallow water. *Oceran Engineering,* pp. 117-133.

CD-Adapco CSP, 2017. *Personal corrospondents, Customer Support Portal.* s.l.:s.n.

CD-Adapco, 2017a. *Deciding on K-Epsilon Model.* [Online]
Available at: file:///C:/Program%20Files/CD-adapco/11.06.011/STAR-CCM+11.06.011/doc/en/online/index.html#page/STARCCMP%2FGUID-C557A500-3E7A-42CB-B02C-5EBDE32F0C86%3Den%3D.html%23

CD-Adapco, 2017b. *User guide Star-CCM+ Version 12.04.011-R8*, s.l.: s.n.

Chen, C., Shiotani, S. & Sasa, K., 2015. Effect of ocean currents on ship navigation in the east China sea. *Ocean Engineering,* pp. 283-293.

Chen, J., Wei, J. & Jiang, W., 2016. Optimization of a twin-skeg container vessel by parametric design and CFD simulations. *International Journal of Naval Architecture and Ocean Engineering 8 ,* pp. 466-474.

Cogliolo, A. & Moretti, P., 2011. *The Environmental Challenge,* Genoa: s.n.

Cressie, N., 1991. *statistics of spatial data.* New York: John Wiley & Sons.

Cura-Hochbaum, A. & Uharek, S., 2014. *PREDICTION OF THE MANOEUVRING BEHAVIOUR OF THE KCSBASED ON VIRTUAL CAPTIVE TESTS.* Berlin, s.n.

Dai, K. & Li, Y., 2019. MANOEUVRING PREDICTION OF KVLCC2 WITH HYDRODYNAMIC DERIVATIVES GENERATED BY A VIRTUAL CAPTIVE MODEL TEST. *POLISH MARITIME RESEARCH 4 (104),* pp. 16-26.

Dalbey, K. et al., 2020. *Dakota, A Multilevel Parallel Object-Oriented Framework for Design Optimization, Parameter Estimation, Uncertainty Quantification, and Sensitivity Analysis: version 6.13 Theory Manual,* Albuquerque: Sandia national laboratories.

Daniel, C. et al., 2014. *Active reward learning,* s.l.: s.n.

Diez, M. & Peri, D., 2010. Robust optimization for ship conceptual design. *ocean Engineering,* pp. 966-977.

Elhadad, A., Duan, W., Deng, R. & Elhanfey, H., 2014. Numerical Analysis for Resistance Calculations of NPL as a Floating Hull for Wave Glider. *Applied Mechanics and Materials,* pp. 38-43.

Elsaeed, G., 2013. Effect of Cross Water Currents on Ships: The State of Art Review. *Australian Journal of Basic and Applied Sciences,* pp. 238-246.

Engineering toolbox, 2021. *Properties of Seawater.* [Online]
Available at: https://www.engineeringtoolbox.com/sea-water-properties-d_840.html

Erikstad, S. & Levander, K., 2012. *System Based Design of offshore support vessels,* Glasgow: s.n.

European Commission , 2013. *Integrating Maritime Transport Emissions in the EU's Greenhouse Gas Reduction Policies ,* s.l.: s.n.

Faltinsen, O. & Zhao, R., 1991. Numerical Prediction of Ship Motions at High Forward Speed. *Philosophical Transactions of the Royal Society of London Series A-Mathematical Physical and Engineering Sciences, 334 (1634),* pp. 241-252.

Ferziger, J. H. & Peric, M., 2002. *Computational Methods for Fluid Dynamics.* s.l.:Springer.

Freindship Systems, 2020. *FGenericCurve,* s.l.: Freindship Systems.

Fujiwara, T., Ueno, M. & Nimura, T., 2001. *An estimation method of wood forces and moments acting on ships.* s.l., s.n.

Gablonsky, J., 2001. *Direct version 2.0 userguide technical report. Technical Report CRSC-TR01-08.* Raleigh, NC: North Carolina State University, Center for Research in Scientific Computation.

Gao, Q. & Vassalos, D., 2011. *Numerical Study of the Roll Decay of Intact and Damaged Ships.* s.l., s.n., pp. 277-282.

Ghassabzadeh, M. & Ghassemi, H., 2013. An innovative method for parametric design of planing tunnel vessel Hull form. *Ocean Engineering,* pp. 14-27.

Grigoropoulos, G. & Chalkias, D., 2010. Hull-form optimization in calm and rough water. *Computer-Aided Design 42,* pp. 977-984.

Haase, M. et al., 2012. *Application of RANSE-based Simulations for Resistance Prediction of Medium-Speed Catamarans at Different Scales.* Launceston, 18th Australasian Fluid Mechanics Conference.

Hansomn, n.d. [Online].

Hanson, A., 2017. *The benefits of using Computational Fluid Dynamics as a tool for innovation.* [Online]
Available at: https://www.pddinnovation.com/computational-fluid-dynamics/

He, S. et al., 2016. Manoeuvring prediction based on CFD generated derivatives. *Journal of Hydrodynamics,* pp. 284-292.

He, S. et al., 2016. Manoeuvring prediction based on CFD generated derivatives. *Journal of Hydrodynamics*, pp. 284-292.

Howett, B., Day, S. & Incecek, A., 2012. *Lowering Carbon Emissions in Shipping Through Improved Hullform Design for Realistic Operating Conditions.* [Online]
Available at:
http://www.lowcarbonshipping.co.uk/files/ucl_admin/LCS%202012/Howett.pdf

Huang, D., Allen, T. T., Notz, W. I. & Zeng, N., 2006. global optimisation of stochastic black-box systems via sequential kriging meta-models. *Journal of global optimisation*, pp. 441-466.

Huang, F. & Yang, C., 2016. Hull form optimisation of a cargo ship for reduced drag. *Journal of Hydrodynamics*, pp. 173-183.

IMO, 2021. *Energy Efficiency Measures.* [Online]
Available at: https://www.imo.org/en/OurWork/Environment/Pages/Technical-and-Operational-Measures.aspx
[Accessed 2021].

Incat Crowther, 2020. *IC18001 - Product Details.* [Online]
Available at: http://www.incatcrowther.com/product/ic18001

Industrial technology, 2020. *CFD CUTS DEVELOPMENT TIME FOR A RACE WINNING ENGINE.* [Online]
Available at: https://www.industrialtechnology.co.uk/products--cfd-cuts-development-time-for-a-race-winning-engine.html

ITTC, 2002a. *Propulsion, Performance Uncertainty Analysis, Example for Propulsion Test,* s.l.: ITTC.

ITTC, 2002b. *Testing and Extrapolation Methods, resistance and resistance tests 7.5-02-02-01,* s.l.: ITTC.

ITTC, 2011a. *Practical Guidelines for Ship CFD Applications,* s.l.: ITTC.

ITTC, 2011b. *Seakeeping Experiments.* s.l., s.n.

ITTC, 2011c. *The Specialist Committee on Computational Fluid Dynamics,* Rio de Janeiro: ITTC.

ITTC, 2014. *Analysis of Speed/Power Trial Data 7.5-04-01-01.2,* s.l.: ITTC.

ITTC, 2017. *ITTC recommended procedures and guidelines: Captive Model Test,* s.l.: ITTC.

Jin, Y. et al., 2017. URANS predictions of wave induced loads and motions on ships in regular head and oblique waves at zero forward speed. *Jouranl of Fluids and Structures,* pp. 178-204.

Jones, D., M, S. & Welch, W., 1998. Efficient global optimization of expensive black-box functions.. *Journal of Global Optimization,* pp. 455-492.

Katsoulis, T., Wang, X. & Kaklis, P. D., 2019. A T-splines-based parametric modeller for computer-aided ship design. *Ocean Ngineering 191.*

Khan, S., 2019. *Small electric boats and their influence on the grid.* [Online]
Available at: https://site.uit.no/ladeteknologi/2019/11/06/small-electric-boats-and-their-influence-on-the-grid/
[Accessed 01 06 2021].

Kim, M. et al., 2016. *A study on ship speed loss due to added resistance in a seaway.* s.l., s.n.

Kobayashi, K., Kohri, I. & Matsushima, Y., 2011. Study of Influence of MRF Method on the Prediction of the Engine Cooling Fan Performance.

Kostas, K., Ginnis, A., Politis, C. & Kaklis, P., 2015. Ship-hull shape optimization with a T-spline based BEM–isogeometric solver. *computer methods and applied mechanics and engineering,* pp. 611-622.

Lal, A. & Elangovan, M., 2008. *CFD Simulation and Validation of Flap Type Wave-Maker,* s.l.: s.n.

Levander, K., 1991. *System Based Passenger Ship Design,* s.l.: s.n.

Liu, Y., Zou, L., Zou, Z. & Haipeng, G., 2018. Predictions of ship maneuverability based on virtual captive model tests. *Engineering Applications of Computational Fluid Mechanics,* pp. 334-353.

Lui, Y., Zou, L. & Z. Z., 2017. Computational fluid dynamics prediction of hydrodynamic forces on a manoeuvring ship including effects of dynamic sinkage and trim. *Journal of engineering for the maritime environment.*

Lungu, A., 2019. A sliding grid based method for the roll decay simulation. *Modern Technologies in Industrial Engineering VII, (ModTech2019).*

Maarsch, M., 2017. *Automated validation and verification process* [Interview] 2017.

Marine Digital, 2021. *Green-tech in Shipping Industry.* [Online]
Available at: https://marine-digital.com/article_green_ship

McTaggart, K., 1997. *Shipmo7: An updated strip theory program for predicting ship motions and sea loads in waves.* [Online]
Available at:
http://oai.dtic.mil/oai/oai?verb=getRecord&metadataPrefix=html&identifier=ADA323840

Ming, W. et al., 2013. Numerical Research on Ship Motions in Oblique Irregular Waves. *Advanced Materials Research*, pp. 1531-1534.

Mofidi, A., 2017. *Ship maneuv Ship maneuvers with discr ers with discretized propeller and coupled pr opeller and coupled propeller model/CFD,* Iowa: University of Iowa.

Mohammadafzali, S., 2015. *A Mathematical Model for the Maneuvering Simulation of a Propelled SPAR Vessel,* St. John's: Memorial University of Newfoundland.

Moraes, H., Vasconcellos, J. & Almeida, P., 2007. Multiple criteria optimization applied to high speed catamaran preliminary design. *Ocean Engineering,* pp. 133-147.

Morton, S., 2011. *Computational stability and control analysis of aircraft using high performance computing and system identification.,* Portsdown West: s.n.

Mousaviraad, S. M., 2010. *CFD prediction of ship response to extreme winds,* Iowa: University of Iowa.

Mucha, P., 2017. *On Simulation-based Ship Maneuvering Prediction in Deep and Shallow Water,* s.l.: University of Duisburg-Essen.

Muck, K., Hoffmann, P. & Bradshaw, P., 1985. The effect of convex surface curvature on turbulent boundary layers. *Jouranl of Fluid Mechanics Volume 161,* pp. 347-369.

Naval Architecture, 2014. *The design spiral.* [Online]
Available at: http://naval-architecture.blogspot.com/2014/04/the-design-spiral.html

Newman, J. N., 1978. *The Theory of Ship Motions.* New York: Academic Press.

Nikolopulos, L. & Boulougouris, E., 2018. A Study on the Statistical Calibration of the Holtrop and Mennen Approximate Power Prediction Method for Full Hull Form, Low Froude Number Vessels. *Journal of Ship Production and Design,* pp. 1-28.

NOAA, 2021. *What is a Plimsoll line?*. [Online]
Available at: https://oceanservice.noaa.gov/facts/plimsoll-line.html#:~:text=The%20Plimsoll%20line%20is%20a,in%20port%20and%20at%20sea.

Offshore Wind, 2017. *UK Offshore Wind Generation on the Rise in 2017 Q2.* [Online]
Available at: https://www.offshorewind.biz/2017/09/29/uk-offshore-wind-generation-on-the-rise-in-2017-q2/

Oldfield, C. & Larmaei, R., 2014. *CFD prediction of hull manoeuvering forces,* Ottawa: STX Marine.

Orihara, H. & Miyata, H., 2003. Evaluation of added resistance in regular incident waves by computational fluid dynamics motion simulation using an overlapping grid system. *Journal of Marine Science and Technology 8 (2),* pp. 47-60.

Papanikolaou, A., 2009. Holistic ship design optimisation. *Ocean Engineering.*

Parkinson, A., Balling, R. & Hedengreen, J., 2013. *Optimization Methods for Engineering Design,* s.l.: Brigham Young University.

Park, J.-H., Choi, J.-E. & Chun, H., 2015. Hull-form optimization of KSUEZMAX to enhance resistance performance. *Ocean Engineering,* pp. 100-114.

Pennino, S. et al., 2020. Development of a New Ship Adaptive Weather Routing Model Based on Seakeeping Analysis and Optimization. *Marine Science and Engineering.*

Peric, M., 2020. *full Scale simulation for marine design,* s.l.: SIEMENS.

Peri, D., Rossetti, M. & Campana, E., 2001. Design Optimization of Ship Hulls via CFD Techniques. *Journal of Shpi Research, Vol. 45, No. 2,* pp. 140-149.

Putra, N., Susanto, A. & Suharyo, O., 2017. Comparative Analysis Results of Towing Tank and Numerical Calculations With Harvald Guldammer Method (Case Study of Propulsion Speed Reduction PC-43). *Journal of Applied Engineering Research,* pp. 10637-106345.

Rahm, S., 2015. *The costly future of green shipping.,* s.l.: s.n.

Raihunen, J. et al., 2019. Optimisation of passenger ship structures in concept design stage. *Ships and Offshore Structures,* pp. 320-334.

Ray, T., Gokarn, R. & Sha, O., 1995. A global optimization model for ship design. *Computers in Industry,* pp. 175-192.

Ricci, A., Janssen, W. D., Wijhe, H. J. & Blocken, B., 2020. CFD simulation of wind forces on ships in ports: Case study for the Rotterdam Cruise Terminal. *Journal of Wind Engineering and Industrial Aerodynamics.*

Roache, P. J., 1998. Verification of Codes and Calculations. *AIAA Journal*, pp. 696-702.

Romanowski, A., Tezdogan, T. & Osman, T., 2019. Development of a CFD methodology for the numerical simulation of irregular sea-states. *Ocean Engineering*, Volume 192.

Royal Institution of Naval Architects, 2018. *Best practices for wave flow simulations (pp38-42).* London: s.n.

Roy, R., Hinduja, S. & Teti, R., 2008. Recent advances in engineering design optimisation: Challenges and future trends. *CIRP Annals - Manufacturing Technology 57*, pp. 697-715.

Sahoo, P., 2007. *Manoeuvering,* Launceston: Australian Maritime College.

Savine, A., 2018. *Sobol Sequence Explained by Antoine Savine.* [Online]
Available at: https://medium.com/@antoine_savine/sobol-sequence-explained-188f422b246b

Savitsky, D., 1964. Hydrodynamic design of planing hulls. *SNAME Mar. Technol* , pp. 71-95.

Scamardella, A. & Piscopo, V., 2014. Passenger ship seakeeping optimization by the Overall Motion Sickness Incidence. *Ocean Engineering,* pp. 86-97.

Schachter, R. D., Ribeiro, H. J. & Da Conceição, C. A., 2016. Dynamic equilibrium evaluation for planing hulls with arbitrary geometry and variable deadrise angles - The Virtual Prismatic Hulls Method. *Ocean Engineering,* pp. 67-92.

Sea Temperature, 2021. *Bergen Sea Temperature.* [Online]
Available at: https://seatemperature.net/current/norway/bergen-hordaland-norway-sea-temperature#:~:text=Average%20annual%20water%20temperature%20on,63%C2%B0F)%20in%20August.

Seo, M., Park, D., Yang, K. & Kim, Y., 2013. Comparative study on computation of ship added resistance in waves. *Ocean Engineering, 73*, pp. 1-15.

Shen, Z., Wan, D. & Carrica, P. M., 2015. Dynamic overset grids in OpenFOAM with application to KCS self-propulsion and maneuvering. *Ocean Engineering.*

Shen, Z. & Wan, D. C. P., 2014-B. *RANS SIMULATIONS OF FREE MANEUVERS WITH MOVING RUDDERS AND PROPELLERS USING OVERSET GRIDS IN OPENFOAM*. s.l., s.n.

Shen, Z.-r., Ye, H.-x. & Wan, D.-c., 2014-A. URANS Simulation of ship motion responses in long-crested irregular waves. *Journal of Hydrodynamics*, pp. 436-448.

Shippo, 2021. *How Long Do Shipments Take?*. [Online]
Available at: https://www.shippo.co.uk/faqs/how-long-do-shipments-take/#:~:text=Time%20on%20the%20Sea&text=The%20time%20it%20can%20take,between%2025%20and%2030%20days.

Siemens Star CCM+, 2020-A. *Deciding on a K-Omega Model*. [Online]
Available at: file:///C:/Program%20Files/Siemens/15.02.007-R8/STAR-CCM+15.02.007-R8/doc/en/online/index.html#page/STARCCMP%2FGUID-37CAC5A4-32E6-4C64-A934-DA52F9B3D063.html%23

Siemens Star CCM+, 2020-B. *K-Omega Model.* [Online]
Available at: file:///C:/Program%20Files/Siemens/15.02.007-R8/STAR-CCM+15.02.007-R8/doc/en/online/index.html#page/STARCCMP%2FGUID-F839E5D6-5A89-4A46-8E2A-239374565CB6.html%23

SIEMENS Star CCM+, 2020-C. *What is Planar Motion Carriage.* [Online]
Available at: file:///C:/Program%20Files/Siemens/15.02.007-R8/STAR-CCM+15.02.007-R8/doc/en/online/index.html#page/STARCCMP%2FGUID-5E85364B-6034-4649-835D-9A6BB7B86140.html

SIEMENS Star CCM+, 2020-D. *Donor search.* [Online]
Available at: file:///C:/Program%20Files/Siemens/15.02.007-R8/STAR-CCM+15.02.007-R8/doc/en/online/index.html#page/STARCCMP%2FGUID-EA52A744-93FD-4F99-B007-064BDFCAA8BF.html

SIEMENS Star CCM+, 2020-E. *Overset mesh reference.* [Online]
Available at: file:///C:/Program%20Files/Siemens/15.02.007-R8/STAR-CCM+15.02.007-R8/doc/en/online/index.html#page/STARCCMP%2FGUID-274B9B9C-54E6-4115-893B-C3AFA8D6F633.html

SIEMENS Star CCM+, 2020-F. *solution data interpolation.* [Online]
Available at: file:///C:/Program%20Files/Siemens/15.02.007-R8/STAR-CCM+15.02.007-

R8/doc/en/online/index.html#page/STARCCMP/GUID-232B553A-E01F-4EEF-9020-557A591A10D3.html#wwID0ESVARD

SIEMENS Star CCM+, 2021. *Body Force Propeller Method.* [Online]
Available at: file:///C:/Program%20Files/Siemens/15.02.007-R8/STAR-CCM+15.02.007-R8/doc/en/online/index.html#page/STARCCMP%2FGUID-20C2FE5D-4A56-441F-98CD-5D5179274F50.html%23

SIEMENS, 2020. *Simulation-driven ship design,* s.l.: Siemens.

SIMMAN, 2008. *Annoucements.* [Online]
Available at: http://www.simman2008.dk/announce.html

SIMMAN, 2014. *SIMMAN 2014.* [Online]
Available at: https://simman2014.dk/

Simonsen, C., Otzen, J., Joncquez, S. & Stern, F., 2013. EFD and CFD for KCS heaving and pitching in regular head waves. *Journal of Marine Science and Technology, 18 (4),* pp. 435-459.

Simonsen, C. et al., 2012. *Maneuvering predictions in the early design phase using CFD generated PMM data.* Gothenburg, s.n.

Simonsen, D., 2004. *PMM model test with DDG51 including uncertainty assessment,* Lyngby: FORCE Technology.

Srinivas, N., Krause, A., Kakade, S. & Seeger, M., 2012. Information-theoretic regret bounds for Gaussian process optimization in the bandit setting. *IEEE Transactions on Information Theory,,* pp. 3250-3265.

Stern, F. et al., 2011. Experience from SIMMAN 2008—The First Workshop on Verification and Validation of Ship Maneuvering Simulation Methods. *Journal of Ship Research, Vol. 55, No. 2,* pp. 135-147.

Stern, F., Wilson, R. & Shao, J., 2006. Quantitative V&V of CFD simulations and certification of CFD codes. *International Journal of Numerical Methods in Fluids, 50 ,* pp. 1335-1355.

Stern, F., Wilson, R. V., Coleman, H. & Paterson, E. G., 2001. Comprehensive approach to verification and validation of CFD simulations - Part 1: Methodology and procedures. *Jouranl of Fluids Engineering-Transcriptions of Asme,,* pp. 793-802.

Terziev, M. et al., 2018. Numerical investigation of the behaviour and performance of ships advancing through restricted shallow waters. *Journal of Fluids and Structures, 76,* p. 185–215.

Tezdogan, T., 2015. *Potential Flow and CFD-Based Hydrodynamic Analyses of Mono- and Multi-Hull Vessels,* Glasgow: s.n.

Tezdogan, T. et al., 2015. Full-scale unsteady RANS CFD simulations of ship behaviourand performance in head seas due to slow steaming. *Ocean Engineering,* pp. 186-206.

Tezdogan, T., Demirel, Y. K., Incecik, A. & Turan, O., 2014b. *Hydrodynamics of heaving twin cylinders in a free surface using an unsteady-RANS method.* Glasgow, s.n.

Tezdogan, T., Incecik, A. & Turan, O., 2014c. Operability assessment of high speed passenger ships based on human comfort criteria. *Ocean Engineering 89,* pp. 32-52.

Tezdogan, T., Incecik, A. & Turan, O., 2016. Full-scale unsteady RANS simulations of vertical ship motions in shallow water. *Ocean Engineering,* pp. 131-145..

The Maritime Executive, 2015. *Numerical Towing Tanks, a practical reality?.* [Online] Available at: https://www.maritime-executive.com/article/numerical-towing-tanks-a-practical-reality#:~:text=Used%20effectively%2C%20CFD%20simulation%20can,order%20to%20meet%20contractual%20obligations.

Torre, S., Burlando, M., Repetto, M. & Ruscelli, D., 2019. *Aerodynamic coefficients on moored ships.* , Beijing, China, s.n., pp. 1-6.

Toxopeu, S., Warlee, F. & Hallman, R., 2008. *Manoeuvring and Seakeeping Tests for 5415M,* Wageningen: MARIN.

United Nations, 2019. *Review of Maritime Transport.* s.l., UN.

University of Strathclyde, 2015. *Analysis of Far Offshore Accommodation.* [Online] Available at: http://www.esru.strath.ac.uk/EandE/Web_sites/14-15/Far_Offshore_Wind/our_work/our_work_files/pages/the_tool.html

Vantorre, M., 1999. *CAPTIVE MANOEUVRING TESTS WITH SHIP MODELS: A REVIEW OF ACTUAL PRACTICE, BASED ON THE 22ND ITTC MANOEUVRING COMMITTEE QUESTIONNAIRE* , Antwerp: s.n.

VPO, 2018. *Vessel performance optimisation: what do the experts say?*. [Online]
Available at: https://vpoglobal.com/2018/01/15/essel-performance-optimisation-experts-say/

Wang, J. & Wan, D., 2018. CFD Investigations of Ship Maneuvering in Waves Using naoe-FOAM-SJTU Solver. *Journal of Marine Science and Application* , pp. 443-458.

Wang, J. & Wan, D., 2020. CFD study of ship stopping maneuver by overset grid technique. *Ocean Engineering.*

Wartsila, 2021. *Ship resistance*. [Online]
Available at: https://www.wartsila.com/encyclopedia/term/ship-resistance

White, P. et al., 2019. *Predictions of Ship Turning Circle Maneuvers Using A Combined Computational Fluid Dynamics and Potential Flow Approach,* Ann Arbor: University of Michigan.

Woolliscroft, M. & Maki, K., 2016. A fast-running CFD formulation for unsteady ship maneuvering performance prediction. *Ocean Engineering*, pp. 154-162.

Y.H. Ozdemir, B. B. T. Y. S. B., 2014. Numerical and experimental study of turbulent free surface flow for a fast ship model. *Brodogradnja Volume 65 Issue 1*, pp. 39-54.

Yang, C. & Huang, F., 2015. Hydrodynamic optimization of a triswach. *Journal of Hydrodynamics*, pp. 856-864.

Yusoff, Y., Ngadiman, M. & Mohad Zain, A., 2011. Overview of NSGA-II optimising machining process parameters. *Advanced in control engineering and information science,* pp. 3978-3983.

Zhang, B., 2009. THE OPTIMIZATION OF THE HULL FORM WITH THE MINIMUM WAVE MAKING RESISTANCE BASED ON RANKINE SOURCE METHOD. *Journal of Hydrodynamics*, pp. 277-284.

Zhou, Y., Daamen, W., Vellinga, T. & Hoogendoorn, S., 2020. Impacts of wind and current on ship behavior in ports and waterways: A quantitative analysis based on AIS data. *Ocean Engieering.*